Numerical modelling of viscoelastic flows based on a log-conformation formulation

Laura Moreno Martínez

Ph.D. thesis in Structural Analysis

Universitat Politècnica de Catalunya
Departament d'Enginyeria Civil i Ambiental

Supervisors: Prof. Ramon Codina i Rovira
Prof. Joan Baiges Aznar

Barcelona, July 2021

A mis padres y a mi hermana.

Acknowledgements

Aquí es donde se supone que le tengo que dar las gracias a las personas que han sido importantes durante esta etapa de casi 5 años. Lo haré lo mejor que pueda e intentaré no enrollarme demasiado.

Así que, primero de todo tengo que darles las gracias a mis directores Ramon Codina y Joan Baiges por darme la oportunidad de trabajar con ellos y por haberme guiado todos estos años. He aprendido infinito con vosotros.

Por supuesto a todos con los que he compartido despacho 102. Empezando por Esther, que me hizo el primer tour por CIMNE y eso ya no se olvida, a Arnau, por ayudarme a dar los primeros pasos en FEMUSS, a Ernesto y a Alexis y sus breves visitas al despacho. Gracias también a Gabriel, porque hemos pasado juntos toda esta etapa. Espero que veles por la perpetuidad de nuestro proyecto fotográfico. A Domingo y a Irene, que aunque estuvieron muy poco tiempo, realmente animaron mucho el despacho 102. A Alejandro, Arnau y Zulkee, mucho ánimo con lo que os queda de tesis.

En especial, gracias a Ino y Samuel, porque realmente fueron compañeros de confinamiento (a distancia) y compartimos los sufrimientos y alegrías, pero sobre todo muchíiiiisimas horas de gmeet (bog-rfuk-hsr) mientras hacíamos los proyectos. Gracias por el apoyo que me habéis dado en todo. No hubiera sido lo mismo sin vosotros.

También gracias a Daniel y David por ser mis compañeros para comer durante la mayor parte de la tesis, porque en el zulo ese con las bombillas medio fundidas hemos compartido nuestros pesares, pero también las cosas que nos salían bien. Y también por nuestras excursiones. Sin vosotros tampoco hubiera sido lo mismo.

No puede faltar en los agradecimientos Pepe. Gracias por compartir estos años conmigo, con todos mis altibajos. Por estar ahí y apoyarme en todo. Se podría decir que la tesis la has sufrido casi tú más que yo.

Por supuesto, gracias a mis padres y a mi hermana porque han sido ese apoyo incondicional todo el tiempo, aunque fuera a distancia. Las horas y horas de teléfono y skype son una prueba de ello. Gracias por creer en mí más de lo que yo creo en mi misma. Si no hubiera sido por vosotros, probablemente jamás me hubiera animado a hacer una tesis doctoral.

Gracias también al resto de mi familia y en concreto a mis abuelos Juan Antonio, Fermina y Luisa, y a mi tía Mari Carmen.

A mis amigos de Barcelona por amenizar tan divinamente bien los fines de semana y endulzar así un poco más la vida: Isa, David, Maria, Isa, Rafa, Cris, Erika, Alba.

A mis amigas de Elda, en particular a Vero y María Salud, por seguir ahí, siguiendo mis peripecias y dándome aliento. A mis amigos de la carrera de matemáticas de la universidad de Alicante con los que aún tengo contacto. Y por último también a mis amigos del máster de Galicia: Marta, Daniel, Enric y Bea, porque siempre están aunque cada uno estemos en una punta del país.

Abstract

Viscoelastic fluids are a type of non-Newtonian fluids which are formed by complex internal structures and high-molecular-weight, whose typical examples are the polymer solutions and molten polymers. Also, the viscoleastic fluid flow presents a combination of two fluid properties: viscosity and elasticity. The main characteristic regarding the behavior of these flows is the strong dependence of the stresses on the flow history. Due to this complexity, computing the viscoelastic fluid flow involves a wide range of difficulties, in particular when elasticity becomes dominant, i.e., when the dimensionless Weissenberg number is high. These difficulties are considered one of the biggest challenges in computational rheology; this is known as the High Weissenberg Number Problem (HWNP).

This study presents different strategies to deal with the numerical shortcomings that appear when the viscoelastic fluid is particularly elastic. These strategies are carried out in the Finite Element (FE) framework and by using the Variational Multiscale (VMS) formulation as stabilization approach. A term-by-term is also design.

The cornerstone of this work is the application of a reformulation of the equations associated to the standard formulation, namely, the logarithmic reformulation, which permits simulating more elastic flows due to the fact that it eliminates the exponential stress profiles in the vicinity of stress singularities.

Another topic addressed in this work is the study of the effect of temperature in viscoelastic fluid flow, where a two-way strategy is considered: the viscoelastic properties have now a dependence with the temperature, and the energy equation takes into account has to consider the viscous dissipation. That study is particularly interesting due to the fact that non-isothermal flow in many industrial applications.

On the other hand, the incorporation of time-dependent subscales for solving the viscoelastic fluid flow problem is crucial to address two issues: the first one related with the instability produced when solving anisotropic space-time discretizations, and the second, the already mentioned exponential growth typical in viscoelastic flows with high Weissenberg number. In this work, time-dependent sub-grid scales are presented for both formulations: standard and logarithmic.

Finally, as the logarithmic formulation is particularly expensive, above all when the scheme considered is monolithic, a fractional step for this formulation is designed, in which the system of equations is defined in a fully decoupled manner. This algorithm is especially useful when purely elastic instabilities need to be captured. These instabilities lead in some cases to elastic turbulence: a physical phenomenon in which the fluid flow becomes chaotic even for low Reynolds numbers.

Resumen

Los fluidos viscoelásticos son un tipo específico de fluidos no Newtonianos formados por una estructura interna muy compleja con alto peso molecular. Los ejemplos típicos de este tipo de fluidos son las soluciones y líquidos poliméricos. Además, los fluidos viscoelásticos presentan la combinación de dos propiedades específicas de los fluidos: viscosidad y elasticidad. Sin embargo, la principal característica relacionada con el comportamiento para estos flujos es la dependencia de la tensiones a la historia del fluido. Debido a su estructura y la complejidad de su comportamiento, resolver el problema de flujo viscoelástico se convierte en algo bastande difícil de abordar, en particular cuando el flujo es elástico, o en otras palabras, cuando el número adimensional Weissenberg es alto. Afrontar estas dificultades se considerada uno de los mayores retos de la reología computacional, y es conocido como el Problema de Alto Número de Weissenberg (HWNP).

Este estudio presenta diferentes estrategias con el fin de evitar las dificultades numéricas que aparecen en estos casos, en que la componente elástica del fluido es muy dominante. Estas estrategias se abordan desde el marco de los Elementos Finitos cuyo método de estabilización será el de Subscalas Variacionales (VMS). Además, se diseña la estabilización término a término basada en estos métodos, que se aplicará a las formulaciones desarrolladas.

Sin embargo, la piedra angular de este trabajo es la aplicación de una reformulación de las ecuaciones que describen el flujo viscoelástico, llamada formulación logaritmica, y que permite la simulación de casos más elásticos debido a que, básicamente, elimina el crecimiento exponencial de las tensiones cerca de singularidades.

Otro tema que se trata en este trabajo es el efecto de la temperatura en los flujos viscoelásticos, donde se considerará un acople bidireccional con el problema térmico. Por un lado, ahora las propiedades del fluido dependen de la temperatura, y por otro, en la ecuación de energía tenemos que considerar la disipación viscosa como fuente térmica. Este estudio es interesante debido a que los fluidos viscoelásticos son sometidos a altas temperaturas en muchas aplicaciones industriales.

Por otra parte, también se explora la incorporación de subescalas dependientes del tiempo en el método de estabilización. Este cambio será crucial para paliar dos tipos de problemas: el primero relacionado con la inestabilidad que se produce cuando resolvemos discretizaciones anisotropicas espacio-tiempo, y la segunda para tratar con el mencionado crecimiento exponencial que aparece cuando los flujos viscoelásticos tienen alto número de Weissenberg. Esta estrategia se aplica tanto a la formulación estándar de las ecuaciones como a la logaritmica.

Finalmente, como la computación de la formulación logaritmica es cara computacionalmente, sobre todo cuando el esquema es de tipo monolítico, se ha diseñado un esquema de paso fraccionado en que el sistema de ecuaciones para esta formulación se desacopla. Este algoritmo resulta especialemnte útil para capturar inestabilidades púramente elásticas. Estas inestabilidades pueden desembocar en turbulencia elástica, que es un fenómeno

físico en que el flujo se vuelve caótico a pesar de contar con un bajo número de Reynolds.

Contents

List of Figures

List of Tables

List of Algorithms

List of Theorems

Chapter 1

Introduction

1.1 Motivation

Viscoelastic fluids are widely employed in a large variety of engineering, medical and natural science applications, such as safety devices capable of absorbing impacts (bulletproof vests, shoe insoles...), some plastics, blood pumps or micro pumps. Moreover, these fluids display distinct features to those shown by pure viscous fluids, for instance turbulent drag reduction [76] or elastic turbulence at low Reynolds number [78]. On the other hand, the production process of polymers is mostly non-isothermal in nature. Since flow properties are strongly dependent both upon rheology and temperature, it is of high interest to understand and make predictions of such type of flows. The combination of high viscosities of polymeric melts and high deformation rates results in the transformation of large amounts of mechanical energy into heat; and consequently in a rising of the material temperature. As remarked in [56], also, non-isothermal nonlinear flow is very relevant in many applications since it is the basis of many complex flow problems with viscoelastic and multiphase fluids. Air flow inside a combustion engine or polymer flow in an injection molding, or fluid flow in a heat exchange are only a few examples of viscous fluids where temperature is an important unknown.

Due to the increment of interest for these fluids and the notable relevance in the industry in recent years and also the particular properties of viscoelastic fluids, the study of numerical tools for the computation of this kind of flows is valuable both from the fundamental and the practical perspectives. This is therefore the motivation of the numerical and mathematical analysis of the governing equations.

Moreover, the computation of this flow leads to several difficulties both numerically and mathematically, above all when elasticity becomes dominant in the fluid. In fact, solving the viscoelastic fluid flow problem for high elasticity (or equivalently, when the dimensionless Weissenberg number is pronounced) is one of the biggest challenges in computational rheology since the 1970s. It is commonly called the *High Weissenberg Number Problem* (HWNP) [128]. It is defined as a numerical phenomenon that causes the iterative computations to breakdown for relatively low Weissenberg numbers, and normally it is expressed as a lack of convergence in the iterative method due to the hyperbolic nature of the differential constitutive equations. In literature some strategies are presented to deal with all these troubles, although the number of works addressing the HWNP is scarce even nowadays. That fact is also a motivation to apply cutting edge methodologies in the computation of the viscoelastic fluid flow and make new contributions in this field.

1.2   Overview

First of all, it is crucial to understand that a viscoelastic fluid - the fluid that will be considered along this work - is a specific type of non-Newtonian fluid. But, what is exactly a non-Newtonian fluid? In nature, most of the fluids can be modelled using the well-known Navier Stokes equations for Newtonian fluids, such as for example water or air. However, these equations are not capable of predicting the behaviour of all fluids, as occurs in the case of non-Newtonian fluids. In those cases, fluid does not follow the law of Newton of viscosity, which means that viscosity is dependent of stresses, and consequently a nonlinear constitutive law equation must be added to the classical Navier-Stokes equations. Also, viscosity can change the fluid behavior to a solid one under certain forces, due to its dependence on the rate of strain, apart from the state variables. Many salt solutions and molten polymers are non-Newtonian fluids, as are many commonly found substances such as honey, toothpaste, corn starch, paint, blood, melted butter or shampoo.

Particularly, viscoelastic fluids are a type of non-Newtonian fluids that mainly exhibits a combination of two main properties. The first one is the viscosity, which is related with the loss of memory, the irreversibility of the state of the fluid and the friction. The second one is the elasticity, which implies that the fluid has memory; this means that the state of stresses will depend of the deformation history. In addition, elasticity implies the production of internal energy storage.

The particular combination of properties is explained by the complex internal structure and high-molecular-weight that these fluids present, whose typical examples are polymer solutions and molten polymers. The main characteristic of polymeric fluids is the presence of macroscopic chains of molecules which will be stretched to out by the drag forces [144]. Moreover the natural tendency of the molecule to retract for this stretched configuration generates an elastic force which contributes to the macroscopic stress tensor. Therefore, whereas viscous materials resist shear flow and strain linearly with time when a stress is applied, elastic materials strain when stretched and immediately return to their original state once the stress is removed.

Also, remarkable effects are triggered by viscoelastic fluid flows when they are stirred, vibrated or given sudden external forces. An example of this is the well-known "rod climbing" effect which appears in some industrial processes [22].

Due to the observation of these effects, Poisson, Maxwell and Boltzman argued that that apart from the viscosity property, these fluids have an instantaneous elasticity. The elasticity "memorizes" all past states of stress. This time scale of all memorized stresses is called relaxation time [97]. In 1929, a constitutive law was written one by Jeffrey which considers both properties, and in 1950, Oldroyd [124] presented another one separating the retardation time from the viscous part and the relaxation time from the polymer part. Nowadays, this model is the simplest and one of the most popular in the literature, employed to test several benchmarks, methods, formulations, etc. In this work, this constitutive law will be the considered in general in all our computations. Giesekus, in 1982 proposed a generalization of the original model written by Jeffrey in which the constitutive equation has an additional nonlinear term [73]. In the literature, other constitutive models can be found, but all of them belong to the same family and present a similar structure, for example the UCM (Upper Convective Maxwell) [126], FENE (Finite Extensible Nonlinear Elastic) [142] and PTT models (Phan-Thien-Tanner) [134].

One of the first attempts to compute numerically a viscoelastic fluid flow in a planar contraction is the work of Crochet and Bezy [55], where problems were reported in the Galerkin formulation when the Weissenberg number increases, in other words, when the

elasticity becomes relevant.

In this sense, the finite element approximation of the flow of viscoelastic fluids presents many difficulties: on the one hand we have to deal with the problem associated to the Navier-Stokes equations, such as the treatment of the convective term or the compatibility of the velocity-pressure approximations. Now the constitutive equation is also highly nonlinear, with the own convective term that triggers a large number of instabilities. Also, even for smooth solutions, additional compatibility conditions must be considered velocity and stress interpolations to control velocity gradients.

In the case of Newtonian fluid flows, numerical instabilities occur when the Reynolds number (that measures the relation between convective and inertial forces) is high, and the solution creates *boundary layers* for problems where non-slip conditions are applied (for example in channels). In comparison, viscoelastic fluid flows create boundary layers due to the high value of the stresses. It is a direct consequence of the hyperbolic nature of the constitutive equation.

Therefore, the numerical computation of viscoelastic fluid flow is considered a challenging problem even for low Weissenberg numbers. When the Weissenberg number increases the number of difficulties make the problem almost unaffordable (that is the well-known *High Weissenberg Number Problem* previously mentioned). Some strategies have been used in the literature in order to increase the Weissenberg number of numerical simulations and, one of them is a reformulation of the equations proposed by Hulsen, Fattal and Kupferman [64, 65], known as the logarithm conformation reformulation. It basically consists in a change of variables to avoid the exponential growth of the stresses when the Weissenberg number is high. This idea will be employed and studied in this work.

1.3   Goals

The aim of this study is the design and development of new numerical schemes, formulations and techniques to solve viscoelastic fluid flows when the Weissenberg number is high, with the objective of simulating the purely elastic instability, as well as exploring thermal-coupling effects. These numerical schemes are all based on the Finite Element framework, and the stabilization technique employed is developed in the context of the Variational Multi-Scale (VMS) method, which allows the use of the same interpolation for the three-fields whose variables are velocity, pressure and stresses. In addition, this formulation is implemented in the in-house code FEMUSS, a High Performance Computing Environment (HPCE).

FEMUSS is an object-oriented finite element code developed in Fortran and able of solving three-dimensional fluid dynamics (incompressible and compressible), solid mechanics, fluid-structure interaction problems or coupled thermal problems among others, in a high performance environment. That allows to compute problems with a large number of elements and solving real problems. It uses PETSC [11], that is a suite of data routines for the scalable (parallel) solution of applications modeled by partial differential equations, including several solvers (iterative and direct type). Among its strengths are the thorough implementation of the generalized theory and the straightforward organization and accessibility of the code, which facilitates the introduction of new models and tools. Nevertheless, since FEMUSS is mostly research-oriented and in constant development, the implementation of new constitutive formulations requires additional changes and improvements to reach the goals of the work.

In order to compute viscoelastic fluid flow problems for high elasticity, we will apply the log-conformation reformulation mentioned previously. It is a reformulation of the

traditional constitutive equations of viscoelastic fluids, which eliminates the instability and linearizes the exponential stress profiles near the stress singularities. Therefore, the formulation seeks to treat the exponential growth of the elastic stresses, allowing to extend the range of Weissenberg numbers for which a numerical solution can be obtained. This reformulation is carried out through a change of variables in function of the conformation tensor which indicates the macromolecular configuration of the polymeric chains.

Thermal coupling with the viscoelastic fluid flow is also a relevant topic in many industrial processes. In comparison with Newtonian cases, now we will need to consider a dependence of temperature in the viscoelastic properties. On the other hand, the study of the effect of *viscous dissipation* will be particularly interesting, due to the fact that fluids reach higher temperatures caused by the internal work. This effect is displayed as a term in the energy equation which accounts for the mechanical part of the viscoelastic fluid that is transformed into heat, i.e., Joule's effect. To address the coupled problem we have to consider an iterative algorithm which updates the parameters needed at each time step, due to the four variables being strongly coupled.

Recent studies indicate that classical residual-based stabilized methods for unsteady incompressible flows may experience difficulties when the time step is small relative to the spatial grid size. These problems can happen, for instance, when small time steps result from the necessity of accuracy to solve transient problems due to the presence of non-linear terms in the differential equations, a very common issue in viscoelastic flow formulations. The approximations used in Variational Multiscale (VMS) methods usually neglect the time derivative of the sub-grid scales, consequently, anisotropic space-time discretizations cannot guarantee stability. We propose the design of stabilization techniques that allow one to compute time-dependent viscoelastic flow problems with high elasticity (or Weissenberg number) and with an anisotropic space-time discretization.

The flow patterns in viscoelastic fluids can be highly dynamic and in some cases chaotic, due to the elastic component of the fluid and the convective nature of the constitutive equation, even in quasi non-inertial flows, where non-linear rheological effects can manifest through the generation of large normal stresses which result in complex flow phenomena causing a *purely elastic instability*, and in some cases producing elastic instability. In our work, problems which exhibit the purely elastic instability phenomena have been studied, and different tools have been employed to obtain an accurate and efficient solution.

Finally, an important topic in numerical analysis is the study of stability and convergence of the applied methods, such a the logarithmic reformulation stabilized using subgrid scales. Due to the fact that a complete analysis of the non-linear problem requires more exhaustive and deep study, in this work we restrict ourselves to analyze the linearized problem.

In view of the above, the aim of this study is divided into the following objectives, each of which corresponds to a chapter in this dissertation:

- Development and implementation of the logarithmic reformulation for the viscoelastic fluid flow problem.

- Study of the thermal coupling, in particular putting the focus in the effect of viscous dissipation.

- Implementation of the dynamic sub-grid scales in order to simulate problems with a smaller time-step in relation with the mesh.

- Study of the purely elastic instabilities.

- Numerical analysis of stability and convergence of the developed methods.

The computational implementation and validation of the models require numerical improvements in areas of the code such as FE formulation, integration scheme, loading configurations and pre- and post-processor interfaces.

1.4 Outline

The work has been organized as follows:

Chapter 2 The *log-conformation reformulation* is applied to the standard viscoelastic fluid flow formulation with the aim of simulating flows with a higher Weissenberg number. However, a slightly different formulation is proposed to the log-conformation formulation in contrast with the original one, which is *non-singular* when the Weissenberg number is close to zero. Moreover different stabilization schemes are presented based on VMS: two residual based ones, and one of a term-by-term type. Some numerical examples demonstrate the benefits of the reformulation, validating solutions with benchmarks found in the literature.

Chapter 3 The thermal coupling with the viscoelastic fluid flow is implemented and studied using a split stabilization. Both formulations, the standard and the logarithmic one are used in this chapter. Temperature dependence of viscoelastic properties is established using two different models, and also viscous dissipation term is added to the energy equation. We explore the effects in the behavior of the temperature in viscoelastic fluids using two different benchmarks to validate the iterative scheme.

Chapter 4 In this chapter we design stabilization techniques that allow one to compute time-dependent viscoelastic flow problems with high elasticity (or Weissenberg number) and with an anisotropic space-time discretization. Yet, there is also an obvious link between the possibility to treat high Weissenberg numbers and the VMS method we propose, since small time steps are required in complex flow cases. Since the logarithmic formulation and the term-by-term formulation are independent, along this chapter both standard and logarithmic formulations are considered, compared and validated in some numerical examples. Moreover, the numerical analysis of the stability in the linearized problem is studied.

Chapter 5 Purely elastic instability is produced at relative low Reynolds number but for a high Weissenberg number. For studying this physical phenomenon, a fractional step scheme for the logarithmic formulation has been designed in order to save in computational cost. The stabilization considered in this scheme is term-by-term for the momentum equation, and also the time-dependent sub-grid scales are considered. The scheme is tested in different benchmarks, and finally employed to reproduce the purely elastic instability.

Chapter 6 In this chapter we analyze a linearization of the logarithmic reformulation of the problem. In order to be able to use the same interpolation for all the unknowns (velocity, pressure and logarithm of the conformation tensor), we employ a stabilized finite element formulation based on the VMS concept developed in previous chapters. The study of the linearized problem already serves to show why the logarithmic reformulation performs better than the standard one for high Weissenberg numbers; this is reflected in the stability and error estimates that we provide in this chapter.

Chapter 7 Finally, the achievements of this study are summed up, final conclusions are drawn and future work lines are outlined.

Note that a chapter in which the state of the art is reviewed is not included at the beginning of the work. The self-contained nature of each chapter lends to include specific literature reviews. Likewise, conclusions related to the specific content of each chapter are pointed out at the end of the same.

1.5   Research dissemination

The work included in this dissertation has resulted in the following scientific publications:

Chapter 2

Moreno L., Codina R., Baiges J. & Castillo E. (2019). Logarithmic conformation reformulation in viscoelastic flow problems approximated by a VMS-type stabilized finite element formulation. *Computer Methods in Applied Mechanics and Engineering*, 354, 706-731.

Chapter 3

Moreno L., Codina R. & Baiges J. (2021).Moreno, L., Codina, R., Baiges, J. (2021). Numerical simulation of non-isothermal viscoelastic fluid flows using a VMS stabilized finite element formulation. *Journal of Non-Newtonian Fluid Mechanics*, 104640.

Chapter 4

Moreno L., Codina R. & Baiges J. (2020). Solution of transient viscoelastic flow problems approximated by a term-by-term VMS stabilized finite element formulation using time-dependent subgrid-scales. *Computer Methods in Applied Mechanics and Engineering*, 367, 113074.

Codina R. & Moreno L. (2021). Stability Analysis of time dependent linearized viscoelastic flow problems using a stabilized finite element formulation in space. *ESAIM. Mathematical Modelling and Numerical Analysis*, Submitted.

Chapter 6

Codina R. & Moreno L. (2021). Analysis of a stabilized finite element approximation for a linearized logarithmic reformulation of the viscoelastic flow problem. *ESAIM. Mathematical Modelling and Numerical Analysis*, 55, 279.

Also part of the work, in particular some contents of Chapter 2 and Chapter 6 are included in the next publication:

Castillo E., Moreno L., Baiges J. & Codina R. (2021). Stabilised Variational Multi-Scale Finite Element Formulations for Viscoelastic Fluids. *Archives of Computational Methods in Engineering*, 1-33.

In addition, part of the work was presented at the following conferences:

Unpublished Conference Presentations

Moreno L., Codina R. & Baiges J. *Thermal coupling simulations with a viscoelastic fluid flow,* IX International Conference on Computational Methods for Coupled Problems in Science and Engineering. Virtual Congress. 14-16 June 2021.

Moreno L., Codina R. & Baiges J. *Solution of transient viscoelastic flow problems approximated by a VMS stabilized finite element formulation using time-dependent subrid-scales*, 14th World Congress on Computational Mechanics (WCCM) ECCOMAS Congress 2020, Virtual Congress, 11-15 January 2021.

Moreno L., Codina R. & Baiges J. *Simulation of non-isothermal viscoelastic fluid flow problem using a VMS stabilized Formulation*, VIII International Conference on Coupled Problems in Science and Engineering, Sitges (Barcelona), 3-5 June 2019.

Chapter 2

Logarithmic conformation reformulation

This chapter is based on the publication:

Moreno L., Codina R., Baiges J. & Castillo E. (2019). Logarithmic conformation reformulation in viscoelastic flow problems approximated by a VMS-type stabilized finite element formulation. *Computer Methods in Applied Mechanics and Engineering*, 354, 706-731.

2.1 Abstract

In this chapter, the log-conformation reformulation originally proposed by Fattal and Kupferman [64] is presented. This formulation allows computing incompressible viscoelastic problems with high Weissenberg numbers which are impossible to solve with the typical three-field formulation. By following this approach, in this work we develop a new stabilized finite element formulation based on the logarithmic reformulation using the Variational Multiscale (VMS) method as stabilization technique, together with a modified log-conformation formulation. Our approach follows the term-by-term stabilization proposed by Castillo and Codina [26] for the standard formulation, which is more effective when there are stress singularities. The formulation can be used when the relaxation parameter is set to zero, and permits a direct steady numerical resolution. The formulation is validated in the classical benchmark flow past a cylinder and in the well-known planar contraction 4:1, achieving very accurate, stable and mesh independent results for highly elastic fluids.

2.2 Background

The main characteristic about the behavior of viscoelastic materials is that stresses do not just depend on current deformation rates, but also on the deformation history. Due to this, time is a crucial element to take into account, because viscoelastic fluids have different responses depending on the time-scales of the deformation.

As it was explained in the Introduction (Chapter 1), computing the flow of these kind of fluids leads to several difficulties, in particular when elasticity becomes dominant, i.e. the dimensionless number known as *Weissenberg number* is high. This number is defined

as We $= \lambda u / L$, where λ is the characteristic relaxation time of the material u is the characteristic velocity of the flow, and L is the characteristic length of the domain. In some articles, another dimensionless number is used for flows with non-constant deformation rate, the *Deborah number*, De $= \lambda / t_c$ written in terms of the relaxation time and the time-scale of observation t_c. In [57] an extensive discussion is done about the suitable uses of each number.

These difficulties in numerically simulating high Weissenberg numbers flows are one of the biggest challenges in computational rheology, commonly named the *High Weissenberg Number Problem* (HWNP) [128]. It is understood as a numerical phenomenon that causes the iterative computations to breakdown for relatively low Weissenberg numbers. Normally, that is expressed as a lack of convergence in the iterative method due to the hyperbolic nature of the differential constitutive equations. The breakdown occurs for a critical value of the Weissenberg number, but it is specific to each particular problem, the spatial discretization and the numerical algorithm. The numerical instability is brought about by the failure of the proper balance of the deformation rate and the convection, and it was identified and discussed by Fattal and Kupferman [65]. It is a fundamental instability, present in all constitutive models and standard numerical methods. Nevertheless, it is demonstrated that constitutive methods can predict other instabilities of mathematical character [106, 108], referred to as *constitutive instabilities,* which can be classified in two: the Hadamard instability, associated with the non-linear fast response of constitutive equations, and the dissipative instability, related to the formulation of the dissipative behavior of viscoelastic models.

The source of the HWNP has thus been identified: on the one hand the loss of positive-definiteness of the conformation tensor, an internal variable which should be symmetric positive-definite to be physically admissible [64, 92]; on the other hand, the large stress gradients, regions with particular high deformation rate, or near stagnation points favor the breakdown of the numerical method, as explained in Fattal and Kupferman in [64, 65]. They describe the cause for this phenomena to be caused by the use of inapropriate approximations to represent the stress tensor, remarking the importance of preserving its positivity. By following these ideas, a new formulation was proposed by Fattal and Kupferman [64]: the log-conformation representation (denoted by LCR), a reformulation of the traditional equations of viscoelastic fluids, which eliminates the instability and linearizes the exponential stress profiles near the stress singularities. Therefore, the formulation seeks to treat the exponential growth of the elastic stresses, allowing to extend the range of Weissenberg numbers for which a numerical solution can be obtained.

However, alternative schemes have been proposed in other works. For example, Vaithianathan and Collins [160] presented two matrix decomposition schemes in order to construct the positive definite conformation tensor, employing the FENE-P model. Balci et al. [12] proposed a square root conformation representation. Afonso et al. [3], developed several matrix kernel-transformation families which can be applied to the conformation tensor equation. Nevertheless, although there are a variety of proposals to deal with the lack of positive-definiteness in the conformation tensor, the logarithm representation is the uniquely capable of linearizing the exponential stress profile.

Since the logarithmic formulation was presented, a great number of works have been written following this novel strategy, applying different methodologies and schemes, in finite volume and finite element (FE) codes. The next first work published applying the log-conformation reformulation is due to Hulsen et al. [93] using the DEVSS/DG formulation for the discretization and a first-order upwind scheme in a FE implementation. Later, Coronado et al. [53] proposed a "simple alternate" form of the log-conformation formulation

implemented in the DEVSS-TG/SUPG FE method, and in comparison with the previous work, fewer code modifications with respect to the standard formulation were required. An analysis between the two previous publications and two new implementations was presented by Kane et al. [98], remarking particularly the treatment of the advective term of the constitutive equation. The final conclusion is that all four formulations are very similar, except the one described by Coronado et al. [53], that is a little less robust due to the linear interpolation of the convective term. Damanik et al. [56] defined a fully coupled monolithic FE approach, using the edge-oriented FE stabilization for the convective term. Saramito [148] and Knechtges [101] recently derived fully implicit versions of the log-conformation formulation that do not involve an algebraic decomposition of the velocity gradient tensor, and which can be linearized and solved by the Newton-Raphson method. Afonso et al. [1, 2] investigated the performance of the log-conformation reformulation using the finite volume method framework in both works, although the second is more interesting because it seeks to predict the rich dynamical transitions in the 4:1 contraction planar benchmark, whereas the first one solves the flow around a cylinder, a problem without singularities. Comminal et al. [51, 52], simulated incompressible viscoelastic flows and the stream-log-conformation methodology, a combination between the log-conformation with the stream function flow formulation (see [103]) that is beneficial for the accuracy and stability of the numerical algorithm. One of the most recent publications belongs to Pimenta et al. [138], who increased the robustness and accuracy of the viscoelastic solver in OpenFoam, implementing there the log-conformation methodology.

Concerning this chapter, we propose a slightly different formulation to the log-conformation formulation. Our formulation is *non-singular* when the Weissenberg number is close to zero, while the original one proposed by Fattal and Kupferman [64] presents some problems because of the inverse of the relaxation time in the equations. The same idea was followed by Saramito [148]; both formulations can be reduced to the Navier-Stokes equations when the Weissenberg number is set to zero. Due to this, continuation methods can be successfully employed to get the optimal convergence in the validated problems. Also, we have to remark that the steady problem can be solved directly, while in most of the references the logarithmic formulation shows a strong time-dependency. As Saramito [148] pointed out, the reason can be that previous methods relied on some finite difference methods for computing the Jacobian matrix and strong non-linearities were considered non-differentiable (see, for example, [56]). Let us stress again the theoretical contribution presented in [148], where the main properties of the typical operators of the formulation are proved.

In this chapter, we apply the efficient logarithmic reformulation to solve the viscoelastic problem with the goal of simulating flows with a high Weissenberg number, using a stabilized formulation based on the Variational Multiscale (VMS) method. This stabilized formulation has its beginnings in the methods introduced by Hughes et al. [91] for the scalar convection-diffusion-reaction problem, and later extended to the Navier-Stokes problem by Codina [38, 40, 41], where the space of the sub-grid scales was taken as orthogonal to the FE space. This idea was adapted to the three-field Navier-Stokes problem in [25] and later to the viscoelastic flow problem in [26].

The mathematical analysis of the formulation can be found in [15, 29]. Other papers can be found concerning the VMS framework for viscoelastic regimes, such as [104, 105], where an Oldroyd-B fluid is considered. By following the same steps, the purpose of this chapter is the design of stabilized formulations which allow computing viscoelastic problems with a high Weissenberg number using the logarithmic reformulation, and testing them for numerical examples where both elastic stress gradients and numerical singularities

are the main features. This chapter is organized as follows: Section 2.3 explains in detail the log-conformation reformulation and the modifications considered; later we report the steps to obtain the strong formulation, the variational equations and consequently the Galerkin FE discretization. Once the main equations are defined, Section 2.4 presents the stabilized FE approach based on the VMS approach; the linearization of the problem is also extensively discussed.

As for the numerical results, they are presented in Section 2.5. First, in Section 2.5.1, a study of the h convergence of the formulations is described for a stationary Oldroyd-B flow, where a manufactured solution is considered. Secondly, in Section 2.5.2, the flow past a cylinder is tested for an Oldroyd-B fluid, comparing the solution obtained for Weissenberg numbers 0.6, 0.7 and 0.9 with other published solutions. The drag force on the cylinder is also contrasted for higher Weissenberg numbers. Then, the well-known 4:1 planar contraction benchmark is elaborated in Section 2.5.3. It is studied for two different Reynolds number values. Finally, we present a three dimensional example in Section 2.5.4, with the aim of showing that the formulation works well in 3D cases. Conclusions are drawn in the last section of the chapter, Section 2.6.

2.3   The modified log-conformation formulation problem

2.3.1   Standard formulation for the viscoelastic flow problem

Let us start presenting the standard equations associated to the viscoelastic flow problem. Let us consider a viscoelastic fluid moving in a domain Ω of $\mathbb{R}^d$ (d=2 or 3) during the time interval $[0, T]$ and let $\partial\Omega$ be the boundary. Assuming the flow to be incompressible and isothermal, the governing equations are the conservation of momentum and mass, which can be expressed as follows:

$$\rho\frac{\partial \boldsymbol{u}}{\partial t} + \rho\boldsymbol{u}\cdot\nabla\boldsymbol{u} - \nabla\cdot\boldsymbol{T} + \nabla p = \boldsymbol{f} \text{ in } \Omega, t \in (0, T), \tag{2.1}$$

$$\nabla\cdot\boldsymbol{u} = 0 \text{ in } \Omega, t \in (0, T), \tag{2.2}$$

where ρ denotes the constant density, $p : \Omega \times (0, T) \to \mathbb{R}$ is the pressure field, $\boldsymbol{u} : \Omega \times (0, T) \to \mathbb{R}^d$ is the velocity field, $\boldsymbol{f} : \Omega \times (0, T) \to \mathbb{R}^d$ is the force field and $\boldsymbol{T} : \Omega \times (0, T) \to \mathbb{R}^d \otimes \mathbb{R}^d$ is the deviatoric extra stress tensor. In general, $\boldsymbol{T}$ is defined in terms of a viscous and a viscoelastic contribution as

$$\boldsymbol{T} = 2\eta_s\nabla^s\boldsymbol{u} + \boldsymbol{\sigma},$$

where η_s represents the effective viscosity (or solvent viscosity), $\nabla^s\boldsymbol{u}$ is the symmetrical part of the velocity gradient and $\boldsymbol{\sigma}$ is the viscoelastic or the elastic stress tensor.

Finally, the constitutive equation for the viscoelastic stress tensor must be defined to close the problem. Even if there is a wide range of different models, we consider the Oldroyd-B model in this work, which is the model of a Newtonian stress supplemented with an extra-stress that satisfies the upper-convected Maxwell equation, and it reads as

$$\frac{1}{2\eta_p}\boldsymbol{\sigma} - \nabla^s\boldsymbol{u} + \frac{\lambda}{2\eta_p}\left(\frac{\partial \boldsymbol{\sigma}}{\partial t} + \boldsymbol{u}\cdot\nabla\boldsymbol{\sigma} - \boldsymbol{\sigma}\cdot\nabla\boldsymbol{u} - (\nabla\boldsymbol{u})^T\cdot\boldsymbol{\sigma}\right) = \boldsymbol{0}, \text{ in } \Omega, t \in (0, T), \tag{2.3}$$

where λ is the relaxation time and η_p represents the polymeric viscosity. Each term of the equation has a particular meaning: $\nabla^s\boldsymbol{u}$ is the source, $\frac{\lambda}{2\eta_p}\boldsymbol{u}\cdot\nabla\boldsymbol{\sigma}$ represents the convective term and $\frac{\lambda}{2\eta_p}\left(\boldsymbol{\sigma}\cdot\nabla\boldsymbol{u} + (\nabla\boldsymbol{u}^T)\cdot\boldsymbol{\sigma}\right)$ are the rotational terms. Note that from this point

we write the polymeric and the effective viscosity in function of the total viscosity η_0. For that, an additional parameter $\beta \in [0, 1]$ is introduced, so that $\eta_s = \beta\eta_0$ and $\eta_p = (1-\beta)\eta_0$.

Calling $\boldsymbol{U} = [\boldsymbol{u}, p, \boldsymbol{\sigma}]$, $\boldsymbol{F}_{\text{std}} = [\boldsymbol{f}, 0, \boldsymbol{0}]$ and defining

$$\mathcal{D}_{\text{std}}(\boldsymbol{U}) := \begin{pmatrix} \rho\dfrac{\partial\boldsymbol{u}}{\partial t} \\ 0 \\ \dfrac{\lambda}{2\eta_p}\dfrac{\partial\boldsymbol{\sigma}}{\partial t} \end{pmatrix},$$

$$\mathcal{L}_{\text{std}}(\hat{\boldsymbol{u}}; \boldsymbol{U}) := \begin{pmatrix} -\nabla\cdot\boldsymbol{\sigma} - 2\eta_s\nabla\cdot(\nabla^s\boldsymbol{u}) + \rho\hat{\boldsymbol{u}}\cdot\nabla\boldsymbol{u} + \nabla p \\ \nabla\cdot\boldsymbol{u} \\ \dfrac{1}{2\eta_p}\boldsymbol{\sigma} - \nabla^s\boldsymbol{u} + \dfrac{\lambda}{2\eta_p}\left(\hat{\boldsymbol{u}}\cdot\nabla\boldsymbol{\sigma} - \boldsymbol{\sigma}\cdot\nabla\hat{\boldsymbol{u}} - (\nabla\hat{\boldsymbol{u}})^T\cdot\boldsymbol{\sigma}\right) \end{pmatrix}, \qquad (2.4)$$

we may write (2.1), (2.2) and (2.3), considering $D_t = D_{\text{std}}$, $\mathcal{L} = \mathcal{L}_{\text{std}}$ and $\boldsymbol{F} = \boldsymbol{F}_{\text{std}}$, as

$$\mathcal{D}_t(\boldsymbol{U}) + \mathcal{L}(\boldsymbol{u}; \boldsymbol{U}) = \boldsymbol{F}. \qquad (2.5)$$

2.3.2 The log-conformation reformulation

Departing from the standard formulation, the logarithmic reformulation will be exposed, and later applied to the standard equations. This model has an interpretation in terms of statistical mechanics, which involves a statistical average of dyadic vector products. First, the *conformation tensor* is defined, taking into account that it must, by definition, be symmetric and positive-definite to be physically-admissible, because this internal variable represents the macromolecular configuration of the polymer chains. It is defined as

$$\boldsymbol{\tau} = \frac{\lambda\boldsymbol{\sigma}}{\eta_p} + \boldsymbol{I}.$$

Consequently, the stress tensor can be expressed as a function of the conformation tensor as $\boldsymbol{\sigma} = \dfrac{\eta_p}{\lambda}(\boldsymbol{\tau} - \boldsymbol{I})$. Then, replacing $\boldsymbol{\sigma}$ in the constitutive equation (2.3) with $\boldsymbol{\tau}$, we can rewrite the Oldroyd-B model in terms of the conformation tensor $\boldsymbol{\tau}$ as

$$\frac{1}{2\lambda}(\boldsymbol{\tau} - \boldsymbol{I}) - \nabla^s\boldsymbol{u} + \frac{1}{2}\left(\frac{\partial\boldsymbol{\tau}}{\partial t} + \boldsymbol{u}\cdot\nabla\boldsymbol{\tau} - \boldsymbol{\tau}\cdot\nabla\boldsymbol{u} - (\nabla\boldsymbol{u})^T\cdot\boldsymbol{\tau}\right) = \boldsymbol{0}. \qquad (2.6)$$

However, in the chapter, we have considered a modification when the conformation tensor is defined, with the aim of allowing $\lambda = 0$, i.e., the Newtonian behavior. To this end, we introduce the relaxation-time parameter $\lambda_0(\lambda)$ linearly dependent with λ, which could be defined as $\lambda_0 = \max\{k\lambda, \lambda_{0,\min}\}$, k being a constant and $\lambda_{0,\min}$ a given threshold. So, if $k = 1$ and $\lambda_{0,\min} = 0$, the original change of variables proposed by Fattal and Kupferman [64] is recovered; however, if k is taken equal to zero, then the three-field Navier-Stokes problem for Newtonian fluids is obtained. It is worth to remark that in the numerical experiments we have found useful to take k small, so that $\lambda_0 < \lambda$; this has allowed us to obtain converged solutions that we have not been able to get for $k = 1$.

Thus, we define

$$\boldsymbol{\tau} = \frac{\lambda_0(\lambda)\boldsymbol{\sigma}}{\eta_p} + \boldsymbol{I}.$$

From this point we use λ_0 instead of $\lambda_0(\lambda)$ to simplify the notation. The constitutive equation (2.3) can be rewritten by following the proposed modification as

$$\frac{1}{2\lambda_0}(\boldsymbol{\tau} - \boldsymbol{I}) - \nabla^s\boldsymbol{u} + \frac{\lambda}{2\lambda_0}\left(\frac{\partial\boldsymbol{\tau}}{\partial t} + \boldsymbol{u}\cdot\nabla\boldsymbol{\tau} - \boldsymbol{\tau}\cdot\nabla\boldsymbol{u} - (\nabla\boldsymbol{u})^T\cdot\boldsymbol{\tau} + 2\nabla^s\boldsymbol{u}\right) = \boldsymbol{0}. \qquad (2.7)$$

The log-conformation reformulation basically consists of a change of variables in terms of the matrix-logarithm of the conformation tensor, that is to say, the conformation tensor is replaced by a new variable $\boldsymbol{\psi} = \log(\boldsymbol{\tau})$. This can be calculated through eigenvalue computation that rotates the $\boldsymbol{\tau}$ tensor into its main principle axes and can be expressed as $\boldsymbol{\psi} = \boldsymbol{R}\log(\boldsymbol{\Lambda})\boldsymbol{R}^T$ because $\boldsymbol{\tau}$ is a symmetric positive definite tensor (for $k \leq 1$) and therefore it can always be diagonalized. In the expression introduced, $\boldsymbol{\Lambda}$ is a diagonal matrix with the eigenvalues of $\boldsymbol{\tau}$, and $\boldsymbol{R}$ is the orthogonal matrix of the eigenvectors of $\boldsymbol{\tau}$.

To sum up, in order to obtain the new formulation the stress tensor must be replaced by $\boldsymbol{\sigma} = \dfrac{\eta_p}{\lambda_0}(\boldsymbol{\tau} - \boldsymbol{I})$, and in turn, the conformation tensor $\boldsymbol{\tau}$ must be written as $\boldsymbol{\tau} = \exp(\boldsymbol{\psi})$ in the standard viscoelastic formulation detailed above, (2.1), (2.2) and (2.3). The new equations of the log-conformation formulation are now expressed as follows:

$$\rho\frac{\partial\boldsymbol{u}}{\partial t} - \frac{\eta_p}{\lambda_0}\nabla\cdot\exp(\boldsymbol{\psi}) - 2\eta_s\nabla\cdot(\nabla^{\mathrm{s}}\boldsymbol{u}) + \rho\boldsymbol{u}\cdot\nabla\boldsymbol{u} + \nabla p = \boldsymbol{f}, \tag{2.8}$$

$$\nabla\cdot\boldsymbol{u} = 0, \tag{2.9}$$

$$\frac{1}{2\lambda_0}(\exp(\boldsymbol{\psi}) - \boldsymbol{I}) - \nabla^{\mathrm{s}}\boldsymbol{u} + \frac{\lambda}{2\lambda_0}\Big(\frac{\partial\exp(\boldsymbol{\psi})}{\partial t} + \boldsymbol{u}\cdot\nabla\exp(\boldsymbol{\psi})$$
$$- \exp(\boldsymbol{\psi})\cdot\nabla\boldsymbol{u} - (\nabla\boldsymbol{u})^T\cdot\exp(\boldsymbol{\psi}) + 2\nabla^{\mathrm{s}}\boldsymbol{u}\Big) = \boldsymbol{0}, \tag{2.10}$$

where the unknowns are the velocity, the pressure, and tensor $\boldsymbol{\psi}$, which depends directly on the viscoelastic stress tensor $\boldsymbol{\sigma}$.

This logarithm reformulation employed reminds of the formulation used by Coronado et al. in [53], although there the conformation tensor was simply replaced by $\exp(\boldsymbol{\psi})$. Another change was introduced in [53] with respect to the original log-conformation reformulation: the decomposition of the gradient of the velocity into three different tensors. However, this has not been taken into account in our formulation. In this sense, the modified log-conformation formulation proposed by Saramito [148] is very similar to our formulation.

Let us introduce some notation, useful in the next subsections. Calling now $\boldsymbol{U} = [\boldsymbol{u}, p, \boldsymbol{\psi}]$ and $\boldsymbol{F}_{\mathrm{log}} = [\boldsymbol{f}, 0, \frac{1}{2\lambda_0}\boldsymbol{I}]$ and defining

$$\mathcal{D}_{\mathrm{log}}(\boldsymbol{U}) := \begin{pmatrix} \rho\dfrac{\partial\boldsymbol{u}}{\partial t} \\ 0 \\ \dfrac{\lambda}{2\lambda_0}\dfrac{\partial\exp(\boldsymbol{\psi})}{\partial t} \end{pmatrix}, \tag{2.11}$$

$$\mathcal{L}_{\mathrm{log}}(\hat{\boldsymbol{u}}; \boldsymbol{U}) := \begin{pmatrix} -\dfrac{\eta_p}{\lambda_0}\nabla\cdot(\exp(\boldsymbol{\psi})) - 2\eta_s\nabla\cdot(\nabla^s\boldsymbol{u}) + \rho\hat{\boldsymbol{u}}\cdot\nabla\boldsymbol{u} + \nabla p \\ \nabla\cdot\boldsymbol{u} \\ \dfrac{1}{2\lambda_0}\exp(\boldsymbol{\psi}) - \nabla^s\boldsymbol{u} + \dfrac{\lambda}{2\lambda_0}(\hat{\boldsymbol{u}}\cdot\nabla(\exp(\boldsymbol{\psi}))) \\ -\exp(\boldsymbol{\psi})\cdot\nabla\hat{\boldsymbol{u}} - (\nabla\hat{\boldsymbol{u}})^T\cdot\exp(\boldsymbol{\psi}) + 2\nabla^s\boldsymbol{u} \end{pmatrix}, \tag{2.12}$$

we may write (2.8)-(2.10) as

$$\mathcal{D}_t(\boldsymbol{U}) + \mathcal{L}(\boldsymbol{u}; \boldsymbol{U}) = \boldsymbol{F}, \tag{2.13}$$

considering $\mathcal{D}_t = \mathcal{D}_{\mathrm{log}}$, $\mathcal{L} = \mathcal{L}_{\mathrm{log}}$ and $\boldsymbol{F} = \boldsymbol{F}_{\mathrm{log}}$. The notation $\hat{\boldsymbol{u}}$ in (2.12) is used to distinguish the different arguments in which the velocity appears. These equations need to be complemented with initial and boundary conditions to close the problem. For the sake of simplicity, in the exposition we only consider the simplest boundary condition

$\boldsymbol{u} = \boldsymbol{0}$ on $\partial\Omega$ for all time. Boundary conditions for the $\boldsymbol{\psi}$ tensor will be similar to those for the elastic stresses $\boldsymbol{\sigma}$ in the standard formulation: they do not need to be prescribed, but imposing them can suppose a significant computational save. We will indicate in our examples where the boundary condition are prescribed.

The problem is completely defined by the initial conditions for the velocity and the new variable $\boldsymbol{\psi}$, which are denoted by $\boldsymbol{u} = \boldsymbol{u}^0$, and $\boldsymbol{\psi} = \boldsymbol{\psi}^0$ at time $t = 0$, with $\boldsymbol{u}^0$ and $\boldsymbol{\psi}^0$ functions defined on the whole domain Ω.

2.3.3   Variational formulation

In order to write the weak form of the problem, let us introduce some notation. The space of square integrable functions in a domain ω is denoted by $L^2(\omega)$, and the space of functions whose distributional derivatives of order up to $m \geq 0$ (integer) belong to $L^2(\omega)$ is denoted by $H^m(\omega)$.

The space $H_0^1(\omega)$ is made up of functions in $H^1(\omega)$ vanishing on $\partial\omega$. The topological dual of $H_0^1(\omega)$ is denoted by $H^{-1}(\Omega)$, the duality pairing being $\langle \cdot, \cdot \rangle$. The L^2 inner product in ω (for scalars, vectors and tensors) is denoted by $(\cdot, \cdot)_\omega$ and the integral over ω of the product of two general functions is written as $\langle \cdot, \cdot \rangle_\omega$, the subscript being omitted when $\omega = \Omega$. The norm in a space X is denoted by $\| \cdot \|_X$, except in the case $X = L^2(\Omega)$, case in which the subscript is omitted.

Using this notation, velocity and pressure FE spaces for the continuous problem are $\boldsymbol{V}_0 = H_0^1(\Omega)^d$ and $\mathcal{Q} = L^2(\Omega)/\mathbb{R}$, and the space for the tensor $\boldsymbol{\psi}$ is denoted by $\boldsymbol{\Upsilon}$ for each fixed time t, where an appropriate regularity is assumed. The weak form of the problem consists in finding $\boldsymbol{U} = [\boldsymbol{u}, p, \boldsymbol{\psi}] : (0, T) \longrightarrow \boldsymbol{\mathcal{X}} := \boldsymbol{V}_0 \times \boldsymbol{Q} \times \boldsymbol{\Upsilon}$, such that the initial conditions are satisfied and:

$$\left(\rho \frac{\partial \boldsymbol{u}}{\partial t}, \boldsymbol{v} \right) + \frac{\eta_p}{\lambda_0}(\exp(\boldsymbol{\psi}), \nabla^s \boldsymbol{v}) + 2(\eta_s \nabla^s \boldsymbol{u}, \nabla^s \boldsymbol{v})$$

$$+ \langle \rho \boldsymbol{u} \cdot \nabla \boldsymbol{u}, \boldsymbol{v} \rangle - (p, \nabla \cdot \boldsymbol{v}) = \langle \boldsymbol{f}, \boldsymbol{v} \rangle, \tag{2.14}$$

$$(q, \nabla \cdot \boldsymbol{u}) = 0, \tag{2.15}$$

$$\left(\frac{1}{2\lambda_0} \exp(\boldsymbol{\psi}) - \nabla^s \boldsymbol{u}, \boldsymbol{\chi} \right) + \frac{\lambda}{2\lambda_0} \left(\frac{\partial \exp(\boldsymbol{\psi})}{\partial t}, \boldsymbol{\chi} \right)$$

$$+ \frac{\lambda}{2\lambda_0} (\boldsymbol{u} \cdot \nabla \exp(\boldsymbol{\psi}) - \exp(\boldsymbol{\psi}) \cdot \nabla \boldsymbol{u}, \boldsymbol{\chi})$$

$$+ \frac{\lambda}{2\lambda_0} \left(-(\nabla \boldsymbol{u})^T \cdot \exp(\boldsymbol{\psi}) + 2\nabla^s \boldsymbol{u}, \boldsymbol{\chi} \right) = \frac{1}{2\lambda_0} \langle \boldsymbol{I}, \boldsymbol{\chi} \rangle, \tag{2.16}$$

for all $\boldsymbol{V} = [\boldsymbol{v}, q, \boldsymbol{\chi}] \in \boldsymbol{\mathcal{X}}$, where it is assumed that $\boldsymbol{f}$ is such that $\langle \boldsymbol{f}, \boldsymbol{v} \rangle$ is well defined. In compact form, the problem can be written as:

$$(\mathcal{D}_t(\boldsymbol{U}), \boldsymbol{V}) + B(\boldsymbol{u}; \boldsymbol{U}, \boldsymbol{V}) = L(\boldsymbol{V}), \tag{2.17}$$

where

$$(\mathcal{D}_t(\boldsymbol{U}), \boldsymbol{V}) = \left(\rho \frac{\partial \boldsymbol{u}}{\partial t}, \boldsymbol{v} \right) + \frac{\lambda}{2\lambda_0} \left(\frac{\partial \exp(\boldsymbol{\psi})}{\partial t}, \boldsymbol{\chi} \right), \tag{2.18}$$

$$B(\hat{\boldsymbol{u}}; \boldsymbol{U}, \boldsymbol{V}) = \frac{\eta_p}{\lambda_0}(\exp(\boldsymbol{\psi}), \nabla^s \boldsymbol{v}) + 2(\eta_s \nabla^s \boldsymbol{u}, \nabla^s \boldsymbol{v}) + \langle \rho \hat{\boldsymbol{u}} \cdot \nabla \boldsymbol{u}, \boldsymbol{v} \rangle$$

$$- (p, \nabla \cdot \boldsymbol{v}) + (\nabla \cdot \boldsymbol{u}, q) + \frac{1}{2\lambda_0}(\exp(\boldsymbol{\psi}), \boldsymbol{\chi}) - (\nabla^s \boldsymbol{u}, \boldsymbol{\chi})$$

$$+ \frac{\lambda}{2\lambda_0} \left(\hat{\boldsymbol{u}} \cdot \nabla \exp(\boldsymbol{\psi}) - \exp(\boldsymbol{\psi}) \cdot \nabla \hat{\boldsymbol{u}} - (\nabla \hat{\boldsymbol{u}})^T \cdot \exp(\boldsymbol{\psi}) + 2\nabla^{\mathrm{s}}\boldsymbol{u}, \boldsymbol{\chi} \right). \quad (2.19)$$

$$L(\boldsymbol{V}) = \langle \boldsymbol{f}, \boldsymbol{v} \rangle + \frac{1}{2\lambda_0} \langle \boldsymbol{I}, \boldsymbol{\chi} \rangle. \quad (2.20)$$

Note that the test function $\boldsymbol{\chi}$ is, from the physical point of view, a stress, whereas $\boldsymbol{\psi}$ is the logarithm of the conformation tensor (and thus, dimensionless). We could also have used a test function for the constitutive equation of the form $\frac{\eta_p}{\lambda_0} \exp(\boldsymbol{\chi})$, where now $\boldsymbol{\chi}$ would be dimensionless. This would simplify the analysis (some stability would follow taking $\boldsymbol{\chi} = \boldsymbol{\psi}$), but complicate significantly the finite element approximations described below.

2.3.4   Linearization of the exponential

Apart from the typical non-linearities associated with the standard viscoelastic problem such as convective or stretching terms, now we have to consider how to process the exponential function of the tensor $\boldsymbol{\psi}$. It has been treated as follows:

$$\exp(\boldsymbol{\psi}) = \exp(\hat{\boldsymbol{\psi}} + \delta\boldsymbol{\psi}) = \exp(\hat{\boldsymbol{\psi}}) \cdot \exp(\delta\boldsymbol{\psi}),$$

where $\delta\boldsymbol{\psi} = \boldsymbol{\psi} - \hat{\boldsymbol{\psi}}$ is considered as the incremental part and $\hat{\boldsymbol{\psi}}$ is a known tensor, which will be calculated at the previous iteration in the linearization scheme. The term $\exp(\delta\boldsymbol{\psi})$ has been linearized in turn through a Taylor expansion with a truncation error of order $(\delta\boldsymbol{\psi})^2$. Therefore the approximation is defined as

$$\exp(\delta\boldsymbol{\psi}) \approx \boldsymbol{I} + \delta\boldsymbol{\psi}.$$

Consequently,

$$\exp(\boldsymbol{\psi}) \approx \exp(\hat{\boldsymbol{\psi}}) \cdot (\boldsymbol{I} + \delta\boldsymbol{\psi}) = \exp(\hat{\boldsymbol{\psi}}) \cdot \boldsymbol{\psi} + \exp(\hat{\boldsymbol{\psi}}) \cdot (\boldsymbol{I} - \hat{\boldsymbol{\psi}}). \quad (2.21)$$

So, inserting the approximation into the system (2.8) - (2.10), the system is linearized around $\hat{\boldsymbol{\psi}}$ as follows

$$\rho \frac{\partial \boldsymbol{u}}{\partial t} - \frac{\eta_p}{\lambda_0} \nabla \cdot (\exp(\hat{\boldsymbol{\psi}}) \cdot \boldsymbol{\psi}) - 2\eta_s \nabla \cdot (\nabla^s \boldsymbol{u}) + \rho \boldsymbol{u} \cdot \nabla \boldsymbol{u} + \nabla p$$

$$= \boldsymbol{f} + \frac{\eta_p}{\lambda_0} \nabla \cdot (-\exp(\hat{\boldsymbol{\psi}}) \cdot \hat{\boldsymbol{\psi}} + \exp(\hat{\boldsymbol{\psi}})), \quad (2.22)$$

$$\nabla \cdot \boldsymbol{u} = 0, \quad (2.23)$$

$$\frac{1}{2\lambda_0} \exp(\hat{\boldsymbol{\psi}}) \cdot \boldsymbol{\psi} - \nabla^s \boldsymbol{u} + \frac{\lambda}{2\lambda_0} \Big(\frac{\partial(\exp(\hat{\boldsymbol{\psi}}) \cdot \boldsymbol{\psi})}{\partial t} + 2\nabla^s \boldsymbol{u}$$

$$+ \boldsymbol{u} \cdot \nabla \Big(\exp(\hat{\boldsymbol{\psi}}) \cdot \boldsymbol{\psi} - \exp(\hat{\boldsymbol{\psi}}) \cdot \hat{\boldsymbol{\psi}} + \exp(\hat{\boldsymbol{\psi}}) \Big)$$

$$- \Big(\exp(\hat{\boldsymbol{\psi}}) \cdot \boldsymbol{\psi} - \exp(\hat{\boldsymbol{\psi}}) \cdot \hat{\boldsymbol{\psi}} + \exp(\hat{\boldsymbol{\psi}}) \Big) \cdot \nabla \boldsymbol{u}$$

$$- (\nabla \boldsymbol{u})^T \cdot \Big(\exp(\hat{\boldsymbol{\psi}}) \cdot \boldsymbol{\psi} - \exp(\hat{\boldsymbol{\psi}}) \cdot \hat{\boldsymbol{\psi}} + \exp(\hat{\boldsymbol{\psi}}) \Big) \Big)$$

$$= \frac{1}{2\lambda_0} (\boldsymbol{I} - \exp(\hat{\boldsymbol{\psi}}) + \exp(\hat{\boldsymbol{\psi}}) \cdot \hat{\boldsymbol{\psi}}) + \frac{\lambda}{2\lambda_0} \left(\frac{\partial(\exp(\hat{\boldsymbol{\psi}}) \cdot \hat{\boldsymbol{\psi}})}{\partial t} - \frac{\partial \exp(\hat{\boldsymbol{\psi}})}{\partial t} \right). \quad (2.24)$$

The variational formulation of this problem is straightforward.

2.3.5 Galerkin finite element discretization

The standard Galerkin approximation for the variational problem, which has been established in (2.17), is described next. Let $\mathcal{T}_h = \{K\}$ be a FE partition of the domain Ω. The diameter of an element $K \in \mathcal{T}_h$ is denoted by h_K and the diameter of the partition is defined as $h = \max\{h_K | K \in \mathcal{T}_h\}$. From $\mathcal{T}_h$ we may construct conforming FE spaces for the velocity, the pressure and the elastic stress, $\boldsymbol{\mathcal{V}}_h \subset \boldsymbol{\mathcal{V}}$, $\mathcal{Q}_h \subset \mathcal{Q}$, $\boldsymbol{\Upsilon}_h \subset \boldsymbol{\Upsilon}$, respectively. Calling $\boldsymbol{\mathcal{X}}_h := \boldsymbol{\mathcal{V}}_h \times \mathcal{Q}_h \times \boldsymbol{\Upsilon}_h$, the Galerkin FE approximation of the problem consists in finding $\boldsymbol{U}_h : (0, T) \longrightarrow \boldsymbol{\mathcal{X}}_h$, such that:

$$(\mathcal{D}_t(\boldsymbol{U}_h), \boldsymbol{V}_h) + B(\boldsymbol{u}_h; \boldsymbol{U}_h, \boldsymbol{V}_h) = L(\boldsymbol{V}_h),$$

for all $\boldsymbol{V}_h = [\boldsymbol{v}_h, q_h, \boldsymbol{\chi}_h] \in \boldsymbol{\mathcal{X}}_h$, and satisfying the appropriate initial conditions.

2.3.6 Monolithic time discretization

For the time discretization, we have used a monolithic approach, although it would also be possible to employ a fractional step technique, as in [27]. There are a lot of possibilities for the discretization in time, but we will restrict ourselves to the classical backward difference (BDF) approximations.

Consider a partition of the interval $[0, T]$ into m subintervals of constant size δt, and let $f(t)$ be a generic time-dependent function. We will denote as f^n the approximation to $f(t^n)$, with $t^n = n\delta t$, $n = 0, 1, 2, \ldots, m$. A BDF approximation to the time derivative of the function f order $k = 1, 2, \ldots$, is given by $\frac{\delta_k f^{n+1}}{\delta t}$, where $\delta_k f^{n+1}$ is defined as

$$\delta_k f^{n+1} = \frac{1}{\gamma_k}\left(f^{n+1} - \sum_{i=0}^{k-1} \varphi_k^i f^{n-i}\right), \tag{2.25}$$

and where γ_k and φ_k^i are parameters. In particular, since the time evolution is not the main emphasis of this work, in the numerical examples we have used the simplest BDF1 scheme (in fact, as a means to reach the stationary solution):

$$\frac{\delta_1 f^{n+1}}{\delta t} = \frac{f^{n+1} - f^n}{\delta t} = \left.\frac{\partial f}{\partial t}\right|_{t^{n+1}} + \mathcal{O}(\delta t).$$

A remark is needed for the time derivative of the exponential. Using approximation (2.21), it is easily shown that the operations "linearization" and "time approximation" commute if we identify $\hat{\boldsymbol{\psi}}^n = \boldsymbol{\psi}^n$. Indeed, in both cases we obtain:

$$\left.\frac{\partial \exp(\boldsymbol{\psi})}{\partial t}\right|_{t^{n+1}} = \frac{1}{\delta t}\Big[\exp(\hat{\boldsymbol{\psi}}^{n+1}) \cdot \boldsymbol{\psi}^{n+1} + \exp(\hat{\boldsymbol{\psi}}^{n+1}) - \exp(\hat{\boldsymbol{\psi}}^{n+1}) \cdot \hat{\boldsymbol{\psi}}^{n+1}$$
$$- \exp(\boldsymbol{\psi}^n)\Big] + \mathcal{O}(\delta t) + \mathcal{O}((\delta\boldsymbol{\psi}^{n+1})^2). \tag{2.26}$$

where $\hat{\boldsymbol{\psi}}^{n+1}$ stands for a previous guess of $\boldsymbol{\psi}^{n+1}$ that depends on the linearization scheme and $\delta\boldsymbol{\psi}^{n+1} = \boldsymbol{\psi}^{n+1} - \hat{\boldsymbol{\psi}}^{n+1}$.

2.4 Design of a stable finite element formulation

2.4.1 Residual based stabilized finite element method

We present in this section two stabilized finite element formulations for computing viscoelastic flows using the logarithm constitutive reformulation, in particular applied to the Oldroyd-B constitutive model.

VMS methods consist in the splitting of the unknown $\boldsymbol{U}$ in a component $\boldsymbol{U}_h$, which can be resolved by the FE space, and the remainder $\tilde{\boldsymbol{U}}$, that will be called sub-grid scale. The framework is based on the work by Hughes et al. [91]. In the context of a three field formulation for flow problems, see [42] and [26]. The sub-grid scale needs to be approximated in a simple manner, with the goal of capturing its effect and yielding a stable formulation. The final number of degrees of freedom is the same as the Galerkin method. Different approaches can be followed to approximate the sub-scale and to choose the space where it is defined.

The problem we wish to approximate is (2.13) in differential form and (2.17) in variational form. Suppose for the moment that $\mathcal{L}(\hat{\boldsymbol{u}}; \cdot)$ is a *linear* operator (for $\hat{\boldsymbol{u}}$ given). After introducing the subscales decomposition and integrating by parts, the VMS method leads to the problem of finding $\boldsymbol{U}_h : (0, T) \longrightarrow \boldsymbol{\mathcal{X}}_h$ such that

$$(\mathcal{D}_t(\boldsymbol{U}_h), \boldsymbol{V}_h) + B(\boldsymbol{u}_h; \boldsymbol{U}_h, \boldsymbol{V}_h) + \sum_K \langle \tilde{\boldsymbol{U}}, \mathcal{L}^*(\boldsymbol{u}_h; \boldsymbol{V}_h) \rangle_K = L(\boldsymbol{V}_h), \qquad (2.27)$$

for all $\boldsymbol{V}_h \in \boldsymbol{\mathcal{X}}_h$, where $\mathcal{L}^*(\hat{\boldsymbol{u}}; \cdot)$ is the formal adjoint operator of $\mathcal{L}(\hat{\boldsymbol{u}}; \cdot)$ and $\tilde{\boldsymbol{U}}$ is the sub-grid scale, which needs to be approximated, without considering boundary conditions.

Let us remark that two different schemes can be followed at this point to get the stabilized problem:

1. Since operator $\mathcal{L}(\hat{\boldsymbol{u}}; \cdot)$ in (2.13) is in fact *non-linear* because of the exponential of $\boldsymbol{\psi}$, the VMS strategy needs to be applied to a certain linearization. The one described previously could be used, but other options are also possible.

2. The alternative is to work with the standard form of the problem (2.5) (depending on the elastic stress $\boldsymbol{\sigma}$), in which operator $\mathcal{L}_{\text{std}}(\hat{\boldsymbol{u}}; \cdot)$ *is* linear, design the stabilized FE problem based on the VMS concept (involving operator $\mathcal{L}_{\text{std}}^*(\hat{\boldsymbol{u}}; \cdot)$) and then change variables to obtain a log-conformation formulation.

Both cases give us different stabilized formulations, although for simplicity only the second one has been considered in this work. Therefore, the adjoint operator we need to consider is

$$\mathcal{L}_{\text{std}}^*(\hat{\boldsymbol{u}}; \boldsymbol{U}) := \begin{pmatrix} \nabla \cdot \boldsymbol{\chi} - 2\eta_s \nabla \cdot (\nabla^s \boldsymbol{v}) - \rho \hat{\boldsymbol{u}} \cdot \nabla \boldsymbol{v} - \nabla q \\ -\nabla \cdot \boldsymbol{v} \\ \dfrac{1}{2\eta_p} \boldsymbol{\chi} + \nabla^s \boldsymbol{v} - \dfrac{\lambda}{2\eta_p} \left(\hat{\boldsymbol{u}} \cdot \nabla \boldsymbol{\chi} + \boldsymbol{\chi} \cdot (\nabla \hat{\boldsymbol{u}})^T + \nabla \hat{\boldsymbol{u}} \cdot \boldsymbol{\chi} \right) \end{pmatrix}. \qquad (2.28)$$

Taking $\tilde{P}$ as the L^2 projection onto the space of sub-grid scales, the approximation we consider for the sub-grid scales within each element is

$$\tilde{\boldsymbol{U}} = \boldsymbol{\alpha} \tilde{P}[\boldsymbol{F} - \mathcal{D}_t(\boldsymbol{U}_h) - \mathcal{L}(\boldsymbol{u}_h; \boldsymbol{U}_h)], \qquad (2.29)$$

where the operators $\mathcal{D}_t$ and $\mathcal{L}$ were defined previously for logarithmic formulation. Moreover, $\boldsymbol{\alpha}$ is a diagonal matrix $\boldsymbol{\alpha} = \text{diag}(\alpha_1 \boldsymbol{I}_d, \alpha_2, \alpha_3 \boldsymbol{I}_{d \times d})$ with $\boldsymbol{I}_d$ the identity on vectors of $\mathbb{R}^d$, $\boldsymbol{I}_{d \times d}$ the identity on second order tensor and the parameters α_i, $i = 1, 2, 3$ are computed as

$$\alpha_1 = \left[c_1 \frac{\eta_0}{h_1^2} + c_2 \frac{\rho |\boldsymbol{u}_h|}{h_2} \right]^{-1}, \qquad (2.30)$$

$$\alpha_2 = \frac{h_1^2}{c_1 \alpha_1}, \qquad (2.31)$$

$$\alpha_3 = \left[c_3\frac{1}{2\eta_p} + c_4\left(\frac{\lambda}{2\eta_p}\frac{|\boldsymbol{u}_h|}{h_2} + \frac{\lambda}{\eta_p}|\nabla\boldsymbol{u}_h|\right)\right]^{-1}, \tag{2.32}$$

where h_1 corresponds to a characteristic element length calculated in the two-dimensional case as the square root of the element area, and in three-dimensional case as the cubic root of the element volume, whereas h_2 represents the characteristic length associated to the element length in the streamline direction (see [46] for more details). On the other side, $|\boldsymbol{u}_h|$ is the Euclidean norm of the velocity while $|\nabla\boldsymbol{u}_h|$ is calculated by means of the Frobenious norm. The dimensionless constants c_i, $i = 1, .., 4$ are algorithmic parameters in the formulation, and the values adopted in this work are $c_1 = 4.0$, $c_2 = 2.0$, $c_3 = 4.0$, $c_4 = 0.25$ for linear elements. Numerical analysis indicates that they have to be of order one [42], and that $c_4 < 1$. Moreover, $c_1 = 4.0$, $c_2 = 2.0$ are the optimal values for the approximation of the one-dimensional convection-diffusion equation. Note that the values for these constants are the same as those used for the standard formulation [26].

Inserting (2.29) in (2.27), with $\boldsymbol{\alpha}$ given above and using the adjoint operator (2.28), we obtain the following problem: find $\boldsymbol{U}_h \in \boldsymbol{\mathcal{X}}_h$ such that

$$(\mathcal{D}_t(\boldsymbol{U}_h), \boldsymbol{V}_h) + B(\boldsymbol{u}_h; \boldsymbol{U}_h, \boldsymbol{V}_h) + S_1(\boldsymbol{u}_h; \boldsymbol{U}_h, \boldsymbol{V}_h) + S_2(\boldsymbol{U}_h, \boldsymbol{V}_h) + S_3(\boldsymbol{u}_h; \boldsymbol{U}_h, \boldsymbol{V}_h)$$
$$= L(\boldsymbol{V}_h) + R_1(\boldsymbol{u}_h; \boldsymbol{V}_h) + R_3(\boldsymbol{u}_h; \boldsymbol{V}_h), \tag{2.33}$$

for all $\boldsymbol{V}_h \in \boldsymbol{\mathcal{X}}_h$, where

$$S_1(\hat{\boldsymbol{u}}_h; \boldsymbol{U}_h, \boldsymbol{V}_h) = \sum_K \alpha_1 \Big\langle \tilde{P}\Big[\rho\frac{\partial\boldsymbol{u}_h}{\partial t} - \frac{\eta_p}{\lambda_0}\nabla\cdot\exp(\boldsymbol{\psi}_h) - 2\eta_s\nabla\cdot(\nabla^s\boldsymbol{u}_h)$$
$$+ \rho\hat{\boldsymbol{u}}_h\cdot\nabla\boldsymbol{u}_h + \nabla p_h\Big],$$
$$- \nabla\cdot\boldsymbol{\chi}_h + 2\eta_s\nabla\cdot(\nabla^s\boldsymbol{v}_h) + \rho\hat{\boldsymbol{u}}_h\cdot\nabla\boldsymbol{v}_h + \nabla q_h\Big\rangle_K, \tag{2.34}$$

$$S_2(\boldsymbol{U}_h, \boldsymbol{V}_h) = \sum_K \alpha_2 \Big\langle \tilde{P}[\nabla\cdot\boldsymbol{u}_h], \nabla\cdot\boldsymbol{v}_h\Big\rangle_K, \tag{2.35}$$

$$S_3(\hat{\boldsymbol{u}}_h; \boldsymbol{U}_h, \boldsymbol{V}_h) = \sum_K \alpha_3 \Big\langle \tilde{P}\Big[\frac{1}{2\lambda_0}\exp(\boldsymbol{\psi}_h) - \nabla^s\boldsymbol{u}_h$$
$$+ \frac{\lambda}{2\lambda_0}\Big(\frac{\partial\exp(\boldsymbol{\psi}_h)}{\partial t} + \hat{\boldsymbol{u}}_h\cdot\nabla\exp(\boldsymbol{\psi}_h)\Big)$$
$$- \exp(\boldsymbol{\psi}_h)\cdot\nabla\hat{\boldsymbol{u}}_h - (\nabla\hat{\boldsymbol{u}}_h)^T\cdot\exp(\boldsymbol{\psi}_h) + 2\nabla^s\boldsymbol{u}_h\Big],$$
$$- \frac{1}{2\eta_p}\boldsymbol{\chi}_h - \nabla^s\boldsymbol{v}_h$$
$$+ \frac{\lambda}{2\eta_p}\Big(\hat{\boldsymbol{u}}_h\cdot\nabla\boldsymbol{\chi}_h + \boldsymbol{\chi}_h\cdot(\nabla\hat{\boldsymbol{u}}_h)^T + \nabla\hat{\boldsymbol{u}}_h\cdot\boldsymbol{\chi}_h\Big)\Big\rangle_K, \tag{2.36}$$

$$R_1(\hat{\boldsymbol{u}}_h; \boldsymbol{V}_h) = \sum_K \alpha_1 \Big\langle \tilde{P}\Big[\boldsymbol{f}\Big], -\nabla\cdot\boldsymbol{\chi}_h + 2\eta_s\nabla\cdot(\nabla^s\boldsymbol{v}_h) + \rho\hat{\boldsymbol{u}}_h\cdot\nabla\boldsymbol{v}_h + \nabla q_h\Big\rangle_K, \tag{2.37}$$

$$R_3(\hat{\boldsymbol{u}}_h; \boldsymbol{V}_h) = \sum_K \alpha_3 \Big\langle \tilde{P}\Big[\frac{1}{2\lambda_0}\boldsymbol{I}\Big], -\frac{1}{2\eta_p}\boldsymbol{\chi}_h - \nabla^s\boldsymbol{v}_h,$$
$$+ \frac{\lambda}{2\eta_p}\Big(\hat{\boldsymbol{u}}_h\cdot\nabla\boldsymbol{\chi}_h + \boldsymbol{\chi}_h\cdot(\nabla\hat{\boldsymbol{u}}_h)^T + \nabla\hat{\boldsymbol{u}}_h\cdot\boldsymbol{\chi}_h\Big)\Big\rangle_K. \tag{2.38}$$

In these equations, $\tilde{P}$ is the projection restricted to the appropriate components of the FE residual $\boldsymbol{R}_h := \boldsymbol{F} - \mathcal{L}(\boldsymbol{u}_h; \boldsymbol{U}_h)$ onto the space of sub-grid scales. It remains only

to define the projection, for which we consider two possibilities. If we consider $\tilde{P} = I$ (identity), then the method is called Algebraic Sub-Grid Scales (ASGS). In the case that $\tilde{P} = P_h^\perp = I - P_h$ (where P_h is the L^2 projection onto the appropriate finite element space), the name of the method is Orthogonal Sub-Grid Scales (OSS). Independently of the choice of the projection $\tilde{P}$, method (2.33) is consistent, since the terms added to the Galerkin ones are proportional to the FE residual $\boldsymbol{R}_h$.

2.4.2 Split-OSS

Method (2.33) is stable for smooth solutions, and displays the appropriate order of convergence, both for $\tilde{P} = I$ and for $\tilde{P} = P_h^\perp$. As it is indicated in [26], the OSGS method seems in general more accurate, whereas ASGS is cheaper because projections are not needed and it is more robust.

   If we consider the case $\tilde{P} = P_h^\perp$, from (2.33) we can design a simplified method, which consists in neglecting the cross local inner-product terms, as well as some other terms that do not contribute to stability.

   Following the considerations made in [28] for the construction of the Split OSGS stabilization for the traditional viscoelastic formulation, the modified method we propose for the log-conformation reformulation is: find $\boldsymbol{U}_h : (0, T) \longrightarrow \boldsymbol{\mathcal{X}}_h$ satisfying the appropriate initial conditions and such that

$$
(\mathcal{D}_t(\boldsymbol{U}_h), \boldsymbol{V}_h) + B(\boldsymbol{u}_h, \boldsymbol{\psi}_h; \boldsymbol{U}_h, \boldsymbol{V}_h) + S_1^\perp(\boldsymbol{u}_h; \boldsymbol{U}_h, \boldsymbol{V}_h) + S_2^\perp(\boldsymbol{U}_h, \boldsymbol{V}_h)
$$
$$
+ S_3^\perp(\boldsymbol{u}_h; \boldsymbol{U}_h, \boldsymbol{V}_h) = L(\boldsymbol{V}_h), \quad (2.39)
$$

for all $\boldsymbol{V}_h \in \boldsymbol{\mathcal{X}}_h$, where

$$
S_1^\perp(\hat{\boldsymbol{u}}_h; \boldsymbol{U}_h, \boldsymbol{V}_h) = \sum_K \alpha_1 \Big\langle P_h^\perp \Big[-\frac{\eta_p}{\lambda_0} \nabla \cdot \exp(\boldsymbol{\psi}) \Big], -\nabla \cdot \boldsymbol{\chi}_h \Big\rangle_K
$$
$$
+ \sum_K \alpha_1 \Big\langle P_h^\perp \Big[\nabla p_h \Big], \nabla q_h \Big\rangle_K + \sum_K \alpha_1 \Big\langle P \Big[\rho \hat{\boldsymbol{u}}_h \cdot \nabla \boldsymbol{u}_h \Big], \rho \hat{\boldsymbol{u}}_h \cdot \nabla \boldsymbol{v}_h \Big\rangle_K \quad (2.40)
$$

$$
S_2^\perp(\boldsymbol{U}_h, \boldsymbol{V}_h) = \sum_K \alpha_2 \Big\langle P_h^\perp [\nabla \cdot \boldsymbol{u}_h], \nabla \cdot \boldsymbol{v}_h \Big\rangle_{K'} \quad (2.41)
$$

$$
S_3^\perp(\hat{\boldsymbol{u}}_h; \boldsymbol{U}_h, \boldsymbol{V}_h) = \sum_K \alpha_3 \Big\langle P_h^\perp [\nabla^s \boldsymbol{u}_h], \nabla^s \boldsymbol{v}_h \Big\rangle_K
$$
$$
+ \frac{\lambda^2}{4\lambda_0 \eta_p} \sum_K \alpha_3 \Big\langle P_h^\perp [\hat{\boldsymbol{u}}_h \cdot \nabla \exp(\boldsymbol{\psi}_h)], \hat{\boldsymbol{u}}_h \cdot \nabla \boldsymbol{\chi}_h \Big\rangle_K
$$
$$
+ \frac{\lambda^2}{4\lambda_0 \eta_p} \sum_K \alpha_3 \Big\langle P_h^\perp [-\exp(\boldsymbol{\psi}_h) \cdot \nabla \hat{\boldsymbol{u}}_h
$$
$$
- (\nabla \hat{\boldsymbol{u}}_h)^T \cdot \exp(\boldsymbol{\psi}_h) + 2\nabla^s \boldsymbol{u}_h], (\boldsymbol{\chi}_h \cdot (\nabla \hat{\boldsymbol{u}}_h)^T + \nabla \hat{\boldsymbol{u}}_h \cdot \boldsymbol{\chi}_h) \Big\rangle_{K'} \quad (2.42)
$$

Method (2.39) is not just a simplification of (2.33). For smooth solutions, both have an optimal convergence rate in h. However, in problems where the solution has strong gradients, we have found (2.39) more robust, similarly to what it is explained in [28]. Therefore, we will refer to S-ASGS when $\tilde{P} = I$ in (2.36), and S-OSGS for the case $\tilde{P} = P_h^\perp = I - P_h$. However note that in both cases (2.40) and (2.41) have been used instead of (2.34) and (2.35), respectively. Note that the last term in (2.42) is unnecessary for stability and could be omitted. We have to remark as the expression (2.42), where the cross local inner-products have been neglected for the the stabilization terms of the

constitutive equation, could lead a lack of convergence in the iterative method. This is extensively justified in Chapter 4, in particular in Section 4.4.2 where an example of convergence failure is exposed to justify that, in our computations, the fully residual is considered in all cases. In other words, $S_3(\hat{\boldsymbol{u}}_h; \boldsymbol{U}_h, \boldsymbol{V}_h)$ in (2.36) is employed instead of $S_3^{\perp}(\hat{\boldsymbol{u}}_h; \boldsymbol{U}_h, \boldsymbol{V}_h)$ in (2.42).

2.4.3 Linearized problem and algorithm

The equations for incompressible viscoelastic flows have a high number of non-linear terms, in particular in the momentum and the constitutive equation. Obviously, these are maintained with the logarithmic reformulation, and furthermore, new non-linearities arising from the exponential function appear, as it has been exposed in Section 2.3.2.

For the convective term of the momentum equation we can use a fixed point scheme or Newton-Raphson's scheme. However, for the non-linear terms in the constitutive equation, we have used a Newton-Raphson linearization always, and it has been decisive to be able to compute some high Weissenberg cases and get the optimal convergence of the method. At each iteration of each time step, the equations written in Algorithm 1 are computed.

Let us make the following remarks about the algorithm used:

- The nonlinear term in the momentum equation can be linearized with the fixed point scheme or with Newton-Raphson's method, but in the algorithm presented the method used is the second.

- The exponential terms that appear both in the momentum equation and in the constitutive equation have been linearized using (2.21), taking the tensor $\hat{\boldsymbol{\psi}}$ as the one obtained from the previous iteration of the current time step.

- The computation of the exponential function, the gradient and the divergence of the exponential function of the variable $\boldsymbol{\psi}_h$ at the previous iteration must be calculated at each iteration.

- All non-linear terms belonging to the constitutive equation, both in the Galerkin terms and in the stabilization, have been linearized using Newton-Raphson's method.

- Stabilization parameters are computed with the values of the unknowns at the previous iterations.

- The iterative treatment of the orthogonal projection is coupled to the linearization of the total system. Specifically, the orthogonal projection of any function f has been approximated as $P_h^{\perp}[f^i] \approx f^i - P_h[f^{i-1}]$, the superscript being the iteration counter.

- Note that the ASGS method associated to the constitutive equation is considered when $\tilde{P} = I$, while the OSS is applied when $\tilde{P} = P_h^{\perp}$.

Apart from the linearization carried out in some terms just explained, we have found extremely useful the application of other techniques that lead to a better convergence. One of them is the under-relaxation scheme, taking as a relaxation parameter $\epsilon = 0.5$, which has been found effective in most of the cases; the second tool employed is the continuation method in terms of the relaxation time λ, which consists in N_{λ} continuation steps of equal size $\delta\lambda = \lambda/N_{\lambda}$. Note that continuation techniques can be employed because of the modification of the log-conformation formulation; if the original logarithmic formulation had

been taken, they could not be used. Besides, the continuation loop and the linearization loop are coupled in the algorithm used.

In the equations displayed in the Algorithm 1 variables $\boldsymbol{u}_h^{j+1,i}, p_h^{j+1,i}, \boldsymbol{\psi}_h^{j+1,i}$ corresponding to the $(j+1)$ time step are denoted by $\boldsymbol{u}_h^i, p_h^i, \boldsymbol{\psi}_h^i$ for simplicity. Regarding the temporal terms, the notation introduced in Section 2.3.6 is employed here.

The equations considered in Algorithm 1 are solved inside of a general algorithm, presented in Algorithm 2, where all considerations made are taken into account.

Algorithm 1 Logarithmic conformation reformulation. Fully discrete and linearized problem at each iteration.

Given $\boldsymbol{u}_h^{i-1}, p_h^{i-1}, \boldsymbol{\psi}_h^{i-1} (i \geq 1)$, solve $\boldsymbol{u}_h^i, p_h^i$ and $\boldsymbol{\psi}_h^i$ from:

$$\left(\rho \frac{\delta_k \boldsymbol{u}_h^i}{\delta t}, \boldsymbol{v}_h\right) + \frac{\eta_p}{\lambda_0}(\exp(\boldsymbol{\psi}_h^{i-1}) \cdot \boldsymbol{\psi}_h^i, \nabla^s \boldsymbol{v}_h) + 2(\eta_s \nabla^s \boldsymbol{u}_h^i, \nabla^s \boldsymbol{v}_h) + \langle \rho \boldsymbol{u}_h^{i-1} \cdot \nabla \boldsymbol{u}_h^i, \boldsymbol{v}_h\rangle$$

$$+ \langle \rho \boldsymbol{u}_h^i \cdot \nabla \boldsymbol{u}_h^{i-1}, \boldsymbol{v}_h\rangle - (p_h^i, \nabla \cdot \boldsymbol{v}_h) + (\nabla \cdot \boldsymbol{u}_h^i, q_h) + \frac{1}{2\lambda_0}(\exp(\boldsymbol{\psi}_h^{i-1}) \cdot \boldsymbol{\psi}_h^i, \boldsymbol{\chi}_h)$$

$$- (\nabla^s \boldsymbol{u}_h^i, \boldsymbol{\chi}_h) + \frac{\lambda}{2\lambda_0}\left(\frac{\delta_k}{\delta t}(\exp(\boldsymbol{\psi}_h^{i-1}) \cdot \boldsymbol{\psi}_h^i) + (\boldsymbol{u}_h^{i-1} \cdot \nabla(\exp(\boldsymbol{\psi}_h^{i-1}) \cdot \boldsymbol{\psi}_h^i), \boldsymbol{\chi}_h)\right)$$

$$+ \frac{\lambda}{2\lambda_0}\left(\boldsymbol{u}_h^i \cdot \nabla\left(\exp(\boldsymbol{\psi}_h^{i-1})\right) - \exp(\boldsymbol{\psi}_h^{i-1}) \cdot \boldsymbol{\psi}_h^i \cdot \nabla \boldsymbol{u}_h^{i-1} - \exp(\boldsymbol{\psi}_h^{i-1}) \cdot \nabla \boldsymbol{u}_h^i, \boldsymbol{\chi}_h\right)$$

$$- \frac{\lambda}{2\lambda_0}\left((\nabla \boldsymbol{u}_h^{i-1})^T \cdot \exp(\boldsymbol{\psi}_h^{i-1}) \cdot \boldsymbol{\psi}_h^i + (\nabla \boldsymbol{u}_h^i)^T \cdot \exp(\boldsymbol{\psi}_h^{i-1}), \boldsymbol{\chi}_h\right)$$

$$+ \frac{\lambda}{2\lambda_0}(2\nabla^s \boldsymbol{u}_h^i, \boldsymbol{\chi}_h)\right) + \sum_K \alpha_1^{i-1}\left\langle -\frac{\eta_p}{\lambda_0}\nabla \cdot (\exp(\boldsymbol{\psi}_h^{i-1}) \cdot \boldsymbol{\psi}_h^i), -\nabla \cdot \boldsymbol{\chi}_h\right\rangle_K$$

$$+ \sum_K \alpha_1^{i-1}\left\langle \nabla p_h^i, \nabla q_h\right\rangle_K + \sum_K \alpha_1^{i-1}\left\langle \rho \boldsymbol{u}_h^{i-1} \cdot \nabla \boldsymbol{u}_h^i + \rho \boldsymbol{u}_h^i \cdot \nabla \boldsymbol{u}_h^{i-1}, \rho \boldsymbol{u}_h^{i-1} \cdot \nabla \boldsymbol{v}_h\right\rangle_K$$

$$+ \sum_K \alpha_2^{i-1}\left\langle \nabla \cdot \boldsymbol{u}_h^i, \nabla \cdot \boldsymbol{v}_h\right\rangle_K + \sum_K \alpha_3^{i-1}\left\langle \tilde{P}\Big[\frac{1}{2\lambda_0}\exp(\boldsymbol{\psi}_h^{i-1}) \cdot \boldsymbol{\psi}_h^i - \nabla^s \boldsymbol{u}_h^i\right.$$

$$+ \frac{\lambda}{2\lambda_0}\Big(\frac{\delta_k}{\delta t}(\exp(\boldsymbol{\psi}_h^{i-1}) \cdot \boldsymbol{\psi}_h^i) + \boldsymbol{u}_h^{i-1} \cdot \nabla(\exp(\boldsymbol{\psi}_h^{i-1}) \cdot \boldsymbol{\psi}_h^i) + \boldsymbol{u}_h^i \cdot \nabla(\exp(\boldsymbol{\psi}_h^{i-1})$$

$$- (\exp(\boldsymbol{\psi}_h^{i-1}) \cdot \boldsymbol{\psi}_h^i) \cdot \nabla \boldsymbol{u}_h^{i-1} - \exp(\boldsymbol{\psi}_h^{i-1}) \cdot \nabla \boldsymbol{u}_h^i - (\nabla \boldsymbol{u}_h^{i-1})^T \cdot (\exp(\boldsymbol{\psi}_h^{i-1}) \cdot \boldsymbol{\psi}_h^i)$$

$$- (\nabla \boldsymbol{u}^i)^T \cdot \exp(\boldsymbol{\psi}_h^{i-1}) + 2\nabla^s \boldsymbol{u}_h^i\Big)\Big], -\frac{1}{2\eta_p}\boldsymbol{\chi}_h - \nabla^s \boldsymbol{v}_h$$

$$+ \frac{\lambda}{2\eta_p}\left(\boldsymbol{u}_h^{i-1} \cdot \nabla \boldsymbol{\chi}_h - \boldsymbol{\chi}_h \cdot (\nabla \boldsymbol{u}_h^{i-1})^T - \nabla \boldsymbol{u}_h^{i-1} \cdot \boldsymbol{\chi}_h\right)\right\rangle_K$$

$$= \langle \boldsymbol{f}, \boldsymbol{v}_h\rangle + \frac{\eta_p}{\lambda_0}(\exp(\boldsymbol{\psi}_h^{i-1}) \cdot \boldsymbol{\psi}_h^{i-1} - \exp(\boldsymbol{\psi}_h^{i-1}), \nabla^s \boldsymbol{v}_h)$$

$$+ \langle \rho \boldsymbol{u}_h^{i-1} \cdot \nabla \boldsymbol{u}_h^{i-1}, \boldsymbol{v}_h\rangle + \frac{1}{2\lambda_0}\left(\boldsymbol{I} - \exp(\boldsymbol{\psi}_h^{i-1}) + \exp(\boldsymbol{\psi}_h^{i-1}) \cdot \boldsymbol{\psi}_h^{i-1}, \boldsymbol{\chi}_h\right)$$

$$+ \frac{\lambda}{2\lambda_0}\left(\frac{\delta_k}{\delta t}\left(\exp(\boldsymbol{\psi}_h^{i-1}) \cdot \boldsymbol{\psi}_h^{i-1} - \exp(\boldsymbol{\psi}_h^{i-1})\right) + \boldsymbol{u}_h^{i-1} \cdot \nabla(\exp(\boldsymbol{\psi}_h^{i-1}) \cdot \boldsymbol{\psi}_h^{i-1}), \boldsymbol{\chi}_h\right)$$

$$+ \frac{\lambda}{2\lambda_0}\left(-\exp(\boldsymbol{\psi}_h^{i-1}) \cdot \boldsymbol{\psi}_h^{i-1}) \cdot \nabla \boldsymbol{u}_h^{i-1} - (\nabla \boldsymbol{u}_h^{i-1})^T \cdot (\exp(\boldsymbol{\psi}_h^{i-1}) \cdot \boldsymbol{\psi}_h^{i-1}, \boldsymbol{\chi}_h)\right)$$

$$+ \sum_K \alpha_1^{i-1}\left\langle -\frac{\eta_p}{\lambda_0}\nabla \cdot (\exp(\boldsymbol{\psi}_h^{i-1}) \cdot \boldsymbol{\psi}_h^{i-1} + \exp(\boldsymbol{\psi}_h^{i-1})), -\nabla \cdot \boldsymbol{\chi}_h\right\rangle_K$$

$$+ \sum_K \alpha_1^{i-1}\left\langle \rho \boldsymbol{u}_h^{i-1} \cdot \nabla \boldsymbol{u}_h^{i-1}, \rho \boldsymbol{u}_h^{i-1} \cdot \nabla \boldsymbol{v}_h\right\rangle_K$$

$$+ \sum_K \alpha_1^{i-1}\left\langle P_h\Big[-\frac{\eta_p}{\lambda_0}\nabla \cdot (\exp(\boldsymbol{\psi}_h^{i-1}))\Big], -\nabla \cdot \boldsymbol{\chi}_h\right\rangle_K$$

$$+ \sum_K \alpha_1^{i-1} \Big\langle P_h \Big[\rho \boldsymbol{u}_h^{i-1} \cdot \nabla \boldsymbol{u}_h^{i-1} \Big], \rho \boldsymbol{u}_h^{i-1} \cdot \nabla \boldsymbol{v}_h \Big\rangle_K$$

$$+ \sum_K \alpha_1^{i-1} \Big\langle P_h \Big[\nabla p_h^{i-1} \Big], \nabla q_h \Big\rangle_K + \sum_K \alpha_2 \Big\langle P_h [\nabla \cdot \boldsymbol{u}_h^{i-1}], \nabla \cdot \boldsymbol{v}_h \Big\rangle_K$$

$$+ \sum_K \alpha_3^{i-1} \Big\langle \tilde{P} \Big[\frac{1}{2\lambda_0} (\boldsymbol{I} - \exp(\boldsymbol{\psi}_h^{i-1}) + \exp(\boldsymbol{\psi}_h^{i-1}) \cdot \boldsymbol{\psi}_h^{i-1})$$

$$+ \frac{\lambda}{2\lambda_0} \Big(\frac{\delta_k}{\delta t} \left(\exp(\boldsymbol{\psi}_h^{i-1}) \cdot \boldsymbol{\psi}_h^{i-1} \right) + \exp(\boldsymbol{\psi}_h^{i-1}) \Big)$$

$$- \boldsymbol{u}_h^{i-1} \cdot \nabla (\exp(\boldsymbol{\psi}_h^{i-1}) \cdot \boldsymbol{\psi}_h^{i-1} - \exp(\boldsymbol{\psi}_h^{i-1}))$$

$$- \left(\exp(\boldsymbol{\psi}_h^{i-1}) \cdot \boldsymbol{\psi}_h^{i-1} - \exp(\boldsymbol{\psi}_h^{i-1}) \right) \cdot \nabla \boldsymbol{u}_h^{i-1}$$

$$- (\nabla \boldsymbol{u}_h^{i-1})^T \cdot (\exp(\boldsymbol{\psi}_h^{i-1}) \cdot \boldsymbol{\psi}_h^{i-1} - \exp(\boldsymbol{\psi}_h^{i-1})) \Big], -\frac{1}{2\eta_p} \boldsymbol{\chi}_h$$

$$- \nabla^s \boldsymbol{v}_h + \frac{\lambda}{2\eta_p} \left(\boldsymbol{u}_h^{i-1} \cdot \nabla \boldsymbol{\chi}_h - \boldsymbol{\chi}_h \cdot (\nabla \boldsymbol{u}_h^{i-1})^T - \nabla \boldsymbol{u}_h^{i-1} \cdot \boldsymbol{\chi}_h \right) \Big\rangle_K$$

2.5 Numerical results

In this section we will show some numerical examples where the benefits of the stabilized formulations applied to the logarithmic formulation will be demonstrated. As it is remarked in Section 2.3.6, most of the results shown have been obtained solving the steady problem directly, although many references and previous approaches with the log-conformation were time-dependent.

The first result presented in Section 2.5.1 is a convergence test that will show the accuracy of the formulation. It is useful to show that it is optimally convergent for smooth solutions. Secondly, in Section 2.5.2, the well-known benchmark flow past a cylinder is tested to compare different quantities, such as the stress tensor around and downstream of the cylinder or the drag coefficient, with the values published in the literature. In Section 2.5.3 we present the classical 4:1 planar contraction flow problem for two different Reynolds numbers, Re = 1.0 and Re = 0.0, with the purpose of validating the results with a number of references. Finally, the last example in Section 2.5.4 is a three dimensional problem, designed as an extension of the two dimensional 4:1 contraction benchmark.

2.5.1 Convergence test

This first numerical results belong to the convergence study of the stabilized formulations employed for the log-conformation problem. The exact solution will be defined by the next set of functions:

$$u_x(x, y) = 2x^2 y(x-1)^2(y-1)(2y-1),$$
$$u_y(x, y) = -2xy^2(x-1)(y-1)^2(2x-1),$$
$$p(x, y) = \sin(2\pi x)\sin(2\pi y),$$
$$\sigma_{xx}(x, y) = 5\sin(2\pi x)\sin(2\pi y),$$
$$\sigma_{yy}(x, y) = -5\sin(2\pi x)\sin(2\pi y),$$
$$\sigma_{xy}(x, y) = \sin(2\pi x)\sin(2\pi y),$$

where the x and y components of the velocity and the stress tensor have been indicated with a subscript.

Algorithm 2 Logarithmic conformation reformulation. General algorithm.

---

read initial condition $\boldsymbol{u}_h^0$

set $p_h^0 = 0$, $\boldsymbol{\psi}_h^0 = \boldsymbol{0}$

set $\lambda^0 = 0$

for $j = 0, ..., m-1$ **do** *(Temporal loop)*

     set $i = 0$

     set $\boldsymbol{u}_h^{j+1,0} = \boldsymbol{u}_h^j$, $p_h^{j+1,0} = p_h^j$, $\boldsymbol{\psi}_h^{j+1,0} = \boldsymbol{\psi}_h^j$

     set the relaxation time to $\lambda^{j+1} = \min(\lambda^j + \lambda/N_\lambda, \lambda)$

     while not converged **do**

         $i \leftarrow i + 1$

         compute exponentials:

         $\exp(\boldsymbol{\psi}^{j+1,i-1})$, $\nabla \cdot \exp(\boldsymbol{\psi}^{j+1,i-1})$ and $\nabla(\exp(\boldsymbol{\psi}^{j+1,i-1}))$

         compute projections:

         $P_h\left[-\dfrac{\eta_p}{\lambda_0}\nabla \cdot \exp(\boldsymbol{\psi}^{j+1,i-1})\right]$, $P_h\left[\nabla p_h^{j+1,i-1}\right]$,

         $P_h\left[\rho\boldsymbol{u}_h^{j+1,i-1}\cdot\nabla\boldsymbol{u}_h^{j+1,i-1}\right]$ and $P_h\left[\nabla \cdot \boldsymbol{u}_h^{j+1,i-1}\right]$

         if $P = P_h^\perp$ in the constitutive equation **then**

             compute projection

             $P_h\Big[\dfrac{1}{2\lambda_0}\exp(\boldsymbol{\psi}_h^{j+1,i-1}) - \nabla^s\boldsymbol{u}_h^{j+1,i-1} + \dfrac{\lambda}{2\lambda_0}\Big(\boldsymbol{u}_h^{j+1,i-1}\cdot\nabla\exp(\boldsymbol{\psi}_h^{j+1,i-1})$

             $+\dfrac{\delta_k}{\delta t}(\exp(\boldsymbol{\psi}_h^{j+1,i-1})) - \exp(\boldsymbol{\psi}_h^{j+1,i-1})\cdot\nabla\boldsymbol{u}_h^{j+1,i-1}$

             $-(\nabla\boldsymbol{u}_h^{j+1,i-1})^T\cdot\exp(\boldsymbol{\psi}_h^{j+1,i-1}) + 2\nabla^s\boldsymbol{u}_h^{j+1,i-1}\Big)\Big]$

         end if

         compute stabilization parameters:

         $\alpha_1^{j+1,i-1}$, $\alpha_2^{j+1,i-1}$ and $\alpha_3^{j+1,i-1}$ with $\boldsymbol{U}^{j+1,i-1}$

         solve equations from Algorithm 1 for $\boldsymbol{u}_h^{j+1,i}$, $p_h^{j+1,i}$ and $\boldsymbol{\psi}_h^{j+1,i}$

         update unknows:

             $\boldsymbol{u}_h^{j+1,i} \leftarrow \epsilon\boldsymbol{u}_h^{j+1,i} + (1-\epsilon)\boldsymbol{u}_h^{j+1,i-1}$

             $p_h^{j+1,i} \leftarrow \epsilon p_h^{j+1,i} + (1-\epsilon)p_h^{j+1,i-1}$

             $\boldsymbol{\psi}_h^{j+1,i} \leftarrow \epsilon\boldsymbol{\psi}_h^{j+1,i} + (1-\epsilon)\boldsymbol{\psi}_h^{j+1,i-1}$

         check convergence

     end while

     set converged values

         $\boldsymbol{u}_h^{j+1} = \boldsymbol{u}_h^{j+1,i}$

         $p_h^{j+1} = p_h^{j+1,i}$

         $\boldsymbol{\psi}_h^{j+1} = \boldsymbol{\psi}_h^{j+1,i}$

end for *(End temporal loop)*

In order to satisfy the constitutive equation (2.10) with the velocity and the tensor $\boldsymbol{\psi}$, we have to add the forcing term

$$\begin{aligned} \boldsymbol{f}_c = & \frac{1}{2\lambda_0} (\exp(\boldsymbol{\psi}) - \boldsymbol{I}) - \nabla^s \boldsymbol{u} \\ & + \frac{\lambda}{2\lambda_0} \left(\boldsymbol{u} \cdot \nabla \exp(\boldsymbol{\psi}) - \exp(\boldsymbol{\psi}) \cdot \nabla \boldsymbol{u} - (\nabla \boldsymbol{u})^T \cdot \exp(\boldsymbol{\psi}) + 2\nabla^s \boldsymbol{u} \right) \end{aligned}$$

to the right-hand-side of the constitutive equation, with $\boldsymbol{u}$ and $\boldsymbol{\psi}$ being the given manufactured solution. Note that tensor $\boldsymbol{\psi}$ is obtained analytically from the stress tensor through the relation defined in Section 2.3.2.

The computational domain is the unit square, discretized using uniform structured meshes of bilinear (Q_1) and biquadratic (Q_2) quadrilateral elements. The range of element sizes employed in this study ranges between $h = 0.003125$ and $h = 0.0125$ for Q_1 elements, and between $h = 0.00625$ and $h = 0.025$ for Q_2 elements.

We have considered three different Weissenberg numbers for every mesh, We $= 0.0$, We $= 0.5$ and We $= 1.0$. These quantities have been calculated with the maximum velocity value as characteristic velocity and the side of the square as characteristic length, taking into account that the expression of the dimensionless number is We $= \frac{\lambda U}{L}$.

Regarding the optimal convergence rate expected, when the mesh is composed of linear elements, it is 2 in velocity and 1 in pressure and $\boldsymbol{\psi}$ for the L^2-norm, but using quadratic elements it is 3 in velocity and 2 in pressure and $\boldsymbol{\psi}$.

For both formulations, S-OSGS and S-ASGS, results are extremely close, so we have only represented the S-ASGS results in Fig. 2.1.

2.5.2 Viscoelastic fluid flow past a cylinder in a channel

In the literature, we can find that this problem has been worked out using both formulations, the log-conformation one and the standard one. The most relevant results obtained with the standard formulation belong to Fan et al. [63] and Alves et al. [5]. In both works results are highly accurate, although their schemes failed for a Weissenberg number around 1. Other authors, who have published results with diverse techniques for the standard formulation, have obtained similar results regarding the numerical breakdown at relatively moderate Weissenberg numbers with an Oldroyd-B fluid, such as Caola et al. [24], Owens et al. [127], or Castillo et al. [26]. Nevertheless, the logarithmic reformulation of the equations allows us to get solutions for higher Weissenberg numbers. We will compare our results with the solutions found in the literature.

Set up

The geometry of a viscoelastic fluid flow past a confined cylinder in a channel considered in this section is depicted in Fig. 2.2. Note that only the half domain has been taken, for symmetry reasons.

Let us describe the boundary conditions of the problem, following the notation included in the sketch of the geometry. For the velocity, we will impose non-slip conditions on the top wall $y = 2R$, Γ_{wall}, and on the cylinder boundary Γ_{cyl}, while symmetry conditions are prescribed along the axis $y = 0$, denoted by Γ_{sym}. In our case, these last conditions are applied imposing the component y of the velocity to be zero. On the other hand, a fully developed parabolic velocity profile and the associated elastic stress profile are imposed at the inlet Γ_{in}:
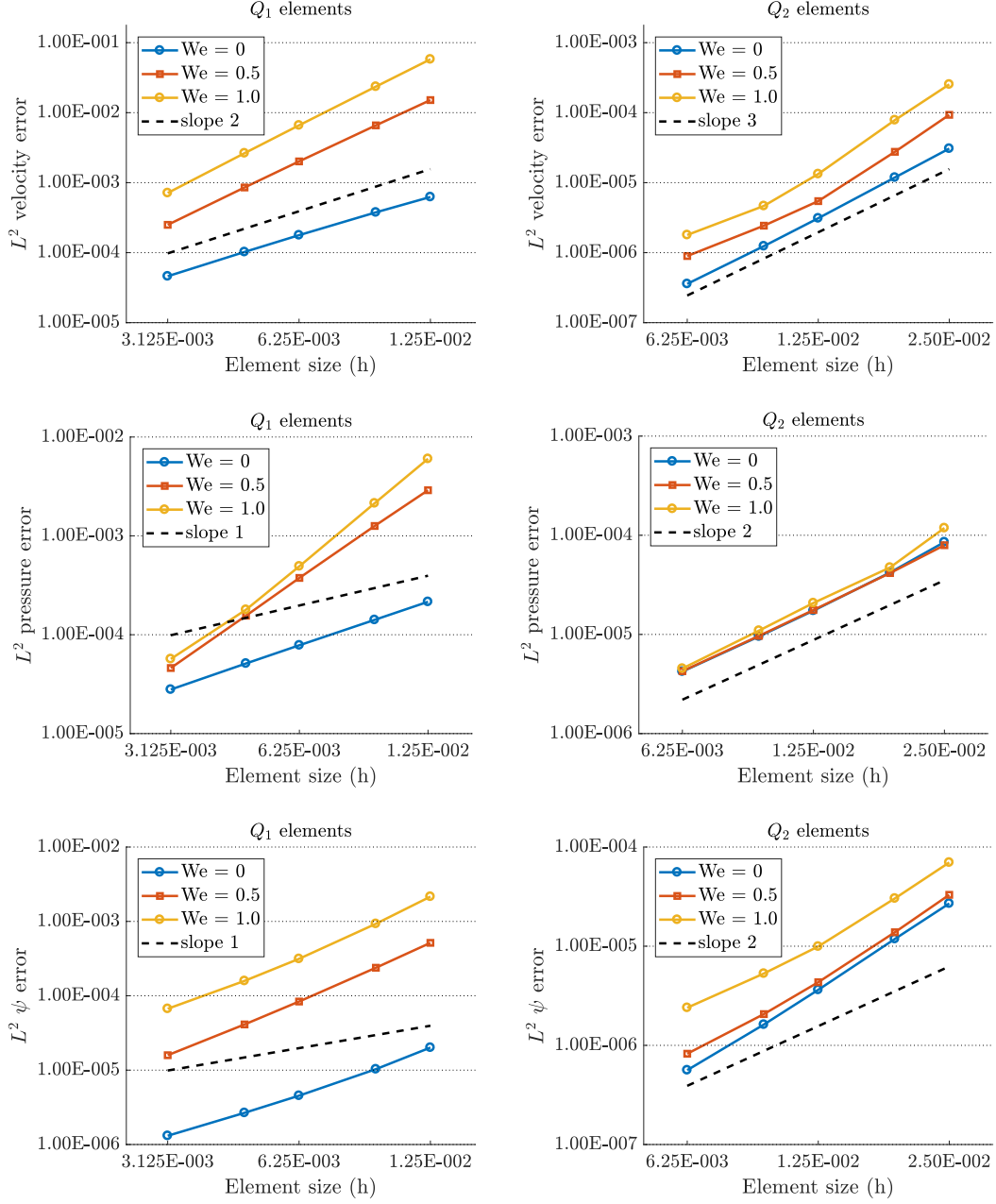
Figure 2.1: Convergence test. Discrete L^2-errors for velocity, pressure and ψ fields using a manufactured solution in quadrilateral elements (Q1 and Q2) with S-ASGS as the stabilization method.
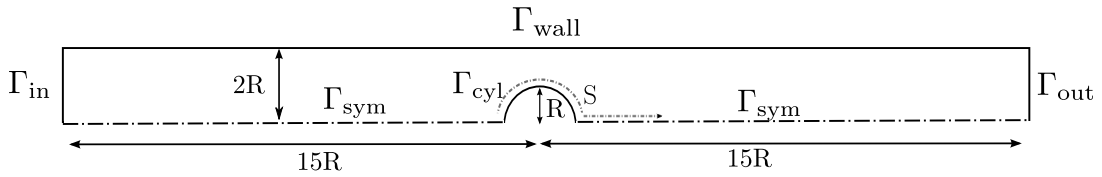
Figure 2.2: Flow past a cylinder. Geometry and computational boundaries.
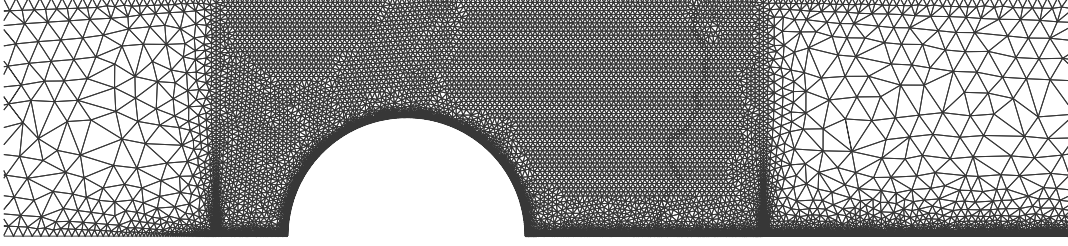
Figure 2.3: Flow past a cylinder. Computational mesh.

Mesh	Nodes	Elements	$h_{\min}$
M1	38 469	71980	0.005
M2	84 378	156 959	0.002
M3	179 645	336 106	0.001

Table 2.1: Flow past a cylinder. Main characteristics of the computational meshes.

$$u_x = \frac{3Q}{4R}\left(1 - \frac{y^2}{(2R)^2}\right), \qquad u_y = 0,$$
$$\sigma_{xx} = 2\lambda\eta_p\left(\frac{\partial u_x}{\partial y}\right)^2, \qquad \sigma_{xy} = \eta_p\left(\frac{\partial u_x}{\partial y}\right), \quad \sigma_{yy} = 0,$$

where Q is the flow rate and R is the radius of the cylinder. Note that the stress conditions will be defined over the inflow boundary using the new variable $\boldsymbol{\psi}$, taking into account the already mentioned relation $\boldsymbol{\psi} = \log\left(\frac{\lambda_0\boldsymbol{\sigma}}{\eta_p}\right)$ in Section 2.3.2. Moreover, the horizontal velocity is left free, the vertical one is set to zero and the pressure is prescribed to zero on the outlet boundary Γ_{out}. The values for the parameters used along all this study are $Q = 1$, $\eta_0 = 1$, $\beta = 0.59$.

We have solved the benchmark for different Weissenberg numbers $\text{We} = \frac{\lambda U}{L_0}$, where the characteristic velocity in this problem is $U = \frac{3Q}{4R}$, and the characteristic length is $L_0 = R$. Furthermore, in all our calculations the convective term of the momentum equation is neglected, as it is customary of this problem.

In order to check the independence of the mesh in the results we have employed three different meshes, with a similar structure. In Fig. 2.3 one of them is displayed, where we can observe its unstructured nature, composed of linear triangles. We have to stand out the refinement of the mesh in the region around the cylinder and downstream, where the maximum values of the stress are achieved. More details about these are found in Table 2.1, which contains the number of nodes, elements and the minimum element size $h_{\min}$ for each mesh.

Drag coefficient results

Although convergence for the dimensionless drag coefficient is a good indicator to check a method, in the literature some discrepancies exist when a moderately high Weissenberg number is considered ($\text{We} \geq 0.7$). Moreover, as the drag coefficient is an integrated quantity over a cylinder, accuracy in the whole of the domain cannot be ensured if this drag coefficient is not adequately reproduced.

Some drag coefficients for different Weissenberg numbers are presented numerically in Table 2.2 and graphically in Fig. 2.4, where our own results (labelled P.S.) are compared to

We	Hulsen M4 [93]	Afonso M30 [2]	Damanik [56]	P.S.
0.1	130.363	-	130.366	130.30
0.2	126.626	-	126.628	126.58
0.3	123.193	-	123.194	123.16
0.4	120.596	-	120.593	120.57
0.5	118.936	118.781	118.828	118.82
0.6	117.792	117.778	117.779	117.80
0.7	117.340	117.350	117.321	117.38
0.8	117.373	117.380	117.347	117.47
0.9	117.787	117.797	117.762	118.01
1.0	118.501	118.662	118.574	118.88
1.1	119.466	119.740	119.657	119.89
1.2	120.650	120.985	120.919	121.14
1.3	-	-	123.350	122.57
1.4	123.587	124.124	123.936	124.14
1.5	-	126.022	125.665	125.85
1.6	127.172	127.759	127.523	127.66
1.7	-	130.012	129.494	129.57
1.8	131.285	132.024	131.578	131.53
1.9	-	134.188	133.754	133.51
2.0	135.839	136.580	136.039	135.53
2.1	not solved	-	138.438	137.57
2.2	not solved	141.801	not solved	139.62
2.3	not solved	-	not solved	141.67
2.4	not solved	146.730	not solved	143.66
2.5	not solved	149.112	not solved	not solved

Table 2.2: Flow past a cylinder. Comparison of drag force coefficient.

those of other authors, who also have applied the log-conformation reformulation, such as Hulsen et al. [93], Afonso et al. [2] or Damanik et al. [56]. Particularly, Hulsen et al. [93] indicate that from a certain Weissenberg value, the solution shows time-dependency and computations do not break down, although some fluctuations are detected when We = 2.0 is reached. However, in our calculations, fluctuations have not been detected and a steady flow has been obtained.

The agreement is acceptable with other publications where the logarithmic reformulation has been made, although from values higher than 1.2 slight discrepancies are detected.

The advantages of using this formulation are notorious: while computations reported in the literature using the standard formulation break down around a Weissenberg number of 0.9, the logarithmic formulation shows good stability for higher values. In our case, we have been capable of simulating fluids with Weissenberg number equal to 2.4.

Stress convergence

As we have commented above, the drag coefficient study is not enough to prove the accuracy of the formulation. Therefore, we have displayed the component x of the stress on the cylinder wall and along the downstream center line with the purpose of contrasting
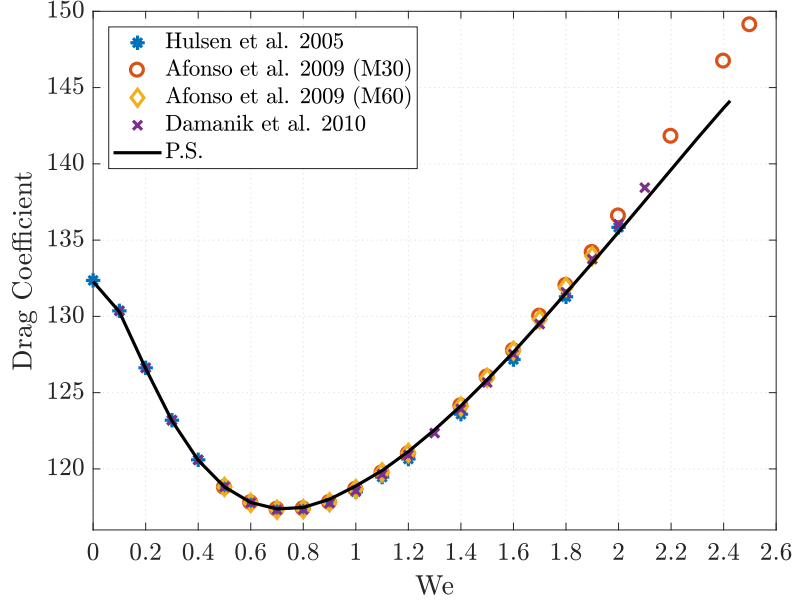
Figure 2.4: Flow past a cylinder. Comparison of drag force coefficient.

our results with those reported by different authors.

Regarding stress convergence when the mesh is refined, as some authors have remarked (Afonso et al. [2], Coronado et al.[53]), there are a lot of discrepancies, particularly when the Weissenberg number begins to increase (We ≥ 0.7). It occurs especially for the maximum peak of stresses situated in the rear wake. Some authors, in spite of using extremely refined meshes and high order methods, cannot be conclusive about the converged results.

A comparison of the first component of the elastic stress profile along the cylinder and downstream at the center line of the domain is shown in Figures 2.5, 2.6 and 2.7; our results are compared with other published results.

We are in agreement with results found in the literature for Weissenberg number equal to 0.6, particularly with Hulsen et al. [93] and Damanik et al. [56], whereas the values shows by Afonso et al. [2] are slightly greater, as it is displayed in Fig. 2.5. Only the result of the thickest mesh (M1) is included here because the values obtained are practically identical for the three meshes, and therefore we can affirm a complete solution independence with respect the mesh used.

However, for the figure presented associated with a Weissenberg number equal to 0.7 (Fig. 2.6), the discrepancies among authors start mainly in the rear wake, in spite of mesh convergence. As it has been commented previously, although this case has been computed by a wide number of authors, high order methods are not conclusive. Regarding our results, these are in agreement with the values reached in the rear wake by Hulsen et al. [93] and Afonso et al. [2] when the finest mesh is employed, although the maximum peak over the cylinder is higher than that plotted by Afonso et al. [2]; in turn, these maximum values are very close to those of the rest of authors compared. Mesh dependency needs to be highlighted for this Weissenberg number at this point, and it is shown in Fig. 2.6 (right), where we can see differences between meshes, especially along the centerline in the wake of the cylinder.

In Fig. 2.7 the results for Weissenberg 0.9 are displayed. As we have remarked before, this solution does not have mesh convergence; this phenomenon has already been
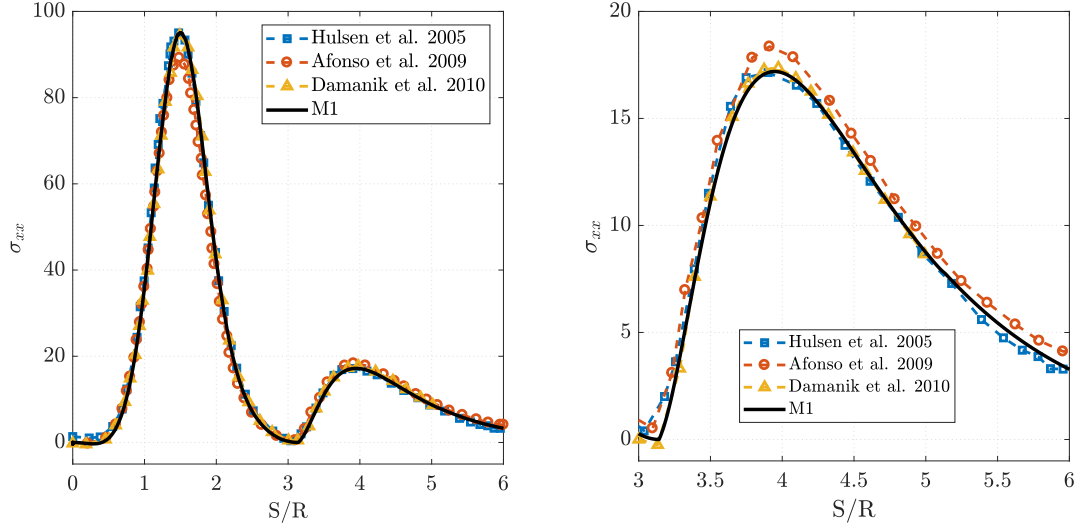
Figure 2.5: Flow past a cylinder. Profile of the first component stress σ_{xx} along cylinder and downstream for We = 0.6.
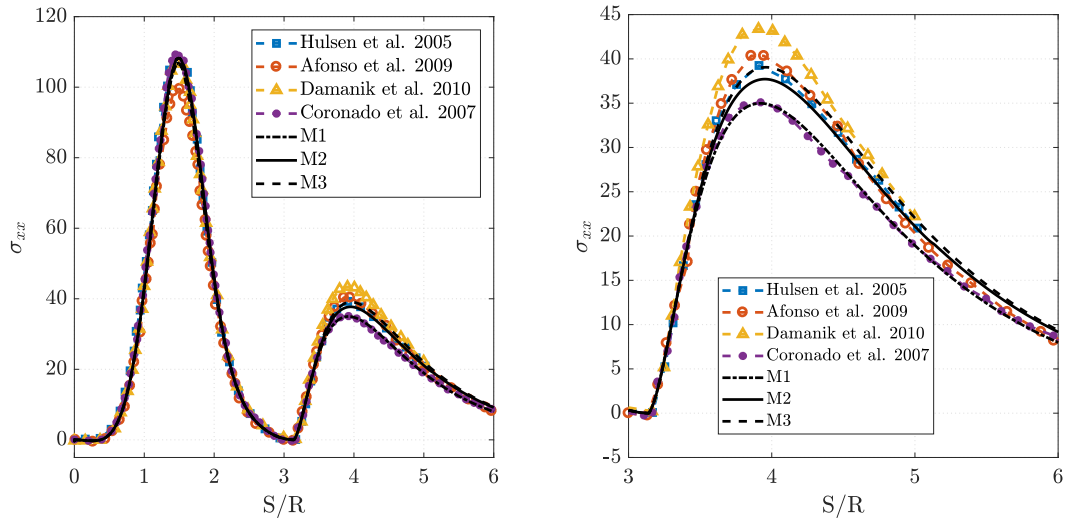
Figure 2.6: Flow past a cylinder. Profile of the first component stress σ_{xx} along cylinder and downstream for We = 0.7.
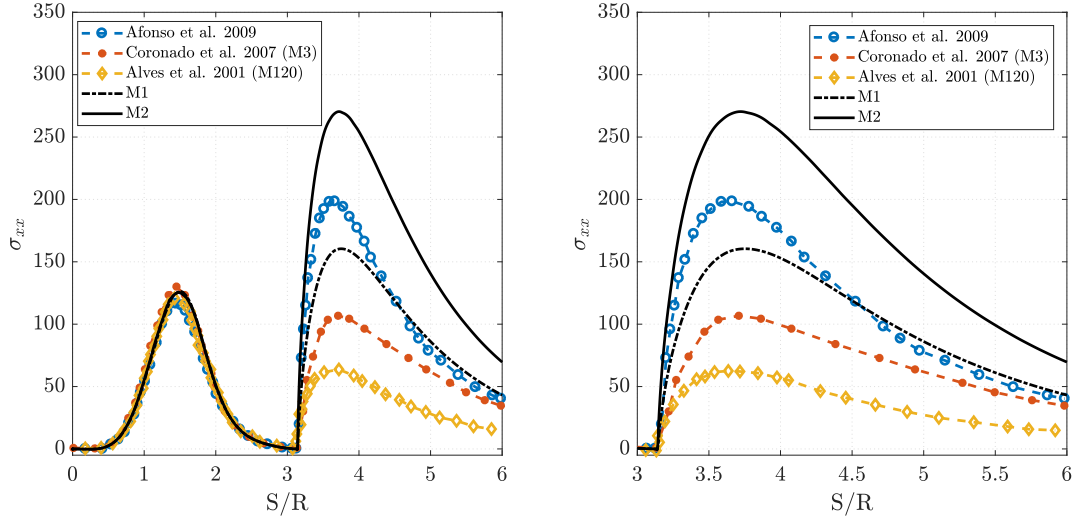
Figure 2.7: Flow past a cylinder. Profile of the first component stress σ_{xx} along cylinder and downstream for We = 0.9.

reported in the literature by some researchers [2, 53, 93]. To show this effect clearly, we have plotted in Fig. 2.7 the values obtained with two different meshes (M1 and M2), so the lack of convergence is demonstrated, because whenever the mesh is refined the maximum values reached along the centerline downstream show a significant increment. The authors referenced above relate this to the behavior of the constitutive model, which models an unlimited extension of the fluid at finite extension rates. For this reason, numerous discrepancies are found between works published when the stress values along the rear wake are plotted, for example between Alves et al. [5], Coronado et al.[53], Afonso et al. [2], and our own results. Nevertheless, the values in points situated around the cylinder are very close in all quoted references.

     Finally, we have illustrated results using mesh M2, with the aim of showing that smooth solutions have been achieved even in more elastic cases. Analogously to the graphs displayed for Weissenberg 0.6, 0.7 and 0.9, in Fig. 2.8 we show the creeping flow around and past the cylinder for greater elasticity values. We are aware of simulations with a Weissenberg number equal o grater than 0.9 do not show mesh-convergence at the rear wake. However, depite of that a significant increasing of the maximum value when Weissenberg number is enlarging can be observed, while the stresses around the wall of the cylinder stay very similar, quasi independent of the elasticity of the fluid.

2.5.3   Contraction 4:1

The next benchmark presented is the well-known 4:1 planar contraction problem in the two dimensional version. This is a suitable example because it is more stringent than other benchmarks when highly elastic problems are studied, due to the singularity which is situated in the corner.

Set up

First of all, we describe the main characteristics of this case. Since the problem is symmetric, we have just considered half of the domain, as it is shown in Fig. 2.10. Moreover,
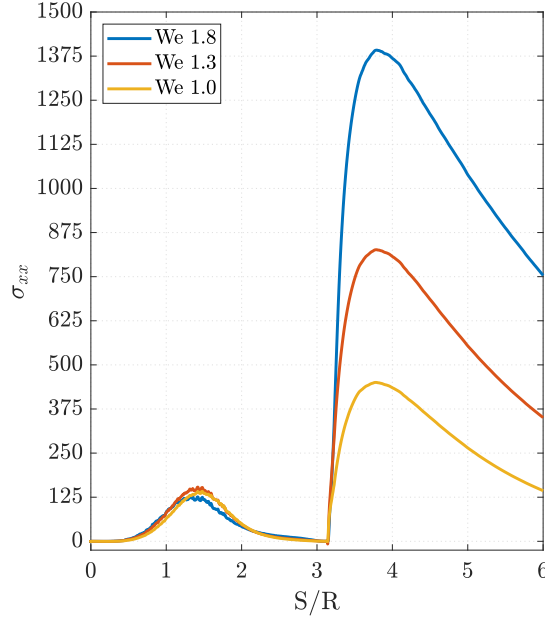
Figure 2.8: Flow past a cylinder. Profile of the first component stress σ_{xx} for high Weissenberg numbers (We=1.0, 1.3, 1.8).

the main characteristic lengths have been already detailed in the figure, taking $H_1 = 4$ and $H_2 = 1$, together with the corner vortex length definition denoted by X_R and the lip vortex X_L. These quantities are useful to compare our results with those of other authors.

Let us describe the boundary conditions associated with this problem. On the solid walls Γ_{wall}, non-slip conditions are imposed for the velocity field and on symmetric boundaries Γ_{sym}, the component y of the velocity is set to zero. Moreover, on the inlet boundary Γ_{in} a fully parabolic velocity profile and stress profile are prescribed:

$$u_x = \frac{3Q}{4H_1}\left(1 - \frac{y^2}{H_1^2}\right), \qquad u_y = 0,$$
$$\sigma_{xx} = 2\lambda\eta_p\left(\frac{\partial u_x}{\partial y}\right)^2, \quad \sigma_{xy} = -\eta_p\left(\frac{\partial u_x}{\partial y}\right), \quad \sigma_{yy} = 0,$$

where Q is the flow rate, set to 1. In this case the characteristic length is $H_2 = 1$, which is the length of the inlet channel, and the characteristic velocity is the mean outflow velocity, $\bar{u}_2 = 1$. Note that the stress conditions will be imposed to the new variable ψ, easily computed from the defined stress functions; these are required in order to avoid the need of using a too large computational domain.

For the outlet boundary Γ_{out}, the x-component of the velocity is left free, and the y-component is set to zero. In addition, the x-component of the normal component of the total Cauchy stress tensor is set to zero. The remaining parameters are $\eta_0 = 1$ and $\beta = 1/9$.

With the characteristic values chosen, We $= \frac{\lambda\bar{u}_2}{H_2}$ and the Reynolds number is

$$\text{Re} = \frac{\rho\bar{u}_2 H_2}{\eta_0},$$

where parameter ρ is the fluid's density.
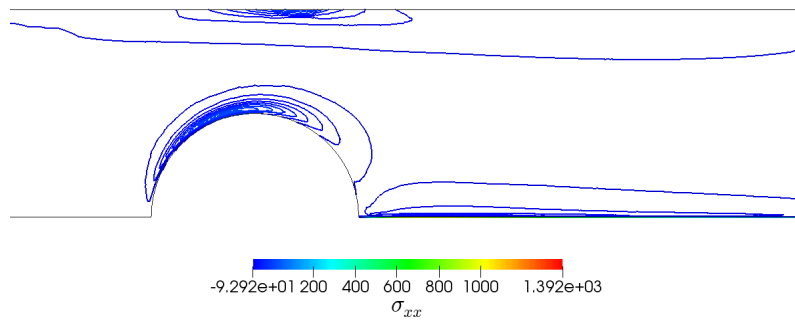
(a) First component of the stresses σ_{xx}
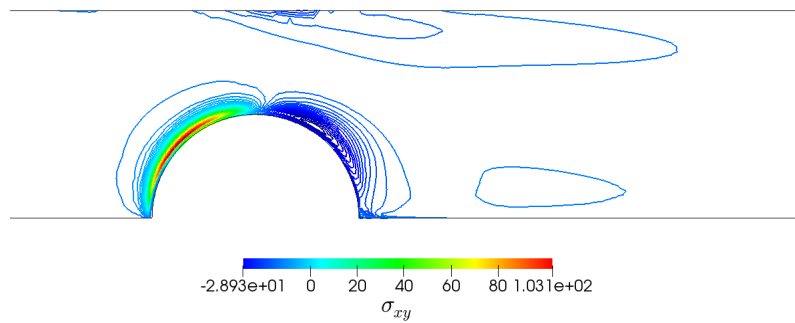
(b) Component xy of the stresses σ_{xy}
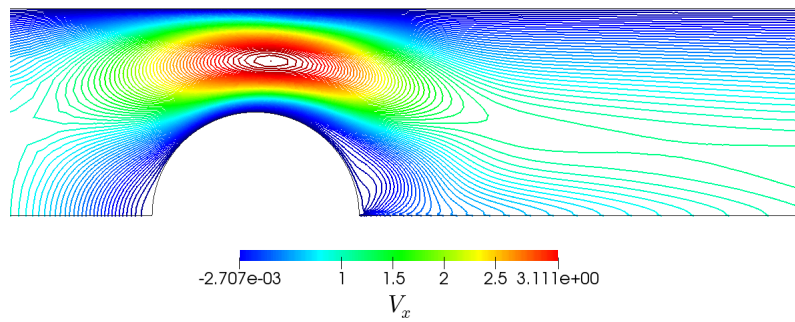
(c) First component of the velocity
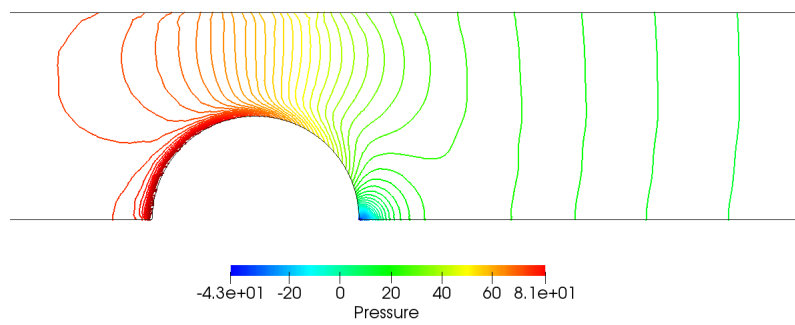
(d) Pressure

Figure 2.9: Flow past a cylinder. Contours near the cylinder.
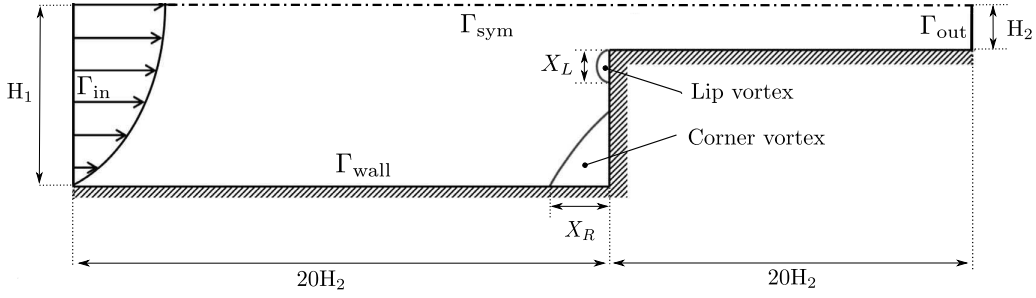
Figure 2.10: Contraction 4:1. Geometry and computational boundaries.

Mesh	Nodes	Elements	$\Delta x_{\min} = \Delta y_{\min}$
M1	10 316	19 770	0.04
M2	12 880	24 712	0.02
M3	20 441	39 242	0.01
M4	28 713	55 693	0.0075
M5	36 513	70 818	0.005

Table 2.3: Contraction 4:1. Main characteristics of the meshes employed.

The main characteristics of the different size meshes used are detailed in Table 2.3. The structure is shared by all of them, although only one is shown in Fig. 2.11. The notation $\Delta x_{\min} = \Delta y_{\min}$ indicates the minimum element sizes in the x and y directions. We have to remark the structured character of the mesh employed near to the contraction, while it is unstructured in the rest of the domain. The results displayed in Section 2.5.3 correspond to mesh M3, while in Section 2.5.3 various mesh sizes are used.

Oldroyd-B flow at Re = 1

In this subsection we will study the problem taking into consideration the inertial effects, in other words, without neglecting the convective term of the momentum equation. So, in order to be capable of comparing our results with others, we have chosen the Reynolds number to be equal to 1. All the authors found in the literature have solved this exact case employing the standard formulation. A wide range of techniques have been carried out to solve this problem: Sato and Richardson [149] and Phillips and Williams et al. [136] describe a semi-Lagrangian finite volume scheme, Nithiarasu et al. [122] propose an explicit characteristic based split (CBS) scheme, whereas Li et al [110] present a mixed finite element scheme, utilizing the DEVSS method for stress stabilization. Castillo et al. [26] proposed a stabilized method using the VMS method with a discontinuity capturing technique which allows to deal with local discontinuities.

In our case, the maximum Weissenberg number achieved by the present scheme is about We = 9.0. This value is smaller than the Weissenberg value that we have been capable of simulating when the Reynolds number is set to zero. This effect is in agreement with the authors quoted before, and is produced by the relevance of the non-linear convective term of the momentum equation. As it is commented before, we have not come upon this problem solved with the logarithmic reformulation in the literature, but the benefits of this formulation are clear in comparison with the standard formulation, allowing us to solve the problem for fluids with much higher elasticity. For example, one of the highest
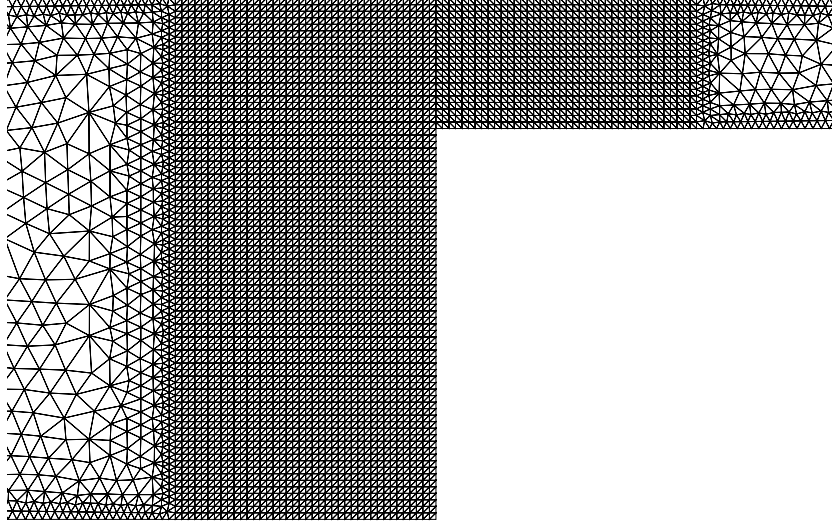
Figure 2.11: Contraction 4:1. Computational mesh.

values reached for the standard formulation is We = 5.0 in the work written by Castillo et al. [26], where it is explained that for We = 5.5 some instabilities appeared, and the scheme is incapable of solving the problem for We = 6.0.

Next, we will present some results, starting with the distribution of streamlines near the contraction for some of Weissenberg numbers, shown in Fig. 2.12. As in other works, the vortex in the corner decreases when We increases, while the lip vortex grows progressively for increasing Weissenberg numbers. This secondary vortex starts to emerge for We ≥ 1.0 (see [26, 110, 122] for discussion). Lip vortices start to merge with the corner vortices at We = 5.5 approximately, but two different centers of rotation are clearly defined. The two centers merge at about We = 6.0. The resulting corner, in some works as [51], is referred as *the third vortex*. So, when the Weissenberg number increases, we observe a divergence of the streamlines upstream of the contraction. The relationship between the corner vortex length (denoted by X_R in Fig. 2.10) and the Weissenberg number is shown in in Fig. 2.13 together with the results of other works in the literature. We have to remark that although the corner vortex sizes are consistent with results published, lip vortex sizes are notably higher than the ones reported in the literature. However, it seems a logical behavior that contributes to the final merge between the two vortices. Both graphs are plotted up to Weissenberg 5.0 because above this value the third vortex appears, annihilating the previous vortices. This phenomenon is clearly visible in Fig. 2.12. A pressure plotting is shown along a cut line near the contraction problem in Fig. 2.14a, where the singularity at the corner is easily identified at $x = 20$. A decreasing of the maximum pressure values is observed whenever the Weissenberg number grows. On the other side, the first elastic stress distribution (σ_{xx}) along $y = -H_2$ is given in Fig. 2.14b for various Weissenberg values using mesh M3. The singularity (at the corner) is located at $x = 20.0$. We can observe that the peak values of the viscoelastic stresses increase with elasticity. We have found differences between the maximum peaks obtained and the results presented in [26], where the standard formulation is employed. Nevertheless, our solution is very close to the distribution shown in the work of Afonso et al. [1], where a study comparing both formulation is developed and where a distribution of the elastic stress

(a) We = 0.0   (b) We = 0.5   (c) We = 1.0

(d) We = 2.0   (e) We = 3.0   (f) We = 4.0

(g) We = 5.0   (h) We = 6.0   (i) We = 7.0
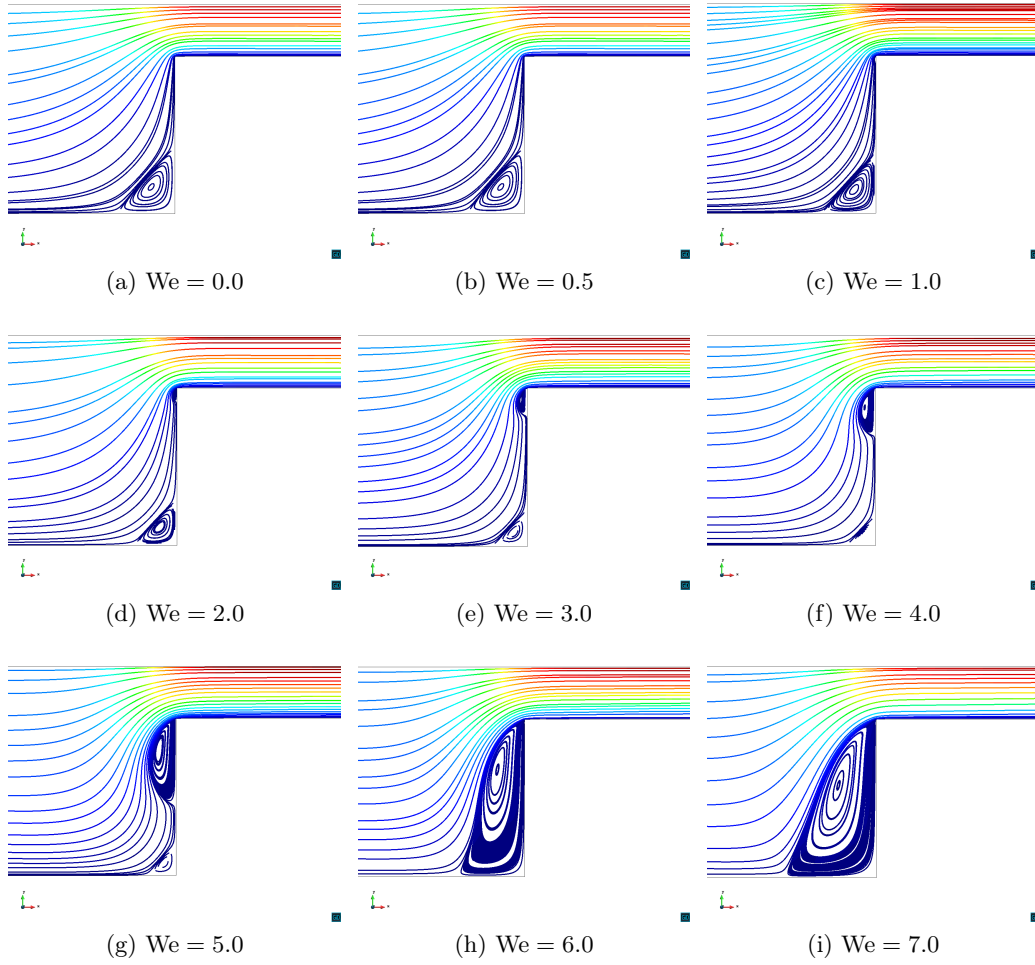
Figure 2.12: Contraction 4:1. Streamlines patterns for different Weissenberg number and Re = 1.0.
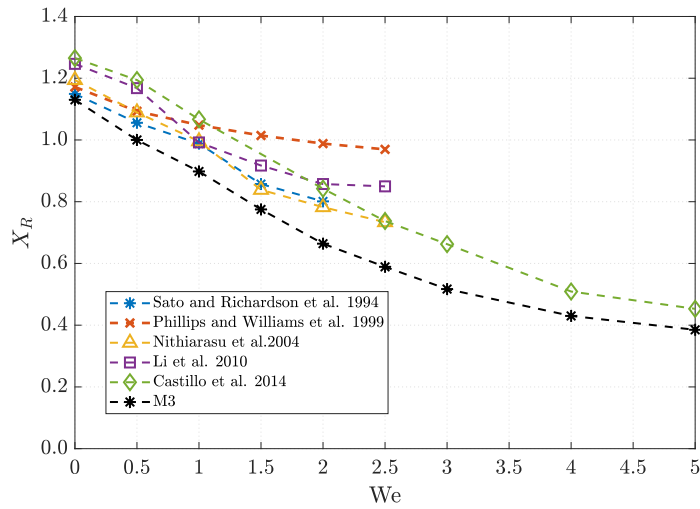
Figure 2.13: Contraction 4:1. Corner length comparison for Re = 1.0, We $\leq$ 5.0.
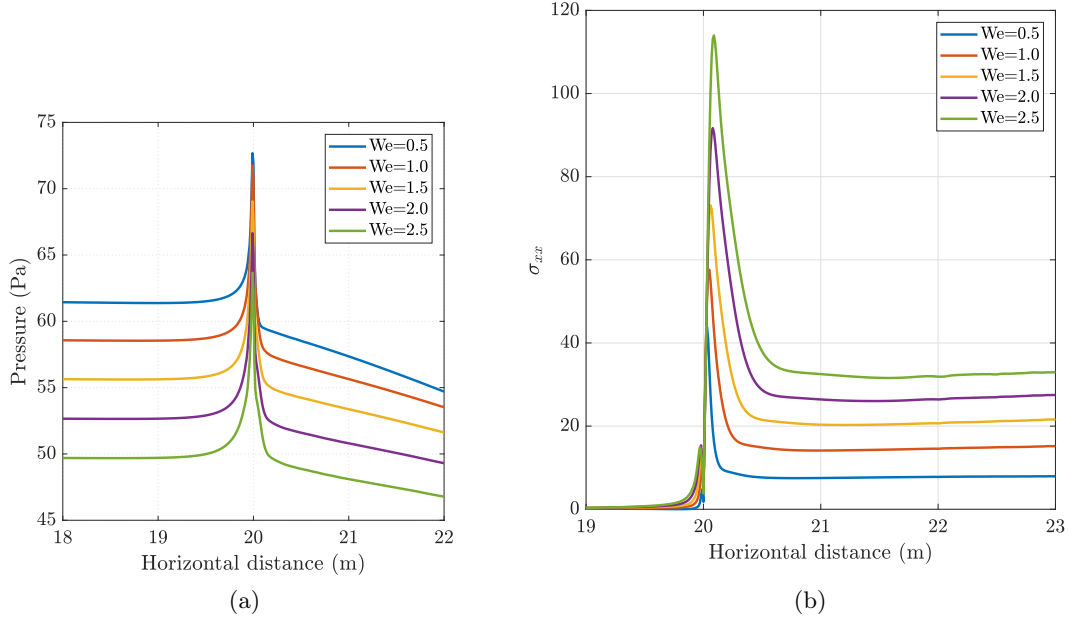
Figure 2.14: Contraction 4:1. Pressure and first elastic stress tensor component in a cut line along $y = -H_2$ near the contraction corner for Re $= 1.0$, We ≤ 2.5.

along the centerline $y = 0$ (symmetry axis), where the solution is smoother, is plotted. By following the same idea, Fig. 2.15 compares solutions in both formulations; we have not found large discrepancies between them, except in the maximum values, where a slight variation is observed when elasticity grows. Moreover, in [1] it is described how these differences are more perceptible from We $= 2.5$, because with the logarithmic formulation the flow becomes unsteady, while with the standard one it diverges at We $= 3.0$. The contours of the extra stresses and pressure provided by the proposed formulation for We$=$ 1.0, 3.0, 5.0 ant 7.0 are displayed in Figs. 2.16 - 2.19. The patterns of the corresponding results are smooth and similar to the ones shown in the literature [26, 110, 122] although there are some differences near to the contraction in the distribution of the component
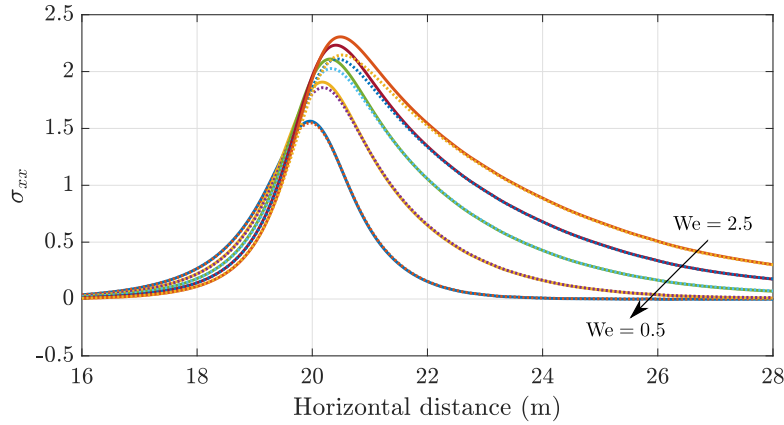
Figure 2.15: Contraction 4:1. First elastic stress component along $y = 0$, Re $= 1.0$.

(a) We = 1.0

(b) We = 3.0

(c) We = 5.0

(d) We = 7.0
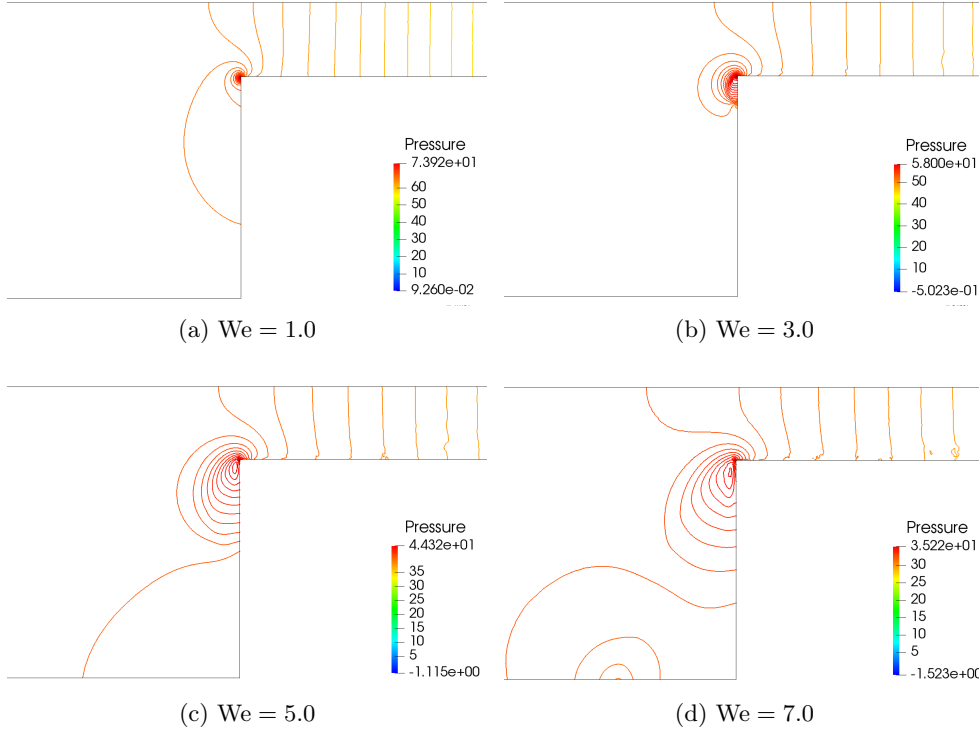
Figure 2.16: Contraction 4:1. Pressure contours around the contraction corner for different Weissenberg numbers and Re=1.0.

σ_{yy} (Fig. 2.18) and σ_{xy} (Fig. 2.19) when the fluid is more elastic (We=3.0 and 5.0, for example). These differences in the distribution of the shear stress could be the cause of the unusual growth and the size of the lip vortex, already explained and shown in Fig. 2.12. On the other side, we can observe that the gradients of the elastic stresses near the contraction corner and the maximum stress value are higher when the Weissenberg number is increased.

Oldroyd-B flow at Re $= 0.01$

There are studies, such as Sato and Richardson [149] and Matallah et al. [117], which indicate that solutions for the Oldroyd-B flow with a Reynolds number Re ≤ 0.01 are almost identical to those for the Oldroyd-B flow with Re $= 0.0$, in other words, those of creeping flow. For this reason, the solutions for Re $= 0.01$ given by the proposed scheme can be compared with studies of creeping flow published in the literature. Recall that in our case Re $= \frac{\rho \bar{u}_2 H_2}{\eta_0}$.

Many references with different numerical schemes present results for the problem considered. For example, Alves et al. [4], analyze the dispersion and the vortex length using several methods, and Kim et al. [100] employ a transient finite element method based on a fractional step scheme and stabilization techniques. Authors quoted in previous sections, as [26, 122], also validate their schemes for Re $= 0.01$; these are included in our comparisons. All the mentioned articles use the standard formulation; however, we have come upon some relevant analysis where a log-conformation reformulation is employed to solve the contraction problem, such as the work by Afonso et al. [1], where a dynamic evaluation of the behavior and the fluctuation of flow at high Weissenberg number is stud-
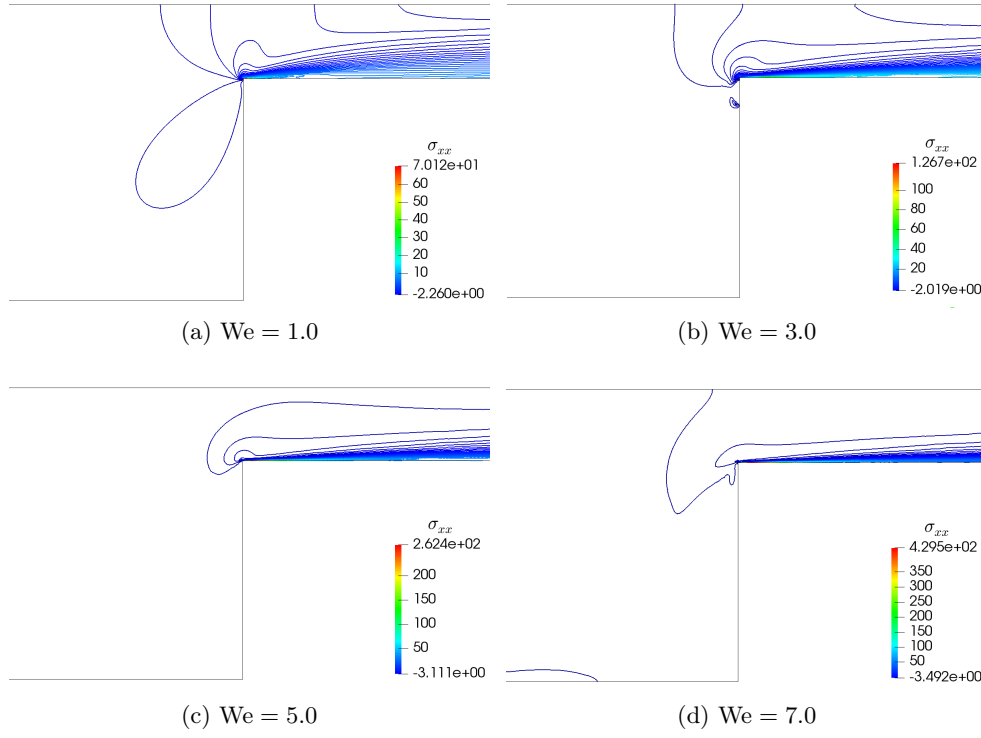
Figure 2.17: Contraction 4:1. Distribution of component xx of the normal elastic stresses at Re=1.0.
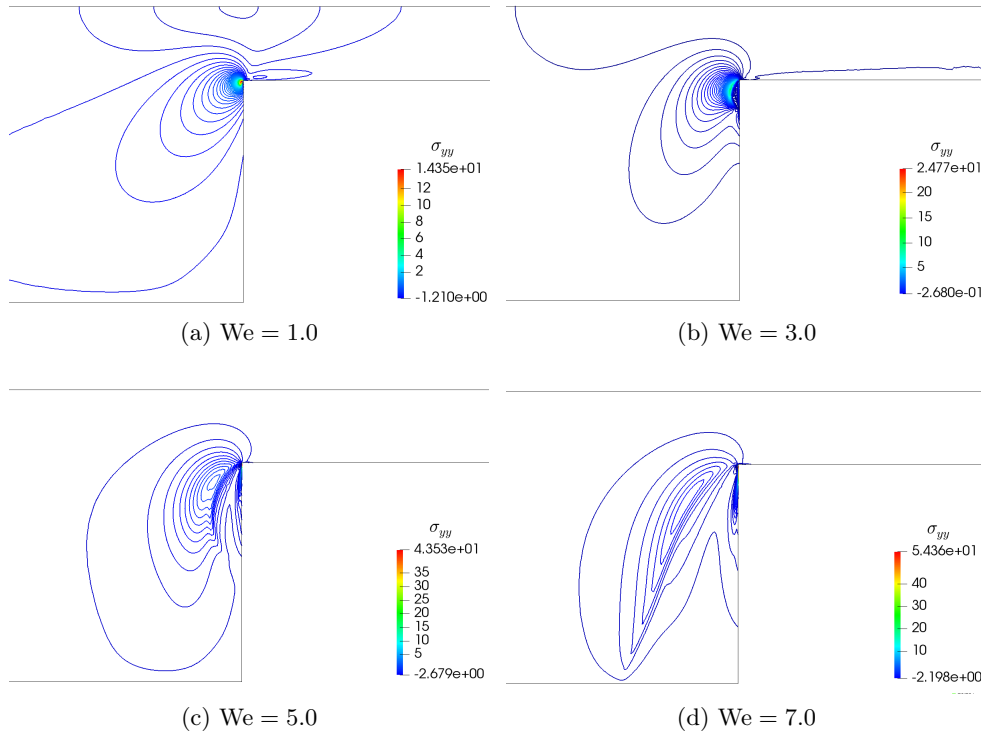
Figure 2.18: Contraction 4:1. Distribution of component yy of the normal elastic stresses at Re=1.0.

(a) We = 1.0   (b) We = 3.0

(c) We = 5.0   (d) We = 7.0
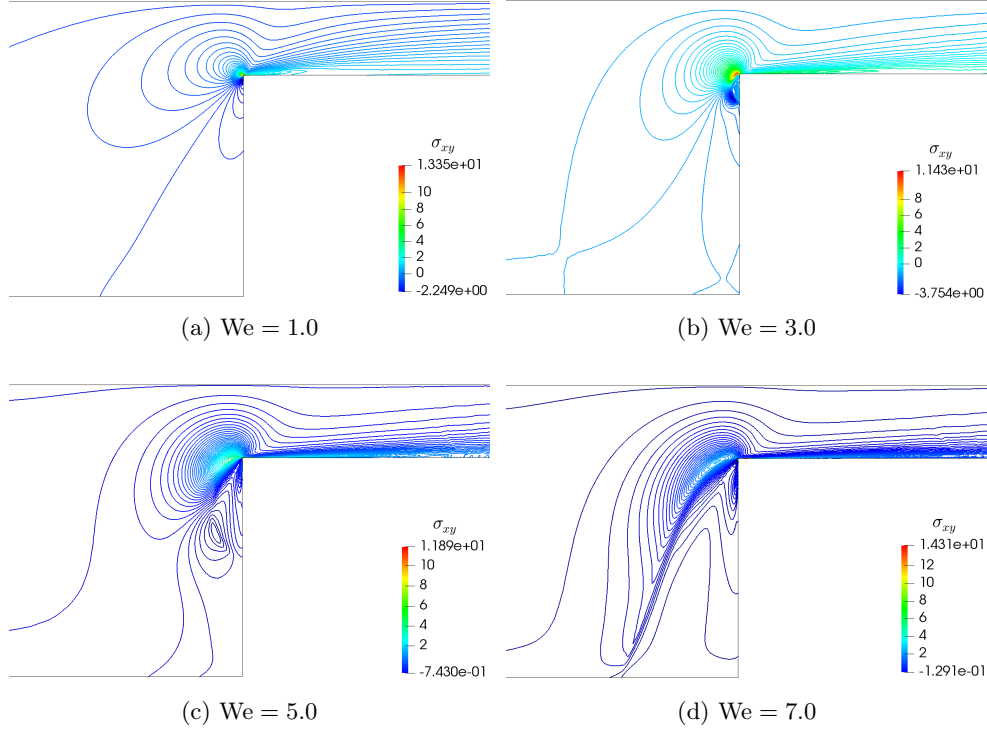
Figure 2.19: Contraction 4:1. Distribution of component xy of the normal elastic stresses at Re=1.0.

ied, Comminal et al. [51], which presents a numerical solution for a Weissenberg number up to 20 with a streamfunction-log-conformation methodology, and Pimenta et al. [138], the most recent study, in which the typical solver available in the OpenFOAM toolbox is modified to get second-order accuracy. All these works consider We $\leq$ 12.

We have illustrated streamlines in Fig. 2.20 for various Weissenberg numbers up to 7.0. The maximum Weissenberg number reached in our case is 15.0 in stationary regime and using the coarsest mesh. We are aware of the lack of accuracy of the results of the highest we reached, because in references [1, 51] the existence of large fluctuations are described for high Weissenberg numbers, whereas we obtain a stable stationary solution. Note that the aim of this work is to validate the formulation, therefore transient terms have just been added to achieve stationary solutions and not to perform truly transient calculations.

The behavior of the vortex is very close to the one described for the Re = 1.0 case. Fig. 2.21 shows the evolution of the corner vortex and later the third vortex size when the Weissenberg number is increased for the three finest meshes. Just as it is exposed in the work of Pimenta et al. [138], the growth of the lip vortex size is shown to be significantly dependent on the mesh resolution, where finer meshes lead to a smaller lip vortex and, consequently, it affects the merge between two vortices and thus to the growth and size of the third vortex.

In Fig. 2.22, the comparison with the literature (references [1, 51]) of the corner size in terms of the Weissenberg number is shown. A survey of the numerical results presented in the literature reveals large discrepancies between the results of the different studies. Our results are in very good agreement with the solutions of Kim et al. [100] for values up to We = 3.0.

(a) We = 0.0   (b) We = 0.5   (c) We = 1.0

(d) We = 2.0   (e) We = 3.0   (f) We = 4.0

(g) We = 5.0   (h) We = 6.0   (i) We = 7.0
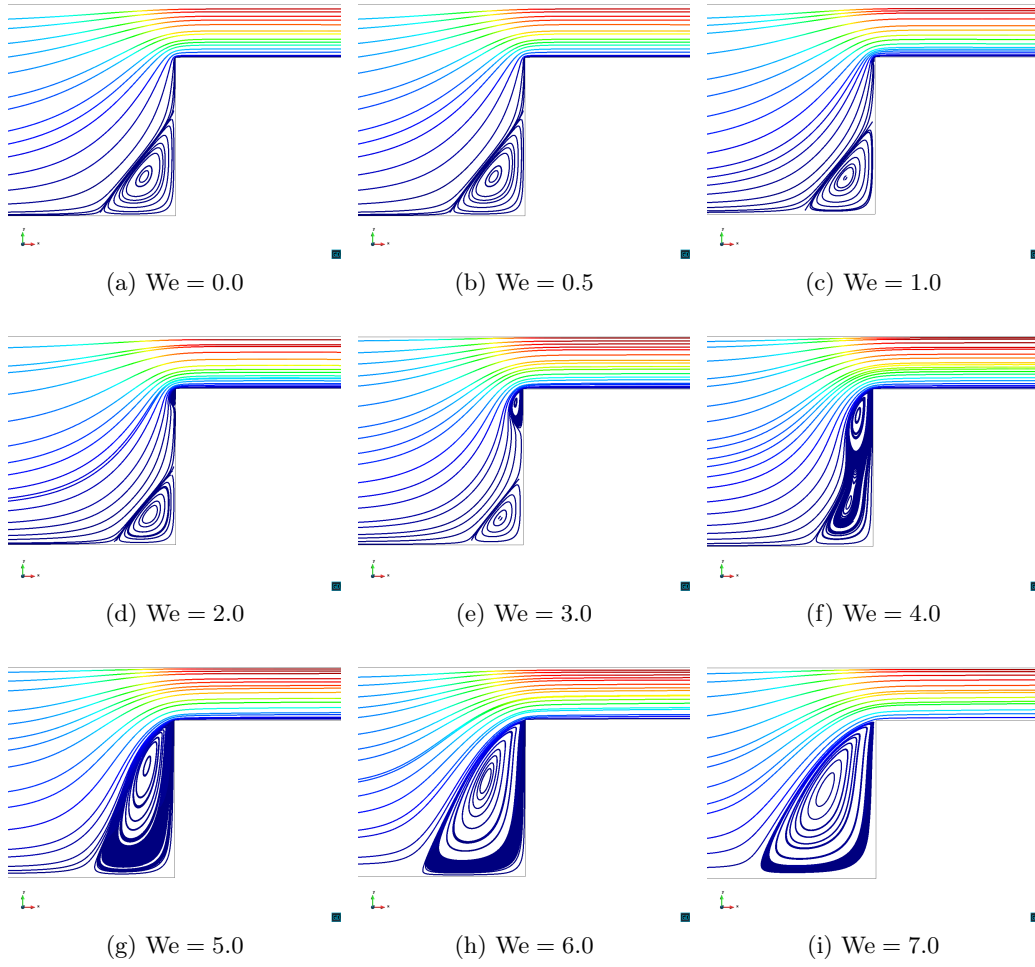
Figure 2.20: Contraction 4:1. Streamlines patterns in the contraction planar for different Weissenberg number for Re = 0.01.
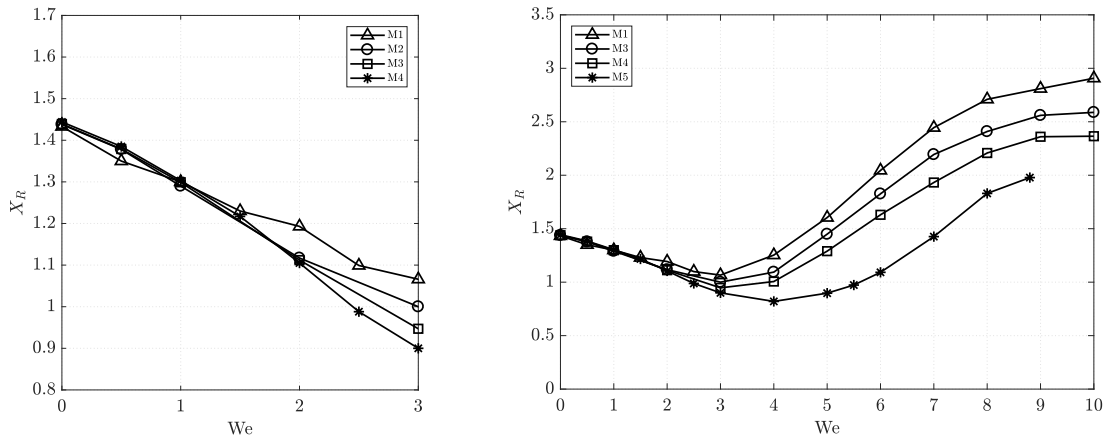
Figure 2.21: Contraction 4:1. Corner vortex length comparison between meshes for Re=0.01.
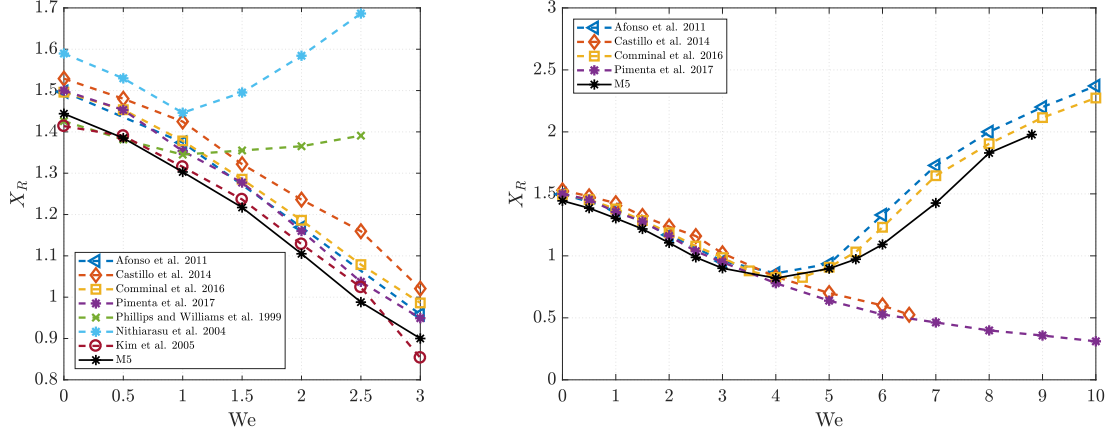
Figure 2.22: Contraction 4:1. Corner vortex length comparison for Re=0.01.

We	Δp (Re=1.0)	Δp (Re=0.01)	We	Δp (Re=1.0)	Δp (Re=0.01)
0.0	64.79	62.95	**6.0**	33.78	32.96
1.0	58.99	58.38	**7.0**	30.56	29.85
2.0	53.24	52.43	**8.0**	29.26	27.48
3.0	47.49	46.60	**9.0**	-	25.11
4.0	42.30	41.33	**10.0**	-	23.09
5.0	37.76	36.80	**11.0**	-	21.42

Table 2.4: Contraction 4:1. Pressure drop for different Weissenberg and Reynolds numbers.

Pressure drop

Finally, a global study has been performed to validate the formulation. As done in Castillo et al. [26], pressure drop for some Weissenberg numbers are included in Fig. 2.4. It is calculated as $\Delta p = p_{inlet} - p_{outlet}$, that is, as the difference between the pressure at the inlet and pressure at the outlet. In both cases, inertial and non-inertial, the same effect occurs: the pressure drop decreases when the elasticity of the fluid is increased, as it is expected from the physical point of view.

2.5.4   Three dimensional case

As a last example, we are going to show a 4:1 contraction problem in its three dimensional version, in order to proof that the proposed formulation is ready for 3D problems. Measures and conditions considered are similar to those in [26].

Set up

The geometry is illustrated in Fig. 2.23 together with some measures. Since the problem is symmetric for low Weissenberg numbers, we have just considered a fourth of the total domain. In [1], the full domain was used in order to be able to capture flow asymmetries or instabilities when the Weissenberg number grows. Both inlet and outlet lengths are the same as in the two dimensional case, long enough for getting a full flow development. Moreover, the characteristic length we have chosen is $H_2 = 1$, which is half of the channel
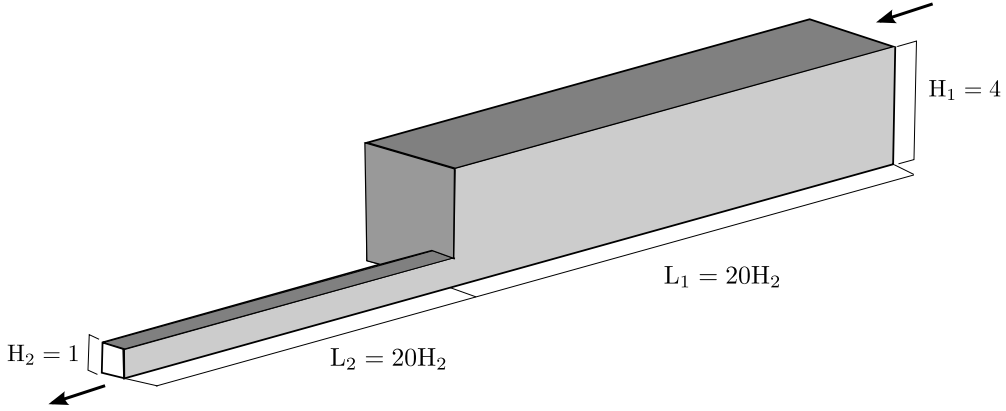
Figure 2.23: Contraction 4:1. Three dimensional geometry and computational boundary.

width of the narrowest part, and the average velocity in the outlet of the channel $\bar{u}_2 = 1$ has been chosen as characteristic velocity.

The boundary conditions are an extension from the two dimensional case, but now the domain has two symmetry boundaries instead of one. The symmetry planes are $y = 0$ and $z = 0$, and the normal velocity to each plane is set to zero. In this problem we have just considered a Weissenberg number of $\mathrm{We} = 1.0$ and the inertial effects have been minimized, taking $\mathrm{Re} = 0.01$.

Higher values of the Weissenberg number would require finer meshes in order to be capable to capture the lip vortex. Nevertheless, we are now trying to study the behavior of the highest Weissenberg number in a three dimensional geometry, as it is done in [26]. The mesh used is formed by 476 852 unstructured tetrahedra and 86 856 nodes.

Some results

Only a few pictures of results will be presented, intending to give an idea of the flow. On the one side, streamlines are shown in Fig. 2.24, where these are plotted on two perpendicular planes. Particularly, in Fig. 2.24b the main corner vortex is clearly appreciated, and also the lip vortex starts to emerge. The similarities with the two dimensional case are remarkable, in spite of the minimum mesh size being notably finer in that problem. In Fig. 2.24c the symmetry with respect to plane $y = z$ of the streamlines can be observed.

Displaying the distribution of the pressure near the contraction is interesting, due to this is one of the most difficult fields to capture suitably geometry presents an abrupt change. The contour lines of this field around the corner are plotted in Fig. 2.25. In Fig. 2.26a a cut line along the contraction is shown, where it is proved as the pressure peak is well captured. Also, in Figure Fig. 2.26b the first component of the elastic stresses is displayed to reinforce the idea of good performance of the simulation capturing the peak produced in the corner. We have to stand out that the results presented in this section pretend to make a qualitative study of the three dimensional problem, neither comparing the results obtained with other publications nor establishing a rigorous analysis of the differences between them.

2.6   Conclusions

In this chapter a FE method has been designed for the log-conformation formulation of Fattal and Kupferman [64], considering a modification with respect to the original formu-
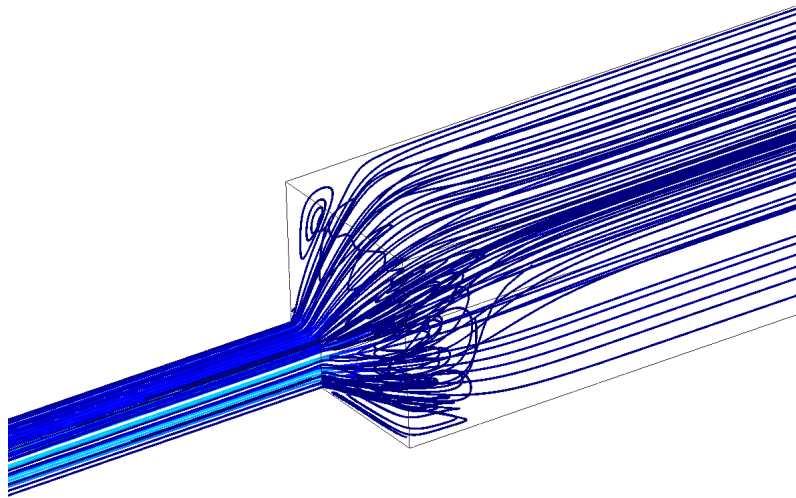
(a) Streamlines in the 3D geometry.
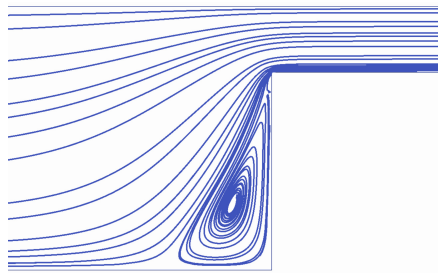
(b) Cut with the plane $y = 0$.
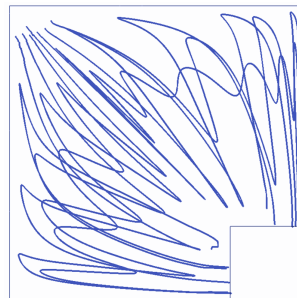
(c) Cut plane a $x = $ cte near to the contraction plane.

Figure 2.24: Contraction 4:1. Streamlines in the three dimensional model in three different views.
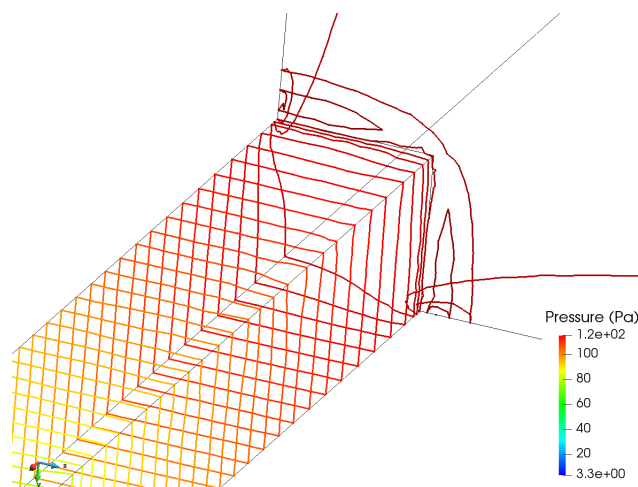
Figure 2.25: Contraction 4:1. Contour lines of the pressure in the three dimensional model.
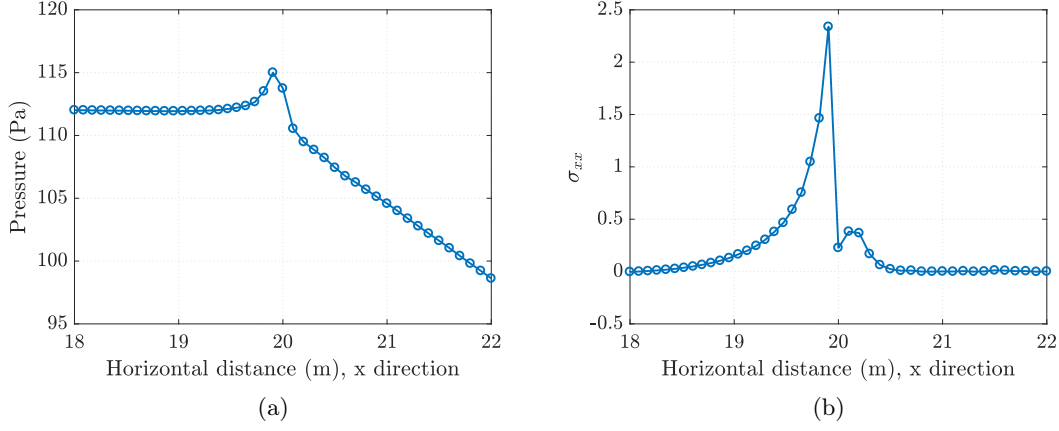
Figure 2.26: Contraction 4:1. Pressure and normal elastic stresses component σ_{xx} near the corner.

lation which is non-singular with respect to the relaxation time parameter and, moreover, that allows a direct steady numerical computation. The spatial approximation is carried out using a stabilized FE method based on the VMS framework. Firstly, a residual-based formulation of the equations is presented, and later the Split-OSS method is developed for the momentum and continuity equations, whereas the constitutive equation can be stabilized using the classical residual-based stabilization, following the steps of [26]. The linearization of the problem has been presented in detail, emphasizing the treatment of the exponential function. The convergence of the proposed method has a strong dependency on this treatment.

The resulting method allows one to obtain globally stable solutions, and has been validated in different benchmarks for high Weissenberg numbers, showing accuracy, optimal convergence for smooth solutions, and robustness even in steady-state computations, reaching accurate results in comparison with other methods reported in the literature. Moreover, the formulation also performs well in the three-dimensional case, with good results from a qualitative point of view.

Chapter 3

Thermal Coupling

This chapter is based on the publication:

3.1 Abstract

In this chapter the effect of temperature in viscoelastic fluid flows is studied applying a stabilized finite element formulation based on both a standard and a log-conformation reformulation (LCR), and the Variational Multiscale (VMS) method as stabilization technique. The log-conformation reformulation turns out to be crucial to solve the cases with a high Weissenberg number. Regarding temperature coupling, a two-way coupling strategy is employed: on the one hand, the dependence of viscoelastic fluid parameters on temperature is established, together with the addition of a new term to the energy equation which takes into account the stress work. The formulations and the iterative algorithms are validated in the well-known flow past a cylinder benchmark. Besides, the extension 1:3 case is studied, in which several scenarios are explored varying the values of the main dimensionless numbers that characterize the problem to see how the flow pattern and temperature distribution change along the channel.

3.2 Background

As it was advanced in the Introduction (Chapter 1), the processes in which polymers are involved are mostly non-isothermal in nature. Flow properties are strongly dependent both on rheology and temperature, therefore there is a high interest to understand the behavior of such type of flows. The combination of high viscosities of polymeric melts and high deformation rates results in the transformation of large amounts of mechanical energy into heat, and consequently in a rising of the material temperature. As remarked in [56], the non-isothermal nonlinear flow is also particularly relevant in many applications, since it is the basis of many complex flow problems with viscoelastic and multiphase fluids. Airflow inside a combustion engine, polymer flow in injection molding, or fluid flow in heat exchange problems, are only a few examples of viscous fluids where the temperature is an important unknown. Concerning viscoelastic materials, stresses now play an important

role on the temperature and temperature history and not only on the deformation (and deformation history). Consequently, the temperature should be an independent variable in the constitutive equations for the stress tensor, as Peters et al. [133] explain in their work. Moreover, the temperature dependence of the linear viscoelastic properties (such as the relaxation time λ) is described by the principle of *time-temperature superposition*. This principle states that all characteristic times of the material depend on temperature similarly and therefore this relation can be described through a function of the temperature. In literature, we have found two main models [68]: the Williams-Landel-Ferry (WLF) function [168] which is widely employed or the Arrhenius relationship [18] (see [113] for a discussion between these two methods). Also, the *time-temperature superposition* principle holds for rheological properties at different constant temperatures, however, it does not describe the consequences of temperature changes in time and space. As it is explained in [133], another difficulty for solving non-isothermal viscoelastic flows comes from the energy equation. Usually, it is assumed that the internal energy of fluids is a function of the temperature uniquely, however, this is not a proper assumption for viscoelastic fluids.

Besides, the energy equation needs to be reconsidered to specify which part of the mechanical power is dissipated and which part is accumulated as elastic energy. One needs to take into account that the deformation of elastic materials is a reversible process since mechanical energy can be stored and released as mechanical energy again. Nevertheless, for purely viscous materials, the deformation is irreversible, due to mechanical energy being completely dissipated. On the contrary, for viscoelastic materials, mechanical energy will be partially stored as elastic energy and partly dissipated. This is taken into account by the stress work in the energy equation, which is computed as the product between stresses and the velocity gradient. For Newtonian fluids it is called *viscous dissipation*, as it is always positive. For viscoelastic fluids we will call it also viscous dissipation if it is positive and this property is exploited.

In literature different works can be found which study the forced convection in pipes and channels using diverse techniques, as [49, 133, 139], and more recent papers as [94] which simulate a 3D viscoelastic flow in a rectangular duct, or [84], where the application to axisymmetric 4:1 contraction flows is developed for non-isothermal flows. Also, the recirculation and thermal regions of viscoelastic flow in the symmetric planar problem for different expansion angles is studied in [150]. Moreover, the optimal control of non-isothermal viscoelastic fluids to minimize vortices and controlling the heat flux is investigated in [102] using finite differences, and also in [54], although in this case using a Newtonian flow but employing the finite element (FE) method. More recently, we found the work [156], where a 3D transient non-isothermal simulation is performed to predict the extrudate shape of viscoelastic fluids emerging from an asymmetric keyhole shaped die.

Regarding free convection examples, numerical experiments can be found in the literature that include these effects, apart from considering the contribution of the stress work into the energy equation, such as Peres et al. [131]. This work explores the significant enhancement of the convection coefficient with respect to the corresponding Newtonian fluid flow, demonstrated experimentally by Hartnett and Kostic [86]. In this case, the variation of the fluid density with temperature is dealt with in a classical way, employing the well-known Boussinesq approximation. Following similar assumptions, in [151], heat transfer is studied in a heated square cavity under the effect of thermal radiation, and [56], where the MIT benchmark 2001 [37] is carried out.

One of the main issues of such simulations, besides robustness and efficiency, is the reliability of the numerical solution. The price to be paid for enhancing the accuracy and robustness properties of such fully coupled approaches is the more expensive solution of

the resulting coupled nonlinear discrete schemes.

In this chapter, we employ two different models to define the constitutive models, both rather similar between them. On the one hand, the Phan-Thien-Tanner (PTT) [134, 135] which is widely employed in non-isothermal fluid flows. The Oldroyd-B model is also used in this work. Also, apart from the standard viscoelastic fluid flow equations, the coupled problem is considered using the log-conformation reformulation introduced first by Fattal and Kupferman in [64, 65], and applied to a FE framework using sub-grid scales in [120], Chapter 2. In the literature, [109] employs the log-conformation reformulation coupled with temperature to study the heat transfer enhancement by elastic turbulence in a curvy channel. Also in [56], the thermal coupling is studied employing the log-conformation reformulation using the FE method.

The Variational Multi-scale Method has been employed to stabilize both, viscoelastic fluid flow and temperature problems, such as it is done in Chapter 2. This stabilized formulation has its beginnings in the methods introduced by Hughes et al. [91] for the scalar convection-diffusion-reaction problem and later extended to the Navier-Stokes problem in [38, 40, 41], where the space of the sub-grid scales was taken as orthogonal to the FE space. This idea was adapted to the three-field Navier-Stokes problem in [25] and later to the viscoelastic flow problem in [26].

Concerning the algorithm employed, it is iterative and non-monolithic, executed in a partitioned manner. This means that in each iteration (or each time-step in the case of a time-dependent simulation) both parameters dependent of temperature in the constitutive and momentum equation and the stress work term in the energy equation are updated.

The purpose of this chapter is to study numerically the effect of the temperature in the viscoelastic fluid flow in two different examples using both the standard and logarithmic reformulation and a term-by-term stabilization scheme. The first example is done to validate the model in the flow past a cylinder. The second one is the 1:3 expansion, an interesting case in which the stationary solution could be asymmetric while the domain is symmetric when the Reynolds number is high enough. In the case of the patterns of viscoelastic fluids other instabilities can be activated because of the elastic component of the fluid, even in flows with low Reynolds number, resulting in a chaotic flow called elastic turbulence [78, 155, 167]. In particular, in [154], the effect in a square-square three-dimensional contraction is studied, obtaining asymmetric flows in a symmetric problem when elasticity grows. Also, in [107] the instabilities and the symmetry of the flow in a symmetric domain are analyzed for flows with high elasticity.

This chapter is structured as follows. In Section 3.3 we present the initial and boundary problem statement, the variational form adopted, the Galerkin FE approximation, and the time discretization. Section 3.5 details the stabilized formulation employed for the thermal coupling. Finally, in Section 3.6 we present the benchmarks computed to validate the code and to explore the effect of temperature in viscoelastic fluid flows. Finally, the conclusions are summarized in Section 3.7.

3.3   Thermally coupled viscoelastic fluid flows

In this section, the equations that involve the coupled problem are presented, taking into account the proper modifications for both the viscoelastic fluid flow problem and the temperature problem.

3.3.1   Initial and boundary value problem

First of all we present briefly the standard equations that describe the viscoelastic fluid flow problem considering that now the different fluid parameters such as relaxation time λ and the total viscosity η_0 have a dependency with the temperature unknown. We consider the fluid moving in a domain denoted by $\Omega \subset \mathbb{R}^d$, taking $d = 2$ or 3 depending on whether the problem is two or three dimensional. The flow takes place during the time interval $[0, T]$. The momentum, continuity, constitutive and energy equations are written as follows:

$$\rho \frac{\partial \boldsymbol{u}}{\partial t} + \rho \boldsymbol{u} \cdot \nabla \boldsymbol{u} - \nabla \cdot (2\eta_s(\vartheta)\nabla^s \boldsymbol{u}) - \nabla \cdot \boldsymbol{\sigma} + \nabla p = \boldsymbol{f} \text{ in } \Omega, t \in]0, T[, \qquad (3.1)$$

$$\nabla \cdot \boldsymbol{u} = 0 \text{ in } \Omega, t \in]0, T[, \qquad (3.2)$$

$$\frac{1}{2\eta_p(\vartheta)} \left(\mathbf{I} + \mathfrak{h}(\boldsymbol{\sigma})\right) \cdot \boldsymbol{\sigma} - \nabla^s \boldsymbol{u} + \frac{\lambda(\vartheta)}{2\eta_p(\vartheta)} \left(\frac{\partial \boldsymbol{\sigma}}{\partial t} + \boldsymbol{u} \cdot \nabla \boldsymbol{\sigma}\right)$$

$$- \frac{\lambda(\vartheta)}{2\eta_p(\vartheta)} \left(\boldsymbol{\sigma} \cdot \nabla \boldsymbol{u} + (\nabla \boldsymbol{u})^T \cdot \boldsymbol{\sigma}\right) = \mathbf{0}, \text{ in } \Omega, t \in]0, T[, \qquad (3.3)$$

$$\rho C_p \left(\frac{\partial \vartheta}{\partial t} + \boldsymbol{u} \cdot \nabla \vartheta\right) - k\Delta\vartheta - \boldsymbol{\sigma} : \nabla^s \boldsymbol{u} = 0, \text{ in } \Omega, t \in]0, T[\qquad (3.4)$$

where ρ denotes the constant density, $p : \Omega \times]0, T[\to \mathbb{R}$ is the pressure field, $\boldsymbol{u} : \Omega \times]0, T[\to \mathbb{R}^d$ is the velocity field, $\vartheta : \Omega \times]0, T[\to \mathbb{R}$ is the temperature field, $\boldsymbol{\sigma} : \Omega \times]0, T[\to \mathbb{R}^d \otimes \mathbb{R}^d$ is the viscoelastic or elastic stress tensor, $\boldsymbol{f} : \Omega \times]0, T[\to \mathbb{R}^d$ is the force field. Note that the third and fourth terms in the left-hand-side of equation (3.1) correspond to the divergence of the deviatoric extra stress tensor, $\boldsymbol{T} : \Omega \times]0, T[\to \mathbb{R}^d \otimes \mathbb{R}^d$, defined in terms of the viscous and the viscoelastic contribution as $\boldsymbol{T} = 2\eta_s \nabla^s \boldsymbol{u} + \boldsymbol{\sigma}$.

In the energy equation (3.4), C_p denotes the specific heat and k is the thermal conductivity, considered constant.

With reference to the constitutive equation (3.3), η_s represents the effective viscosity (or solvent viscosity), $\nabla^s \boldsymbol{u}$ is the symmetrical part of the velocity gradient and λ is the relaxation time and η_p represents the polymeric viscosity. Note that equations (3.1)-(3.3) are written for the isothermal case in the Section 2.3.1 in the Chapter 2, with the difference that now η_p, η_s and λ are allowed to depend on the temperature ϑ, although λ and η_p must scale in the same way with respect to it and therefore its quotient can be evaluated with a reference temperature ϑ_0 (see below). In Section 2.3.1 also the meaning of each term of the constitutive equation is explained, together with the relation between total viscosity η_0 and effective (or solvent) and polymeric viscosity. Nevertheless the relation will be recalled here. For that, an additional parameter $\beta \in [0, 1]$ is introduced, so that $\eta_s = \beta\eta_0$ and $\eta_p = (1 - \beta)\eta_0$. Finally, $\mathfrak{h}(\boldsymbol{\sigma})$ is a tensor that adopts different expressions depending on the constitutive equation considered. In the case of the Oldroyd-B model, tensor $\mathfrak{h}(\boldsymbol{\sigma})$ is taken as a null tensor; however for the Giesekus model [73] this tensor is equal to $\frac{\varepsilon\lambda}{\eta_p}\boldsymbol{\sigma}$, where ε is the constant called *mobility factor*, and is related to the elongational behavior of the fluids and considered to be positive. Similarly, for the Phan-Thien-Tanner (PTT) model [134] the tensor adopts the form $\frac{\varepsilon\lambda}{\eta_p}\mathrm{tr}\,(\boldsymbol{\sigma})\,\mathbf{I}$, where $\mathrm{tr}(\boldsymbol{\sigma})$ is the trace of the stress tensor. Note that when $\varepsilon = 0$ the two models reduce to the Oldroyd-B rheological model. Also, we have to remark that, in the Giesekus and PTT models, another non-linearity is considered in the constitutive equation, defined by the product $\mathfrak{h}(\boldsymbol{\sigma}) \cdot \boldsymbol{\sigma}$. This term enables a simple qualitative description of several well-known properties of viscoelastic fluids, namely, shear-thinning, the non-zero second normal stress coefficient and the stress overshoot in transient shear flows [121]. The PTT model is one of the most used approaches in the literature when non-isothermal viscoelastic fluid flow problems are addressed, and
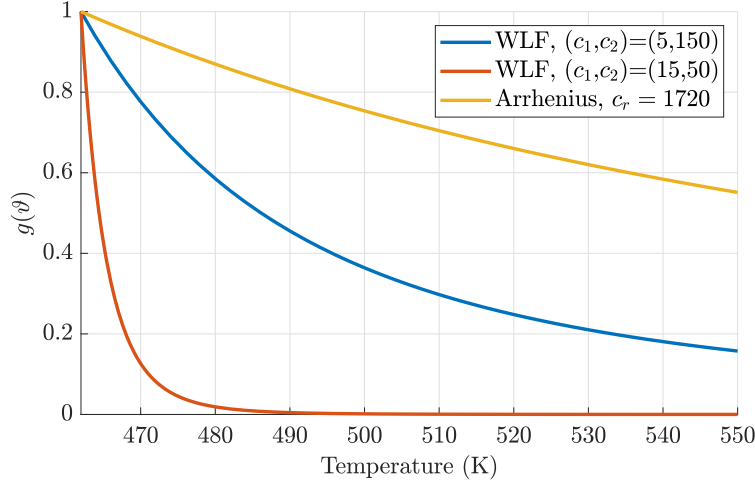
Figure 3.1: Comparison between different models for the temperature dependence for the viscoelastic fluid flow parameters considering $\vartheta_0 = 462$ K.

we will also consider it for some numerical computations. In [102], it is argued that the motivation of using the linearized PTT mode instead of the Oldroyd-B model is that it avoids some shortcomings when the Weissenberg number increases, due to the non-linear term discussed and a positive parameter related to the elongational behavior of the fluid which tends to lower the stresses resulting from the computations.

As it was explained in the background (Section 3.2 of this chapter), the temperature dependence of the viscoelastic properties is defined by the principle of *time-temperature superposition*, in which that dependence is established through temperature functions. There are different functions to define accurately this relation, although the most used ones are those presented next. The first one is the Williams-Landel-Ferry (WLF) function [168], defined as follows:

$$g_{\mathrm{wlf}}(\vartheta) = \exp\left[-\frac{c_a(\vartheta - \vartheta_0)}{c_b + (\vartheta - \vartheta_0)}\right]$$

where ϑ_0 is the reference temperature and c_a and c_b are constants. Typical extreme sets of WLF parameters (c_a, c_b) are $(5, 150)$ for temperatures relatively far from the glass transition temperature ϑ_g, leading to thermorheological coupling, and $(15, 50)$ for temperatures relatively close to ϑ_g. The second one employed in this work is the Arrhenius function, it is given by

$$g_{\mathrm{a}}(\vartheta) = \exp\left[c_r\left(\frac{1}{\vartheta} - \frac{1}{\vartheta_0}\right)\right]$$

where in this case c_r is a constant parameter and ϑ_0 is the reference temperature given in Kelvin. The constant c_r is considered 1720 K, as done in [123, 150]. In Figure 3.1 the two extreme set of parameters for the Williams-Landel-Ferry function, and the Arrhenius function considering $c_r = 1720$ K have been plot. In both functions, the temperature of reference has been fixed to 462 K to compare the shape of the curves. Note that for the WLF function, if ϑ_0 is near the glass transition temperature; viscosity and relaxation time vary significantly with ϑ, as it can be observed in the plots. As it was advanced in the introduction, in the work of Lomellini [113], an extensive discussion is presented about which of the two methods (WLF or Arrhenius) is more accurate, the conclusion being that the WLF approach is quite general as it applies to a lot of materials as polymer melt

solutions and organic and inorganic glass-forming liquids when the temperature approaches the glass transition. However, an Arrhenius behavior is reported to better fit polyolefins and polycaprolactam liquids. To sum up, the conclusion is that the WLF model is the best representation of the data over the whole temperature range. Finally, the relation between temperature and viscoelastic properties is established as follows:

$$\lambda(\vartheta) = \lambda(\vartheta_0)g(\vartheta)$$
$$\eta_0(\vartheta) = \eta_0(\vartheta_0)g(\vartheta)$$

where g is the shift factor that will be equal to g_{wlf} or g_{a} depending on the considered model, and $\lambda(\vartheta_0)$ and $\eta_0(\vartheta_0)$ are known values for the reference temperature ϑ_0. Note that considering the previous expressions, in equation (3.3) the quotient $\frac{\lambda(\vartheta)}{\eta_0(\vartheta)}$ is a constant. Therefore, from this point we define $\Lambda(\vartheta_0)$ as $\Lambda(\vartheta_0) = \frac{\lambda(\vartheta_0)}{\eta_0(\vartheta_0)}$.

In the case of taking into account free convection, the Boussinesq approximation will be considered, adding a body force term in the momentum equation (3.1):

$$\gamma \boldsymbol{g}(\vartheta - \vartheta_0)$$

where γ is the thermal expansion coefficient and $\boldsymbol{g}$ is the gravity acceleration vector.

Now, a remark about the modification in the energy equation (3.4) must be done. Following the work of Peters and Baaijens [133] two additional terms are considered in the energy equations when the PTT model is considered as the constitutive equation. The energy balance equation is in this case as follows:

$$\rho C_p \left(\frac{\partial \vartheta}{\partial t} + \boldsymbol{u} \cdot \nabla \vartheta \right) - k\Delta\vartheta = \alpha\boldsymbol{\sigma} : \nabla^s \boldsymbol{u} + (1-\alpha)\frac{\text{tr}(\boldsymbol{\sigma})}{2\bar{\lambda}}, \text{ in } \Omega, t \in]0, T[$$

where α is a constant, and $\bar{\lambda} = \lambda \left(1 + \frac{\lambda\varepsilon\text{tr}(\boldsymbol{\sigma})}{\eta_p} \right)^{-1}$. Note that the two last terms on the right-hand side have been added to the classical energy equation, although for the case $\alpha = 1$ the standard expression would be recovered. The first term is the contribution of the entropy elasticity and the second expresses the contribution of the energy elasticity. In [133] it is argued that there are two extreme cases: $\alpha = 1$ that corresponds with the case of pure entropy elasticity and $\alpha = 0$ that is the case of pure energy elasticity. In the same work, the authors demonstrate that the effect of the parameter α is very small because with a fully-developed shear flow there will be no internal energy storage, and only stress work matters. Therefore, as it remarked in [131] the two α terms will cancel up and the final result will be mathematically equivalent to setting $\alpha = 1$, which is also argued in other works [48, 165]. Following the same arguments, in this work we will suppose that the parameter α is 1 in all cases. Therefore, the considered energy equation is (3.4). Note that in the case of coupling with an Oldroyd-B fluid, the expression for the energy equation would also be (3.4). The heat source term is thus the classical one, i.e. the product between stresses and the symmetric gradient of velocities and represents the internal heat produced by internal work.

Therefore the differential equations of the initial and boundary value problem for the standard formulation are (3.1)-(3.4).

From this point, in order to distinguish operators between standard and log-conformation reformulations, we will employ the subscripts "std" and "log", respectively. Let us define

$\boldsymbol{U} = [\boldsymbol{u}, p, \boldsymbol{\sigma}, \vartheta]$, $\boldsymbol{F}_{\mathrm{std}} = [\boldsymbol{f}, 0, \boldsymbol{0}, 0]$,

$$\mathcal{L}_{\mathrm{std}}(\hat{\boldsymbol{U}}; \boldsymbol{U}) := \begin{pmatrix} -\nabla \cdot \boldsymbol{\sigma} - \nabla \cdot (2\eta_s(\hat{\vartheta})\nabla^s \boldsymbol{u}) + \rho \hat{\boldsymbol{u}} \cdot \nabla \boldsymbol{u} + \nabla p \\ \nabla \cdot \boldsymbol{u} \\ \dfrac{1}{2\eta_p(\hat{\vartheta})}(\mathbf{I} + \mathfrak{h}(\hat{\boldsymbol{\sigma}})) \cdot \boldsymbol{\sigma} - \nabla^s \boldsymbol{u} + \Lambda(\vartheta_0)\left(g_{\mathrm{std}}(\hat{\boldsymbol{u}}, \boldsymbol{\sigma})\right) \\ \rho C_p \hat{\boldsymbol{u}} \cdot \nabla \vartheta - k\Delta\vartheta - \hat{\boldsymbol{\sigma}} : \nabla^s \hat{\boldsymbol{u}} \end{pmatrix} \tag{3.5}$$

and

$$\mathcal{D}_{\mathrm{std}}\left(\hat{\vartheta}; \boldsymbol{U}\right) := \begin{pmatrix} \rho \dfrac{\partial \boldsymbol{u}}{\partial t} \\ 0 \\ \Lambda(\vartheta_0)\dfrac{\partial \boldsymbol{\sigma}}{\partial t} \\ \rho C_p \dfrac{\partial \vartheta}{\partial t} \end{pmatrix},$$

where $g_{\mathrm{std}}(\hat{\boldsymbol{u}}, \boldsymbol{\sigma}) = \hat{\boldsymbol{u}} \cdot \nabla \boldsymbol{\sigma} - \boldsymbol{\sigma} \cdot \nabla \hat{\boldsymbol{u}} - (\nabla \hat{\boldsymbol{u}})^T \cdot \boldsymbol{\sigma}$ are the convective and the rotational terms. Equations (3.1), (3.2) and (3.3) can be rewritten, considering $\mathcal{D}_t = \mathcal{D}_{\mathrm{std}}$, $\mathcal{L} = \mathcal{L}_{\mathrm{std}}$ and $\boldsymbol{F} = \boldsymbol{F}_{\mathrm{std}}$, as:

$$\mathcal{D}_t(\vartheta; \boldsymbol{U}) + \mathcal{L}(\boldsymbol{U}; \boldsymbol{U}) = \boldsymbol{F}. \tag{3.6}$$

These equations need to be completed with initial and boundary conditions to close the problem. For simplicity, we suppose the boundary condition for the velocity $\boldsymbol{u} = \boldsymbol{0}$ on $\partial\Omega$ for all time. Elastic stress conditions do not need to be prescribed. Finally, for the temperature, similarly to the velocity, we suppose $\vartheta = 0$ on $\partial\Omega$, in other words, we assume homogeneous Dirichlet boundary conditions for both velocity and temperature. This will allow us to simplify the writing, for example because unknowns and test functions of the variational form of the problem will belong to the same space. However, in the numerical examples we shall use non-homogeneous boundary conditions that can be implemented as usual by shifting the unknowns with the boundary-value functions. Regarding the initial conditions, we will set velocity, stresses and temperature to $\boldsymbol{u} = \boldsymbol{u}^0$, $\boldsymbol{\sigma} = \boldsymbol{\sigma}^0$ and $\vartheta = \vartheta^0$ at time $t = 0$ where $\boldsymbol{u}^0$, $\boldsymbol{\sigma}^0$ and ϑ^0 are functions defined on the whole domain Ω.

Now, we will define the set of equations in strong form for the log-conformation reformulation (see [120], or the Chapter 2 for more details), taking into account the modifications considered above regarding the viscoelastic parameters and the additional term for the energy equation. The reformulation is derived basically from a change of variables, where the stress tensor is replaced by $\boldsymbol{\sigma} = \dfrac{\eta_p}{\lambda_0}(\boldsymbol{\tau} - \mathbf{I})$, and in turn, the conformation tensor $\boldsymbol{\tau}$ is written as $\boldsymbol{\tau} = \exp(\boldsymbol{\psi})$ in (3.1), (3.2) and (3.3). Particularly, λ_0 is linearly dependent with λ and is defined as $\lambda_0 = \max\{k\lambda, \lambda_{0,\min}\}$, being k a constant and $\lambda_{0,\min}$ a given threshold. As it is detailed in [120], in the numerical experiments we have found useful to take k small, so that $\lambda_0 < \lambda$; this has allowed us to obtain converged solutions that we have not been able to get for $k = 1$. Clearly, for $k \leq 1$ we can ensure that the conformation tensor is always symmetric and positive. In the case of thermal coupling, λ_0 also depends on the temperature through the dependence with λ. Therefore, the strong form of the problem consists in finding $\boldsymbol{u}$, p, $\boldsymbol{\psi}$, ϑ solving the next set of equations over the domain Ω and in the interval $[0, T]$:

$$\rho\frac{\partial \boldsymbol{u}}{\partial t} - \nabla \cdot \frac{\eta_p(\vartheta)}{\lambda_0(\vartheta)}\exp(\boldsymbol{\psi}) - \nabla \cdot 2\eta_s(\vartheta)\nabla^s \boldsymbol{u} + \rho \boldsymbol{u} \cdot \nabla \boldsymbol{u} + \nabla p = \boldsymbol{f}, \tag{3.7}$$

$$\nabla \cdot \boldsymbol{u} = 0, \tag{3.8}$$

$$\frac{1}{2\lambda_0(\vartheta)}\left(\exp(\boldsymbol{\psi}) - \boldsymbol{I}\right) \cdot \left(\mathfrak{h}(\exp(\boldsymbol{\psi})) + \boldsymbol{I}\right) - \nabla^{\mathrm{s}}\boldsymbol{u} + \frac{\lambda(\vartheta)}{2\lambda_0(\vartheta)}\left(\frac{\partial \exp(\boldsymbol{\psi})}{\partial t}\right.$$

$$+ \boldsymbol{u} \cdot \nabla \exp(\boldsymbol{\psi}) - \exp(\boldsymbol{\psi}) \cdot \nabla\boldsymbol{u} - (\nabla\boldsymbol{u})^T \cdot \exp(\boldsymbol{\psi}) + 2\nabla^{\mathrm{s}}\boldsymbol{u}\bigg) = \boldsymbol{0}, \tag{3.9}$$

$$\rho C_p \left(\frac{\partial \vartheta}{\partial t} + \boldsymbol{u} \cdot \nabla\vartheta\right) - k\Delta\vartheta - \left(\frac{\eta_p(\vartheta)}{\lambda_0(\vartheta)}\exp(\boldsymbol{\psi}) - \boldsymbol{I}\right) : \nabla^s \boldsymbol{u} = 0. \tag{3.10}$$

Considering again the expressions of viscoelastic parameters, we can define $\Upsilon_1(\vartheta_0) = \frac{\eta_p(\vartheta_0)}{\lambda_0(\vartheta_0)}$ and $\Upsilon_2(\vartheta_0) = \frac{\lambda(\vartheta_0)}{2\lambda_0(\vartheta_0)}$. Analogously to what was done for the standard formulation, calling $\boldsymbol{U} = [\boldsymbol{u}, p, \boldsymbol{\psi}, \vartheta]$ and $\boldsymbol{F}_{\log} = [\boldsymbol{f}, 0, \boldsymbol{0}, 0]$, the differential equation of the problem can be written as $\mathcal{D}_{\log}(\vartheta; \boldsymbol{U}) + \mathcal{L}_{\log}(\boldsymbol{U}; \boldsymbol{U}) = \boldsymbol{F}_{\log}$, where

$$\mathcal{L}_{\log}(\hat{\boldsymbol{U}}; \boldsymbol{U}) := \begin{pmatrix} -\nabla \cdot \Upsilon_1(\vartheta_0)\exp(\boldsymbol{\psi}) - \nabla \cdot 2\eta_s(\hat{\vartheta})\nabla^s\boldsymbol{u} + \rho\hat{\boldsymbol{u}} \cdot \nabla\boldsymbol{u} + \nabla p \\ \nabla \cdot \boldsymbol{u} \\ \frac{1}{2\lambda_0(\hat{\vartheta})}\left(\exp(\hat{\boldsymbol{\psi}}) - \boldsymbol{I}\right) \cdot \left(\mathfrak{h}(\exp(\boldsymbol{\psi})) + \boldsymbol{I}\right) - \nabla^s\boldsymbol{u} + \Upsilon_2(\vartheta_0)g_{\log}(\hat{\boldsymbol{u}}; \boldsymbol{u}, \boldsymbol{\psi}) \\ \rho C_p\left(\hat{\boldsymbol{u}} \cdot \nabla\vartheta\right) - k\Delta\vartheta - \left(\Upsilon_1(\vartheta_0)\exp(\hat{\boldsymbol{\psi}}) - \boldsymbol{I}\right) : \nabla^s\hat{\boldsymbol{u}} \end{pmatrix}$$
$$\tag{3.11}$$

and

$$\mathcal{D}_{\log}(\boldsymbol{U}) := \begin{pmatrix} \rho\dfrac{\partial \boldsymbol{u}}{\partial t} \\ 0 \\ \Upsilon_2(\vartheta_0)\dfrac{\partial \exp(\boldsymbol{\psi})}{\partial t} \\ \rho C_p\dfrac{\partial \vartheta}{\partial t} \end{pmatrix},$$

where $g_{\log}(\hat{\boldsymbol{u}}; \boldsymbol{u}, \boldsymbol{\psi}) = \hat{\boldsymbol{u}} \cdot \nabla\left(\exp(\boldsymbol{\psi})\right) - \exp(\boldsymbol{\psi}) \cdot \nabla\hat{\boldsymbol{u}} - (\nabla\hat{\boldsymbol{u}})^T \cdot \exp(\boldsymbol{\psi}) + 2\nabla^s\boldsymbol{u}$ are the convective and rotational terms.

In this case the boundary and initial conditions are similar to the ones described above, but now instead of $\boldsymbol{\sigma}$ we have the dimensionless tensor $\boldsymbol{\psi}$, which will adopt the value $\boldsymbol{\psi} = \boldsymbol{\psi}^0$ at time $t = 0$.

3.3.2 Variational form

The notation employed for the spaces and that is important for defining the variational form of the problem is properly indicated in Section 2.3.3 of the Chapter 2. Using this notation, velocity, pressure and stress FE spaces for the continuous problem are: $\boldsymbol{V}_0 = H_0^1(\Omega)^d$ for the velocity, $\mathcal{Q} = L^2(\Omega)/\mathbb{R}$ for the pressure, $\boldsymbol{\Upsilon} = H^1(\Omega)_{\mathrm{sym}}^{d \times d}$ for the stresses in the standard formulation (the subscript standing for symmetric tensors), and for the temperature $\mathcal{T} = H_0^1(\Omega)$ for each fixed time t. Therefore, the weak form of the coupled for the standard formulation problem consists in finding $\boldsymbol{U} = [\boldsymbol{u}, p, \boldsymbol{\sigma}, \vartheta] :]0, T[\longrightarrow \boldsymbol{\mathcal{X}} := \boldsymbol{V}_0 \times \mathcal{Q} \times \boldsymbol{\Upsilon} \times \mathcal{T}$, such that the initial conditions are satisfied and:

$$\left(\rho\frac{\partial \boldsymbol{u}}{\partial t}, \boldsymbol{v}\right) + (\boldsymbol{\sigma}, \nabla^s\boldsymbol{v}) + 2(\eta_s(\vartheta)\nabla^s\boldsymbol{u}, \nabla^s\boldsymbol{v}) + \langle\rho\boldsymbol{u} \cdot \nabla\boldsymbol{u}, \boldsymbol{v}\rangle - (p, \nabla \cdot \boldsymbol{v}) = \langle\boldsymbol{f}, \boldsymbol{v}\rangle,$$

$$(q, \nabla \cdot \boldsymbol{u}) = 0,$$

$$\left(\frac{1}{2\eta_p(\vartheta)}\left(\boldsymbol{I} + \mathfrak{h}(\boldsymbol{\sigma})\right) \cdot \boldsymbol{\sigma}, \boldsymbol{\chi}\right) - (\nabla^s\boldsymbol{u}, \boldsymbol{\chi}) + \Lambda(\vartheta_0)\left(\frac{\partial \boldsymbol{\sigma}}{\partial t} + \boldsymbol{u} \cdot \nabla\boldsymbol{\sigma}, \boldsymbol{\chi}\right)$$

$$-\Lambda(\vartheta_0)\left(\boldsymbol{\sigma} \cdot \nabla\boldsymbol{u} + (\nabla\boldsymbol{u})^T \cdot \boldsymbol{\sigma}, \boldsymbol{\chi}\right) = 0,$$

$$\rho C_p \left(\frac{\partial \vartheta}{\partial t} + \boldsymbol{u} \cdot \nabla \vartheta, \xi \right) + (k \nabla \vartheta, \nabla \xi) - (\boldsymbol{\sigma} : \nabla^s \boldsymbol{u}, \xi) = 0,$$

for all $\boldsymbol{V} = [\boldsymbol{v}, q, \boldsymbol{\chi}, \xi] \in \boldsymbol{\mathcal{X}}$. In compact form, the problem can be written as:

$$\mathcal{G}_{\mathrm{std}}(\vartheta; \boldsymbol{U}, \boldsymbol{V}) + B_{\mathrm{std}}(\boldsymbol{U}; \boldsymbol{U}, \boldsymbol{V}) = L_{\mathrm{std}}(\boldsymbol{V}), \tag{3.12}$$

for all $\boldsymbol{V} \in \boldsymbol{\mathcal{X}}$, where

$$\mathcal{G}_{\mathrm{std}}(\boldsymbol{U}, \boldsymbol{V}) = \left(\rho \frac{\partial \boldsymbol{u}}{\partial t}, \boldsymbol{v} \right) + \Lambda(\vartheta_0) \left(\frac{\partial \boldsymbol{\sigma}}{\partial t}, \boldsymbol{\chi} \right) + \rho C_p \left(\frac{\partial \vartheta}{\partial t}, \xi \right), \tag{3.13}$$

$$B_{\mathrm{std}}(\hat{\boldsymbol{U}}; \boldsymbol{U}, \boldsymbol{V}) = 2(\eta_s(\hat{\vartheta}) \nabla^s \boldsymbol{u}, \nabla^s \boldsymbol{v}) + \langle \rho \hat{\boldsymbol{u}} \cdot \nabla \boldsymbol{u}, \boldsymbol{v} \rangle + (\boldsymbol{\sigma}, \nabla^s \boldsymbol{v})$$

$$- (p, \nabla \cdot \boldsymbol{v}) + (q, \nabla \cdot \boldsymbol{u}) + \left(\frac{1}{2\eta_p(\hat{\vartheta})} (\mathbf{I} + \mathfrak{h}(\hat{\boldsymbol{\sigma}})) \cdot \boldsymbol{\sigma}, \boldsymbol{\chi} \right)$$

$$- (\nabla^s \boldsymbol{u}, \boldsymbol{\chi}) + \Lambda(\vartheta_0) \left(\hat{\boldsymbol{u}} \cdot \nabla \boldsymbol{\sigma} - \boldsymbol{\sigma} \cdot \nabla \hat{\boldsymbol{u}} - (\nabla \hat{\boldsymbol{u}})^T \cdot \boldsymbol{\sigma}, \boldsymbol{\chi} \right)$$

$$+ \rho C_p (\hat{\boldsymbol{u}} \cdot \nabla \vartheta, \xi) + (k \nabla \vartheta, \nabla \xi) - (\hat{\boldsymbol{\sigma}} : \nabla^s \hat{\boldsymbol{u}}, \xi), \tag{3.14}$$

$$L_{\mathrm{std}}(\boldsymbol{V}) = \langle \boldsymbol{f}, \boldsymbol{v} \rangle. \tag{3.15}$$

Analogously, considering now the logarithmic reformulation of the viscoelastic flow problem, the spaces for the velocity, pressure and temperature for the continuous problems are the ones defined above for the standard formulation. However, now the space for tensor $\boldsymbol{\psi}$ is denoted by $\bar{\boldsymbol{\Upsilon}}$ for each fixed time t, where an appropriate regularity is assumed (see [120]). So, in this case the weak form of the problem consists in finding $\boldsymbol{U} = [\boldsymbol{u}, p, \boldsymbol{\psi}, \vartheta]$: $]0, T[\longrightarrow \bar{\boldsymbol{\mathcal{X}}} := \boldsymbol{V}_0 \times \mathcal{Q} \times \bar{\boldsymbol{\Upsilon}} \times \mathcal{T}$, such that the initial conditions are satisfied and for all $\boldsymbol{V} = [\boldsymbol{v}, q, \boldsymbol{\chi}, \xi] \in \boldsymbol{\mathcal{X}}$,

$$\mathcal{G}_{\mathrm{log}}(\vartheta; \boldsymbol{U}, \boldsymbol{V}) + B_{\mathrm{log}}(\boldsymbol{U}; \boldsymbol{U}, \boldsymbol{V}) = L_{\mathrm{log}}(\vartheta; \boldsymbol{V}), \tag{3.16}$$

where each term is defined as

$$\mathcal{G}_{\mathrm{log}}(\hat{\vartheta}; \boldsymbol{U}, \boldsymbol{V}) = \left(\rho \frac{\partial \boldsymbol{u}}{\partial t}, \boldsymbol{v} \right) + \left(\Upsilon_2(\vartheta_0) \frac{\partial \exp(\boldsymbol{\psi})}{\partial t}, \boldsymbol{\chi} \right) + \rho C_p \left(\frac{\partial \vartheta}{\partial t}, \xi \right), \tag{3.17}$$

$$B_{\mathrm{log}}(\hat{\boldsymbol{U}}; \boldsymbol{U}, \boldsymbol{V}) = (\Upsilon_1(\vartheta_0) \exp(\boldsymbol{\psi}), \nabla^s \boldsymbol{v}) + 2(\eta_s(\hat{\vartheta}) \nabla^s \boldsymbol{u}, \nabla^s \boldsymbol{v}) + \langle \rho \hat{\boldsymbol{u}} \cdot \nabla \boldsymbol{u}, \boldsymbol{v} \rangle$$

$$- (p, \nabla \cdot \boldsymbol{v}) + (\nabla \cdot \boldsymbol{u}, q) + \left(\frac{1}{2\lambda_0(\hat{\vartheta})} (\exp(\boldsymbol{\psi} - \mathbf{I})) \cdot \left(\mathfrak{h}(\exp(\hat{\boldsymbol{\psi}})) + \mathbf{I} \right), \boldsymbol{\chi} \right)$$

$$- (\nabla^s \boldsymbol{u}, \boldsymbol{\chi}) + (\Upsilon_2(\vartheta_0) (\hat{\boldsymbol{u}} \cdot \nabla \exp(\boldsymbol{\psi}) - \exp(\boldsymbol{\psi}) \cdot \nabla \hat{\boldsymbol{u}}), \boldsymbol{\chi})$$

$$- \left(\Upsilon_2(\vartheta_0) \left((\nabla \hat{\boldsymbol{u}})^T \cdot \exp(\boldsymbol{\psi}) - 2\nabla^s \boldsymbol{u} \right), \boldsymbol{\chi} \right)$$

$$+ \rho C_p (\hat{\boldsymbol{u}} \cdot \nabla \vartheta, \xi) + (k \nabla \vartheta, \nabla \xi) - \left(\Upsilon_1(\vartheta_0) \left(\exp(\hat{\boldsymbol{\psi}}) - \mathbf{I} : \nabla^s \hat{\boldsymbol{u}} \right), \xi \right), \tag{3.18}$$

$$L_{\mathrm{log}}(\hat{\vartheta}; \boldsymbol{V}) = \langle \boldsymbol{f}, \boldsymbol{v} \rangle. \tag{3.19}$$

Note that the space of the test functions is the same as for the standard formulation, i.e., the change of variables is made for the stress unknown, but not for the stress test function as it was indicated in the Section 2.3.3 of the Chapter 2.

For the coupled problem, we have to consider several dimensionless numbers to characterize the problem. On the one hand, we have the Reynolds number, which comes from the Navier-Stokes equations and relates inertial and viscous forces. Secondly, we have the

Weissenberg number, a dimensionless number essential to characterize viscoelastic fluid flow problems. This, as it was already defined, indicates the relevance of the elastic terms of the constitutive equation, and compares elastic forces with viscous forces. Regarding the dimensionless number associated with the energy equation, we have selected the Prandtl number, which relates transport with thermal diffusivity. Finally, we need a global dimensionless number able to describe how strong is the coupling between the fluid flow and the temperature model. With this finality, we consider the Brinkman number, which compares the inertial power with the heat conduction. Therefore we have a total of four dimensionless number to define each coupled problem:

$$\text{Reynolds number:}\qquad \text{Re} = \frac{\rho L U}{\eta_0}, \quad \text{Prandtl number:}\qquad \text{Pr} = \frac{\eta_0 C_p}{k_f},$$

$$\text{Weissenberg number:}\quad \text{We} = \frac{\lambda U}{L}, \quad \text{Brinkman number:}\quad \text{Br} = \frac{\eta_0 U^2}{k_f \left(\vartheta_w - \vartheta_i \right)},$$

where L is the characteristic length, U the characteristic velocity of the problem, ϑ_w is the temperature on a reference wall and ϑ_i is the temperature at the inflow. The remaining parameters that appear in the previous expressions are properties that correspond to the viscoelastic fluid flow problem or the temperature problem, and which are explained in the previous sections.

3.4   Galerkin finite element discretization and time discretization

Once the variational problems for both formulations (3.12) and (3.16) have been defined, the Galerkin approximation can be established. The FE partition of the domain Ω is denoted by $\mathcal{P}_h = \{K\}$. Likewise, the diameter of an element $K \in \mathcal{P}_h$ is denoted by h_K and the diameter of the partition is defined as $h = \max\{h_K | K \in \mathcal{P}_h\}$.

So, for the standard formulation, from $\mathcal{P}_h$ we may construct conforming FE spaces for the velocity, the pressure, the elastic stress and the temperature, $\boldsymbol{\mathcal{V}}_h \subset \boldsymbol{\mathcal{V}}$, $\mathcal{Q}_h \subset \mathcal{Q}$, $\boldsymbol{\Upsilon}_h \subset \boldsymbol{\Upsilon}$ and $\mathcal{T}_h \subset \mathcal{T}$, respectively. Calling $\boldsymbol{\mathcal{X}}_h := \boldsymbol{\mathcal{V}}_h \times \mathcal{Q}_h \times \boldsymbol{\Upsilon}_h \times \mathcal{T}_h$, the Galerkin FE approximation of the problem consists in finding $\boldsymbol{U}_h :]0, T[\longrightarrow \boldsymbol{\mathcal{X}}_h$, such that:

$$\mathcal{G}_{\text{std}}(\vartheta_h; \boldsymbol{U}_h, \boldsymbol{V}_h) + B_{\text{std}}(\boldsymbol{U}_h; \boldsymbol{U}_h, \boldsymbol{V}_h) = L_{\text{std}}(\boldsymbol{V}_h),$$

for all $\boldsymbol{V}_h = [\boldsymbol{v}_h, q_h, \boldsymbol{\chi}_h, \xi_h] \in \boldsymbol{\mathcal{X}}_h$, and satisfying the appropriate initial conditions.

Now, for the logarithmic conformation reformulation, from $\mathcal{T}_h$ we construct the FE space for the new variable $\boldsymbol{\psi}$, $\bar{\boldsymbol{\Upsilon}}_h \subset \bar{\boldsymbol{\Upsilon}}$. $\bar{\boldsymbol{\mathcal{X}}}_h := \boldsymbol{\mathcal{V}}_h \times \mathcal{Q}_h \times \bar{\boldsymbol{\Upsilon}}_h \times \mathcal{T}_h$ is the Galerkin FE space now, and the Galerkin approximation consists in finding $\boldsymbol{U}_h :]0, T[\longrightarrow \bar{\boldsymbol{\mathcal{X}}}_h$, such that

$$\mathcal{G}_{\log}(\vartheta_h; \boldsymbol{U}_h, \boldsymbol{V}_h) + B_{\log}(\boldsymbol{U}_h; \boldsymbol{U}_h, \boldsymbol{V}_h) = L_{\log}(\vartheta_h; \boldsymbol{V}_h),$$

for all $\boldsymbol{V}_h = [\boldsymbol{v}_h, q_h, \boldsymbol{\chi}_h, \xi_h] \in \boldsymbol{\mathcal{X}}_h$. We have to remark that the Galerkin approximation is not enough to obtain a stable formulation unless convective terms are not relevant and the appropriate compatibility conditions on the FE spaces hold. Therefore, the next section presents a stable formulation. Regarding the time discretization in this chapter the backward differencing (BDF) scheme is considered, in particular BDF1. The first order scheme is not the best discretization to capture time-dependent responses. However, the numerical examples presented in this chapter have a steady-state solution, and therefore a BDF1 scheme with a uniform partition of size δt will be suitable in these cases. The time

step level will be denoted with a superscript. In Section 2.3.6 the BDF approximation is properly defined. Moreover, for the log-conformation reformulation we need to obtain the linearized expression for the time derivative of the exponential, such as it was explained the Chapter 2.

3.5 Stabilized finite element formulation

In this section, we will describe briefly the stabilized formulation employed for the thermal coupling. For both formulations, standard and logarithmic, the stabilization used departs from the Variational Multi-Scale (VMS) method, widely described in [91]. This method was already described briefly in Section 2.4 of Chapter 2. The method consists in splitting the unknowns $\boldsymbol{U}$ into two different parts: the component that is computed by the FE space, denoted by $\boldsymbol{U}_h$ and the part that cannot be solved by the FE space, called subgrid scale and which is denoted by $\tilde{\boldsymbol{U}}$. The stabilized method employed in this chapter is analogous to the one presented in [25] for the standard formulation and the one presented in Chapter 2 for the log-conformation reformulation for the viscoelastic fluid flow. As the main ideas of the stabilization method have been already presented previously, in this section we restrict us to the extension to the thermal coupling.

3.5.1 Residual-based VMS methods

Firstly, we present the case of the standard formulation. Suppose that $\mathcal{L}_{\mathrm{std}}(\hat{\boldsymbol{U}}; \cdot)$ is a linear operator for a given $\hat{\boldsymbol{U}} = [\hat{\boldsymbol{u}}, \hat{p}, \hat{\boldsymbol{\sigma}}, \hat{\vartheta}]$ known. Introducing the sub-grid scale, and integrating by parts, the method consists in finding $\boldsymbol{U}_h :]0, T[\longrightarrow \boldsymbol{\mathcal{X}}_h$, such that

$$\mathcal{G}_{\mathrm{std}}(\vartheta_h; \boldsymbol{U}_h, \boldsymbol{V}_h) + B_{\mathrm{std}}(\boldsymbol{U}_h; \boldsymbol{U}_h, \boldsymbol{V}_h) + \sum_K \langle \tilde{\boldsymbol{U}}, \mathcal{L}^*(\boldsymbol{U}_h; \boldsymbol{V}_h) \rangle_K = L_{\mathrm{std}}(\boldsymbol{V}_h), \qquad (3.20)$$

for all $\boldsymbol{V}_h \in \boldsymbol{\mathcal{X}}_h$, where $\mathcal{L}^*(\hat{\boldsymbol{U}}; \cdot)$ is the formal adjoint of $\mathcal{L}_{\mathrm{std}}(\hat{\boldsymbol{U}}; \cdot)$, typically without considering boundary conditions, $\tilde{\boldsymbol{U}}$ is the sub-grid scale, which needs to be approximated and has components $\tilde{\boldsymbol{U}} = \left[\tilde{\boldsymbol{u}}, \tilde{p}, \tilde{\boldsymbol{\sigma}}, \tilde{\vartheta} \right]$. All approximations have been considered continuous; in this case expression (3.20) is justified in [44]. Similarly, for the log-conformation reformulation, we have to find $\boldsymbol{U}_h :]0, T[\longrightarrow \bar{\boldsymbol{\mathcal{X}}}_h$ such that

$$\mathcal{G}_{\mathrm{log}}(\vartheta_h; \boldsymbol{U}_h, \boldsymbol{V}_h) + B_{\mathrm{log}}(\boldsymbol{U}_h; \boldsymbol{U}_h, \boldsymbol{V}_h) + \sum_K \langle \tilde{\boldsymbol{U}}, \mathcal{L}^*(\boldsymbol{U}_h; \boldsymbol{V}_h) \rangle_K = L_{\mathrm{log}}(\vartheta_h; \boldsymbol{V}_h), \quad (3.21)$$

for all $\boldsymbol{V}_h \in \boldsymbol{\mathcal{X}}_h$. Let us remark that for both formulations (standard and logarithmic) the same operator $\mathcal{L}^* \left(\hat{\boldsymbol{U}}; \boldsymbol{V} \right)$ is used:

$$\mathcal{L}^*(\hat{\boldsymbol{U}}; \boldsymbol{V}) := \begin{pmatrix} \nabla \cdot \boldsymbol{\chi} - \nabla \cdot (2\eta_s(\hat{\vartheta})\nabla^s \boldsymbol{v}) - \rho \hat{\boldsymbol{u}} \cdot \nabla \boldsymbol{v} - \nabla q \\ -\nabla \cdot \boldsymbol{v} \\ \dfrac{1}{2\eta_p(\hat{\vartheta})} (\mathbf{I} + \mathfrak{h}(\hat{\boldsymbol{\sigma}})) \cdot \boldsymbol{\chi} + \nabla^s \boldsymbol{v} - \Lambda(\vartheta_0) \left(\hat{\boldsymbol{u}} \cdot \nabla \boldsymbol{\chi} + g^*(\hat{\boldsymbol{u}}, \boldsymbol{\chi}) \right) \\ \rho C_p \hat{\boldsymbol{u}} \cdot \nabla \xi - k \Delta \xi \end{pmatrix}, \qquad (3.22)$$

where in this case $g^*(\hat{\boldsymbol{u}}, \boldsymbol{\chi}) = \boldsymbol{\chi} \cdot (\nabla \hat{\boldsymbol{u}})^T + \boldsymbol{\chi} \cdot \nabla \hat{\boldsymbol{u}}$. As the operators $\mathcal{D}_t$ and $\mathcal{L}$ were defined previously for both formulations, the sub-grid scales can be written in terms of the finite element component:

$$\tilde{\boldsymbol{U}} = \boldsymbol{\alpha} \tilde{P}[\boldsymbol{F} - \mathcal{D}_t(\vartheta_h; \boldsymbol{U}_h) - \mathcal{L}(\boldsymbol{U}_h; \boldsymbol{U}_h)], \qquad (3.23)$$

where we denote as $\tilde{P}$ the L^2 projection onto the space of sub-grid scales. The ASGS (Algebraic Sub-Grid Scales) method is recovered if $\tilde{P}$ is the projection onto the space of FE residuals; however if $\tilde{P}$ is taken as the orthogonal projection to the FE space, $P^{\perp}$, then the OSGS (Orthogonal Sub-Grid Scales) method would be recovered.

Regarding matrix $\boldsymbol{\alpha}$ that appears in expression (3.23), it is the diagonal matrix of stabilization terms, $\boldsymbol{\alpha} = \mathrm{diag}(\alpha_1 \boldsymbol{I}_d, \alpha_2, \alpha_3 \boldsymbol{I}_{d \times d}, \alpha_4)$ with $\boldsymbol{I}_d$ the identity on vectors of $\mathbb{R}^d$, $\boldsymbol{I}_{d \times d}$ the identity on second order tensors and the parameters α_i, $i = 1, 2, 3, 4$ are computed as

$$\alpha_1 = \left[c_1 \frac{\eta_0(\vartheta_h)}{h_1^2} + c_2 \frac{\rho |\boldsymbol{u}_h|}{h_2} \right]^{-1}, \tag{3.24}$$

$$\alpha_2 = \frac{h_1^2}{c_1 \alpha_1}, \tag{3.25}$$

$$\alpha_3 = \left[c_3 \frac{1}{2 \eta_p(\vartheta_h)} + c_4 \Lambda(\vartheta_0) \left(\frac{|\boldsymbol{u}_h|}{h_2} + |\nabla \boldsymbol{u}_h| \right) \right]^{-1}, \tag{3.26}$$

$$\alpha_4 = \left[c_5 \frac{k}{h_1^2} + c_6 \frac{\rho C_p |\boldsymbol{u}_h|}{h_2} \right]^{-1}, \tag{3.27}$$

where c_i with $i = 1, .., 6$ are constants, h_1 is the characteristic length computed as the square root of the element area or the cubic root of the element volume depending on the dimension of the case, and h_2 is another characteristic length computed as the element length in the streamline direction (see [46] for more details). The constants $c_i, i = 1, .., 6$ are algorithmic parameters in the formulation. The values employed in this chapter for the numerical simulations are: $c_1 = 4.0$, $c_2 = 1.0$, $c_3 = 4.0$, $c_4 = 0.25$, $c_5 = 4.0$ and $c_6 = 2.0$. We keep these values constants for all flows.

Inserting (3.23) in (3.20) for the standard formulation, with $\boldsymbol{\alpha}$ given above and using the adjoint operator (3.22), we obtain the following problem: find $\boldsymbol{U}_h :]0, T[\longrightarrow \boldsymbol{\mathcal{X}}_h$ such that

$$
\begin{aligned}
(\mathcal{G}_{\mathrm{std}}(\vartheta_h; \boldsymbol{U}_h), \boldsymbol{V}_h) &+ B_{\mathrm{std}}(\boldsymbol{U}_h; \boldsymbol{U}_h, \boldsymbol{V}_h) + S_{1,\mathrm{std}}(\boldsymbol{u}_h, \vartheta_h; \boldsymbol{U}_h, \boldsymbol{V}_h) + S_2(\boldsymbol{U}_h, \boldsymbol{V}_h) \\
&+ S_{3,\mathrm{std}}(\boldsymbol{U}_h; \boldsymbol{U}_h, \boldsymbol{V}_h) + S_{4,\mathrm{std}}(\boldsymbol{u}_h, \boldsymbol{\sigma}_h; \boldsymbol{U}_h, \boldsymbol{V}_h) = L_{\mathrm{std}}(\boldsymbol{V}_h) + R_{1,\mathrm{std}}(\boldsymbol{u}_h, \vartheta_h; \boldsymbol{V}_h),
\end{aligned}
\tag{3.28}
$$

for all $\boldsymbol{V}_h \in \boldsymbol{\mathcal{X}}_h$. The details of each stabilized term can be found in the work of Castillo and Codina [25], with exception of the expression $S_{4,\mathrm{std}}$, which corresponds to stabilization terms of the energy equation. These terms are:

$$
\begin{aligned}
S_{1,\mathrm{std}}\left(\hat{\boldsymbol{u}}_h, \hat{\vartheta}_h; \boldsymbol{U}_h, \boldsymbol{V}_h \right) = \sum_K \alpha_1 \Bigg\langle &\tilde{P} \left[\rho \frac{\partial \boldsymbol{u}_h}{\partial t} - \nabla \cdot \boldsymbol{\sigma}_h - \nabla \cdot 2 \eta_s(\hat{\vartheta}_h) \nabla^s \boldsymbol{u}_h \right. \\
&\left. + \rho \hat{\boldsymbol{u}}_h \cdot \nabla \boldsymbol{u}_h + \nabla p_h \right], \\
&-\nabla \cdot \boldsymbol{\chi}_h + \nabla \cdot 2 \eta_s(\hat{\vartheta}_h) \nabla^s \boldsymbol{v}_h + \rho \hat{\boldsymbol{u}}_h \cdot \nabla \boldsymbol{v}_h + \nabla q_h \Bigg\rangle_K,
\end{aligned}
\tag{3.29}
$$

$$
S_2\left(\boldsymbol{U}_h, \boldsymbol{V}_h \right) = \sum_K \alpha_2 \left\langle \tilde{P} \left[\nabla \cdot \boldsymbol{u}_h \right], \nabla \cdot \boldsymbol{v}_h \right\rangle_K, \tag{3.30}
$$

$$
\begin{aligned}
S_{3,\mathrm{std}}\left(\hat{\boldsymbol{U}}_h; \boldsymbol{U}_h, \boldsymbol{V}_h \right) = \sum_K \alpha_3 \Bigg\langle &\tilde{P} \left[\frac{1}{2 \eta_p(\hat{\vartheta}_h)} (\boldsymbol{I} + \mathfrak{h}(\hat{\boldsymbol{\sigma}}_h)) \boldsymbol{\sigma}_h - \nabla^s \boldsymbol{u}_h \right. \\
&\left. + \Lambda(\vartheta_0) \left(\frac{\partial \boldsymbol{\sigma}_h}{\partial t} + g_{\mathrm{std}}(\hat{\boldsymbol{u}}_h; \boldsymbol{\sigma}_h) \right) \right],
\end{aligned}
$$

$$- \frac{1}{2\eta_p(\hat{\vartheta}_h)} \left(\mathbf{I} + \mathfrak{h}(\hat{\boldsymbol{\sigma}}_h) \right) \cdot \boldsymbol{\chi}_h - \nabla^s \boldsymbol{v}_h$$

$$+ \Lambda(\vartheta_0) \left(\hat{\boldsymbol{u}}_h \cdot \nabla \boldsymbol{\chi}_h + g^*(\hat{\boldsymbol{u}}_h, \boldsymbol{\chi}_h) \right) \big\rangle_K, \tag{3.31}$$

$$S_{4,\text{std}}(\hat{\boldsymbol{u}}_h, \hat{\boldsymbol{\sigma}}_h; \boldsymbol{U}_h, \boldsymbol{V}_h) = \sum_K \alpha_4 \left\langle \tilde{P} \left[\rho C_p \left(\frac{\partial \vartheta_h}{\partial t} + \hat{\boldsymbol{u}}_h \cdot \nabla \vartheta_h \right) - k\Delta\vartheta_h - \hat{\boldsymbol{\sigma}}_h : \nabla^s \hat{\boldsymbol{u}}_h \right],$$

$$-\rho C_p \hat{\boldsymbol{u}}_h \cdot \nabla \xi_h + k\Delta \xi_h \big\rangle_K, \tag{3.32}$$

$$R_{1,\text{std}}\left(\hat{\boldsymbol{u}}_h, \hat{\vartheta}_h; \boldsymbol{V}_h \right) = \sum_K \alpha_1 \left\langle \tilde{P}[\boldsymbol{f}], -\nabla \cdot \boldsymbol{\chi}_h + \nabla \cdot 2\eta_s(\hat{\vartheta}_h)\nabla^s \boldsymbol{v}_h \right.$$

$$+ \rho \hat{\boldsymbol{u}}_h \cdot \nabla \boldsymbol{v}_h + \nabla q_h \big\rangle_K. \tag{3.33}$$

Recall that if $\tilde{P} = I$ we obtain the ASGS method, and if $\tilde{P} = P_h^\perp = I - P_h$ the we would be considering the OSGS method.

Analogously, in the case of the stabilization formulation for the logarithmic case, inserting (3.23) in (3.21) and using the adjoint operator defined in (3.22), we obtain the following problem: find $\boldsymbol{U}_h :]0,T[\longrightarrow \boldsymbol{\mathcal{X}}_h$ such that

$$(\mathcal{G}_{\text{log}}(\vartheta_h; \boldsymbol{U}_h), \boldsymbol{V}_h) + B_{\text{log}}(\boldsymbol{U}_h; \boldsymbol{U}_h, \boldsymbol{V}_h) + S_{1,\text{log}}(\boldsymbol{u}_h, \vartheta_h; \boldsymbol{U}_h, \boldsymbol{V}_h) + S_2(\boldsymbol{U}_h, \boldsymbol{V}_h)$$

$$+ S_{3,\text{log}}(\boldsymbol{U}_h; \boldsymbol{U}_h, \boldsymbol{V}_h) + S_{4,\text{log}}(\boldsymbol{U}_h; \boldsymbol{U}_h, \boldsymbol{V}_h) = L_{\text{log}}(\boldsymbol{V}_h) + R_{1,\text{log}}(\boldsymbol{u}_h, \vartheta_h; \boldsymbol{V}_h). \tag{3.34}$$

In this case, $S_{i,\text{log}}$, with $i = 1, 2, 3$ and $R_{j,\text{log}}$ with $j = 1, 3$ are detailed in [120] and the only difference is that now we have to consider the temperature-dependence of the viscoelastic variables. These terms are

$$S_{1,\text{log}}(\hat{\boldsymbol{u}}_h, \hat{\vartheta}_h; \boldsymbol{U}_h, \boldsymbol{V}_h) = \sum_K \alpha_1 \left\langle \tilde{P} \left[\rho \frac{\partial \boldsymbol{u}_h}{\partial t} - \nabla \cdot (\Upsilon_1(\vartheta_0) \exp(\boldsymbol{\psi}_h)) - \nabla \cdot (2\eta_s(\hat{\vartheta})\nabla^s \boldsymbol{u}_h) \right. \right.$$

$$+ \rho \hat{\boldsymbol{u}}_h \cdot \nabla \boldsymbol{u}_h + \nabla p_h \Big],$$

$$-\nabla \cdot \boldsymbol{\chi}_h + \nabla \cdot (2\eta_s(\hat{\vartheta}_h)\nabla^s \boldsymbol{v}_h) + \rho \hat{\boldsymbol{u}}_h \cdot \nabla \boldsymbol{v}_h + \nabla q_h \big\rangle_K, \tag{3.35}$$

$$S_{2,\text{log}}(\boldsymbol{U}_h, \boldsymbol{V}_h) = \sum_K \alpha_2 \left\langle \tilde{P}[\nabla \cdot \boldsymbol{u}_h], \nabla \cdot \boldsymbol{v}_h \right\rangle_K, \tag{3.36}$$

$$S_{3,\text{log}}(\hat{\boldsymbol{u}}_h, \hat{\vartheta}_h; \boldsymbol{U}_h, \boldsymbol{V}_h) = \sum_K \alpha_3 \left\langle \tilde{P} \left[\frac{1}{2\lambda_0(\hat{\vartheta}_h)} \left(\exp(\boldsymbol{\psi}_h) - \mathbf{I} \right) \cdot (\mathfrak{h}(\exp(\boldsymbol{\psi}_h)) + \mathbf{I}) - \nabla^s \boldsymbol{u}_h \right. \right.$$

$$+ \Upsilon_2(\vartheta_0) \left(\frac{\partial \exp(\boldsymbol{\psi}_h)}{\partial t} + g_{\text{log}}(\hat{\boldsymbol{u}}_h; \boldsymbol{u}_h, \boldsymbol{\psi}_h) \right) \Big],$$

$$-\frac{1}{2\eta_p(\hat{\vartheta}_h)} \boldsymbol{\chi}_h - \nabla^s \boldsymbol{v}_h + \Lambda(\vartheta_0)(\vartheta_0) \left(\hat{\boldsymbol{u}}_h \cdot \nabla \boldsymbol{\chi}_h + g^*(\hat{\boldsymbol{u}}_h, \boldsymbol{\chi}_h) \right) \big\rangle_K, \tag{3.37}$$

$$R_{1,\text{log}}(\hat{\boldsymbol{u}}_h, \hat{\vartheta}_h; \boldsymbol{V}_h) = \sum_K \alpha_1 \left\langle \tilde{P}[\boldsymbol{f}], -\nabla \cdot \boldsymbol{\chi}_h + \nabla \cdot (2\eta_s(\hat{\vartheta}_h)\nabla^s \boldsymbol{v}_h) + \rho \hat{\boldsymbol{u}}_h \cdot \nabla \boldsymbol{v}_h + \nabla q_h \right\rangle_K. \tag{3.38}$$

Regarding $S_{4,\text{log}}$, it is as follows:

$$S_{4,\text{log}}\left(\hat{\boldsymbol{U}}_h; \boldsymbol{U}_h, \boldsymbol{V}_h \right) = \sum_K \alpha_4 \left\langle \tilde{P} \left[\rho C_p \hat{\boldsymbol{u}}_h \cdot \nabla \vartheta_h - k\Delta\vartheta_h, \right. \right.$$

$$- \left(\Upsilon_1(\vartheta_0) \exp(\hat{\boldsymbol{\psi}}_h) - \mathbf{I} \right) : \nabla^s \hat{\boldsymbol{u}}_h \Big], -\rho C_p \hat{\boldsymbol{u}}_h \cdot \nabla \xi_h + k\Delta \xi_h \big\rangle_K, \tag{3.39}$$

The same considerations made for the standard formulation about the projections and the different stabilization methods carry over to the log-conformation reformulation.

3.5.2   Split-OSS stabilization

This stabilization method comes from considering two assumptions in the residual-based VMS methods. The first one is that the projection considered is $\tilde{P} = P_h^\perp$, and the second one is to neglect the cross local inner-product terms together with other terms that do not contribute to stability. The result is a simplified method that is not consistent but whose convergence rate in h is optimal, as explained in [25]. The split strategy is only considered over the stabilization terms of the momentum equation, and the reason for this is detailed in [119]. If the split term-by-term in the constitutive equation is done, convergence for the non-linear iterations turns out to be very difficult to attain.

Therefore for the standard formulation, the stabilization considered finally consists in finding $\boldsymbol{U}_h :]0, T[\longrightarrow \boldsymbol{\mathcal{X}}_h$ such that

$$
(\mathcal{G}_{\text{std}}(\vartheta_h; \boldsymbol{U}_h), \boldsymbol{V}_h) + B_{\text{std}}(\boldsymbol{U}_h; \boldsymbol{U}_h, \boldsymbol{V}_h) + S_{1,\text{std}}^\perp(\boldsymbol{u}_h; \boldsymbol{U}_h, \boldsymbol{V}_h) + S_2^\perp(\boldsymbol{U}_h, \boldsymbol{V}_h)
$$
$$
+ S_{3,\text{std}}^\perp(\boldsymbol{U}_h; \boldsymbol{U}_h, \boldsymbol{V}_h) + S_{4,\text{std}}^\perp(\boldsymbol{u}_h, \boldsymbol{\sigma}_h; \boldsymbol{U}_h, \boldsymbol{V}_h) = L_{\text{std}}(\boldsymbol{V}_h). \quad (3.40)
$$

for all $\boldsymbol{V}_h \in \boldsymbol{\mathcal{X}}_h$. For $S_{i,\text{std}}^\perp$ with $i = 2, 3, 4$ we consider the same expression detailed in (3.30), (3.31) and (3.32) for $S_{i,\text{std}}$, but now taking into account that $\tilde{P} = P_h^\perp$ as it has been specified above. The expression of $S_{1,\text{std}}^\perp$ in (3.28) is now as follows:

$$
S_{1,\text{std}}^\perp(\hat{\boldsymbol{u}}_h; \boldsymbol{U}_h, \boldsymbol{V}_h) = \sum_K \alpha_1 \left\langle P_h^\perp[\nabla \cdot \boldsymbol{\sigma}_h], \nabla \cdot \boldsymbol{\chi}_h \right\rangle_K + \sum_K \alpha_1 \left\langle P_h^\perp[\nabla p_h], q_h \right\rangle_K
$$
$$
+ \sum_K \alpha_1 \left\langle P_h^\perp[\nabla \rho \hat{\boldsymbol{u}}_h \cdot \nabla \boldsymbol{u}_h], \rho \hat{\boldsymbol{u}}_h \cdot \nabla \boldsymbol{v}_h \right\rangle_K. \quad (3.41)
$$

For the log-conformation reformulation we have the following stabilized form: find $\boldsymbol{U}_h :]0, T[\longrightarrow \boldsymbol{\mathcal{X}}_h$ such that

$$
(\mathcal{G}_{\text{log}}(\vartheta_h; \boldsymbol{U}_h), \boldsymbol{V}_h) + B_{\text{log}}(\boldsymbol{U}_h; \boldsymbol{U}_h, \boldsymbol{V}_h) + S_{1,\text{log}}^\perp(\boldsymbol{u}_h, \vartheta_h; \boldsymbol{U}_h, \boldsymbol{V}_h) + S_2^\perp(\boldsymbol{U}_h, \boldsymbol{V}_h)
$$
$$
+ S_{3,\text{log}}^\perp(\boldsymbol{U}_h; \boldsymbol{U}_h, \boldsymbol{V}_h) + S_{4,\text{log}}^\perp(\boldsymbol{U}_h; \boldsymbol{U}_h, \boldsymbol{V}_h) = L_{\text{log}}(\boldsymbol{V}_h), \quad (3.42)
$$

for all $\boldsymbol{V}_h \in \boldsymbol{\mathcal{X}}_h$. As in the standard formulation, for the terms $S_{i,\text{log}}^\perp$ with $i = 2, 3, 4$, we can consider the expressions detailed in (3.36), (3.37), (3.39) taking $\tilde{P} = P_h^\perp$. The expression of $S_{1,\text{log}}^\perp$ in (3.42) is now as follows:

$$
S_{1,\text{log}}^\perp(\hat{\boldsymbol{u}}_h, \hat{\vartheta}_h; \boldsymbol{U}_h, \boldsymbol{V}_h) = \sum_K \alpha_1 \left\langle P_h^\perp\left[\nabla \cdot (\Upsilon_1(\vartheta_0) \exp(\boldsymbol{\psi}_h))\right], \nabla \cdot \boldsymbol{\chi}_h \right\rangle_K
$$
$$
+ \sum_K \alpha_1 \left\langle P_h^\perp\left[\nabla p_h\right], \nabla q_h \right\rangle_K + \sum_K \alpha_1 \left\langle P_h^\perp\left[\rho \hat{\boldsymbol{u}}_h \cdot \nabla \boldsymbol{u}_h\right], \rho \hat{\boldsymbol{u}}_h \cdot \nabla \boldsymbol{v}_h \right\rangle_K.
$$

There are many benefits associated to the use a split term-by-term stabilization instead of a residual-based one: the first one is the simplicity, since some cross-local products have been neglected, the second one is that some negative terms that do not contribute to stability have been deleted, therefore the scheme is more stable. Moreover, the scheme has turned out to be more efficient in solving problems with high gradients and when the Weissenberg number is relatively high in viscoelastic fluid flow problems [31, 120]. Furthermore, cumbersome elementwise terms of the form $\nabla \cdot \eta \nabla^s \boldsymbol{v}_h$, with η a variable function depending on temperature, do not need to be evaluated. Note that for the stabilization terms associated to the constitutive equation, $S_{3,\text{log}}^\perp$, we are not neglected the inner products, and the reason is justified in Chapter 4, Section 4.4.2.

3.5.3   Linearization and algorithm

The set of equations of the thermally coupled problem with incompressible viscoelastic flows presents a high number of non-linear terms, in particular in the momentum and in the constitutive equation. Regarding the algorithm employed, it is displayed in Algorithm 3 (only considering the standard formulation, however for the log-conformation reformulation the algorithm would be analogous). Apart from the points enumerated in Section 2.4.3 that are considered also in that case, we have to make the the following remarks about the algorithm used:

- It is iterative for the coupling, but monolithic for the fluid flow problem. It means that in each time-step the parameters dependent on temperature for solving the viscoelastic fluid flow problem and the stress work for the temperature problem are continuously updated.

- The nonlinear term in the momentum equation can be linearized with a fixed point scheme or with Newton-Raphson's method.

- In the case of the log-conformation reformulation, the exponential terms that appear both in the momentum equation and in the constitutive equation have been linearized using a Taylor development (see Chapter 2), taking the tensor $\hat{\boldsymbol{\psi}}$ as the one obtained from the previous iteration of the current time step.

3.6   Numerical results

In this section several numerical examples are presented. Firstly, the flow past a cylinder is studied, using the standard formulation together with the PTT constitutive equation, and taking the Williams-Landel-Ferry function to establish the relations between temperature and viscoelastic parameters. The second example is the extension 1:3, where the log-conformation reformulation is employed and the Arrhenius function is used, instead of the WLF, as dependence method between temperature and viscoelastic properties. All computations have been performed using the Split-OSS stabilization explained in Section 3.5.2. Likewise, for each case the formulation chosen corresponds to that of the reference of comparison, when possible.

3.6.1   Flow around a cylinder

The first example is the well-known flow past a cylinder, a typical benchmark to check formulations for simulating viscoelastic fluid flows. This has been extensively studied by Peters and Baaijens [7] to evaluate the performance of constitutive equations for both polymer solutions and melts, although supposing an isothermal flow. Moreover, these authors also explore the non-isothermal case in [133]. There, the numerical result is obtained using a stabilized discontinuous Galerkin method for the viscoelastic equations, and a regular Galerkin method employing a bi-quadratic interpolation of the temperature to solve the temperature equation. Coupling is carried out using a fixed point iteration. The authors also discuss the differences in the stress field between isothermal and non-isothermal problems, as we will do.

Algorithm 3 General algorithm for thermal coupling using VMS.

---

read initial condition $\boldsymbol{u}_h^0$ and ϑ_h^0

set $p_h^0 = 0$, $\boldsymbol{\psi}_h^0 = \boldsymbol{0}$

for $j = 0, ..., m-1$ **do** *(Temporal loop)*

 set $k{=}0$

 set $\boldsymbol{u}_h^{j+1,0} = \boldsymbol{u}_h^j$, $p_h^{j+1,0} = p_h^j$, $\boldsymbol{\sigma}_h^{j+1,0} = \boldsymbol{\sigma}_h^j$

 while not converged **do** *(Coupling loop)*

  $k \leftarrow k + 1$

  set $i = 0$

  set $\boldsymbol{u}_h^{j+1,k,0} = \boldsymbol{u}_h^{j,k}$, $p_h^{j+1,k,0} = p_h^{j,k}$, $\boldsymbol{\sigma}_h^{j+1,k,0} = \boldsymbol{\sigma}_h^{j,k}$

  set $\lambda^{j+1,k} = \lambda(\vartheta_h^{j+1,k-1})$ and $\eta_0^{j+1,k} = \eta_0(\vartheta_h^{j+1,k-1})$

  while not converged **do**

   $i \leftarrow i + 1$

   compute "residuals": $\mathbf{R}_{u1}$, $\mathbf{R}_{u2}$, $\mathbf{R}_{u3}$, $\mathbf{R}_\sigma$

   compute projections: $P_h\left[\mathbf{R}_{u1}\right]$, $P_h\left[\mathbf{R}_{u2}\right]$, $P_h\left[\mathbf{R}_{u3}\right]$, $P_h\left[\mathbf{R}_\sigma\right]$

   compute stabilization parameters:

    $\alpha_1^{j+1,k,i-1}$, $\alpha_2^{j+1,k,i-1}$ and $\alpha_3^{j+1,k,i-1}$ with $\boldsymbol{U}^{j+1,k,i-1}$

   solve viscoelastic fluid flow equations for $\boldsymbol{u}_h^{j+1,k,i}$, $p_h^{j+1,k,i}$ and $\boldsymbol{\sigma}_h^{j+1,k,i}$

   check convergence

  end while

  set converged values

   $\boldsymbol{u}_h^{j+1,k} = \boldsymbol{u}_h^{j+1,k,i}$

   $p_h^{j+1,k} = p_h^{j+1,k,i}$

   $\boldsymbol{\sigma}_h^{j+1,k} = \boldsymbol{\sigma}_h^{j+1,k,i}$

  set the stress work as $\boldsymbol{\sigma}_h^{j+1,k} : \nabla \boldsymbol{u}_h^{j+1,k}$

  set $i = 0$

  set $\vartheta_h^{j+1,k,0} = \vartheta_h^{j,k}$

  compute stabilization parameter $\alpha_4^{j+1,k,i-1}$ with $\boldsymbol{u}_h^{j+1,k}$

  while not converged **do**

   $i \leftarrow i + 1$

   compute "residual" $\mathbf{R}_\vartheta$

   compute projection $P_h\left[\mathbf{R}_\vartheta\right]$

   solve the energy equation for $\vartheta_h^{j+1,k,i}$ considering the stress work

   check convergence

  end while

  set converged values

   $\vartheta_h^{j+1,k} = \vartheta_h^{j+1,k,i}$

 end while *(End coupling loop)*

 set converged values

  $\boldsymbol{u}_h^{j+1} = \boldsymbol{u}_h^{j+1,k}$

  $p_h^{j+1} = p_h^{j+1,k}$

  $\boldsymbol{\sigma}_h^{j+1} = \boldsymbol{\sigma}_h^{j+1,k}$

  $\vartheta_h^{j+1} = \vartheta_h^{j+1,k}$

end for *(End temporal loop)*
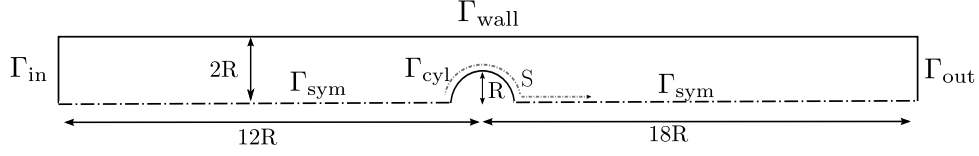
Figure 3.2: Non-isothermal flow past a cylinder. Geometry and computational boundaries.

Setup

The computational domain extends 12 times the length of the radius upstream of the cylinder centre and 18 times downstream, as shown in Figure 3.2.

First, we define the parameters of the non-isothermal viscoelastic fluid flow problem. The relaxation time for the reference temperature $\lambda(\vartheta_0)$ is 0.1 s, the total viscosity for the reference temperature is $\eta_0(\vartheta_0) = 1.0 \times 10^4$ Pa $\cdot$ s and the parameter β is set to 0.5. As it has been explained, the total viscosity and relaxation time are temperature-dependent, and this relation is defined by the WLF function g_{wlf}, defined in Section 3.3.1. In this case the constants c_1 and c_2 of this function are set as 4.54 and 150.36, respectively. The mobility parameter ε of the PTT constitutive model is 0.1. The density is $\rho = 921$ kg$\cdot$m^{-3}, the specific heat is $C_p = 1.5$ kJ$\cdot$kg$\cdot$K^{-1} and the conductivity k is fixed to 0.17 W$\cdot$m$\cdot$K^{-1}. The reference temperature ϑ_0 is set to 462 K.

Regarding the boundary conditions of the problem, for the velocity no-slip conditions are imposed on the top wall Γ_{wall} and the cylinder surface Γ_{cyl}, and symmetry conditions are prescribed along the axis Γ_{sym}. On the other hand, a fully developed parabolic velocity profile and the associated elastic stress are prescribed at the inlet Γ_{in}. These are given by:

$$u_x = \frac{3Q}{8\mathrm{R}} \left(1 - \frac{y^2}{(2\mathrm{R})^2} \right), \qquad u_y = 0,$$

$$\sigma_{xx} = 2\lambda(\vartheta_0)(1-\beta)\eta_0(\vartheta_0) \left(\frac{\partial u_x}{\partial y} \right)^2, \quad \sigma_{xy} = (1-\beta)\eta_0(\vartheta_0) \left(\frac{\partial u_x}{\partial y} \right), \quad \sigma_{yy} = 0,$$

where Q is the flow rate, and R is the cylinder radius. Note that stresses are prescribed using the Oldroyd-B model and with the only purpose of accelerating convergence. For the outlet Γ_{out}, the horizontal velocity is left free, the vertical velocity is taken equal to zero and the pressure is prescribed to zero. On the other hand, regarding the temperature boundary conditions, the reference temperature ϑ_0 is imposed at the inlet Γ_{in} and on the top wall Γ_{wall} as 462 K.

We will compute the problem for different Weissenberg numbers (already defined in Section 3.3.2) We $= \lambda U/R$ where U is the characteristic velocity, written as a function of the flow rate as $U = 3Q/8\mathrm{R}$; R is the cylinder radius defined above. As considered in reference [133], the convective term of the momentum equation is neglected in all the computations.

About the FE discretization considered, the mesh has 58591 linear elements and 36174 nodes. We have to remark that the refinement around the cylinder wall is significant, as shown in Figure 3.3, where the mesh is partially shown. Although all simulations have a steady-state solution, all of them have been computed using a temporal discretization to facilitate the convergence of the iterative algorithm. For all the cases, the scheme used is BDF1 (as explained in Section 3.4), and the time step is fixed to $\delta t = 5 \times 10^{-5}$ s.
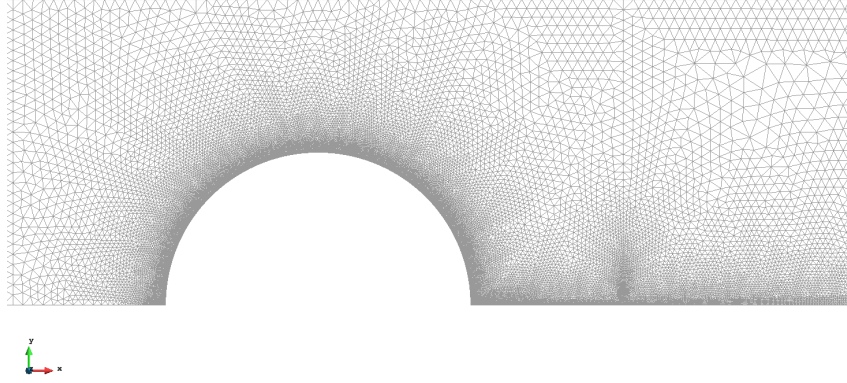
Figure 3.3: Non-isothermal flow past a cylinder. Zoom of computational mesh employed.

Results

Results of the simulation for We = 4.0 are shown in Figures 3.4 and 3.5. In particular, Figure 3.4 shows the distribution of the temperature in the vicinity of the cylinder while Figure 3.5 displays the distribution of the stresses in the same location.

- For the distribution of the temperature, this field rises significantly downstream, reaching the maximum temperature at 474.42 K. The difference of temperature between the initial or the temperature fixed on the walls at 462 K and the maximum temperature reached is the consequence of the stress work, represented by the term added to the energy equation, expressed as the product between the stresses and the symmetric gradient of the velocity field. In comparison with the typical models associated with Newtonian fluid flows, the viscoelastic fluid flow has a new *source* of heat, which is represented in the Figure 3.4. On the other hand, in comparison with [133], the maximum value reached is slightly smaller, although the general distribution of the temperature field is similar to the one obtained by the authors of this reference.

- Regarding the distribution of the stresses in Figure 3.5 near the cylinder, the maximum values are reached in two significant locations: one in the top of the wall of the cylinder, and another one at a point downstream, located in the centerline (or symmetric boundary) of the domain.

The temperature effect over the stress field can be shown in Figure 3.6, where the isothermal case is compared with the non-isothermal case, and both cases considering We = 4.0. As this figure shows, a significant reduction in stresses is found when the temperature coupling is considered. That reduction is located both over the wall of the cylinder and downstream. In [133], the reduction reached in the stresses is over 40% comparing two cases. Although in our computations this difference is not so pronounced as in the reference work, the reduction is equally considerable, over the 30%.

In Figure 3.7, a comparison between the difference of temperatures is performed between the viscoelastic case for We = 4 and the Newtonian viscous case. At first sight, the major difference is that the viscoelastic case reaches higher temperatures than the Newtonian case; however, the temperature distribution on the cylinder and downstream is also significantly different. While in the viscoelastic case the maximum peak of temperature is reached downstream, in the Newtonian case it is reached on the cylinder. On the other hand, computations were executed for some Weissenberg numbers to study the differences
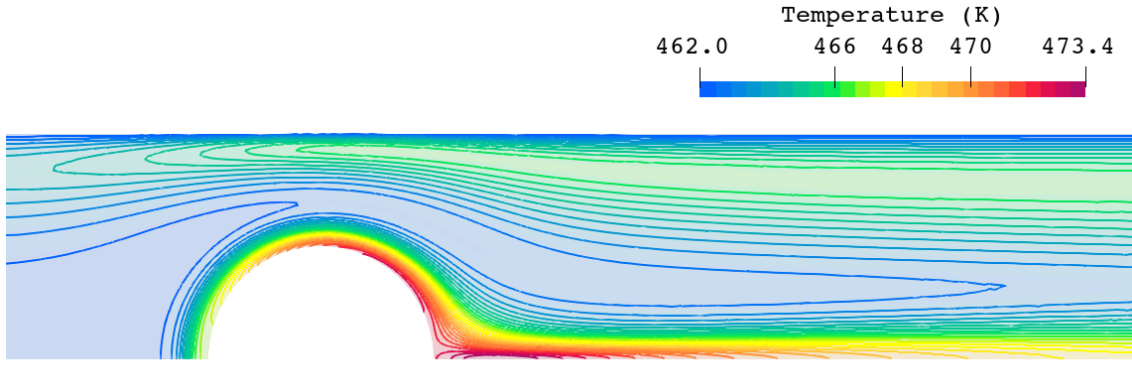
Figure 3.4: Non-isothermal flow past a cylinder. Distribution of temperature ϑ around the cylinder. We = 4.

Figure 3.5: Non-isothermal flow past a cylinder. Distribution of stresses. Above: component σ_{xx}, middle: component σ_{yy} , and below: component σ_{xy} around the cylinder. We = 4.
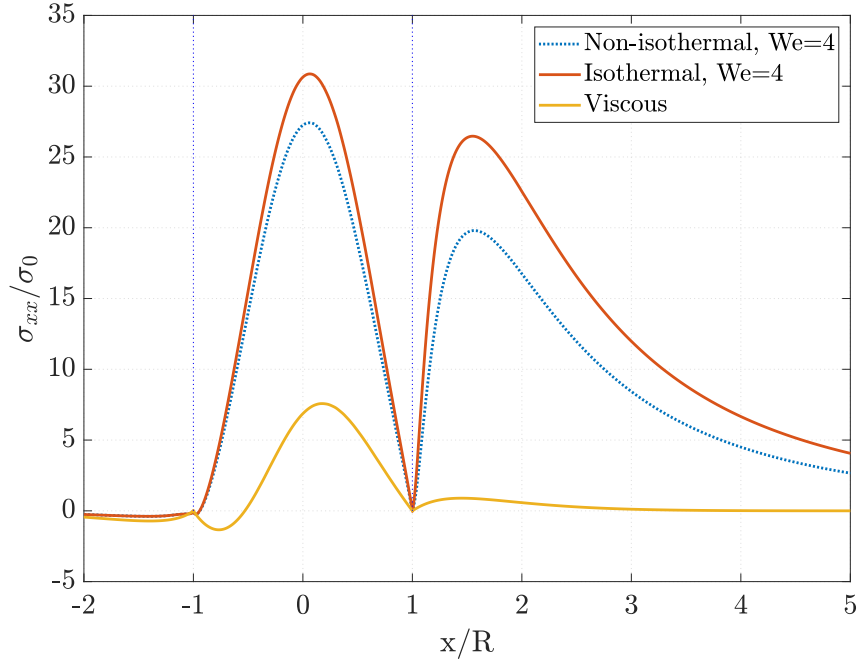
Figure 3.6: Non-isothermal past flow a cylinder. Stress component σ_{xx} around and down-stream of cylinder in isothermal and non-isothermal cases.

between temperatures. The parameter $\Delta\vartheta = \vartheta - \vartheta_0$ (difference between reference tem-perature and temperature distribution), around the cylinder is plotted in Figure 3.8. The results in these last figures seem to be coherent: while the Weissenberg number increases, the stresses also do, and therefore by the definition of *viscous dissipation* the internal work is more relevant, causing an increase of the temperature around the cylinder and down-stream. Results are in agreement with the graph shown in [133] from a qualitative point of view. Quantitatively, the comparison is not meaningful, as we have not performed mesh convergence studies and these are not presented in [133], either.

3.6.2   1:3 Expansion

In this section, the case of the 1:3 expansion is simulated. This benchmark is motivated by the work of Shahbani-Zahiri et al. [150], where a complete study is done of this problem, exploring the solution for different expansion angles. That is an important example due to the formation and growth of symmetric and asymmetric regions that play an important role in the viscous dissipation, temperature distribution, and heat transfer rate. Following ideas similar to those exposed in the cited paper, we study the temperature effect over the patterns. On the one hand, both the fluid inertia and elasticity have a significant effect on the flow pattern of non-isothermal viscoelastic fluids, and therefore, the research of the effects of elastic properties and inertial force on the heat transfer is relevant and worth. In the literature, more papers treat this problem for a low Reynolds (when bifurcation effects are not present) than for a relatively high Reynolds number. When the Reynolds number is around 50 or 100 the flow of Newtonian fluids is known to give rise to an asymmetric pattern: larger and smaller recirculation zones appear behind the step change. This phenomenon is characteristic in planar expansions, and it is suggested in [125] that this could be explained by the Coanda effect. This effect explains that any perturbation of the flow field, pushing the main flow to one of the sides of the expansion, gives rise to
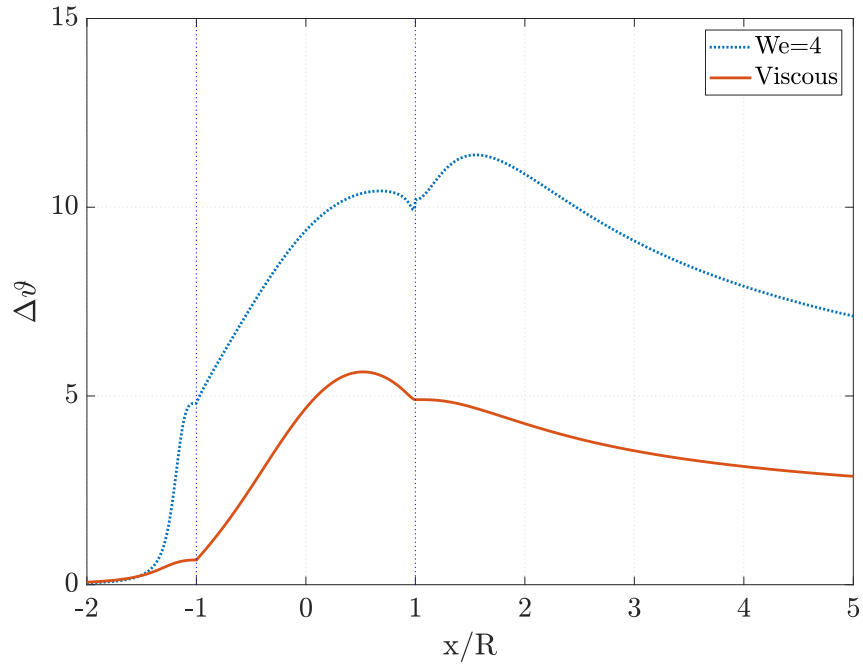
Figure 3.7: Non-isothermal flow past a cylinder. Increase of temperatures around the cylinder and downstream for Newtonian fluid and a viscoelastic fluid, We = 4.
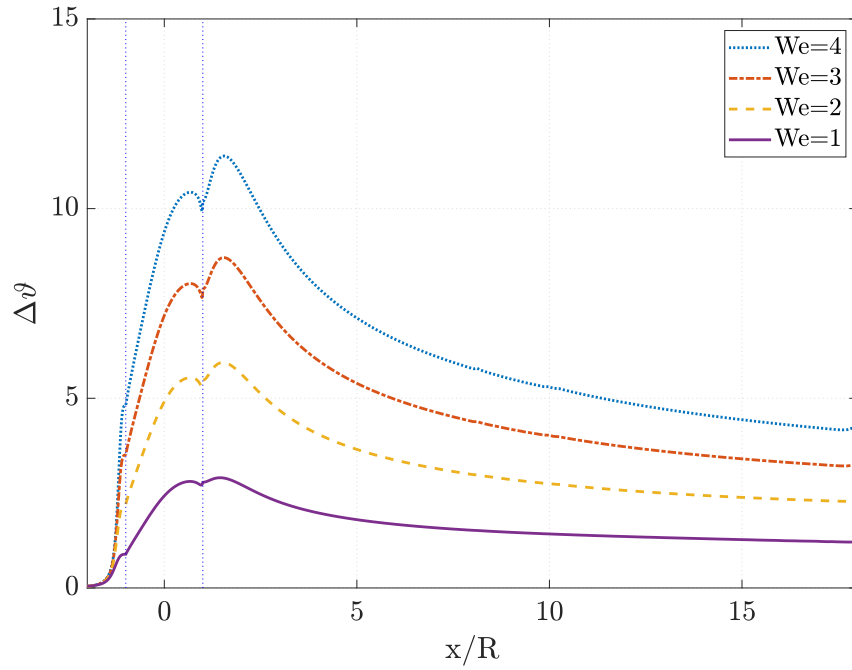
Figure 3.8: Non-isothermal flow past a cylinder. Increase of temperatures around the cylinder and downstream for several Weissenberg numbers.

Mesh	NY	$\Delta y_{\min}$	NX1	NX2	$\Delta x_{\min}$	Nodes	Elements
M1	20	0.0050	140	400	0.0072	11 781	11 200
M3	52	0.0019	358	1024	0.0027	72 384	73 829

Table 3.1: 1:3 expansion. Main characteristics of the meshes employed.

larger velocities and lower pressures. Consequently, the asymmetry will naturally tend to be accentuated. This example has an additional peculiarity: the asymmetry of the steady-state solution if the Reynolds number is greater or equal than 40 or/and if the Elasticity number El = We/Re is greater than 0.1, even if the geometry is symmetrical. This asymmetry was accurately studied in the literature, under theoretical, experimental, and numerical works with Newtonian fluids, such as [66], [59], or the work developed by Hawa et al. [88], where a bifurcation analysis and linear stability study is carried out. Additionally we have to remark the works [145] and [125]. In [125], Oliveira studies the bifurcation in different isothermal scenarios that include Newtonian and viscoelastic fluid flows, simulating the problem with a finite volume method for a FENE type constitutive model.

In [150] the constitutive model employed is the so called exponential Phan Thien-Tanner (EPTT) model, similar to the PTT model explained in this chapter, with the difference that the exponential of $\mathfrak{h}(\boldsymbol{\sigma})$ is considered, using the notation introduced in Section 3.3.1. In our computations, the Oldroyd-B constitutive model is employed, but instead of the standard formulation, the log-conformation approach is used. This formulation seems to be more adequate than the standard one due to the high Weissenberg number reached in some computations.

In this section, apart from studying the thermal coupling, we will explore also the effect of the four dimensionless numbers that characterize the problem; how the flow pattern, and the temperature distribution change as the Weissenberg number (elasticity) increases or the Prandtl and the Brinkman number vary. Note that in the reference work [150] only the inertial and the elasticity influence are reported.

Setup

The computational geometry for this problem is represented in Figure 3.9a. In this case, the parameters of the model are as follows: h = 0.1 m (not to be confused with the mesh size), H = 0.3 m, $\theta = 60°$. Regarding the lengths of the three parts of the duct, these are set as: $L_1 = 60h$ m, $L_3 = 120h$ m and L_2 is calculated taking into account the angle of the expansion, therefore it is set as $L_2 = \frac{1}{5\sqrt{3}}$ m. Regarding the computational mesh, different grids have been employed for the computations, but all of them considering Q1 (bilinear) elements, following the structure displayed in Figure 3.9b. The characteristics of the meshes are detailed in Table 3.1 where NY1 indicates the number of the mesh cells in the y-direction of the channel. Moreover, NX1 and NX2 are the number of mesh cells for the first and second sections of the channel in the x-direction.

The Reynolds number can be computed using the maximum inlet velocity (from this point it will be indicated as $\text{Re}_{\max} = \rho U_{\max} L / \eta_0$) or using the average of the incoming velocity (denoted by $\text{Re}_{\text{avg}} = \rho U_{\text{avg}} L / \eta_0$ to avoid future confusions). The characteristic length is taken as h (height of the small channel). The remaining fluid parameters are: $\eta_0 = 4.07$ Pa · s, $\rho = 1226$ kg · m^{-3}, and $\beta = 0.5$ (recall that $\eta_s = \beta \eta_0$, $\eta_p = (1 - \beta)\eta_0$). For the Arrhenius function, the constant c_r is 1720 K. Regarding the temperature param-
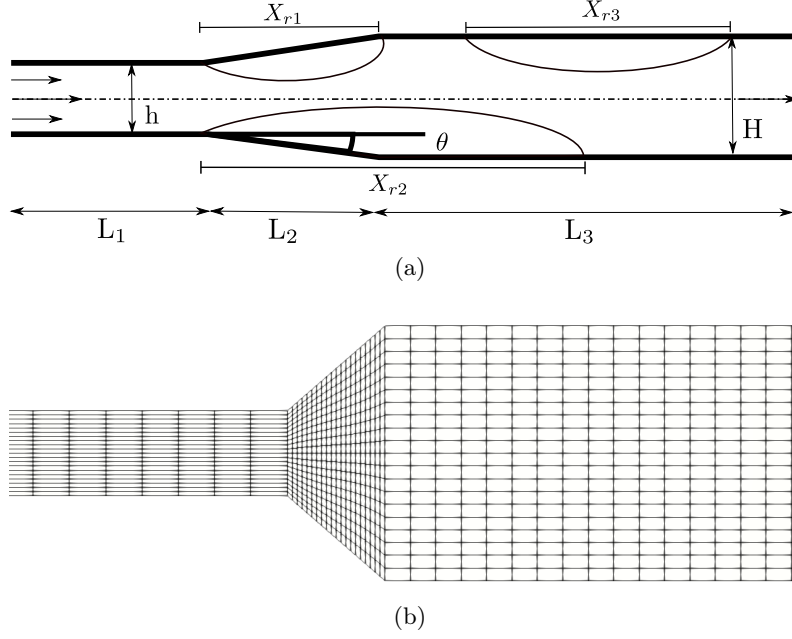
Figure 3.9: 1:3 expansion. Computational geometry and scheme of vortices (a) and computational mesh (b).

eters, these are the specific heat C_p and conductivity k, computed using the Brinkman number and the Prandtl number, which are suitably defined at the end of Section 3.3.2. The reference temperature ϑ_0 is set to 463.5 K. Now we define the boundary conditions. For the velocity, no-slip conditions are imposed on the walls of the channel Γ_{wall} and a fully developed parabolic velocity profile together with the associated elastic stress are prescribed at the inlet Γ_{in}. These are given by:

$$u_x = \frac{3Q}{4\text{h}}\left(1 - \frac{y}{\text{h}^2}\right), \qquad\qquad u_y = 0,$$

$$\sigma_{xx} = 2\lambda(\vartheta_0)(1-\beta)\eta_0(\vartheta_0)\left(\frac{\partial u_x}{\partial y}\right)^2, \quad \sigma_{xy} = (1-\beta)\eta_0(\vartheta_0)\left(\frac{\partial u_x}{\partial u_y}\right), \quad \sigma_{yy} = 0,$$

where Q is the flow rate, and h is the height of the small channel. For the outlet Γ_{out}, the horizontal velocity is left free, the vertical velocity is taken equal to zero and the pressure is prescribed to zero, constant. On the other hand, regarding the temperature boundary conditions, the reference temperature ϑ_0 is imposed at the inlet Γ_{in} and on the top wall Γ_{wall} to 563.15 K. Note that the inlet fluid is 100 K colder than the temperature of the walls.

Newtonian case. Validation

The Newtonian case is computed for the isothermal case first for validations, as this case is widely reported in the literature. Later the results will be compared with the thermal-coupling case. Very similar results are obtained for meshes M1 and M3, showing that the results obtained can be used for comparison with the literature. In particular, this comparison is done using the results of mesh M3, although mesh M1 is employed to study the trend of the vortices when different dimensionless numbers are changed. As it is explained in [125], in most earlier calculations of the phenomenon, the asymmetric flow was usually triggered by introducing a slight geometrical asymmetry in the symmetric

Authors	Critical Reynolds
Oliveira et. al [125]	54.0
Fearn et al. [66]	53.9
Drikakis et al. [59]	53.3
Hawa and Rusak [88]	53.8
Mishra and Jayaraman [118]	53.0
Present Study	53.5

Table 3.2: 1:3 expansion. Comparison of critical Reynolds in literature for the pitchfork bifurcation.

configuration or by adding a small perturbation to the velocity profile imposed at the inlet or to the whole initial velocity field (see, for example, [59, 61, 66, 88, 118]). In our case, as happened in the work of Oliveira et al. [125], no artificial devices have been required if the ASGS stabilization is employed. However, if the stabilization is of split-type and the Reynolds number is low, the bifurcation must be triggered using a bifurcation produced by a higher Reynolds number as an initial solution, for example. In the case of Newtonian fluid considering the isothermal case, the critical Reynolds number at which bifurcation occurs found for our computations is $Re_c = 53.5$. Comparing with the literature, this approach is rather accurate, considering that different methods have been applied in each case. For example, in the work of Oliveira et al. [125] the critical value is $Re_c = 54$ using a finite volume method; for Fearn et al. [66] it was $Re_c = 53.9$ using in that case a FE framework. We can find also the work of Drikakis [59] which uses a fourth-order finite-difference method and the critical Reynolds value is $Re_c = 53.3$. In the literature, we find also other examples such as the work of Hawa and Rusak [88], which employ a stream function finite-difference formulation and where the critical Reynolds number is $Re_c = 53.8$. In Table 3.2, this comparison is summarized. The goal of this study is not to be accurate in the exact location of this critical number, but to validate the algorithm and check the thermal coupling for considering later the viscoelastic case from a qualitative point of view.

For the coupling with the temperature, we consider a Weissenberg number equal to zero to study the differences with the isothermal case. On the other hand, we fix the Prandtl number to 1 and the Brinkman number also to 1. The Reynolds and the Weissenberg numbers are computed taking the average of the fluid velocity at the channel inlet. The parameters of the problem are determined according to the values of these dimensionless numbers.

In Figures 3.10 and 3.11 several plots of the stationary solution have been taken for different Reynolds numbers to show some aspects of this problem: the streamlines in each case and the distribution of the temperatures. All the plots correspond to the non-isothermal Newtonian case, although the pattern of vortices is similar in all the computation cases.

- It can be observed in Figure 3.10 that for Re = 10 and Re = 30 the solution is symmetric, although we can see as the length of the vortices is higher as the Reynolds number increases. For Re = 50 the solution has bifurcated and presents an asymmetry: now the vortex on the top is smaller than the vortex in the bottom. Finally, for Re = 100 we can see that apart from the non-symmetric solution, a new vortex has emerged on the top, although displaced downstream. In other words, when the inertial forces are more dominant in comparison with the viscous forces, the fluid flow becomes unstable and the asymmetry appears.

- Regarding the contours of temperature, we can see graphically the effect of the viscous dissipation. As it was specified in the Setup section of the problem, the temperature at the inlet of the channel is 100 K lower than on the walls. Despite this fact, viscous dissipation generates energy in the flowing fluid, reaching the maximum peak when the fluid flow does the transition from the small part of the channel to the wider part. This effect is due to the formation of symmetric recirculation regions, causing a displacement of the maximum peak of heat in the central zone. Moreover, we have to stand out that the maximum value of temperature is moved into the channel when the Reynolds number increases. When Re grows and there is a formation of asymmetric vortices, the location of the maximum temperature zone slightly diverges to the wall where the smaller vortices are formed. Therefore, the maximum temperature zone is generated in the vicinity of the largest vortex and close to its center. These results are in agreement with the results reported by Shahbani-Zahiri [150].

In Figure 3.11 we plot also streamlines and temperature contours for a higher Reynolds number.

- For Re = 150 we can remark that the vortices have been enlarged in comparison with the case Re = 100, and how the vortex on the top starts to split into two separated vortices. For Re = 200, the plot of streamlines shows the appearance of a new vortex near the bottom wall, apart from the evident enlargement of some of the other vortices.

- The distribution of temperature displays a pronounced gradient of temperatures, and note that the small channel transports a cold flux. In this case, it seems clear that the advection velocity in the energy equation has an important role in this change of temperature distribution. Even the maximum peak of temperatures is not located now at the center of the channel, it can be found in one of the asymmetric vortices.

Now, we will compare the length of the vortices between different cases (isothermal and non-isothermal). Note that in Figure 3.9a a general scheme of the vortices is plotted in the domain, apart from the general notation to describe this domain. This comparison is displayed in Figure 3.12, considering both cases: the isothermal (plotted in blue) and the non-isothermal (plotted in red) cases for the Newtonian fluid flow.

- At the first sight, the length of the vortices in the non-isothermal case is higher than in the isothermal scenario, but that is not the only difference, also the critical Reynolds number where the bifurcation occurs has changed significantly. As we have analyzed previously, while the first bifurcation occurs for a critical Reynolds around 53-54 for the isothermal case, if the thermal coupling is considered, that first bifurcation is found around a $Re_c = 30$.

- The difference between Reynolds numbers is even more pronounced for the second bifurcation: while in the isothermal case the critical Reynolds is 117 (from this point a third vortex emerges in the same side of the channel than the smaller vortex, as represented in Figure 3.9a), in the non-isothermal case the critical number is around 60. In this last case, the third vortex grows significantly, even overtaking in length vortex X_{r1} (that occurs for Re = 150, for example).
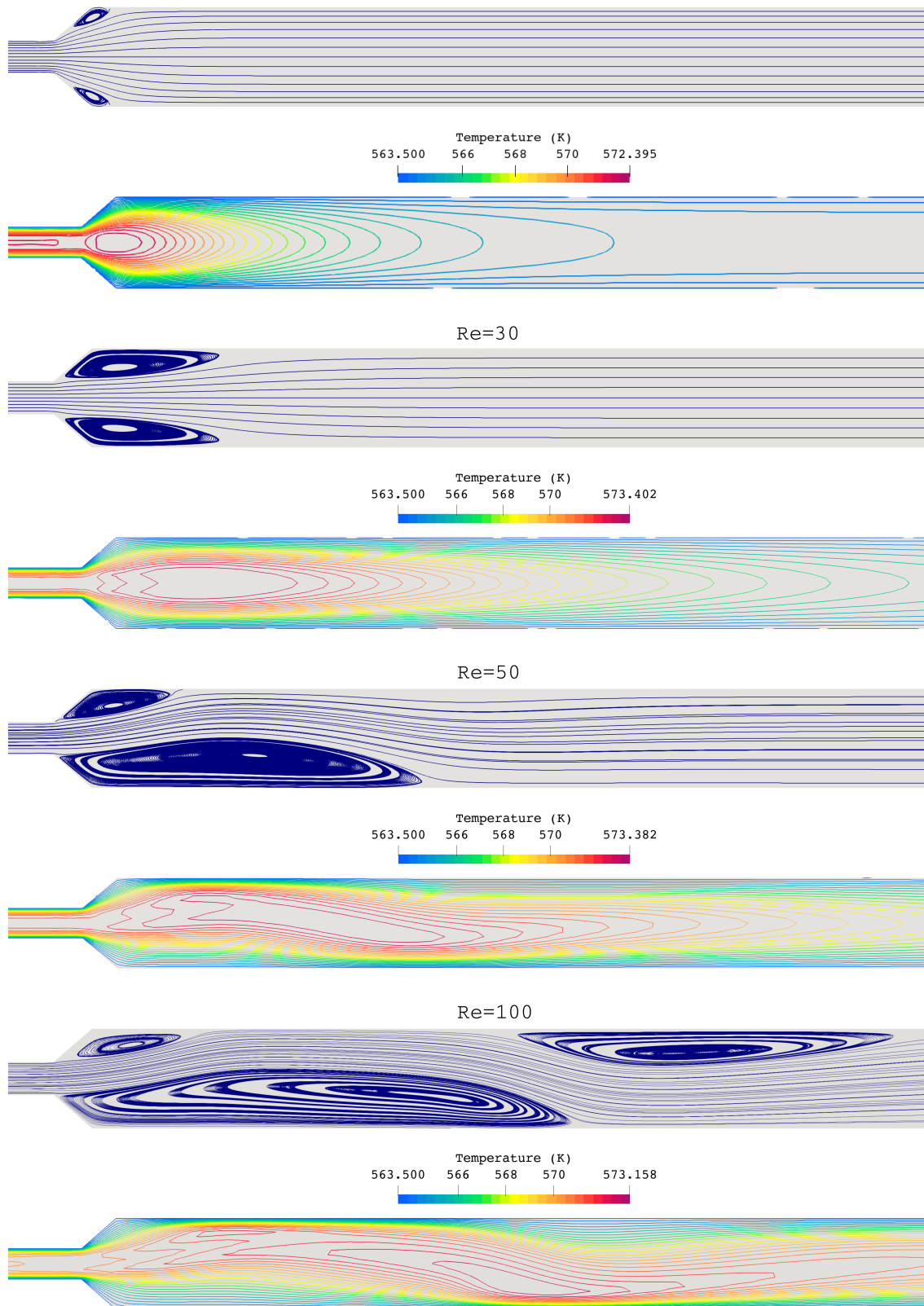
Figure 3.10: Streamlines and temperature contours for Re = 10, 30, 50 and 100.
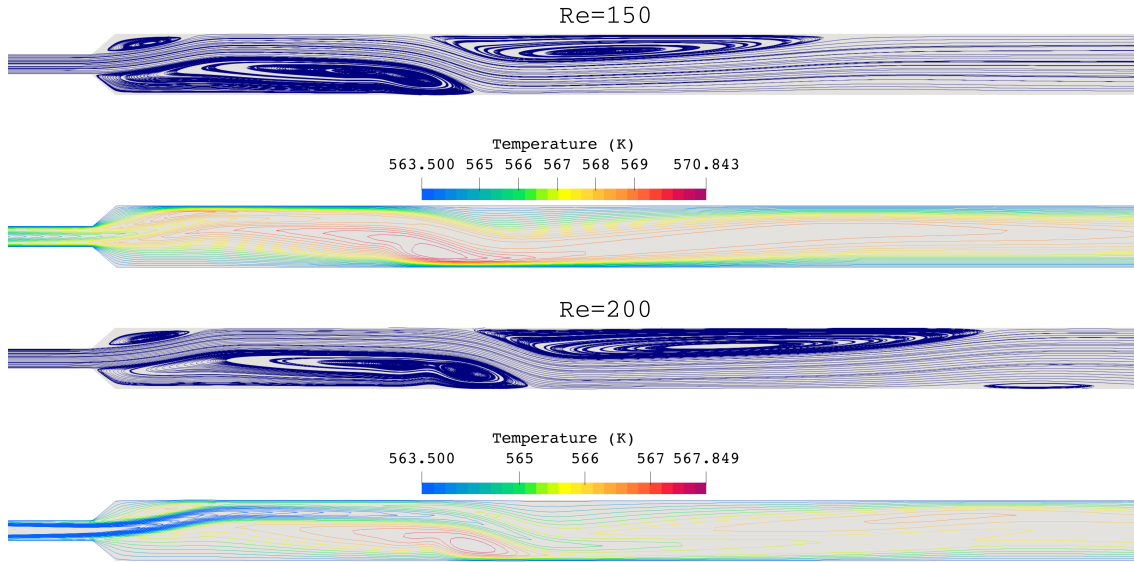
Figure 3.11: 1:3 expansion. Streamlines and temperature contours for Re = 150 and Re = 200.
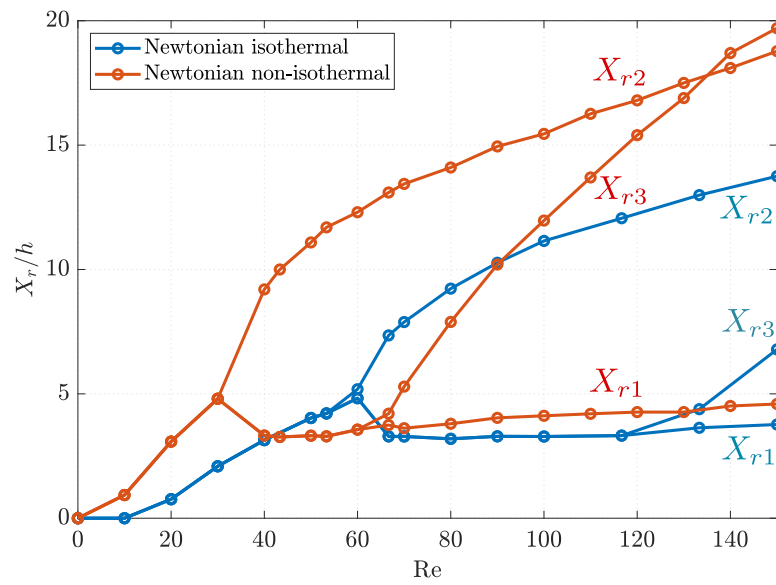
Figure 3.12: 1:3 expansion. Length of vortices versus the Reynolds number for the Newtonian fluid flow.

Weissenberg number study

As it was commented previously, for non-Newtonian viscoelastic flows the number of independent parameters that can be varied increments significantly. We can now modify the Weissenberg number or the β (that measures the balance between polymeric and solvent viscosity) parameters, for example, apart from the Reynolds number. We have to remark that the log-conformation reformulation to solve the problem in the case of high Weissenberg numbers has been crucial to obtaining solutions, despite the increment of the computational cost associated with that formulation [120].

In this study, the main results will put the focus on how viscoelasticity influences the variation of upper and lower vortices in the example we are analyzing. In this sense, we can observe the plots in Figure 3.13, where a comparison of the length of vortices for varying Reynolds numbers is displayed. The bifurcation plot for the viscoelastic liquid for different Weissenberg numbers is compared with that of the Newtonian case. As it is concluded in Oliveira et al. [125], two main conclusions can be drawn:

- The first one is the fact that the critical Reynolds number in which the bifurcation (transition between symmetric and asymmetric solution) is produced is delayed to higher values. For the Newtonian case, that number is around 53.3, and in our computations, for We = 1 it is around 60, and for We = 2 the critical number is around 67. Therefore, we can conclude that viscoelasticity is a stabilizing factor, retarding the appearance of the asymmetric solution. In terms of the elastic forces, we can conclude that when these are more relevant in relation with viscous forces, then the fluid flow is more stable.

- The second one is the size of the vortices. In general, for viscoelastic cases, the size is smaller when it is compared with the Newtonian case (see Figure 3.13a), in particular for the higher vortex X_{r1}. For the smaller vortex, a contrary effect occurs: the size is higher. Therefore, we can conclude that the difference between vortices is lower in the presence of elasticity. That occurs clearly in a Reynolds number range between 0 and 100; when the Reynolds number is more relevant, the effect of viscoelasticity is not that remarkable in this aspect.

- In Figure 3.13b we compare the size of the vortices with the Weissenberg number, with a range of We from 0 to 2. This plot reinforces the previous idea: that elasticity is a stabilizing factor of the bifurcation. The difference between vortices is smaller (the smaller vortex increases while the larger vortex decreases) when the Weissenberg number increases, until the symmetry of the solution is recovered for a We = 2.

In Figure 3.14, the effect of temperature is analyzed in the viscoelastic case, in particular taking We = 1. A similar effect as the one reported in the Newtonian case is reproduced here: an increase of vortex length and the asymmetry appearing at a low Reynolds number for the non-isothermal case.Also, a comparison between non-isothermal cases considering different Weissenberg numbers (We = 1, 2, 3) together with the Newtonian case was carried out; however, no significant differences were found referring to the vortex length or the Reynolds number where the asymmetry occurs. The reason seems to be that the length of the vortices is dominated mainly by the Prandtl number when the coupling is considered.

Despite the length of the vortex not being affected by elasticity, in Figure 3.15 the maximum temperature peaks are plotted in both cases: the Newtonian one and the viscoelastic case considering We = 1. As in the previous benchmark, an increase of temperature is noticed when the viscoelastic fluid flow is contemplated.
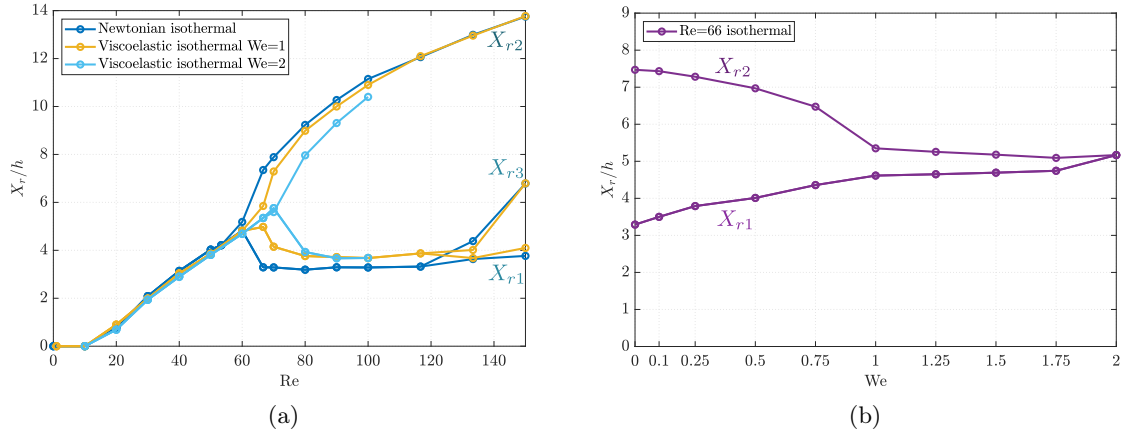
Figure 3.13: 1:3 expansion. Length of vortices versus the Reynolds number (a), and length of vortices versus the Weissenberg number for Reynolds 66.67 (b).
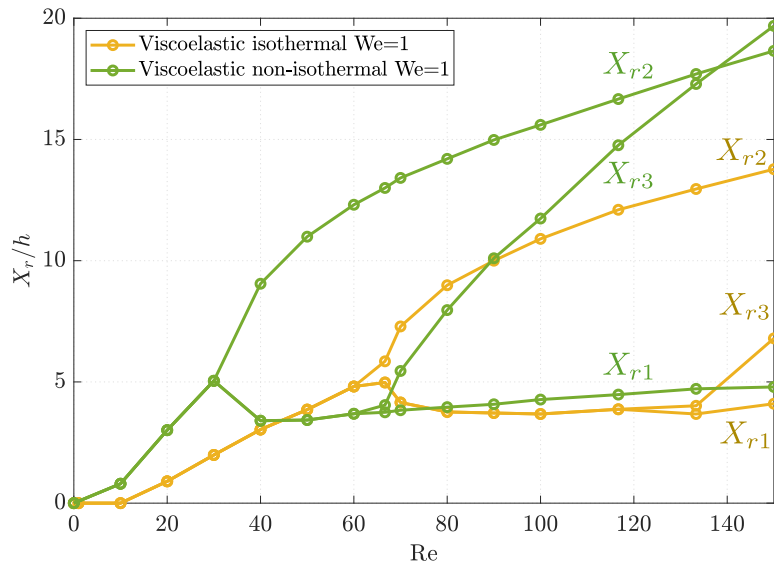
Figure 3.14: 1:3 expansion. Viscoelastic fluid flow considering the coupling for temperature with $Pr = 1$, $Br = 1$.
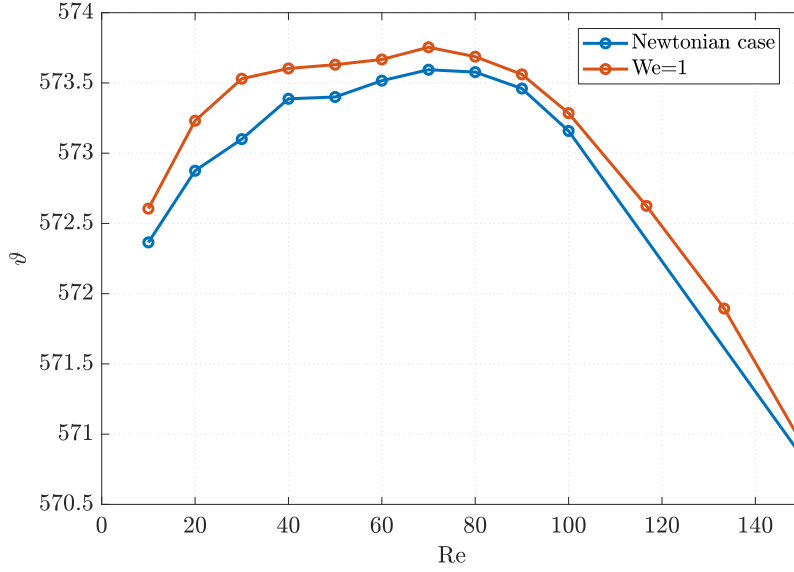
Figure 3.15: 1:3 expansion. Maximum peaks of temperatures with Pr = 1, Br = 1.

Prandtl number study

The influence of the Prandtl number on the temperature and on the vortices length is investigated to see how the flow pattern changes when it is increased. In Figure 3.16 we can observe with more detail that effect.

- Firstly, in Figure 3.16a we compare the vortices for three different Prandtl number, varying the Reynolds number. Apart from the fact that the vortices are smaller in general when the Prandtl number is greater, also the critical Reynolds where the bifurcation occurs changes. While for Pr = 1 and Pr = 100 the first bifurcation is situated at Re = 30 approximately, for Pr = 250 it is located at Re = 40. The second bifurcation suffers a more pronounced displacement regarding Reynolds number: for Pr = 1 it is located at Re = 60 but for Pr = 100 it is at Re = 80 and for Pr = 250 at Re = 100.

- Second, fixing the Reynolds number to 40 and varying the Prandtl number (see Figure 3.16b) we obtain a reduction of the length of the vortices, reaching a symmetrical solution for Pr = 250. However, for a smaller Prandtl, the solution is asymmetric. In this aspect, the effect is similar to the Weissenberg number influence: the increase of Pr gives a more *stable* solution. In terms of the heat convection forces in relation with the diffusivity, we can state that the flow pattern is more stable when the heat convection forces are significantly higher than the heat diffusion.

The temperature contours can be observed in Figure 3.17 for two different Prandtl numbers considering in both cases Re = 40, Br = 1 and We = 0.1. Two main comments can be done about the distribution of this field.

- The temperature contours are significantly different between the two cases. When the Prandtl number is small (Pr = 1), the thermal diffusivity is dominant compared to the convective term, and despite the inlet temperature being colder than on the walls, that fact does not affect the temperature distribution. In that case, the
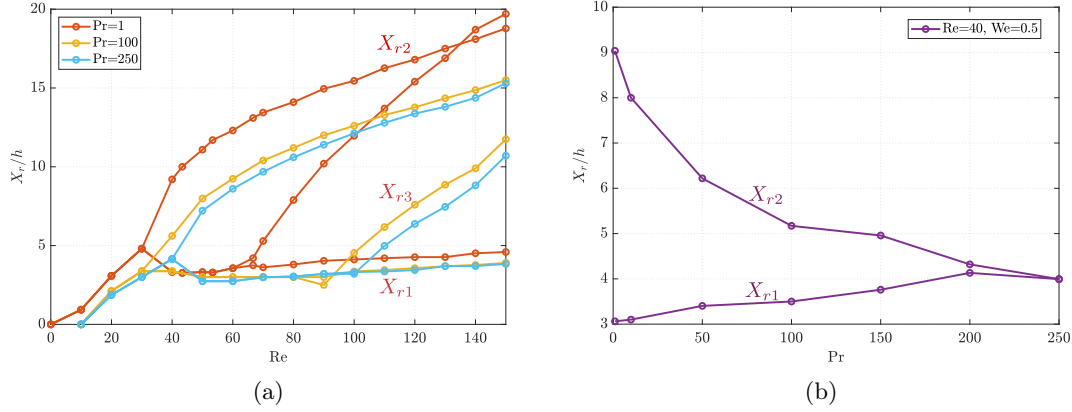
Figure 3.16: 1:3 expansion. Effect of Prandtl number on vortex length, We = 0.1, Br = 1. Length of vortices versus the Reynolds number (a), and length of vortices versus the Prandtl number for Re = 40 (b).

temperature is higher at the center of the duct, due to the effect of the viscous dissipation.

- However, in the case of Pr = 100, the convective term is now dominant, and therefore the cold inlet flow is distributed along the whole duct. For this reason, the gradient of the temperature is more pronounced in a channel cross-section (varying between 463.27 K to 570 K), and the maximum of temperatures induced by the internal work of the elastic fluid concentrates in the vortices. That effect is similar to the one reported in the case Pr = 1 and high Reynolds number (see Figure 3.11). In that case, the convective forces were also dominant but induced by a high advection velocity instead of a high heat capacity in comparison with the conductivity of the fluid flow.

Brinkman number study

Until this point, the effect of the Reynolds, Weissenberg, and Prandtl dimensionless numbers has been studied and characterized. In all the previous cases we have considered the Brinkman number as 1, as it was considered in the reference work [150]. y studying the influence for the four dimensionless numbers characteristics of the problem, we will see also how the Brinkman number affects the flow pattern. Note that this number compares the inertial power with the heat conduction, as explained previously. This dimensionless number can be understood as a global number that measures the coupling between flow and temperature. Therefore, following the same procedure as for the other dimensionless numbers studies, we display two different plots, represented in Figure 3.18.

- The first one (Figure 3.18a) represents the comparison of the vortex length for a range of Reynolds numbers and three Brinkman numbers: 1, 50, and 100. Note that for clarity, the same color is employed for representing the vortices of the same Brinkman number; nevertheless, different linestyles have been used to distinguish more clearly the length of each vortex and compare them. Let us remark that for computations where the Brinkman number is high, such as Br = 50 or Br = 100,

(a) Pr=1
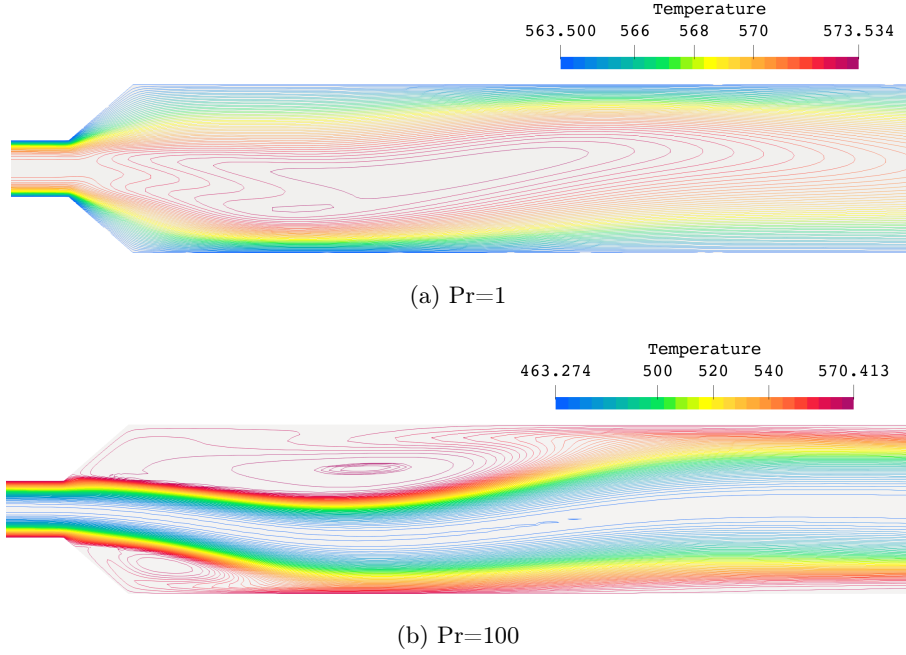
(b) Pr=100

Figure 3.17: 1:3 expansion. Distribution of temperature in the domain considering We = 0.1, Br = 1 and Re = 40 for two different Prandtl numbers: Pr = 1 (a) and Pr = 100 (b).

new vortices emerge for low Reynolds number, also the size of the vortices is larger than in the case of Br = 1. Regarding the asymmetry, it occurs for a lower Reynolds number, (Re = 20) for Br = 50 and Br = 100, and also three vortices of different size appear simultaneously. For low Brinkman number, until Re = 66 the third vortex does not appear, while for Br = 50, it occurs for approximately Re = 30. The fourth vortex emerges also for a low Reynolds number (Re = 45 in the case of Br = 100) in contrast with the low Brinkman number case, in which it is located at Re = 200 (see Figure 3.11).

- In Figure 3.18b, the lengths of the vortices are represented, fixing the Re = 40, We = 0.1 and Pr = 1. In this plot, the Brinkman effect can be observed with major clarity. For a decreasing Br the flow is stabilized until a stable symmetrical state is reached. In other words, the asymmetry is reduced and it is completely attenuated when the Brinkman number is 1. Otherwise, as the Brinkman number increases the flux becomes more *unstable*.

3.7   Conclusions

Throughout this work, the effect of the temperature coupling with viscoelastic fluid flows has been studied and analyzed. First of all, sub-grid scale VMS-stabilization methods have been proposed to obtain an accurate solution for high elastic flows. In this concern, two different formulations have been employed: both the standard and the log-conformation reformulation have been coupled with temperature. The log-conformation reformulation has been crucial for solving simulations with a high Weissenberg number, for which it is otherwise impossible to obtain converged solutions. Referring to the coupling, it is carried out in two different ways: on the one hand, viscoelastic properties are now temperature-

(a)   (b)
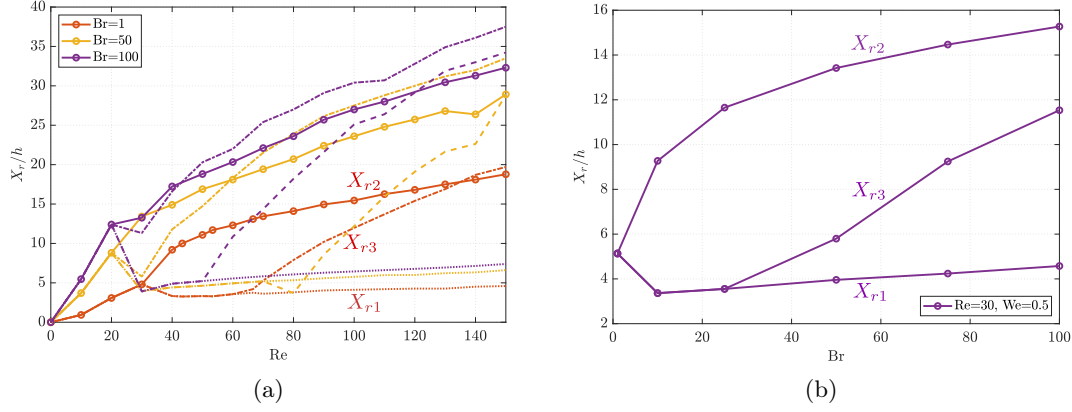
Figure 3.18: 1:3 expansion. Effect of Brinkman number in vortex length, We = 0.1, Pr = 1. Length of vortices versus the Reynolds number (a), and length of vortices versus the Brinkman number for Re = 30 (b).

dependent through defined functions. On the other, the energy equation has to consider the mechanical part of the elastic flow which is transformed into heat.

Regarding the numerical simulations, of the observed effects, two are the most remarkable: the first one is the increase of temperatures when the Weissenberg number increases, and the second one is a stress reduction in comparison with isothermal cases. However, in the particular case of the 1:3 expansion, also a thermal coupling effect to the flow pattern in the channel is found. In that case, we can observe that the asymmetric solution appears for lower Reynolds number in comparison with the isothermal case or a higher size of the vortices that emerge in both sides of the channel is observed. Moreover, the flow pattern is strongly influenced by the parameters that define the problem and for this reason, that influence has been explored varying the Prandtl number and the Brinkman number apart from the Reynolds and Weissenberg numbers. As a general trend and for the models considered herein, the flow is more stable for low Re, high We, low Br and high Pr.

Chapter 4

Time-dependent subgrid-scales

This chapter is based on the publication:

Moreno L., Codina R. & Baiges J. (2020). Solution of transient viscoelastic flow problems approximated by a term-by-term VMS stabilized finite element formulation using time-dependent subgrid-scales. *Computer Methods in Applied Mechanics and Engineering*, 367, 113074.

4.1   Abstract

In this chapter, some finite element stabilized formulations for transient viscoelastic flow problems are presented. These are based on the Variational Multiscale (VMS) method, following the approach introduced in Castillo and Codina, *Comput. Meth. Appl. Mech. Eng.*, vol. 349, pp. 701 - 721 (2019), for the Navier-Stokes problem, the main feature of the method being that the time derivative term in the subgrid-scales is not neglected. The main advantage of considering time-dependent sub-grid scales is that stable solutions for anisotropic space-time discretizations are obtained; however other benefits related with elastic problems are found along this study. Additionally, a split term-by-term stabilization method is discussed and redesigned, where only the momentum equation is approached using a term-by-term methodology, and which turns out to be much more efficient than other residual-based formulations. The proposed methods are designed for the standard and logarithmic formulations in order to deal with high Weissenberg number problems in addition to anisotropic space-time discretizations, ensuring stability in all cases. The proposed formulations are validated in several benchmarks such as the flow over a cylinder problem and the lid-driven cavity problem, obtaining stable and accurate results. A comparison between formulations and stabilization techniques is done to demonstrate the efficiency of time-dependent sub-grid scales and the term-by-term methodologies.

4.2   Background

Recent studies indicate that classical residual-based stabilized methods for unsteady incompressible flows may experience difficulties when the time step is small relative to the spatial grid size. For example, Bochev et al. [20] argue that spatial stabilization in conjunction with finite differencing in time implies destabilizing terms and that $\delta t > Ch^2$ is a sufficient condition to avoid instabilities (where δt is the time step size, C a positive con-

stant and h the spatial grid size), although they are not conclusive about the necessity of this condition. Nevertheless, for anisotropic space-time discretizations (partitions in which h and δt are independently refined), this inequality is not necessarily satisfied [9], and in fact complications in residual-based stabilized methods are reported. These problems can happen, for instance, when small time steps result from the necessity of accuracy to solve transient problems due to the presence of non-linear terms in the differential equations, a very common issue in viscoelastic flow formulations. The results presented by Bochev et al. [19] explain why fully discrete formulations experience problems when $\delta t \to 0$, putting the focus on the coercivity of the stabilized variational equation. These instabilities are encountered particularly in early stages of the time integration.

In particular, the approximations used in Variational Multiscale (VMS) methods [91] usually neglect the time derivative of the sub-grid scales, resulting in the inequality $\delta t > Ch^2$ being required to obtain stable solutions. Consequently, anisotropic space-time discretizations cannot guarantee stability, as it is argued by Codina et al. [47]. The sub-grid scales obtained neglecting the time derivative are denoted in [40] with the term *quasi-static.* In this sense, the work [47] results crucial, because the authors explore all the properties of the discrete formulation that is obtained when the temporal dependency of subgrid scales is accounted for. This idea, which is widely developed in the quoted paper, avoids some inconsistencies, allowing to solve turbulent flows accurately [50]. In addition, the computational effort is reduced significantly due to the reduction of non-linear iterations needed to solve at each time step.

In a more recent publication [30], the authors present the benefits of the tracking of sub-grid scales in time for the Navier-Stokes incompressible problem using various stabilized methods, including a residual-based VMS method and a method whose structure is split term-by-term, where the use of orthogonal projections results in an optimal order non-consistent method. This work demonstrates that, considering dynamic sub-grid scales, the anisotropic time-space discretization is completely stable, i.e. the inequality $\delta t > Ch^2$ does not need to be satisfied. By following these ideas, the present chapter pursues to expand transient subgrid-scale methods to the viscoelastic flow problem. The interest of a term-by-term stabilization in the stationary viscoelastic problem was identified in [28], where it is shown that some terms of standard residual-based formulations that do not contribute to stability may in fact lead to wrong localization of peaks of pressure and stress.

The computation of viscoelastic flows leads to its own difficulties, as it was explained in Chapter 2, especially when elasticity becomes dominant, i.e., when the dimensionless number known as the *Weissenberg number* is high. In these cases, the numerical instability is caused by the lack of balance between deformation rate and convection, as identified by Fattal and Kupferman [65]. The source of the so called High Weissenberg Number Problem (HWNP) is associated with the loss of positive-definiteness of the conformation tensor [64, 91], and the existence of large stress gradients and regions with high deformation rate that cause the numerical methods to fail. A new formulation was proposed by Fattal and Kupferman [64, 65] in order to deal with these shortcomings: the so called Logarithmic Conformation Representation. This formulation arises from the traditional equations of viscoelastic fluids together with a change of variables, with the objective of eliminating instabilities, allowing to extend the range of Weissenberg numbers which can be computed. In this sense, in Chapter 2 this reformulation is applied using a stabilized formulation based on the VMS method, which will be the basis of some of the stabilized formulations employed here.

Although it is not the objective of this chapter to discuss complex applications of the

logarithmic formulation, let us mention that it has opened the door to approximate complex viscoelastic flow problems, as the droplet formation in [114] (using a finite volume method) or the simulation of centrifugal ventricular assist devices in [87], where the logarithm of a shape tensor entering the viscoelastic model is taken (and, as in our case, a VMS formulation is employed).

To sum up, the purpose of the present chapter is the design of stabilization techniques that allow one to compute time-dependent viscoelastic flow problems with high elasticity (or Weissenberg number) and with an anisotropic space-time discretization. High elasticities are expected to be achieved by the use of the logarithmic formulation of the problem, whereas the anisotropic space-time discretization will be possible because of the term-by-term VMS method with transient subgrid scales we present. Yet, there is also an obvious link between the possibility to treat high Weissenberg numbers and the VMS method we propose, since small time steps are required in complex flow cases. Since the logarithmic formulation and the term-by-term formulation are independent, along this chapter both standard and logarithmic formulations are considered, compared and validated in some numerical examples.

The structure of the chapter is as follows: Section 4.3 explains the main features of the standard and logarithmic formulations in the strong and variational form for an Oldroyd-B fluid. At the end of this section, the Galerkin finite element (FE) and the time discretization are described. Once the main equations are set, Section 4.4 exposes the stabilized FE approach based on the VMS method considering the dynamic sub-grid scales through two different forms: the residual-based stabilization and the split term-by-term stabilization, where the particularities of the formulation design are discussed numerically. In Section 4.5 the stability analysis of the formulation is presented. The numerical results are exposed in Section 4.6, where three different benchmarks are computed and analysed to validate the formulations. Finally, conclusions are collected in the last section of the chapter, Section 4.7.

4.3 Viscoelastic flow problem

4.3.1 Strong form

The definition of the viscoelastic flow problem understood as a boundary problem written in both, standard and logarithmic formulation is performed in Chapter 2, in particular in Section 2.3. Therefore, see this section to see more details. The notation of the main operators of the problem will be the same as the one detailed there.

4.3.2 Variational form

In contrast with the analogous section in Chapter 2, the variational form of the standard and the logarithmic formulations is also detailed. The notation followed for the spaces in this section is the same as in the firsts paragraphs of Section 2.3.3. Using that notation, the spaces for continuous standard problem can be taken as: $\boldsymbol{\Upsilon} = H^1(\Omega)^{d \times d}_{\text{sym}}$ (symmetric second order tensor with components in $H^1(\Omega)$) for the stress field, $\boldsymbol{V}_0 = H^1_0(\Omega)^d$ for the velocity field and $\mathcal{Q} = L^2(\Omega)/\mathbb{R}$ for the pressure for each fixed time t (the regularity for the stress space could be relaxed).

The weak form of the problem consists in finding $\boldsymbol{U} = [\boldsymbol{u}, p, \boldsymbol{\sigma}] :]0, T[\longrightarrow \boldsymbol{\mathcal{X}} := \boldsymbol{V}_0 \times$

$\boldsymbol{Q} \times \boldsymbol{\Upsilon}$, such that the initial conditions are satisfied and:

$$\left(\rho\frac{\partial \boldsymbol{u}}{\partial t}, \boldsymbol{v}\right) + (\boldsymbol{\sigma}, \nabla^s \boldsymbol{v}) + 2(\eta_s \nabla^s \boldsymbol{u}, \nabla^s \boldsymbol{v}) + \langle \rho \boldsymbol{u} \cdot \nabla \boldsymbol{u}, \boldsymbol{v}\rangle - (p, \nabla \cdot \boldsymbol{v}) = \langle \boldsymbol{f}, \boldsymbol{v}\rangle,$$

$$(q, \nabla \cdot \boldsymbol{u}) = 0,$$

$$\frac{1}{2\eta_p}(\boldsymbol{\sigma}, \boldsymbol{\chi}) - (\nabla^s \boldsymbol{u}, \boldsymbol{\chi}) + \frac{\lambda}{2\eta_p}\left(\frac{\partial \boldsymbol{\sigma}}{\partial t} + \boldsymbol{u} \cdot \nabla \boldsymbol{\sigma} - \boldsymbol{\sigma} \cdot \nabla \boldsymbol{u} - (\nabla \boldsymbol{u})^T \cdot \boldsymbol{\sigma}, \boldsymbol{\chi}\right) = 0,$$

for all $\boldsymbol{V} = [\boldsymbol{v}, q, \boldsymbol{\chi}] \in \boldsymbol{\mathcal{X}}$, where it is assumed that $\boldsymbol{f}$ is such that $\langle \boldsymbol{f}, \boldsymbol{v}\rangle$ is well defined. In compact form, the problem can be written as:

$$\mathcal{G}_{\text{std}}(\boldsymbol{U}, \boldsymbol{V}) + B_{\text{std}}(\boldsymbol{u}; \boldsymbol{U}, \boldsymbol{V}) = L_{\text{std}}(\boldsymbol{V}), \tag{4.1}$$

for all $\boldsymbol{V} \in \boldsymbol{\mathcal{X}}$, where

$$\mathcal{G}_{\text{std}}(\boldsymbol{U}, \boldsymbol{V}) = \left(\rho\frac{\partial \boldsymbol{u}}{\partial t}, \boldsymbol{v}\right) + \frac{\lambda}{2\eta_0}\left(\frac{\partial \boldsymbol{\sigma}}{\partial t}, \boldsymbol{\chi}\right), \tag{4.2}$$

$$B_{\text{std}}(\hat{\boldsymbol{u}}; \boldsymbol{U}, \boldsymbol{V}) = 2(\eta_s \nabla^s \boldsymbol{u}, \nabla^s \boldsymbol{v}) + \langle \rho \hat{\boldsymbol{u}} \cdot \nabla \boldsymbol{u}, \boldsymbol{v}\rangle + (\boldsymbol{\sigma}, \nabla^s \boldsymbol{v})$$

$$- (p, \nabla \cdot \boldsymbol{v}) + (q, \nabla \cdot \boldsymbol{u}) + \frac{1}{2\eta_p}(\boldsymbol{\sigma}, \boldsymbol{\chi}) - (\nabla^s \boldsymbol{u}, \boldsymbol{\chi})$$

$$+ \frac{\lambda}{2\eta_p}\left(\hat{\boldsymbol{u}} \cdot \nabla \boldsymbol{\sigma} - \boldsymbol{\sigma} \cdot \nabla \hat{\boldsymbol{u}} - (\nabla \hat{\boldsymbol{u}})^T \cdot \boldsymbol{\sigma}, \boldsymbol{\chi}\right), \tag{4.3}$$

$$L_{\text{std}}(\boldsymbol{V}) = \langle \boldsymbol{f}, \boldsymbol{v}\rangle. \tag{4.4}$$

Considering now the logarithmic reformulation of the viscoelastic flow problem, the spaces for the velocity and pressure for the continuous problems are the ones defined above for the standard formulation, and now, the space for tensor $\boldsymbol{\psi}$ is denoted by $\bar{\boldsymbol{\Upsilon}}$ for each fixed time t, where an appropriate regularity is assumed, such as it is expressed in Section 2.3.3 in Chapter 2. The weak form of the problem consists in finding $\boldsymbol{U} = [\boldsymbol{u}, p, \boldsymbol{\psi}] :]0, T[\longrightarrow \bar{\boldsymbol{\mathcal{X}}} := \boldsymbol{V}_0 \times \boldsymbol{Q} \times \bar{\boldsymbol{\Upsilon}}$, such that the initial conditions are satisfied and (2.14) - (2.16) hold for all $\boldsymbol{V} = [\boldsymbol{v}, q, \boldsymbol{\chi}] \in \boldsymbol{\mathcal{X}}$. Again taking into account the new definition of $\boldsymbol{U}$ for this formulation, the problem can be written as:

$$\mathcal{G}_{\log}(\boldsymbol{U}, \boldsymbol{V}) + B_{\log}(\boldsymbol{u}; \boldsymbol{U}, \boldsymbol{V}) = L_{\log}(\boldsymbol{V}), \tag{4.5}$$

where each term is defined as

$$\mathcal{G}_{\log}(\boldsymbol{U}, \boldsymbol{V}) = \left(\rho\frac{\partial \boldsymbol{u}}{\partial t}, \boldsymbol{v}\right) + \frac{\lambda}{2\lambda_0}\left(\frac{\partial \exp(\boldsymbol{\psi})}{\partial t}, \boldsymbol{\chi}\right), \tag{4.6}$$

$$B_{\log}(\hat{\boldsymbol{u}}; \boldsymbol{U}, \boldsymbol{V}) = \frac{\eta_p}{\lambda_0}(\exp(\boldsymbol{\psi}), \nabla^s \boldsymbol{v}) + 2(\eta_s \nabla^s \boldsymbol{u}, \nabla^s \boldsymbol{v}) + \langle \rho \hat{\boldsymbol{u}} \cdot \nabla \boldsymbol{u}, \boldsymbol{v}\rangle - (p, \nabla \cdot \boldsymbol{v})$$

$$+ (\nabla \cdot \boldsymbol{u}, q) + \frac{1}{2\lambda_0}(\exp(\boldsymbol{\psi}), \boldsymbol{\chi}) - (\nabla^s \boldsymbol{u}, \boldsymbol{\chi})$$

$$+ \frac{\lambda}{2\lambda_0}\left(\boldsymbol{u} \cdot \nabla \exp(\boldsymbol{\psi}) - \exp(\boldsymbol{\psi}) \cdot \nabla \boldsymbol{u} - (\nabla \boldsymbol{u})^T \cdot \exp(\boldsymbol{\psi}) + 2\nabla^s \boldsymbol{u}, \boldsymbol{\chi}\right), \tag{4.7}$$

$$L_{\log}(\boldsymbol{V}) = \langle \boldsymbol{f}, \boldsymbol{v}\rangle + \frac{1}{2\lambda_0}\langle \boldsymbol{I}, \boldsymbol{\chi}\rangle. \tag{4.8}$$

4.3.3 Galerkin finite element discretization and time discretization

First, the Galerkin approximation for the variational problems, which have been established in (4.1) and (4.5), will be described for both formulations. Let start defining the

notation which we will employ in this section. The finite element partition of the domain Ω is $\mathcal{T}_h = \{K\}$. Likewise, the diameter of an element $K \in \mathcal{T}_h$ is denoted by h_K and the diameter of the partition is defined as $h = \max\{h_K | K \in \mathcal{T}_h\}$.

In the particular case of the standard formulation, from $\mathcal{T}_h$ we may construct conforming finite element spaces for the velocity, the pressure and the elastic stress, $\boldsymbol{\mathcal{V}}_h \subset \boldsymbol{\mathcal{V}}$, $\mathcal{Q}_h \subset \mathcal{Q}$, $\boldsymbol{\Upsilon}_h \subset \boldsymbol{\Upsilon}$, respectively. So, calling $\boldsymbol{\mathcal{X}}_h := \boldsymbol{\mathcal{V}}_h \times \mathcal{Q}_h \times \boldsymbol{\Upsilon}_h$, the Galerkin FE approximation of the standard problem consists in finding $\boldsymbol{U}_h :]0, T[\longrightarrow \boldsymbol{\mathcal{X}}_h$, such that:

$$\mathcal{G}_{\mathrm{std}}(\boldsymbol{U}_h, \boldsymbol{V}_h) + B_{\mathrm{std}}(\boldsymbol{u}_h; \boldsymbol{U}_h, \boldsymbol{V}_h) = \boldsymbol{F}_{\mathrm{std}}(\boldsymbol{V}_h),$$

for all $\boldsymbol{V}_h = [\boldsymbol{v}_h, q_h, \boldsymbol{\chi}_h] \in \boldsymbol{\mathcal{X}}_h$, and satisfying the appropriate initial conditions.

On the other hand, for the logarithmic conformation reformulation, from $\mathcal{T}_h$ we construct the finite element space for the new variable $\boldsymbol{\psi}$, $\bar{\boldsymbol{\Upsilon}}_h \subset \bar{\boldsymbol{\Upsilon}}$. So, $\bar{\boldsymbol{\mathcal{X}}}_h := \boldsymbol{\mathcal{V}}_h \times \mathcal{Q}_h \times \bar{\boldsymbol{\Upsilon}}_h$ is the Galerkin FE now, and the Galerkin approximation consists in finding $\boldsymbol{U}_h :]0, T[\longrightarrow \bar{\boldsymbol{\mathcal{X}}}_h$, such that

$$\mathcal{G}_{\mathrm{log}}(\boldsymbol{U}_h, \boldsymbol{V}_h) + B_{\mathrm{log}}(\boldsymbol{u}_h; \boldsymbol{U}_h, \boldsymbol{V}_h) = \boldsymbol{F}_{\mathrm{log}}(\boldsymbol{V}_h),$$

for all $\boldsymbol{V}_h = [\boldsymbol{v}_h, q_h, \boldsymbol{\chi}_h] \in \boldsymbol{\mathcal{X}}_h$.

It is well known that the Gakerkin approximation is unstable unless convective terms are not relevant and appropriate compatibility conditions between $\mathcal{Q}_h$ and $\boldsymbol{\mathcal{V}}_h$, on the one hand, and between $\boldsymbol{\mathcal{V}}_h$ and $\boldsymbol{\Upsilon}_h$, on the other hand, are met (see for example [26] and references therein). In the next section we will present a stable formulation, able in particular to deal with continuous approximations for all fields, which is the situation we shall consider.

We define now the discretization in time as a backward differencing (BDF) scheme as it was defined in expression (2.25) in Section 2.3.6, using the same notation. Particularly, first and second order backward differencing schemes (respectively referenced as BDF1 and BDF2) have been implemented in this work, based on the approximations:

$$\frac{\delta_1 f^{n+1}}{\delta t} = \frac{f^{n+1} - f^n}{\delta t} = \left.\frac{\partial f}{\partial t}\right|_{t^{n+1}} + \mathcal{O}(\delta t),$$

$$\frac{\delta_2 f^{n+1}}{\delta t} = \frac{3f^{n+1} - 4f^n + f^{n-1}}{2\delta t} = \left.\frac{\partial f}{\partial t}\right|_{t^{n+1}} + \mathcal{O}(\delta t^2).$$

In any case, the stabilized finite element method which will be exposed is independent of the time scheme used.

4.4   Stabilized finite element formulation

In this section, two different stabilized finite element methods for computing viscoelastic flows will be presented: the first is purely based on the finite element residual, and the second one is a term-by-term method. However, both depart from the framework described in [91], and already described in Chapter 2. For more details about this development, see [25]. Additionally, we will develop these methods for the two different formulations considered in this chapter: the well-known standard viscoelastic formulation and for the logarithmic reformulation. Note that the stabilization methods proposed are suitable for the three field Newtonian problem too, which is recovered by considering the parameter λ equal to zero.

4.4.1   Residual-based VMS methods

The problem that we pretend to approximate is (3.6) in strong form for both standard (2.17) and logarithmic (4.5) formulations.

Firstly, we will deal with the standard formulation. Let us suppose that $\mathcal{L}_{\text{std}}(\hat{\boldsymbol{u}}; \cdot)$ is a linear operator for a given $\hat{\boldsymbol{u}}$. Introducing the sub-grid scale decomposition and integrating by parts, the method leads to find $\boldsymbol{U}_h :]0, T[\longrightarrow \boldsymbol{\mathcal{X}}_h$ such that

$$\mathcal{G}_{\text{std}}(\boldsymbol{U}_h, \boldsymbol{V}_h) + B_{\text{std}}(\boldsymbol{u}_h; \boldsymbol{U}_h, \boldsymbol{V}_h) + \sum_K \langle \tilde{\boldsymbol{U}}, \mathcal{L}^*(\boldsymbol{u}_h; \boldsymbol{V}_h) \rangle_K = L_{\text{std}}(\boldsymbol{V}_h), \qquad (4.9)$$

for all $\boldsymbol{V}_h \in \boldsymbol{\mathcal{X}}_h$, where $\mathcal{L}^*(\boldsymbol{u}_h; \boldsymbol{V}_h)$ is the formal adjoint of the operator of $\mathcal{L}_{\text{std}}(\hat{\boldsymbol{u}}; \cdot)$, typically without considering boundary conditions, $\tilde{\boldsymbol{U}}$ is the sub-grid scale, which needs to be approximated and has components $\tilde{\boldsymbol{U}} = [\tilde{\boldsymbol{u}}, \tilde{p}, \tilde{\boldsymbol{\sigma}}]$. To justify (4.9), see e.g. [44], and recall that we are considering all approximations continuous. In fact, the sub-grid scales can also be approximated using bubble functions, as in [105].

Analogously, for the logarithmic formulation, method leads to find $\boldsymbol{U}_h :]0, T[\longrightarrow \bar{\boldsymbol{\mathcal{X}}}_h$ such that

$$\mathcal{G}_{\log}(\boldsymbol{U}_h, \boldsymbol{V}_h) + B_{\log}(\boldsymbol{u}_h; \boldsymbol{U}_h, \boldsymbol{V}_h) + \sum_K \langle \tilde{\boldsymbol{U}}, \mathcal{L}^*(\boldsymbol{u}_h; \boldsymbol{V}_h) \rangle_K = L_{\log}(\boldsymbol{V}_h), \qquad (4.10)$$

for all $\boldsymbol{V}_h \in \boldsymbol{\mathcal{X}}_h$. Let us remark that for both formulations (standard and logarithmic) the same operator $\mathcal{L}^*(\hat{\boldsymbol{u}}; \cdot)$ will be employed, following the process described in [120]:

$$\mathcal{L}^*(\hat{\boldsymbol{u}}; \boldsymbol{V}) := \begin{pmatrix} \nabla \cdot \boldsymbol{\chi} - 2\eta_s \nabla \cdot (\nabla^s \boldsymbol{v}) - \rho \hat{\boldsymbol{u}} \cdot \nabla \boldsymbol{v} - \nabla q \\ -\nabla \cdot \boldsymbol{v} \\ \dfrac{1}{2\eta_p} \boldsymbol{\chi} + \nabla^s \boldsymbol{v} - \dfrac{\lambda}{2\eta_p} \left(\hat{\boldsymbol{u}} \cdot \nabla \boldsymbol{\chi} + \boldsymbol{\chi} \cdot (\nabla \hat{\boldsymbol{u}})^T + \nabla \hat{\boldsymbol{u}} \cdot \boldsymbol{\chi} \right) \end{pmatrix}.$$

This is due to the fact that we have not changed variables in the stress test function.

Once operators $\mathcal{D}_t$ and $\mathcal{L}$ are defined for both formulations, the sub-grid scales can be written in terms of the finite element component as

$$\frac{\partial \tilde{\boldsymbol{U}}}{\partial t} + \boldsymbol{\alpha}^{-1} \tilde{\boldsymbol{U}} = \tilde{P}[\boldsymbol{F} - \mathcal{D}_t(\boldsymbol{U}_h) - \mathcal{L}(\boldsymbol{u}_h; \boldsymbol{U}_h)], \qquad (4.11)$$

where we denote $\tilde{P}$ as the L^2 projection onto the space of sub-grid scales.

Note that the most classical approach, the Algebraic Sub-Grid Scale (ASGS) method is recovered if $\tilde{P}$ is the projection onto the space of FE residuals. On the contrary, if $\tilde{P}$ is taken as the orthogonal projection to the FE space, the Orthogonal Sub-Scale Stabilization (OSGS) method [39] is recovered. On the other hand, $\boldsymbol{\alpha}$ is taken as a diagonal matrix of stabilization parameters, $\boldsymbol{\alpha} = \text{diag}(\alpha_1 \boldsymbol{I}_d, \alpha_2, \alpha_3 \boldsymbol{I}_{d \times d})$, with $\boldsymbol{I}_d$ the identity on vectors of $\mathbb{R}^d$, $\boldsymbol{I}_{d \times d}$ the identity on second order tensors, and parameters α_i, $i = 1, 2, 3$, being defined as in expressions (2.30)-(2.32), and originally in [26].

Now, inserting the solution of (4.11) with $\boldsymbol{\alpha}$ given by (2.30)-(2.32) into (4.9), we obtain the following residual-based stabilization method: find $\boldsymbol{U}_h :]0, T[\longrightarrow \boldsymbol{\mathcal{X}}_h$ such that

$$\mathcal{G}_{\text{std}}(\boldsymbol{U}_h, \boldsymbol{V}_h) + B_{\text{std}}(\boldsymbol{u}_h; \boldsymbol{U}_h, \boldsymbol{V}_h) + \sum_K \langle \tilde{p}, -\nabla \cdot \boldsymbol{v}_h \rangle_K$$

$$+ \sum_K \langle \tilde{\boldsymbol{u}}, \nabla \cdot \boldsymbol{\chi}_h - 2\eta_s \nabla \cdot (\nabla^s \boldsymbol{v}_h) - \rho \boldsymbol{u}_h \cdot \nabla \boldsymbol{v}_h - \nabla q_h \rangle_K$$

$$+ \sum_{K} \left\langle \tilde{\boldsymbol{\sigma}}, \frac{1}{2\eta_p} \boldsymbol{\chi}_h + \nabla^s \boldsymbol{v}_h - \frac{\lambda}{2\eta_p} \left(\boldsymbol{u}_h \cdot \nabla \boldsymbol{\chi}_h + \boldsymbol{\chi}_h \cdot (\nabla \boldsymbol{u}_h)^T + \nabla \boldsymbol{u}_h \cdot \boldsymbol{\chi}_h \right) \right\rangle_K$$

$$= \langle \boldsymbol{f}, \boldsymbol{v}_h \rangle, \tag{4.12}$$

where $\tilde{\boldsymbol{u}}$, $\tilde{p}$ and $\tilde{\boldsymbol{\sigma}}$ are the sub-grid scales of the momentum, the continuity and the constitutive equation, respectively, and $B_{\text{std}}(\hat{\boldsymbol{u}}_h; \boldsymbol{U}_h, \boldsymbol{V}_h)$ is given in (4.3).

The sub-grid scales are the solution to the problem:

$$\rho \frac{\partial \tilde{\boldsymbol{u}}}{\partial t} + \alpha_1^{-1} \tilde{\boldsymbol{u}} = \tilde{P} \left[\boldsymbol{f} - \left(\rho \frac{\partial \boldsymbol{u}_h}{\partial t} - \nabla \cdot \boldsymbol{\sigma}_h - 2\eta_s \nabla \cdot (\nabla^s \boldsymbol{u}_h) + \rho \boldsymbol{u}_h \cdot \nabla \boldsymbol{u}_h + \nabla p_h \right) \right],$$
$$\tag{4.13}$$

$$\alpha_2^{-1} \tilde{p} = - \tilde{P} \left[\nabla \cdot \boldsymbol{u}_h \right], \tag{4.14}$$

$$\frac{\lambda}{2\eta_p} \frac{\partial \tilde{\boldsymbol{\sigma}}}{\partial t} + \alpha_3^{-1} \tilde{\boldsymbol{\sigma}} = \tilde{P} \left[-\frac{1}{2\eta_p} \boldsymbol{\sigma}_h + \nabla^s \boldsymbol{u}_h \right]$$

$$+ \tilde{P} \left[-\frac{\lambda}{2\eta_p} \left(\frac{\partial \boldsymbol{\sigma}_h}{\partial t} + \boldsymbol{u}_h \cdot \nabla \boldsymbol{\sigma}_h - \boldsymbol{\sigma}_h \cdot \nabla \boldsymbol{u}_h - (\nabla \boldsymbol{u}_h)^T \cdot \boldsymbol{\sigma}_h \right) \right]. \tag{4.15}$$

Note that the stabilization terms added to the Galerkin method in (4.12) are proportional to the finite element residuals of the momentum, the continuity and the constitutive equation. Due to this, the stabilized method defined by (4.12) will be denoted as a residual-based VMS method. Furthermore the prefix *orthogonal* will be added if $\tilde{P} = P_h^\perp$.

On the other hand, if the time derivatives of the velocity sub-grid scale (in equation (4.13)) and the stress sub-grid scale (in equation (4.15)) are neglected, the method is usually called *quasi-static,* otherwise it will be denoted as *dynamic*. Particularly, when $\tilde{P} = P_h^\perp$, two additional simplifications can be done:

1. $P_h^\perp \left[\frac{\partial \boldsymbol{u}_h}{\partial t} \right] = 0$ and $P_h^\perp \left[\frac{\partial \boldsymbol{\sigma}_h}{\partial t} \right] = 0$.

2. $P_h^\perp [\boldsymbol{f}] \approx 0$.

If these approximations are adopted, a weakly consistent method is obtained, although if $\boldsymbol{f}$ is a finite element function, full consistency is recovered. The initial condition for the velocity and stress sub-grid scales in (4.13) and (4.15) can be taken as zero [10].

For the logarithmic reformulation, equation (4.10), considering the expression of the sub-grid scales (4.11) it can be expressed as

$$\mathcal{G}_{\log}(\boldsymbol{U}_h, \boldsymbol{V}_h) + B_{\log}(\boldsymbol{u}_h; \boldsymbol{U}_h, \boldsymbol{V}_h)$$

$$+ \sum_{K} \langle \tilde{\boldsymbol{u}}, \nabla \cdot \boldsymbol{\chi}_h - 2\eta_s \nabla \cdot (\nabla^s \boldsymbol{v}_h) - \rho \boldsymbol{u}_h \cdot \nabla \boldsymbol{v}_h - \nabla q_h \rangle_K$$

$$+ \sum_{K} \langle \tilde{p}, -\nabla \cdot \boldsymbol{v}_h \rangle_K + \sum_{K} \left\langle \tilde{\boldsymbol{\sigma}}, \frac{1}{2\eta_p} \boldsymbol{\chi}_h + \nabla^s \boldsymbol{v}_h \right\rangle_K$$

$$+ \sum_{K} \left\langle \tilde{\boldsymbol{\sigma}}, -\frac{\lambda}{2\eta_p} \left(\boldsymbol{\chi}_h \cdot (\nabla \boldsymbol{u}_h)^T + \nabla \boldsymbol{u}_h \cdot \boldsymbol{\chi}_h \right) \right\rangle_K$$

$$= \langle \boldsymbol{f}, \boldsymbol{v}_h \rangle + \frac{1}{2\lambda_0} \langle \boldsymbol{I}, \boldsymbol{\chi} \rangle,$$

where $\tilde{\boldsymbol{u}}$, $\tilde{p}$ and $\tilde{\boldsymbol{\psi}}$ are the sub-grid scales of the momentum, the continuity and the constitutive equation respectively, and $B_{\log}$ is the bilinear form of the problem when the

logarithmic formulation is considered. We have to remark that the sub-grid scale of the constitutive equation, for simplicity, has also been computed as $\tilde{\boldsymbol{\sigma}}$ in the logarithmic case, considering $\tilde{\boldsymbol{\sigma}} = \dfrac{\eta_p}{\lambda_0} \left(\exp\left(\tilde{\boldsymbol{\psi}}\right) - \mathbf{I} \right)$. As a residual-based VMS method is applied, sub-grid scales are defined as follows:

$$\rho \frac{\partial \tilde{\boldsymbol{u}}}{\partial t} + \alpha_1^{-1} \tilde{\boldsymbol{u}} = \tilde{P} \left[\boldsymbol{f} - \left(\rho \frac{\partial \boldsymbol{u}_h}{\partial t} - \frac{\eta_p}{\lambda_0} \nabla \cdot \exp(\boldsymbol{\psi}_h) \right) \right]$$
$$+ \tilde{P} \left[-2\eta_s \nabla \cdot (\nabla^s \boldsymbol{u}_h) + \rho \boldsymbol{u}_h \cdot \nabla \boldsymbol{u}_h + \nabla p_h \right], \tag{4.16}$$

$$\alpha_2^{-1} \tilde{p} = \tilde{P} \left[-\nabla \cdot \boldsymbol{u}_h \right], \tag{4.17}$$

$$\frac{\lambda}{2\eta_p} \frac{\partial \tilde{\boldsymbol{\sigma}}}{\partial t} + \alpha_3^{-1} \tilde{\boldsymbol{\sigma}} = \tilde{P} \left[-\frac{1}{2\lambda_0} \exp(\boldsymbol{\psi}_h) + \nabla^s \boldsymbol{u}_h \right]$$
$$- \tilde{P} \left[\frac{\lambda}{2\lambda_0} \left(\frac{\partial \exp(\boldsymbol{\psi}_h)}{\partial t} + \boldsymbol{u}_h \cdot \nabla \exp(\boldsymbol{\psi}_h) \right) \right]$$
$$+ \tilde{P} \left[\frac{\lambda}{2\lambda_0} \left(\exp(\boldsymbol{\psi}_h) \cdot \nabla \boldsymbol{u}_h + (\nabla \boldsymbol{u}_h)^T \cdot \exp(\boldsymbol{\psi}_h) - 2\nabla^s \boldsymbol{u}_h \right) \right] \tag{4.18}$$

Note that the stabilized parameters $\boldsymbol{\alpha}$ are the same as those defined by the standard formulation (2.30)-(2.32).

4.4.2   Term-by-term stabilized formulation

Motivation

The method proposed here has been motivated by the fact that not all the terms of the product of $\nabla \cdot \boldsymbol{\chi}_h - 2\eta_s \nabla \cdot (\nabla^s \boldsymbol{v}_h) - \rho \boldsymbol{u}_h \cdot \nabla \boldsymbol{v}_h - \nabla q_h$, and the terms that contribute to $\tilde{\boldsymbol{u}}$ in (4.12) provide stability. Likewise, the same occurs for the constitutive equation adjoint,

$$\frac{1}{2\eta_p} \boldsymbol{\chi}_h + \nabla^s \boldsymbol{v}_h - \frac{\lambda}{2\eta_p} \left(\boldsymbol{u}_h \cdot \nabla \boldsymbol{\chi}_h + \boldsymbol{\chi}_h \cdot (\nabla \boldsymbol{u}_h)^T + \nabla \boldsymbol{u}_h \cdot \boldsymbol{\chi}_h \right),$$

and terms of $\tilde{\boldsymbol{\sigma}}$. Therefore, some of these terms can be neglected without loss of stability. This is the key idea in term-by-term stabilization methods (developed, for example in [25, 38, 143]). For the stationary viscoelastic problem, the convenience of using this split stabilization for the momentum equation was identified in [28].

Let us consider the expressions (4.13) and (4.15), taking into account that $\tilde{P} = P_h^\perp$, $P_h^\perp[\boldsymbol{f}] \approx \mathbf{0}$, $P_h^\perp\left[\frac{\partial \boldsymbol{u}_h}{\partial t} \right] = 0$ and $P_h^\perp\left[\frac{\partial \boldsymbol{\sigma}_h}{\partial t} \right] = 0$. Therefore we can rewrite them as follows:

$$\rho \frac{\partial \tilde{\boldsymbol{u}}}{\partial t} + \alpha_1^{-1} \tilde{\boldsymbol{u}} = P_h^\perp \left[\nabla \cdot \boldsymbol{\sigma}_h \right] + P_h^\perp \left[2\eta_s \nabla \cdot (\nabla^s \boldsymbol{u}_h) \right] - P_h^\perp \left[\rho \boldsymbol{u}_h \cdot \nabla \boldsymbol{u}_h \right] - P_h^\perp \left[\nabla p_h \right],$$
$$\tag{4.19}$$

$$\frac{\lambda}{2\eta_p} \frac{\partial \tilde{\boldsymbol{\sigma}}}{\partial t} + \alpha_3^{-1} \tilde{\boldsymbol{\sigma}} = -P_h^\perp \left[\frac{1}{2\eta_p} \boldsymbol{\sigma}_h \right] + P_h^\perp \left[\nabla^s \boldsymbol{u}_h \right]$$
$$- P_h^\perp \left[\frac{\lambda}{2\eta_p} \boldsymbol{u}_h \cdot \nabla \boldsymbol{\sigma}_h \right] + P_h^\perp \left[\frac{\lambda}{2\eta_p} \left(\boldsymbol{\sigma}_h \cdot \nabla \boldsymbol{u}_h + (\nabla \boldsymbol{u}_h)^T \cdot \boldsymbol{\sigma}_h \right) \right]. \tag{4.20}$$

The key ingredient that allows to consider any of these terms instead the residual based VMS is the orthogonal projection $P_h^\perp$. The right-hand-side (RHS) of (4.19) and (4.20) is not zero when the FE solution is replaced by the continuous solution, and consequently the method is not consistent. Nevertheless, the consistency error is optimal [41].
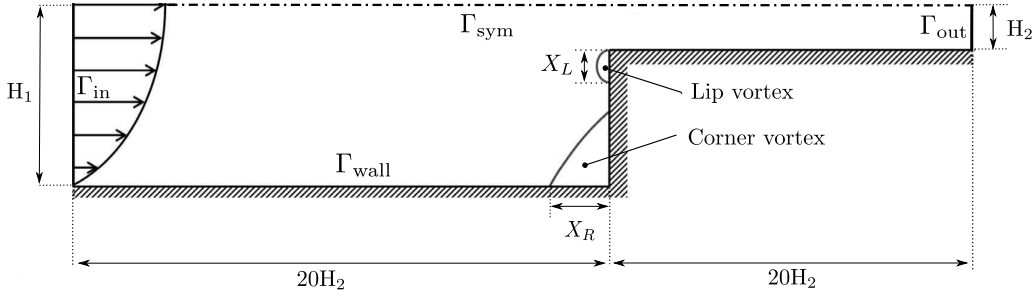
Figure 4.1: Contraction 4:1. Domain and boundary conditions for the fail test.

Additionally, some of the terms in the RHS of (4.19) and (4.20) can be neglected, like the second term of (4.19), because they do not contribute to stability. The three remaining terms help to improve stability, the first one giving control of the divergence of the viscoelastic stresses, the third one on the convective term and the fourth one on the pressure gradient. Similar considerations can be applied to modify equation (4.20), now considering that $P_h^\perp[\boldsymbol{\sigma}_h] = \mathbf{0}$.

As explained earlier, the previous splitting and simplification technique results in an a priori weakly consistent method. However, when the splitting approach is used in the constitutive equation (4.20) the method fails to converge when applied to simple numerical tests. This convergence failure is independent of the approximation properties (stability and accuracy) of the method, but clearly limits its applicability. This breakdown is produced by the fact that the full residual (the sum of all terms) is usually small whereas each separate term is large (considering absolute terms). Consequently, in numerical solutions, the split term-by-term method for the constitutive equation is not as efficient as the residual-based one. It is remarkable that this phenomenon occurs also in simple stationary problems, as shown in the next example. Yet, it has to be stressed that this is a phenomenon encountered in practice that we have never observed when the term-by-term formulation for the momentum equation is used. From the computational point of view, it would be desirable to employ it also for the constitutive equation, but the following example explains why it is not possible.

Example of convergence failure of the term-by-term stabilization of the constitutive equation

In this subsection, we will briefly describe the numerical example and the results obtained when the lack of convergence for the term-by-term stabilization occurs. We have considered the well-known 4:1 contraction benchmark (see Figure 4.1) in a stationary version, with a Weissenberg number equal to 4.0 and Reynolds number equal to 0.01, as it is considered in Section 2.5.3 of the Chapter 2, considering the same boundary conditions. The space discretization consists of 7784 nodes and 14793 triangular elements, whose minimum element size is $h_{\min} = 0.05$, as it is plotted in Figure 2.11.

In Table 4.1, the different values for the terms of the constitutive equation residual are plotted for a numerical integration point situated approximately at coordinates $(17.5, -3.5)$ and for each component together with the total residual, indicated in the last row. Other points have also been checked, and the same effect is observed in all of them. The values represented in Table 4.1 correspond to inner-iteration 20. A continuation iterative scheme in terms of the relaxation time λ has been employed, using 15 continuation steps. Within

Residual terms	comp xx	comp yy	comp xy
$\dfrac{1}{2\eta_p}\boldsymbol{\sigma}_h$	0.82002	0.68599	0.80990
$-\nabla^s \boldsymbol{u}_h$	0.35160	-0.41654	-0.44841
$\dfrac{\lambda}{2\eta_p}\hat{\boldsymbol{u}}_h \cdot \nabla \boldsymbol{\sigma}_h$	2.89475	-1.30149	0.74938
$-\dfrac{\lambda}{2\eta_p}\left(\boldsymbol{\sigma}_h \cdot \nabla \hat{\boldsymbol{u}}_h + (\nabla \hat{\boldsymbol{u}}_h)^T \cdot \boldsymbol{\sigma}_h\right)$	-4.29379	-0.59164	-2.14322
Full residual	-0.22741	-1.62369	-1.03234

Table 4.1: Values adopted by each term using the term-by-term stabilization in the constitutive equation for each tensor component for the contraction 4:1 benchmark. Inneriteration 20.

each of them, a fixed point iterative scheme has been employed, so that $\hat{\boldsymbol{u}}_h$ in Table 4.1 is the velocity at the previous iteration of the one considered.

As it can be observed, in components xx and xy of the residual, the full residual has a smaller value than other terms such as the rotational or the convective terms separately (in absolute value). When this effect happens, the iterative scheme for the term-by-term formulation fails. Note that this occurs when the Weissenberg number is significant; if it is low, convergence does not experiment this kind of problems.

Final design

In view of the previous discussion, the method must be designed carefully. For this reason, along the present chapter the method denoted as term-by-term (S-OSS) will be built as a split term-by-term for the momentum equation, and the full residual-based VMS, explained in subsection 4.4.1, for the constitutive equation.

Under the described circumstances and following this splitting approach, we can split $\tilde{\boldsymbol{u}} = \tilde{\boldsymbol{u}}_1 + \tilde{\boldsymbol{u}}_2 + \tilde{\boldsymbol{u}}_3$, while the stress sub-grid scale remains as $\tilde{\boldsymbol{\sigma}}$. Therefore, the term-by-term finite element formulation proposed consists in finding $\boldsymbol{U}_h = [\boldsymbol{u}_h, p_h, \boldsymbol{\sigma}_h] : (0, T) \longrightarrow \boldsymbol{\mathcal{X}}_h$ such that

$$
\mathcal{G}_{\text{std}}(\boldsymbol{U}_h, \boldsymbol{V}_h) + B_{\text{std}}(\boldsymbol{u}_h; \boldsymbol{U}_h, \boldsymbol{V}_h) + \sum_K \langle \tilde{\boldsymbol{u}}_1, -\rho \boldsymbol{u}_h \cdot \nabla \boldsymbol{v}_h \rangle_K
$$
$$
+ \sum_K \langle \tilde{\boldsymbol{u}}_2, -\nabla q_h \rangle_K + \sum_K \langle \tilde{\boldsymbol{u}}_3, \nabla \cdot \boldsymbol{\chi}_h \rangle_K + \sum_K \langle \tilde{p}, -\nabla \cdot \boldsymbol{v}_h \rangle_K
$$
$$
+ \sum_K \left\langle \tilde{\boldsymbol{\sigma}}, \frac{1}{2\eta_p}\boldsymbol{\chi}_h + \nabla^s \boldsymbol{v} - \frac{\lambda}{2\eta_p}\left(\boldsymbol{u}_h \cdot \nabla \boldsymbol{\chi}_h + \boldsymbol{\chi}_h \cdot (\nabla \boldsymbol{u}_h)^T + \nabla \boldsymbol{u}_h \cdot \boldsymbol{\chi}_h\right) \right\rangle_K
$$
$$
= \langle \boldsymbol{f}, \boldsymbol{v}_h \rangle,
$$

for all $[\boldsymbol{v}_h, q_h, \boldsymbol{\sigma}_h] \in \boldsymbol{\mathcal{X}}_h$, where B_{std} is the bilinear form defined in (4.3), and the sub-grid scales $\tilde{\boldsymbol{u}}_1, \tilde{\boldsymbol{u}}_2, \tilde{\boldsymbol{u}}_3, \tilde{p}$, are the solution of the evolution problems:

$$
\rho \frac{\partial \tilde{\boldsymbol{u}}_1}{\partial t} + \alpha_1^{-1} \tilde{\boldsymbol{u}}_1 = -P_h^{\perp}\left[\rho \boldsymbol{u}_h \cdot \nabla \boldsymbol{u}_h\right], \tag{4.21}
$$

$$
\rho \frac{\partial \tilde{\boldsymbol{u}}_2}{\partial t} + \alpha_1^{-1} \tilde{\boldsymbol{u}}_2 = -P_h^{\perp}\left[\nabla p_h\right], \tag{4.22}
$$

$$
\rho \frac{\partial \tilde{\boldsymbol{u}}_3}{\partial t} + \alpha_1^{-1} \tilde{\boldsymbol{u}}_3 = P_h^{\perp}\left[\nabla \cdot \boldsymbol{\sigma}_h\right], \tag{4.23}
$$

$$\alpha_2^{-1}\tilde{p} = -P_h^{\perp}\left[\nabla \cdot \boldsymbol{u}_h\right], \tag{4.24}$$

while the sub-grid scale $\tilde{\boldsymbol{\sigma}}$ is the solution of (4.15), defined in the previous section. Parameters α_i, $i = 1, 2, 3$ are the stabilization terms, already defined in (2.30)-(2.32). The proposed method is not residual-based, and therefore, is not consistent in the sense used in the finite element context, although it has an optimal consistency error.

Finally, the term-by-term stabilization proposed for the log-conformation formulation consists in finding $\boldsymbol{U}_h = [\boldsymbol{u}_h, p_h, \boldsymbol{\psi}_h] : (0, T) \longrightarrow \bar{\boldsymbol{\mathcal{X}}}_h$ such that

$$\mathcal{G}_{\log}(\boldsymbol{U}_h, \boldsymbol{V}_h) + B_{\log}(\boldsymbol{u}_h; \boldsymbol{U}_h, \boldsymbol{V}_h) + \sum_K \langle \tilde{\boldsymbol{u}}_1, -\rho \boldsymbol{u}_h \cdot \nabla \boldsymbol{v}_h \rangle_K$$

$$+ \sum_K \langle \tilde{\boldsymbol{u}}_2, -\nabla q_h \rangle_K + \sum_K \langle \tilde{\boldsymbol{u}}_3, \nabla \cdot \boldsymbol{\chi}_h \rangle_K + \sum_K \langle \tilde{p}, -\nabla \cdot \boldsymbol{v}_h \rangle_K$$

$$+ \sum_K \left\langle \tilde{\boldsymbol{\sigma}}, \frac{1}{2\eta_p}\boldsymbol{\chi}_h + \nabla^s \boldsymbol{v} - \frac{\lambda}{2\eta_p}\left(\boldsymbol{u}_h \cdot \nabla \boldsymbol{\chi}_h + \boldsymbol{\chi}_h \cdot (\nabla \boldsymbol{u}_h)^T + \nabla \boldsymbol{u}_h \cdot \boldsymbol{\chi}_h\right) \right\rangle_K$$

$$= \langle \boldsymbol{f}, \boldsymbol{v}_h \rangle,$$

for all $[\boldsymbol{v}_h, q_h, \boldsymbol{\chi}_h] \in \boldsymbol{\mathcal{X}}_h$, where $B_{\log}$ is the bilinear form defined in (4.7), the sub-grid scale $\tilde{\boldsymbol{u}}_3$, is now defined as the solution of:

$$\rho\frac{\partial \tilde{\boldsymbol{u}}_3}{\partial t} + \alpha_1^{-1}\tilde{\boldsymbol{u}}_3 = P_h^{\perp}\left[\frac{\eta_p}{\lambda_0}\nabla \cdot \exp(\boldsymbol{\psi}_h)\right]. \tag{4.25}$$

The sub-grid scales $\tilde{\boldsymbol{u}}_1$, $\tilde{\boldsymbol{u}}_2$, and $\tilde{p}$ are solutions of (4.21), (4.22), (4.24), respectively, and the sub-grid scale $\tilde{\boldsymbol{\sigma}}$ is the solution of (4.18). Additionally, the parameters $\alpha_i, i = 1, 2, 3$ are defined in (2.30)-(2.32).

4.4.3 Discretization of the equations for the sub-grid scales

The time dependent behavior of the sub-grid scales is widely analyzed in [9, 47], although in this subsection we try to describe the main ideas for the two methods presented in this chapter: the residual-based method and the term-by-term one. For both, we have used the BDF1 scheme to discretize the defined sub-grid scales. Particularly, in the case of the split stabilization method, sub-grid scales (4.21) -(4.23) and the elastic stress sub-grid scale (4.15) can be written as

$$\tilde{\boldsymbol{u}}_1^{n+1} = \left(\rho\frac{1}{\delta t} + \frac{1}{\alpha_1^{n+1}}\right)^{-1}\left(\rho\frac{1}{\delta t}\tilde{\boldsymbol{u}}_1^n - \rho P_h^{\perp}\left[\boldsymbol{u}_h^{n+1} \cdot \nabla \boldsymbol{u}_h^{n+1}\right]\right),$$

$$\tilde{\boldsymbol{u}}_2^{n+1} = \left(\rho\frac{1}{\delta t} + \frac{1}{\alpha_1^{n+1}}\right)^{-1}\left(\rho\frac{1}{\delta t}\tilde{\boldsymbol{u}}_2^n - P_h^{\perp}\left[\nabla p_h^{n+1}\right]\right),$$

$$\tilde{\boldsymbol{u}}_3^{n+1} = \left(\rho\frac{1}{\delta t} + \frac{1}{\alpha_1^{n+1}}\right)^{-1}\left(\rho\frac{1}{\delta t}\tilde{\boldsymbol{u}}_3^n + P_h^{\perp}\left[\nabla \cdot \boldsymbol{\sigma}_h^{n+1}\right]\right),$$

$$\tilde{\boldsymbol{\sigma}}^{n+1} = \left(\frac{\lambda}{2\eta_p}\frac{1}{\delta t} + \frac{1}{\alpha_3^{n+1}}\right)^{-1}\left(\frac{\lambda}{2\eta_p}\frac{1}{\delta t}\tilde{\boldsymbol{\sigma}}^n + \tilde{P}\left[-\frac{1}{2\eta_p}\boldsymbol{\sigma}_h^{n+1} + \nabla^s \boldsymbol{u}_h^{n+1}\right.\right.$$

$$\left.\left. -\frac{\lambda}{2\eta_p}\left(\frac{\delta \boldsymbol{\sigma}_h^{n+1}}{\delta t} + \boldsymbol{u}_h^{n+1} \cdot \nabla \boldsymbol{\sigma}_h^{n+1} - \boldsymbol{\sigma}_h^{n+1} \cdot \nabla \boldsymbol{u}_h^{n+1} - (\nabla \boldsymbol{u}_h^{n+1})^T \cdot \boldsymbol{\sigma}_h^{n+1}\right)\right]\right).$$

From these expressions, we can conclude that the sub-grid scales depend directly on $\alpha_{1\text{dyn}} = \left(\rho\frac{1}{\delta t} + \frac{1}{\alpha_1}\right)^{-1}$ and $\alpha_{3\text{dyn}} = \left(\frac{\lambda}{2\eta_p}\frac{1}{\delta t} + \frac{1}{\alpha_3}\right)^{-1}$, where $\alpha_{1\text{dyn}}$ and $\alpha_{3\text{dyn}}$ redefine the

classical stabilitation parameters and now depend on the time-step size. The procedure is analogous for the logarithmic formulation, now considering (4.21), (4.22) and (4.25) for $\tilde{\boldsymbol{u}}_1^{n+1}$, $\tilde{\boldsymbol{u}}_2^{n+1}$ and $\tilde{\boldsymbol{u}}_3^{n+1}$, respectively, and (4.18) for $\tilde{\boldsymbol{\sigma}}^{n+1}$; the same expressions for $\alpha_{1\mathrm{dyn}}$ and $\alpha_{3\mathrm{dyn}}$ are used.

Concerning the new definition of the stabilization parameters, an extremely relevant study about the instability that appears when the ASGS method and the *quasi-static* sub-grid scales are employed is developed by Bochev et al. in [19]. They relate this instability to the reduction of δt if h (element size of mesh) remains fixed, i.e. for anisotropic space-time discretizations. However, the instability described disappears automatically if $\delta t \geq C\alpha_1^{n+1}$, where C is a positive constant. Therefore it seems clear that the stabilization parameter and the time step size must be related in the *quasi-static* stabilized finite element methods. This question is justified in [30], remarking that when this inequality holds, it will be unnecessary to use dynamic sub-grid scales.

Furthermore, we can observe that for the viscoelastic flow problem parameter α_3 is also modified, but no references exist about the possible effects that this change could produce. This question will be explored and discussed along the numerical examples, in the Section 4.6.

Finally, let us remark that aspects related to the treatment of the logarithm of the conformation tensor can be found in Chapter 2 and references therein (see also [101] for a non-standard implementation of this approach).

4.4.4   Linearization and algorithm

As we have seen, the equations for incompressible viscoelastic flows have a high number of non-linear terms which must be treated.

The algorithm employed in the time-dependent subscales problem is similar to the one detailed in Algorithm 1, although we have to remark some differences:

- The linearization of the convective term of the momentum equation is done using the Newton-Raphson scheme.

- Stabilization parameters are computed with the values of the unknowns at the previous iterations and the time step size (δt).

- Dynamic subgrid-scales are computed each time-step, using the subgrid-scale of the previous time step j, the orthogonal projection of the "residual", the time step size δt and the stabilization parameters that now are dynamics.

In the equations displayed in Algorithm 4 variables $\boldsymbol{u}_h^{j+1,i}, p_h^{j+1,i}, \boldsymbol{\psi}_h^{j+1,i}$ corresponding to the $j + 1$ time step are denoted by $\boldsymbol{u}_h^i, p_h^i, \boldsymbol{\psi}_h^i$ for simplicity. Moreover, the subscales $\tilde{\boldsymbol{u}}_1^j$, $\tilde{\boldsymbol{u}}_2^j, \tilde{\boldsymbol{u}}_3^j, \tilde{\boldsymbol{\sigma}}^j$ corresponding with the previous time step j are denoted here as $\tilde{\boldsymbol{u}}_1, \tilde{\boldsymbol{u}}_2, \tilde{\boldsymbol{u}}_3, \tilde{\boldsymbol{\sigma}}$, omitting the superscript. In addition, we have defined $\boldsymbol{E} = \exp(\boldsymbol{\psi}^{j+1,i-1})$ as the exponential of the variable $\boldsymbol{\psi}$ computed in the previous iteration and $\boldsymbol{R} = \exp(\boldsymbol{\psi}^{j+1,i-1})\boldsymbol{\psi}^{j+1,i-1} - \exp(\boldsymbol{\psi}^{j+1,i-1})$ for clarity. Note that in Algorithms 4 and 5 the Split-OSS stabilization is considered. Lastly, we define the next expressions using known fields from the previous iteration:

$$\mathbf{R}_{u1} = \rho \boldsymbol{u}_h^{j+1,i-1} \cdot \nabla \boldsymbol{u}_h^{j+1,i-1}$$

$$\mathbf{R}_{u2} = \nabla p_h^{j+1,i-1}$$

$$\mathbf{R}_{u3} = -\frac{\eta_p}{\lambda_0} \nabla \cdot \boldsymbol{E}$$

$$\mathbf{R}_\psi = \frac{1}{2\lambda_0}\boldsymbol{E} - \nabla^s\boldsymbol{u}_h^{j+1,i-1} + \frac{\lambda}{2\lambda_0}\Big(\boldsymbol{u}_h^{j+1,i-1}\cdot\nabla\boldsymbol{E}$$
$$- \boldsymbol{E}\cdot\nabla\boldsymbol{u}_h^{j+1,i-1} - (\nabla\boldsymbol{u}_h^{j+1,i-1})^T\cdot\boldsymbol{E} + 2\nabla^s\boldsymbol{u}_h^{j+1,i-1}\Big)$$

Regarding the temporal terms, the notation introduced in Section 2.3.6 and Section 4.3.3 is employed here. The equations considered in Algorithm 4 are solved inside a general algorithm, presented in Algorithm 5, where all considerations made are taken into account.

Algorithm 4 Logarithmic conformation reformulation using time-dependet subscales. Fully discrete and linearized problem at each iteration.

Given $\boldsymbol{u}_h^{i-1}$, p_h^{i-1}, $\boldsymbol{\psi}_h^{i-1}(i \geq 1)$, $\tilde{\boldsymbol{u}}_1$, $\tilde{\boldsymbol{u}}_2$, $\tilde{\boldsymbol{u}}_3$ and $\tilde{\boldsymbol{\sigma}}$ solve for $\boldsymbol{u}_h^i$, p_h^i and $\boldsymbol{\psi}_h^i$ from:

$$\left(\rho\frac{\delta_k\boldsymbol{u}_h^i}{\delta t},\boldsymbol{v}_h\right) + \frac{\eta_p}{\lambda_0}(\boldsymbol{E}\cdot\boldsymbol{\psi}_h^i,\nabla^s\boldsymbol{v}_h) + 2(\eta_s\nabla^s\boldsymbol{u}_h^i,\nabla^s\boldsymbol{v}_h) + \langle\rho\boldsymbol{u}_h^{i-1}\cdot\nabla\boldsymbol{u}_h^i,\boldsymbol{v}_h\rangle$$
$$+ \langle\rho\boldsymbol{u}_h^i\cdot\nabla\boldsymbol{u}_h^{i-1},\boldsymbol{v}_h\rangle - (p_h^i,\nabla\cdot\boldsymbol{v}_h) + (\nabla\cdot\boldsymbol{u}_h^i,q_h) + \frac{1}{2\lambda_0}(\boldsymbol{E}\cdot\boldsymbol{\psi}_h^i,\boldsymbol{\chi}_h)$$
$$- (\nabla^s\boldsymbol{u}_h^i,\boldsymbol{\chi}_h) + \frac{\lambda}{2\lambda_0}\left(\frac{\delta_k}{\delta t}(\boldsymbol{E}\cdot\boldsymbol{\psi}_h^i) + (\boldsymbol{u}_h^{i-1}\cdot\nabla(\boldsymbol{E}\cdot\boldsymbol{\psi}_h^i),\boldsymbol{\chi}_h\right)$$
$$+ \frac{\lambda}{2\lambda_0}\left(\boldsymbol{u}_h^i\cdot\nabla\boldsymbol{E} - \boldsymbol{E}\cdot\boldsymbol{\psi}_h^i\cdot\nabla\boldsymbol{u}_h^{i-1} - \boldsymbol{E}\cdot\nabla\boldsymbol{u}_h^i,\boldsymbol{\chi}_h\right)$$
$$- \frac{\lambda}{2\lambda_0}\left((\nabla\boldsymbol{u}_h^{i-1})^T\cdot\boldsymbol{E}\cdot\boldsymbol{\psi}_h^i + (\nabla\boldsymbol{u}_h^i)^T\cdot\boldsymbol{E},\boldsymbol{\chi}_h\right)$$
$$+ \frac{\lambda}{2\lambda_0}(2\nabla^s\boldsymbol{u}_h^i,\boldsymbol{\chi}_h)\Big) + \sum_K\alpha_{1\mathrm{dyn}}^{i-1}\left\langle -\frac{\eta_p}{\lambda_0}\nabla\cdot(\boldsymbol{E}\cdot\boldsymbol{\psi}_h^i),-\nabla\cdot\boldsymbol{\chi}_h\right\rangle_K$$
$$+ \sum_K\alpha_{1\mathrm{dyn}}^{i-1}\left\langle\nabla p_h^i,\nabla q_h\right\rangle_K + \sum_K\alpha_{2\mathrm{dyn}}^{i-1}\left\langle\nabla\cdot\boldsymbol{u}_h^i,\nabla\cdot\boldsymbol{v}_h\right\rangle_K$$
$$+ \sum_K\alpha_{1\mathrm{dyn}}^{i-1}\left\langle\rho\boldsymbol{u}_h^{i-1}\cdot\nabla\boldsymbol{u}_h^i + \rho\boldsymbol{u}_h^i\cdot\nabla\boldsymbol{u}_h^{i-1},\rho\boldsymbol{u}_h^{i-1}\cdot\nabla\boldsymbol{v}_h\right\rangle_K$$
$$+ \sum_K\alpha_{3\mathrm{dyn}}^{i-1}\Big\langle\frac{1}{2\lambda_0}\boldsymbol{E}\cdot\boldsymbol{\psi}_h^i - \nabla^s\boldsymbol{u}_h^i + \frac{\lambda}{2\lambda_0}\Big(\frac{\delta_k}{\delta t}(\boldsymbol{E}\cdot\boldsymbol{\psi}_h^i) + \boldsymbol{u}_h^{i-1}\cdot\nabla(\boldsymbol{E}\cdot\boldsymbol{\psi}_h^i)$$
$$+ \boldsymbol{u}_h^i\cdot\nabla\boldsymbol{E} - (\boldsymbol{E}\cdot\boldsymbol{\psi}_h^i)\cdot\nabla\boldsymbol{u}_h^{i-1} - \boldsymbol{E}\cdot\nabla\boldsymbol{u}_h^i - (\nabla\boldsymbol{u}_h^{i-1})^T\cdot(\boldsymbol{E}\cdot\boldsymbol{\psi}_h^i)$$
$$- (\nabla\boldsymbol{u}^i)^T\cdot\boldsymbol{E} + 2\nabla^s\boldsymbol{u}_h^i\Big),-\frac{1}{2\eta_p}\boldsymbol{\chi}_h - \nabla^s\boldsymbol{v}_h$$
$$+ \frac{\lambda}{2\eta_p}\left(\boldsymbol{u}_h^{i-1}\cdot\nabla\boldsymbol{\chi}_h - \boldsymbol{\chi}_h\cdot(\nabla\boldsymbol{u}_h^{i-1})^T - \nabla\boldsymbol{u}_h^{i-1}\cdot\boldsymbol{\chi}_h\right)\Big\rangle_K$$
$$= \langle\boldsymbol{f},\boldsymbol{v}_h\rangle + \frac{\eta_p}{\lambda_0}(\boldsymbol{R},\nabla^s\boldsymbol{v}_h) + \langle\rho\boldsymbol{u}_h^{i-1}\cdot\nabla\boldsymbol{u}_h^{i-1},\boldsymbol{v}_h\rangle + \frac{1}{2\lambda_0}\left(\boldsymbol{I} - \boldsymbol{R} + \frac{\lambda}{2\lambda_0}\frac{\delta_k}{\delta t}\boldsymbol{R},\boldsymbol{\chi}_h\right)$$
$$+ \frac{\lambda}{2\lambda_0}\left(\boldsymbol{u}_h^{i-1}\cdot\nabla(\boldsymbol{E}\cdot\boldsymbol{\psi}_h^{i-1}) - (\boldsymbol{E}\cdot\boldsymbol{\psi}_h^{i-1})\cdot\nabla\boldsymbol{u}_h^{i-1} - (\nabla\boldsymbol{u}_h^{i-1})^T\cdot(\boldsymbol{E}\cdot\boldsymbol{\psi}_h^{i-1}),\boldsymbol{\chi}_h\right)$$
$$+ \sum_K\alpha_{1\mathrm{dyn}}^{i-1}\left\langle -\frac{\eta_p}{\lambda_0}\nabla\cdot\boldsymbol{R},-\nabla\cdot\boldsymbol{\chi}_h\right\rangle_K$$
$$+ \sum_K\alpha_{1\mathrm{dyn}}^{i-1}\left\langle\rho\boldsymbol{u}_h^{i-1}\cdot\nabla\boldsymbol{u}_h^{i-1},\rho\boldsymbol{u}_h^{i-1}\cdot\nabla\boldsymbol{v}_h\right\rangle_K$$
$$+ \sum_K\alpha_{1\mathrm{dyn}}^{i-1}\left\langle\frac{\rho}{\delta t}\tilde{\boldsymbol{u}}_1 + P_h\left[\mathbf{R}_{u1}\right],\rho\boldsymbol{u}_h^{i-1}\cdot\nabla\boldsymbol{v}_h\right\rangle_K$$
$$+ \sum_K\alpha_{1\mathrm{dyn}}^{i-1}\left\langle\frac{\rho}{\delta t}\tilde{\boldsymbol{u}}_2 + P_h\left[\mathbf{R}_{u2}\right],\nabla q_h\right\rangle_K + \sum_K\alpha_2\left\langle P_h[\nabla\cdot\boldsymbol{u}_h^{i-1}],\nabla\cdot\boldsymbol{v}_h\right\rangle_K$$
$$+ \sum_K\alpha_{1\mathrm{dyn}}^{i-1}\left\langle\frac{\rho}{\delta t}\tilde{\boldsymbol{u}}_3 + P_h\left[\mathbf{R}_{u3}\right],-\nabla\cdot\boldsymbol{\chi}_h\right\rangle_K$$

$$+ \sum_K \alpha_{3\mathrm{dyn}}^{i-1} \Big\langle \frac{1}{2\lambda_0}(\boldsymbol{I} - \boldsymbol{R}) + \frac{\lambda}{2\lambda_0}\Big(\frac{\delta_k}{\delta t}\boldsymbol{R} - \boldsymbol{u}_h^{i-1} \cdot \nabla\left(\boldsymbol{E} \cdot \boldsymbol{\psi}_h^{i-1}\right)\Big)$$

$$- \left(\boldsymbol{E} \cdot \boldsymbol{\psi}_h^{i-1}\right) \cdot \nabla \boldsymbol{u}_h^{i-1} - (\nabla \boldsymbol{u}_h^{i-1})^T \cdot \left(\boldsymbol{E} \cdot \boldsymbol{\psi}_h^{i-1}\right), -\frac{1}{2\eta_p}\boldsymbol{\chi}_h - \nabla^s \boldsymbol{v}_h$$

$$+ \frac{\lambda}{2\eta_p}\left(\boldsymbol{u}_h^{i-1} \cdot \nabla \boldsymbol{\chi}_h - \boldsymbol{\chi}_h \cdot (\nabla \boldsymbol{u}_h^{i-1})^T - \nabla \boldsymbol{u}_h^{i-1} \cdot \boldsymbol{\chi}_h\right) \Big\rangle_K$$

$$+ \sum_K \alpha_{3\mathrm{dyn}}^{i-1} \Big\langle \frac{\lambda}{2\eta_p}\frac{1}{\delta t}\tilde{\boldsymbol{\sigma}} + P_h\left[\mathbf{R}_\psi\right], -\frac{1}{2\eta_p}\boldsymbol{\chi}_h - \nabla^s \boldsymbol{v}_h$$

$$+ \frac{\lambda}{2\eta_p}\left(\boldsymbol{u}_h^{i-1} \cdot \nabla \boldsymbol{\chi}_h - \boldsymbol{\chi}_h \cdot (\nabla \boldsymbol{u}_h^{i-1})^T - \nabla \boldsymbol{u}_h^{i-1} \cdot \boldsymbol{\chi}_h\right) \Big\rangle_K$$

Algorithm 5 Logarithmic conformation reformulation using time-dependent subscales. General algorithm for Split-OSS stabilization.

---

read initial condition $\boldsymbol{u}_h^0$ (or compute $\boldsymbol{u}_h^0 = \mathrm{P}_h\left[\boldsymbol{u}_h^0\right]$)

set $p_h^0 = 0$, $\boldsymbol{\psi}_h^0 = \boldsymbol{0}$ (or compute $p_h^0 = \mathrm{P}_h\left[p_h^0\right]$, $\boldsymbol{\psi}_h^0 = \mathrm{P}_h\left[\boldsymbol{\psi}_h^0\right]$) **for** j=0,...,m-1 **do** *(Temporal loop)*

    set $i=0$

    set $\boldsymbol{u}_h^{j+1,0} = \boldsymbol{u}_h^j$, $p_h^{j+1,0} = p_h^j$, $\boldsymbol{\psi}_h^{j+1,0} = \boldsymbol{\psi}_h^j$

    while not converged **do**

        $i \leftarrow i + 1$

        compute exponentials: $\boldsymbol{E}$, $\nabla \cdot \boldsymbol{E}$ and $\nabla \boldsymbol{E}$

        compute "residuals": $\mathbf{R}_{u1}$, $\mathbf{R}_{u2}$, $\mathbf{R}_{u3}$, $\mathbf{R}_\psi$

        compute projections: $P_h\left[\mathbf{R}_{u1}\right]$, $P_h\left[\mathbf{R}_{u2}\right]$, $P_h\left[\mathbf{R}_{u3}\right]$, $P_h\left[\mathbf{R}_\psi\right]$

        compute stabilization parameters:

            $\alpha_{1\mathrm{dyn}}^{j+1,i-1}$, $\alpha_2^{j+1,i-1}$ and $\alpha_{3\mathrm{dyn}}^{j+1,i-1}$ with $\boldsymbol{U}^{j+1,i-1}$ and δt

        solve equations in Algorithm 4 for $\boldsymbol{u}_h^{j+1,i}$, $p_h^{j+1,i}$ and $\boldsymbol{\psi}_h^{j+1,i}$

        check convergence

    end while

    compute dynamic subscales

$$\tilde{\boldsymbol{u}}_1^{j+1} = \alpha_{1\mathrm{dyn}}^{j+1,i}\left(\frac{\rho}{\delta t}\tilde{\boldsymbol{u}}_1^j - \left(\mathbf{R}_{u1} - P_h\left[\mathbf{R}_{u1}\right]\right)\right)$$

$$\tilde{\boldsymbol{u}}_2^{j+1} = \alpha_{1\mathrm{dyn}}^{j+1,i}\left(\frac{\rho}{\delta t}\tilde{\boldsymbol{u}}_2^j - \left(\mathbf{R}_{u2} - P_h\left[\mathbf{R}_{u2}\right]\right)\right)$$

$$\tilde{\boldsymbol{u}}_3^{j+1} = \alpha_{1\mathrm{dyn}}^{j+1,i}\left(\frac{\rho}{\delta t}\tilde{\boldsymbol{u}}_3^j - \left(\mathbf{R}_{u3} - P_h\left[\mathbf{R}_{u3}\right]\right)\right)$$

$$\tilde{\boldsymbol{\sigma}}^{j+1} = \alpha_{3\mathrm{dyn}}^{j+1,i}\left(\frac{\lambda}{2\eta_p}\frac{1}{\delta t}\tilde{\boldsymbol{\sigma}}^j - \left(\mathbf{R}_\psi - P_h\left[\mathbf{R}_\psi\right]\right)\right)$$

    set converged values

$$\boldsymbol{u}_h^{j+1} = \boldsymbol{u}_h^{j+1,i}$$

$$p_h^{j+1} = p_h^{j+1,i}$$

$$\boldsymbol{\psi}_h^{j+1} = \boldsymbol{\psi}_h^{j+1,i}$$

    (End temporal loop)

4.5 Analysis of stability

In this section the numerical analysis of the formulation considering time-dependent sub-grid scales is presented, although restricted to the linearized problem. For this reason, we will consider the advection velocity $\boldsymbol{a} : \Omega \times \,]0, t_{\mathrm{f}}[\,\to \mathbb{R}^d$ as a given velocity field, and, in the constitutive equation, the gradient of velocities $\nabla \boldsymbol{a}$ also known. It is assumed that $\boldsymbol{a} \in L^\infty(]0, t_{\mathrm{f}}[; W^{1,\infty}(\Omega)^d)$, with $\nabla \cdot \boldsymbol{a} = 0$, $\boldsymbol{n} \cdot \boldsymbol{a} = 0$ on $\partial\Omega$. For the logarithmic formulation, the exponential is considered linearized, as follows: if we consider $\exp(\hat{\boldsymbol{\psi}})$ and $\hat{\boldsymbol{\psi}}$ known, we can denote these tensors as $\boldsymbol{E} = \exp(\hat{\boldsymbol{\psi}})$ and $\boldsymbol{S} = \hat{\boldsymbol{\psi}}$, respectively, and introduce $\boldsymbol{R} = \boldsymbol{E} \cdot \boldsymbol{S} - \boldsymbol{E}$.

The fully discrete problem is obtained after discretizing in time. To this end, we consider the BDF1 scheme. Let $0 = t^0 < t^1 < \ldots < t^N = t_{\mathrm{f}}$ be a uniform partition of the time interval of size $\delta t = t^i - t^{i-1}$, $i = 1, \ldots, N$. We will use a superscript to denote the time step counter, indicating by n the time level up to which the solution is known. We employ the notation $\delta f^n := f^{n+1} - f^n$ and $\delta_t f^n := \frac{\delta f^n}{\delta t}$ for any time dependent function f, f^n being an approximation to $f(t^n)$.

The present analysis follows the same lines on the one presented in [47], developed for the stabilized finite element approximation for the incompressible flow problems, where the sub-grid scales are considered time-dependent. In particular, the work [30] presents a term-by-term stabilization approach using orthogonal sub-grid scales, which is also analyzed following the same ideas. The analysis developed in this section aims at emphasizing the effect of tracking the sub-scales in time for the viscoelastic fluid flow problem from the analytical perspective.

4.5.1 Linearized problem

Let us describe the stabilized FE method we analyze in the following. We will not derive it here, as it was presented in detail in [119]. Let us only describe the main ingredients. The starting point is the VMS approach, splitting the unknowns into their FE component and their SGS. The SGSs are considered *time dependent*, and *orthogonal* to the FE space in the $L^2(\Omega)$ sense. An important remark is required here: for the velocity SGS, this orthogonality is to the FE space *without boundary conditions*, i.e., without imposing that velocities vanish on the boundary. We will call $\boldsymbol{\mathcal{V}}_h \subset H^1(\Omega)^d$ this space, and $P_h : L^2(\Omega)^d \longrightarrow \boldsymbol{\mathcal{V}}_h$ the $L^2(\Omega)$ projection onto $\boldsymbol{\mathcal{V}}_h$ (we use the same symbol P_h as for the $L^2(\Omega)$ projection onto $\boldsymbol{\Upsilon}_h$ or $\bar{\boldsymbol{\Upsilon}}_h$). Note that $\boldsymbol{\mathcal{V}}_h^\perp \subset \boldsymbol{\mathcal{V}}_{h,0}^\perp$, $\perp$ standing for $L^2(\Omega)$ orthogonality, and also that for any function f defined on Ω the function $P_h^\perp(f) \in \boldsymbol{\mathcal{V}}_h^\perp$ converges to zero as $h \to 0$ in any suitable norm at the optimal rate provided by the FE interpolation. This would *not* happen if P_h is replaced by the $L^2(\Omega)$ projection onto $\boldsymbol{\mathcal{V}}_{h,0}$. The method to be analyzed has as starting point the decompositions $\boldsymbol{u} \approx \boldsymbol{u}_h + \tilde{\boldsymbol{u}}_1 + \tilde{\boldsymbol{u}}_2 + \tilde{\boldsymbol{u}}_3$, $p \approx p_h$, $\boldsymbol{\sigma} \approx \boldsymbol{\sigma}_h + \tilde{\boldsymbol{\sigma}}$. The velocity SGSs $\tilde{\boldsymbol{u}}_1$, $\tilde{\boldsymbol{u}}_2$, $\tilde{\boldsymbol{u}}_3 \in \boldsymbol{\mathcal{V}}_h^\perp$ are considered to be independent for the design of the method (see [28]). For the pressure, we could also introduce a pressure SGS $\tilde{p} \in \mathcal{Q}_h^\perp$, but this would only introduce a marginal added value in the stability results. Finally, there is only one stress SGS, $\tilde{\boldsymbol{\sigma}} \in \boldsymbol{\Upsilon}_h^\perp$ for the standard formulation, and likewise for the LCR, for the reasons explained in [120]. To simplify the exposition, we shall consider that spaces $\mathcal{Q}_h$ and $\boldsymbol{\Upsilon}_h$ are made of *continuous* functions. Moreover, we will consider that $P_h^\perp[\boldsymbol{f}] = \boldsymbol{0}$. For simplicity $\tilde{p}$ will be fixed to zero. Although all these assumptions are not crucial, they permit to simplify the analysis. After adequate approximations for the SGSs and neglecting some terms that do not contribute to stability, the method to be analyzed for the standard formulation reads as follows: given $\boldsymbol{u}_h^n \in \boldsymbol{\mathcal{V}}_{h,0}$, $\tilde{\boldsymbol{u}}_i^n \in \boldsymbol{\mathcal{V}}_h^\perp$, $i = 1, 2, 3$, $\boldsymbol{\sigma}_h^n \in \boldsymbol{\Upsilon}_h$

and $\tilde{\boldsymbol{\sigma}}^n \in \boldsymbol{\Upsilon}_h^\perp$, find $\boldsymbol{u}_h^{n+1} \in \boldsymbol{\mathcal{V}}_{h,0}$, $\tilde{\boldsymbol{u}}_i^{n+1} \in \boldsymbol{\mathcal{V}}_h^\perp$, $i = 1, 2, 3$, $\boldsymbol{\sigma}_h^{n+1} \in \boldsymbol{\Upsilon}_h$, $p_h^{n+1} \in \mathcal{Q}_h$ and $\tilde{\boldsymbol{\sigma}}^{n+1} \in \boldsymbol{\Upsilon}_h^\perp$ such that

$$
(\rho\delta\boldsymbol{u}_h^n, \boldsymbol{v}_h) + \left(\frac{\lambda}{2\eta_p}\delta\boldsymbol{\sigma}_h^n, \boldsymbol{\chi}_h\right) + \delta t\left(\boldsymbol{\sigma}_h^{n+1} + 2\eta_s\nabla^s\boldsymbol{u}_h^{n+1}, \nabla^s\boldsymbol{v}_h\right) + \delta t\left(\rho\boldsymbol{a}\cdot\nabla\boldsymbol{u}_h^{n+1}, \boldsymbol{v}_h\right)
$$

$$
- \delta t\left(p_h^{n+1}, \nabla\cdot\boldsymbol{v}_h\right) + \delta t\left(\nabla\cdot\boldsymbol{u}_h^{n+1}, q_h\right) + \delta t\left(\frac{1}{2\eta_p}\boldsymbol{\sigma}_h^{n+1} - \nabla^s\boldsymbol{u}_h^{n+1}, \boldsymbol{\chi}_h\right)
$$

$$
+ \delta t\frac{\lambda}{2\eta_p}\left(\boldsymbol{a}\cdot\nabla\boldsymbol{\sigma}_h^{n+1} - \boldsymbol{\sigma}_h^{n+1}\cdot\nabla\boldsymbol{a} - (\nabla\boldsymbol{a})^T\cdot\boldsymbol{\sigma}_h^{n+1}, \boldsymbol{\chi}_h\right) - \delta t\left(\tilde{\boldsymbol{u}}_1^{n+1}, \rho\boldsymbol{a}\cdot\nabla\boldsymbol{v}_h\right)
$$

$$
- \delta t\left(\tilde{\boldsymbol{u}}_2^{n+1}, \nabla q_h\right) + \delta t\left(\tilde{\boldsymbol{u}}_3^{n+1}, \nabla\cdot\boldsymbol{\chi}_h\right) - \delta t\left(\tilde{p}^{n+1}, \nabla\cdot\boldsymbol{v}_h\right)
$$

$$
+ \delta t\left(\tilde{\boldsymbol{\sigma}}^{n+1}, \frac{1}{2\eta_p}\boldsymbol{\chi}_h + \nabla^s\boldsymbol{v}_h - \frac{\lambda}{2\eta_p}\left(\boldsymbol{a}\cdot\nabla\boldsymbol{\chi}_h + \boldsymbol{\chi}_h\cdot(\nabla\boldsymbol{a})^T + \nabla\boldsymbol{a}\cdot\boldsymbol{\chi}_h\right)\right)
$$

$$
- \delta t\left\langle\boldsymbol{f}^{n+1}, \boldsymbol{v}_h\right\rangle = 0, \tag{4.26}
$$

$$
\rho\delta\tilde{\boldsymbol{u}}_1^n + \delta t\alpha_1^{-1}\tilde{\boldsymbol{u}}_1^{n+1} = -\delta t P_h^\perp[\rho\boldsymbol{a}\cdot\nabla\boldsymbol{u}_h^{n+1}], \tag{4.27}
$$

$$
\rho\delta\tilde{\boldsymbol{u}}_2^n + \delta t\alpha_1^{-1}\tilde{\boldsymbol{u}}_2^{n+1} = -\delta t P_h^\perp[\nabla p_h^{n+1}], \tag{4.28}
$$

$$
\rho\delta\tilde{\boldsymbol{u}}_3^n + \delta t\alpha_1^{-1}\tilde{\boldsymbol{u}}_3^{n+1} = \delta t P_h^\perp[\nabla\cdot\boldsymbol{\sigma}_h^{n+1}], \tag{4.29}
$$

$$
\delta t\alpha_2^{-1}\tilde{p}^{n+1} = -\delta t P_h^\perp[\nabla\cdot\boldsymbol{u}_h^{n+1}], \tag{4.30}
$$

$$
\frac{\lambda}{2\eta_p}\delta\tilde{\boldsymbol{\sigma}}^n + \delta t\alpha_3^{-1}\tilde{\boldsymbol{\sigma}}^{n+1} = \delta t\tilde{P}\left[-\frac{1}{2\eta_p}\boldsymbol{\sigma}_h^{n+1} + \nabla^s\boldsymbol{u}_h^{n+1}\right.
$$

$$
\left. -\frac{\lambda}{2\eta_p}\left(\frac{\delta\boldsymbol{\sigma}_h^n}{\delta t} + \boldsymbol{a}\cdot\nabla\boldsymbol{\sigma}_h^{n+1} - \boldsymbol{\sigma}_h^{n+1}\cdot\nabla\boldsymbol{a} - (\nabla\boldsymbol{a})^T\cdot\boldsymbol{\sigma}_h^{n+1}\right)\right]. \tag{4.31}
$$

where α_1 and α_3 are the stabilization parameters (the notation of [30] has been kept), computed within each element K and at each time level $n + 1$ as

$$
\alpha_1^{-1} = c_1\frac{\eta_0}{h^2} + \frac{\|\boldsymbol{a}\|_{L^\infty(K)}}{h}, \tag{4.32}
$$

$$
\alpha_3^{-1} = c_3\frac{1}{2\eta_p} + c_4\left(\frac{\lambda}{2\eta_p}\frac{\|\boldsymbol{a}\|_{L^\infty(K)}}{h} + \frac{\lambda}{\eta_p}\|\nabla\boldsymbol{a}\|_{L^\infty(K)}\right), \tag{4.33}
$$

where c_i, $i = 1, 2, 3, 4$, are algorithmic constants (see [31, 44] for an overview of the motivation to obtain α_1, α_3 and the choice of the algorithmic constants). Observe that equations (4.27)-(4.31) result from the time evolution of the SGSs; these are in fact ordinary differential equations that need to be integrated in time at the numerical integration points of the FE mesh.

Let us move now to the LCR. For simplicity, the superscript $n+1$ is omitted for tensors $\boldsymbol{R}$, $\boldsymbol{E}$ described at the beginning of the section. Therefore, the linearized equations in variational form of the log-conformation formulation are expressed as: Given $\boldsymbol{u}_h^n$ and $\boldsymbol{\sigma}_h^n$, find $\boldsymbol{u}_h^{n+1}$, $\boldsymbol{\psi}_h^{n+1}$, $\tilde{\boldsymbol{u}}_1^{n+1}$, $\tilde{\boldsymbol{u}}_2^{n+1}$, $\tilde{\boldsymbol{u}}_3^{n+1}$, $\tilde{\boldsymbol{\sigma}}^{n+1}$ and p_h^{n+1} such that

$$
(\rho\delta\boldsymbol{u}_h^n, \boldsymbol{v}_h) + \left(\frac{\lambda}{2\lambda_0}\delta P_h\left[\boldsymbol{E}\cdot\boldsymbol{\psi}_h^n\right], \boldsymbol{\chi}_h\right) + \delta t\left(\frac{\eta_p}{\lambda_0}P_h\left[\boldsymbol{E}\cdot\boldsymbol{\psi}_h^{n+1}\right] + 2\eta_s\nabla^s\boldsymbol{u}_h^{n+1}, \nabla^s\boldsymbol{v}_h\right)
$$

$$
+ \delta t\left(\rho\boldsymbol{a}\cdot\nabla\boldsymbol{u}_h^{n+1}, \boldsymbol{v}_h\right) - \delta t\left(p_h^{n+1}, \nabla\cdot\boldsymbol{v}_h\right) + \delta t\left(\nabla\cdot\boldsymbol{u}_h^{n+1}, q_h\right)
$$

$$
+ \delta t\left(\frac{1}{2\lambda_0}P_h\left[\boldsymbol{E}\cdot\boldsymbol{\psi}_h^{n+1}\right] - \nabla^s\boldsymbol{u}_h^{n+1}, \boldsymbol{\chi}_h\right)
$$

$$
+ \delta t\left(\frac{\lambda}{2\lambda_0}\left(2\nabla^s\boldsymbol{u}_h^{n+1} + \boldsymbol{a}\cdot\nabla P_h\left[\boldsymbol{E}\cdot\boldsymbol{\psi}_h^{n+1}\right]\right), \boldsymbol{\chi}_h\right)
$$

$$+ \delta t \frac{\lambda}{2\lambda_0} \left(-P_h \left[\boldsymbol{E} \cdot \boldsymbol{\psi}_h^{n+1} \right] \cdot \nabla \boldsymbol{a} - (\nabla \boldsymbol{a})^T \cdot P_h \left[\boldsymbol{E} \cdot \boldsymbol{\psi}_h^{n+1} \right], \boldsymbol{\chi}_h \right)$$

$$- \delta t \left(\tilde{\boldsymbol{u}}_1^{n+1}, \rho \boldsymbol{a} \cdot \nabla \boldsymbol{v}_h \right) - \delta t \left(\tilde{\boldsymbol{u}}_2^{n+1}, \nabla q_h \right) + \delta t \left(\tilde{\boldsymbol{u}}_3^{n+1}, \nabla \cdot \boldsymbol{\chi}_h \right)$$

$$+ \delta t \left(\tilde{\boldsymbol{\sigma}}^{n+1}, \frac{1}{2\eta_p} \boldsymbol{\chi}_h + \nabla^s \boldsymbol{v}_h - \frac{\lambda}{2\eta_p} \left(\boldsymbol{a} \cdot \nabla \boldsymbol{\chi}_h + \boldsymbol{\chi}_h \cdot (\nabla \boldsymbol{a})^T + \nabla \boldsymbol{a} \cdot \boldsymbol{\chi}_h \right) \right)$$

$$- \delta t \left(\tilde{p}^{n+1}, \nabla \cdot \boldsymbol{v}_h \right) - \delta t \left\langle \boldsymbol{f}_u^{n+1}, \boldsymbol{v}_h \right\rangle - \delta t \left\langle \boldsymbol{f}_\psi^{n+1}, \boldsymbol{\chi}_h \right\rangle = 0 \qquad (4.34)$$

$$\rho \delta \tilde{\boldsymbol{u}}_1^n + \delta t \alpha_1^{-1} \tilde{\boldsymbol{u}}_1^{n+1} = -\delta t P_h^\perp \left[\rho \boldsymbol{a} \cdot \nabla \boldsymbol{u}_h^{n+1} \right], \qquad (4.35)$$

$$\rho \delta \tilde{\boldsymbol{u}}_2^n + \delta t \alpha_1^{-1} \tilde{\boldsymbol{u}}_2^{n+1} = -\delta t P_h^\perp \left[\nabla p_h^{n+1} \right], \qquad (4.36)$$

$$\rho \delta \tilde{\boldsymbol{u}}_3^n + \delta t \alpha_1^{-1} \tilde{\boldsymbol{u}}_3^{n+1} = \delta t P_h^\perp \left[\frac{\eta_p}{\lambda_0} \nabla \cdot P_h \left[\boldsymbol{E} \cdot \boldsymbol{\psi}_h^{n+1} \right] \right], \qquad (4.37)$$

$$\delta t \alpha_2^{-1} \tilde{p}^{n+1} = -\delta t P_h^\perp \left[\nabla \cdot \boldsymbol{u}_h^{n+1} \right],$$

$$\frac{\lambda}{2\eta_p} \delta \tilde{\boldsymbol{\sigma}}^n + \delta t \alpha_3^{-1} \tilde{\boldsymbol{\sigma}}^{n+1} = \delta t P_h^\perp \left[-\frac{1}{2\lambda_0} P_h \left[\boldsymbol{E} \cdot \boldsymbol{\psi}_h^{n+1} \right] + \nabla \boldsymbol{u}_h^{n+1} \right.$$

$$- \frac{\lambda}{2\lambda_0} \left(\boldsymbol{a} \cdot \nabla P_h \left[\boldsymbol{E} \cdot \boldsymbol{\psi}_h^{n+1} \right] - P_h \left[\boldsymbol{E} \cdot \boldsymbol{\psi}_h^{n+1} \right] \cdot \nabla \boldsymbol{a} \right)$$

$$\left. - \frac{\lambda}{2\lambda_0} (\nabla \boldsymbol{a})^T \cdot P_h \left[\boldsymbol{E} \cdot \boldsymbol{\psi}_h^{n+1} \right] - 2\nabla^s \boldsymbol{u}_h \right) \right], \qquad (4.38)$$

where:

$$\boldsymbol{f}_u^{n+1} := \boldsymbol{f}^{n+1} - \frac{\eta_p}{\lambda_0} \nabla \cdot \boldsymbol{R},$$

$$\boldsymbol{f}_\psi^{n+1} := \frac{1}{2\lambda_0} \left(\boldsymbol{I} + \boldsymbol{R} \right) + \frac{\lambda}{2\lambda_0} \left(\boldsymbol{a} \cdot \nabla \boldsymbol{R} - \boldsymbol{R} \cdot \nabla \boldsymbol{a} - (\nabla \boldsymbol{a})^T \cdot \boldsymbol{R} \right).$$

As it has been said, we will take $\tilde{p} = 0$, i. e., $\alpha_2 = 0$. The parameters α_1 and α_3 are still given by (4.32) and (4.33), respectively.

4.5.2   Stability analysis in terms of the sub-grid scales

In this section we will prove stability considering that the SGSs are independent unknowns, deferring to the following section stability results in terms of the FE unknowns only. Let us remark here that the stability results to be obtained are *independent* of the expression of the stabilization parameters α_1 and α_3.

Preliminaries

First of all, let us introduce some additional notation, required for the development of the numerical analysis:

1. Consider a sequence $F = \{f^n\}$, with index n with range from 1 to $n = N$, the number of time intervals of the partition in time. Then for $1 \leq p < \infty$ we can say that $F \in \ell^p(X)$ if $\sum_{n=1}^N \delta t \|f^n\|_X^p \leq C < \infty$, and $F \in \ell^\infty(X)$ if $\max_{n=1,\dots,N} \|f^n\| \leq C < \infty$, where C denotes a generic constant.

2. Given two sequences of functions defined in Ω, $F = \{f^n\}$, and $G = \{g^n\}$, with f^0 and g^0 also given, we will make use of the following discrete version of the integration-by-parts formula:

$$\sum_{n=0}^{N-1} \left\langle \delta f^n, g^{n+1} \right\rangle = - \sum_{n=0}^{N-1} \left\langle f^n, \delta g^n \right\rangle + \left\langle f^N, g^N \right\rangle - \left\langle f^0, g^0 \right\rangle. \qquad (4.39)$$

3. On the other hand, a useful tool will be the classical inverse estimate, which holds for quasi-uniform finite element partitions as those we are using: given a finite element function f_h, there exists a constant C_{inv} such that

$$\|\nabla f_h\| \leq \frac{C_{\text{inv}}}{h} \|f_h\| \tag{4.40}$$

4. We will remark the assumptions we will need on the data. We will consider that $\boldsymbol{u}^0 \in \boldsymbol{L}^2(\Omega)$ and $\boldsymbol{\sigma}^0 \in \boldsymbol{L}^2(\Omega)^{d \times d}_{\text{sym}}$, and therefore $\|\boldsymbol{u}_h^0\|$, $\|\boldsymbol{\sigma}_h^0\|$, $\|\tilde{\boldsymbol{u}}^0\|$ and $\|\tilde{\boldsymbol{\sigma}}^0\|$ will be bounded uniformly in h.

5. In the case of the log-formulation, we also consider $\boldsymbol{\psi}_h^0 \in \boldsymbol{L}^2(\Omega)^{d \times d}_{\text{sym}}$, and $\|P_h\left(\boldsymbol{E} \cdot \boldsymbol{\psi}_h^0\right)\|$ bounded uniformly in h.

6. Concerning the force term, the assumption of $\boldsymbol{f} \in L^2\left(0, T; \boldsymbol{L}^2(\Omega)\right)$ leads to stability. We consider T fixed and bounded. For the time discrete problem, the counterpart of $\boldsymbol{f} \in L^2\left(0, T; \boldsymbol{L}^2(\Omega)\right)$ is $\{\boldsymbol{f}^n\} \in \ell^2\left(\boldsymbol{L}^2(\Omega)\right)$.

Stability bounds for the standard formulation

The first result we will prove is the classical stability, in which only velocity and stresses are implied but not the pressure. In particular, for the standard formulation, the components involved are the finite element component of the velocity and stresses and the sub-grid scales of the velocity and the stresses (Theorem 4.1). In the case of the logarithmic formulation, the analogous result is proved in Theorem 4.2.

The stability obtained for $\tilde{\boldsymbol{u}}^{n+1}$ and $\tilde{\boldsymbol{\sigma}}^{n+1}$ will be proved in terms of $\boldsymbol{u}^{n+1}$, $\boldsymbol{\sigma}^{n+1}$ and p^{n+1} (and in terms of $\boldsymbol{u}^{n+1}$, $\boldsymbol{\psi}^{n+1}$ and p^{n+1} in case of the logarithmic formulation) using dual norms (Theorems 4.3, 4.4, 4.5). Finally, the previous results can be proved for a natural norm, under the condition of stabilization parameters α_1 and α_3 depending on the time step size (Theorem 4.6).

Theorem 4.1 (Stability bounds for the standard formulation). *Let $\boldsymbol{u}_h^{n+1}$, p_h^{n+1} and $\boldsymbol{\sigma}_h^{n+1}$ be the solution of (4.26) and $\tilde{\boldsymbol{u}}_1^{n+1}$, $\tilde{\boldsymbol{u}}_2^{n+1}$, $\tilde{\boldsymbol{u}}_3^{n+1}$, $\tilde{\boldsymbol{\sigma}}^{n+1}$ solutions of (4.27), (4.28), (4.29) and (4.31) respectively. Suppose that $\boldsymbol{a}$ is known, $\nabla \cdot \boldsymbol{a} = 0$, $n \cdot \boldsymbol{a} = 0$ on $\partial\Omega$, and $\nabla \boldsymbol{a}$ have components in L^∞. The following stability bounds hold for all $\delta t > 0$ and λ small enough:*

$$\max_{n=0,\ldots,N-1} \left\{ \rho\|\boldsymbol{u}_h^{n+1}\|^2 + \frac{\lambda}{2\eta_p}\|\boldsymbol{\sigma}_h^{n+1}\|^2 + \rho\left(\|\tilde{\boldsymbol{u}}_1^{n+1}\|^2 + \|\tilde{\boldsymbol{u}}_2^{n+1}\|^2 + \|\tilde{\boldsymbol{u}}_3^{n+1}\|^2\right) \right.$$

$$\left. + \frac{\lambda}{2\eta_p}\|\tilde{\boldsymbol{\sigma}}^{n+1}\|^2 \right\} + \sum_{n=0}^{N-1} \delta t 2\eta_s \|\nabla \boldsymbol{u}_h^{n+1}\|^2$$

$$+ \sum_{n=0}^{N-1} \delta t \frac{1}{2\eta_p}\|\boldsymbol{\sigma}_h^{n+1}\|^2 + \sum_{n=0}^{N-1} \delta t \|\alpha_3^{-1/2}\tilde{\boldsymbol{\sigma}}^{n+1}\|^2$$

$$+ \sum_{n=0}^{N-1} \delta t \left(\|\alpha_1^{-1/2}\tilde{\boldsymbol{u}}_1^{n+1}\|^2 + \|\alpha_1^{-1/2}\tilde{\boldsymbol{u}}_2^{n+1}\|^2 + \|\alpha_1^{-1/2}\tilde{\boldsymbol{u}}_3^{n+1}\|^2\right)$$

$$\lesssim C \sum_{n=0}^{N-1} \delta t \frac{\lambda}{\rho}\|\boldsymbol{f}^{n+1}\|^2 + \rho\|\boldsymbol{u}_h^0\|^2 + \frac{\lambda}{2\eta_p}\|\boldsymbol{\sigma}_h^0\|^2$$

Therefore, if $\{\boldsymbol{f}^n\} \in \ell^2(\boldsymbol{L}^2(\Omega))$, $\boldsymbol{u}^0 \in \boldsymbol{L}^2(\Omega)$, and $\boldsymbol{\sigma}^0 \in \boldsymbol{L}^2(\Omega)^{d \times d}_{\text{sym}}$ we have that

$$\{\boldsymbol{u}_h^n\} \in \ell^\infty\left(\boldsymbol{L}^2(\Omega)\right) \cap \ell^2\left(\boldsymbol{H}^1(\Omega)\right); \{\tilde{\boldsymbol{u}}_1^n\}, \{\tilde{\boldsymbol{u}}_2^n\}, \{\tilde{\boldsymbol{u}}_3^n\} \in \ell^\infty\left(\boldsymbol{L}^2(\Omega)\right);$$

$$\{\alpha_1^{-1/2}\tilde{\boldsymbol{u}}_1^n\},\{\alpha_1^{-1/2}\tilde{\boldsymbol{u}}_2^n\},\{\alpha_1^{-1/2}\tilde{\boldsymbol{u}}_3^n\} \in \ell^2\left(\boldsymbol{L}^2(\Omega)\right);$$

$$\{\boldsymbol{\sigma}_h^n\},\{\tilde{\boldsymbol{\sigma}}^n\} \in \ell^\infty\left(\boldsymbol{L}^2(\Omega)_{\text{sym}}^{d\times d}\right);\{\alpha_3^{-1/2}\tilde{\boldsymbol{\sigma}}^n\} \in \ell^2\left(\boldsymbol{L}^2(\Omega)_{\text{sym}}^{d\times d}\right).$$

Proof. In order to obtain stability bounds for the finite element solution, first of all we test (4.26) by $\boldsymbol{v}_h = \boldsymbol{u}_h^{n+1}$, $q_h = p_h^{n+1}$ and $\boldsymbol{\chi}_h = \boldsymbol{\sigma}_h^{n+1}$. Under the suppositions of the Theorem, we have $\left(\boldsymbol{a}\cdot\nabla\boldsymbol{u}_h^{n+1},\boldsymbol{u}_h^{n+1}\right) = 0$ and $\left(\boldsymbol{a}\cdot\nabla\boldsymbol{\sigma}_h^{n+1},\boldsymbol{\sigma}_h^{n+1}\right) = 0$.

$$\rho\underbrace{\left(\delta\boldsymbol{u}_h^n,\boldsymbol{u}_h^{n+1}\right)}_{(1)} + \frac{\lambda}{2\eta_p}\underbrace{\left(\delta\boldsymbol{\sigma}_h^n,\boldsymbol{\sigma}_h^{n+1}\right)}_{(2)} + \delta t\left(\boldsymbol{\sigma}_h^{n+1},\nabla^s\boldsymbol{u}_h^{n+1}\right)$$

$$+ \delta t 2\eta_s\left(\nabla^s\boldsymbol{u}_h^{n+1},\nabla^s\boldsymbol{u}_h^{n+1}\right) + \delta t\left(\boldsymbol{a}\cdot\nabla\boldsymbol{u}_h^{n+1},\boldsymbol{u}_h^{n+1}\right)$$

$$- \delta t\left(p_h^{n+1},\nabla\cdot\boldsymbol{u}_h^{n+1}\right) + \delta t\left(\nabla\cdot\boldsymbol{u}_h^{n+1},p_h^{n+1}\right)$$

$$+ \delta t\frac{1}{2\eta_p}\left(\boldsymbol{\sigma}_h^{n+1},\boldsymbol{\sigma}_h^{n+1}\right) - \delta t\left(\nabla^s\boldsymbol{u}_h^{n+1},\boldsymbol{\sigma}_h^{n+1}\right) + \delta t\frac{\lambda}{2\eta_p}\left(\boldsymbol{a}\cdot\nabla\boldsymbol{\sigma}_h^{n+1},\boldsymbol{\sigma}_h^{n+1}\right)$$

$$+ \underbrace{\delta t\frac{\lambda}{2\eta_p}\left(-\boldsymbol{\sigma}_h^{n+1}\cdot\nabla\boldsymbol{a} - (\nabla\boldsymbol{a})^T\cdot\boldsymbol{\sigma}_h^{n+1},\boldsymbol{\sigma}_h^{n+1}\right)}_{(3)}$$

$$- \sum_K \delta t\left(\tilde{\boldsymbol{u}}_1^{n+1},\rho\boldsymbol{a}\cdot\nabla\boldsymbol{u}_h^{n+1}\right)_K - \sum_K \delta t\left(\tilde{\boldsymbol{u}}_2^{n+1},\nabla p_h^{n+1}\right)$$

$$+ \sum_K \delta t\left(\tilde{\boldsymbol{u}}_3^{n+1},\nabla\cdot\boldsymbol{\sigma}_h^{n+1}\right)_K + \sum_K \delta t\left(\tilde{\boldsymbol{\sigma}}^{n+1},\frac{1}{2\eta_p}\boldsymbol{\sigma}_h^{n+1} + \nabla^s\boldsymbol{u}_h^{n+1}\right)_K$$

$$- \sum_K \delta t\left(\tilde{\boldsymbol{\sigma}}^{n+1},\frac{\lambda}{2\eta_p}\left(\boldsymbol{a}\cdot\nabla\boldsymbol{\sigma}_h^{n+1} + \boldsymbol{\sigma}_h^{n+1}\cdot(\nabla\boldsymbol{a})^T + \nabla\boldsymbol{a}\cdot\boldsymbol{\sigma}_h^{n+1}\right)\right)_K$$

$$= \underbrace{\delta t\left(\boldsymbol{f}^{n+1},\boldsymbol{u}_h^{n+1}\right)}_{(4)}.$$

Now, we can add up the resulting equalities from $n = 0$ to an arbitrary time level M and consider the equality

$$(a, a - b) = \frac{1}{2}a^{\boldsymbol{2}} - \frac{1}{2}b^2 + \frac{1}{2}(a - b)^2.$$

In particular, if a and b are consecutive terms of a series, the term $\frac{1}{2}a^{\boldsymbol{2}} - \frac{1}{2}b^2$ would be a telescoping series. Therefore, the following equality is employed adding up the resulting equalities from $n = 0$ to an arbitrary time level M:

$$\sum_{n=0}^M \left(u^{n+1} - u^n\right) = u^M - u^0.$$

Therefore, for any sequence $\{u^n\}$:

$$(1) = \sum_{n=0}^M \rho\left(\delta\boldsymbol{u}_h^n,\boldsymbol{u}_h^{n+1}\right) = \frac{1}{2}\sum_{n=0}^M \rho\left\|\delta\boldsymbol{u}_h^n\right\|^2 + \frac{1}{2}\rho\left\|\boldsymbol{u}_h^{M+1}\right\|^2 - \frac{1}{2}\rho\left\|\boldsymbol{u}_h^0\right\|^2,$$

$$(2) = \sum_{n=0}^M \frac{\lambda}{2\eta_p}\left(\delta\boldsymbol{\sigma}_h^n,\boldsymbol{\sigma}_h^{n+1}\right) = \frac{1}{2}\sum_{n=0}^M \frac{\lambda}{2\eta_p}\left\|\delta\boldsymbol{\sigma}_h^n\right\|^2 + \frac{1}{2}\frac{\lambda}{2\eta_p}\left\|\boldsymbol{\sigma}_h^{M+1}\right\|^2 - \frac{1}{2}\frac{\lambda}{2\eta_p}\left\|\boldsymbol{\sigma}_h^0\right\|^2,$$

$$(3) = -\sum_{n=0}^M \delta t\frac{\lambda}{2\eta_p}\left(\boldsymbol{\sigma}_h^{n+1}\cdot\nabla\boldsymbol{a} + (\nabla\boldsymbol{a})^T\cdot\boldsymbol{\sigma}_h^{n+1},\boldsymbol{\sigma}_h^{n+1}\right) \geq -\sum_{n=0}^M \delta t\frac{\lambda}{\eta_p}\left\|\nabla\boldsymbol{a}\right\|_{L^\infty(\Omega)}\left\|\boldsymbol{\sigma}_h^{n+1}\right\|^2.$$

Also considering the inequality $\left(\boldsymbol{f}^{n+1}, \boldsymbol{u}_h^{n+1}\right) \leq \frac{\gamma}{2}\left\|\boldsymbol{f}^{n+1}\right\|^2 + \frac{1}{2\gamma}\left\|\boldsymbol{u}_h^{n+1}\right\|^2 \ \forall \gamma > 0$, and taking the constant γ as $\gamma = \dfrac{\lambda\varepsilon_0}{\rho}$:

$$(4) = \sum_{n=0}^{M} \delta t\left(\boldsymbol{f}^{n+1}, \boldsymbol{u}_h^{n+1}\right) \leq \sum_{n=0}^{M} \delta t\frac{\lambda\varepsilon_0}{2\rho}\left\|\boldsymbol{f}^{n+1}\right\|^2 + \sum_{n=0}^{M} \delta t\frac{\rho}{2\lambda\varepsilon_0}\left\|\boldsymbol{u}_h^{n+1}\right\|^2.$$

The last term is absorbed by the LHS using the discrete Gronwall Lemma (see [89]) with $\gamma > 1$. To sum up, we obtain the follow expression:

$$\begin{aligned}
&\frac{1}{2}\rho\left\|\boldsymbol{u}_h^{M+1}\right\|^2 + \frac{1}{2}\sum_{n=0}^{M}\rho\left\|\delta\boldsymbol{u}_h^n\right\|^2 + \frac{1}{2}\frac{\lambda}{2\eta_p}\left\|\boldsymbol{\sigma}_h^{M+1}\right\|^2 + \frac{1}{2}\sum_{n=0}^{M}\frac{\lambda}{2\eta_p}\left\|\delta\boldsymbol{\sigma}_h^n\right\|^2 \\
&\quad + \sum_{n=0}^{M}\delta t 2\eta_s\left\|\nabla^s\boldsymbol{u}_h^{n+1}\right\|^2 + \sum_{n=0}^{M}\delta t\left(\frac{1}{2\eta_p} - \frac{\lambda}{\eta_p}\|\nabla\boldsymbol{a}\|_{L^\infty(\Omega)}\right)\left\|\boldsymbol{\sigma}_h^{n+1}\right\|^2 \\
&\quad - \sum_{n=0}^{M}\delta t\left(\tilde{\boldsymbol{u}}_1^{n+1}, \rho\boldsymbol{a}\cdot\nabla\boldsymbol{u}_h^{n+1}\right) - \sum_{n=0}^{M}\delta t\left(\tilde{\boldsymbol{u}}_2^{n+1}, \nabla p_h^{n+1}\right) \\
&\quad + \sum_{n=0}^{M}\delta t\left(\tilde{\boldsymbol{u}}_3^{n+1}, \nabla\cdot\boldsymbol{\sigma}_h^{n+1}\right) + \sum_{n=0}^{M}\delta t\left(\tilde{\boldsymbol{\sigma}}^{n+1}, \frac{1}{2\eta_p}\boldsymbol{\sigma}_h^{n+1} + \nabla^s\boldsymbol{u}_h^{n+1}\right) \\
&\quad - \sum_{n=0}^{M}\delta t\left(\tilde{\boldsymbol{\sigma}}^{n+1}, \frac{\lambda}{2\eta_p}\left(\boldsymbol{a}\cdot\nabla\boldsymbol{\sigma}_h^{n+1} + \boldsymbol{\sigma}_h^{n+1}\cdot(\nabla\boldsymbol{a})^T + \nabla\boldsymbol{a}\cdot\boldsymbol{\sigma}_h^{n+1}\right)\right) \\
&\lesssim \left(\sum_{n=0}^{M}\delta t\frac{\lambda\varepsilon_0}{2\rho}\left\|\boldsymbol{f}^{n+1}\right\|^2 + \rho\left\|P_h[\boldsymbol{u}^0]\right\|^2 + \frac{\lambda}{2\eta_p}\left\|P_h[\boldsymbol{\sigma}^0]\right\|^2\right).
\end{aligned} \tag{4.41}$$

Now, multiplying (4.27) by $\tilde{\boldsymbol{u}}_1^{n+1}$, integrating over the whole domain and adding up the result from $n = 0$ to $n = M$, we get

$$\begin{aligned}
\rho\left\|\tilde{\boldsymbol{u}}_1^{M+1}\right\|^2 &+ \sum_{n=0}^{M}\rho\left\|\delta\tilde{\boldsymbol{u}}_1^n\right\|^2 + \sum_{n=0}^{M}\delta t\left\|\alpha_1^{-1/2}\tilde{\boldsymbol{u}}_1^{n+1}\right\|^2 \\
&\lesssim -\sum_{n=0}^{M}\delta t\left(\tilde{\boldsymbol{u}}_1^{n+1}, P_h^\perp\left[\rho\boldsymbol{a}\cdot\nabla\boldsymbol{u}_h^{n+1}\right]\right) + \rho\left\|\tilde{\boldsymbol{u}}_1^0\right\|^2.
\end{aligned} \tag{4.42}$$

Proceeding analogously for the remaining subgrid-scale expressions, (4.28) is multiplied by $\tilde{\boldsymbol{u}}_2^{n+1}$, (4.29) by $\tilde{\boldsymbol{u}}_3^{n+1}$ and (4.31) by $\tilde{\boldsymbol{\sigma}}^{n+1}$:

$$\begin{aligned}
\rho\left\|\tilde{\boldsymbol{u}}_2^{M+1}\right\|^2 &+ \sum_{n=0}^{M}\rho\left\|\delta\tilde{\boldsymbol{u}}_2^n\right\|^2 + \sum_{n=0}^{M}\delta t\left\|\alpha_1^{-1/2}\tilde{\boldsymbol{u}}_2^{n+1}\right\|^2 \\
&\lesssim -\sum_{n=0}^{M}\delta t\left(\tilde{\boldsymbol{u}}_2^{n+1}, P_h^\perp\left[\nabla p_h^{n+1}\right]\right) + \rho\left\|\tilde{\boldsymbol{u}}_2^0\right\|^2,
\end{aligned} \tag{4.43}$$

$$\begin{aligned}
\rho\left\|\tilde{\boldsymbol{u}}_3^{M+1}\right\|^2 &+ \sum_{n=0}^{M}\rho\left\|\delta\tilde{\boldsymbol{u}}_3^n\right\|^2 + \sum_{n=0}^{M}\delta t\left\|\alpha_1^{-1/2}\tilde{\boldsymbol{u}}_3^{n+1}\right\|^2 \\
&\lesssim \sum_{n=0}^{M}\delta t\left(\tilde{\boldsymbol{u}}_3^{n+1}, P_h^\perp\left[\nabla\cdot\boldsymbol{\sigma}_h^{n+1}\right]\right) + \rho\left\|\tilde{\boldsymbol{u}}_3^0\right\|^2,
\end{aligned} \tag{4.44}$$

$$\frac{\lambda}{2\eta_p}\|\tilde{\boldsymbol{\sigma}}^{M+1}\|^2 + \sum_{n=0}^{M}\frac{\lambda}{2\eta_p}\|\delta\tilde{\boldsymbol{\sigma}}^n\|^2 + \sum_{n=0}^{M}\delta t\|\alpha_3^{-1/2}\tilde{\boldsymbol{\sigma}}^{n+1}\|^2$$

$$\lesssim \sum_{n=0}^{M}\delta t\left(\tilde{\boldsymbol{\sigma}}^{n+1}, \tilde{P}\left[-\frac{1}{2\eta_p}\boldsymbol{\sigma}_h^{n+1} + \nabla^s\boldsymbol{u}_h^{n+1}\right.\right.$$

$$\left.\left. -\frac{\lambda}{2\eta_p}\left(\boldsymbol{a}\cdot\nabla\boldsymbol{\sigma}_h^{n+1} - \boldsymbol{\sigma}_h^{n+1}\cdot\nabla\boldsymbol{a} - (\nabla\boldsymbol{a})^T\cdot\boldsymbol{\sigma}_h^{n+1}\right)\right]\right)$$

$$+ \frac{\lambda}{2\eta_p}\|\tilde{\boldsymbol{\sigma}}^0\|^2. \tag{4.45}$$

Finally, adding up equations (4.41)-(4.45) some terms are cancelled. Note that for any $L^2(\Omega)$-vector function $\boldsymbol{v}$ we have $\left(\tilde{\boldsymbol{u}}^{n+1}, \boldsymbol{v}\right) = \left(\tilde{\boldsymbol{u}}^{n+1}, P_h^\perp[\boldsymbol{v}]\right)$ and for any $L^2(\Omega)^{d\times d}$-tensor $\left(\tilde{\boldsymbol{\sigma}}^{n+1}, \boldsymbol{\chi}\right) = \left(\tilde{\boldsymbol{\sigma}}^{n+1}, \tilde{P}[\boldsymbol{\chi}]\right)$. Moreover, once the equations are added we obtain among others the following terms that also must be bounded before writing the final equality:

$$\sum_{n=0}^{M}\delta t\left(\tilde{\boldsymbol{\sigma}}^{n+1}, \underbrace{\frac{1}{\eta_p}\boldsymbol{\sigma}_h^{n+1}}_{(1)} - \underbrace{\frac{\lambda}{\eta_p}\left(\boldsymbol{\sigma}_h^{n+1}\cdot\nabla\boldsymbol{a} + (\nabla\boldsymbol{a})^T\cdot\boldsymbol{\sigma}_h^{n+1}\right)}_{(2)}\right) \tag{4.46}$$

$$(1) = \sum_{n=0}^{M}\delta t\left(\tilde{\boldsymbol{\sigma}}^{n+1}, \frac{1}{\eta_p}\boldsymbol{\sigma}_h^{n+1}\right)$$

$$\geq -\sum_{n=0}^{M}\delta t\frac{1}{\eta_p}\left[\frac{\varepsilon_1}{2}\|\tilde{\boldsymbol{\sigma}}^{n+1}\|^2 + \frac{1}{2\varepsilon_1}\|\boldsymbol{\sigma}_h^{n+1}\|^2\right],$$

$$(2) = -\sum_{n=0}^{M}\delta t\left(\tilde{\boldsymbol{\sigma}}^{n+1}, \frac{\lambda}{\eta_p}\left(\boldsymbol{\sigma}_h^{n+1}\cdot\nabla\boldsymbol{a} + (\nabla\boldsymbol{a})^T\cdot\boldsymbol{\sigma}_h^{n+1}\right)\right)$$

$$\geq -\sum_{n=0}^{M}\delta t\frac{\lambda}{\eta_p}\|\nabla\boldsymbol{a}\|_{L^\infty\Omega)}\left[\frac{\varepsilon_2}{2}\|\tilde{\boldsymbol{\sigma}}^{n+1}\|^2 + \frac{1}{2\varepsilon_2}\|\boldsymbol{\sigma}_h^{n+1}\|^2\right].$$

Note that for adequate ε_1 and ε_2 these terms are absorbed by $\frac{\lambda}{2\eta_p}\|\boldsymbol{\sigma}_h^{M+1}\|^2$ and $\frac{\lambda}{2\eta_p}\|\tilde{\boldsymbol{\sigma}}^{M+1}\|^2$ respectively, applying the discrete Gronwall Lemma. Therefore, the final inequality is as follows:

$$\rho\left\|\boldsymbol{u}_h^{M+1}\right\|^2 + \frac{\lambda}{2\eta_p}\left\|\boldsymbol{\sigma}_h^{M+1}\right\|^2 + \rho\|\tilde{\boldsymbol{u}}_1^{M+1}\|^2 + \rho\|\tilde{\boldsymbol{u}}_2^{M+1}\|^2 + \rho\|\tilde{\boldsymbol{u}}_3^{M+1}\|^2 + \frac{\lambda}{2\eta_p}\|\tilde{\boldsymbol{\sigma}}^{M+1}\|^2$$

$$+ \rho\sum_{n=0}^{M}\|\delta\boldsymbol{u}_h^n\|^2 + \sum_{n=0}^{M}\frac{\lambda}{2\eta_p}\|\delta\boldsymbol{\sigma}_h^n\|^2 + \rho\left(\sum_{n=0}^{M}\|\delta\tilde{\boldsymbol{u}}_1^n\|^2 + \sum_{n=0}^{M}\|\delta\tilde{\boldsymbol{u}}_2^n\|^2 + \sum_{n=0}^{M}\|\delta\tilde{\boldsymbol{u}}_3^n\|^2\right)$$

$$+ \sum_{n=0}^{M}\frac{\lambda}{2\eta_p}\|\delta\tilde{\boldsymbol{\sigma}}^n\|^2 + \sum_{n=0}^{M}\delta t 2\eta_s\left\|\nabla^s\boldsymbol{u}_h^{n+1}\right\|^2$$

$$+ \sum_{n=0}^{M}\delta t\frac{1}{2\eta_p}\left(1 - \lambda\|\nabla\boldsymbol{a}\|_{L^\infty(\Omega)} - \frac{1}{\varepsilon_1} - \frac{\lambda}{\varepsilon_2}\|\nabla\boldsymbol{a}\|_{L^\infty(\Omega)}\right)\|\boldsymbol{\sigma}_h^{n+1}\|^2$$

$$+ \sum_{n=0}^{M}\delta t\|\alpha_1^{-1/2}\tilde{\boldsymbol{u}}_1^{n+1}\|^2 + \sum_{n=0}^{M}\delta t\|\alpha_1^{-1/2}\tilde{\boldsymbol{u}}_2^{n+1}\|^2 + \sum_{n=0}^{M}\delta t\|\alpha_1^{-1/2}\tilde{\boldsymbol{u}}_3^{n+1}\|^2$$

$$+ \sum_{n=0}^{M} \delta t \|\alpha_3^{-1/2} \tilde{\boldsymbol{\sigma}}^{n+1}\|^2$$

$$\lesssim \sum_{n=0}^{M} \delta t \frac{\lambda \varepsilon_0}{2\rho} \|\boldsymbol{f}^{n+1}\|^2 + \rho \|P_h[\boldsymbol{u}^0]\|^2 + \rho \left(\|\tilde{\boldsymbol{u}}_1^0\|^2 + \|\tilde{\boldsymbol{u}}_2^0\|^2 + \|\tilde{\boldsymbol{u}}_3^0\|^2 \right)$$

$$+ \frac{\lambda}{2\eta_p} \|P_h[\boldsymbol{\sigma}^0]\|^2 + \frac{\lambda}{2\eta_p} \|\tilde{\boldsymbol{\sigma}}^0\|^2,$$

from where the theorem follows for λ small enough. $\qquad\qquad\qquad\qquad\qquad\square$

Stability bounds for the log-conformation reformulation

We can prove now a similar stability estimate for the LCR:

Theorem 4.2 (Stability bounds for the logarithmic formulation). *Let $\boldsymbol{u}_h^{n+1}$, p_h^{n+1} and $\boldsymbol{\psi}_h^{n+1}$ be the solution of (4.34) and $\tilde{\boldsymbol{u}}_1^{n+1}$, $\tilde{\boldsymbol{u}}_2^{n+1}$, $\tilde{\boldsymbol{u}}_3^{n+1}$, $\tilde{\boldsymbol{\sigma}}^{n+1}$ solutions of (4.35), (4.36), (4.37) and (4.38) respectively. The following stability bounds hold for all $\delta t > 0$ and the λ small enough and cosidering that the assumptions of Theorem 4.1 holds:*

$$\max_{n=0,\dots,N-1} \left\{ \rho \|\boldsymbol{u}_h^{n+1}\|^2 + \frac{\lambda}{2\lambda_0} \frac{\eta_p}{\lambda_0} \|P_h\left[\boldsymbol{E} \cdot \boldsymbol{\psi}_h^{n+1}\right]\|^2 + \rho \|\tilde{\boldsymbol{u}}_1^{n+1}\|^2 + \rho \|\tilde{\boldsymbol{u}}_2^{n+1}\|^2 \right.$$

$$\left. + \rho \|\tilde{\boldsymbol{u}}_3^{n+1}\|^2 + \frac{\lambda}{2\eta_p} \|\tilde{\boldsymbol{\sigma}}^{n+1}\|^2 \right\} + \sum_{n=0}^{N-1} \delta t 2\eta_s \|\nabla \boldsymbol{u}_h^{n+1}\|^2$$

$$+ \sum_{n=0}^{N-1} \delta t \frac{\eta_p}{\lambda_0^2} \|P_h\left[\boldsymbol{E} \cdot \boldsymbol{\psi}_h^{n+1}\right]\|^2 + \sum_{n=0}^{N-1} \delta t \|\alpha_3^{-1/2} \tilde{\boldsymbol{\sigma}}^{n+1}\|^2$$

$$+ \sum_{n=0}^{N-1} \delta t \left(\|\alpha_1^{-1/2} \tilde{\boldsymbol{u}}_1^{n+1}\|^2 + \|\alpha_1^{-1/2} \tilde{\boldsymbol{u}}_2^{n+1}\|^2 + \|\alpha_1^{-1/2} \tilde{\boldsymbol{u}}_3^{n+1}\|^2 \right)$$

$$\lesssim \sum_{n=0}^{M} \frac{\lambda}{2\rho} \delta t \|\boldsymbol{f}_u^{n+1}\|^2 + \sum_{n=0}^{M} \frac{\lambda}{2} \frac{\eta_p}{\lambda_0} \delta t \|\boldsymbol{f}_\psi^{n+1}\|^2$$

$$+ \rho \|\boldsymbol{u}^0\|^2 + \frac{\lambda}{2\lambda_0} \frac{\eta_p}{\lambda_0} \|P_h\left[\boldsymbol{E} \cdot \boldsymbol{\psi}_h^0\right]\|^2 .$$

Therefore, if $\{\boldsymbol{f}_{\boldsymbol{u}}^n\}, \{\boldsymbol{f}_{\boldsymbol{\psi}}^n\} \in \ell^2(\boldsymbol{L}^2(\Omega))$, $\boldsymbol{u}_h^0 \in \boldsymbol{L}^2(\Omega)$, and $P_h\left[\boldsymbol{E} \cdot \boldsymbol{\psi}_h^0\right] \in \boldsymbol{L}^2(\Omega)_{\mathrm{sym}}^{d \times d}$ we have that

$$\{\boldsymbol{u}_h^n\} \in \ell^\infty \left(\boldsymbol{L}^2(\Omega) \right) \cap \ell^2 \left(\boldsymbol{H}^1(\Omega) \right) ; \{\tilde{\boldsymbol{u}}_1^n\}, \{\tilde{\boldsymbol{u}}_2^n\}, \{\tilde{\boldsymbol{u}}_3^n\} \in \ell^\infty \left(\boldsymbol{L}^2(\Omega) \right) ;$$

$$\{\alpha_1^{-1/2} \tilde{\boldsymbol{u}}_1^n\}, \{\alpha_1^{-1/2} \tilde{\boldsymbol{u}}_2^n\}, \{\alpha_1^{-1/2} \tilde{\boldsymbol{u}}_3^n\} \in \ell^2 \left(\boldsymbol{L}^2(\Omega) \right) ;$$

$$\{\tilde{\boldsymbol{\sigma}}^n\}, \{P_h\left[\boldsymbol{E} \cdot \boldsymbol{\psi}_h^n\right]\} \in \ell^\infty \left(\boldsymbol{L}^2(\Omega)_{\mathrm{sym}}^{d \times d} \right) ; \{\alpha_3^{-1/2} \tilde{\boldsymbol{\sigma}}^n\} \in \ell^2 \left(\boldsymbol{L}^2(\Omega)_{\mathrm{sym}}^{d \times d} \right) .$$

Proof. In order to obtain stability bounds for the finite element solution, first of all we test (4.34) by $\boldsymbol{v}_h = \boldsymbol{u}_h^{n+1}$, $q_h = p_h^{n+1}$ and $\boldsymbol{\chi}_h = \frac{\eta_p}{\lambda_0} P_h\left[\boldsymbol{E} \cdot \boldsymbol{\psi}_h^{n+1}\right]$. Using the assumptions of Theorem 4.1, we have $\left(\boldsymbol{a} \cdot \nabla \boldsymbol{u}_h^{n+1}, \boldsymbol{u}_h^{n+1} \right) = 0$ and

$$\left(\boldsymbol{a} \cdot \nabla P_h\left[\boldsymbol{E} \cdot \boldsymbol{\psi}_h^{n+1}\right], \frac{\eta_p}{\lambda_0} P_h\left[\boldsymbol{E} \cdot \boldsymbol{\psi}_h^{n+1}\right] \right) = 0.$$

Again, for simplicity, $\tilde{p}$ will be fixed equal to zero along the analysis. We have that

$$
\rho \underbrace{\left(\delta \boldsymbol{u}_h^n, \boldsymbol{u}_h^{n+1}\right)}_{(1)} + \underbrace{\frac{\lambda}{2\lambda_0} \frac{\eta_p}{\lambda_0} \left(\delta P_h \left[\boldsymbol{E} \cdot \boldsymbol{\psi}_h^n\right], P_h \left[\boldsymbol{E} \cdot \boldsymbol{\psi}_h^{n+1}\right]\right)}_{(2)} + \delta t 2\eta_s \left(\nabla^s \boldsymbol{u}_h^{n+1}, \nabla^s \boldsymbol{u}_h^{n+1}\right)
$$

$$
+ \underbrace{\frac{\eta_p}{\lambda_0} \delta t \left(P_h \left[\boldsymbol{E} \cdot \boldsymbol{\psi}_h^{n+1}\right], \nabla^s \boldsymbol{u}_h^{n+1}\right)}_{(3)} + \delta t \left\langle \boldsymbol{a} \cdot \nabla \boldsymbol{u}_h^{n+1}, \boldsymbol{u}_h^{n+1}\right\rangle
$$

$$
- \delta t \left(p_h^{n+1}, \nabla \cdot \boldsymbol{u}_h^{n+1}\right) + \delta t \left(\nabla \cdot \boldsymbol{u}_h^{n+1}, p_h^{n+1}\right)
$$

$$
+ \delta t \frac{1}{2\lambda_0} \frac{\eta_p}{\lambda_0} \left(P_h \left[\boldsymbol{E} \cdot \boldsymbol{\psi}_h^{n+1}\right], P_h \left[\boldsymbol{E} \cdot \boldsymbol{\psi}_h^{n+1}\right]\right) - \underbrace{\frac{\eta_p}{\lambda_0} \delta t \left(\nabla^s \boldsymbol{u}_h^{n+1}, P_h \left[\boldsymbol{E} \cdot \boldsymbol{\psi}_h^{n+1}\right]\right)}_{(3)}
$$

$$
+ \delta t \frac{\lambda}{2\lambda_0} \frac{\eta_p}{\lambda_0} \left(\boldsymbol{a} \cdot \nabla P_h \left[\boldsymbol{E} \cdot \boldsymbol{\psi}_h^{n+1}\right], P_h \left[\boldsymbol{E} \cdot \boldsymbol{\psi}_h^{n+1}\right]\right)
$$

$$
+ \underbrace{\frac{\lambda}{2\lambda_0} \frac{\eta_p}{\lambda_0} \delta t \left(2\nabla^s \boldsymbol{u}_h^{n+1}, P_h \left[\boldsymbol{E} \cdot \boldsymbol{\psi}_h^{n+1}\right]\right)}_{(3)}
$$

$$
- \underbrace{\delta t \frac{\lambda}{2\lambda_0} \frac{\eta_p}{\lambda_0} \left(P_h \left[\boldsymbol{E} \cdot \boldsymbol{\psi}_h^{n+1}\right] \cdot \nabla \boldsymbol{a} + (\nabla \boldsymbol{a})^T \cdot P_h \left[\boldsymbol{E} \cdot \boldsymbol{\psi}_h^{n+1}\right], P_h \left[\boldsymbol{E} \cdot \boldsymbol{\psi}_h^{n+1}\right]\right)}_{(4)}
$$

$$
- \sum_K \delta t \left(\nabla \cdot \boldsymbol{u}_h^{n+1}, \tilde{p}^{n+1}\right)_K - \sum_K \delta t \left(\tilde{\boldsymbol{u}}_1^{n+1}, \rho \boldsymbol{a} \cdot \nabla \boldsymbol{u}_h^{n+1}\right)_K
$$

$$
- \sum_K \delta t \left(\tilde{\boldsymbol{u}}_2^{n+1}, \nabla p_h^{n+1}\right)_K + \sum_K \frac{\eta_p}{\lambda_0} \delta t \left(\tilde{\boldsymbol{u}}_3^{n+1}, P_h \left[\boldsymbol{E} \cdot \boldsymbol{\psi}_h^{n+1}\right]\right)_K
$$

$$
+ \sum_K \delta t \left(\tilde{\boldsymbol{\sigma}}^{n+1}, \frac{1}{2\lambda_0} P_h \left[\boldsymbol{E} \cdot \boldsymbol{\psi}_h^{n+1}\right] + \nabla^s \boldsymbol{u}_h^{n+1}\right)_K
$$

$$
+ \sum_K \delta t \left(\tilde{\boldsymbol{\sigma}}^{n+1}, -\frac{\lambda}{2\lambda_0} \left(\boldsymbol{a} \cdot \nabla P_h \left[\boldsymbol{E} \cdot \boldsymbol{\psi}_h^{n+1}\right]\right.\right.
$$

$$
\left.\left. + P_h \left[\boldsymbol{E} \cdot \boldsymbol{\psi}_h^{n+1}\right] \cdot (\nabla \boldsymbol{a})^T + \nabla \boldsymbol{a} \cdot P_h \left[\boldsymbol{E} \cdot \boldsymbol{\psi}_h^{n+1}\right]\right)\right)_K
$$

$$
= \underbrace{\delta t \left(\boldsymbol{f}_u^{n+1}, \boldsymbol{u}_h^{n+1}\right)}_{(5)} + \underbrace{\delta t \left(\boldsymbol{f}_\psi^{n+1}, \frac{\eta_p}{\lambda_0} P_h \left[\boldsymbol{E} \cdot \boldsymbol{\psi}_h^{n+1}\right]\right)}_{(6)}.
$$

Following the same strategy that in the proof of Theorem 4.1:

$$
(1) = \sum_{n=0}^M \rho \left(\delta \boldsymbol{u}_h^n, \boldsymbol{u}_h^{n+1}\right) = \frac{1}{2} \sum_{n=0}^M \rho \left(\delta \boldsymbol{u}_h^n\right)^2 + \frac{1}{2}\rho \left\|\boldsymbol{u}_h^{M+1}\right\|^2 - \frac{1}{2}\rho \left\|\boldsymbol{u}_h^0\right\|^2,
$$

$$
(2) = \sum_{n=0}^M \frac{\lambda}{2\lambda_0} \frac{\eta_p}{\lambda_0} \left(\delta P_h \left[\boldsymbol{E} \cdot \boldsymbol{\psi}_h^n\right], P_h \left[\boldsymbol{E} \cdot \boldsymbol{\psi}_h^{n+1}\right]\right)
$$

$$
= \frac{1}{2} \sum_{n=0}^M \frac{\lambda}{2\lambda_0} \frac{\eta_p}{\lambda_0} \left\|\delta P_h \left[\boldsymbol{E} \cdot \boldsymbol{\psi}_h^n\right]\right\|^2 + \frac{1}{2} \frac{\lambda}{2\lambda_0} \frac{\eta_p}{\lambda_0} \left\|P_h \left[\boldsymbol{E} \cdot \boldsymbol{\psi}_h^{M+1}\right]\right\|^2
$$

$$
- \frac{1}{2} \frac{\lambda}{2\lambda_0} \frac{\eta_p}{\lambda_0} \left\|P_h \left[\boldsymbol{E} \cdot \boldsymbol{\psi}_h^0\right]\right\|^2,
$$

$$(3) = \sum_{n=0}^{M} \frac{\lambda}{\lambda_0} \frac{\eta_p}{\lambda_0} \delta t \left(\nabla^s \boldsymbol{u}_h^{n+1}, P_h \left[\boldsymbol{E} \cdot \boldsymbol{\psi}_h^{n+1} \right] \right)$$

$$\geq - \sum_{n=0}^{M} \eta_p \frac{\lambda}{\lambda_0} \delta t \left[\frac{1}{2\varepsilon_0 \lambda_0^2} \left\| P_h \left[\boldsymbol{E} \cdot \boldsymbol{\psi}_h^{n+1} \right] \right\|^2 + \frac{\varepsilon_0}{2} \left\| \nabla^s \boldsymbol{u}_h^{n+1} \right\|^2 \right],$$

$$(4) = - \sum_{n=0}^{M} \delta t \frac{\lambda}{2\lambda_0} \frac{\eta_p}{\lambda_0} \left(P_h \left[\boldsymbol{E} \cdot \boldsymbol{\psi}_h^{n+1} \right] \cdot \nabla \boldsymbol{a} + (\nabla \boldsymbol{a})^T \cdot P_h \left[\boldsymbol{E} \cdot \boldsymbol{\psi}_h^{n+1} \right], P_h \left[\boldsymbol{E} \cdot \boldsymbol{\psi}_h^{n+1} \right] \right)$$

$$\geq - \sum_{n=0}^{M} \delta t \frac{\lambda}{2\lambda_0} \frac{\eta_p}{\lambda_0} \left\| \nabla \boldsymbol{a} \right\|_{L^\infty(\Omega)} \left\| P_h \left[\boldsymbol{E} \cdot \boldsymbol{\psi}_h^{n+1} \right] \right\|^2.$$

Considering the inequality $\left(\boldsymbol{f}^{n+1}, \boldsymbol{u}_h^{n+1} \right) \leq \frac{\gamma}{2} \left\| \boldsymbol{f}^{n+1} \right\|^2 + \frac{1}{2\gamma} \left\| \boldsymbol{u}_h^{n+1} \right\|^2, \forall \gamma > 0$, and taking the constant γ as $\gamma = \dfrac{\lambda \varepsilon_1}{\rho}$, $\varepsilon_1 > 0$ and supposing $\left\| \boldsymbol{f}_u^{n+1} \right\|$ bounded.

$$(5) = \sum_{n=0}^{M} \delta t \left(\boldsymbol{f}_u^{n+1}, \boldsymbol{u}_h^{n+1} \right) \leq \sum_{n=0}^{M} \frac{\lambda \varepsilon_1}{2\rho} \delta t \left\| \boldsymbol{f}_u^{n+1} \right\|^2 + \sum_{n=0}^{M} \frac{\rho}{2\lambda \varepsilon_1} \delta t \left\| \boldsymbol{u}_h^{n+1} \right\|^2. \qquad (4.47)$$

Analogously, applying the same strategy that for expression (4.47) and supposing $\left\| \boldsymbol{f}_\psi^{n+1} \right\|$ bounded, considering $\varepsilon_2 > 0$ and taking the constant γ as $\gamma = \lambda \varepsilon_2$ in Young's inequality:

$$(6) = \sum_{n=0}^{M} \delta t \left(\boldsymbol{f}_\psi^{n+1}, \frac{\eta_p}{\lambda_0} P_h \left[\boldsymbol{E} \cdot \boldsymbol{\psi}_h^{n+1} \right] \right)$$

$$\leq \sum_{n=0}^{M} \delta t \frac{\eta_p}{\lambda_0} \frac{\lambda \varepsilon_2}{2} \left\| \boldsymbol{f}_\psi^{n+1} \right\|^2 + \sum_{n=0}^{M} \delta t \frac{\eta_p}{\lambda_0} \frac{1}{2\lambda \varepsilon_2} \left\| P_h \left[\boldsymbol{E} \cdot \boldsymbol{\psi}_h^{n+1} \right] \right\|^2.$$

The last term is absorbed by the LHS due to the discrete Gronwall Lemma with $\alpha > 1$. To sum up we obtain the following expression:

$$\frac{1}{2} \rho \left\| \boldsymbol{u}_h^{M+1} \right\|^2 + \frac{1}{2} \sum_{n=0}^{M} \rho \left\| \delta \boldsymbol{u}_h^n \right\| + \frac{1}{2} \frac{\lambda}{2\lambda_0} \frac{\eta_p}{\lambda_0} \left\| P_h \left[\boldsymbol{E} \cdot \boldsymbol{\psi}_h^{M+1} \right] \right\|^2$$

$$+ \frac{1}{2} \sum_{n=0}^{M} \frac{\lambda}{2\lambda_0} \frac{\eta_p}{\lambda_0} \left\| \delta P_h \left[\boldsymbol{E} \cdot \boldsymbol{\psi}_h^n \right] \right\|^2 + \sum_{n=0}^{M} \delta t \left(2\eta_s - \eta_p \frac{\varepsilon_0}{2} \frac{\lambda}{\lambda_0} \right) \left\| \nabla^s \boldsymbol{u}_h^{n+1} \right\|^2$$

$$+ \sum_{n=0}^{M} \delta t \frac{\eta_p}{\lambda_0} \left(\frac{1}{2\lambda_0} - \frac{\lambda}{2\varepsilon_0 \lambda_0^2} - \frac{\lambda}{\lambda_0} \left\| \nabla \boldsymbol{a} \right\|_{L^\infty(\Omega)} \right) \left\| P_h \left[\boldsymbol{E} \cdot \boldsymbol{\psi}_h^{n+1} \right] \right\|^2$$

$$- \sum_{n=0}^{M} \delta t \left(\tilde{\boldsymbol{u}}_1^{n+1}, \rho \boldsymbol{a} \cdot \nabla \boldsymbol{u}_h^{n+1} \right) - \sum_{n=0}^{M} \delta t \left(\tilde{\boldsymbol{u}}_2^{n+1}, \nabla p_h^{n+1} \right)$$

$$+ \sum_{n=0}^{M} \delta t \frac{\eta_p}{\lambda_0} \left(\tilde{\boldsymbol{u}}_3^{n+1}, \nabla \cdot P_h \left[\boldsymbol{E} \cdot \boldsymbol{\psi}_h^{n+1} \right] \right)$$

$$+ \sum_{n=0}^{M} \delta t \left(\tilde{\boldsymbol{\sigma}}^{n+1}, \frac{1}{2\lambda_0} P_h \left[\boldsymbol{E} \cdot \boldsymbol{\psi}_h^{n+1} \right] + \nabla^s \boldsymbol{u}_h^{n+1} - \frac{\lambda}{2\lambda_0} \left(\boldsymbol{a} \cdot \nabla P_h \left[\boldsymbol{E} \cdot \boldsymbol{\psi}_h^{n+1} \right] \right. \right.$$

$$\left. \left. + P_h \left[\boldsymbol{E} \cdot \boldsymbol{\psi}_h^{n+1} \right] \cdot (\nabla \boldsymbol{a})^T + \nabla \boldsymbol{a} \cdot P_h \left[\boldsymbol{E} \cdot \boldsymbol{\psi}_h^{n+1} \right] \right) \right)$$

$$\lesssim \sum_{n=0}^{M} \frac{\lambda\varepsilon_1}{2\rho}\delta t \left\| \boldsymbol{f}_u^{n+1} \right\|^2 + \sum_{n=0}^{M} \frac{\lambda\varepsilon_2}{2}\frac{\eta_p}{\lambda_0}\delta t \left\| \boldsymbol{f}_\psi^{n+1} \right\|^2 + \rho \left\| P_h(\boldsymbol{u}^0) \right\|^2$$

$$+ \frac{\lambda}{2\lambda_0}\frac{\eta_p}{\lambda_0} \left\| P_h \left[\boldsymbol{E}\cdot\boldsymbol{\psi}_h^0 \right] \right\|^2, \tag{4.48}$$

taking the ε_i $i = 0,1,2$ suitable.

Now, we multiply (4.35) by $\tilde{\boldsymbol{u}}_1^{n+1}$, integrate over the whole domain and add up the result from $n=0$ to $n=M$:

$$\rho\left\|\tilde{\boldsymbol{u}}_1^{M+1}\right\|^2 + \sum_{n=0}^{M}\rho\left\|\delta\tilde{\boldsymbol{u}}_1^n\right\|^2 + \sum_{n=0}^{M}\delta t\left\|\alpha_1^{-1/2}\tilde{\boldsymbol{u}}_1^{n+1}\right\|^2$$

$$\lesssim -\sum_{n=0}^{M}\delta t\left(\tilde{\boldsymbol{u}}_1^{n+1}, P_h^\perp\left[\rho\boldsymbol{a}\cdot\nabla\boldsymbol{u}_h^{n+1}\right]\right) + \rho\left\|\tilde{\boldsymbol{u}}_1^0\right\|^2, \tag{4.49}$$

Analogously, we multiply (4.36) by $\tilde{\boldsymbol{u}}_2^{n+1}$, (4.37) by $\tilde{\boldsymbol{u}}_3^{n+1}$ and (4.38) by $\tilde{\boldsymbol{\sigma}}^{n+1}$, to obtain:

$$\rho\left\|\tilde{\boldsymbol{u}}_2^{M+1}\right\|^2 + \sum_{n=0}^{M}\rho\left\|\delta\tilde{\boldsymbol{u}}_2^n\right\|^2 + \sum_{n=0}^{M}\delta t\left\|\alpha_1^{-1/2}\tilde{\boldsymbol{u}}_2^{n+1}\right\|^2$$

$$\lesssim -\sum_{n=0}^{M}\delta t\left(\tilde{\boldsymbol{u}}_2^{n+1}, P_h^\perp\left[\nabla p_h^{n+1}\right]\right) + \rho\left\|\tilde{\boldsymbol{u}}_2^0\right\|^2, \tag{4.50}$$

$$\rho\left\|\tilde{\boldsymbol{u}}_3^{M+1}\right\|^2 + \sum_{n=0}^{M}\rho\left\|\delta\tilde{\boldsymbol{u}}_3^n\right\|^2 + \sum_{n=0}^{M}\delta t\left\|\alpha_1^{-1/2}\tilde{\boldsymbol{u}}_3^{n+1}\right\|^2$$

$$\lesssim \sum_{n=0}^{M}\delta t\frac{\eta_p}{\lambda_0}\left(\tilde{\boldsymbol{u}}_3^{n+1}, P_h^\perp\left[\nabla\cdot P_h\left[\boldsymbol{E}\cdot\boldsymbol{\psi}_h^{n+1}\right]\right]\right) + \rho\left\|\tilde{\boldsymbol{u}}_3^0\right\|^2, \tag{4.51}$$

$$\frac{\lambda}{2\eta_p}\left\|\tilde{\boldsymbol{\sigma}}^{M+1}\right\|^2 + \sum_{n=0}^{M}\frac{\lambda}{2\eta_p}\left\|\delta\tilde{\boldsymbol{\sigma}}^n\right\|^2 + \sum_{n=0}^{M}\delta t\left\|\alpha_3^{-1/2}\tilde{\boldsymbol{\sigma}}^{n+1}\right\|^2$$

$$\lesssim \sum_{n=0}^{M}\delta t\left(\tilde{\boldsymbol{\sigma}}^{n+1}, \tilde{P}\left[-\frac{1}{2\lambda_0}P_h\left[\boldsymbol{E}\cdot\boldsymbol{\psi}_h^{n+1}\right] + \nabla^s\boldsymbol{u}_h^{n+1} - \frac{\lambda}{\lambda_0}\nabla^s\boldsymbol{u}_h^{n+1}\right.\right.$$

$$-\frac{\lambda}{2\lambda_0}\left(\boldsymbol{a}\cdot\nabla P_h\left[\boldsymbol{E}\cdot\boldsymbol{\psi}_h^{n+1}\right] - P_h\left[\boldsymbol{E}\cdot\boldsymbol{\psi}_h^{n+1}\right]\cdot(\nabla\boldsymbol{a})^T\right.$$

$$\left.\left.\left.-\nabla\boldsymbol{a}\cdot P_h\left[\boldsymbol{E}\cdot\boldsymbol{\psi}_h^{n+1}\right]\right)\right]\right) + \frac{\lambda}{2\eta_p}\left\|\tilde{\boldsymbol{\sigma}}^0\right\|^2. \tag{4.52}$$

Adding equations (4.48)-(4.52), some terms are cancelled. The next terms must be bounded considering that for any $L^2(\Omega)$-vector function $\boldsymbol{v}$ we have $\left(\tilde{\boldsymbol{u}}^{n+1}, \boldsymbol{v}\right) = \left(\tilde{\boldsymbol{u}}^{n+1}, P_h^\perp[\boldsymbol{v}]\right)$ and for any $L^2(\Omega)^{d\times d}$-tensor $\left(\tilde{\boldsymbol{\sigma}}^{n+1}, \boldsymbol{\chi}\right) = \left(\tilde{\boldsymbol{\sigma}}^{n+1}, \tilde{P}[\boldsymbol{\chi}]\right)$:

$$\sum_{n=0}^{M}\delta t\Big(\tilde{\boldsymbol{\sigma}}^{n+1}, \underbrace{\frac{1}{\lambda_0}P_h\left[\boldsymbol{E}\cdot\boldsymbol{\psi}_h^{n+1}\right]}_{(1)} + \underbrace{\frac{\lambda}{\lambda_0}\nabla^s\boldsymbol{u}_h^{n+1}}_{(2)}$$

$$+\underbrace{\frac{\lambda}{\lambda_0}\left(-P_h\left[\boldsymbol{E}\cdot\boldsymbol{\psi}_h^{n+1}\right]\cdot(\nabla\boldsymbol{a})^T - \nabla\boldsymbol{a}\cdot P_h\left[\boldsymbol{E}\cdot\boldsymbol{\psi}_h^{n+1}\right]\right)}_{(3)}\Big)$$

$$(1) = \sum_{n=0}^{M} \delta t \left(\tilde{\boldsymbol{\sigma}}^{n+1}, \frac{1}{\lambda_0} \left\| P_h \left[\boldsymbol{E} \cdot \boldsymbol{\psi}_h^{n+1} \right] \right\| \right) = 0,$$

$$(2) = \sum_{n=0}^{M} \delta t \left(\tilde{\boldsymbol{\sigma}}^{n+1}, \frac{\lambda}{\lambda_0} \nabla^s \boldsymbol{u}_h^{n+1} \right)$$

$$\geq - \sum_{n=0}^{M} \delta t \frac{\lambda}{\lambda_0} \frac{1}{\eta_p} \left[\frac{1}{2\varepsilon_4} \left\| \tilde{\boldsymbol{\sigma}}^{n+1} \right\|^2 + \eta_p^2 \frac{\varepsilon_4}{2} \left\| \nabla^s \boldsymbol{u}_h^{n+1} \right\|^2 \right],$$

$$(3) = \sum_{n=0}^{M} \delta t \left(\tilde{\boldsymbol{\sigma}}^{n+1}, -\frac{\lambda}{\lambda_0} P_h \left[\boldsymbol{E} \cdot \boldsymbol{\psi}_h^{n+1} \right] \cdot (\nabla \boldsymbol{a})^T - \frac{\lambda}{\lambda_0} \nabla \boldsymbol{a} \cdot P_h \left[\boldsymbol{E} \cdot \boldsymbol{\psi}_h^{n+1} \right] \right)$$

$$\geq - \sum_{n=0}^{M} \delta t \frac{\lambda}{\eta_p} \left\| \nabla \boldsymbol{a} \right\|_{L^\infty(\Omega)} \left[\frac{1}{2\varepsilon_5} \left\| \tilde{\boldsymbol{\sigma}}^{n+1} \right\|^2 + \frac{\varepsilon_5}{2} \frac{\eta_p^2}{\lambda_0^2} \left\| P_h \left[\boldsymbol{E} \cdot \boldsymbol{\psi}_h^{n+1} \right] \right\|^2 \right].$$

Moreover, the discrete Gronwall Lemma can be employed in the last terms. Finally, we obtain the next inequality:

$$\rho \left\| \boldsymbol{u}_h^{M+1} \right\|^2 + \frac{\lambda}{2\lambda_0} \frac{\eta_p}{\lambda_0} \left\| P_h \left[\boldsymbol{E} \cdot \boldsymbol{\psi}_h^{M+1} \right] \right\|^2 + \rho \left\| \tilde{\boldsymbol{u}}_1^{M+1} \right\|^2 + \rho \left\| \tilde{\boldsymbol{u}}_2^{M+1} \right\|^2$$

$$+ \rho \left\| \tilde{\boldsymbol{u}}_3^{M+1} \right\|^2 + \frac{\lambda}{2\lambda_0} \left\| \tilde{\boldsymbol{\sigma}}^{M+1} \right\|^2 + \rho \sum_{n=0}^{M} \left\| \delta \boldsymbol{u}_h^n \right\|^2 + \sum_{n=0}^{M} \frac{\lambda}{2\lambda_0} \left\| \delta P_h \left[\boldsymbol{E} \cdot \boldsymbol{\psi}_h^n \right] \right\|^2$$

$$+ \rho \sum_{n=0}^{M} \left\| \delta \tilde{\boldsymbol{u}}_1^n \right\|^2 + \rho \sum_{n=0}^{M} \left\| \delta \tilde{\boldsymbol{u}}_2^n \right\|^2 + \rho \sum_{n=0}^{M} \left\| \delta \tilde{\boldsymbol{u}}_3^n \right\|^2 + \sum_{n=0}^{M} \frac{\lambda}{2\eta_p} \left\| \delta \tilde{\boldsymbol{\sigma}}^n \right\|^2$$

$$+ \sum_{n=0}^{M} \delta t \left(2\eta_s - \eta_p \frac{\varepsilon_0}{2} \frac{\lambda}{\lambda_0} - \eta_p \frac{\varepsilon_4}{2} \frac{\lambda}{\lambda_0} \right) \left\| \nabla^s \boldsymbol{u}_h^{n+1} \right\|^2$$

$$+ \sum_{n=0}^{M} \delta t \frac{\eta_p}{\lambda_0} \left(\frac{1}{2\lambda_0} - \frac{\lambda}{2\varepsilon_0 \lambda_0^2} - \left(\frac{\lambda}{2\lambda_0} + \frac{\varepsilon_5 \lambda}{2\lambda_0} \right) \left\| \nabla \boldsymbol{a} \right\|_{L^\infty(\Omega)} \right) \left\| P_h \left[\boldsymbol{E} \cdot \boldsymbol{\psi}_h^{n+1} \right] \right\|^2$$

$$+ \sum_{n=0}^{M} \delta t \left\| \alpha_1^{-1/2} \tilde{\boldsymbol{u}}_1^{n+1} \right\|^2 + \sum_{n=0}^{M} \delta t \left\| \alpha_1^{-1/2} \tilde{\boldsymbol{u}}_2^{n+1} \right\|^2 + \sum_{n=0}^{M} \delta t \left\| \alpha_1^{-1/2} \tilde{\boldsymbol{u}}_3^{n+1} \right\|^2$$

$$+ \sum_{n=0}^{M} \delta t \left\| \alpha_3^{-1/2} \tilde{\boldsymbol{\sigma}}^{n+1} \right\|^2$$

$$\lesssim \sum_{n=0}^{M} \frac{\lambda \varepsilon_1}{2\rho} \delta t \left\| \boldsymbol{f}_u^{n+1} \right\|^2 + \sum_{n=0}^{M} \frac{\lambda \varepsilon_2}{2} \frac{\eta_p}{\lambda_0} \delta t \left\| \boldsymbol{f}_\psi^{n+1} \right\|^2 + \rho \left\| P_h(\boldsymbol{u}^0) \right\|^2$$

$$+ \frac{\lambda}{2\lambda_0} \frac{\eta_p}{\lambda_0} \left\| P_h \left[\boldsymbol{E} \cdot \boldsymbol{\psi}_h^0 \right] \right\|^2 + \rho \left\| \tilde{\boldsymbol{u}}_1^0 \right\|^2 + \rho \left\| \tilde{\boldsymbol{u}}_2^0 \right\|^2 + \rho \left\| \tilde{\boldsymbol{u}}_3^0 \right\|^2 + \frac{\lambda}{2\eta_p} \left\| \tilde{\boldsymbol{\sigma}}^0 \right\|^2$$

from where the theorem follows for λ small enough. $\square$

4.5.3 Stability analysis in terms of the finite element unknowns

Preliminaries

The stability obtained for $\tilde{\boldsymbol{u}}^{n+1}$ and $\tilde{\boldsymbol{\sigma}}^{n+1}$ will be translated now into stability in terms of $\boldsymbol{u}_h^{n+1}$, $\boldsymbol{\sigma}_h^{n+1}$ and p_h^{n+1} (and in terms of $\boldsymbol{u}_h^{n+1}$, $\boldsymbol{\psi}_h^{n+1}$ and p_h^{n+1} in the case of the LCR) using

first dual norms (Theorems 4.3, 4.4, 4.5). Later, these results will be extended to a natural norm if a certain relationship between the time step size and the stabilization parameters α_1 and α_3 holds (Theorem 4.6). If this relationship does not hold, the stability results to be obtained are rather weak. For the case of the transient Stokes problem, they can be improved by obtaining bounds for the discrete time derivative as done in [**?**]; in fact, this technique also allows one to obtain explicit estimates for the pressure. However, we will not pursue this path in this work, as for the problem we consider that would require stringent and unrealistic conditions on the Reynolds and Weissenberg numbers. The result obtained from Theorem 4.1 gives stability for $\{\boldsymbol{u}_h^n\}$, $\{\tilde{\boldsymbol{u}}^n\}$, $\{\boldsymbol{\sigma}_h^n\}$ and $\{\tilde{\boldsymbol{\sigma}}^n\}$, and Theorem 4.2 for $\{P_h\left[\boldsymbol{E}\cdot\boldsymbol{\psi}^n\right]\}$ instead for $\{\boldsymbol{\sigma}_h^n\}$. In the following we shall see that from these results we can get stability on the following terms:

$$\boldsymbol{m}_1^n := \rho\boldsymbol{a}\cdot\nabla\boldsymbol{u}_h^n, \tag{4.53}$$

$$\boldsymbol{m}_2^n := \nabla p_h^n, \tag{4.54}$$

$$\boldsymbol{m}_3^n := -\nabla\cdot\boldsymbol{\sigma}_h^n, \tag{4.55}$$

$$\boldsymbol{m}_4^n := \frac{1}{2\eta_p}\boldsymbol{\sigma}_h^n - \nabla^s\boldsymbol{u}_h^n + \frac{\lambda}{2\eta_p}\left(\boldsymbol{a}\cdot\nabla\boldsymbol{\sigma}_h^n - \boldsymbol{\sigma}_h^n\cdot\nabla\boldsymbol{a} - (\nabla\boldsymbol{a})^T\cdot\boldsymbol{\sigma}_h^n\right),$$

for $n = 1, ..., N$. In case of the logarithmic formulation $\boldsymbol{m}_1^n$ and $\boldsymbol{m}_2^n$ are defined as in the standard formulation, however $\boldsymbol{m}_3^n$ and $\boldsymbol{m}_4^n$ must be redefined:

$$\boldsymbol{m}_3^n := -\frac{\eta_p}{\lambda_0}\nabla\cdot P_h\left[\boldsymbol{E}\cdot\boldsymbol{\psi}_h^n\right], \tag{4.56}$$

$$\boldsymbol{m}_4^n := \frac{1}{2\lambda_0}P_h\left[\boldsymbol{E}\cdot\boldsymbol{\psi}_h^n\right] - \nabla^s\boldsymbol{u}_h^n + \frac{\lambda}{2\lambda_0}\left(2\nabla^s\boldsymbol{u}_h^n + \boldsymbol{a}\cdot\nabla P_h\left[\boldsymbol{E}\cdot\boldsymbol{\psi}_h^n\right]\right.$$
$$\left. - P_h\left[\boldsymbol{E}\cdot\boldsymbol{\psi}_h^n\right]\cdot\nabla\boldsymbol{a} - (\nabla\boldsymbol{a})^T\cdot P_h\left[\boldsymbol{E}\cdot\boldsymbol{\psi}_h^n\right]\right). \tag{4.57}$$

The term $\boldsymbol{m}_1^n$ provides control on the convective derivative, $\boldsymbol{m}_2^n$ over the gradient of the pressure, $\boldsymbol{m}_3^n$ on the divergence of the stress tensor and $\boldsymbol{m}_4^n$ on some terms of the constitutive equation. On the other hand, we will want to have control over the orthogonal component of the three terms $\boldsymbol{m}_1^n$, $\boldsymbol{m}_2^n$ and $\boldsymbol{m}_3^n$. However, we do not have control over these components separately, as explained in [41]. Moreover also the control over the term $\boldsymbol{m}_4^n$ will be pursued.

We will follow the same procedure presented as in [47]. As indicated there, in the general situation without imposing any condition on δt, α_1 or α_3, we will prove stability in a rather weak dual norm. However if we assume a condition between α_1 and α_3, and δt it is possible to improve this stability for the classical one of stabilized finite element methods.

Let us describe the dual norm in which stability will be first proved. Given a sequence $F = \{f^n\}$, of scalar, vector or tensor functions on Ω, we define the following norms: Given a sequence $F = \{f^n\}$, of scalar or vector functions defined on Ω, we define the following norms:

$$\|F\|_{X_i} := \left(\sum_{n=0}^{N}\delta t\,\|f^n\|^2\right)^{1/2} + \sum_{n=0}^{N-1}\delta t\left\|\alpha_i^{1/2}\delta_t f^n\right\| + \max_{n=0,...,N}\left\{\alpha_i^{1/2}\,\|f^n\|\right\}, \tag{4.58}$$

with $i = 1, 3$. These norms endow the spaces of sequences

$$X_i = \left\{F = \{f^n\}\mid F \in \ell^2\left(L^2\left(\Omega\right)\right), \left\{\alpha_i^{1/2}\delta_t f^n\right\} \in \ell^1\left(L^2\left(\Omega\right)\right),\right.$$

$$\left\{\alpha_i^{1/2} f^n\right\} \in \ell^\infty \left(L^2(\Omega)\right)\right\}$$

of a Banach structure. Note that $\{\delta_t f^n\} \in \ell^1 \left(L^2(\Omega)\right)$ and $F \in \ell^\infty \left(L^2(\Omega)\right)$ certainly define strong topologies, but the factors $\alpha_1^{1/2}$ and $\alpha_3^{1/2}$ prevent from any comparison between the different terms. Let now X_i' be the dual space of X_i, the duality pairing being

$$\langle F, G \rangle_{X_i \times X_i'} := \sum_{n=1}^{N} \delta t \langle f^n, g^n \rangle,$$

with $F = \{f^n\} \in X_i$, $G = \{g^n\} \in X_i'$. The norm in X_i' is given by

$$\|G\|_{X_i'} := \sup_{F \in X, F \neq 0} \frac{\langle F, G \rangle_{X_i \times X_i'}}{\|F\|_{X_i}}. \tag{4.59}$$

Stability in dual norms

Let us start proving some stability for $\{m_i^n\}$, $i = 1, 2, 3$, in the norm of X_1'. Recall that the $L^2(\Omega)$ projection onto $\boldsymbol{\mathcal{V}}_h$ is P_h, whereas $P_h^\perp$ is the $L^2(\Omega)$ projection onto $\boldsymbol{\mathcal{V}}_h^\perp$. The $L^2(\Omega)$ projection onto the velocity FE space $\boldsymbol{\mathcal{V}}_{h,0}$ will be denoted by $P_{h,0}$.

Theorem 4.3 (Stability in the dual norm X_1' for the momentum equation terms). *Under assumptions of Theorem 4.1 and $2c_3 \leq c_1$, where c_1 and c_3 are the constants of the stabilization terms α_1 and α_3 respectively, there is a constant C such that*

$$\left\|\left\{\alpha_1^{1/2} P_h^\perp \left[m_1^n\right]\right\}\right\|_{X_1'} + \left\|\left\{\alpha_1^{1/2} P_h^\perp \left[m_2^n\right]\right\}\right\|_{X_1'} + \left\|\left\{\alpha_1^{1/2} P_h^\perp \left[m_3^n\right]\right\}\right\|_{X_1'}$$
$$+ \left\|\left\{\alpha_1^{1/2} P_{h,0} \left[m_1^n + m_2^n + m_3^n\right]\right\}\right\|_{X_1'} \leq C$$

Proof. Let $\{v^n\} \in X$ be arbitrary sequences, which can be split as $v^n = v_h^n + v_b^n + \tilde{v}^n$ with $v_h^n = P_h[v^n]$. On the one hand we can write equations (4.27)-(4.29) as

$$\rho \delta \tilde{u}_i^n + \delta t \alpha_1^{-1} \tilde{u}_i^{n+1} = -\delta t P_h^\perp \left[m_i^{n+1}\right], \ i = 1, 2, 3$$

Multiplying each equation by $\alpha_1^{1/2} \tilde{v}^{n+1}$, integrating over Ω, and adding up the result from $n = 0$ to $N - 1$, integrating by parts using the discrete integrator formula and using the Cauchy-Schwartz inequality, we have

$$\sum_{n=0}^{N-1} \delta t \alpha_1^{1/2} \left(P_h^\perp \left[m_i^{n+1}\right], \tilde{v}^{n+1}\right)$$

$$= -\sum_{n=0}^{N-1} \rho \alpha_1^{1/2} \left(\delta \tilde{u}_i^n, \tilde{v}^{n+1}\right) - \sum_{n=0}^{N-1} \delta t \alpha_1^{-1/2} \left(\tilde{u}_i^{n+1}, \tilde{v}^{n+1}\right)$$

$$= \sum_{n=0}^{N-1} \rho \alpha_1^{1/2} \left(\tilde{u}_i^n, \delta \tilde{v}^n\right) - \rho \alpha_1^{1/2} \left(\tilde{u}_i^N, \tilde{v}^N\right) + \rho \alpha_1^{1/2} \left(\tilde{u}_i^0, \tilde{v}^0\right)$$

$$- \sum_{n=0}^{N-1} \delta t \alpha_1^{-1/2} \left(\tilde{u}_i^{n+1}, \tilde{v}^{n+1}\right)$$

$$\lesssim \rho \max_{n=0,\ldots,N-1} \{\|\tilde{u}_i^n\|\} \sum_{n=0}^{N-1} \delta t \alpha_1^{1/2} \|\delta_t \tilde{v}^n\| \tag{4.60}$$

$$+ 2\rho \max_{n=0,\dots,N-1} \{\|\tilde{\boldsymbol{u}}_i^n\|\} \, \alpha_1^{1/2} \max_{n=0,\dots,N} \{\|\tilde{\boldsymbol{v}}^n\|\}$$

$$+ \left(\sum_{n=0}^{N-1} \delta t \left\| \alpha_1^{-1/2} \tilde{\boldsymbol{u}}_i^{n+1} \right\|^2 \right)^{1/2} \left(\sum_{n=0}^{N-1} \delta t \left\| \tilde{\boldsymbol{v}}^{n+1} \right\|^2 \right)^{1/2}. \tag{4.61}$$

Now, using Theorem 4.1 and the definition of norm X_1 (4.58), we can conclude that

$$\left\langle \{\boldsymbol{v}^n\}, \alpha_1^{1/2} \left\{ P_h^\perp [\boldsymbol{m}_i^n] \right\} \right\rangle_{X_1 \times X_1'} = \sum_{n=0}^{N-1} \delta t \alpha_1^{1/2} \left(P_h^\perp [\boldsymbol{m}_i^{n+1}], \tilde{\boldsymbol{v}}^{n+1} \right)$$

$$\lesssim C \left\| \{\boldsymbol{v}^n\} \right\|_{X_1}.$$

Consequently, adding the three inequalities for $i = 1, 2, 3$ we have bounded

$$\left\| \left\{ \alpha_1^{1/2} P_h^\perp [\boldsymbol{m}_1^n] \right\} \right\|_{X_1'} + \left\| \left\{ \alpha_1^{1/2} P_h^\perp [\boldsymbol{m}_2^n] \right\} \right\|_{X_1'} + \left\| \left\{ \alpha_1^{1/2} P_h^\perp [\boldsymbol{m}_3^n] \right\} \right\|_{X_1'} \le C \tag{4.62}$$

The next step is to control the finite element component, that is, to say, the term

$$P_h \left[\boldsymbol{m}_1^n + \boldsymbol{m}_2^n + \boldsymbol{m}_3^n \right].$$

Let us define, for simplicity, the sequence $\boldsymbol{m}_s^n = \sum_{i=1}^3 \boldsymbol{m}_i^n$. For this, we take equation (4.26), considering $q_h = 0$ and $\boldsymbol{\chi}_h = \boldsymbol{0}$, and $\boldsymbol{v}_h$ as defined at the beginning of the proof. Therefore, employing similar arguments to the previous development, we have that

$$\sum_{n=0}^{N-1} \delta t \alpha_1^{1/2} \left(P_h [\boldsymbol{m}_s^{n+1}], \boldsymbol{v}_h^{n+1} \right)$$

$$= \sum_{n=0}^{N-1} \delta t \alpha_1^{1/2} \left(\boldsymbol{a} \cdot \nabla \boldsymbol{u}_h^{n+1} + \nabla p_h^{n+1} - \nabla \cdot \boldsymbol{\sigma}_h^{n+1}, \boldsymbol{v}_h^{n+1} \right)$$

$$= \sum_{n=0}^{N-1} \delta t \alpha_1^{1/2} \left\langle \boldsymbol{f}^{n+1}, \boldsymbol{v}_h^{n+1} \right\rangle - \sum_{n=0}^{N-1} \alpha_1^{1/2} \left(\delta \boldsymbol{u}_h^n, \boldsymbol{v}_h^{n+1} \right) - \sum_{n=0}^{N-1} 2\eta_s \delta t \alpha_1^{1/2} \left(\nabla^s \boldsymbol{u}_h^{n+1}, \nabla^s \boldsymbol{v}_h^{n+1} \right)$$

$$+ \sum_{n=0}^{N-1} \delta t \alpha_1^{1/2} \left(\tilde{\boldsymbol{u}}_1^{n+1}, \boldsymbol{a} \cdot \nabla \boldsymbol{v}_h^{n+1} \right) - \sum_{n=0}^{N-1} \delta t \alpha_1^{1/2} \left(\tilde{\boldsymbol{\sigma}}^{n+1}, \nabla^s \boldsymbol{v}_h^{n+1} \right)$$

$$\lesssim \alpha_1^{1/2} \max_{n=1,\dots,N} \{\|\boldsymbol{v}_h^n\|\} \sum_{n=0}^{N-1} \delta t \left\| \boldsymbol{f}^{n+1} \right\| + \max_{n=1,\dots,N} \{\|\boldsymbol{u}_h^n\|\} \sum_{n=0}^{N-1} \delta t \alpha_1^{1/2} \left\| \delta_t \boldsymbol{v}_h^n \right\|$$

$$+ 2 \max_{n=0,\dots,N} \{\|\boldsymbol{u}_h^n\|\} \alpha_1^{1/2} \max_{n=1,\dots,N} \{\|\boldsymbol{v}_h^n\|\} + \sum_{n=0}^{N-1} \delta t 2 \eta_s^{1/2} \left\| \nabla^s \boldsymbol{u}_h^{n+1} \right\| \left\| \boldsymbol{v}_h^{n+1} \right\|$$

$$+ \sum_{n=0}^{N-1} \delta t \alpha_1^{-1/2} \left\| \tilde{\boldsymbol{u}}_1^{n+1} \right\| \left\| \boldsymbol{v}_h^{n+1} \right\| + \sum_{n=0}^{N-1} \delta t \alpha_3^{-1/2} \left\| \tilde{\boldsymbol{\sigma}}^{n+1} \right\| \left\| \boldsymbol{v}_h^{n+1} \right\|. \tag{4.63}$$

In particular, the three last terms have been obtained using the inverse estimate (4.40) together with the definition of α_1 and α_3, which in particular imply:

$$\frac{\eta_0}{h} \alpha_1^{1/2} \le C \eta_0^{1/2}, \quad \frac{\|\boldsymbol{a}\|_{L^\infty(K)}}{h} \le \alpha_1^{-1}, \quad \frac{\alpha_1^{1/2}}{h} \le \alpha_3^{-1/2}.$$

The last inequality holds under the condition $2c_3 \leq c_1$, being c_1 and c_3 the constants of the stabilization parameters α_1 and α_3. Using now the assumptions on the data, Cauchy's inequality for the last three terms of (4.63) and finally using Theorem 4.1, it follows that

$$
\left\langle \{\boldsymbol{v}^n\}, \alpha_1^{1/2} \{P_h\left[\boldsymbol{m}_s^n\right]\} \right\rangle_{X_1 \times X_1'} = \sum_{n=0}^{N-1} \delta t \alpha_1^{1/2} \left(P_h\left[\boldsymbol{m}_s^{n+1}\right], \boldsymbol{v}_h^{n+1}\right)
$$
$$
\lesssim C \left\|\{\boldsymbol{v}^n\}\right\|_{X_1}.
$$

Therefore

$$
\left\|\left\{\alpha_1^{1/2} P_h\left[\boldsymbol{m}_1^n + \boldsymbol{m}_2^n + \boldsymbol{m}_3^n\right]\right\}\right\|_{X_1'} \leq C \tag{4.64}
$$

The theorem follows from the addition of (4.62) and (4.64).

This result is analogous for the logarithmic formulation case, considering (4.56) and replacing $\nabla \cdot \boldsymbol{\sigma}_h^{n+1}$ by $\dfrac{\eta_p}{\lambda_0} \nabla \cdot P_h\left[\boldsymbol{E} \cdot \boldsymbol{\psi}_h^{n+1}\right]$ in (4.63). $\square$

Now we can proceed to prove a similar result for the constitutive equation. Since the stress or the logarithm of the conformation tensor have no boundary conditions, we will be able to prove stability for $\{P_h[\alpha_3^{1/2}\boldsymbol{m}_4^n]\}$ and $\{P_h^\perp[\alpha_3^{1/2}\boldsymbol{m}_4^n]\}$, that is to say, for the whole sequence $\{\alpha_3^{1/2}\boldsymbol{m}_4^n\}$.

Theorem 4.4 (Stability in the dual norm X_3' for the constitutive equation)**.** *Under the assumptions of the Theorem 4.1, assume also $2c_3 \leq c_1$, where c_1 and c_3 are the constants of the stabilization terms α_1 and α_3 respectively. Then, there is a constant C such that*

$$
\left\|\left\{\alpha_3^{1/2}\boldsymbol{m}_4^n\right\}\right\|_{X_3'} \leq C
$$

Proof. Let $\{\boldsymbol{\tau}^n\} \in X$ be an arbitrary sequence, which can be split on $\boldsymbol{\tau}^n = \boldsymbol{\tau}_h^n + \tilde{\boldsymbol{\tau}}^n$, with $\boldsymbol{\tau}_h^n = P_h\left[\boldsymbol{\tau}^n\right]$. We can write (4.31) as

$$
\frac{\lambda}{2\eta_p}\delta\tilde{\boldsymbol{\sigma}}^n + \delta t \alpha_3^{-1}\tilde{\boldsymbol{\sigma}}^{n+1} = -\delta t P_h^\perp\left[\boldsymbol{m}_4^{n+1}\right]
$$

Now, we follow the same procedure as in Theorem 4.3: multiplying by $\alpha_3^{1/2}\boldsymbol{\chi}_h^{n+1}$, integrating over Ω and adding up the result from $n=0$ to $N-1$, integrating by parts using the discrete integration formula and using the Cauchy-Schwartz inequality, we have

$$
\sum_{n=0}^{N-1} \delta t \alpha_3^{1/2} \left(P_h^\perp\left[\boldsymbol{m}_4^{n+1}\right], \tilde{\boldsymbol{\chi}}^{n+1}\right)
$$
$$
= -\sum_{n=0}^{N-1} \frac{\lambda}{2\eta_p}\alpha_3^{1/2}\left(\delta\tilde{\boldsymbol{\sigma}}^n, \tilde{\boldsymbol{\chi}}^{n+1}\right) - \sum_{n=0}^{N-1} \delta t \alpha_3^{-1/2}\left(\tilde{\boldsymbol{\sigma}}^{n+1}, \tilde{\boldsymbol{\chi}}^{n+1}\right)
$$
$$
= \sum_{n=0}^{N-1} \frac{\lambda}{2\eta_p}\alpha_3^{1/2}\left(\tilde{\boldsymbol{\sigma}}^n, \delta\tilde{\boldsymbol{\chi}}^n\right) - \frac{\lambda}{2\eta_p}\alpha_3^{1/2}\left(\tilde{\boldsymbol{\sigma}}^N, \tilde{\boldsymbol{\chi}}^N\right) + \frac{\lambda}{2\eta_p}\alpha_3^{1/2}\left(\tilde{\boldsymbol{\sigma}}^0, \tilde{\boldsymbol{\chi}}^0\right)
$$
$$
- \sum_{n=0}^{N-1} \delta t \alpha_3^{-1/2}\left(\tilde{\boldsymbol{\sigma}}^{n+1}, \tilde{\boldsymbol{\chi}}^{n+1}\right)
$$
$$
\lesssim \frac{\lambda}{2\eta_p} \max_{n=0,\dots,N-1} \{\|\tilde{\boldsymbol{\sigma}}^n\|\} \sum_{n=0}^{N-1} \delta t \alpha_3^{1/2} \|\delta_t \tilde{\boldsymbol{\chi}}^n\|
$$

$$+ \frac{\lambda}{\eta_p} \max_{n=0,\dots,N-1} \{\|\tilde{\boldsymbol{\sigma}}^n\|\} \, \alpha_3^{1/2} \max_{n=0,\dots,N} \{\|\tilde{\boldsymbol{\chi}}^n\|\}$$

$$+ \left(\sum_{n=0}^{N-1} \delta t \left\| \alpha_3^{-1/2} \tilde{\boldsymbol{\sigma}}^{n+1} \right\|^2 \right)^{1/2} \left(\sum_{n=0}^{N-1} \delta t \left\| \tilde{\boldsymbol{\chi}}^{n+1} \right\|^2 \right)^{1/2}. \tag{4.65}$$

Therefore, using Theorem 4.1 and the definition of the norm in X_3 (4.58), we can conclude that

$$\left\langle \{\boldsymbol{\chi}^n\}, \alpha_3^{1/2} \left\{ P_h^\perp [\boldsymbol{m}_4^n] \right\} \right\rangle_{X_3 \times X_3'} = \sum_{n=0}^{N-1} \delta t \alpha_3^{1/2} \left(P_h^\perp [\boldsymbol{m}_4^{n+1}], \tilde{\boldsymbol{\chi}}^{n+1} \right)$$

$$\lesssim C \left\| \{\boldsymbol{\chi}_h^n\} \right\|_{X_3}. \tag{4.66}$$

The next step is to control the finite element component, that is, $P_h [\boldsymbol{m}_4^n]$. Now, we use equation (4.26), considering $q_h = 0$ and $\boldsymbol{v}_h = \boldsymbol{0}$, and $\boldsymbol{\chi}_h$ as defined at the beginning of the proof. Therefore, employing similar arguments to the previous development, we have that

$$\sum_{n=0}^{N-1} \delta t \alpha_3^{1/2} \left(P_h [\boldsymbol{m}_4^{n+1}], \boldsymbol{\chi}_h^{n+1} \right)$$

$$= \sum_{n=0}^{N-1} \delta t \alpha_3^{1/2} \left(\frac{1}{2\eta_p} \boldsymbol{\sigma}_h^{n+1} - \nabla^s \boldsymbol{u}_h^{n+1}, \boldsymbol{\chi}_h^{n+1} \right)$$

$$+ \sum_{n=0}^{N-1} \delta t \alpha_3^{1/2} \frac{\lambda}{2\eta_p} \left(\boldsymbol{a} \cdot \nabla \boldsymbol{\sigma}_h^{n+1} - \boldsymbol{\sigma}_h^{n+1} \cdot \nabla \boldsymbol{a} - (\nabla \boldsymbol{a})^T \cdot \boldsymbol{\sigma}_h^{n+1}, \boldsymbol{\chi}_h^{n+1} \right)$$

$$= - \sum_{n=0}^{N-1} \alpha_3^{1/2} \frac{\lambda}{2\eta_p} \left(\delta \boldsymbol{\sigma}_h^n, \boldsymbol{\chi}_h^{n+1} \right) - \sum_{n=0}^{N-1} \delta t \alpha_3^{1/2} \left(\tilde{\boldsymbol{u}}_3^{n+1}, \nabla \cdot \boldsymbol{\chi}_h^{n+1} \right)$$

$$- \sum_{n=0}^{N-1} \delta t \alpha_3^{1/2} \left(\tilde{\boldsymbol{\sigma}}^{n+1}, \frac{1}{2\eta_p} \boldsymbol{\chi}_h - \frac{\lambda}{2\eta_p} \left(\boldsymbol{a} \cdot \nabla \boldsymbol{\chi}_h + \boldsymbol{\chi}_h \cdot (\nabla \boldsymbol{a})^T + \nabla \boldsymbol{a} \cdot \boldsymbol{\chi}_h \right) \right)$$

$$\lesssim \frac{\lambda}{2\eta_p} \max_{n=1,\dots,N} \{\|\boldsymbol{\sigma}_h^n\|\} \sum_{n=0}^{N-1} \delta t \alpha_3^{1/2} \|\delta \boldsymbol{\chi}_h^n\| + 2 \frac{\lambda}{2\eta_p} \max_{n=0,\dots,N} \{\|\boldsymbol{\sigma}_h^n\|\} \, \alpha_3^{1/2} \max_{n=1,\dots,N} \{\|\boldsymbol{\chi}_h^n\|\}$$

$$+ \sum_{n=0}^{N-1} \delta t \alpha_3^{-1/2} \left\| \tilde{\boldsymbol{\sigma}}^{n+1} \right\| \left\| \boldsymbol{\chi}_h^{n+1} \right\| + \sum_{n=0}^{N-1} \delta t \alpha_1^{-1/2} \left\| \tilde{\boldsymbol{u}}_3^{n+1} \right\| \left\| \boldsymbol{\chi}_h^{n+1} \right\|. \tag{4.67}$$

In particular, the three last terms have been obtained using the inverse estimate (4.40) together with the definitions of α_1 and α_3, which in particular imply:

$$\frac{C}{2\eta_0} \le \alpha_3^{-1}, \quad \frac{\lambda}{2\eta_0} \frac{\|\boldsymbol{a}\|_{L^\infty(K)}}{h} \le \alpha_3^{-1}, \quad \frac{\lambda}{2\eta_0} \|\nabla \boldsymbol{a}\|_{L^\infty(K)} \le \alpha_3^{-1}, \quad \frac{\alpha_3^{1/2}}{h} \le \alpha_1^{-1/2}.$$

As in Theorem 4.3, the last inequality holds under the assumption $2c_3 \le c_1$, being c_1 and c_3 the constants of the stabilization parameters α_1 and α_3.

Using the assumptions on the data, Cauchy's inequality for the last two terms of (4.67) and finally using Theorem 4.1, it follows that

$$\left\langle \{\boldsymbol{\chi}^n\}, \alpha_3^{1/2} \left\{ P_h [\boldsymbol{m}_4^n] \right\} \right\rangle_{X_3 \times X_3'} = \sum_{n=0}^{N-1} \delta t \alpha_3^{1/2} \left(P_h [\boldsymbol{m}_4^{n+1}], \boldsymbol{\chi}_h^{n+1} \right)$$

$$\lesssim \|\{\boldsymbol{\chi}_h^n\}\|_{X_3}. \tag{4.68}$$

The theorem follows from (4.66) and (4.68). For the logarithmic formulation, there are slight differences in the proof. In that case we have to consider the expression of $\boldsymbol{m}_4^n$ (4.57). So, in the step where the finite element component is controlled, we will use equation (4.34), considering $q_h = 0$ and $\boldsymbol{v}_h = \boldsymbol{0}$, and $\boldsymbol{\chi}_h$ as defined above. Therefore, we have that

$$\sum_{n=0}^{N-1} \delta t \alpha_3^{1/2} \left(P_h \left[\boldsymbol{m}_4^{n+1} \right], \boldsymbol{\chi}_h^{n+1} \right)$$

$$= \sum_{n=0}^{N-1} \delta t \alpha_3^{1/2} \left(\frac{1}{2\lambda_0} P_h \left[\boldsymbol{E} \cdot \boldsymbol{\psi}_h^{n+1} \right] - \nabla^s \boldsymbol{u}_h^{n+1}, \boldsymbol{\chi}_h^{n+1} \right)$$

$$+ \sum_{n=0}^{N-1} \delta t \alpha_3^{1/2} \frac{\lambda}{2\lambda_0} \left(2\nabla^s \boldsymbol{u}_h^{n+1} + \boldsymbol{a} \cdot \nabla P_h \left[\boldsymbol{E} \cdot \boldsymbol{\psi}_h^{n+1} \right] \right.$$

$$\left. - P_h \left[\boldsymbol{E} \cdot \boldsymbol{\psi}_h^{n+1} \right] \cdot \nabla \boldsymbol{a} - (\nabla \boldsymbol{a})^T \cdot P_h \left[\boldsymbol{E} \cdot \boldsymbol{\psi}_h^{n+1} \right], \boldsymbol{\chi}_h^{n+1} \right)$$

$$= - \sum_{n=0}^{N-1} \alpha_3^{1/2} \frac{\lambda}{2\lambda_0} \left(\delta P_h \left[\boldsymbol{E} \cdot \boldsymbol{\psi}_h^{n} \right], \boldsymbol{\chi}_h^{n+1} \right) - \sum_{n=0}^{N-1} \delta t \alpha_3^{1/2} \left(\tilde{\boldsymbol{u}}_3^{n+1}, \nabla \cdot \boldsymbol{\chi}_h^{n+1} \right)$$

$$- \sum_{n=0}^{N-1} \delta t \alpha_3^{1/2} \left(\tilde{\boldsymbol{\sigma}}^{n+1}, \frac{1}{2\eta_p} \boldsymbol{\chi}_h - \frac{\lambda}{2\eta_p} \left(\boldsymbol{a} \cdot \nabla \boldsymbol{\chi}_h + \boldsymbol{\chi}_h \cdot (\nabla \boldsymbol{a})^T + \nabla \boldsymbol{a} \cdot \boldsymbol{\chi}_h \right) \right) \right)$$

$$\leq \frac{\lambda}{2\lambda_0} \max_{n=1,\dots,N} \left\{ \| P_h \left[\boldsymbol{E} \cdot \boldsymbol{\psi}_h^n \right] \| \right\} \sum_{n=0}^{N-1} \delta t \alpha_3^{1/2} \| \delta_t \boldsymbol{\chi}_h^n \|$$

$$+ 2 \frac{\lambda}{2\lambda_0} \max_{n=0,\dots,N} \left\{ \| P_h \left[\boldsymbol{E} \cdot \boldsymbol{\psi}_h^n \right] \| \right\} \alpha_3^{1/2} \max_{n=1,\dots,N} \left\{ \| \boldsymbol{\chi}_h^n \| \right\}$$

$$+ C \sum_{n=0}^{N-1} \delta t \alpha_3^{-1/2} \| \tilde{\boldsymbol{\sigma}}^{n+1} \| \, \| \boldsymbol{\chi}_h^{n+1} \| + C \sum_{n=0}^{N-1} \delta t \alpha_1^{-1/2} \| \tilde{\boldsymbol{u}}_3^{n+1} \| \, \| \boldsymbol{\chi}_h^{n+1} \|.$$

and this result will be analogous to the one obtained for the standard formulation. $\qquad \square$

Following the same structure as in the analysis done in [47], we include another theorem, which is easily obtained from Theorem 4.3 and Theorem 4.4. For the proof, the case of the backward Euler time integration must be considered in all this section. Therefore the next inequalities will be taken into account; both used, in the proof of Theorems 4.1 and 4.2:

$$\rho \sum_{n=0}^{M} \| \delta \boldsymbol{u}_h^n \|^2 + \rho \left(\sum_{n=0}^{M} \| \delta \tilde{\boldsymbol{u}}_1^n \|^2 + \sum_{n=0}^{M} \| \delta \tilde{\boldsymbol{u}}_2^n \|^2 + \sum_{n=0}^{M} \| \delta \tilde{\boldsymbol{u}}_3^n \|^2 \right) \leq C, \tag{4.69}$$

$$\sum_{n=0}^{M} \frac{\lambda}{2\eta_p} \| \delta \boldsymbol{\sigma}_h^n \|^2 + \sum_{n=0}^{M} \frac{\lambda}{2\eta_p} \| \delta \tilde{\boldsymbol{\sigma}}^n \|^2 \leq C. \tag{4.70}$$

For the logarithmic formulation, the inequality to consider would be:

$$\sum_{n=0}^{M} \frac{\lambda}{2\lambda_0} \| \delta P_h \left[\boldsymbol{E} \cdot \boldsymbol{\psi}_h^n \right] \|^2 + \sum_{n=0}^{M} \frac{\lambda}{2\eta_p} \| \delta \tilde{\boldsymbol{\sigma}}^n \|^2 \leq C. \tag{4.71}$$

Now we will define the following norm, that will replace norm $\|\cdot\|_{X_i}$ (4.58):

$$\|F\|_{Y_i} := \left(\sum_{n=0}^{N} \max\{\delta t, \alpha_i\} \|f^n\|^2 \right)^{1/2}. \tag{4.72}$$

Theorem 4.5 (Stability in the dual norm Y'). *Under the assumptions of Theorems 4.3 and 4.4, assume also that $\{\boldsymbol{f}^n\} \in \ell^2(\boldsymbol{L}^2(\Omega))$, $\boldsymbol{u}_h^0 \in \boldsymbol{L}^2(\Omega)$ and $\boldsymbol{\sigma}_h^0 \in \boldsymbol{L}^2(\Omega)$. Then there are constants C_1 and C_2 such that*

a) $\left\| \left\{ \alpha_1^{1/2} P_h^{\perp} [\boldsymbol{m}_1^n] \right\} \right\|_{Y_1'} + \left\| \left\{ \alpha_1^{1/2} P_h^{\perp} [\boldsymbol{m}_2^n] \right\} \right\|_{Y_1'} + \left\| \left\{ \alpha_1^{1/2} P_h^{\perp} [\boldsymbol{m}_3^n] \right\} \right\|_{Y_1'},$

$\qquad + \left\| \left\{ \alpha_1^{1/2} P_{h,0} [\boldsymbol{m}_1^n + \boldsymbol{m}_2^n + \boldsymbol{m}_3^n] \right\} \right\|_{Y_1'} \leq C_1$

b) $\left\| \left\{ \alpha_3^{1/2} \boldsymbol{m}_4^n \right\} \right\|_{Y_3'} \leq C_2.$

Proof. For the terms of the momentum equation, a), the only difference with Theorem 4.4 is that the following terms must be bounded as follows:

$$\sum_{n=0}^{N-1} \rho \alpha_1^{1/2} \left(\delta \tilde{\boldsymbol{u}}_i^n, \tilde{\boldsymbol{v}}^{n+1} \right) \leq \left(\sum_{n=0}^{N-1} \rho \|\delta \tilde{\boldsymbol{u}}_i^n\|^2 \right)^{1/2} \left(\sum_{n=0}^{N-1} \rho \alpha_1 \|\tilde{\boldsymbol{v}}^n\|^2 \right)^{1/2}, \tag{4.73}$$

$$\sum_{n=0}^{N-1} \rho \alpha_1^{1/2} \left(\delta \boldsymbol{u}_h^n, \boldsymbol{v}_h^{n+1} \right) \leq \left(\sum_{n=0}^{N-1} \rho \|\delta \boldsymbol{u}_h^n\|^2 \right)^{1/2} \left(\sum_{n=0}^{N-1} \rho \alpha_1 \|\boldsymbol{v}_h^n\|^2 \right)^{1/2}. \tag{4.74}$$

The first expression would be employed in step (4.61), where the sub-grid scales are bounded, and the second expression would be used in step (4.63). In this last case the fields in the finite element space are bounded. Using the properties defined previously, (4.73) and (4.74) will be bounded finally by $C \|\boldsymbol{v}^n\|_Y$, from where the result a) follow as in Theorem 4.3.

Now in order to bound the terms corresponding to the constitutive equation, b), the inequality used is:

$$\sum_{n=0}^{N-1} \frac{\lambda}{2\eta_p} \alpha_3^{1/2} \left(\delta \tilde{\boldsymbol{\sigma}}^n, \tilde{\boldsymbol{\chi}}^{n+1} \right) \leq \left(\sum_{n=0}^{N-1} \frac{\lambda}{2\eta_p} \|\delta \tilde{\boldsymbol{\sigma}}^n\|^2 \right)^{1/2} \left(\sum_{n=0}^{N-1} \frac{\lambda}{2\eta_p} \alpha_3 \|\tilde{\boldsymbol{\chi}}^n\|^2 \right)^{1/2}. \tag{4.75}$$

Employing, again, the properties defined previously (4.70), we can bound (4.75) by $C \|\boldsymbol{\chi}^n\|_Y$, from where the result b) follows analogously as in Theorem 4.4.

For the logarithmic formulation the arguments would be analogous for a) and b). The only difference is that in b) the inequality for bounding the finite element space component is the next one:

$$\sum_{n=0}^{N-1} \frac{\lambda}{2\lambda_0} \alpha_3^{1/2} \left(\delta P_h [\boldsymbol{E} \cdot \boldsymbol{\psi}_h^n], \boldsymbol{\chi}_h^{n+1} \right) \leq \left(\sum_{n=0}^{N-1} \frac{\lambda}{2\lambda_0} \|\delta P_h [\boldsymbol{E} \cdot \boldsymbol{\psi}_h^n]\|^2 \right)^{1/2} \left(\sum_{n=0}^{N-1} \frac{\lambda}{2\lambda_0} \alpha_3 \|\boldsymbol{\chi}_h^n\|^2 \right)^{1/2}. \tag{4.76}$$

And finally using (4.71), the expression above would be bounded by $C \|\boldsymbol{\chi}_h^n\|_Y$. $\qquad \square$

Stability in natural norms

From the last Theorem 4.5 the next result is straightforward to prove the next result, which holds the inequality $\delta t \geq C\alpha_i$ for $i = 1, 3$ is satisfied.

Theorem 4.6 (Stability in the natural norm). *Under the assumptions of Theorem 4.5, assume also that the stabilization parameters satisfy $\alpha_1 \leq C\delta t$ and $\alpha_3 \leq C\delta t$ as $h \to 0$ and $\delta t \to 0$, and suppose that $\{\boldsymbol{f}^n\} \in \ell^2\left(\boldsymbol{L}^2(\Omega)\right)$, $\boldsymbol{u}_h^0 \in \boldsymbol{L}^2(\Omega)$ and $\boldsymbol{\sigma}_h^0 \in \boldsymbol{L}^2(\Omega)$. Then, there are constants C_1 and C_2 such that*

$$a) \sum_{n=0}^{N} \delta t \left\|\left\{\alpha_1^{1/2} P_h^{\perp}\left[\boldsymbol{m}_1^n\right]\right\}\right\| + \sum_{n=0}^{N} \delta t \left\|\left\{\alpha_1^{1/2} P_h^{\perp}\left[\boldsymbol{m}_2^n\right]\right\}\right\| + \sum_{n=0}^{N} \delta t \left\|\left\{\alpha_1^{1/2} P_h^{\perp}\left[\boldsymbol{m}_3^n\right]\right\}\right\|$$

$$+ \sum_{n=0}^{N} \delta t \left\|\left\{\alpha_1^{1/2} P_{h,0}\left[\boldsymbol{m}_1^n + \boldsymbol{m}_2^n + \boldsymbol{m}_3^n\right]\right\}\right\| \leq C_1$$

$$b) \sum_{n=0}^{N} \delta t \left\|\left\{\alpha_3^{1/2} \boldsymbol{m}_4^n\right\}\right\| \leq C_2$$

Proof. If inequalities $\alpha_1 \leq C\delta t$ and $\alpha_3 \leq C\delta t$ hold, it is immediately proved from the definition of expression (4.72) that $Y = \ell^2\left(\boldsymbol{L}^2(\Omega)\right)$. As this space is reflexive, this implies that $Y = Y'$. Therefore this theorem is proved through the Theorem 4.5 directly. $\qquad\square$

According to Theorem 4.6, we have control on the component of $\boldsymbol{m}_1 + \boldsymbol{m}_2 + \boldsymbol{m}_3$ in $\boldsymbol{\mathcal{V}}_{h,0}$ and $\boldsymbol{\mathcal{V}}_h^{\perp}$, but it remains to prove stability on the component in $\boldsymbol{\mathcal{V}}_h$ associated to functions defined on $\partial\Omega$. As discussed in previous works [41, 45], this is done by prescribing a (mild) condition on the FE mesh.

Corollary 4.6.1. *Under the assumptions of Theorem 4.6, suppose also that the FE mesh is such that given $\boldsymbol{a}, \boldsymbol{v}_h \in \boldsymbol{\mathcal{V}}_h$, $q_h \in \mathcal{Q}_h$, $\boldsymbol{\chi}_h \in \boldsymbol{\Upsilon}_h$ and $\boldsymbol{z}_h := \rho \boldsymbol{a} \cdot \nabla \boldsymbol{v}_h + \nabla q_h - \nabla \cdot \boldsymbol{\chi}_h$, there holds*

$$\|\boldsymbol{z}_h\| \leq c_{\mathrm{m}}\left(\|P_{h,0}\left[\boldsymbol{z}_h\right]\| + \left\|P_h^{\perp}\left[\boldsymbol{z}_h\right]\right\|\right), \text{ for a constant } c_{\mathrm{m}} > 0.$$

Then:

$$\sum_{n=0}^{N} \delta t \left\|\alpha_1^{1/2}\left[\boldsymbol{m}_1^n + \boldsymbol{m}_2^n + \boldsymbol{m}_3^n\right]\right\|^2 \leq C. \tag{4.77}$$

Proof. Let $\boldsymbol{z}_h^n = \alpha_1^{1/2}\left[\boldsymbol{m}_1^n + \boldsymbol{m}_2^n + \boldsymbol{m}_3^n\right]$. From the assumption made we have that

$$\|\{\boldsymbol{z}_h^n\}\|_{\ell^2(L^2(\Omega)^d)} \lesssim \|\{P_{h,0}[\boldsymbol{z}_h^n]\}\|_{\ell^2(L^2(\Omega)^d)} + \|\{P_h^{\perp}[\boldsymbol{z}_h^n]\}\|_{\ell^2(L^2(\Omega)^d)}$$

$$\lesssim \|\{P_{h,0}[\boldsymbol{z}_h^n]\}\|_{\ell^2(L^2(\Omega)^d)} + \sum_{i=1}^{3}\left\|\left\{\alpha_1^{1/2} P_h^{\perp}\left[\boldsymbol{m}_i^n\right]\right\}\right\|_{\ell^2(L^2(\Omega)^d)}^2,$$

from where the result follows using Theorem 4.6. $\qquad\square$

To sum up, this numerical analysis shows that the use of time-dependent sub-grid scales in a viscoelastic fluid flow formulation is a stable method. In this section a simple linearized problem has been analyzed. The main features of the formulation are to consider the SGSs as dynamic, orthogonal to the FE space and assigning one velocity SGS for each of the terms of the momentum equation that need to be stabilized. In comparison with

other works where the Navier-Stokes equations are considered, apart from giving stability for velocity and pressure, also stability for stresses in the case of the standard formulation and for the tensor $\boldsymbol{\psi}$ in the case of the logarithmic formulation have been proved. In addition, we have proved control over the divergence of stresses, apart from the convective derivative and the pressure gradient, and for the constitutive equation, gaining stability over all of these terms. Also observe the constants in the stability estimates do not depend on the coefficients of the equation; therefore, they do not blow up as $\eta_0 \to 0$ or $\lambda \to 0$.

4.6   Numerical results

This section aims to show the importance of dynamic sub-grid scales to solve viscoelastic problems, and particularly the suitability of the term-by-term stabilization method described along the chapter for both possible formulations, standard and logarithmic. First of all, in Section 4.6.1, a convergence analysis for several discretization schemes is performed. Secondly, in Section 4.6.2, we display the typical flow over a cylinder problem for Re = 100, where the different formulations proposed are compared for several Weissenberg numbers and time steps δt. Thirdly, a dynamic lid-driven cavity flow problem is presented in Section 4.6.3 in order to discuss the efficiency and stability of the dynamics sub-grid scales in a more complex benchmark for two different cases: a stationary one with Re = 0, and a dynamic forced regime with Re = 100. Finally the formulation is tested in a three-dimensional lid driven cavity in Section 4.6.4 as an extension of the two-dimensional dynamic version.

4.6.1   Convergence test

This numerical example is done with the goal of studying the convergence of the temporal schemes using time-dependent sub-grid scales. This convergence study has been carried out for both, standard and logarithmic formulations. As it was detailed in Section 2.5.1, the domain is a unit square, in this case discretized by 256 elements Q1. Regarding the boundary and the initial conditions are prescribed following the time-dependent analytical solutionfor the standard formulation:

$$
\begin{aligned}
u_x(x,y) &= (4x+6)f(t), & \sigma_{xx}(x,y) &= (2x+3)f(t),\\
u_y(x,y) &= -(4y-6)f(t), & \sigma_{yy}(x,y) &= (2y+3)f(t),\\
p(x,y) &= xf(t), & \sigma_{xy}(x,y) &= (x+y)f(t),
\end{aligned}
$$

where the x and y components of the velocity and the stress tensor have been indicated with a subscript, and $f(t) = \cos(4\pi t)\exp(-t)$. These velocity, pressure and elastic stress fields do not satisfy the momentum or constitutive equation. On the other hand, for the logarithmic formulation instead of stresses we define the solution over the variable $\boldsymbol{\psi}$ and therefore the analytical solution will be:

$$
\begin{aligned}
u_x(x,y) &= (4x+6)f(t), & \psi_{xx}(x,y) &= (2x+3)f(t),\\
u_y(x,y) &= -(4y-6)f(t), & \psi_{yy}(x,y) &= (2y+3)f(t),\\
p(x,y) &= xf(t), & \psi_{xy}(x,y) &= (x+y)f(t),
\end{aligned}
$$

Therefore we have to add a some forcing terms in the equations in the domain Ω. For the standard case these are as follows:

$$
\boldsymbol{f}_{\mathrm{mom}} = \rho\frac{\partial \boldsymbol{u}}{\partial t} + \rho\boldsymbol{u}\cdot\nabla\boldsymbol{u} - \nabla\cdot(2\eta_s\nabla^s\boldsymbol{u} + \boldsymbol{\sigma}) + \nabla p
$$

Scheme	$\boldsymbol{u}$	p	$\boldsymbol{\sigma}$ or $\boldsymbol{\psi}$
		Rate of convergence	
BDF1	1	0	1
BDF2	2	1	2
BDF3	3	2	3
CN	2	1	2

Table 4.2: Convergence test. Rate of convergence expected.

$$f_{\text{cont}} = \nabla \cdot \boldsymbol{u}$$

$$\boldsymbol{f}_{\text{cons}} = \frac{1}{2\eta_p}\boldsymbol{\sigma} - \nabla^s\boldsymbol{u} + \frac{\lambda}{2\eta_p}\left(\frac{\partial\boldsymbol{\sigma}}{\partial t} + \boldsymbol{u}\cdot\nabla\boldsymbol{\sigma} - \boldsymbol{\sigma}\cdot\nabla\boldsymbol{u} - (\nabla\boldsymbol{u})^T\cdot\boldsymbol{\sigma}\right)$$

Analogously, for the logarithmic formulation, the force terms are:

$$\boldsymbol{f}_{\text{mom}} = \rho\frac{\partial\boldsymbol{u}}{\partial t} - \frac{\eta_p}{\lambda_0}\nabla\cdot\exp(\boldsymbol{\psi}) - 2\eta_s\nabla\cdot(\nabla^{\text{s}}\boldsymbol{u}) + \rho\boldsymbol{u}\cdot\nabla\boldsymbol{u} + \nabla p$$

$$f_{\text{cont}} = \nabla \cdot \boldsymbol{u}$$

$$\boldsymbol{f}_{\text{cons}} = \frac{1}{2\lambda_0}(\exp(\boldsymbol{\psi}) - \boldsymbol{I}) - \nabla^{\text{s}}\boldsymbol{u} + \frac{\lambda}{2\lambda_0}\Big(\frac{\partial\exp(\boldsymbol{\psi})}{\partial t}$$

$$+ \boldsymbol{u}\cdot\nabla\exp(\boldsymbol{\psi}) - \exp(\boldsymbol{\psi})\cdot\nabla\boldsymbol{u} - (\nabla\boldsymbol{u})^T\cdot\exp(\boldsymbol{\psi}) + 2\nabla^{\text{s}}\boldsymbol{u}\Big)$$

The stabilized finite element formulation employed in this test is the Split-OSS, tested for a stationary problem in Section 2.5.1 (Chapter 2). In this case the error is measured in different norms, $\ell^\infty\left(L^2\left(\Omega\right)\right)$ which is the maximum of the sequence of spatial L^2-norms of the solution and $\ell^2\left(H^1\left(\Omega\right)\right)$, which is the ℓ^2-norm of the sequence of spatial H^1-norms of the solution. The convergence has been checked for four different temporal schemes: BDF1, BDF2, BDF3 and Crank-Nicolson (CN). The Weissenberg numbers considered are We $= 0.25$, We $= 0.5$ and We $= 1$ (considering the Weissenberg number as the dimensionless number defined by this expression We $= \frac{\lambda U}{L}$). The optimal convergence rate expected is presented in Table 4.2. Results for the standard formulation are presented in Figure 4.2, and for the logarithmic formulation in Figure 4.3. The pressure field has not been plotted in none of these figures, although the convergence is optimal as for the other unknowns.

4.6.2   Flow over a cylinder

In this subsection, the well-known flow over a cylinder problem is used to achieve several objectives: firstly, to compare the various stabilization methods proposed (dynamic and quasi-static formulations) in terms of stability when the time step is small, and when the Weissenberg number increases. Secondly, the solution obtained with the proposed formulations when using rather coarse meshes is compared with the one obtained with a fine mesh, assessing the suitability of the methods when using coarse meshes. Lastly, the behavior of velocity sub-grid scales is studied comparing the results of the residual-based and the term-by-term formulations.

Setup

The computational domain is defined as a rectangle of length 16 and width 8, with a unitary cylinder centered at point (4,0), as it is plotted in Figure 4.4.
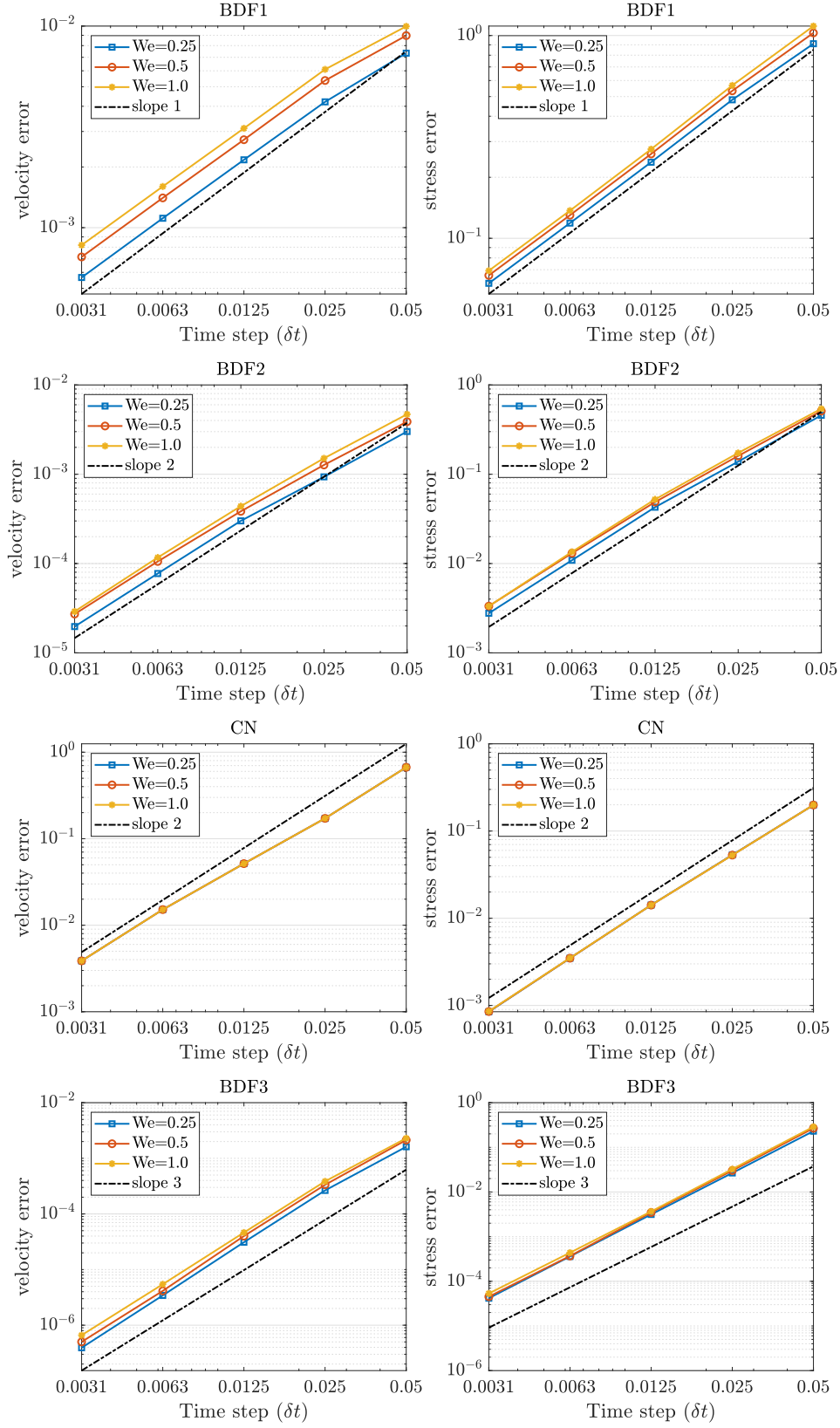
Figure 4.2: Convergence test. Discrete $\ell^\infty(L^2(\Omega))$-errors for velocity and stress fields using BDF1, BDF2, CN and BDF3 schemes for standard formulation.
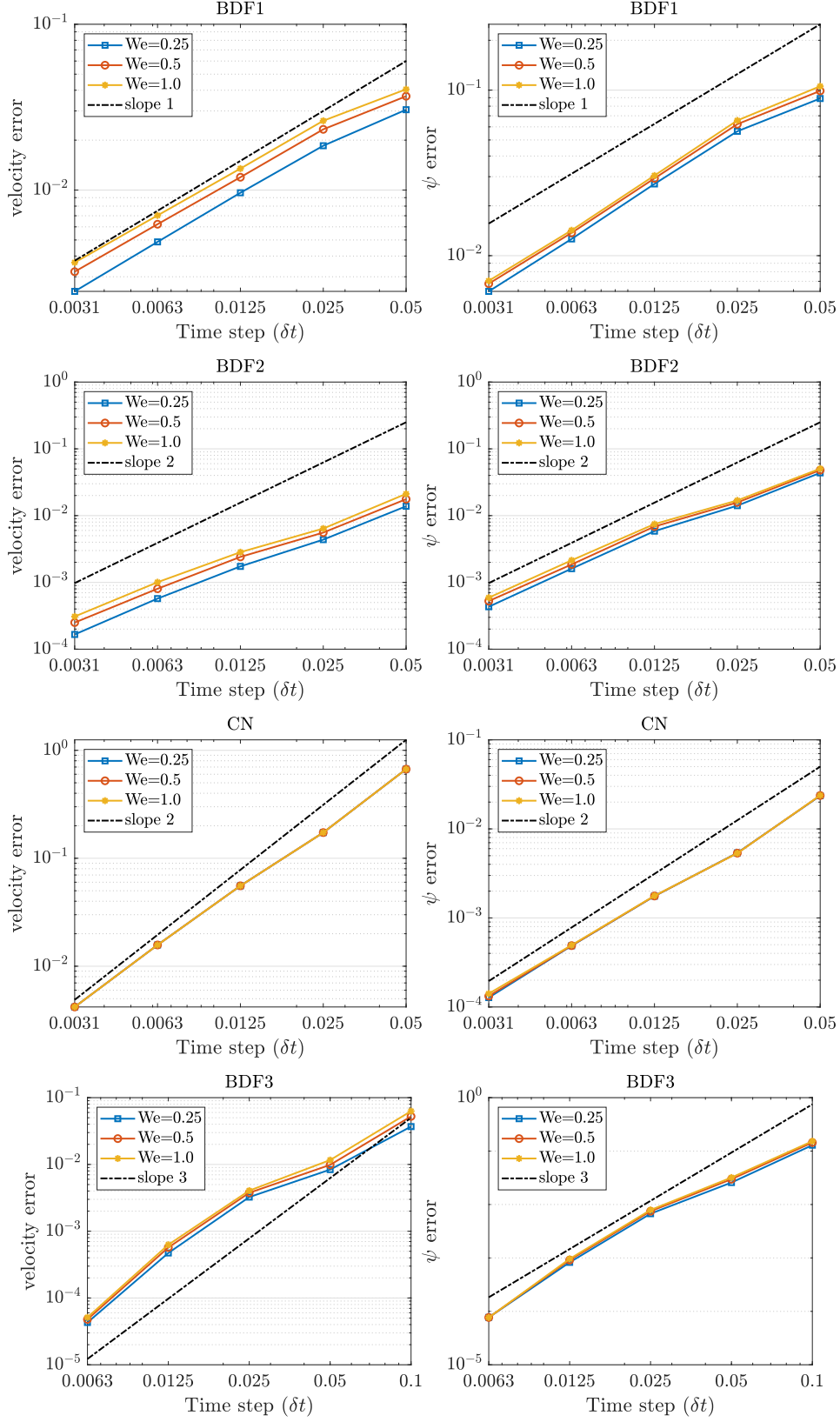
Figure 4.3: Convergence test. Discrete $\ell^\infty(L^2(\Omega))$-errors for velocity and $\boldsymbol{\psi}$ fields using BDF1, BDF2, CN and BDF3 schemes for logarithmic formulation.
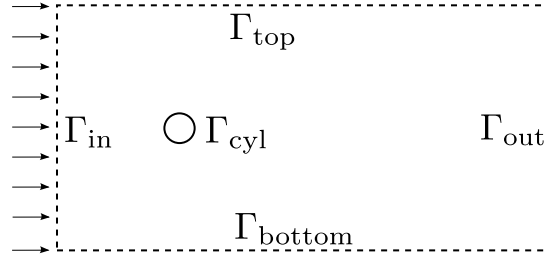
Figure 4.4: Flow over an unconfined cylinder. Domain and computational boundaries.
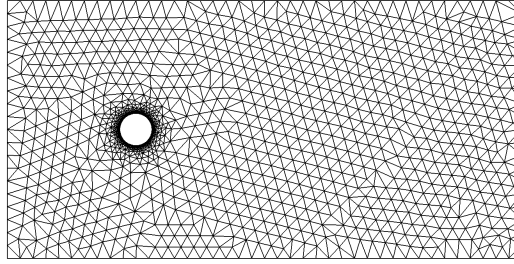
Figure 4.5: Flow over an unconfined cylinder. Computational mesh.

The boundary conditions of the problem are as follows. The inflow velocity of the problem is prescribed in Γ_{in} as $u_x = 1$ and $u_y = 0$, while Γ_{top} and Γ_{bottom} are considered fictitious walls where $u_y = 0$ and u_x is left free. For the outflow boundary Γ_{out} the velocity is left free in both components, and finally, for the wall of the cylinder Γ_{cyl} non-slip conditions are set, that is, velocity is set to zero. Note that the stress components have been let free in all boundaries.

The benchmark has been computed for different Weissenberg numbers, defined by We $= \frac{\lambda U}{L}$, where U and L are the characteristic velocity and length respectively, and the Reynolds number, defined by Re $= \frac{\rho U L}{\eta_0}$, has been set to 100. The viscoelastic fluid parameters are: $\rho = 1$, $\beta = 0.5$ and $\eta_0 = 0.01$.

The mesh used to compute this numerical example is rather coarse, due to the fact that we aim to check that our methods do not need to fulfill the $\delta t \geq C h^2$ inequality in order to obtain stable solutions. In other words, we show that the formulation proposed is independent of the space-time discretization, without looking for an accurate result. In particular, the mesh employed is unstructured, with an element size around the cylinder of $h_{\min} = 0.01$, and coarser at the rest of the domain (maximum element size $h_{\max} = 0.4$). For the computation of this benchmark a BDF1 time discretization scheme has been used; the time step considered will be indicated in each case.

Stability study

First of all, we pretend to show the stability of the proposed formulation employing the time-dependent sub-grid scales explained in previous subsections, in comparison with the quasi-static formulation. We have considered the orthogonal residual based VMS formulation (see [26]) and the term-by-term stabilization in the standard formulation. Also, a wide range of time step sizes have been contemplated to show numerically that the dy-

P1 elements	Time step (δt)			
Method	0.050	0.0250	3.125×10^{-3}	1.562×10^{-3}
Static-OSS	Solved	Failed	-	-
Dyn-OSS	Solved	Solved	Solved	Solved
Static-SOSS	Solved	Solved	Solved	Failed
Dyn-SOSS	Solved	Solved	Solved	Solved

Table 4.3: Flow over an unconfined cylinder. Stability study: solved and failed cases for We = 0.125, $\alpha_{1,\min} \approx 1.156 \times 10^{-3}$ using P1 elements.

P2 elements	Time step (δt)			
Method	0.025	0.0125	3.906×10^{-4}	1.953×10^{-4}
Static-OSS	Solved	Failed	-	-
Dyn-OSS	Solved	Solved	Solved	Solved
Static-SOSS	Solved	Solved	Solved	Failed
Dyn-SOSS	Solved	Solved	Solved	Solved

Table 4.4: Flow over an unconfined cylinder. Stability study: solved and failed cases We = 0.125, $\alpha_{1,\min} \approx 7.4 \times 10^{-5}$ using P2 elements.

namic formulation is more stable than the quasi-static one, in particular for time steps up to $\delta t \approx \alpha_{1,\min}$ (minimum of the first stabilization parameter) for linear (P1) and quadratic (P2) elements.

Regarding the space discretization, Figure 4.5 has been employed to elaborate this comparative, resulting in $\alpha_{1,\min} \approx 1.156 \times 10^{-3}$ when P1 elements are considered. For P2 elements the minimum stabilization parameter is $\alpha_{1,\min} \approx 7.4 \times 10^{-5}$. Note that $\alpha_{1,\min}$ is a value obtained from each problem, and depends directly on the h (element size) magnitude.

In all these cases, the Weissenberg number has been fixed to 0.125, that is a low value, in order to avoid failures associated with a high elasticity.

Results are summarized in Table 4.3, where the suffix *Static* indicates the cases solved through a quasi-static method, whereas *Dyn* refers to the dynamic sub-grid scale methods. On the other hand, the term-by-term stabilization method is denoted by *SOSS* and *OSS* is labeled for the residual-based orthogonal VMS method. In both cases, linear and quadratic elements, the dynamic method is the most efficient, as it has been argued in the preceding section. In both cases (P1 and P2 elements), the most unstable stabilization method is the quasi-static formulation together with the residual-based stabilization, which is not able to solve the problem for $\delta t \lesssim 21\alpha_{1,\min}$ for linear elements. The quasi-static formulation using a split stabilization is particularly stable in comparison with the residual based. In this case, for both types of elements, the scheme presents instabilities approximately when $\delta t \approx \alpha_{1,\min}$. For smaller time steps, only the dynamic stabilization methods achieve convergence of the problem. Note that the instability in principle appears when the inequality $\delta t \geq C\alpha_1^{n+1}$ is not fulfilled.

A second comparative study has been carried out. In this case, the high Weissenberg number instability has been tested, solving the flow past a cylinder problem for several Weissenberg numbers. Let us recall that this dimensionless number represents the elasticity in the flow, therefore when elasticity is high the computation of the flow leads to several difficulties, among them, the exponential growth of the elastic stresses. In Table 4.5, the dynamic formulation of the residual-based and the term-by-term stabilization for the standard formulation and the logarithmic formulation are tested for different Weissenberg

	Weissenberg (We)			
Formulation	0.125	0.25	0.375	0.5
Std-OSS	Solved	Failed	-	-
Std-SOSS	Solved	Solved	Solved	Failed
Log-OSS	Solved	Solved	Failed	-
Log-SOSS	Solved	Solved	Solved	Solved

Table 4.5: Flow over an unconfined cylinder. Stability study: solved and failed cases for the two dynamic formulations (Std: Standard and Log: Logarithmic), $\delta t = 0.1$.

	Weissenberg (We)			
Formulation	0.125	0.165	0.25	0.5
Std-Static	Solved	Failed	-	-
Std-Dyn	Solved	Solved	Solved	Failed
Log-Static	Solved	Solved	Failed	-
Log-Dyn	Solved	Solved	Solved	Solved

Table 4.6: Flow over an unconfined cylinder. Stability study: solved and failed cases for S-OSS formulations, using dynamic and quasi-static sub-grid scales, $\delta t = 0.1$.

numbers. In all cases, the time step is fixed at $\delta t = 0.1$, and continuation techniques have not been employed.

Residual-based methods are the less stable ones and they fail for Weissenberg numbers equal to 0.25 and 0.375, for standard and logarithmic formulations, respectively. It is remarkable that the split term-by-term stabilization methods show a suitable robustness in spite of using the standard formulation, as it can be observed in Table 4.5 for We = 0.375. Nevertheless, the logarithmic formulation together with the dynamic sub-grid scales is the most effective method: while the other methods are not able to converge for We = 0.5, the dynamic logarithmic formulation is capable of converging in this case.

The conclusion is that for problems with a δt sufficiently small such that the inequality $\delta t \geq C\alpha_1^{n+1}$ is not satisfied (at a certain time step n), and whose Weissenberg number is particularly high, only a dynamic term-by-term logarithmic formulation will be effective. We have tested numerically that if, for instance, $\delta t = 1.562 \times 10^{-3}$ for P1 elements is used, only the dynamic term-by-term stabilization is stable (see Table 4.3). However, if we contemplate a flow with a Weissenberg number equal to 0.5, this model would not be able to converge unless a logarithmic formulation is used.

Finally, a study has been performed, putting the focus on the Split-OSS methods and how the dynamic formulation can affect stability not only when the time step is small, but also in terms of elasticity. In Table 4.6 the most significant results have been summarized, the conclusion being that dynamic formulations are more efficient avoiding elastic instabilities, permitting the computation of fluid flows with a higher Weissenberg number. For example, for the logarithmic conformation formulation, $\alpha_{1,\min} \approx \alpha_{1dyn,\min} \approx 0.119 \times 10^{-2}$, i.e., the stabilization parameter of the momentum equation remains similar in both problems, dynamic and quasi-static, while the constitutive stabilization parameter differs significantly ($\alpha_{3,\min} \approx 0.335 \times 10^{-2}$ and $\alpha_{3dyn,\min} \approx 0.562 \times 10^{-4}$). This is due to the structure of the dynamic parameter, which apart from depending on time step size also depends on the parameter λ, directly related with the dimensionless Weissenberg number.

It is clear that the logarithmic formulation is more expensive than the standard one due to the computations of the exponential of the variable $\boldsymbol{\psi}$, among others [120]; this
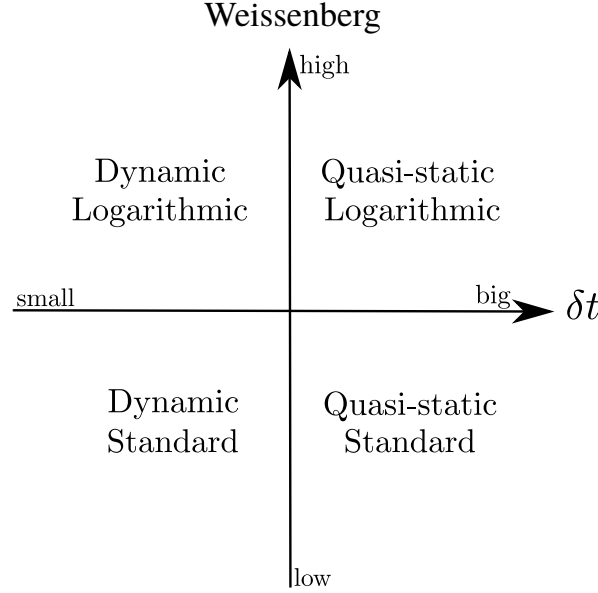
Figure 4.6: A general scheme of S-OSS formulations (standard and logarithmic) and methods (quasistatic or dynamic sub-grid scales) for solving viscoelastic transient problems depending of the characteristics of the problem.

needs to be taken into account when selecting the proper formulation and stabilization method for a given problem. In Figure 4.6 a general scheme has been displayed for the Split-OSS formulations, where the characteristics of the problem determine the use of dynamic/quasi-static sub-grid scales and logarithmic/standard formulations. The vertical axis represents the Weissenberg number magnitude, and the horizontal axis corresponds the size of the time step. In this case, labels "big" and "small" refer to magnitudes in comparison with the stabilization parameter $\alpha_{1,\min}$ and the quoted inequality $\delta t \geq C\alpha_1^{n+1}$ for all n. Note that the thresholds are not sharp, due to the fact that the dynamic stabilization is also useful to deal with some high Weissenberg problems and it could avoid the need of using the logarithmic formulation to solve them, which is much more expensive from the computational point of view. Obviously, the dynamic stabilization can also be used in the case of large time steps, although in this case the quasi-static version might also work and it is cheaper; the important point is that the dynamic formulation *must* be used for small time steps (small in the sense explained above).

Comparison between methods

In this subsection we compare the solution obtained by using the proposed methods considering a low Weissenberg value, set to 0.125.

Firstly, in Figure 4.7, pressure, velocity and stress have been plotted for the solution obtained with the dynamic term-by-term formulation, considering a time step $\delta t = 0.1$,

(a) P1 elements

(b) P2 elements

(c) P1 elements

(d) P2 elements

(e) P1 elements
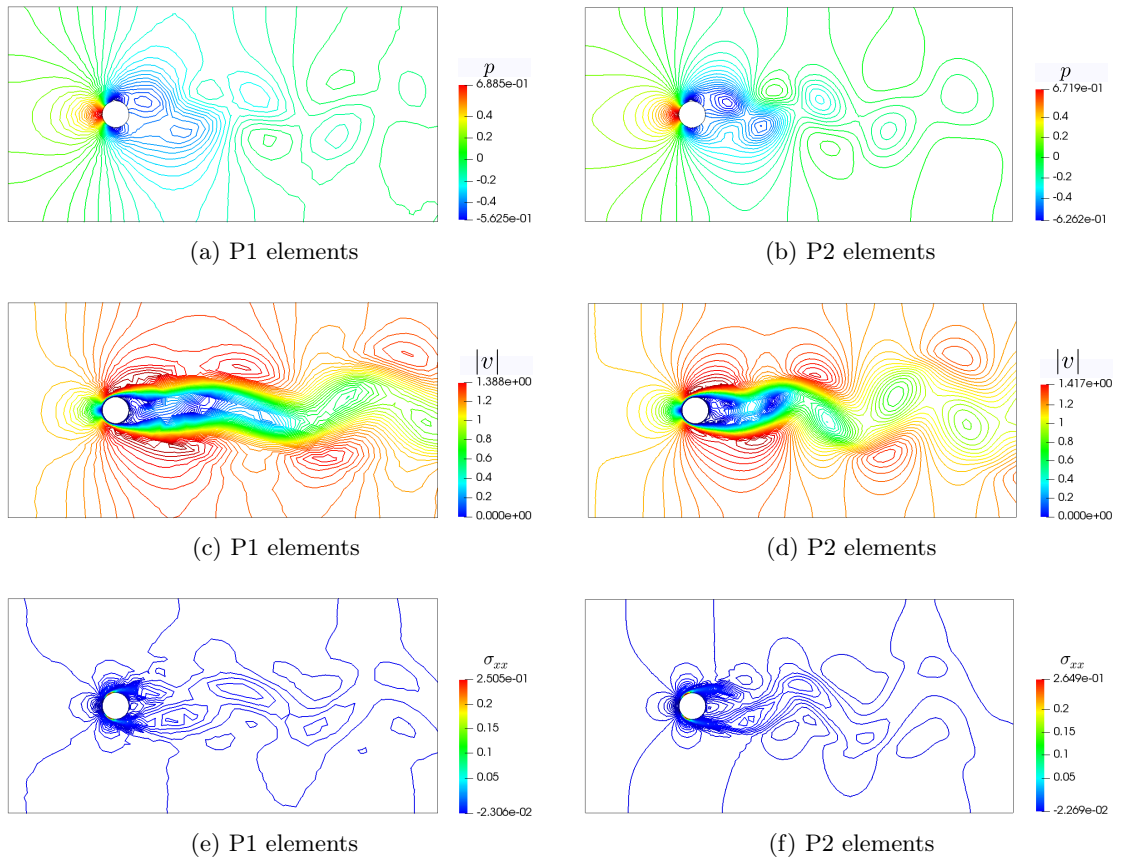
(f) P2 elements

Figure 4.7: Flow over an unconfined cylinder. Contours of the pressure, velocity and component xx of the elastic stress, $\delta t = 0.1$.

for linear (left) and quadratic (right) elements. The differences found between the results obtained with P1 and P2 elements are due to the coarse discretization used; due to this, solutions obtained using P2 elements are more accurate and less mesh-dependent. Note that for higher Weissenberg numbers, the results are very similar qualitatively, with the exception of the elastic stress tensor, whose maximum values increase significantly on the wall of the cylinder.

The evolution of the main fields in a downstream point situated at $(6,0)$ is displayed in order to compare the solution between stabilization methods in Figure 4.8. The graphs show curves along time when oscillatory solutions are achieved for the second component of the velocity, the pressure and the xx component of the stresses. Also, results are depicted for different time step sizes: for $\delta t = 0.1$ and for $\delta t = 1.5625 \times 10^{-3}$, in other words, $\delta t \approx \alpha_{1,\min}$. For the smaller time step, only the dynamic methods are stable, as detailed in Table 4.3, for this reason only OSS and S-OSS dynamic cases are taken into account.

As explained in [30], the instability derived from the space-time discretization restriction can be identified in the evolution of pressure, as shown in Figure 4.8c when the static OSS stabilization method is used.

On the other hand, in Figure 4.8a we can observe that the quasi-static sub-grid scales together with the residual-based stabilization is the less dissipative one, followed by the dynamic sub-grid scales version. In comparison, the term-by-term formulation is more diffusive than the orthogonal residual-based methods. Additionally, the dynamic formulation is also more dissipative than the quasi-static version. We need to remark that the differences between the residual-based and the term-by-term formulations appreciated in Figure 4.8 are caused directly by the coarse mesh employed, since for finer discretizations no significant differences are found. This figure helps to understand why the dynamic formulation for the term-by-term formulation is in general more stable, and this is because when the approximation is not fine enough, it tends to be more diffusive than the quasi-static and residual-based counterpart.

The next figures show an interesting result. In Figures 4.9 and 4.10 the components x and y of the sub-grid scales are plotted for both dynamic formulations utilized: the orthogonal residual, denoted by $\tilde{\boldsymbol{u}}$, and the split term-by-term, denoted in Figures 4.9 and 4.10 as $\tilde{\boldsymbol{u}}_1$, $\tilde{\boldsymbol{u}}_2$ and $\tilde{\boldsymbol{u}}_3$. At first sight, the sub-grid scales obtained by the split formulation are very different to the ones of the orthogonal residual method. The existence of a difference between both methods is evident, because while in the term-by-term formulation only local inner products of the convective term, the pressure gradient and the divergence of the stress are considered, the residual stabilization takes into account all of the cross product terms of these operators applied to the unknowns and the test functions. Furthermore, the sub-grid scales of the velocity are not similar in both methods. However, when the three sub-grid scales are added (denoted by $\sum_{i=1}^{3} \tilde{\boldsymbol{u}}_i$), the result is very similar to the sub-grid scales obtained with the residual based formulation, as illustrated in Figures 4.9 and 4.10. This effect has already been reported for the Navier-Stokes problem in [30]. The results for quadratic elements are shown in Figure 4.10. The general trend is similar too, although the presence of the Laplacian term in the residual-based formulation is probably the cause for the observed differences. These figures serve to justify the splitting of the velocity sub-grid scales that we have assumed to motivate the method proposed in this chapter (see the second paragraph on Section 4.4.2)

In this case, the solutions obtained with the logarithmic formulations are identical to the standard formulation. For this reason, the type of formulation (standard or logarithmic reformulation) has not been specified in this comparative.
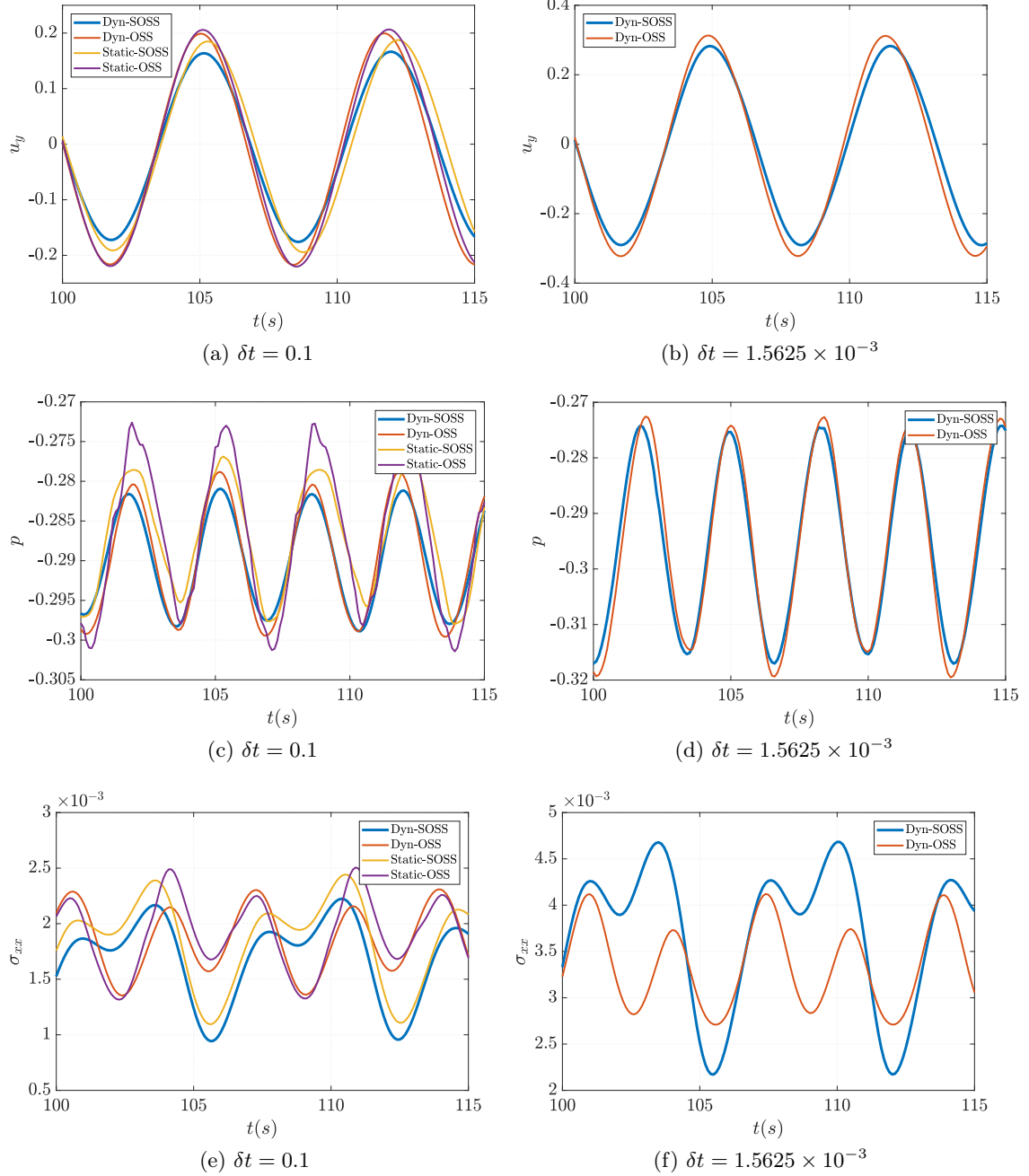
Figure 4.8: Flow over an unconfined cylinder. Comparison of the evolution of the fields between the different stabilization methods for $\delta t = 0.1$ (left) and $\delta t = 0.0015625$ (right) at the point downstream (6,0).
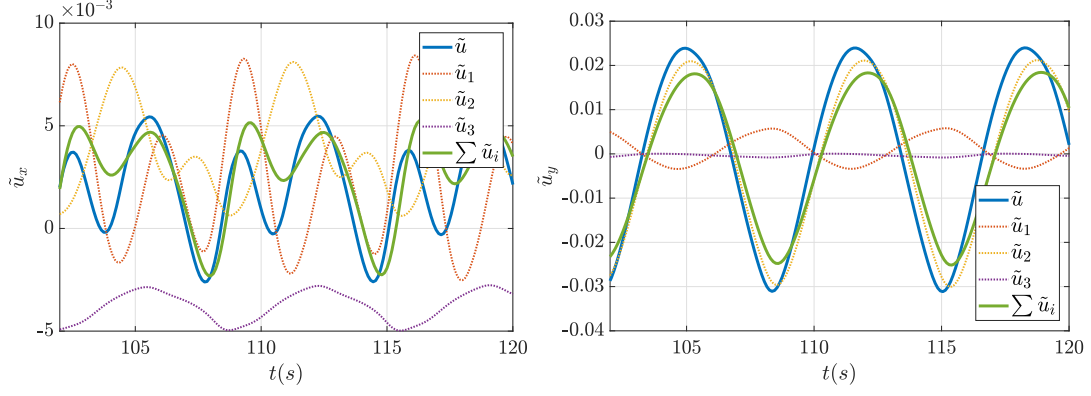
Figure 4.9: Flow over an unconfined cylinder. Comparison of evolution of the sub-grid scales at $\delta t = 0.1$ using P1 elements at the point downstream (6,0).
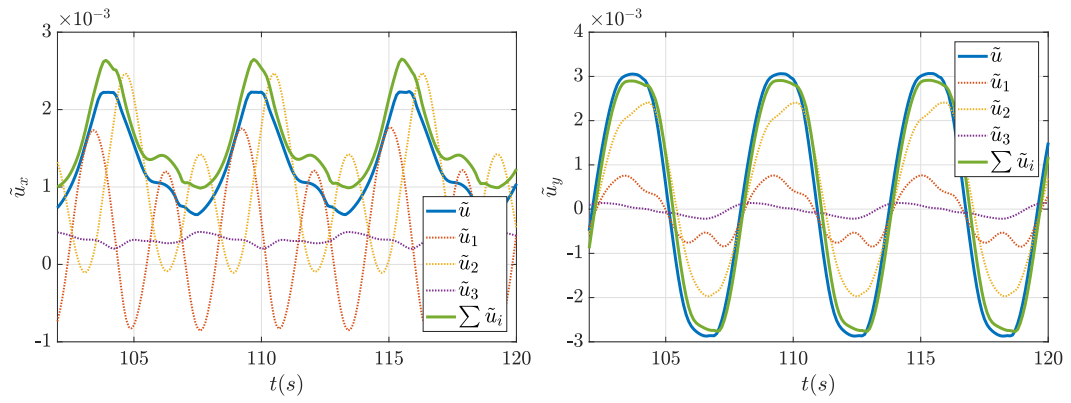
Figure 4.10: Flow over an unconfined cylinder. Comparison of the evolution of the sub-grid scales at $\delta t = 0.1$ using P2 elements at the point downstream (6,0).
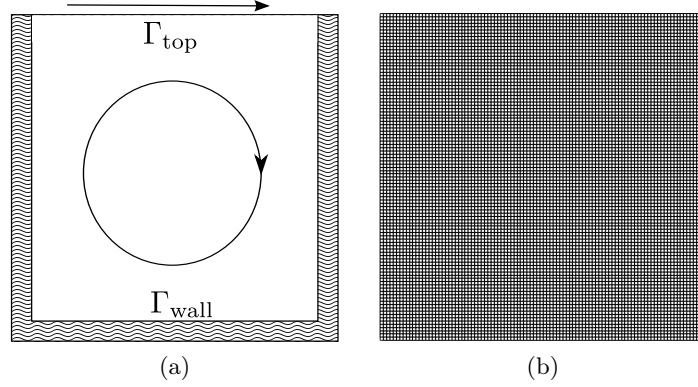
Figure 4.11: Lid-driven cavity. Schematic representation of computational boundaries (a) and computational mesh (b).

4.6.3 Lid-driven cavity flow problem

The lid-driven cavity flow is a good example to illustrate the differences that can be generated by the viscoelastic contribution in the fluid, due to the elastic stresses dependence on the previous deformation history. In this case, we have solved it to prove that the dynamic term-by-term formulation is also efficient.

Steady-state case at $\mathrm{Re} = 0$

A fluid confined in the unit square is considered, whose boundaries are solid walls except the top boundary, which has a prescribed velocity in the x direction, as shown in Figure 4.11a. Because the viscoelastic fluid cannot sustain deformation at a stagnation point, the motion of the lid must be smooth and the gradient of the velocity should be zero at corners. For this reason, on the boundary Γ_{top} the horizontal velocity has been chosen as follows:

$$u_x(x, 1, t) = 8 \left[1 + \tanh \left(8 \left(t - \frac{1}{2} \right) \right) \right] x^2 (1 - x)^2,$$

$$u_y(x, 1, t) = 0,$$

where the function $1 + \tanh \left(8 \left(t - \frac{1}{2} \right) \right)$ has a smooth transition, being zero at $t = 0$; u_x attains the maximum value $(u = 1)$ when $t > \frac{1}{2}$ at the center, $x = \frac{1}{2}$. In Γ_{wall}, velocity is set to zero in both components. The inflow boundary conditions for the elastic stress tensor are not needed since there is no inflow boundary in this problem. As characteristic velocity, the maximum lid velocity has been taken to compute the dimensionless numbers, and the characteristic length is 1, the size of each square's side. The considered Weissenberg number is We $= 1.0$, and the Reynolds number Re $= 0$. Referring to the spatial discretization, a structured mesh composed by 10 000 bilinear Q1 elements is used (see Figure 4.11b) and the time step considered is $\delta t = 0.0025$. Concerning to the time discretization scheme, a BDF1 scheme has been used.

This test is carried out with the aim of comparing the accuracy of the dynamic and the quasi-static stabilization methods in a stationary problem, comparing the results with other authors [27, 52, 65, 148]. In our case neither continuation iterative methods to treat the convergence, nor additional sub-relaxation schemes have been employed.

In Table 4.7 we show that the problem is solved successfully only for the combination of the logarithmic formulation and the dynamic sub-grid scale stabilization. The steady

Formulation	Stabilization S-OSS	
	Quasi-static	Dynamic
Standard	Failed - time step 265	Failed - time step 1316
Logarithmic	Failed - time step 240	Solved

Table 4.7: Lid-driven cavity. Comparison between different formulations with $We = 1.0$, $Re = 0$, $\delta t = 0.0025$. The time step at which convergence fails is indicated in each case

state tolerance is 10^{-5}, and for each time step three non-linear Newton-Raphson iterations are employed. As in the cylinder example, $\alpha_{1,\min} \approx 0.83 \times 10^{-5} \approx \alpha_{1\text{dyn},\min}$, therefore the dynamic sub-grid scales for the momentum equations are not peremptory because the instability is not originated by a small time step. In this case, the high Weissenberg number is the main problem. If we compare the stabilization methods, we see that $\alpha_{3,\min} \approx 0.25$, whereas $\alpha_{3\text{dyn},\min} \approx 0.239 \times 10^{-2}$. This notable difference is due to the structure of parameter $\alpha_{3\text{dyn},\min}$, which depends directly on the magnitude of λ. This structure of the parameter combined with the log-conformation formulation allows to properly solve this problem. It can be observed that while the quasi-static options fail early in the simulation, even in the log-conformation reformulation, the dynamic stabilization is, from this point of view, much more efficient for high Weissenberg numbers.

It must be remarked that although in [27], convergence was achieved with a quasi-static and standard formulation, a fractional step scheme was used to solve it, together with some continuation and sub-relaxation methods to help convergence, while in our case only a monolithic method with a fixed point iterative scheme without extra sub-relaxation artifacts is considered.

In Figure 4.12, cuts of the velocity components have been displayed, whereas in Figure 4.13 cuts of the components of $\boldsymbol{\psi}$ are plotted with the aim of comparing the results with other works such as [52, 65, 85]. The results are extremely similar to those by Fattal and Kupferman. For the component ψ_{yy}, the solution is compared with the results in [52]. The small differences found between our work and other publications probably are due to the differences with the mesh used. For example, in [52] the mesh employed is extremely fine near the boundaries in contrast with the uniform relatively coarse mesh used in our case.

Dynamic case at $Re = 100$

In this case the boundary conditions are similar to the steady-state case, with the exception of the condition imposed over the boundary Γ_{top}, where now the horizontal velocity has been selected as:

$$u_x(x, 1, t) = 16x^2(1 - x)^2 \sin(\pi t),$$
$$u_y(x, 1, t) = 0.$$

The $\sin(\pi t)$ term has been added to force the lid velocity to be time dependent and dynamic. Additionally, the Reynolds number ($Re = \frac{\rho U L}{\eta_0}$) will be considered equal to 100.

The mesh and time-step size considered are the ones defined in the stationary case, but in this occasion the time discretization scheme is BDF2. We will show the results obtained under the assumptions commented, and these will be compared with the solution shown in [27], where the authors studied the same benchmark in the quasi-static case employing a fractional step method developed in the same work.

If the time step is small, the quasi-static method is incapable of solving the dynamic problem, considering that now the stabilization parameter is $\alpha_{1,\min} \approx 4.1 \times 10^{-4}$. In Figure
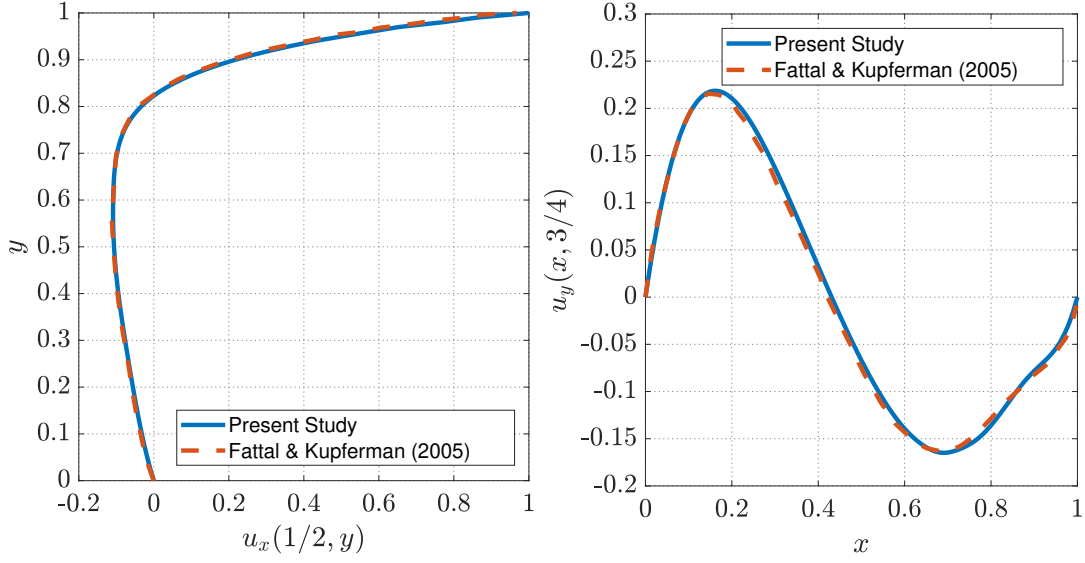
Figure 4.12: Lid-driven cavity. Results at time $t = 8$, for We $= 1$ and Re $= 0$. Velocity profiles along the lines $x = 1/2$ and $y = 3/4$.

4.14, streamlines are displayed for two different time steps, $t = 1.5$ and $t = 2.0$, and in Figure 4.15 the component σ_{xy} of the stress has been plotted. These results are shown in order to do a qualitative study, similar snapshots are presented in [30]. In addition, in Figure 4.15 the isolines that correspond to the component xy of the stress sub-grid scale have been presented as isocontours. The same case has been checked for the dynamic logarithmic formulation, obtaining similar results.

4.6.4   Three-dimensional case

In order to check that the proposed stabilization method works well also in the three-dimensional case, we have simulated the lid driven cavity problem in the 3D case. The problem is just an extension of the two-dimensional case developed in subsection 4.6.3.

Setup

The three-dimensional lid driven cavity problem is solved for an unit cube, as displayed in Figure 4.16a. On the top of the lid (denoted by Γ_{top} in the scheme) the components of the velocity are prescribed to:

$$u_x(x, y, 1, t) = 256x^2(1 - x)^2 y^2 (1 - y)^2 \sin(\pi t),$$
$$u_y(x, y, 1, t) = 0,$$
$$u_z(x, y, 1, t) = 0,$$

and velocity is fixed to zero at the rest of boundaries (Γ_{wall}). Similar to Subsection 4.6.3, the boundary condition imposed on the top is due to two reasons: on the one hand the necessity of imposing a smooth condition at the corners, and on the other hand the necessity of a time-dependent boundary to make the problem dynamic. As in the two-dimensional case, no boundary conditions are required for the stresses. The physical properties considered for the problem are a Weissenberg number of 0.5 and a Reynolds number equal to 100.
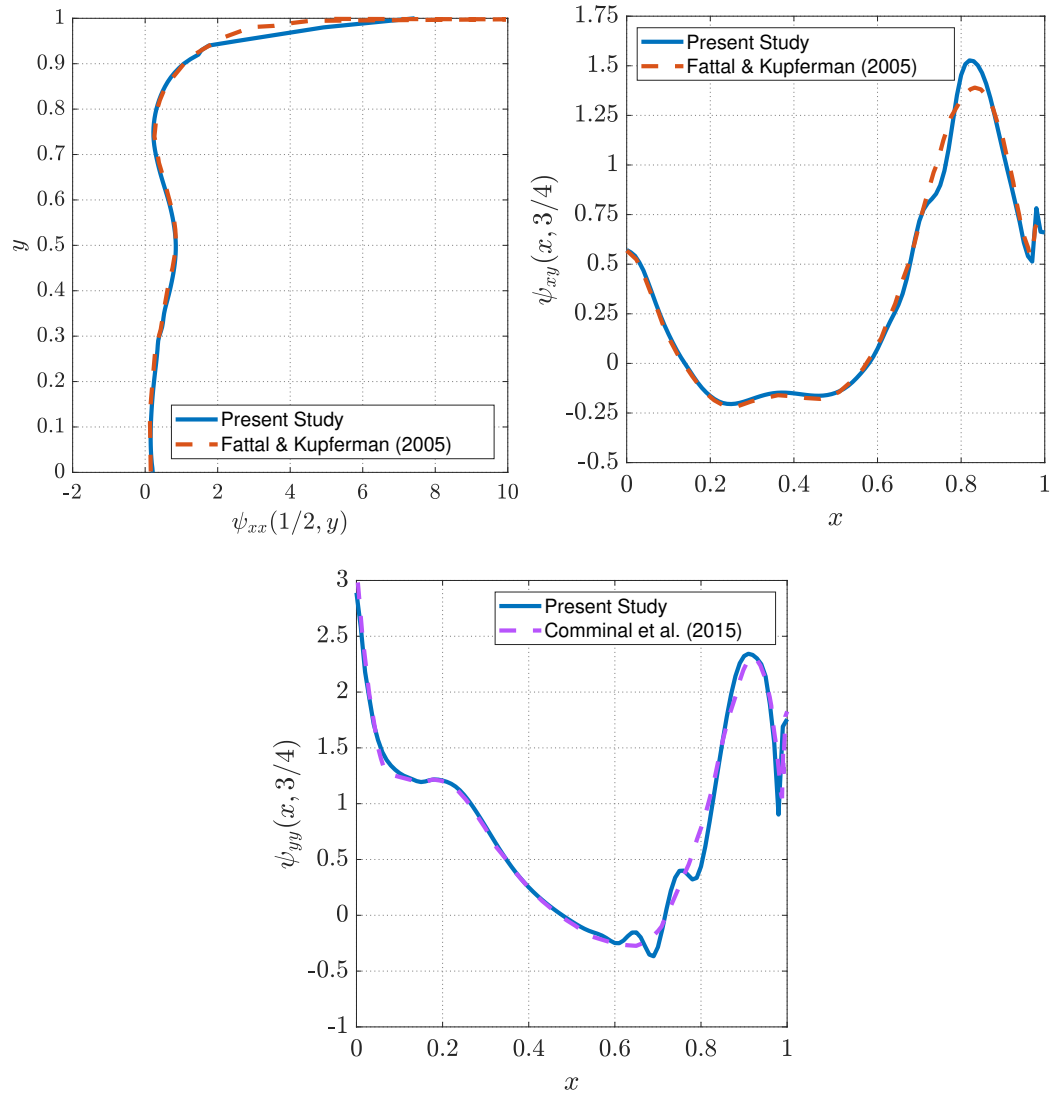
Figure 4.13: Lid-driven cavity. Results at time $t = 8$, for We = 1 and Re = 0. $\boldsymbol{\psi}$ profiles along the lines $x = 1/2$ and $y = 3/4$.

(a) $t = 1.5$ (b) $t = 2.0$
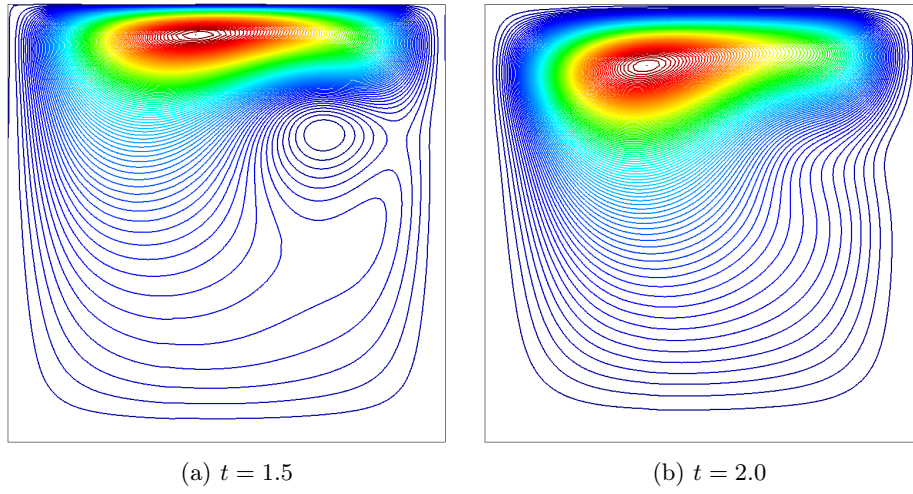
Figure 4.14: Lid-driven cavity. Streamlines using the dynamic Split-OSS method for $We = 1$ and $Re = 100$.

(a) $t = 1.5$ (b) $t = 2.0$

(c) $t = 1.5$ (d) $t = 2.0$
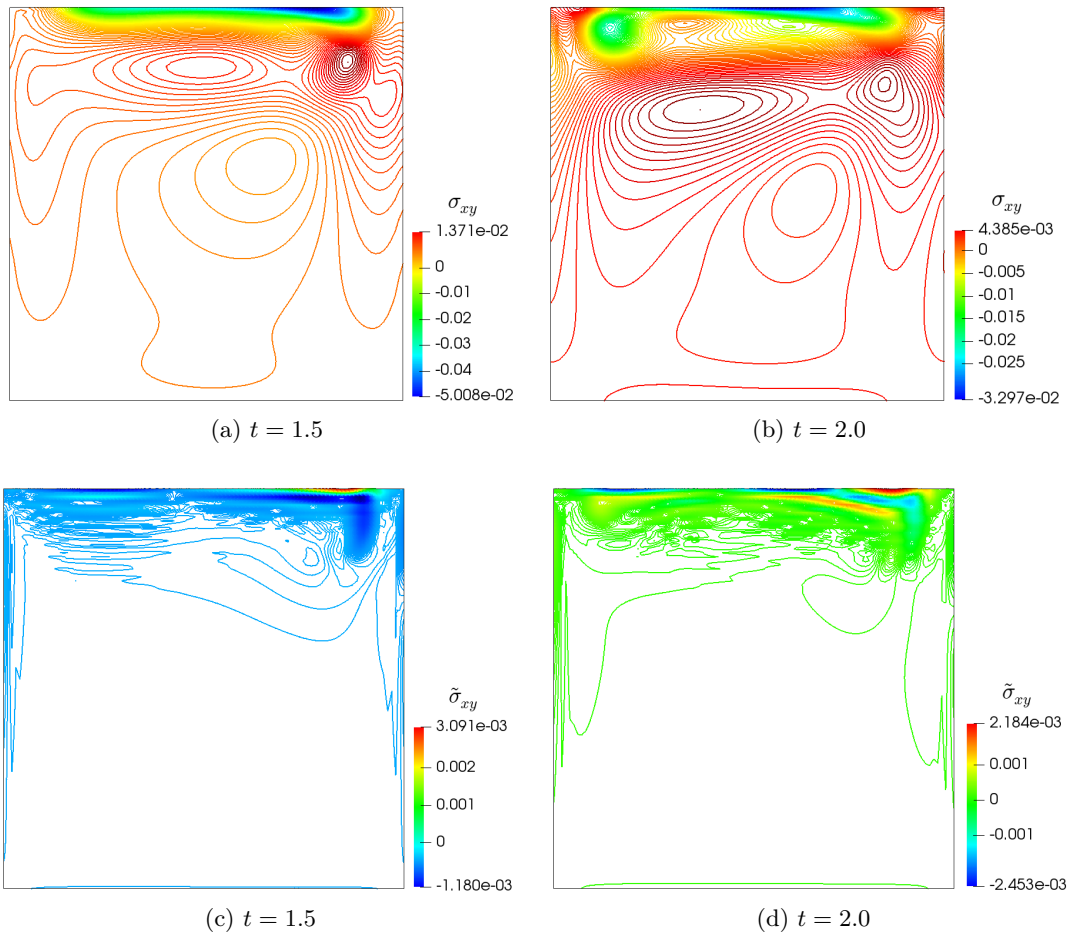
Figure 4.15: Lid-driven cavity. Contours of the component xy of the stresses (top), and of the sub-grid scale (bottom), using the Split OSS method for $We = 1$ and $Re = 100$.
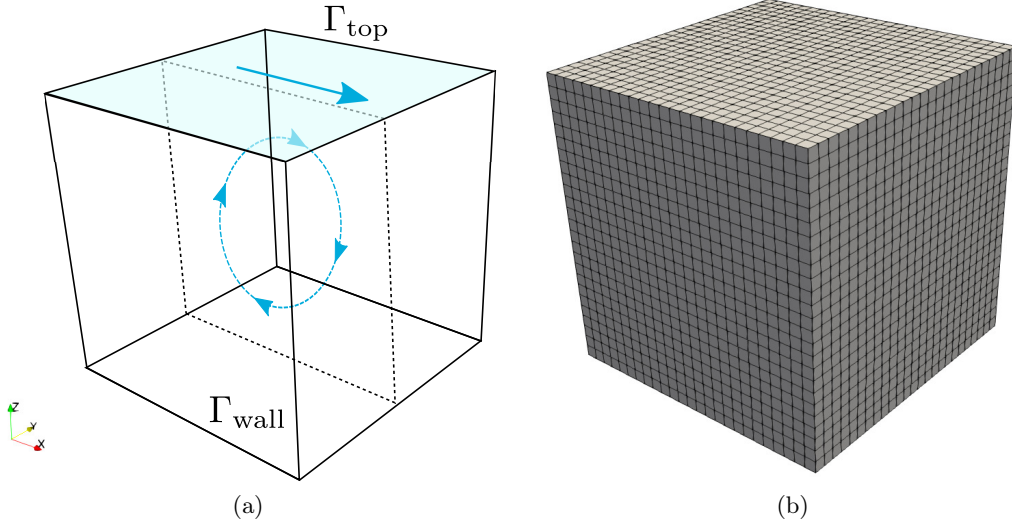
Figure 4.16: Lid-driven cavity. Schematic representation 3D and computational boundaries (a) and computational mesh (b).

The numerical spatial discretization consists in 15625 trilinear Q1 hexaedral elements, and 17 576 nodes, plotted in Figure 4.16b. Finally, referring to the time discretization, a BDF1 time integrator is employed together with a time step size of $\delta t = 0.01$ and a time interval from 0 to 2 seconds.

Results

The aim of this problem is to demonstrate that the dynamic sub-grid scale formulation is able to solve three-dimensional cases; we do not have any reference to compare the accuracy of our results, although the mesh employed can be considered coarse for the problem being solved. No significant differences have been found between our results and those reported in [27].

In Figure 4.17 we have plotted isolines of some relevant fields in cuts defined by planes $x = 0.5$, $y = 0.5$ and $z = 0.5$, at time $t = 1.5$. In particular, Figure 4.17a shows the distribution of the pressure, Figure 4.17b the first component of the velocity, and finally, Figures 4.17c and 4.17d display the distribution of the component xy of the stresses and the sub-grid scales of the stresses, respectively. The problem has been run using the dynamic term-by-term standard and logarithmic formulations, obtaining very similar results.

Streamlines in the cut-plane $y = 0.5$ and for two different times ($t = 1.5$ and $t = 2.0$) are shown in Figure 4.18.

4.7   Conclusions

Along this chapter, various dynamic sub-grid scales VMS-stabilization methods have been proposed with the goal of solving viscoelastic flow problems. The main ideas have been applied to the log-conformation reformulation [64] of the viscoelastic equations, originally proposed in [120]. For both formulations (standard and logarithmic), two different stabilization methods have been designed: one based on the residual of the equations, and the second one based on a split term-by-term stabilization for the momentum equation. The stabilized methods defined in this chapter allow to solve time-dependent problems typically

(a)

(b)

(c)

(d)
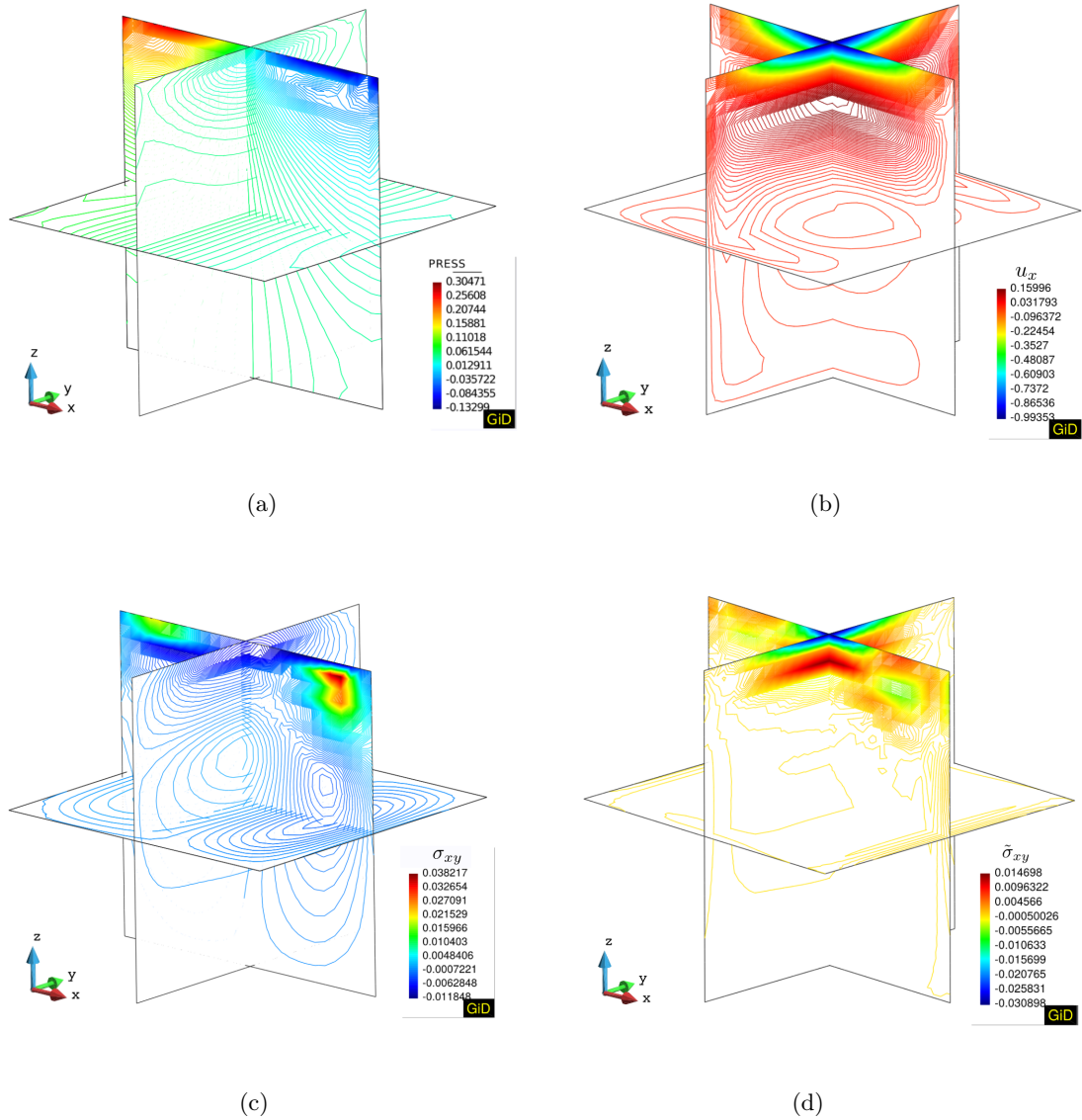
Figure 4.17: Lid-driven cavity. Contours in some cuts for different fields in the 3D domain at $t = 1.5$.

(a) $t = 1.5$ (b) $t = 2.0$
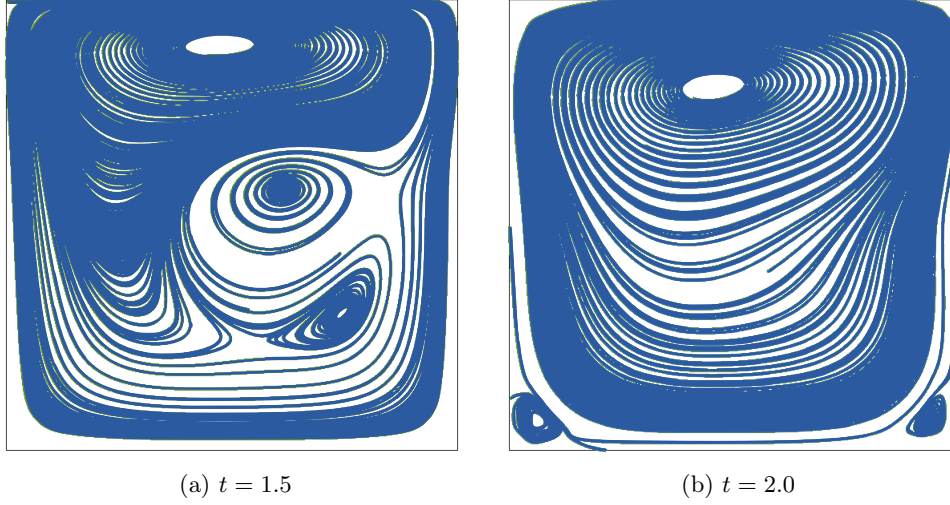
Figure 4.18: Lid-driven cavity. Streamlines in a cut-plane $y = 0.5$ of the three dimensional domain.

where two different sources of instability can appear simultaneously: the one originated by anisotropic space-time refinement when the time step is small and the well-known stress exponential growth typical of high Weissenberg numbers of viscoelastic problems.

The stability analysis of a VMS-based stabilized FE method for a linearized viscoelastic flow problem discretized in time using the BDF1 scheme, using both the standard formulation and the LCR. First, we have obtained stability for the FE component and the SGSs in standard norms; the results obtained are the expected ones (Theorems 4.1 and 4.2). Of particular relevance is the $\ell^\infty (L^2(\Omega)^d)$ stability obtained for the SGSs, which is a direct consequence of considering them dynamic. The stability bounds for the SGSs can be translated into additional stability for the FE components of the unknowns. This is done first in rather weak dual norms (Theorems 4.3 and 4.4), with a certain improvement if the dissipative nature of the BDF1 scheme is employed (Theorem 4.5). Furthermore, if the classical condition relating the time step size and the stabilization parameters is assumed, a classical stability estimate can be derived (Theorem 4.6). In all results proven, the constants in the stability estimates do not depend on the physical properties of the problem being solved. All these results serve to assess that the formulation proposed is stable in the terms that could be expected. From this stability one could prove convergence using more or less standard arguments.

The proposed methods have been analyzed extensively in several benchmarks, using linear and quadratic elements, structured and unstructured meshes, doing different comparatives between the quasi-static and dynamic stabilization methods to show the efficiency and robustness of the new strategies. The results obtained are particularly remarkable due to the high Weissenberg number reached with the dynamic formulation, which remains stable even if the standard formulation is considered, apart from evident benefits in anisotropic space-time discretizations when the time step is small. In all our numerical experiments, we have found the term-by-term stabilization for the momentum equation more robust than the residual-based one, and the dynamic version of the sub-grid scales more robust than the quasi-static one. This is independent of whether the standard or the logarithmic formulations are employed, the latter being obviously more successful than the former in reaching high Weissenberg numbers. Therefore, the combination of

dynamic sub-grid scales in the term-by-term stabilization and the logarithmic formulation of the equations is capable of solving problems with higher elasticity than all the other options.

Chapter 5

The purely elastic instability

5.1 Abstract

The aim of this chapter is to reproduce problems which show the purely elastic phenomena. For this, different tools have been employed to obtain an accurate and efficient solution. First, the logarithmic formulation is crucial to deal with the high Weissenberg number problems and to obtain converged solutions. Second, we have included time-dependent sub-grid scales in our finite element term-by-term stabilization approach, based on the variational multiscale (VMS) method, in order to obtain stable solutions. This allows us to avoid instabilities related with small time step in relation with the spatial grid discretization, a common issue in viscoelastic flow formulations. Third, the problem has been implemented using a fractional step scheme to reduce an expensive computational cost, and important savings are shown in this respect. The numerical scheme has been tested using some numerical examples, and finally, a case which shows the purely elastic instability has been computed.

5.2 Background

The flow patterns in viscoelastic fluids can be highly dynamic and, in some cases, chaotic due to the elastic component of the fluid and the convective nature of the constitutive equation. That behavior is common even in quasi non-inertial flows [58]. In these cases non-linear rheological effects can manifest through the generation of large normal stresses which result in complex flow phenomena causing elastic turbulence [155]. Elastic turbulence was experimentally observed first by Steinberg and Groisman [78], and although there is no common agreement on the definition of "turbulence", the term is employed in this context due to the fact that this phenomenon showing many characteristics similar to inertial turbulence: the flow exhibits an increment in resistance and fluid elasticity, intensified mixing of mass and a wide range of activated temporal and spatial frequencies. The dominant process depends strongly on the values of the Weissenberg number, and occurs for relatively low Reynolds numbers. In [80] it is shown that elasticity-induced turbulence can be obtained through a moderate increase in the We number. In these conditions, the features of the flow are comparable to those observed in hydrodynamic turbulence for high Reynolds number.

This flow regime is found in applications such as microfluids and the addition of polymers to the fluid can be employed to accelerate the phenomena, for example in mixing [79], emulsification and heat transfer [159]. The study of the dynamics of microscopic objects

in fluctuating flows is also an application of these kind of solutions [112]. Moreover, other typical situations where this physical phenomenon can be observed are the flow in microchannels or cross-flows, where the increment in normal stresses promotes the generation of boundary layers with patterns similar to those of viscous turbulence [60, 141].

Regarding numerical simulation, elastic turbulence is especially challenging due to several reasons, such as those specified in [83]. On the one hand the constitutive models of viscoelastic fluids are based on rudimentary approximations and do not put the focus on relevant aspects of polymer dynamics. On the other hand, advanced techniques and schemes are required to deal with sharp gradients, a typical ingredient in the polymer stress field [95, 140]. Lastly, the required time step is small, as a consequence of the high viscosity of the fluid [169]. In [154], the effect of the contraction ratio in the dynamic response of the flow in a square-square three-dimensional contractions is analysed using experimental and numerical results, where asymmetric flows in a symmetric problem are created increasing the elasticity of the flow. In [107], the instabilities and the asymmetry of the flow in a symmetric domain are analysed for flows with high Weissenberg number using the Leonov constitutive model.

The usual constitutive models that modelize viscoelastic fluid flow, such as the Oldroyd-B and the FENE-P models, are coupled systems of partial differential equations for the velocity, the pressure and the polymer stress tensor. This last one is by nature positive definite, and it has been proved that the loss of this property leads to several instabilities [97]. In the literature, we can find a wide number of numerical tools to deal with this problem. One of the most popular ones is to include global artificial diffusivity in the model, in other words, add a Laplacian term to the evolution equation for the polymer stress. The numerical simulations which have employed this technique are in qualitative agreement with experiments. However, as indicated in [83], the values of diffusivity are required to be three to six orders of magnitude greater than those appropriate for real polymers [161]. Other numerical schemes have been proposed in order to avoid using artificial diffusivity, such as the logarithmic conformation reformulation, proposed originally by Fattal and Kupferman [64] and employed in this work. These numerical schemes have been compared with simulations using artificial diffusivity at high or moderate Reynolds numbers, and quantative discrepancies have emerged. For these reasons, alternative methods should be preferred to the use of artificial diffusivity. On the contrary, in the case of low Reynolds numbers, several studies on elastic turbulence have employed artificial diffusivity, and the work of Gupta et al. [83] demonstrates that there exist particular cases in which the effect of artificial diffusivity is especially adverse.

Elastic turbulence has been proposed as an efficient technique for mixing in very low Reynolds flows, such as in microchannel flows [6], and as indicated in [17]. Despite the great technological interest, this phenomenon is still only partially understood from the theoretical point of view. Laboratory experiments in curvilinear channels have demonstrated that very viscous polymer solutions in the elastic turbulence regime are very efficient for small-scale mixing [79]. In the literature we found different works that investigate elastic turbulence under this perspective, using numerical simulation. In the work written by Berti et al. [17] the phenomenon is investigated for polymer solutions in a two-dimensional Kolmogorov shear flow. The results obtained are in agreement with experimental observations. Recently, numerical and analytical investigations have been used to obtain the instability diagram as a function of the Weissenberg and the Reynolds number as done in [21].

Two dimensional elastic turbulence has also been explored for Taylor-Couette flows by some authors from several perspectives: theoretical [70, 129], in several experiments [130]

and lastly in the numerical simulations by Buel et al. [162]. In the problem in which geometry is restricted to the axisymmetric flow, the transition is coupled with an increment of the velocity fluctuations. Transition to a wave pattern beyond a critical Weissenberg number occurs via a supercritical Hopf bifurcation, although the most unstable modes occur for the non-axisymetric case and bifurcation diagrams were obtained using the Oldroyd-B model. However, in [162], the flow of a viscoelastic fluid in a 2D Taylor Couette is reproduced, using a micron scale, and the turbulence which is observed is only produced by the elastic component of the fluid. In this letter, simulations are performed using OpenFOAM and employing the log-conformation tensor method to stabilize the formulation.

On the other hand, we have to remark that in elastic turbulence, the characteristic power-law dependence between the kinetic energy E and the frequency f is $E(f) \sim f^{-\alpha}$ in the power spectra of the fluctuating velocity field is different to the usual turbulence. The exponent α shows non-monotonic behaviour as a function of the radial position. In [162] the authors indicate that in constrast wih the 3D elastic turbulence where the characteristic exponent is typically $\alpha > 3$, in the numerical 2D experiment the exponent is $\alpha > 2$, attributing this change to the smaller spatial dimension. In the experiments performed by Groisman and Steinberg [78] the power law scaling is $\alpha = 3.5$, and the more recent theories are in agreement with these exponents. In this sense, we found especially relevant the work developed by Fouxon and Lebedev [70]. In this chapter, the authors established a power-law spectrum for the velocity, which is not associated with a flux of a conserved quantity. The elastic turbulence case with Re $<< 1$ and We > 1, some simplifications are considered in the mathematical development. Finally, the inequality $\alpha > 3$ is proved.

In this work the logarithmic formulation is employed, it is crucial to treat the high Weissenberg number problem and obtain converged solutions. The formulation employed in this chapter has been already specified in Chapter 2. Moreover, time-dependent subgrid-scales are included in the finite element term-by-term stabilization approach, based on the Variational Multiscale (VMS) method [91] to obtain stable solutions. This allows us to avoid instabilities related with a small time step in relation with the spatial grid discretization, a common issue in viscoelastic flow formulations (see Chapter 4 for more details).

As a novelty, in this chapter fractional step schemes are designed and implemented to reduce the computational cost of solving the logarithmic formulation using a monolithic scheme. Equations are solved in a uncoupled way and using correction steps. Fractional step methods introduce an additional temporal error, that has to be at least of the order of the time integration scheme used to approximate time derivatives if this order is to be preserved.

The interest in fractional step methods applied to incompressible flows started with the works of Chorin [36] and Temam [158], who introduced fractional step methods at the continous level. However, in this chapter, fractional step methods are introduced at the purely algebraic level, when the equations have already been discretized in space and in time. In [8] and [81] we can find overviews of these strategies for the case of the incompressible Navier-Stokes equations for Newtonian fluids can be found. In the case of viscoelastic flows, the main difficulty is the appearance of the stress, a new variable that evolves in time. The uncoupling will need to satisfy two conditions: on the one hand the stability of the time discretization must be preserved together with the accuracy order. We have to stand out the work of Castillo et al. [27], which proposes a fractional step method following the option of the purely algebraic approach. In this case, apart from uncoupling the velocity from the pressure in the momentum equation, it is necessary to

uncoupled the elastic stress. In the literature, other fractional schemes have been reported for solving viscoelastic fluid flows, the most popular is the one known as the Θ-method, proposed first for Newtonian fluids in [75] and later extended to the viscoelastic fluid flow problem in [152] and [147].

This chapter will follow similar steps to the ones detailed in [27] for the standard formulation, but now applied to the logarithmic formulation, presenting two fractional step methods with first and second order splitting errors. In both cases, the first step is the momentum equation to compute an intermediate velocity that will be corrected later. However, while for the first order scheme the intermediate velocity is calculated without considering the pressure and the variable ψ, for the second order scheme extrapolated values for the pressure and the ψ variable are taken into account with the aim of improving the approximation of the intermediate velocity. With the second step we obtain the intermediate ψ values employing the intermediate velocity computed in the previous step. The third step has the structure of a discrete pressure Poisson equation, and the fourth and fifth steps correspond to the velocity and ψ correction step, respectively. Another interesting algebraic approach in fractional step methods is the interpretation of fractional step methods as an inexact LU factorization of the main matrix of the system, when this system has already been discretized. Some high order algebraic pressure segregation algorithms also could be designed following this point of view. In the literature we found [72], where the Navier-Stokes problem is solved applying this approach. This idea is also developed for the standard formulation of the viscoelastic problem in [27].

To summarize, the goal of this study is twofold: on the one hand, it is the design and implementation of a fractional step method with the aim of reducing the computational cost of the logarithmic formulation computations. In this sense, two different fractional methods are designed for the logarithmic formulation. The first order scheme is obtained from a straightforward segregation of the pressure and the variable ψ in the momentum equation. That is the main difference with the second order scheme, case in which a first order extrapolation of these variables is employed. The second objective is the computation of the purely elastic instabilities in the viscoelastic fluid flow by using all the tools presented.

This chapter is divided into different sections: The viscoelastic fluid flow written in the logarithmic formulation is introduced in Section 5.3. In Section 5.4 we detail the numerical approximation considered; Section 5.5 exposes the fractional step algorithm designed and Section 5.6 shows the final algebraic formulation including the stabilization. Some remarks concerning the linearized problem are presented in Section 5.7. Finally, in Section 5.8 the numerical results obtained are explained. The main conclusions of the chapter are discussed in Section 5.9.

5.3   The viscoelastic flow problem

5.3.1   Strong form

In this section, the viscoelastic fluid flow problem written in the logarithmic formulation is presented. As the contents are similar to those presented in section 2.3 in Chapter 2, only the most relevant aspects will be briefly summarized. Note that the logarithmic formulation one proposed there is slightly different to the one proposed originally by Fattal and Kupferman [64], and that the modification allows one to take $\lambda = 0$. Finally the strong form is defined by the system of equations (2.8)-(2.10), which can be found in Section 2.3.2.

5.3.2 Variational form

The variational form of the problem is explained in Section 2.3.3. Note that the definition of the main spaces and notation is established there. To indicate again the main operators of the problem, the weak form will be explicitly written again. Therefore, the weak form of the problem consists in finding $\boldsymbol{U} = [\boldsymbol{u}, p, \boldsymbol{\psi}] : (0, T) \longrightarrow \boldsymbol{\mathcal{X}} := \boldsymbol{V}_0 \times \boldsymbol{Q} \times \boldsymbol{\Upsilon}$, such that the initial conditions are satisfied and:

$$\mathcal{D}_{\mathrm{t}}(\boldsymbol{U}, \boldsymbol{V}) + B(\boldsymbol{u}; \boldsymbol{U}, \boldsymbol{V}) = L(\boldsymbol{V}), \tag{5.1}$$

where each term is defined as

$$\mathcal{D}_{\mathrm{t}}(\boldsymbol{U}, \boldsymbol{V}) = \left(\rho \frac{\partial \boldsymbol{u}}{\partial t}, \boldsymbol{v} \right) + \frac{\lambda}{2\lambda_0} \left(\frac{\partial \exp(\boldsymbol{\psi})}{\partial t}, \boldsymbol{\chi} \right), \tag{5.2}$$

$$B(\hat{\boldsymbol{u}}; \boldsymbol{U}, \boldsymbol{V}) = \frac{\eta_p}{\lambda_0} (\exp(\boldsymbol{\psi}), \nabla^s \boldsymbol{v}) + 2(\eta_s \nabla^s \boldsymbol{u}, \nabla^s \boldsymbol{v}) + \langle \rho \hat{\boldsymbol{u}} \cdot \nabla \boldsymbol{u}, \boldsymbol{v} \rangle - (p, \nabla \cdot \boldsymbol{v})$$

$$+ (\nabla \cdot \boldsymbol{u}, q) + \frac{1}{2\lambda_0} (\exp(\boldsymbol{\psi}), \boldsymbol{\chi}) - (\nabla^s \boldsymbol{u}, \boldsymbol{\chi})$$

$$+ \frac{\lambda}{2\lambda_0} \left(\boldsymbol{u} \cdot \nabla \exp(\boldsymbol{\psi}) - \exp(\boldsymbol{\psi}) \cdot \nabla \boldsymbol{u} - (\nabla \boldsymbol{u})^T \cdot \exp(\boldsymbol{\psi}) + 2\nabla^s \boldsymbol{u}, \boldsymbol{\chi} \right), \tag{5.3}$$

$$L(\boldsymbol{V}) = \langle \boldsymbol{f}, \boldsymbol{v} \rangle + \frac{1}{2\lambda_0} \langle \boldsymbol{I}, \boldsymbol{\chi} \rangle. \tag{5.4}$$

for all $\boldsymbol{V} = [\boldsymbol{v}, q, \boldsymbol{\chi}] \in \boldsymbol{\mathcal{X}}$.

5.4 Numerical approximation

5.4.1 Galerkin finite element discretization

Let $\mathcal{T}_h = \{K\}$ be a FE partition of the domain Ω. The diameter of an element $K \in \mathcal{T}_h$ is denoted by h_K and the diameter of the partition is defined as $h = \max\{h_K | K \in \mathcal{T}_h\}$. From $\mathcal{T}_h$ we may construct conforming FE spaces for the velocity, the pressure and the elastic stress, $\boldsymbol{\mathcal{V}}_h \subset \boldsymbol{\mathcal{V}}$, $\mathcal{Q}_h \subset \mathcal{Q}$, $\boldsymbol{\Upsilon}_h \subset \boldsymbol{\Upsilon}$, respectively. Calling $\boldsymbol{\mathcal{X}}_h := \boldsymbol{\mathcal{V}}_h \times \mathcal{Q}_h \times \boldsymbol{\Upsilon}_h$, the Galerkin FE approximation of the problem consists in finding $\boldsymbol{U}_h : (0, T) \longrightarrow \boldsymbol{\mathcal{X}}_h$, such that:

$$(\mathcal{D}_t(\boldsymbol{U}_h), \boldsymbol{V}_h) + B(\boldsymbol{u}_h; \boldsymbol{U}_h, \boldsymbol{V}_h) = L(\boldsymbol{V}_h), \tag{5.5}$$

for all $\boldsymbol{V}_h = [\boldsymbol{v}_h, q_h, \boldsymbol{\chi}_h] \in \boldsymbol{\mathcal{X}}_h$, and satisfying the appropriate initial conditions.

5.4.2 Monolithic time discretization

First of all we will detail the time discretization of problem (5.5) using a monolithic approach, that is to say, when all the components of $\boldsymbol{U}_h$ are solved at the same time. For the time discretization, we will employ classical backward difference (BDF) approximations. The details of the general scheme definition can be found in Section 2.3.6 in Chapter 2.

In the present section only the cases considered will be specified, i. e., $k = 1$ and 2. The BDF formulas re:

$$\frac{\delta_1 f^{n+1}}{\delta t} = \frac{f^{n+1} - f^n}{\delta t} = \left. \frac{\partial f}{\partial t} \right|_{t^{n+1}} + \mathcal{O}(\delta t).$$

$$\frac{\delta_2 f^{n+1}}{\delta t} = \frac{3}{2} \left(\frac{f^{n+1} - \frac{4}{3} f^n + \frac{1}{3} f^{n-1}}{\delta t} \right) = \left. \frac{\partial f}{\partial t} \right|_{t^{n+1}} + \mathcal{O}(\delta t^2).$$

In the case of the time-derivative of the exponential, considering the Taylor development for the following approximation (2.21), we obtain the approximation:

$$\frac{\partial \exp(\boldsymbol{\psi})}{\partial t}\bigg|_{t^{n+1}} = \frac{1}{\delta t}\Big[\exp(\hat{\boldsymbol{\psi}}^{n+1})\cdot\boldsymbol{\psi}^{n+1} + \exp(\hat{\boldsymbol{\psi}}^{n+1}) - \exp(\hat{\boldsymbol{\psi}}^{n+1})\cdot\hat{\boldsymbol{\psi}}^{n+1}$$
$$- \exp(\boldsymbol{\psi}^n)\Big] + \mathcal{O}(\delta t) + \mathcal{O}((\delta\boldsymbol{\psi}^{n+1})^2). \tag{5.6}$$

Analogously, for BDF2:

$$\frac{\partial \exp(\boldsymbol{\psi})}{\partial t}\bigg|_{t^{n+1}} = \frac{3}{2}\frac{1}{\delta t}\Big[\exp(\hat{\boldsymbol{\psi}}^{n+1})\cdot\boldsymbol{\psi}^{n+1} + \exp(\hat{\boldsymbol{\psi}}^{n+1}) - \exp(\hat{\boldsymbol{\psi}}^{n+1})\cdot\hat{\boldsymbol{\psi}}^{n+1}$$
$$- \frac{4}{3}\exp(\boldsymbol{\psi}^n) + \frac{1}{3}\exp(\boldsymbol{\psi}^{n-1})\Big] + \mathcal{O}(\delta t^2) + \mathcal{O}((\delta\boldsymbol{\psi}^{n+1})^2). \tag{5.7}$$

where $\hat{\boldsymbol{\psi}}^{n+1}$ stands for a previous guess of $\boldsymbol{\psi}^{n+1}$ that depends on the linearization scheme and $\delta\boldsymbol{\psi}^{n+1} = \boldsymbol{\psi}^{n+1} - \hat{\boldsymbol{\psi}}^{n+1}$. We will also use the extrapolation operators of order k, defined as $\hat{f}_k^{n+1} = f^{n+1} + \mathcal{O}(\delta t^k)$, which for $k = 1$ and 2 are given by

$$\hat{f}_1^{n+1} = f^n \tag{5.8}$$
$$\hat{f}_2^{n+1} = 2f^n - f^{n-1}. \tag{5.9}$$

Therefore, using BDF schemes, the time discretization of (5.5) can be written in expanded form as follows: for $n = 1, 2, ...$, find $[\boldsymbol{u}_h^{n+1}, p_h^{n+1}, \boldsymbol{\psi}_h^{n+1}] \in \boldsymbol{\mathcal{X}}_h$, such that

$$\left(\rho\frac{\delta_k \boldsymbol{u}_h^{n+1}}{\delta t}, \boldsymbol{v}_h\right) + \frac{\eta_p}{\lambda_0}(\exp(\boldsymbol{\psi}_h^{n+1}), \nabla^s \boldsymbol{v}_h) + 2(\eta_s \nabla^s \boldsymbol{u}_h^{n+1}, \nabla^s \boldsymbol{v}_h)$$
$$+ \langle \rho \boldsymbol{u}_h^{n+1}\cdot\nabla \boldsymbol{u}_h^{n+1}, \boldsymbol{v}_h\rangle - (p_h^{n+1}, \nabla\cdot\boldsymbol{v}_h) = \langle \boldsymbol{f}_h^{n+1}, \boldsymbol{v}_h\rangle, \tag{5.10}$$
$$(q_h, \nabla\cdot\boldsymbol{u}_h^{n+1}) = 0, \tag{5.11}$$
$$\left(\frac{1}{2\lambda_0}\exp(\boldsymbol{\psi}_h) - \nabla^s \boldsymbol{u}_h^{n+1}, \boldsymbol{\chi}_h\right) + \frac{\lambda}{2\lambda_0}\left(\frac{\delta_k \exp(\boldsymbol{\psi}_h)}{\delta t}, \boldsymbol{\chi}_h\right)$$
$$+ \frac{\lambda}{2\lambda_0}\left(\boldsymbol{u}_h^{n+1}\cdot\nabla\exp(\boldsymbol{\psi}_h^{n+1}) - \exp(\boldsymbol{\psi}_h^{n+1})\cdot\nabla\boldsymbol{u}_h^{n+1}, \boldsymbol{\chi}_h\right)$$
$$+ \frac{\lambda}{2\lambda_0}\left(-(\nabla\boldsymbol{u}_h^{n+1})^T\cdot\exp(\boldsymbol{\psi}_h^{n+1}) + 2\nabla^s \boldsymbol{u}_h^{n+1}, \boldsymbol{\chi}_h\right) = \frac{1}{2\lambda_0}\langle \boldsymbol{I}, \boldsymbol{\chi}_h\rangle, \tag{5.12}$$

for all $[\boldsymbol{v}_h, q_h, \boldsymbol{\chi}_h] \in \boldsymbol{\mathcal{X}}_h$.

5.4.3   Algebraic system

The problem defined by (5.10)-(5.12) is an algebraic system, considering the nodal unknowns of the finite element functions $[\boldsymbol{u}_h^{n+1}, p_h^{n+1}, \boldsymbol{\psi}_h^{n+1}] \in \boldsymbol{\mathcal{X}}_h$. Regarding the algebraic notation, the arrays of the nodal unknowns are expressed by upright case symbols: in bold case for the velocity $\boldsymbol{u}_h$ and the variable $\boldsymbol{\psi}_h$ and in light case for the pressure p_h. In the case of the tensor $\boldsymbol{\psi}$ we will use the well-known Voigt notation. Therefore the components of $\boldsymbol{\psi}_h$ at a node a will be written as Ψ_i^a, where i runs from 1 to 3 in a two-dimensional case and from 1 to 6 in a three-dimensional case. The superscript E in some matrices indicates that $\exp(\boldsymbol{\psi})$ computed in the previous iteration is employed for their calculation. The dependence of matrices $K_{\boldsymbol{u}}$ and $K_{\boldsymbol{\psi}}$ on $\mathbf{U}$ will be explicitly expressed. Taking into

account these considerations about notation, the algebraic structure of problem defined by equations (5.10)-(5.12) is as follows:

$$M_{\boldsymbol{u}}\frac{\delta_k}{\delta t}\mathbf{U}^{n+1} + K_{\boldsymbol{u}}\left(\mathbf{U}^{n+1}\right)\mathbf{U}^{n+1} + G\mathrm{P}^{n+1} - D_{\boldsymbol{\psi}}^{\mathrm{E}}\boldsymbol{\Psi}^{n+1} = \mathbf{F}_{\boldsymbol{u}}^{\mathrm{E}}, \qquad (5.13)$$

$$D\mathbf{U}^{n+1} = \mathbf{0}, \qquad (5.14)$$

$$M_{\boldsymbol{\psi}}^{\mathrm{E}}\frac{\delta_k}{\delta t}\boldsymbol{\Psi}^{n+1} + K_{\boldsymbol{\psi}}^{\mathrm{E}}\left(\mathbf{U}^{n+1}\right)\boldsymbol{\Psi}^{n+1} - S\mathbf{U}^{n+1} = \mathbf{F}_{\boldsymbol{\psi}}^{\mathrm{E}}. \qquad (5.15)$$

Lastly, the identification of the different terms in (5.10)-(5.12) that contribute to the matrices is straightforward. Moreover, system (5.13)-(5.15) can be written as follows:

$$\begin{bmatrix} A_{11} & A_{12} & A_{13} \\ A_{21} & A_{22} & 0 \\ A_{31} & 0 & 0 \end{bmatrix} \begin{bmatrix} \mathbf{U}^{n+1} \\ \boldsymbol{\Psi}^{n+1} \\ \mathrm{P}^{n+1} \end{bmatrix} = \begin{bmatrix} \mathbf{F}_1^{n+1} \\ \mathbf{F}_2^{n+1} \\ \mathrm{F}_3^{n+1} \end{bmatrix} \qquad (5.16)$$

where

$$A_{11} = \frac{1}{\gamma_k \delta t}M_{\boldsymbol{u}} + K_{\boldsymbol{u}}\left(\mathbf{U}^{n+1}\right), \qquad A_{12} = -D_{\boldsymbol{\psi}}^{\mathrm{E}},$$

$$A_{21} = -S, \qquad\qquad A_{22} = \frac{1}{\gamma_k \delta_K}M_{\boldsymbol{\psi}}^{\mathrm{E}} + K_{\boldsymbol{\psi}}^{\mathrm{E}}(\mathbf{U})^{n+1},$$

$$A_{13} = G, \qquad\qquad A_{31} = D,$$

$$\mathbf{F}_1 = \mathbf{F}_{\boldsymbol{u}}^{\mathrm{E}} + \frac{1}{\delta t\gamma_k}\left(\sum_{i=0}^{k-1}\varphi_k^i\mathbf{U}^{n-i}\right), \quad \mathrm{F}_3 = 0,$$

$$\mathbf{F}_2 = \mathbf{F}_{\boldsymbol{\psi}}^{\mathrm{E}} + \frac{1}{\delta t\gamma_k}\left(\sum_{i=0}^{k-1}\varphi_k^i\boldsymbol{\Psi}^{n-i}\right).$$

5.5 Fractional step method

In this section, we propose two fractional step methods following an extension of the schemes developed for the standard formulation of the viscoelastic fluid flow problem in [27]. At the same time, these methods can be understood as pressure-correction schemes applied to the viscoelastic fluid flow problem. In this case, we need a guess for the variable $\boldsymbol{\psi}$, apart from a guess for the velocity. After computing these fields, we will need to correct the velocity. Such as it is explained in [27], the main ideas could be used to design velocity-correction-type methods or momentum-pressure Poisson equation formulations, as in references [8, 43].

The approach explained here consists in the splitting at the pure algebraic level, as was explained in the background of this chapter (see also [132]). In particular we only present the extrapolation point of view: the main ideas referred to the inexact factorization are widely explained for the viscoelastic fluid flow problem in [27]. For the logarithmic formulation the methodology would be analogous.

The method presented here is a fractional step method using the extrapolation of the variables. The unknowns need to be segregated from an equation and then corrected. For the standard formulation, the variables to be extrapolated are the pressure and the stress in the momentum equation, to compute a velocity guess. In the logarithmic case, the variables extrapolated are also pressure, and now the variable $\boldsymbol{\psi}$ to obtain that velocity guess. The other variables are computed using this velocity guess and, at the end, we have to correct the velocity. Now, we will write the algebraic system defined in (5.13)-(5.15) in this equivalent form:

$$M_{\boldsymbol{u}}\frac{\delta_k}{\delta t}\tilde{\mathbf{U}}^{n+1} + K_{\boldsymbol{u}}\left(\tilde{\mathbf{U}}^{n+1}\right)\tilde{\mathbf{U}}^{n+1} + G\hat{\mathrm{P}}_{k'-1}^{n+1} - D_{\boldsymbol{\psi}}^{\mathrm{E}}\hat{\boldsymbol{\Psi}}_{k'-1}^{n+1} = \mathbf{F}_{\boldsymbol{u}}^{\mathrm{E}}, \quad (5.17)$$

$$M_{\boldsymbol{u}}\frac{\delta_k}{\delta t}\left(\mathbf{U}^{n+1}-\tilde{\mathbf{U}}^{n+1}\right)+N_{\boldsymbol{u}}+G\left(\mathrm{P}^{n+1}-\hat{\mathrm{P}}_{k'-1}^{n+1}\right)-D_{\boldsymbol{\psi}}^{\mathrm{E}}\left(\boldsymbol{\Psi}^{n+1}-\hat{\boldsymbol{\Psi}}_{k'-1}^{n+1}\right)=\mathbf{0}, \quad (5.18)$$

$$M_{\boldsymbol{\psi}}^{\mathrm{E}}\frac{\delta_k}{\delta t}\tilde{\boldsymbol{\Psi}}^{n+1}+K_{\boldsymbol{\psi}}^{\mathrm{E}}\left(\tilde{\mathbf{U}}^{n+1}\right)\tilde{\boldsymbol{\Psi}}^{n+1}-S\tilde{\mathbf{U}}^{n+1}=\mathbf{F}_{\boldsymbol{\psi}}^{\mathrm{E}}, \quad (5.19)$$

$$M_{\boldsymbol{\psi}}^{\mathrm{E}}\frac{\delta_k}{\delta t}\left(\boldsymbol{\Psi}^{n+1}-\tilde{\boldsymbol{\Psi}}^{n+1}\right)+\mathbf{N}_{\boldsymbol{\psi}}^{n+1}-S\left(\mathbf{U}^{n+1}-\tilde{\mathbf{U}}^{n+1}\right)=\mathbf{0}, \quad (5.20)$$

$$-D\tilde{\mathbf{U}}^{n+1}+\gamma_k\delta t D M_{\boldsymbol{u}}^{-1}\mathbf{N}_{\boldsymbol{u}}^{n+1}+\gamma_k\delta t D M_{\boldsymbol{u}}^{-1}G\left(\mathrm{P}^{n+1}-\hat{\mathrm{P}}_{k'-1}^{n+1}\right)$$
$$-\gamma_k\delta t D M_{\boldsymbol{u}}^{-1}D_{\boldsymbol{\psi}}^{\mathrm{E}}\left(\boldsymbol{\Psi}^{n+1}-\hat{\boldsymbol{\Psi}}_{k'-1}^{n+1}\right)=\mathbf{0}, \quad (5.21)$$

where

$$\mathbf{N}_{\boldsymbol{u}}^{n+1}=K_{\boldsymbol{u}}\left(\mathbf{U}^{n+1}\right)\mathbf{U}^{n+1}-K_{\boldsymbol{u}}\left(\tilde{\mathbf{U}}^{n+1}\right)\tilde{\mathbf{U}}^{n+1},$$

$$\mathbf{N}_{\boldsymbol{\psi}}^{n+1}=K_{\boldsymbol{\psi}}^{\mathrm{E}}\left(\mathbf{U}^{n+1}\right)\boldsymbol{\Psi}^{n+1}-K_{\boldsymbol{\psi}}^{\mathrm{E}}\left(\tilde{\mathbf{U}}^{n+1}\right)\tilde{\boldsymbol{\Psi}}^{n+1}.$$

In this set of equations, we have denoted $\tilde{\mathbf{U}}^{n+1}$ and $\tilde{\boldsymbol{\Psi}}^{n+1}$ as the auxiliary variables, in other words, the guess variables that later must be corrected. On the other hand we have denoted by $\hat{g}_{k'-1}^{n+1}$ the extrapolated variables, where the order of the extrapolation is indicated by the subscript $k'-1$ at time t^{n+1} of the function g (explained in Section 5.4.2 for the cases $k'-1=1,2$). In the case $k'-1=0$, $\hat{g}_0^{n+1}=0$ is taken. Moreover, the difference $\delta_k\tilde{g}^{n+1}$ is calculated using $\tilde{g}^{n+1}$ and g^m for time steps m previous to $n+1$, g now being either $\mathbf{U}$ or $\boldsymbol{\Psi}$. Equivalently to the scheme for the standard formulation developed in [27], we have now that adding up (5.17) and (5.18) we recover (5.13); also, adding up (5.19) and (5.20) we also recover (5.15). Finally equation (5.21) is recover multiplying (5.18) by $\gamma_k\delta t D M_{\boldsymbol{u}}^{-1}$ and using (5.14). Observe that the last equation (5.21) can be seen as a Poisson-type equation for the pressure. Note the difference between k and k': while the first indicates the order of the time integration, k' determines the order of the uncoupling of the variables that are extrapolated. The choice of these can be done independently, although a proper balance between them is required to achieve a certain order of the final approximation is needed. In our case we take $k'=k$, and the steps that we consider will be the following:

1. Compute $\tilde{\mathbf{U}}^{n+1}$ from (5.17).

2. Compute $\tilde{\boldsymbol{\Psi}}^{n+1}$ from (5.19).

3. Compute an approximation to P^{n+1} by solving (5.21), but neglecting the term $\mathbf{N}_{\boldsymbol{u}}^{n+1}$ and replacing $\boldsymbol{\Psi}^{n+1}$ by $\tilde{\boldsymbol{\Psi}}^{n+1}$.

4. Compute an approximation to $\mathbf{U}^{n+1}$ from (5.18) but neglecting $\mathbf{N}_{\boldsymbol{u}}^{n+1}$.

5. Compute an approximation to $\boldsymbol{\Psi}^{n+1}$ from (5.20) but neglecting $\mathbf{N}_{\boldsymbol{\psi}}^{n+1}$.

Following these steps, we obtain the fractional step method that allows us to uncouple the calculation of each variable. The following remarks are similar to the ones done for the standard formulation in [27], and briefly summarized here. On the one hand the matrix $DM_{\boldsymbol{u}}^{-1}G$ that appears in the equation (5.21) is approximated by the matrix resulting from the direct approximation of the Laplacian. Regarding the order of the scheme, it is of $\mathcal{O}(\delta t^k)$ for a given spatial discretization. If we assume that this is true up to time n and that the scheme is stable, and the approximation defined by (5.17)-(5.21), it follows that it is also true at time step $n+1$. Note that if the order of extrapolation is higher than $k-1$

$(k' > k)$, then the order of the error would be dominated by the time integration scheme. Also note that the scheme is stable for $k' = 1, 2$; in the case $k' = 3$ (not considered here) we would obtain $\hat{P}_2^{n+1} = 2P^n - P^{n-1}$ that is known to give an unstable scheme (for more details see [8], for example). On the other hand, while for $k = 1$ we obtain an extension to viscoelastic flows of the classical first order fractional step method, for $k = 2$ we obtain an extension of second order scheme that keeps the pressure gradient at the previous time step in the momentum equation. Lastly, as it was advanced, for the fractional step scheme of the logarithmic formulation we will need to do some remarks. Superscript E in matrices M_{ψ}^{E}, K_{ψ}^{E}, D_{ψ}^{E} indicates that the computation of the exponential of variable ψ at the previous iteration is required. Also, we have to consider the right-hand-side matrices $\mathbf{F}_{\boldsymbol{u}}^{\mathrm{E}}$ and $\mathbf{F}_{\psi}^{\mathrm{E}}$ that are computed to obtain the linearization of the exponential considered (see Section 2.4.3 for more details). In Algorithm 6, the schemes of first and second order are presented. Note that the sixth step is not necessary. It is written only with the aim of observing how the scheme can be understood as a inexact block LU-decomposition.

Algorithm 6 First and second order fractional schemes ($k = 1, 2$) for the logarithmic formulation.

---

1. **Compute the intermediate velocity** using pressure and ψ variable values extrapolated.

$$M_{\boldsymbol{u}}\frac{\delta_k}{\delta t}\tilde{\mathbf{U}}^{n+1} + K_{\boldsymbol{u}}\left(\tilde{\mathbf{U}}^{n+1}\right)\tilde{\mathbf{U}}^{n+1} + G\hat{\mathrm{P}}_{k'-1}^{n+1} - D_{\psi}^{\mathrm{E}}\hat{\boldsymbol{\Psi}}_{k'-1}^{n+1} = \mathbf{F}_{\boldsymbol{u}}^{\mathrm{E}} \longrightarrow \tilde{\mathbf{U}}^{n+1}$$

2. **Compute the intermediate ψ** using the intermediate velocity computed in the previous step.

$$M_{\psi}^{\mathrm{E}}\frac{\delta_k}{\delta t}\tilde{\boldsymbol{\Psi}}^{n+1} + K_{\psi}^{\mathrm{E}}\left(\tilde{\mathbf{U}}^{n+1}\right)\tilde{\boldsymbol{\Psi}}^{n+1} - S\tilde{\mathbf{U}}^{n+1} = \mathbf{F}_{\psi}^{\mathrm{E}} \longrightarrow \tilde{\boldsymbol{\Psi}}^{n+1}$$

3. **Compute the intermediate pressure** using both intermediate velocities and ψ computed in the two previous steps:

$$-D\tilde{\mathbf{U}}^{n+1} + \gamma_k\delta t DM_{\boldsymbol{u}}^{-1}\mathbf{N}_{\boldsymbol{u}}^{n+1} + \gamma_k\delta t DM_{\boldsymbol{u}}^{-1}G\left(\tilde{\mathrm{P}}^{n+1} - \hat{\mathrm{P}}_{k'-1}^{n+1}\right)$$
$$-\gamma_k\delta t DM_{\boldsymbol{u}}^{-1}D_{\psi}^{\mathrm{E}}\left(\tilde{\boldsymbol{\Psi}}^{n+1} - \hat{\boldsymbol{\Psi}}_{k'-1}^{n+1}\right) = \mathbf{0} \longrightarrow \tilde{\mathrm{P}}^{n+1}$$

4. **Compute the velocity correction**:

$$M_{\boldsymbol{u}}\frac{\delta_k}{\delta t}\left(\mathbf{U}^{n+1} - \tilde{\mathbf{U}}^{n+1}\right) + \mathbf{N}_{\boldsymbol{u}}^{n+1} + G\left(\tilde{\mathrm{P}}^{n+1} - \hat{\mathrm{P}}_{k'-1}^{n+1}\right)$$
$$-D_{\psi}^{\mathrm{E}}\left(\tilde{\boldsymbol{\Psi}}^{n+1} - \hat{\boldsymbol{\Psi}}_{k'-1}^{n+1}\right) = \mathbf{0} \longrightarrow \mathbf{U}^{n+1}$$

5. **Compute the ψ correction**:

$$M_{\psi}^{\mathrm{E}}\frac{\delta_k}{\delta t}\left(\boldsymbol{\Psi}^{n+1} - \tilde{\boldsymbol{\Psi}}^{n+1}\right) + \mathbf{N}_{\psi}^{n+1} - S\left(\mathbf{U}^{n+1} - \tilde{\mathbf{U}}^{n+1}\right) = \mathbf{0} \longrightarrow \boldsymbol{\Psi}^{n+1}$$

6. **Pressure correction**: $\mathrm{P}^{n+1} = \tilde{\mathrm{P}}^{n+1} \longrightarrow \mathrm{P}^{n+1}$

5.6   Stabilized finite element formulation

In this section we present the stabilization employed, based on the Variational Multiscale (VMS) methods. That is explained in Section 2.4. Two different considerations must be remarked about the stabilization considered for solving the cases included in this chapter.

The first one is that the stabilization considered for implementing the fractional scheme is of term-by-term type, which is described in Section 2.4.2. As it is explained there, this stabilization is not consistent but being shows optimal convergence in h. Apart from having a simpler stabilization due to the fact that there are less terms implied, it is proved in Chapter 2 that it is more robust solving problems with high stress gradients.

The second consideration is that also the dynamic subscales have been introduced in this approach, such as developed in Section 4.4.2 of Chapter 4. That allow us to face anisotropic space-time discretizations and also permits to solve more elastic problems as explained in Chapter 4. Therefore, in this section the stabilized finite element formulation will be briefly described, and solely the discrete equations will be written. Then, we will discuss the changes in the algebraic structure for the fractional step method.

5.6.1   Stabilized monolithic formulation

In general stabilized finite element methods consist in modifying the Galerkin discrete formulation by adding additional terms designed to enhance stability. The method proposed in this case replaces the finite element problem (5.5) by the following problem. The term-by-term stabilization proposed for the log-conformation formulation consists in finding $\boldsymbol{U}_h = [\boldsymbol{u}_h, p_h, \boldsymbol{\psi}_h] : (0, T) \longrightarrow \bar{\boldsymbol{\mathcal{X}}}_h$ such that

$$
\begin{aligned}
(\mathcal{D}_t(\boldsymbol{U}_h), \boldsymbol{V}_h) &+ B(\boldsymbol{u}_h; \boldsymbol{U}_h, \boldsymbol{V}_h) + \sum_K \langle \tilde{\boldsymbol{u}}_1, -\rho \boldsymbol{u}_h \cdot \nabla \boldsymbol{v}_h \rangle_K \\
&+ \sum_K \langle \tilde{\boldsymbol{u}}_2, -\nabla q_h \rangle_K + \sum_K \langle \tilde{\boldsymbol{u}}_3, \nabla \cdot \boldsymbol{\chi}_h \rangle_K + \sum_K \langle \tilde{p}, -\nabla \cdot \boldsymbol{v}_h \rangle_K \\
&+ \sum_K \left\langle \tilde{\boldsymbol{\sigma}}, \frac{1}{2\eta_p} \boldsymbol{\chi}_h + \nabla^s \boldsymbol{v}_h - \frac{\lambda}{2\eta_p} \left(\boldsymbol{u}_h \cdot \nabla \boldsymbol{\chi}_h + \boldsymbol{\chi}_h \cdot (\nabla \boldsymbol{u}_h)^T + \nabla \boldsymbol{u}_h \cdot \boldsymbol{\chi}_h \right) \right\rangle_K \\
&= \langle \boldsymbol{f}, \boldsymbol{v}_h \rangle,
\end{aligned}
\tag{5.22}
$$

for all $[\boldsymbol{v}_h, q_h, \boldsymbol{\sigma}_h] \in \boldsymbol{\mathcal{X}}_h$, where $\mathcal{D}_t$ is the operator which involves the time-dependent terms, defined in (5.2) and B is the form of the logarithm problem defined in (5.3). A term-by-term stabilization has several advantages in comparison with residual-type ones, for example it is more effective achieving converged solutions in the presence of strong gradients, an it is definitely more robust due to the fact that terms that do not give stability are neglected. Although this method is not consistent, it has an optimal convergence rate, as it was advanced previously.

In addition, an important remark is needed. For the fractional step methods described here, the Split-OSS method has been implemented for both, *quasistatic* and *dynamic* subscales. The time-dependent subscales or *dynamic* subscales applied to the viscoelastic fluid flow problem have been properly discussed and developed in Chapter 4, where the main advantages were enumerated.

Therefore, for expression (5.22) the sub-grid scales $\tilde{\boldsymbol{u}}_1$, $\tilde{\boldsymbol{u}}_2$, $\tilde{\boldsymbol{u}}_3$, $\tilde{p}$ and $\tilde{\boldsymbol{\sigma}}$ are computed in a different manner depending on whether they are time-dependent or not. In the case of considering *dynamic* subscales, they are the solution of the next evolution problems; however if the *quasistatic* approach is considered, the computation is straightforward,

neglecting the time-derivative of the subgrid-scales in each equation (5.23)-(5.27):

$$\rho\frac{\partial \tilde{\boldsymbol{u}}_1}{\partial t} + \alpha_1^{-1}\tilde{\boldsymbol{u}}_1 = -P_h^{\perp}\left[\rho\boldsymbol{u}_h \cdot \nabla\boldsymbol{u}_h\right], \tag{5.23}$$

$$\rho\frac{\partial \tilde{\boldsymbol{u}}_2}{\partial t} + \alpha_1^{-1}\tilde{\boldsymbol{u}}_2 = -P_h^{\perp}\left[\nabla p_h\right], \tag{5.24}$$

$$\rho\frac{\partial \tilde{\boldsymbol{u}}_3}{\partial t} + \alpha_1^{-1}\tilde{\boldsymbol{u}}_3 = P_h^{\perp}\left[\frac{\eta_p}{\lambda_0}\nabla \cdot \exp(\boldsymbol{\psi}_h)\right]. \tag{5.25}$$

$$\alpha_2^{-1}\tilde{p} = -P_h^{\perp}\left[\nabla \cdot \boldsymbol{u}_h\right], \tag{5.26}$$

$$\frac{\lambda}{2\eta_p}\frac{\partial \tilde{\boldsymbol{\sigma}}}{\partial t} + \alpha_3^{-1}\tilde{\boldsymbol{\sigma}} = P_h^{\perp}\left[-\frac{1}{2\lambda_0}\exp(\boldsymbol{\psi}_h) + \nabla^s\boldsymbol{u}_h\right.$$
$$-\frac{\lambda}{2\lambda_0}\left(\frac{\partial \exp(\boldsymbol{\psi}_h)}{\partial t} + \boldsymbol{u}_h \cdot \nabla \exp(\boldsymbol{\psi}_h)\right)$$
$$\left.+\frac{\lambda}{2\lambda_0}\left(\exp(\boldsymbol{\psi}_h) \cdot \nabla\boldsymbol{u}_h + (\nabla\boldsymbol{u}_h)^T \cdot \exp(\boldsymbol{\psi}_h) - 2\nabla^s\boldsymbol{u}_h\right)\right] \tag{5.27}$$

Parameters α_i, $i = 1, 2, 3$ are the stabilization terms, already defined in (2.30)-(2.32). Note that P_h denotes the L^2 projection onto the appropriate finite element space, without considering boundary conditions. Also $P_h^{\perp} = I - P_h$ is the orthogonal projection, where I is the identity. Regarding the discretization of the equations of the dynamic sub-grid scales, a BDF1 scheme is employed as follows (see Section 4.4.3 for more details):

$$\tilde{\boldsymbol{u}}_1^{n+1} = \left(\rho\frac{1}{\delta t} + \frac{1}{\alpha_1^{n+1}}\right)^{-1}\left(\rho\frac{1}{\delta t}\tilde{\boldsymbol{u}}_1^n - \rho P_h^{\perp}\left[\boldsymbol{u}_h^{n+1} \cdot \nabla\boldsymbol{u}_h^{n+1}\right]\right),$$

$$\tilde{\boldsymbol{u}}_2^{n+1} = \left(\rho\frac{1}{\delta t} + \frac{1}{\alpha_1^{n+1}}\right)^{-1}\left(\rho\frac{1}{\delta t}\tilde{\boldsymbol{u}}_2^n - P_h^{\perp}\left[\nabla p_h^{n+1}\right]\right),$$

$$\tilde{\boldsymbol{u}}_3^{n+1} = \left(\rho\frac{1}{\delta t} + \frac{1}{\alpha_1^{n+1}}\right)^{-1}\left(\rho\frac{1}{\delta t}\tilde{\boldsymbol{u}}_3^n + P_h^{\perp}\left[\frac{\eta_p}{\lambda_0}\nabla \cdot \exp(\boldsymbol{\psi}_h^{n+1})\right]\right),$$

$$\tilde{\boldsymbol{\sigma}}^{n+1} = \left(\frac{\lambda}{2\eta_p}\frac{1}{\delta t} + \frac{1}{\alpha_3^{n+1}}\right)^{-1}\left(\frac{\lambda}{2\eta_p}\frac{1}{\delta t}\tilde{\boldsymbol{\sigma}}^n + P_h^{\perp}\left[-\frac{1}{2\lambda_0}\exp(\boldsymbol{\psi}_h^{n+1}) + \nabla^s\boldsymbol{u}_h^{n+1}\right.\right.$$
$$-\frac{\lambda}{2\lambda_0}\left(\frac{\delta_k \exp(\boldsymbol{\psi}_h^{n+1})}{\delta t} + \boldsymbol{u}_h^{n+1} \cdot \nabla \exp(\boldsymbol{\psi}_h^{n+1})\right)$$
$$\left.\left.+\frac{\lambda}{2\lambda_0}\left(\exp(\boldsymbol{\psi}_h^{n+1}) \cdot \nabla\boldsymbol{u}_h^{n+1} + (\nabla\boldsymbol{u}_h^{n+1})^T \cdot \exp(\boldsymbol{\psi}_h^{n+1}) - 2\nabla^s\boldsymbol{u}_h^{n+1}\right)\right]\right).$$

From these expressions, we can conclude that the sub-grid scales depend directly on $\alpha_{1\mathrm{dyn}} = \left(\rho\frac{1}{\delta t} + \frac{1}{\alpha_1}\right)^{-1}$ and $\alpha_{3\mathrm{dyn}} = \left(\frac{\lambda}{2\eta_p}\frac{1}{\delta t} + \frac{1}{\alpha_3}\right)^{-1}$, where $\alpha_{1\mathrm{dyn}}$ and $\alpha_{3\mathrm{dyn}}$ redefine the classical stabilitation parameters and now depend on the time-step size. The time discretization of (5.22) can be performed as for the Galerkin method, in other words, using BDF schemes of order k, partial time derivatives have to be replaced by $\delta_k/\delta t$ and all unknowns need to be evaluated at time step $n + 1$.

5.6.2 Algebraic formulation and fractional step scheme

From the expression (5.22), we can now define the algebraic system to solve at each time step considering the stabilization term as:

$$
\begin{bmatrix} A_{s,11} & A_{s,12} & A_{13} \\ A_{s,21} & A_{s,22} & 0 \\ A_{31} & 0 & A_{s,33} \end{bmatrix} \begin{bmatrix} \mathbf{U}^{n+1} \\ \boldsymbol{\Psi}^{n+1} \\ \mathrm{P}^{n+1} \end{bmatrix} = \begin{bmatrix} \mathbf{F}^{n+1}_{s,1} \\ \mathbf{F}^{n+1}_{s,2} \\ \mathrm{F}^{n+1}_{s,3} \end{bmatrix} \tag{5.28}
$$

The subscript s indicates the matrices that have contributions from the stabilization terms. Also, note that if time-dependent subscales are considered we have to include the contribution of the subgrid-scale of the previous time step that comes from the BDF1 scheme employed for the discretization of the equations of the dynamic sub-grid scales. Comparing this expression (5.28) with the algebraic structure of the Galerkin approach (5.16), we can find the presence of the term $A_{s,33}$, which comes from the stabilization term of the pressure introduced by the expression given by $\tilde{\boldsymbol{u}}_2$, $\sum_K \alpha_1 \left\langle P_h^\perp [\nabla p_h], q_h \right\rangle$. Regarding matrices A_{13} and A_{31} of the Galerkin method; they remain unaltered due to the term-by-term stabilization chosen and the use of orthogonal projections.

On the other hand, neither the time derivative of the velocity nor the time derivative of $\exp(\boldsymbol{\psi})$ appear in the stabilization terms; therefore matrices $M_{\boldsymbol{u}}$ and $M_{\boldsymbol{\psi}}$, which are symmetric and positive definite, are the only matrices is multiplied by $1/\delta t$ in (5.28). However, if the time-dependent sub-grid scales are employed, then the factor $1/\delta t$ also appears in the computation of the stabilization parameters, and in the right-hand-side of the system due to the discretization of the subscales.

The fractional step methods proposed for the Galerkin method can be easily extended to the stabilized finite element method. The major difference is that now the matrices have contributions of the stabilization terms and the contribution to the discrete equation for the pressure.

Algorithm 7 First and second order fractional schemes ($k = 1, 2$) for the logarithmic formulation with dynamic subscales.

1. **Compute the intermediate velocity** using pressure and $\boldsymbol{\psi}$ variable values extrapolated.

$$
M_{\boldsymbol{u}} \frac{\delta_k}{\delta t} \tilde{\mathbf{U}}^{n+1} + K_{s,\boldsymbol{u}} \left(\tilde{\mathbf{U}}^{n+1} \right) \tilde{\mathbf{U}}^{n+1} + G\hat{\mathrm{P}}^{n+1}_{k'-1} - D^{\mathrm{E}}_{s,\boldsymbol{\psi}} \hat{\boldsymbol{\Psi}}^{n+1}_{k'-1} = \mathbf{F}^{\mathrm{E}}_{s,\boldsymbol{u}} + \tilde{\mathbf{F}}_{\boldsymbol{u}}
$$
$$
\longrightarrow \tilde{\mathbf{U}}^{n+1}
$$

2. **Compute the intermediate $\boldsymbol{\psi}$** using the intermediate velocity computed in the previous step.

$$
M^{\mathrm{E}}_{\boldsymbol{\psi}} \frac{\delta_k}{\delta t} \tilde{\boldsymbol{\Psi}}^{n+1} + K^{\mathrm{E}}_{s,\boldsymbol{\psi}} \left(\tilde{\mathbf{U}}^{n+1} \right) \tilde{\boldsymbol{\Psi}}^{n+1} - S_s \tilde{\mathbf{U}}^{n+1} = \mathbf{F}^{\mathrm{E}}_{s,\boldsymbol{\psi}} + \tilde{\mathbf{F}}_{\boldsymbol{\psi}} \longrightarrow \tilde{\boldsymbol{\Psi}}^{n+1}
$$

3. **Compute the intermediate pressure** using both intermediate velocities and $\boldsymbol{\psi}$ computed in the two previous steps:

$$
-D\tilde{\mathbf{U}}^{n+1} + L_s^\perp \tilde{\mathrm{P}} + \gamma_k \delta t D M_{\boldsymbol{u}}^{-1} \mathbf{N}^{n+1}_{\boldsymbol{u}} + \gamma_k \delta t D M_{\boldsymbol{u}}^{-1} G \left(\tilde{\mathrm{P}}^{n+1} - \hat{\mathrm{P}}^{n+1}_{k'-1} \right)
$$
$$
- \gamma_k \delta t D M_{\boldsymbol{u}}^{-1} D^{\mathrm{E}}_{\boldsymbol{\psi}} \left(\tilde{\boldsymbol{\Psi}}^{n+1} - \hat{\boldsymbol{\Psi}}^{n+1}_{k'-1} \right) = \mathbf{0} \longrightarrow \tilde{\mathrm{P}}^{n+1}
$$

4. **Compute the velocity correction**:

$$M_{\boldsymbol{u}}\frac{\delta_k}{\delta t}\left(\mathbf{U}^{n+1} - \tilde{\mathbf{U}}^{n+1}\right) + \mathbf{N}_{\boldsymbol{u}}^{n+1} + G\left(\tilde{\mathbf{P}}^{n+1} - \hat{\mathbf{P}}_{k'-1}^{n+1}\right)$$
$$- D_{\boldsymbol{\psi}}^{\mathrm{E}}\left(\tilde{\boldsymbol{\Psi}}^{n+1} - \hat{\boldsymbol{\Psi}}_{k'-1}^{n+1}\right) = \mathbf{0} \longrightarrow \mathbf{U}^{n+1}$$

5. **Compute the ψ correction**:

$$M_{\boldsymbol{\psi}}^{\mathrm{E}}\frac{\delta_k}{\delta t}\left(\boldsymbol{\Psi}^{n+1} - \tilde{\boldsymbol{\Psi}}^{n+1}\right) + \mathbf{N}_{\boldsymbol{\psi}}^{n+1} - S\left(\mathbf{U}^{n+1} - \tilde{\mathbf{U}}^{n+1}\right) = \mathbf{0} \longrightarrow \boldsymbol{\Psi}^{n+1}$$

6. **Pressure correction**: $\mathrm{P}^{n+1} = \tilde{\mathrm{P}}^{n+1} \longrightarrow \mathrm{P}^{n+1}$

5.7   Linearized problem

As the equations to be solved are strongly nonlinear, an iterative scheme is required to deal with these non-linearities. Moreover, it is important to remark the treatment made for the orthogonal projections $P_h^{\perp}$:

- A fixed-point-type method is employed to evaluate the stabilization terms. They are calculated using a known velocity $\boldsymbol{u}_h$ for the convective terms and $\boldsymbol{\psi}_h$ for the exponential terms. Those variables are taken either from the previous iteration of the iterative scheme (in case of computing the intermediate or the final steps) or directly from the previous time step. Note that that does not affect the order of convergence.

- The non-linearity in $K_{s,\boldsymbol{u}}\left(\tilde{\mathbf{U}}^{n+1}\right)\tilde{\mathbf{U}}^{n+1}$ can be treated using either a fixed-point or a Newton-Raphson scheme. Due to the fact that the δt must be taken small for fractional step schemes in comparison with the monolithic ones, few iterations are needed to converge. Note also that term $K_{s,\boldsymbol{\psi}}^{\mathrm{E}}\left(\tilde{\mathbf{U}}^{n+1}\right)\tilde{\boldsymbol{\Psi}}^{n+1}$ does not need to be linearized with respect to the velocity variable, due to the fact that the intermediate velocity being known from the first step.

- Regarding the exponential terms, note that the linearization based in Taylor's expansion is considered (see Section 2.3.4). The terms $-D_{s,\boldsymbol{\psi}}^{\mathrm{E}}\hat{\boldsymbol{\Psi}}_{k'-1}^{n+1}$ and $\mathbf{F}_{s,\boldsymbol{u}}^{\mathrm{E}}$ located on the first step do not need to be linearized since in that case the variable $\hat{\boldsymbol{\Psi}}_{k'-1}^{n+1}$ being extrapolated and, therefore, it is a known value. Also, the terms computed in the second step that involve $K_{s,\boldsymbol{\psi}}^{\mathrm{E}}\left(\tilde{\mathbf{U}}^{n+1}\right)\tilde{\boldsymbol{\Psi}}^{n+1}$ and $\mathbf{F}_{s,\boldsymbol{\psi}}^{\mathrm{E}}$, are computed using a fixed point scheme method.

- Also, the treatment of the orthogonal projection $P_h^{\perp}$ must be detailed. For a function f, we compute $P_h^{\perp}[f] = f - P_h[f]$, and the matrices resulting from the orthogonal projection of the unknowns have a "wider stencil", when compared with that of the Galerkin method. To avoid that, the i-th iteration of n-th time step can be approximated as $P_h^{\perp}[f] \approx f^{n,i} - P_h\left[f^{n,i-1}\right]$ (evaluating the projection in the unknown function f in the previous iteration) or $P_h^{\perp}[f] \approx f^{n,i} - P_h\left[f^{n-1}\right]$ (evaluating the projection in f at the previous time step).

5.8   Numerical results

Some numerical examples will be presented in this section where the fractional step method for the logarithmic formulation is applied. First we test the scheme to validate the effectiveness. Then we apply the fractional scheme to study the pure elastic instability. The first result presented in Section 5.8.1 is a convergence test that will show the accuracy of the formulation for the two different schemes. It is important to show that the designed scheme is optimally convergent for smooth solutions. In the second example, developed in Section 5.8.2, the benefits of the fractional step in comparison with a monolithic scheme are explored for a case with a high elasticity. In that case we consider the lid-driven cavity problem presented in Chapter 4. The main objective is to check solutions using different schemes and time rates employed. In Section 5.8.3 the array of cylinders case is studied, where the flow has a temporal response when the Weissenberg number is high enough. This instability, as reported in the introduction of this chapter, is known as the pure elastic instability. For a certain Weissenberg number, the fluid flow can become chaotic, the phenomenon known as elastic turbulence.

5.8.1   Convergence test

This convergence study has been carried out for the logarithmic formulation to test the designed and implemented fractional step scheme. The domain considered is a unit square, using a uniform structured mesh discretized by 625 bilinear elements. Regarding the boundary and the initial conditions, they are prescribed according to the time-dependent analytical solution:

$$
\begin{aligned}
u_x(x,y) &= (4x+6)f(t), & \psi_{xx}(x,y) &= (2x+3)f(t), \\
u_y(x,y) &= -(4y-6)f(t), & \psi_{yy}(x,y) &= (2y+3)f(t), \\
p(x,y) &= xf(t), & \psi_{xy}(x,y) &= (x+y)f(t),
\end{aligned}
$$

where the x and y components of the velocity and the stress tensor have been indicated with a subscript, and $f(t) = \cos(4\pi t)\exp(-t)$. Note that this manufactured solution belongs to the finite element space, therefore the spatial error is negligible; thus the error measured corresponds uniquely to the temporal scheme. These velocity, pressure and ψ fields do not satisfy the momentum and constitutive equation. Therefore we have to add a some forcing terms in the equations in the domain Ω:

$$
\begin{aligned}
\boldsymbol{f}_{\mathrm{mom}} &= \rho\frac{\partial \boldsymbol{u}}{\partial t} - \frac{\eta_p}{\lambda_0}\nabla\cdot\exp(\boldsymbol{\psi}) - 2\eta_s\nabla\cdot(\nabla^{\mathrm{s}}\boldsymbol{u}) + \rho\boldsymbol{u}\cdot\nabla\boldsymbol{u} + \nabla p \\
\boldsymbol{f}_{\mathrm{cont}} &= \nabla\cdot\boldsymbol{u} \\
\boldsymbol{f}_{\mathrm{cons}} &= \frac{1}{2\lambda_0}(\exp(\boldsymbol{\psi}) - \boldsymbol{I}) - \nabla^{\mathrm{s}}\boldsymbol{u} + \frac{\lambda}{2\lambda_0}\Big(\frac{\partial\exp(\boldsymbol{\psi})}{\partial t} \\
&\quad + \boldsymbol{u}\cdot\nabla\exp(\boldsymbol{\psi}) - \exp(\boldsymbol{\psi})\cdot\nabla\boldsymbol{u} - (\nabla\boldsymbol{u})^T\cdot\exp(\boldsymbol{\psi}) + 2\nabla^{\mathrm{s}}\boldsymbol{u}\Big)
\end{aligned}
$$

The BDF1 and BDF2 schemes are selected for time integration, using time-dependent subgrid scales and the Split-OSS stabilized formulation. The results are plotted in Figure 5.1, in which the first column shows the results using BDF1 for each variable of the problem and in the second column the errors corresponding to the BDF2 scheme are displayed. The time step size for BDF1 ranges from $\delta t = 1.6\cdot 10^{-4}$ to $\delta t = 2.5\cdot 10^{-3}$; for BDF2, the time step size goes from $\delta t = 6.25\cdot 10^{-4}$ to $\delta t = 10^{-2}$. Concerning the optimal convergence rate expected it is, in the case of a first order scheme, of 1 in velocity and ψ and 0 for

pressures; in case of the second order scheme. These optimal convergence rates is 2 for the velocity and ψ, and 1 for the pressure field. That optimal convergence rates are displayed together with the different $\ell^\infty(L^2(\Omega))$-errors for each time step size in the graphs shown in Figure 5.1. In all cases the optimal convergence is reached.

5.8.2 Lid-driven cavity flow problem

The lid-driven cavity flow problem is a good example to show the performance and benefits of the fractional step scheme in contrast with a monolithic iterative scheme. Moreover, the benefits of using the dynamic sub-grid scales in the fractional step case will be highlighted.

Setup

The problem consists in a fluid confined in a unit square. Two different cases will be tested in this section: the first one is considering Re $= 0$, whose solution is stationary, and the second is a forced dynamic case with Re $= 100$. All the boundaries are considered solid walls with exception of the top boundary (see the scheme of Figure 5.2). For the case with Re $= 0$, the velocity will be prescribed in the boundary (Γ_{top}), as:

$$u_x(x, 1, t) = 8 \left[1 + \tanh \left(8 \left(t - \frac{1}{2} \right) \right) \right] x^2 (1 - x)^2,$$
$$u_y(x, 1, t) = 0,$$

The hyperbolic tangent permits a smooth transition from 0 at $t = 0$ to, 1 for $t > \frac{1}{2}$ at $x = \frac{1}{2}$. In the Γ_{wall} the velocity is fixed to zero in both components. Concerning the elastic stress tensor conditions, they do not need to be prescribed in this case. For the dynamic case with Re $= 100$, in the boundary (Γ_{top}) the horizontal velocity is chosen as:

$$u_x(x, 1, t) = 16x^2 (1 - x)^2 \sin(\pi t),$$
$$u_y(x, 1, t) = 0.$$

Note that the sin function forces a time-dependent solution. In both cases, the characteristic velocity to compute the dimensionless numbers is taken as the maximum lid velocity, and the characteristic length is set to 1, which is the length of each side of the square. The Weissenberg numbers studied are We $= 0.5$ and We $= 1$. The spatial discretization considered is formed by 10 000 bilinear Q1 elements for the finest mesh (100×100) and 1225 for the coarse mesh (35×35). In all the cases the time discretization employed is the BDF2, scheme and the time step considered is $\delta t = 0.0025$. Moreover, the Split-OSS together with the use of dynamic sub-grid scales is used as stabilization for all the computations.

Comparing monolithic and fractional step schemes

The finality of this case is the study of the solution using both schemes: the monolithic one and the fractional step scheme to compare robustness, accuracy, computational times and number of internal iterations. Firstly the solution of the static case (Re $= 0.0$) is analysed. Observe that in our computation neither continuation iterative methods nor additional sub-relaxation schemes have been used to improve the convergence of the scheme. The robustness of the methods using different scenarios are analyzed in Table 5.1, on the one hand using monolithic or fractional step schemes, secondly using the standard or the logarithmic formulation and thirdly considering dynamic or quasistatic sub-grid scales. All these cases have been analyzed for a coarse mesh and We $= 0.5$. As shown in Chapter
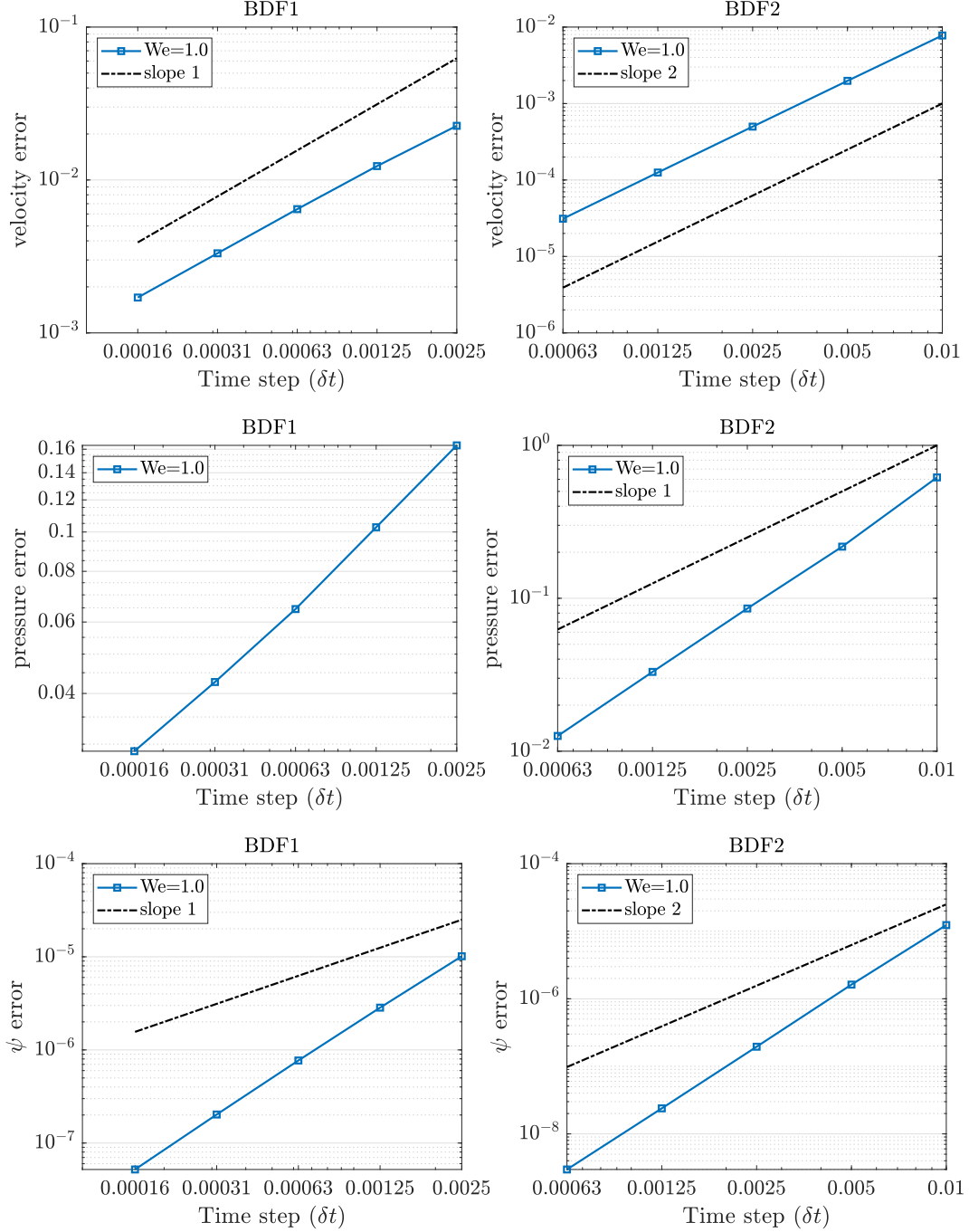
Figure 5.1: Convergence test. Discrete $\ell^\infty(L^2(\Omega))$-errors for velocity, pressure and $\boldsymbol{\psi}$ fields using BDF1 and BDF2 schemes for the fractional step using the logarithmic formulation.
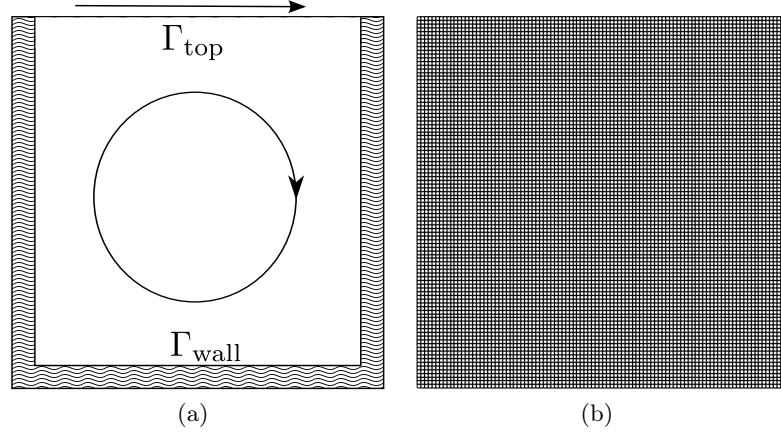
Figure 5.2: Lid-driven cavity. Schematic representation of computational boundaries (a) and computational mesh (b).

		Stabilization S-OSS	
Scheme	**Formulation**	Quasi-static	Dynamic
Monolithic	Standard	Failed - time step 310	Failed - time step 1840
Monolithic	Logarithmic	Failed - time step 450	Solved
Fractional Step	Standard	Failed - time step 692	Failed - time step 1781
Fractional Step	Logarithmic	Failed - time step 593	Solved

Table 5.1: Lid-driven cavity. Comparison between different formulations and schemes with We = 0.5, Re = 0, $\delta t = 0.0025$ considering a mesh of 35×35. The time step at which convergence fails is indicated in each case.

4, the combination between logarithmic and time-dependent sub-grid scales is the only combination which permits to obtain a converged solutions and that is achieved in both monolithic and fractional step schemes. In all cases the tolerance to reach to the steady state is 10^{-5}. The remaining combinations suffer a breakdown in a particular time step, which is indicated also in the table. This instability is not originated by a small time step in relation with the mesh used; only the elasticity (translated to the Weissenberg number) is the unique cause that produces this breakdown.

In Figure 5.3, cuts in $y = 3/4$ for the second component of the velocity (a) and for ψ_{xy} (b) are displayed with the objective of comparing results obtained using the two schemes for We = 0.5 and We = 1.0 considering the stationary solution when Re = 0.0. In addition, a comparison with other works as [65] was carried out for We = 1.0. Results are very close, almost identical, between the two schemes although some little discrepancy is found in comparison with the literature. Another comparison between the two schemes is performed in Figure 5.4 in this case the evolution in time of two different points close to the top boundary, in particular Point 1 which has coordinates (0.12, 0.98) and Point 2 (0.87, 0.98). In both points the evolution in time of the module of the components of the variable ψ is potted. Again, we can observe as the same tracking evolution is recorded for both schemes, ensuring good accuracy of the fractional step scheme.

Now, a table comparing the monolithic time integrator against the fractional step scheme will be presented for two different cases studied in this section. This is shown in Table 5.2. The quotient between the CPU time using the fractional step scheme over the
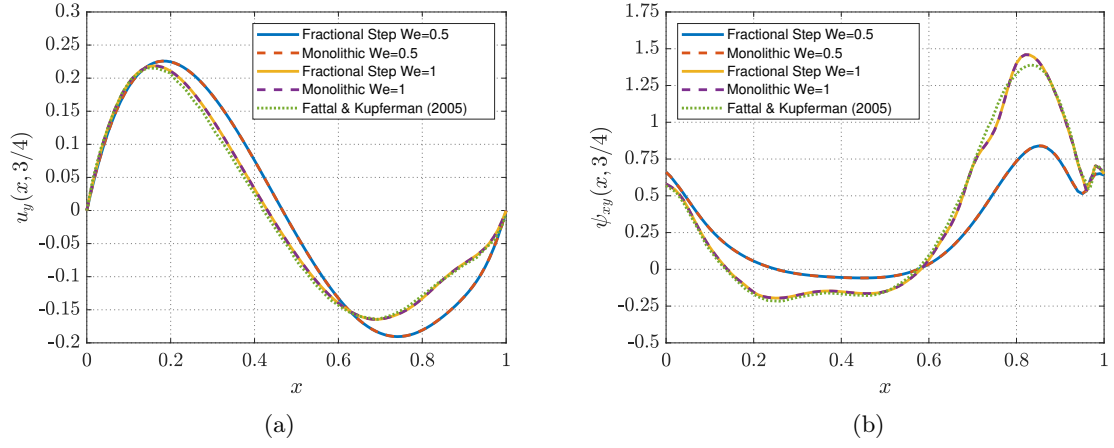
Figure 5.3: Lid-driven cavity. Result at time $t = 8$, Re $= 0.0$, We $= 1$ along the line $y = 3/4$.
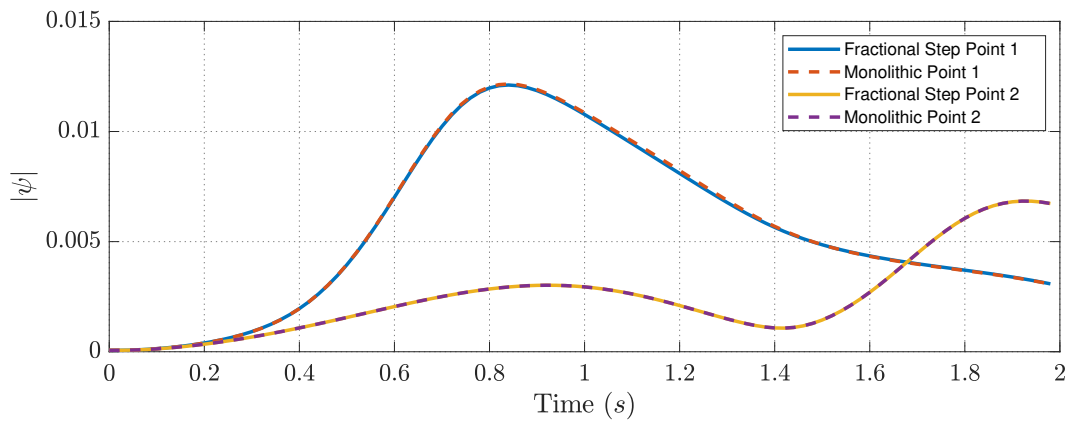

Figure 5.4: Lid-driven cavity. Evolution in time for the ψ field in two different points. Point 1=(0.12 , 0.98); Point 2=(0.87 , 0.98). Re $= 100$, We $= 1$.

Case	Total time ratio	Solver time ratio
We=0.5, Re=0.0	0.48	0.10
We=1.0, Re=100	0.49	0.07

Table 5.2: Lid-driven cavity. Ratio CPU time. Computational mesh 100×100.

	Monolithic	Fractional Step		
Case	$\overline{\text{nni}}$ / $\overline{\text{nsi}}$	$\overline{\text{nni}}_u$ / $\overline{\text{nsi}}_u$	$\overline{\text{nni}}_\psi$ / $\overline{\text{nsi}}_\psi$	$\overline{\text{nsi}}_p$
We=0.5, Re=0.0	7 / 31	8 / 14	2 / 3	98
We=1.0, Re=100	4 / 28	4 / 5	2 / 2	91

Table 5.3: Lid-driven cavity. Average of number of iterations of the monolithic and fractional step algorithms. Computational mesh 100×100.

CPU time spent in the monolithic approach is calculated, to determine the computational savings. Note that for the comparison, a sequential implementation has been used in all cases to avoid discrepancies derived from a parallel computation. Results presented in this table have two columns: on the one hand we show the total CPU time needed by the algorithm and on the other, the time employed by the solver to obtain the solution once the system is built. The savings in CPU time are remarkable, achieving an approximately reduction of 50% of the total time and around 90-93% in the solver time for the cases explored.

In Table 5.3 the number of iterations required in each case is summarized: on the one hand the number of iterations required by the solver to obtain the solution of the system and, on the other, the number of nonlinear internal iterations to obtain converged results. We denote by $\overline{\text{nni}}$ the average number of nonlinear iterations to reach convergence and $\overline{\text{nsi}}$ the average number of iterations required by the solver. In these examples, the number of iterations needed in the monolithic case is greater for the linear solver. The subsystems for each step in case of the fractional step scheme are smaller and better conditioned, and consequently it is translated into a reduction of the number of iterations required. In our examples we have used the same solver for all subsystems. Also, the solver iterations in momentum and constitutive equations is significantly smaller than for the pressure equation. That is a general trend in Newtonian flows and not specific of our problem.

5.8.3   Array of cylinders

The array of cylinders problem has been reported in the literature to present a elastic instability from a critical Weissenberg number. However, it has also received considerable attention since some years ago [71, 99] due to the wide range of engineering applications of polymeric flow in a porous media. The physical experiments which use the periodic array demonstrated an increment of the flow resistance derived from the presence of polymer [35, 164]. Furthermore, the flow through that array is well-known as a complex problem, since it involves a mixture of elongational and shear flow behavior. The first studies considered an infinite array in both the lateral and axial directions in order to do the wall effects negligible. The viscoelastic case [96] considered the channel obstructed by two rows of cylinders, proving that the resistance of the flow monotonically decreased with the flow rate. In the work of Skarsis et al. [153] the Deborah number is defined based on the shear-rate-dependent relaxation time and the average flow rate across the minimum gap. Due to the Reynolds number being significant small (of order of 10^{-10}), the increased
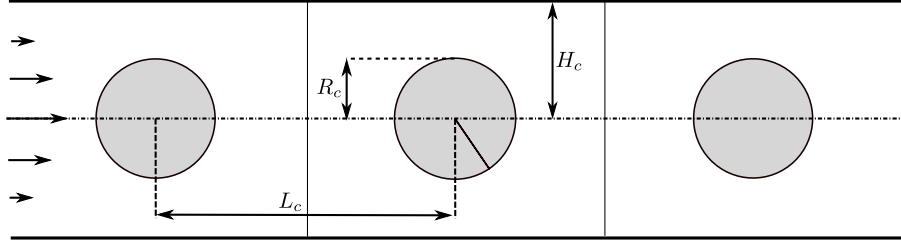
Figure 5.5: Array of cylinders. Schematic representation of the geometry.

pressure drop was only a consequence of the elasticity of the fluid. Moreover, in the work of Chmielewski et al. [33, 34] shown as the pressure fluctuations at some critical De were observed. That indicated the presence of a flow instability, and confirmed the development of unsteady flow patterns. Finally, it was concluded that the increase in the flow resistance corresponds to the amplitude in the time-dependence and asymmetry in the solution.

In this section three different works will be taken as reference. The first one is that corresponding to Liu et al. [111], in which the problem in widely studied using three different models: Giesekus, FENE-P and Chilcott-Rallison (CR), although the flow and stress fields predicted by the three constitutive models are similar. In this chapter, several situations are considered, as different separation length between cylinders, and different Weissenberg numbers. The distribution of the main fields and the values adopted by the drag force were studied. This work will be useful to validate the algorithm proposed.

The second and third are the works papers of Grilli et al. [77] and [163], in which the transition to the elastic instability is investigated. In these two papers, the Lagrangian framework is used, in particular the Smoothed Particle Hydrodynamics (SPH) method [74], which is a meshless technique where a set of ordinary differential equations are solved for discrete elements of fluid (particles). This example is studied using the Oldoyd-B constitutive equation, the same that we will employ in this work.

Setup

The computational geometry in this case is reported in Figure 5.5, where the radius of each cylinder is $R_c = 1$, and is placed on the center line of a two-dimensional channel with half-height $H_c = 2$. The fluid that flows between the channel is driven by a constant body force F. The spatial period considered between cylinders is taken as $L_c = 6$ and $L_c = 2.5$. Concerning the computational mesh, it is unstructured, composed by Q1 elements, with a refinement close to the cylinder, as it is shown in Figure 5.6. The mesh is composed by 12006 nodes and 11462 elements.

Now we will define the boundary conditions considered. On the one hand, no-slip velocity boundary conditions are applied to the solid channel walls and on the cylinder surface. On the other hand, periodic boundary conditions are considered along the streamwise direction, and therefore, reproducing a periodic array structure of cylinders. The Reynolds number considered to rule out the effect of inertia is $\mathrm{Re} = \rho R_c \langle \boldsymbol{u} \rangle / \eta_0 = 2.4 \times 10^{-2}$, where $\langle \boldsymbol{u} \rangle$ is the average of velocity. The total viscosity η_0 involves two contributions: the polymeric viscosity and the solvent viscosity (as it was explained previously). For this problem, the solvent viscosity is $\eta_s = 24.58$ and the polymeric viscosity $\eta_p = 17.08$, and therefore, the factor β is 0.59. On the other hand, the Weissenberg number is calculated in this case as $\mathrm{We} = \lambda \langle \boldsymbol{u} \rangle / R_c$, and in particular in this problem, the Weissenberg numbers adopted are in the interval $[0 : 1.6]$.

(a) (b)
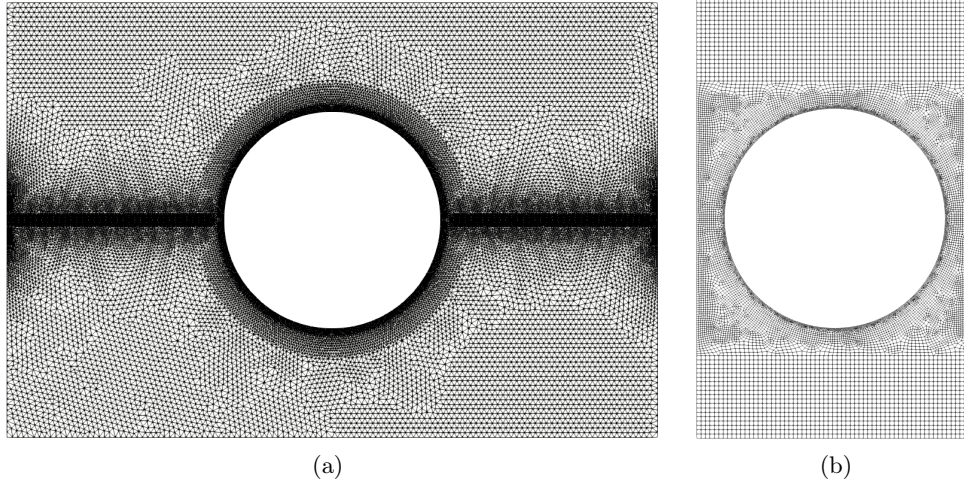
Figure 5.6: Array of cylinders. Meshes employed.

Validation with $L_c = 6$

First of all we validate with the literature the results in the case in which the distance between cylinders is 6. The case is tested using different meshes. In this case, the presence of other cylinders does not affect appreciably the Stokes flow kinematics. The main change (and it is rather subtle) is that the gradient of pressure decreases, as it is reported in [111]. The effect of increasing We on the velocity field can be seen in Figure 5.7a. One of the effects that must be highlighted is how axial velocity on the centerline, next to the downstream stagnation point, increases when We does. For $x > 1.5$ the velocity decreases relative to the less elastic solution (We=0.2). This result is specially interesting due to the proximity of the cylinders, the effect on the velocity field is that this downstream shift is convected increasingly as We is increased. Therefore the velocity upstream of the following cylinder also shows a decrease with respect to a Newtonian flow. Figure 5.7b shows a cross sectional plot of the component v_x of the velocities along the periodic boundary at $x = 3$, where a local minimum can be observed, located on the centerline. These results have been validated with the work of Liu et al. [111].

Elastic instability with $L_c = 2.5$

We have to stand out that, contrary to the case $L_c = 6$, the Newtonian flow in the space between cylinders is characterized by the presence of two rotating vortices, as it is described in [163], making the fluid motion shear dominated instead of elongation dominated (see the Figure 5.8d). As Vazquez-Quesada et al. pointed out, there is no existence of a strong elongational flow in the wake stagnation line due to the closely placed cylinders. The problem, in this case, is characterized by a flow regime where local numerical convergence was already achieved. Therefore, fluctuations in the flow quantities come from a physical origin. In the contour stresses that are shown in Figure 5.8, the maximum peaks of stresses remain at the solid boundaries, in particular on the cylinder. In contrast with a larger cylinder spacing, the polymer molecules along the centerline are at equilibrium due to the recirculation. As explained in [111], the stagnation points where the recirculation region is produced do not appear to produce a lot of molecular extension, in other words, molecules are not relaxed when they go along the streamlines near the boundary of the separated

(a)   (b)
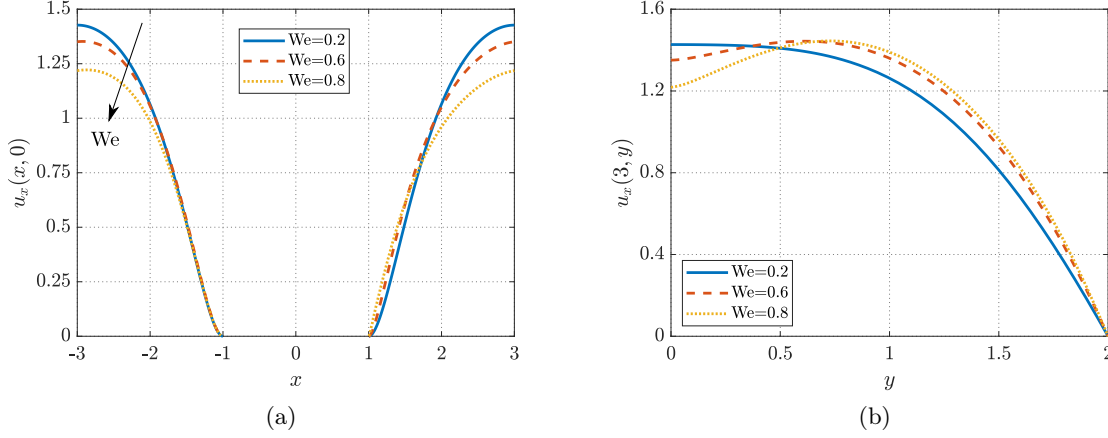
Figure 5.7: Array of cylinders with $L_c = 6$. (a) Profile of v_x along the symmetry line $y = 0$ and (b) across the periodic boundary $x = 3$ for different Weissenberg numbers.

flow. As a result there is a region of "high molecular extension" away from the cylinder surface and upstream from $x = 0$. The distribution of the stresses can be compared with the one shown in [111], although in this case the stresses have been normalized if the model employed is the Chilcott-Rallison (CR) one. On the other hand, in the literature it is reported an increment of the flow resistance in the viscoelastic flow through a porous media and confined arrays for some experiments, but not reproduced numerically. In [157] a wide range of steady simulations around a periodic array were studied using several constitutive models, presenting different behaviors; although in all the cases similar qualitative results were obtained. For example the initial drag reduction, and then an significant increment is reported from We=1. In [163] it is reported that the instability of the previous numerical methods to capture the elastic instability driving the flow towards a more dissipative flow regime could be a possible cause of the discrepancies. Vazquez-Quesada et al. [163] argue that if the transition towards the inestability could be described as a Hopf bifurcation of the mathematical solution, the standard numerical computations will follow the steady branch, while the flow reported is clearly time-dependent. As it is explained in [163], the experimental observation supporting the idea of elastic instability is that an increment in fluctuations of the flow quantities is reported as the We number increase. In Figure 5.9, this effect can be observed: oscillations reported increase as one Weissenberg number does. Moreover, the instability is activated before when the Weissenberg number is higher. In our computations the fluctuations appear for We $= 1.3$. For smaller Weissenberg numbers, the simulations remains stationary in our case. We have to remark several difficulties to achieve a converged solution. For that, the time step employed was $\delta t = 0.0025$.

In Figure 5.10 the point with coordinates $(0, 1.1)$, located downstream of the cylinder, is tracked for the pressure field. We have to remark that several points around the cylinder were tracked to study the evolution in time of the different fields, although the fluctuations reported are similar in all of them. The first graph, Fig. 5.10a, the oscillations captured along 150 seconds are shown. It is the period of time in which the instability becomes more relevant until it reaches a regular and stable oscillations. The second plot, Fig. 5.10b is only a "zoom" of Fig. 5.10a, in which only 20 seconds of oscillations are represented. Finally, in Figure 5.10c the Fourier Transform (FFT) is computed in order to study the frequencies. This plot shows two main modes: one of frequency 1 Hz and another of 0.5
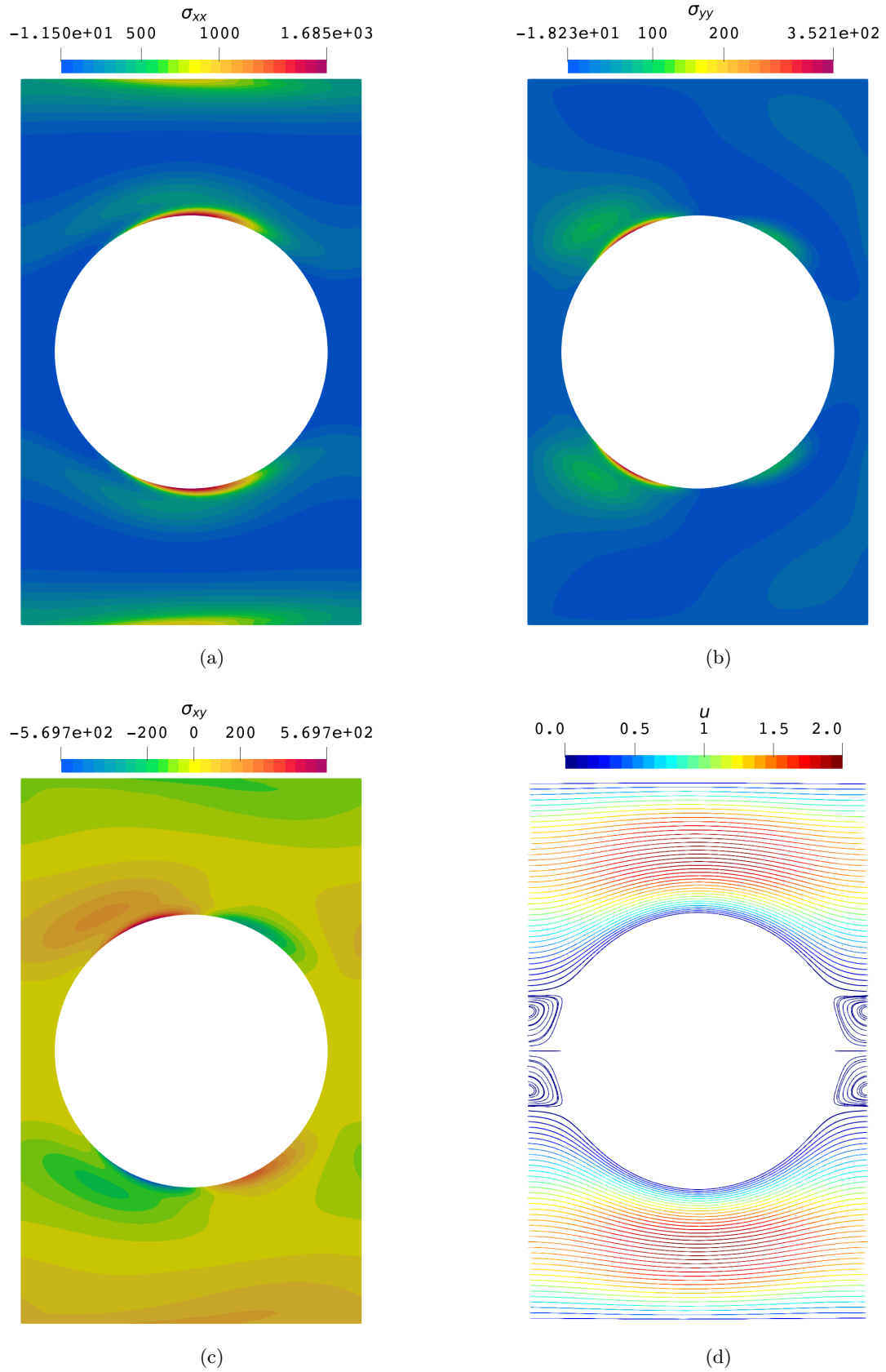
Figure 5.8: Array of cylinders: Contours of stresses and streamlines for We=0.5.
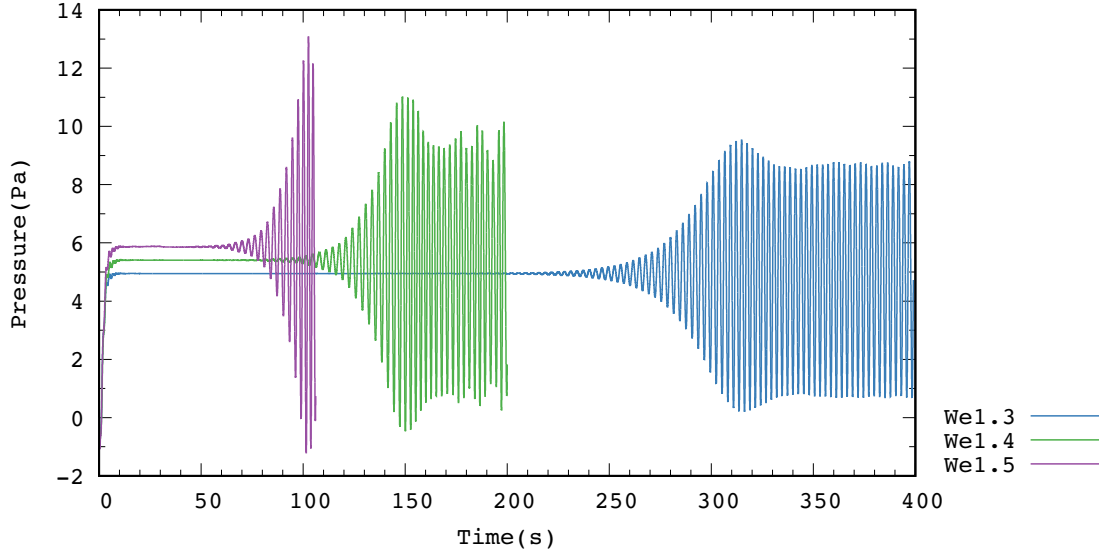
Figure 5.9: Array of cylinders. Tracking of the point (0, 1.1) for different Weissenberg numbers.

Hz approximately.

Although elastic turbulence has not been reported in our examples, clearly a bifurcation has been detected, related with the purely elastic inestability.

5.9   Conclusions

In this chapter, fractional step methods for the logarithmic conformation reformulation have been designed for the first and the second order schemes using a pure algebraic approach. In this fractional scheme, also the time-dependent sub-grid scales are contemplated, allowing to compute anisotropic spatial-time discretizations. In addition, for the viscoelastic case, that implementation permits to compute more elastic cases. Moreover, the use of fractional step schemes implies important savings in computational cost, as it has been highlighted in the cavity benchmark included in the numerical results. Also the fractional step algorithm is validated for an analytical solution, showing an optimal rate of convergence in time for the three variables which are involved.

Finally, using these tools, an elastic instability has been reproduced in the case of the array of cylinders, showing a time-dependent behavior in the solution when the Weissenberg number is high enough, even considering a Reynolds number very low, whose order is 10^{-2}.
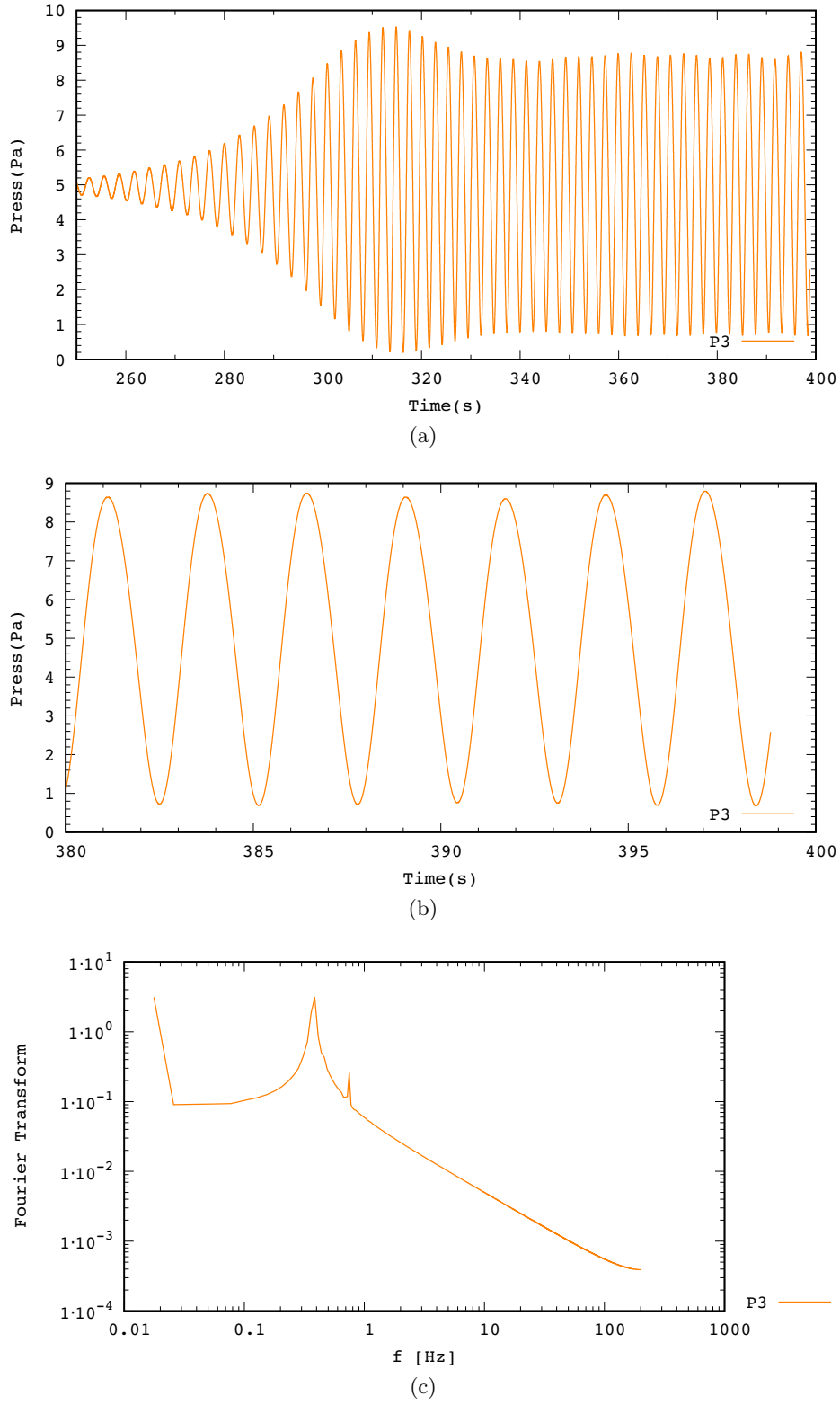
Figure 5.10: Array of cylinders. Tracking of the point (0, 1.1) of the pressure field in the time interval [0,400] (a), and in the time interval [380-400] (b). Fourier transform is plotted in (c).

Chapter 6

Analysis of stability and convergence

This chapter is based on the publication:

Codina, R., & Moreno, L. (2021). Analysis of a stabilized finite element approximation for a linearized logarithmic reformulation of the viscoelastic flow problem. *ESAIM. Mathematical Modelling and Numerical Analysis*, 55, 279.

6.1   Abstract

In this chapter the numerical analysis of a finite element method is presented for a linearized viscoelastic flow problem. In particular, we analyze a linearization of the logarithmic reformulation of the problem, which in particular should be able to produce results for Weissenberg numbers higher than the standard one. In order to be able to use the same interpolation for all the unknowns (velocity, pressure and logarithm of the conformation tensor), we employ a stabilized finite element formulation based on the Variational Multi-Scale concept. The study of the linearized problem already serves to show why the logarithmic reformulation performs better than the standard one for high Weissenberg numbers; this is reflected in the stability and error estimates that we provide in this chapter.

6.2   Background

Computing viscoelastic fluid flows when the fluid presents a dominant elastic behavior is one of the biggest challenges of the computational rheology field nowadays. The equations that model the viscoelastic fluid flow problem present several instabilities which have been studied for example in [67, 144]. These instabilities become important when elasticity becomes dominant, in other words, when the Weissenberg number is high as it was mentioned in previous chapters. The numerical instability was studied by Fattal and Kupferman [64], who explained that it is present in the constitutive models and the standard numerical methods. Constitutive equations could present also other type of instabilities from a mathematical point of view, referred to as *constitutive instabilities* [106, 108]. These can be classified in two: the Hadamard instability, which is a consequence of the non-linear fast response of the constitutive equation, and the dissipative instability, related to the *dissipative* behavior of viscoelastic models. However, the reasons for the HWNP are different: one is the loss of positive-definiteness of the conformation tensor, which is an internal

variable that must be positive-definite to be physically admissible [64, 92], and the second is the appearance of regions with large strain gradients. From the numerical point of view, Fattal and Kupferman [64, 65] focussed the origin of the problem in the inappropriate approximations to represent the stress tensor, standing out the necessity of preserving the positivity of the conformation tensor. By following these ideas the logarithmic conformation reformulation was proposed in [64] as a formulation of the equations which overcomes the instability and linearizes the exponential stress profiles near the stress singularities. The formulation treats the exponential growth of the elastic stresses, allowing to extend the usual range of Weissenberg numbers which can be considered to simulate viscoelastic fluid flows. In this chapter we will use the logarithmic reformulation developed in Chapter 2. In contrast with the original one, our change of variables will be non-singular when the Weissenberg number is close to zero and the flow is Newtonian; a similar idea was presented in [148].

In addition to the instabilities mentioned, viscoelastic fluid flows present some compatibility restrictions when the Galerkin finite element (FE) approximation is undertaken. First, velocity and pressure FE spaces must satisfy the well known inf-sup condition for incompressible flows [23] and, secondly, there is another inf-sup condition that needs to be satisfied between stresses and velocities [146]. This is studied for example for the Navier-Stokes problem in [16, 42]; the same requirements are met in the viscoelastic case. Stable interpolations are proposed in [116], whose analysis can be found in [69]. At the continuous level, these inf-sup conditions are satisfied and the problem can be shown to have a unique solution in the slow viscoelastic case [67, 144]; see also [82, 90] for some results concerning strong solutions.

Referring to the FE approximation, there are several works which analyze the stationary Oldroyd-B problem and present optimal error estimates. For instance, [13] is one of the first works that shows the existence of FE approximations assuming that the continuous problem admits sufficiently smooth and sufficiently small solution; bounds for the error are also provided. In [137], the authors establish the existence and a priori error estimates using the EVSS (Elastic Viscous Split Stress) method, aimed to circumvent the inf-sup condition between velocities and stresses. More recently, in [115] the authors present an error analysis of a particular Oldroyd-B model with the limiting Weissenberg number going to infinity, assuming a suitable regularity of the exact solution for FE and finite volume methods. The time-dependent Oldroyd-B problem has also been studied, for example in [62], using the SUPG method, aimed to circumvent convection instabilities.

In this chapter, the log-conformation reformulation is applied together with a stabilized FE formulation based on the Variational Multi-Scale (VMS) method which aims at circumventing the inf-sup conditions and dealing with convection dominated flows at the same time, as it was considered in the previous chapters. The VMS concept was presented first by Hughes et al. [91] for the convection-diffusion-reaction problem. These ideas were applied and extended in [38, 40–42] for the Navier-Stokes problem and the three-field Stokes problem considering the space of the sub-grid scales orthogonal to the FE space. The viscoelastic fluid flow problem was stabilized following a VMS framework in [28, 29] and in the logarithmic formulation the method was tested in Chapter 2 for some numerical examples in which the Weissenberg number is relevant. This type of stabilization is also applied in [104, 105].

The present chapter can be considered a continuation of the work presented in [29, 42]. In [42] a VMS formulation for the three-field Stokes problem was presented and analyzed. The same approach was followed in [29], in this case applied to a linearized version of the stationary *standard* formulation of the viscoelastic flow problem, using the Oldroyd-B

model. The linearization is based on considering given the advection velocity and the velocity gradient in the rotational terms of the constitutive equation. The purpose of this chapter is to extend this analysis to the *logarithmic reformulation* of the viscoelastic problem. This analysis will serve to explain its improved performance with respect to the standard formulation when the Weissenberg number is high. This would be difficult to observe in the full nonlinear problem, since conditions to ensure existence of solutions and their finite element approximation pose stringent requirements on the Reynolds and Weissenberg numbers of the problem, even in the time dependent case; for the standard formulation and using a similar approach as the one we follow here, this analysis can be found in [14].

This chapter is organized as follows: In Section 6.3, the logarithmic formulation is described, starting from the standard viscoelastic Oldoryd-B fluid flow equations; Section 6.4 presents the FE method employed, based on the VMS approach. In Section 6.5 the numerical analysis is developed; in particular, in Section 6.5.2 stability and convergence are proved for a mesh dependent norm, while in Section 6.5.3 results are obtained for natural norms. Finally, conclusions are drawn in Section 6.6.

6.3 The stationary logarithmic linearized viscoelastic problem

In this section the linearized boundary value problem will be defined for the viscoelastic fluid flow equations written in the logarithmic conformation reformulation. All of the details concerning the reformulation of the standard equations into this logarithmic formulation are explained in Chapter 2.

6.3.1 Linearized boundary value problem

To motivate the linearized problem to be analyzed, let us consider a Newton-Raphson linearization such as it is explained in the Section 2.3.4. Since we consider $\exp(\hat{\boldsymbol{\psi}})$ and $\hat{\boldsymbol{\psi}}$ known, we can denote these tensors as $\boldsymbol{E} = \exp(\hat{\boldsymbol{\psi}})$ and $\boldsymbol{S} = \hat{\boldsymbol{\psi}}$, respectively, and introduce $\boldsymbol{R} = \boldsymbol{E} \cdot \boldsymbol{S} - \boldsymbol{E}$. The linearized equations of the log-conformation formulation are now expressed as follows:

$$-\frac{\eta_p}{\lambda_0}\nabla \cdot (\boldsymbol{E} \cdot \boldsymbol{\psi} - \boldsymbol{R}) - 2\eta_s \nabla \cdot (\nabla^{\mathrm{s}}\boldsymbol{u}) + \rho\boldsymbol{a} \cdot \nabla\boldsymbol{u} + \nabla p = \boldsymbol{f}, \tag{6.1}$$

$$\nabla \cdot \boldsymbol{u} = 0, \tag{6.2}$$

$$\frac{1}{2\lambda_0}(\boldsymbol{E} \cdot \boldsymbol{\psi} - \boldsymbol{R} - \boldsymbol{I}) - \nabla^{\mathrm{s}}\boldsymbol{u} + \frac{\lambda}{2\lambda_0}\left(\boldsymbol{a} \cdot \nabla (\boldsymbol{E} \cdot \boldsymbol{\psi} - \boldsymbol{R})\right.$$
$$\left. - (\boldsymbol{E} \cdot \boldsymbol{\psi} - \boldsymbol{R}) \cdot \nabla\boldsymbol{a} - (\nabla\boldsymbol{a})^T \cdot (\boldsymbol{E} \cdot \boldsymbol{\psi} - \boldsymbol{R}) + 2\nabla^{\mathrm{s}}\boldsymbol{u}\right) = \boldsymbol{0}, \tag{6.3}$$

where the unknowns are the velocity, the pressure, and tensor $\boldsymbol{\psi}$. Note the presence of the last term $2\nabla^{\mathrm{s}}\boldsymbol{u}$, which will have a crucial role in the dependence of the error estimate to be obtained with the Weissenberg number.

Let us introduce some notation, useful in the next subsections. In this case, calling

$U = [u, p, \psi]$, the main linearized operator is defined as

$$\mathcal{L}(U) := \begin{pmatrix} -\dfrac{\eta_p}{\lambda_0} \nabla \cdot (E \cdot \psi) - 2\eta_s \nabla \cdot (\nabla^s u) + \rho a \cdot \nabla u + \nabla p \\[2mm] \nabla \cdot u \\[2mm] \dfrac{1}{2\lambda_0} E \cdot \psi - \nabla^s u + \dfrac{\lambda}{2\lambda_0} (a \cdot \nabla (E \cdot \psi) \\[1mm] - (E \cdot \psi) \cdot \nabla a - (\nabla a)^T \cdot (E \cdot \psi) + 2\nabla^s u) \end{pmatrix}, \tag{6.4}$$

If we also introduce

$$F := \begin{pmatrix} f - \dfrac{\eta_p}{\lambda_0} \nabla \cdot R \\[2mm] 0 \\[2mm] \dfrac{1}{2\lambda_0} (I + R) + \dfrac{\lambda}{2\lambda_0} (a \cdot \nabla R - R \cdot \nabla a - (\nabla a)^T \cdot R) \end{pmatrix} =: \begin{pmatrix} f_u \\[2mm] 0 \\[2mm] f_\psi \end{pmatrix}, \tag{6.5}$$

we may write (2.8)-(2.10) as

$$\mathcal{L}(U) = F, \tag{6.6}$$

which again needs to be supplied with the boundary condition $u = 0$ on $\partial\Omega$.

6.3.2   Variational formulation

Considering the notation defined in Section 2.3.3, this weak form consists in finding $U = [u, p, \psi] \in \mathcal{X} := \mathcal{V} \times \mathcal{Q} \times \Upsilon$ such that

$$\frac{\eta_p}{\lambda_0} (E \cdot \psi, \nabla^s v) + 2(\eta_s \nabla^s u, \nabla^s v) + \langle \rho a \cdot \nabla u, v \rangle - (p, \nabla \cdot v)$$
$$= \langle f, v \rangle + \frac{\eta_p}{\lambda_0} (R, \nabla^s v), \tag{6.7}$$

$$(q, \nabla \cdot u) = 0, \tag{6.8}$$

$$\frac{1}{2\lambda_0} (E \cdot \psi, \chi) - (\nabla^s u, \chi) + \frac{\lambda}{2\lambda_0} (a \cdot \nabla (E \cdot \psi) - E \cdot \psi \cdot \nabla a$$
$$- (\nabla a)^T \cdot E \cdot \psi + 2\nabla^s u, \chi) = \frac{1}{2\lambda_0} (I + R, \chi)$$
$$+ \frac{\lambda}{2\lambda_0} (a \cdot \nabla R, \chi) + \frac{\lambda}{2\lambda_0} (-R \cdot \nabla a - (\nabla a)^T \cdot R, \chi), \tag{6.9}$$

for all $V = [v, q, \chi] \in \mathcal{X}$, where it is assumed that f, R and E are such that the known terms are well defined. In compact form, the problem can be written as:

$$B(U, V) = L(V), \tag{6.10}$$

where

$$B(U, V) = \frac{\eta_p}{\lambda_0} (E \cdot \psi, \nabla^s v) + 2(\eta_s \nabla^s u, \nabla^s v) + \langle \rho a \cdot \nabla u, v \rangle - (p, \nabla \cdot v)$$
$$+ (\nabla \cdot u, q) + \frac{1}{2\lambda_0} (E \cdot \psi, \chi) - (\nabla^s u, \chi)$$
$$+ \frac{\lambda}{2\lambda_0} (a \cdot \nabla (E \cdot \psi) - E \cdot \psi \cdot \nabla a - (\nabla a)^T \cdot E \cdot \psi + 2\nabla^s u, \chi), \tag{6.11}$$

$$L(V) = \langle f, v \rangle + \frac{\eta_p}{\lambda_0} (R, \nabla^s v) + \frac{1}{2\lambda_0} (I + R, \chi) + \frac{\lambda}{2\lambda_0} (a \cdot \nabla R, \chi)$$

$$+ \frac{\lambda}{2\lambda_0} \left(-\boldsymbol{R} \cdot \nabla \boldsymbol{a} - (\nabla \boldsymbol{a})^T \cdot \boldsymbol{R}, \boldsymbol{\chi} \right). \tag{6.12}$$

As it is explained in Section 2.3.3, test function $\boldsymbol{\chi}$ is a stress, whereas the dimensionless unknown $\boldsymbol{\psi}$ is the logarithm of the conformation tensor. We could also have used a test function for the constitutive equation of the form $\frac{\eta_p}{\lambda_0} \exp(\boldsymbol{\chi})$, where now $\boldsymbol{\chi}$ would be dimensionless. This would simplify the analysis (some stability would follow taking $\boldsymbol{\chi} = \boldsymbol{\psi}$), but complicate significantly the FE approximations described below. Note that, strictly speaking, the space of stress test functions could be taken as the L^2 projection onto $L^2(\Omega)^{d \times d}$ of functions of the form $\boldsymbol{E} \cdot \boldsymbol{\varphi}$ properly scaled, for example by a factor $\frac{\eta_p}{\lambda_0}$, with $\boldsymbol{\varphi}$ belonging to the space of trial solutions.

We will not analyze the continuous problem (6.10), but simply assume that there exists a solution that is smooth enough. As for the standard formulation, this requires λ to be small enough and, in the case of the linearization we consider, the following condition on the velocity $\boldsymbol{a}$ which will also be needed in the discrete problem:

Assumption H1 $\boldsymbol{a} \in \mathcal{C}^0(\bar{\Omega})^d$, $\nabla \cdot \boldsymbol{a} = 0$, $\boldsymbol{a}$ and $\nabla \boldsymbol{a}$ have components in $L^\infty(\Omega)$.

$\boldsymbol{E}$ and $\boldsymbol{R}$ have components in $L^\infty(\Omega)$.

$\boldsymbol{E}$ is invertible with a bounded inverse.

6.3.3   Stability of the Galerkin finite element discretization

The standard Galerkin approximation for the variational problem, which has been established in (6.10), is described next. The notation employed is that defined in Section 2.3.5.

Although *any* conforming approximation could be considered using the approach to be described, and this means that pressures and stresses could be discontinuous (see [29]), for conciseness we will restrict to continuous interpolations for these fields.

The condition that the convective derivative of the stress be square integrable will follow from **H1** and choosing the stresses continuous, for example. Calling $\boldsymbol{\mathcal{X}}_h := \boldsymbol{\mathcal{V}}_h \times \mathcal{Q}_h \times \boldsymbol{\Upsilon}_h$, the Galerkin FE approximation of the problem consists in finding $\boldsymbol{U}_h \in \boldsymbol{\mathcal{X}}_h$, such that:

$$B_\psi(\boldsymbol{U}_h, \boldsymbol{V}_h) = L(\boldsymbol{V}_h), \tag{6.13}$$

for all $\boldsymbol{V}_h = [\boldsymbol{v}_h, q_h, \boldsymbol{\chi}_h] \in \boldsymbol{\mathcal{X}}_h$, where B_ψ is obtained from B given in (6.11) replacing $\boldsymbol{E} \cdot \boldsymbol{\psi}_h$ by $P_\psi[\boldsymbol{E} \cdot \boldsymbol{\psi}_h]$, where P_ψ is the L^2 projection onto $\boldsymbol{\Upsilon}_h$.

As in the standard formulation, problem (6.13) lacks stability unless appropriate inf-sup conditions hold. Likewise, convective terms are not bounded, and these may dominate those that can be controlled.

6.4   Stabilized finite element method

The numerical method analysed is a non-residual type stabilization. This method has been detailed extensively in Section 2.4.2.

Following the considerations made in [28] for the construction of the Split-OSS method for the traditional viscoelastic formulation, the modified method we propose for the log-conformation reformulation is: find $\boldsymbol{U}_h \in \boldsymbol{\mathcal{X}}_h$ such that

$$B_{\mathrm{stab}}(\boldsymbol{U}_h, \boldsymbol{V}_h) = B_\psi(\boldsymbol{U}_h, \boldsymbol{V}_h) + B^*(\boldsymbol{U}_h, \boldsymbol{V}_h) = L(\boldsymbol{V}_h) \tag{6.14}$$

for all $\boldsymbol{V}_h \in \boldsymbol{\mathcal{X}}_h$, where $B^*(\boldsymbol{U}_h, \boldsymbol{V}_h)$ represents the stabilizing part of the model, defined as

$$B^*(\boldsymbol{U}_h, \boldsymbol{V}_h) = S_1^\perp(\boldsymbol{U}_h, \boldsymbol{V}_h) + S_2^\perp(\boldsymbol{U}_h, \boldsymbol{V}_h) + S_3^\perp(\boldsymbol{u}_h; \boldsymbol{U}_h, \boldsymbol{V}_h), \qquad (6.15)$$

where

$$S_1^\perp(\boldsymbol{U}_h, \boldsymbol{V}_h) = \sum_K \alpha_1 \Big\langle P_u^\perp \Big[-\frac{\eta_p}{\lambda_0} \nabla \cdot P_\psi [\boldsymbol{E} \cdot \boldsymbol{\psi}_h] \Big], -\nabla \cdot \boldsymbol{\chi}_h \Big\rangle_K$$
$$+ \sum_K \alpha_1 \Big\langle P_u^\perp [\nabla p_h], \nabla q_h \Big\rangle_K + \sum_K \alpha_1 \Big\langle P_u^\perp [\rho \boldsymbol{a} \cdot \nabla \boldsymbol{u}_h], \rho \boldsymbol{a} \cdot \nabla \boldsymbol{v}_h \Big\rangle_K, \quad (6.16)$$

$$S_2^\perp(\boldsymbol{U}_h, \boldsymbol{V}_h) = \sum_K \alpha_2 \Big\langle P_p^\perp [\nabla \cdot \boldsymbol{u}_h], \nabla \cdot \boldsymbol{v}_h \Big\rangle_K, \qquad (6.17)$$

$$S_3^\perp(\boldsymbol{U}_h, \boldsymbol{V}_h) = \sum_K \alpha_3 \Big\langle P_\psi^\perp [\boldsymbol{R}_\psi],$$
$$-\nabla^\mathrm{s} \boldsymbol{v}_h + \frac{\lambda}{2\eta_p} \big(\boldsymbol{a} \cdot \nabla \boldsymbol{\chi}_h + \boldsymbol{\chi}_h \cdot (\nabla \boldsymbol{a})^T + \nabla \boldsymbol{a} \cdot \boldsymbol{\chi}_h \big) \Big\rangle_K, \qquad (6.18)$$

and where $\boldsymbol{R}_\psi$ is the residual of the constitutive equation

$$\boldsymbol{R}_\psi = -\nabla^\mathrm{s} \boldsymbol{u}_h + \frac{\lambda}{2\lambda_0} \big(\boldsymbol{a} \cdot \nabla P_\psi [\boldsymbol{E} \cdot \boldsymbol{\psi}_h] - P_\psi [\boldsymbol{E} \cdot \boldsymbol{\psi}_h] \cdot \nabla \boldsymbol{a}$$
$$-(\nabla \boldsymbol{a})^T \cdot P_\psi [\boldsymbol{E} \cdot \boldsymbol{\psi}_h] + 2\nabla^\mathrm{s} \boldsymbol{u}_h \big). \qquad (6.19)$$

The L^2 projections onto the FE spaces for velocity (without boundary conditions), pressure and stress have respectively been denoted by P_u, P_p and, as already mentioned, P_ψ. The projection onto the velocity space with boundary conditions will be denoted $P_{u,0}$.

The method is a mix of an orthogonal term-by-term formulation for the momentum equation and continuity equation and a residual-based formulation for the constitutive equation. For smooth solutions, both have an optimal convergence rate in h. However, in problems where the solution has strong gradients, we have found (6.15) more robust, similarly to what it is explained in [28]. For a detailed motivation and numerical experimentation using this method, see [120].

In the numerical analysis below we will also use the notation

$$P_\psi [\boldsymbol{E} \cdot \boldsymbol{\psi}_h] \cdot \nabla \boldsymbol{a} + (\nabla \boldsymbol{a})^T \cdot P_\psi [\boldsymbol{E} \cdot \boldsymbol{\psi}_h] = \dot{\boldsymbol{\psi}}_h^* + \dot{\boldsymbol{\psi}}_h^{**},$$

and

$$P_\psi [\boldsymbol{E} \cdot \boldsymbol{\psi}_h] \cdot (\nabla \boldsymbol{a})^T + \nabla \boldsymbol{a} \cdot P_\psi [\boldsymbol{E} \cdot \boldsymbol{\psi}_h] = \dot{\boldsymbol{\psi}}_h^* - \dot{\boldsymbol{\psi}}_h^*,$$

where $\dot{\boldsymbol{\psi}}_h^* = P_\psi [\boldsymbol{E} \cdot \boldsymbol{\psi}_h] \cdot \nabla^\mathrm{s} \boldsymbol{a} + \nabla^\mathrm{s} \boldsymbol{a} \cdot P_\psi [\boldsymbol{E} \cdot \boldsymbol{\psi}_h]$ and $\dot{\boldsymbol{\psi}}_h^{**} = P_\psi [\boldsymbol{E} \cdot \boldsymbol{\psi}_h] \cdot \nabla^\mathrm{as} \boldsymbol{a} - \nabla^\mathrm{as} \boldsymbol{a} \cdot P_\psi [\boldsymbol{E} \cdot \boldsymbol{\psi}_h]$. In these expressions, $\nabla^\mathrm{as} \boldsymbol{a}$ represents the skew-symmetric part of the velocity gradient, given by

$$\nabla^\mathrm{as} \boldsymbol{a} = \frac{1}{2} \Big[\nabla \boldsymbol{a} - (\nabla \boldsymbol{a})^T \Big].$$

6.5 Numerical analysis

6.5.1 Preliminaries

We assume that there is a constant c_inv, independent of the mesh size h, such that

$$\| \nabla v_h \|_K \leq c_\mathrm{inv} h^{-1} \| v_h \|_K, \qquad (6.20)$$

for all FE functions v_h defined on $K \in \mathcal{T}_h$, which can be either scalars, vectors or tensors. We will also make use of Korn's inequality, which holds for the conforming approximation that we consider:

$$\|\boldsymbol{v}_h\|^2_{H^1(\Omega)} \leq c_L \|\nabla^{\mathrm{s}} \boldsymbol{v}_h\|^2 \text{ with } \boldsymbol{v}_h = \boldsymbol{0} \text{ on } \partial\Omega,$$

$c_L > 0$ being a constant. As usual, C will denote a generic positive constant, possibly different at different occurrences. A fixed constant will be identified with a subscript.

We will need a condition on the interpolating spaces that holds in the case of equal order interpolations, and that can be written as [29, 42]:

Assumption H2 Given $\boldsymbol{a}, \boldsymbol{v}_h \in \boldsymbol{\mathcal{V}}_h, q_h \in \mathcal{Q}_h, \boldsymbol{\psi}_h \in \boldsymbol{\Upsilon}_h$ and

$$\boldsymbol{z}_h \coloneqq \rho \boldsymbol{a} \cdot \nabla \boldsymbol{v}_h + \nabla q_h - \nabla \cdot P_\psi[\boldsymbol{E} \cdot \boldsymbol{\psi}_h],$$

there holds $\|\boldsymbol{z}_h\| \leq c_{\mathrm{m}} \left(\|P_{u,0}[\boldsymbol{z}_h]\| + \left\| P_u^\perp[\boldsymbol{z}_h] \right\| \right),$ for a constant

$c_{\mathrm{m}} > 0.$

For a piecewise linear velocity $\boldsymbol{a}$ this assumption is known to hold; here we assume that $\boldsymbol{a}$ is such that it is satisfied.

6.5.2   Stability and convergence in a mesh-dependent norm

The norm in which the results will be first presented is

$$\begin{aligned}
\|\boldsymbol{V}_h\|^2_W = {}& 2\eta_s \|\nabla^s \boldsymbol{v}_h\|^2 + \frac{\eta_p}{\lambda_0^2} \|P_\psi[\boldsymbol{E} \cdot \boldsymbol{\varphi}_h]\|^2 \\[2mm]
& + \sum_K \alpha_u \left\| \rho \boldsymbol{a} \cdot \nabla \boldsymbol{v}_h + \nabla q_h - \frac{\eta_p}{\lambda_0} \nabla \cdot P_\psi[\boldsymbol{E} \cdot \boldsymbol{\varphi}_h] \right\|^2_K \\[2mm]
& + \sum_K \alpha_u \left\| P_u^\perp[\rho \boldsymbol{a} \cdot \nabla \boldsymbol{v}_h] \right\|^2_K + \sum_K \alpha_u \left\| P_u^\perp[\nabla q_h] \right\|^2_K \\[2mm]
& + \sum_K \alpha_u \left\| P_u^\perp \left[\frac{\eta_p}{\lambda_0} \nabla \cdot P_\psi[\boldsymbol{E} \cdot \boldsymbol{\varphi}_h] \right] \right\|^2_K \\[2mm]
& + \sum_K \alpha_p \|\nabla \cdot \boldsymbol{v}_h\|^2_K + \sum_K \alpha_\psi \left\| \frac{\lambda}{2\lambda_0} \left(\boldsymbol{a} \cdot \nabla P_\psi[\boldsymbol{E} \cdot \boldsymbol{\varphi}_h] - \dot{\boldsymbol{\varphi}}_h^{**} \right) \right\|^2_K,
\end{aligned} \tag{6.21}$$

considering $\boldsymbol{V}_h = [\boldsymbol{v}_h, q_h, \boldsymbol{\varphi}_h] \in \boldsymbol{\mathcal{X}}_h$ (note again that $\boldsymbol{\varphi}_h$ is dimensionless). This is clearly homogeneous velocity boundary conditions considered, since if $\|\boldsymbol{V}_h\| = 0$, $\boldsymbol{v}_h = \boldsymbol{0}$ because of the first term (using Körn's inequality), $P_\psi[\boldsymbol{E} \cdot \boldsymbol{\varphi}_h] = \boldsymbol{0}$ for $\eta_p > 0$ because of the second term (and, in fact, $\boldsymbol{\varphi}_h = \boldsymbol{0}$ because of Assumption H3 stated later), and, finally, $q_h = 0$ because of the thirs term and the definition of $\mathcal{Q}$.

To simplify the analysis, we shall consider that the stabilization parameters are constant, computed with the $L^\infty(\Omega)$ norm of the advection velocity and its gradient. The analysis of variable stabilization parameters, including non-uniform meshes, can be done using the techniques in [41].

The main stability result, which implies existence and uniqueness of discrete solutions, is the following:

Theorem 6.1 (Stability). *Suppose that H1 and H2 hold. For λ small enough, there is a constant $C > 0$ such that*

$$\inf_{\boldsymbol{U}_h \in \boldsymbol{\mathcal{X}}_h} \sup_{\boldsymbol{V}_h \in \boldsymbol{\mathcal{X}}_h} \frac{B_{\mathrm{stab}}(\boldsymbol{U}_h, \boldsymbol{V}_h)}{\|\boldsymbol{U}_h\|_W \|\boldsymbol{V}_h\|_W} \geq C,$$

provided the constants $c_i, i = 1, .., 4$ defined in (2.30)-(2.32) are large enough.

Proof. Given $\boldsymbol{U}_h \in \boldsymbol{\mathcal{X}}_h$, consider $\boldsymbol{U}_{h1} = \left[\lambda^* \boldsymbol{u}_h, \lambda^* p_h, \frac{\eta_p}{\lambda_0} P_\psi [\boldsymbol{E} \cdot \boldsymbol{\psi}_h] \right]$, where $\lambda^* = \frac{\lambda - \lambda_0}{\lambda_0} > 0$. We assume that $\lambda > \lambda_{0,\min}$, since the case of very small elasticity is easier to prove and it is not our focus. Now, using skew symmetry of the convective terms (from assumption H1), we obtain:

$$
\begin{aligned}
B_{\text{stab}}(\boldsymbol{U}_h, &\boldsymbol{U}_{h1}) = \\
&= B_\psi(\boldsymbol{U}_h, \boldsymbol{U}_{h1}) + B^*(\boldsymbol{U}_h, \boldsymbol{U}_{h1}) \\
&= \underbrace{\frac{\eta_p}{\lambda_0} \lambda^* \left(P_\psi[\boldsymbol{E} \cdot \boldsymbol{\psi}_h], \nabla^{\mathrm{s}} \boldsymbol{u}_h \right)}_{(1)} + 2\eta_s \lambda^* (\nabla^{\mathrm{s}} \boldsymbol{u}_h, \nabla^{\mathrm{s}} \boldsymbol{u}_h) \\
&\quad + \underbrace{\frac{1}{2\lambda_0} \frac{\eta_p}{\lambda_0} \left(P_\psi[\boldsymbol{E} \cdot \boldsymbol{\psi}_h], P_\psi[\boldsymbol{E} \cdot \boldsymbol{\psi}_h] \right)}_{} \\
&\quad \underbrace{- \frac{\eta_p}{\lambda_0} \left(\nabla^{\mathrm{s}} \boldsymbol{u}_h, P_\psi[\boldsymbol{E} \cdot \boldsymbol{\psi}_h] \right)}_{(1)} \\
&\quad - \frac{\lambda}{2\lambda_0} \frac{\eta_p}{\lambda_0} \underbrace{\left(P_\psi[\boldsymbol{E} \cdot \boldsymbol{\psi}_h] \cdot \nabla \boldsymbol{a}, P_\psi[\boldsymbol{E} \cdot \boldsymbol{\psi}_h] \right)}_{(2)} \\
&\quad - \frac{\lambda}{2\lambda_0} \frac{\eta_p}{\lambda_0} \underbrace{\left((\nabla \boldsymbol{a})^T \cdot P_\psi[\boldsymbol{E} \cdot \boldsymbol{\psi}_h], P_\psi[\boldsymbol{E} \cdot \boldsymbol{\psi}_h] \right)}_{(2)} \\
&\quad + \frac{\lambda}{2\lambda_0} \frac{\eta_p}{\lambda_0} \underbrace{\left(2\nabla^{\mathrm{s}} \boldsymbol{u}_h, P_\psi[\boldsymbol{E} \cdot \boldsymbol{\psi}_h] \right)}_{(1)} \\
&\quad + \sum_K \alpha_u \left\langle P_u^\perp \left[\frac{\eta_p}{\lambda_0} \nabla \cdot P_\psi[\boldsymbol{E} \cdot \boldsymbol{\psi}_h] \right], \frac{\eta_p}{\lambda_0} \nabla \cdot P_\psi[\boldsymbol{E} \cdot \boldsymbol{\psi}_h] \right\rangle \\
&\quad + \sum_K \alpha_u \lambda^* \left\langle P_u^\perp[\nabla p_h], \nabla p_h \right\rangle + \sum_K \alpha_u \lambda^* \left\langle P_u^\perp[\rho \boldsymbol{a} \cdot \nabla \boldsymbol{u}_h], \rho \boldsymbol{a} \cdot \nabla \boldsymbol{u}_h \right\rangle \\
&\quad + \sum_K \alpha_p \lambda^* \left\langle P_p^\perp[\nabla \cdot \boldsymbol{u}_h], \nabla \cdot \boldsymbol{u}_h \right\rangle \\
&\quad + \sum_K \alpha_\psi \Big\langle P_\psi^\perp \left[\lambda^* \nabla^{\mathrm{s}} \boldsymbol{u}_h + \frac{\lambda}{2\lambda_0} \left(\boldsymbol{a} \cdot \nabla P_\psi[\boldsymbol{E} \cdot \boldsymbol{\psi}_h] - \dot{\boldsymbol{\psi}}_h^* - \dot{\boldsymbol{\psi}}_h^{**} \right) \right], \\
&\quad \underbrace{-\lambda^* \nabla^{\mathrm{s}} \boldsymbol{u}_h + \frac{\lambda}{2\lambda_0} \left(\boldsymbol{a} \cdot \nabla P_\psi[\boldsymbol{E} \cdot \boldsymbol{\psi}_h] + \dot{\boldsymbol{\psi}}_h^* - \dot{\boldsymbol{\psi}}_h^{**} \right) \Big\rangle}_{(3)} .
\end{aligned}
$$

Let us bound the terms in this expression. From now on, ε with a subscript will denote a constant resulting from Young's inequality, which will be repeatedly used together with Schwarz's inequality, one can easily obtain:

$$
\begin{aligned}
(1) \quad &\geq \quad -2\eta_p \lambda^* \left[\frac{1}{2\varepsilon_0 \lambda_0^2} \left\| P_\psi[\boldsymbol{E} \cdot \boldsymbol{\psi}_h] \right\|^2 + \frac{\varepsilon_0}{2} \left\| \nabla^{\mathrm{s}} \boldsymbol{u}_h \right\|^2 \right], \\
(2) \quad &\geq \quad -\frac{\lambda \eta_p}{\lambda_0^2} \left\| \nabla \boldsymbol{a} \right\|_{L^\infty(\Omega)} \left\| P_\psi[\boldsymbol{E} \cdot \boldsymbol{\psi}_h] \right\|^2, \\
(3) \quad &\geq \quad -(\lambda^*)^2 \sum_K \alpha_\psi \left\| \nabla^{\mathrm{s}} \boldsymbol{u}_h \right\|_K^2
\end{aligned}
$$

$$+ \sum_K \alpha_\psi \left(\frac{\lambda}{2\lambda_0} \right)^2 \left\| P_\psi^\perp \left[\boldsymbol{a} \cdot \nabla P_\psi [\boldsymbol{E} \cdot \boldsymbol{\psi}_h] - \dot{\boldsymbol{\psi}}_h^{**} \right] \right\|_K^2$$

$$- \sum_K \alpha_\psi \left(\frac{\lambda}{2\lambda_0} \right)^2 4 \left\| \nabla^{\mathrm{s}} \boldsymbol{a} \right\|_{L^\infty(K)}^2 \left\| P_\psi [\boldsymbol{E} \cdot \boldsymbol{\psi}_h] \right\|_K^2 ,$$

from where

$$B_{\mathrm{stab}}(\boldsymbol{U}_h, \boldsymbol{U}_{h1}) \geq \sum_K \left(2\eta_s \lambda^* - \eta_p \lambda^* \varepsilon_0 - (\lambda^*)^2 \alpha_\psi \right) \left\| \nabla^{\mathrm{s}} \boldsymbol{u}_h \right\|_K^2$$

$$+ \sum_K \left[\frac{\eta_p}{\lambda_0^2} \left(1 - \frac{\lambda^*}{\varepsilon_0} - \lambda \left\| \nabla \boldsymbol{a} \right\|_{L^\infty(K)} \right) \right.$$

$$\left. - \alpha_\psi \left(\frac{\lambda}{2\lambda_0} \right)^2 4 \left\| \nabla^{\mathrm{s}} \boldsymbol{a} \right\|_{L^\infty(K)}^2 \right] \left\| P_\psi [\boldsymbol{E} \cdot \boldsymbol{\psi}_h] \right\|_K^2$$

$$+ \sum_K \alpha_u \left\| P_u^\perp \left[\frac{\eta_p}{\lambda_0} \nabla \cdot P_\psi [\boldsymbol{E} \cdot \boldsymbol{\psi}_h] \right] \right\|_K^2 + \sum_K \alpha_u \left\| P_u^\perp [\lambda^* \nabla p_h] \right\|_K^2$$

$$+ \sum_K \alpha_u \left\| P_u^\perp [\lambda^* \rho \boldsymbol{a} \cdot \nabla \boldsymbol{u}_h] \right\|_K^2 + \sum_K \alpha_p \left\| P_p^\perp [\lambda^* \nabla \cdot \boldsymbol{u}_h] \right\|_K^2$$

$$+ \sum_K \alpha_\psi \left(\frac{\lambda}{2\lambda_0} \right)^2 \left\| P_\psi^\perp \left[\frac{\lambda}{2\lambda_0} \left(\boldsymbol{a} \cdot \nabla P_\psi [\boldsymbol{E} \cdot \boldsymbol{\psi}_h] - \dot{\boldsymbol{\psi}}_h^{**} \right) \right] \right\|_K^2 . \tag{6.22}$$

Even if $\alpha_u = \alpha_p = \alpha_\psi = 0$, this estimate yields some stability provided λ is small enough. In fact, this would be the estimate for the Galerkin method, which is the same as for the continuous problem. For the latter it would be possible to obtain pressure stability and stability for the velocity gradient through the use of appropriate inf-sup conditions. In the discrete case, we will not use these, but we will see how the stabilization terms allow us to prove the theorem.

Let us introduce $\boldsymbol{v}_1 \equiv P_{u,0}(\rho \boldsymbol{a} \cdot \nabla \boldsymbol{u}_h + \nabla p_h - \frac{\eta_p}{\lambda_0} \nabla \cdot P_\psi [\boldsymbol{E} \cdot \boldsymbol{\psi}_h])$ and consider $\boldsymbol{V}_{h1} = \alpha_u \lambda^* [\boldsymbol{v}_1, 0, \boldsymbol{0}]$. Taking this test function, using Schwarz's and Young's inequalities and the inverse estimate (6.20) we get

$$B_{\mathrm{stab}}(\boldsymbol{U}_h, \boldsymbol{V}_{h1}) = B_\psi(\boldsymbol{U}_h, \boldsymbol{V}_{h1}) + B^*(\boldsymbol{U}_h, \boldsymbol{V}_{h1})$$

$$= B^*(\boldsymbol{U}_h, \boldsymbol{V}_{h1}) + \sum_K \alpha_u \lambda^* \left\langle \frac{\eta_p}{\lambda_0} P_\psi [\boldsymbol{E} \cdot \boldsymbol{\psi}_h], \nabla^{\mathrm{s}} \boldsymbol{v}_1 \right\rangle_K$$

$$+ \sum_K \alpha_u \lambda^* \left\langle \rho \boldsymbol{a} \cdot \nabla \boldsymbol{u}_h, \boldsymbol{v}_1 \right\rangle_K - \sum_K \alpha_u \lambda^* \left\langle p_h, \nabla \cdot \boldsymbol{v}_1 \right\rangle_K$$

$$- \sum_K \alpha_u \lambda^* \left[\frac{\varepsilon_1}{2} \left\| \boldsymbol{v}_1 \right\|_K^2 + \frac{1}{2\varepsilon_1} (2\eta_s)^2 \frac{c_{\mathrm{inv}}^2}{h^2} \left\| \nabla^{\mathrm{s}} \boldsymbol{u}_h \right\|_K^2 \right].$$

The last term is obtained from the next inequality, by using the Young's inequality and the inverse estimate (6.20):

$$\sum_K \alpha_u \lambda^* 2\eta_s \left(\nabla^{\mathrm{s}} \boldsymbol{u}_h, \nabla^{\mathrm{s}} \boldsymbol{v}_1 \right) \geq - \sum_K \alpha_u \lambda^* \left[\frac{\varepsilon_1}{2} \left\| \boldsymbol{v}_1 \right\|_K^2 + \frac{1}{2\varepsilon_1} (2\eta_s)^2 \frac{c_{\mathrm{inv}}^2}{h^2} \left\| \nabla^{\mathrm{s}} \boldsymbol{u}_h \right\|_K^2 \right]$$

Integrating by parts the second and fourth terms, using the continuity assumed for the interpolation and the advection velocity, we get

$$B_{\mathrm{stab}}(\boldsymbol{U}_h, \boldsymbol{V}_{h1}) \geq B^*(\boldsymbol{U}_h, \boldsymbol{V}_{h1}) + \left(1 - \frac{\varepsilon_1}{2} \right) \sum_K \alpha_u \lambda^* \left\| \boldsymbol{v}_1 \right\|_K^2$$

$$- \frac{1}{2\varepsilon_1} \left(2\eta_s\right)^2 \frac{c_{\mathrm{inv}}^2}{h^2} \sum_K \alpha_u \lambda^* \|\nabla^{\mathrm{s}} \boldsymbol{u}_h\|_K^2. \tag{6.23}$$

Now we need to bound the stabilizing terms:

$$
\begin{aligned}
B^*(\boldsymbol{U}_h, \boldsymbol{V}_{h1}) = {} & \underbrace{\sum_K \alpha_u^2 \lambda^* \left\langle P_u^\perp \left[\rho \boldsymbol{a} \cdot \nabla \boldsymbol{u}_h\right], \rho \boldsymbol{a} \cdot \nabla \boldsymbol{v}_1 \right\rangle}_{(1)} \\
& + \underbrace{\sum_K \alpha_u \alpha_p \lambda^* \left\langle P_p^\perp \left[\nabla \cdot \boldsymbol{u}_h\right], \nabla \cdot \boldsymbol{v}_1 \right\rangle}_{(2)} \\
& + \sum_K \alpha_u \alpha_\psi \lambda^* \left\langle P_\psi^\perp \left[-\nabla^{\mathrm{s}} \boldsymbol{u}_h + \frac{\lambda}{2\lambda_0} \boldsymbol{a} \cdot \nabla P_h \left[\boldsymbol{E} \cdot \boldsymbol{\psi}_h\right]\right], -\nabla^{\mathrm{s}} \boldsymbol{v}_1 \right\rangle \\
& + \underbrace{\sum_K \alpha_u \alpha_\psi \lambda^* \left\langle P_\psi^\perp \left[\frac{\lambda}{2\lambda_0} \left(-P_h \left[\boldsymbol{E} \cdot \boldsymbol{\psi}_h\right] \cdot \nabla \boldsymbol{a} - (\nabla \boldsymbol{a})^t \cdot P_h \left[\boldsymbol{E} \cdot \boldsymbol{\psi}_h\right] + 2\nabla^{\mathrm{s}} \boldsymbol{u}_h\right)\right], -\nabla^{\mathrm{s}} \boldsymbol{v}_1 \right\rangle}_{(3)}
\end{aligned}
$$
$$\tag{6.24}$$

Repeated application of Schwarz's, Young's and the inequality $\|a + b + c\|^2 \leq 4 \|a\|^2 + 4 \|b\|^2 + 2 \|c\|^2$ and the inverse estimate (6.20) allow us to bound the stabilizing terms:

$$
\begin{aligned}
(1) \quad \geq \quad & -\sum_K \alpha_u^2 \lambda^* \|\boldsymbol{a}\|_K \frac{\rho}{h} \left(\frac{1}{2\varepsilon_2} \left\|P_u^\perp \left[\rho \boldsymbol{a} \cdot \nabla \boldsymbol{u}_h\right]\right\|_K^2 + \frac{\varepsilon_2}{2} c_{\mathrm{inv}}^2 \|\boldsymbol{v}_1\|_K^2\right) \\[2mm]
(2) \quad \geq \quad & -\sum_K \alpha_p \lambda^* \left(\frac{1}{2\varepsilon_3} \left\|P_p^\perp \left[\nabla \cdot \boldsymbol{u}_h\right]\right\|_K^2 + \frac{\varepsilon_3}{2} \frac{c_{\mathrm{inv}}^2}{h^2} \alpha_u^2 \|\boldsymbol{v}_1\|_K^2\right) \\[2mm]
(3) \quad \geq \quad & -2\frac{1}{2\varepsilon_4} \lambda^* \sum_K \alpha_\psi \left(\lambda^*\right)^2 \|\nabla^{\mathrm{s}} \boldsymbol{u}_h\|_K^2 \\
& -4\frac{1}{2\varepsilon_4} \lambda^* \sum_K \alpha_\psi \left\|P_\psi^\perp \left[\frac{\lambda}{2\lambda_0} \left(\boldsymbol{a} \cdot \nabla P_h \left[\boldsymbol{E} \cdot \boldsymbol{\psi}_h\right] - \boldsymbol{\psi}_h^{**}\right)\right]\right\|_K^2 \\
& -4\frac{1}{2\varepsilon_4} \lambda^* \sum_K \alpha_\psi \left(\frac{\lambda}{2\lambda_0}\right)^2 4 \|\nabla^{\mathrm{s}} \boldsymbol{a}\|_{L^\infty(K)}^2 \|P_h \left[\boldsymbol{E} \cdot \boldsymbol{\psi}_h\right]\|_K^2 \\
& -\frac{\varepsilon_4}{2} \lambda^* \sum_K \alpha_u^2 \alpha_\psi \frac{c_{\mathrm{inv}}^2}{h^2} \|\boldsymbol{v}_1\|_K^2
\end{aligned}
$$

Finally, the next expression is obtained:

$$
\begin{aligned}
B_{\mathrm{stab}}(\boldsymbol{U}_h, \boldsymbol{V}_{h1}) \geq {} & \lambda^* \sum_K \alpha_u C_u \|\boldsymbol{v}_1\|_K^2 \\
& - \lambda^* \sum_K \alpha_u \left(\frac{1}{\varepsilon_1} 2\eta_s^2 \alpha_u \frac{c_{\mathrm{inv}}^2}{h^2} + \frac{1}{\varepsilon_4} \alpha_\psi \left(\lambda^*\right)^2\right) \|\nabla^{\mathrm{s}} \boldsymbol{u}_h\|_K^2 \\
& - \frac{1}{2\varepsilon_2} \lambda^* \sum_K \alpha_u^2 \|\boldsymbol{a}\|_{L^\infty(K)} \frac{\rho}{h} \left\|P_u^\perp \left[\rho \boldsymbol{a} \cdot \nabla \boldsymbol{u}_h\right]\right\|_K^2 - \frac{1}{2\varepsilon_3} \lambda^* \sum_K \alpha_p \left\|P_p^\perp \left[\nabla \cdot \boldsymbol{u}_h\right]\right\|_K^2 \\
& - 4\frac{1}{2\varepsilon_4} \lambda^* \sum_K \alpha_\psi \left\|P_\psi^\perp \left[\frac{\lambda}{2\lambda_0} \left(\boldsymbol{a} \cdot \nabla P_\psi[\boldsymbol{E} \cdot \boldsymbol{\psi}_h] - \boldsymbol{\psi}_h^{**}\right)\right]\right\|_K^2
\end{aligned}
$$

$$- 4 \frac{1}{2\varepsilon_4} \lambda^* \sum_K \alpha_\psi \left(\frac{\lambda}{2\lambda_0} \right)^2 4 \left\| \nabla^{\mathrm{s}} \boldsymbol{a} \right\|_{L^\infty(K)}^2 \left\| P_\psi [\boldsymbol{E} \cdot \boldsymbol{\psi}_h] \right\|_K^2 , \tag{6.25}$$

where
$$C_u := 1 - \frac{\varepsilon_1}{2} - c_{\mathrm{inv}}^2 \alpha_u \left[\frac{\varepsilon_2}{2} \left\| \boldsymbol{a} \right\|_{L^\infty(K)} \frac{\rho}{h} + \frac{\varepsilon_3}{2} \frac{\alpha_p}{h^2} + \frac{\varepsilon_4}{2} \frac{\alpha_\psi \alpha_u}{h^2} \right] , \tag{6.26}$$
and ε_i, $i = 2, 3, 4$ come again from different instances of the application of Young's inequality.

Let us consider now the test function $\boldsymbol{V}_{h2} = \alpha_p \lambda^* [\boldsymbol{0}, q_2, \boldsymbol{0}]$, with $q_2 \equiv P_p [\nabla \cdot \boldsymbol{u}_h]$.

$$B_{\mathrm{stab}} (\boldsymbol{U}_h, \boldsymbol{V}_{h2}) = \underbrace{\lambda^* \sum_K \alpha_p (\nabla \cdot \boldsymbol{u}_h, q_2)}_{(1)} + \underbrace{\lambda^* \sum_K \alpha_u \alpha_p \left\langle P_u^\perp [\nabla p_h], \nabla q_2 \right\rangle}_{(2)}$$

Using the same tools as above we get

$$(1) = \lambda^* \sum_K \alpha_p \left\| P_p [\nabla \cdot \boldsymbol{u}_h] \right\|_K^2$$

$$(2) \geq -\lambda^* \sum_K \alpha_u \left(\frac{\varepsilon_5}{2} \left\| P_u^\perp [\nabla p_h] \right\|_K^2 + \frac{1}{2\varepsilon_5} \alpha_p^2 \frac{c_{\mathrm{inv}}^2}{h^2} \left\| P_p [\nabla \cdot \boldsymbol{u}_h] \right\|_K^2 \right)$$

Therefore, the final inequality is:

$$B_{\mathrm{stab}} (\boldsymbol{U}_h, \boldsymbol{V}_{h2}) \geq \lambda^* \sum_K \alpha_p C_p \left\| P_p [\nabla \cdot \boldsymbol{u}_h] \right\|_K^2 - \lambda^* \sum_K \alpha_u \frac{\varepsilon_5}{2} \left\| P_u^\perp [\nabla p_h] \right\|_K^2 , \tag{6.27}$$

where
$$C_p := 1 - \frac{1}{2\varepsilon_5} \alpha_p \alpha_u \frac{c_{\mathrm{inv}}^2}{h^2} . \tag{6.28}$$

The next step is to consider the test function $\boldsymbol{V}_{h3} = \alpha_\psi [\boldsymbol{0}, 0, \boldsymbol{\psi}_3]$, with

$$\boldsymbol{\psi}_3 := P_\psi \left(\lambda^* \nabla^{\mathrm{s}} \boldsymbol{u}_h + \frac{\lambda}{2\lambda_0} \left(\boldsymbol{a} \cdot \nabla P_\psi [\boldsymbol{E} \cdot \boldsymbol{\psi}_h] - \dot{\boldsymbol{\psi}}_h^* - \dot{\boldsymbol{\psi}}_h^{**} \right) \right) .$$

The process of bounding $B_{\mathrm{stab}}(\boldsymbol{U}_h, \boldsymbol{V}_{h3})$ is similar to that of bounding $B_{\mathrm{stab}}(\boldsymbol{U}_h, \boldsymbol{V}_{h1})$. Again, one has to apply repeatedly the same inequalities as before. Bounding first the Galerkin terms one gets:

$$\begin{aligned} B_{\mathrm{stab}}(\boldsymbol{U}_h, \boldsymbol{V}_{h3}) &= B(\boldsymbol{U}_h, \boldsymbol{V}_{h3}) + B^*(\boldsymbol{U}_h, \boldsymbol{V}_{h3}) \\ &= B^*(\boldsymbol{U}_h, \boldsymbol{V}_{h3}) + \underbrace{\sum_K \alpha_\psi \frac{1}{2\lambda_0} \left(P_h [\boldsymbol{E} \cdot \boldsymbol{\psi}_h], \boldsymbol{\psi}_3 \right)}_{(1)} \\ &\quad + \underbrace{\sum_K \alpha_\psi \left(\lambda^* \nabla^{\mathrm{s}} \boldsymbol{u}_h + \frac{\lambda}{2\lambda_0} \left(\boldsymbol{a} \cdot \nabla P_h [\boldsymbol{E} \cdot \boldsymbol{\psi}_h] - \dot{\boldsymbol{\psi}}_h^* - \dot{\boldsymbol{\psi}}_h^{**} \right), \boldsymbol{\psi}_3 \right)}_{(2)} \end{aligned}$$

Using the equality $(a + b - c)^2 = a^2 + b^2 + c^2 + 2ab - 2ac - 2bc$ for (2):

$$(1) \geq -\sum_K \alpha_\psi \left[\frac{1}{2\varepsilon_6} \frac{1}{2\lambda_0^2} \left\| P_h [\boldsymbol{E} \cdot \boldsymbol{\psi}_h] \right\|_K^2 + \frac{\varepsilon_6}{2} \left\| \boldsymbol{\psi}_3 \right\|_K^2 \right]$$

$$(2) \geq \sum_K \alpha_\psi \, \|P_\psi \, [\lambda^* \nabla^s \boldsymbol{u}_h]\|_K^2 + \sum_K \alpha_\psi \left\| P_\psi \left[\frac{\lambda}{2\lambda_0} \dot{\boldsymbol{\psi}}_h^* \right] \right\|_K^2$$

$$+ \sum_K \alpha_\psi \left\| P_\psi \left[\frac{\lambda}{2\lambda_0} \left(\boldsymbol{a} \cdot \nabla P_h \, [\boldsymbol{E} \cdot \boldsymbol{\psi}_h] - \dot{\boldsymbol{\psi}}_h^{**} \right) \right] \right\|_K^2$$

$$\underbrace{+ 2 \sum_K \alpha_\psi \left\langle P_\psi \, [\lambda^* \nabla^s \boldsymbol{u}_h] , P_\psi \left[\frac{\lambda}{2\lambda_0} \left(\boldsymbol{a} \cdot \nabla P_h \, [\boldsymbol{E} \cdot \boldsymbol{\psi}_h] - \dot{\boldsymbol{\psi}}_h^{**} \right) \right] \right\rangle_K}_{(a)}$$

$$\underbrace{- 2 \sum_K \alpha_\psi \left\langle P_\psi \, [\lambda^* \nabla^s \boldsymbol{u}_h] , P_\psi \left[\frac{\lambda}{2\lambda_0} \dot{\boldsymbol{\psi}}_h^* \right] \right\rangle_K}_{(b)}$$

$$\underbrace{- 2 \sum_K \alpha_\psi \left\langle P_\psi \left[\frac{\lambda}{2\lambda_0} \left(\boldsymbol{a} \cdot \nabla P_h \, [\boldsymbol{E} \cdot \boldsymbol{\psi}_h] - \dot{\boldsymbol{\psi}}_h^{**} \right) \right] , P_\psi \left[\frac{\lambda}{2\lambda_0} \dot{\boldsymbol{\psi}}_h^* \right] \right\rangle_K}_{(c)}.$$

The terms denoted by (a), (b) and (c) are bounded as follows:

$$(a) \geq -2 \sum_K \alpha_\psi \left[\frac{1}{2\varepsilon_7} \|P_\psi \, [\lambda^* \nabla^s \boldsymbol{u}_h]\|_K^2 + \frac{\varepsilon_7}{2} \left\| P_\psi \left[\frac{\lambda}{2\lambda_0} \left(\boldsymbol{a} \cdot \nabla P_h \, (\boldsymbol{E} \cdot \boldsymbol{\psi}_h) - \dot{\boldsymbol{\psi}}_h^{**} \right) \right] \right\|_K^2 \right]$$

$$(b) \geq -2 \sum_K \alpha_\psi \left[\frac{1}{2\varepsilon_8} \|P_\psi \, [\lambda^* \nabla^s \boldsymbol{u}_h]\|_K^2 + \frac{\varepsilon_8}{2} \left\| P_\psi \left[\frac{\lambda}{2\lambda_0} \dot{\boldsymbol{\psi}}_h^* \right] \right\|_K^2 \right]$$

$$(c) \geq -2 \sum_K \alpha_\psi \left[\frac{1}{2\varepsilon_9} \left\| P_\psi \left[\frac{\lambda}{2\lambda_0} \left(\boldsymbol{a} \cdot \nabla P_h \, (\boldsymbol{E} \cdot \boldsymbol{\psi}_h) - \dot{\boldsymbol{\psi}}_h^{**} \right) \right] \right\|_K^2 + \frac{\varepsilon_9}{2} \left\| P_\psi \left[\frac{\lambda}{2\lambda_0} \dot{\boldsymbol{\psi}}_h^* \right] \right\|_K^2 \right]$$

And finally once the Galerkin terms are bounded gets:

$$B_{\text{stab}}(\boldsymbol{U}_h, \boldsymbol{V}_{h3}) \geq B^*(\boldsymbol{U}_h, \boldsymbol{V}_{h3}) - \frac{1}{2\lambda_0^2} \sum_K \frac{1}{2\varepsilon_6} \|P_\psi [\boldsymbol{E} \cdot \boldsymbol{\psi}_h]\|_K^2$$

$$- \frac{1}{2\lambda_0^2} \sum \frac{\varepsilon_6}{2} \alpha_\psi \|\boldsymbol{\psi}_3\|_K^2 + \sum_K \alpha_\psi \left(1 - \frac{1}{\varepsilon_7} - \frac{1}{\varepsilon_8} \right) \|P_\psi [\lambda^* \nabla^s \boldsymbol{u}_h]\|_K^2$$

$$+ \sum_K \alpha_\psi \left(1 - \varepsilon_8 - \varepsilon_9 \right) \left\| P_\psi \left[\frac{\lambda}{2\lambda_0} \dot{\boldsymbol{\psi}}_h^* \right] \right\|_K^2$$

$$+ \sum_K \alpha_\psi \left(1 - \varepsilon_7 - \frac{1}{\varepsilon_9} \right) \left\| P_\psi \left[\frac{\lambda}{2\lambda_0} \left(\boldsymbol{a} \cdot \nabla P_\psi [\boldsymbol{E} \cdot \boldsymbol{\psi}_h] - \dot{\boldsymbol{\psi}}_h^{**} \right) \right] \right\|_K^2, \qquad (6.29)$$

whereas for the stabilization terms one can get

$$B^*(\boldsymbol{U}_h, \boldsymbol{V}_{h3}) = \underbrace{\sum_K \alpha_u \alpha_\psi \left\langle P_u^\perp \left[\frac{\eta_p}{\lambda_0} \boldsymbol{\nabla} \cdot P_h \, [\boldsymbol{E} \cdot \boldsymbol{\psi}_h] \right] , \nabla \cdot \boldsymbol{\psi}_3 \right\rangle}_{(1)}$$

$$+ \sum_K \alpha_\psi^2 \left\langle P_\psi^\perp \left[\lambda^* \nabla^s \boldsymbol{u}_h + \frac{\lambda}{2\lambda_0} \left(\boldsymbol{a} \cdot \nabla P_h \, [\boldsymbol{E} \cdot \boldsymbol{\psi}_h] - \dot{\boldsymbol{\psi}}_h^{**} - \dot{\boldsymbol{\psi}}_h^* \right) \right] , \right.$$

$$\underbrace{\left. \frac{\lambda}{2\eta_p} \left(\boldsymbol{a} \cdot \nabla \boldsymbol{\psi}_3 + \boldsymbol{\psi}_3 \cdot (\nabla \boldsymbol{a})^T + \nabla \boldsymbol{a} \cdot \boldsymbol{\psi}_3 \right) \right\rangle}_{(2)}$$

Using inequality $-\|a+b+c\| \geq -4\|a\|^2 - 4\|b\|^2 - 2\|c\|^2$ for (2):

$$(1) \quad \geq \quad -\sum_K \alpha_u \left[\frac{1}{2\varepsilon_{10}} \left(\frac{\eta_p}{\lambda_0}\right)^2 \left\| P_u^\perp \left[\nabla \cdot P_h \left[\boldsymbol{E} \cdot \boldsymbol{\psi}_h\right]\right] \right\|^2 + \frac{\varepsilon_{10}}{2} \frac{c_{\text{inv}}^2}{h^2} \alpha_\psi^2 \|\boldsymbol{\psi}_3\|_K^2 \right]$$

$$(2) \quad \geq \quad -2\frac{1}{2\varepsilon_{11}} \sum_K \alpha_\psi \left\| P_\psi^\perp \left(\lambda^* \nabla^s \boldsymbol{u}_h\right) \right\|_K^2$$

$$-4\frac{1}{2\varepsilon_{11}} \sum_K \alpha_\psi \left\| P_\psi^\perp \left[\frac{\lambda}{2\lambda_0} \left(\boldsymbol{a} \cdot \nabla P_h \left[\boldsymbol{E} \cdot \boldsymbol{\psi}_h\right] - \dot{\boldsymbol{\psi}}_h^{**} \right) \right] \right\|_K^2$$

$$-4\frac{1}{2\varepsilon_{11}} \sum_K \alpha_\psi \left\| P_\psi^\perp \left[\frac{\lambda}{2\lambda_0} \dot{\boldsymbol{\psi}}_h^* \right] \right\|_K^2 - \frac{\varepsilon_{11}}{2} \sum_K \alpha_\psi \left[4\alpha_\psi^2 \left(\frac{\lambda}{2\eta_p} \frac{\|\boldsymbol{a}\|_K}{h} \right)^2 \right.$$

$$\left. +4\alpha_\psi^2 \left(\frac{\lambda}{2\eta_p} \|\nabla^s \boldsymbol{a}\|_{L^\infty(K)} \right)^2 + 2\alpha_\psi^2 \left(\frac{\lambda}{2\eta_p} \|\nabla^{\text{as}} \boldsymbol{a}\|_K \right)^2 \right] \|\boldsymbol{\psi}_3\|_K^2 .$$

Therefore the stabilization terms are bounded as:

$$B^*(\boldsymbol{U}_h, \boldsymbol{V}_{h3}) \geq -\sum_K \alpha_u \left(\frac{\eta_p}{\lambda_0}\right)^2 \left[\frac{1}{2\varepsilon_{10}} \left\| P_u^\perp \left[\nabla \cdot P_\psi [\boldsymbol{E} \cdot \boldsymbol{\psi}_h]\right] \right\|_K^2 \right]$$

$$-2\frac{1}{2\varepsilon_{11}} \sum_K \alpha_\psi \left\| P_\psi^\perp [\lambda^* \nabla^s \boldsymbol{u}_h] \right\|_K^2$$

$$-4\frac{1}{2\varepsilon_{11}} \sum_K \alpha_\psi \left\| P_\psi^\perp \left[\frac{\lambda}{2\lambda_0} \left(\boldsymbol{a} \cdot \nabla P_\psi[\boldsymbol{E} \cdot \boldsymbol{\psi}_h] - \dot{\boldsymbol{\psi}}_h^{**} \right) \right] \right\|_K^2$$

$$-4\frac{1}{2\varepsilon_{11}} \sum_K \alpha_\psi \left\| P_\psi^\perp \left[\frac{\lambda}{2\lambda_0} \dot{\boldsymbol{\psi}}_h^* \right] \right\|_K^2$$

$$-\sum_K \alpha_\psi \left[\frac{\varepsilon_{10}}{2} \frac{c_{\text{inv}}^2}{h^2} \alpha_\psi \alpha_u + \frac{\varepsilon_{11}}{2} \left\{ 4\alpha_\psi^2 \left(\frac{\lambda}{2\eta_p} \frac{\|\boldsymbol{a}\|_{L^\infty(K)}}{h} \right)^2 \right.\right.$$

$$\left.\left. +4\alpha_\psi^2 \left(\frac{\lambda}{2\eta_p} \|\nabla^s \boldsymbol{a}\|_{L^\infty(K)} \right)^2 + 2\alpha_\psi^2 \left(\frac{\lambda}{2\eta_p} \|\nabla^{\text{as}} \boldsymbol{a}\|_{L^\infty(K)} \right)^2 \right\} \right] \|\boldsymbol{\psi}_3\|_K^2. \quad (6.30)$$

Let us introduce the constant

$$C_\psi := \frac{1}{2\eta_p} \frac{\varepsilon_6}{2} \alpha_\psi + \frac{\varepsilon_{10}}{2} \frac{c_{\text{inv}}^2}{h^2} \alpha_\psi \alpha_u + \frac{\varepsilon_{11}}{2} \left\{ 4\alpha_\psi^2 \left(\frac{\lambda}{2\eta_p} \frac{\|\boldsymbol{a}\|_{L^\infty(K)}}{h} \right)^2 \right.$$

$$\left. +4\alpha_\psi^2 \left(\frac{\lambda}{2\eta_p} \|\nabla^s \boldsymbol{a}\|_{L^\infty(K)} \right)^2 + 2\alpha_\psi^2 \left(\frac{\lambda}{2\eta_p} \|\nabla^{\text{as}} \boldsymbol{a}\|_{L^\infty(K)} \right)^2 \right\} \quad (6.31)$$

and consider the inequality

$$\|\boldsymbol{\psi}_3\|_K^2 \geq \quad -2\|P_\psi[\lambda^* \nabla^s \boldsymbol{u}_h]\|^2 - 4\left\| P_\psi \left[\frac{\lambda}{2\lambda_0} \left(\boldsymbol{a} \cdot \nabla P_\psi[\boldsymbol{E} \cdot \boldsymbol{\psi}_h] - \dot{\boldsymbol{\psi}}_h^{**} \right) \right] \right\|^2$$

$$-4\left\| P_\psi \left[\frac{\lambda}{2\lambda_0} \dot{\boldsymbol{\psi}}_h^* \right] \right\|^2 .$$

Now using (6.30) in (6.29) we obtain:

$$B_{\text{stab}}(\boldsymbol{U}_h, \boldsymbol{V}_{h3}) \geq -\frac{1}{2\lambda_0} \sum_K \alpha_\psi \frac{1}{2\varepsilon_6} \|P_\psi[\boldsymbol{E} \cdot \boldsymbol{\psi}_h]\|_K^2$$

$$+ \sum_K \alpha_\psi \left(1 - \frac{1}{\varepsilon_7} - \frac{1}{\varepsilon_8} - 2C_\psi \right) \| P_\psi [\lambda^* \nabla^{\mathrm{s}} \boldsymbol{u}_h] \|_K^2$$

$$+ \sum_K \alpha_\psi \left(1 - \varepsilon_8 - \varepsilon_9 - 4C_\psi \right) \left\| P_\psi \left[\frac{\lambda}{2\lambda_0} \dot{\boldsymbol{\psi}}_h^* \right] \right\|_K^2$$

$$+ \sum_K \alpha_\psi \left(1 - \varepsilon_7 - \frac{1}{\varepsilon_9} - 4C_\psi \right) \left\| P_\psi \left[\frac{\lambda}{2\lambda_0} \left(\boldsymbol{a} \cdot \nabla P_\psi [\boldsymbol{E} \cdot \boldsymbol{\psi}_h] - \dot{\boldsymbol{\psi}}_h^{**} \right) \right] \right\|_K^2$$

$$- \frac{1}{2\varepsilon_{10}} \sum_K \alpha_u \left(\frac{\eta_p}{\lambda_0} \right)^2 \left\| P_u^\perp \left[\nabla \cdot P_\psi [\boldsymbol{E} \cdot \boldsymbol{\psi}_h]] \right] \right\|_K^2$$

$$- 2 \frac{1}{2\varepsilon_{11}} \sum_K \alpha_\psi \left\| P_\psi^\perp [\lambda^* \nabla^{\mathrm{s}} \boldsymbol{u}_h] \right\|_K^2$$

$$- 4 \frac{1}{2\varepsilon_{11}} \sum_K \alpha_\psi \left\| P_\psi^\perp \left[\frac{\lambda}{2\lambda_0} \left(\boldsymbol{a} \cdot \nabla P_\psi [\boldsymbol{E} \cdot \boldsymbol{\psi}_h] - \dot{\boldsymbol{\psi}}_h^{**} \right) \right] \right\|_K^2$$

$$- 4 \frac{1}{2\varepsilon_{11}} \left(\frac{\lambda}{2\lambda_0} \right)^2 \sum_K \alpha_\psi 4 \| \nabla^{\mathrm{s}} \boldsymbol{a} \|_{L^\infty(K)}^2 \| P_\psi [\boldsymbol{E} \cdot \boldsymbol{\psi}_h] \|_K^2 . \tag{6.32}$$

It can be checked that the constants ε_i, $i = 1, .., 11$ arising from Young's inequality can be taken such that

$$C_u > 0, \quad C_p > 0, \quad C_\psi > 0,$$

where C_u, C_p and C_ψ are given in (6.26), (6.28) and (6.31), respectively.

Lastly, let us consider $\boldsymbol{V}_h = \boldsymbol{U}_{h1} + \theta_1 \boldsymbol{V}_{h1} + \theta_2 \boldsymbol{V}_{h2} + \theta_3 \boldsymbol{V}_{h3}$. The parameters θ_i can be chosen small enough so as to obtain, from (6.25), (6.27) and (6.32):

$$B_{\mathrm{stab}}(\boldsymbol{U}_h, \boldsymbol{V}_h) \geq 2\eta_s \sum_K C_1 \| \nabla^{\mathrm{s}} \boldsymbol{u}_h \|_K^2 + \frac{\eta_p}{\lambda_0^2} \sum_K C_2 \| P_\psi [\boldsymbol{E} \cdot \boldsymbol{\psi}_h] \|_K^2$$

$$+ \sum_K \alpha_u C_3 \left\| P_{u,0} \left[\rho \boldsymbol{a} \cdot \nabla \boldsymbol{u}_h + \nabla p_h - \frac{\eta_p}{\lambda_0} \nabla \cdot P_\psi [\boldsymbol{E} \cdot \boldsymbol{\psi}_h] \right] \right\|_K^2$$

$$+ \sum_K \alpha_u C_4 \left\| P_u^\perp \left[\frac{\eta_p}{\lambda_0} \nabla \cdot P_\psi [\boldsymbol{E} \cdot \boldsymbol{\psi}_h] \right] \right\|_K^2 + \sum_K \alpha_u C_5 \left\| P_u^\perp [\nabla p_h] \right\|_K^2$$

$$+ \sum_K \alpha_u C_6 \left\| P_u^\perp [\rho \boldsymbol{a} \cdot \nabla \boldsymbol{u}_h] \right\|$$

$$+ \sum_K \alpha_p C_7 \left\| P_p^\perp [\nabla \cdot \boldsymbol{u}_h] \right\|_K^2 + \sum_K \alpha_p C_8 \| P_p [\nabla \cdot \boldsymbol{u}_h] \|^2$$

$$+ \sum_K \alpha_\psi C_9 \left\| P_\psi^\perp \left[\frac{\lambda}{2\lambda_0} \left(\boldsymbol{a} \cdot \nabla P_\psi [\boldsymbol{E} \cdot \boldsymbol{\psi}_h] - \dot{\boldsymbol{\psi}}_h^{**} \right) \right] \right\|_K^2$$

$$+ \sum_K \alpha_\psi C_{10} \left\| P_\psi \left[\frac{\lambda}{2\lambda_0} \left(\boldsymbol{a} \cdot \nabla P_\psi [\boldsymbol{E} \cdot \boldsymbol{\psi}_h] - \dot{\boldsymbol{\psi}}_h^{**} \right) \right] \right\|_K^2$$

$$+ \sum_K \alpha_\psi C_{11} \| P_\psi [\nabla^{\mathrm{s}} \boldsymbol{u}_h] \|_K^2 + \sum_K \alpha_\psi C_{12} \left\| P_\psi \left[\frac{\lambda}{2\lambda_0} \dot{\boldsymbol{\psi}}_h^* \right] \right\|_K^2 , \tag{6.33}$$

with the various constants appearing in this expression given by

$$C_1 = \lambda^* - \frac{\eta_p \varepsilon_0 \lambda^*}{2\eta_s} - \frac{(\lambda^*)^2 \alpha_\psi}{2\eta_s} - \frac{\theta_1 \lambda^* \alpha_u}{2\eta_s} \left(\frac{1}{2\varepsilon_1} (2\eta_s)^2 \alpha_u \frac{c_{\mathrm{inv}}^2}{h^2} + 2 \frac{1}{2\varepsilon_4} (\lambda^*)^2 \alpha_\psi \right)$$

$$- \frac{\theta_3 \alpha_\psi}{2\eta_s} 2 \frac{\eta_p}{\lambda_0} \frac{1}{2\varepsilon_{11}} (\lambda^*)^2 \,,$$

$$C_2 = \left(1 - \frac{\lambda^*}{\varepsilon_0} - \frac{\lambda}{\lambda_0} \|\nabla \boldsymbol{a}\|_{L^\infty(K)} \right) - \frac{\lambda_0^2}{\eta_p} \alpha_\psi \left(\frac{\lambda}{2\lambda_0} \right)^2 4 \|\nabla^{\mathrm{s}} \boldsymbol{a}\|_{L^\infty(K)}^2 \left(1 - \theta_1 4 \frac{1}{2\varepsilon_4} \lambda^* \right)$$

$$- \theta_3 \frac{\lambda_0^2}{\eta_p} \left(\frac{1}{2\lambda_0} \frac{1}{2\varepsilon_6} + 4 \frac{1}{2\varepsilon_{11}} \left(\frac{\lambda}{2\lambda_0} \right)^2 \alpha_\psi 4 \|\nabla^{\mathrm{s}} \boldsymbol{a}\|_{L^\infty(K)}^2 \right) \,,$$

$$C_3 = \lambda^* \theta_1 C_u = \lambda^* \theta_1 \left(1 - \frac{\varepsilon_1}{2} - c_{\mathrm{inv}}^2 \alpha_u \left[\frac{\varepsilon_2}{2} \|\boldsymbol{a}\|_{L^\infty(K)} \frac{\rho}{h} + \frac{\varepsilon_3}{2} \frac{\alpha_p}{h^2} + \frac{\varepsilon_4}{2} \frac{\alpha_\psi}{h^2} \alpha_u \right] \right) \,,$$

$$C_4 = 1 - \theta_3 \frac{1}{2\varepsilon_{10}} \,,$$

$$C_5 = \lambda^* \left(1 - \frac{\varepsilon_5}{2} \theta_2 \right) \,,$$

$$C_6 = (\lambda^*)^2 \left(1 - \lambda^* \theta_1 \frac{1}{2\varepsilon_2} \alpha_u \|\boldsymbol{a}\|_{L^\infty(K)} \frac{\rho}{h} \right) \,,$$

$$C_7 = \lambda^* \left(\lambda^* - \theta_1 \frac{1}{2\varepsilon_3} \right) \,,$$

$$C_8 = \lambda^* \theta_2 C_p = \lambda^* \theta_2 \left(1 - \frac{1}{2\varepsilon_5} \alpha_p \alpha_u \frac{c_{\mathrm{inv}}^2}{h^2} \right) \,,$$

$$C_9 = 1 - 4 \frac{1}{2\varepsilon_4} \lambda^* - \theta_3 4 \frac{1}{2\varepsilon_{11}} \,,$$

$$C_{10} = \theta_3 \left(1 - \varepsilon_7 - \frac{1}{\varepsilon_9} - 4C_\psi \right) \,,$$

$$C_{11} = \theta_3 \left(1 - \frac{1}{\varepsilon_7} - \frac{1}{\varepsilon_8} - 2C_\psi \right) \,,$$

$$C_{12} = \theta_3 \left(1 - \varepsilon_8 - \varepsilon_9 - 4C_\psi \right) \,,$$

all positive for λ small enough and the constants c_i of the stability parameters large enough, and bounded by virtue of Assumption H2. Note that these constants will be larger for smaller values of λ, and the constants C in the inf-sup condition stated by the Theorem will also be larger. There is a tradeoff between the smallness of λ and that of C when the velocity or its gradients are large (or viscosities are small).

Comparing the terms in the right-hand-side of (6.33) and the definition (6.21), it is seen that the former bounds $\left\| P_{u,0} \left[\rho \boldsymbol{a} \cdot \nabla \boldsymbol{u}_h + \nabla p_h - \frac{\eta_p}{\lambda_0} \nabla \cdot P_\psi[\boldsymbol{E} \cdot \boldsymbol{\psi}_h] \right] \right\|$ and $\left\| P_u^\perp \left[\rho \boldsymbol{a} \cdot \nabla \boldsymbol{u}_h + \nabla p_h - \frac{\eta_p}{\lambda_0} \nabla \cdot P_\psi[\boldsymbol{E} \cdot \boldsymbol{\psi}_h] \right] \right\|$. Assumption H2 allows us to guarantee that it also bounds $\left\| \rho \boldsymbol{a} \cdot \nabla \boldsymbol{u}_h + \nabla p_h - \frac{\eta_p}{\lambda_0} \nabla \cdot P_\psi[\boldsymbol{E} \cdot \boldsymbol{\psi}_h] \right\|$. Therefore, for each $\boldsymbol{U}_h$ we have found $\boldsymbol{V}_h$ such that

$$B_{\mathrm{stab}}(\boldsymbol{U}_h, \boldsymbol{V}_h) \geq C \|\boldsymbol{U}_h\|_W^2 \,.$$

In fact, it is seen from (6.33) that we could have included term $\alpha_\psi C_{12} \left\| P_\psi \left[\frac{\lambda}{2\lambda_0} \dot{\boldsymbol{\psi}}_h^* \right] \right\|^2$ in the working norm, which gives control on the FE part of $P_\psi[\boldsymbol{E} \cdot \boldsymbol{\psi}_h] \cdot \nabla^{\mathrm{s}} \boldsymbol{a} + \nabla^{\mathrm{s}} \boldsymbol{a} \cdot P_\psi[\boldsymbol{E} \cdot \boldsymbol{\psi}_h]$. On the other hand, it is easily checked that $\|\boldsymbol{V}_h\|_W \leq C \|\boldsymbol{U}_h\|_W$; we will omit the immediate proof. Using this fact we have shown that for each $\boldsymbol{U}_h \in \boldsymbol{\mathcal{X}}_h$ there exist $\boldsymbol{V}_h \in \boldsymbol{\mathcal{X}}_h$ such that

$$B_{\mathrm{stab}}(\boldsymbol{U}_h, \boldsymbol{V}_h) \geq C \|\boldsymbol{U}_h\|_W \|\boldsymbol{V}_h\|_W \,,$$

from where theorem follows. $\square$

Now, we will define the error function of the method. Let us consider a FE space $\mathcal{W}_h$, made of piecewise continuous polynomial functions of degree k_v. Given a function $v \in H^{k_v+1}(\Omega)$, for $i = 0, 1$ the interpolation errors $\varepsilon_i(v)$ are defined as

$$\inf_{v_h \in \mathcal{W}_h} \sum_K \|v - v_h\|_{H^i(K)} \leq Ch^{k_v''+1-i} \sum_K \|v\|_{H^{k_v''+1}(K)} =: \sum_K \varepsilon_{i,K}(v) =: \varepsilon_i(v),$$

where $k_v'' = \min(k_v, k_v')$. We will denote from this point by $\tilde{v}_h$ the best approximation of v in $\mathcal{W}_h$. Note that $\varepsilon_0(v) = h\varepsilon_1(v)$. In the case of $v = \boldsymbol{\psi}$, it is understood that $\varepsilon_i(\boldsymbol{\psi}) := \inf_{\boldsymbol{\psi}_h \in \boldsymbol{\Upsilon}_h} \sum_K \|\boldsymbol{E} \cdot \boldsymbol{\psi} - \boldsymbol{E} \cdot \boldsymbol{\psi}_h\|_{H^i(K)}$.

The objective of what follows is to show that the error function of the method we propose is:

$$\mathcal{E}(h) := \sqrt{\eta_0}\varepsilon_1(\boldsymbol{u}) + \sqrt{\eta_0} \sum_K \sqrt{\mathrm{Re}_K}\varepsilon_{1,K}(\boldsymbol{u})$$

$$+ \frac{\sqrt{\eta_0}}{\lambda_0}\varepsilon_0(\boldsymbol{\psi}) + \frac{\sqrt{\eta_0}}{\lambda_0} \sum_K \sqrt{\mathrm{We}_K}\varepsilon_{0,K}(\boldsymbol{\psi}) + \frac{1}{\sqrt{\eta_0}}\varepsilon_0(p), \qquad (6.34)$$

where

$$\mathrm{Re}_K := \frac{\rho\|\boldsymbol{a}\|_{L^\infty(K)}h}{\eta_0}, \qquad \mathrm{We}_K := \frac{\lambda\|\boldsymbol{a}\|_{L^\infty(K)}}{h}$$

are the element (or cell) Reynolds and Weissenberg numbers, respectively.

At this point, a very important remark is needed. In [29] it is proved that the FE method proposed for the *standard* formulation of the viscoelastic flow problem is stable and has an error function similar to (6.34) but with *a major difference*: while in the standard case the factor multiplying the term with $\varepsilon_0(\boldsymbol{\sigma})$ is of the order of We_K, now the factor multiplying the second term with $\varepsilon_0(\boldsymbol{\psi})$ is of the order of $\sqrt{\mathrm{We}_K}$ and, moreover, with the factor λ_0^{-1} in front. This is a very important improvement, as the growth of the error with the elasticity of the flow will be significantly reduced in the log-conformation formulation with respect to the standard one. In the linearized problem we consider, the reason for the improvement can be traced back to the last term $2\nabla^s\boldsymbol{u}$ that appears in (2.10). Obviously, the growth of the error with the element Reynolds number is the same.

Lemma 6.2 (Consistency). *Let $\boldsymbol{U} \in \boldsymbol{\mathcal{X}}$ be the solution of the continuous problem and $\boldsymbol{U}_h \in \boldsymbol{\mathcal{X}}_h$ the FE solution. If $\boldsymbol{f} \in \boldsymbol{\mathcal{V}}_h$ and $\boldsymbol{U}$ is regular enough, so that $B_{\mathrm{stab}}(\boldsymbol{U}, \boldsymbol{V}_h)$ is well defined, then*

$$B_{\mathrm{stab}}(\boldsymbol{U} - \boldsymbol{U}_h, \boldsymbol{V}_h) \leq C\mathcal{E}(h)\|\boldsymbol{V}_h\|_W, \qquad (6.35)$$

for all $\boldsymbol{V}_h \in \boldsymbol{\mathcal{X}}_h$, where $\mathcal{E}(h)$ is defined by (6.34).

Proof. Galerkin terms do not contribute to the consistency error. In addition, the contribution of the constitutive and the continuity equations in the stabilization terms are residual based, therefore the consistency is satisfied by construction. Therefore we only have to show as $S_1^\perp$ has consistency error bounded as the Lemma indicates. This is proved from the fact that the orthogonal projection $P^\perp$ onto an appropriate FE space satisfies $\|P^\perp(v)\| \leq C\varepsilon_0(v)$ for any function v. Details are omitted. $\qquad\square$

To show that the interpolation error is also $\mathcal{E}(h)$ we require a technical assumption that states that any element $\boldsymbol{\chi}_h \in \boldsymbol{\Upsilon}_h$, $\boldsymbol{E} \cdot \boldsymbol{\chi}_h$ is close to a finite element function and its derivatives are close to the derivatives of a finite element function. Note that if $\boldsymbol{\chi}_h$ is

a stress, we may scale it by $\frac{\lambda_0}{\eta_p}$ to make it dimensionless. The condition we need may be expressed as follows:

Assumption H3 For all $\boldsymbol{\chi}_h \in \boldsymbol{\Upsilon}_h$ if $\mathcal{M}$ is a bounded linear operator of $\boldsymbol{\chi}_h$ and $\nabla \boldsymbol{\chi}_h$ and there holds

$$\|\mathcal{M}(\boldsymbol{\chi}_h, \nabla \boldsymbol{\chi}_h)\| \leq C \|\mathcal{M}(P_\psi [\boldsymbol{E} \cdot \boldsymbol{\chi}_h], \nabla P_\psi [\boldsymbol{E} \cdot \boldsymbol{\chi}_h])\|$$

Lemma 6.3 (Interpolation error). *Let $\boldsymbol{U} \in \boldsymbol{\mathcal{X}}$ be the solution of the continuous problem, assumed to be regular enough, and $\tilde{\boldsymbol{U}}_h \in \boldsymbol{\mathcal{X}}_h$ its best FE approximation. Then, under assumption H3, the following estimates hold:*

$$B_{\mathrm{stab}}(\boldsymbol{U} - \tilde{\boldsymbol{U}}_h, \boldsymbol{V}_h) \leq C\mathcal{E}(h)\|\boldsymbol{V}_h\|_W, \tag{6.36}$$

$$\|\boldsymbol{U} - \tilde{\boldsymbol{U}}_h\|_W \leq C\mathcal{E}(h). \tag{6.37}$$

Proof. Set $\boldsymbol{e}_u = \boldsymbol{u} - \tilde{\boldsymbol{u}}_h$; $\boldsymbol{e}_p = p - \tilde{p}_h$ and $\boldsymbol{e}_\psi = \boldsymbol{\psi} - \tilde{\boldsymbol{\psi}}_h$. Firstly we will prove inequality (6.37):

$$\left\|\boldsymbol{U} - \tilde{\boldsymbol{U}}_h\right\|_W^2 = 2\eta_s \|\nabla^{\mathrm{s}}\boldsymbol{e}_u\|^2 + \frac{\eta_p}{\lambda_0^2} \|P_\psi[\boldsymbol{E} \cdot \boldsymbol{e}_\psi]\|^2$$

$$+ \underbrace{\sum_K \alpha_u \left\|\rho\boldsymbol{a} \cdot \nabla\boldsymbol{e}_u + \nabla\boldsymbol{e}_p - \frac{\eta_p}{\lambda_0}\nabla \cdot P_\psi[\boldsymbol{E} \cdot \boldsymbol{e}_\psi]\right\|_K^2}_{(1)}$$

$$+ \underbrace{\sum_K \alpha_u \left\|P_u^\perp[\rho\boldsymbol{a} \cdot \nabla\boldsymbol{e}_u]\right\|_K^2}_{(2)} + \underbrace{\sum_K \alpha_u \left\|P_u^\perp[\nabla\boldsymbol{e}_p]\right\|_K^2}_{(3)}$$

$$+ \underbrace{\sum_K \alpha_u \left\|P_u^\perp\left[\frac{\eta_p}{\lambda_0}\nabla \cdot P_\psi[\boldsymbol{E} \cdot \boldsymbol{e}_\psi]\right]\right\|_K^2}_{(4)}$$

$$+ \underbrace{\sum_K \alpha_p \|\nabla \cdot \boldsymbol{e}_u\|_K^2}_{(5)} + \underbrace{\sum_K \alpha_\psi \left\|\frac{\lambda}{2\lambda_0}\left(\boldsymbol{a} \cdot \nabla P_\psi[\boldsymbol{E} \cdot \boldsymbol{e}_\psi] - \dot{\boldsymbol{e}}_\psi^{**}\right)\right\|_K^2}_{(6)},$$

where

$$(1) \leq \sum_K \alpha_u \left(2\|\rho\boldsymbol{a} \cdot \nabla\boldsymbol{e}_u\|_K^2 + 2\|\nabla\boldsymbol{e}_p\|_K^2 + \left\|\frac{\eta_p}{\lambda_0}\nabla \cdot P_\psi[\boldsymbol{E} \cdot \boldsymbol{e}_\psi]\right\|_K^2\right)$$

$$\leq \sum_K \alpha_u \left(2\rho^2 \|\boldsymbol{a}\|_{L^\infty(K)}^2 \varepsilon_1^2(\boldsymbol{u}) + \frac{2}{h^2}\varepsilon_0^2(p) + \frac{1}{h^2}\frac{\eta_p^2}{\lambda_0^2}\varepsilon_0^2(\boldsymbol{\psi})\right),$$

$$(2) \leq \sum_K \alpha_u \rho^2 \|\boldsymbol{a}\|_{L^\infty(K)}^2 \varepsilon_1^2(\boldsymbol{u}),$$

$$(3) \leq \sum_K \alpha_u \frac{1}{h^2}\varepsilon_0^2(p),$$

$$(4) \leq \sum_K \alpha_u \frac{1}{h^2}\frac{\eta_p^2}{\lambda_0^2}\varepsilon_0^2(\boldsymbol{\psi}),$$

$$(5) \leq \sum_K \alpha_p \varepsilon_1^2(\boldsymbol{u}),$$

$$(6) \leq \sum_K \alpha_\psi \left(\left(\frac{\lambda}{2\lambda_0}\right)^2 \|\boldsymbol{a}\|_{L^\infty(K)}^2 \frac{1}{h^2} \varepsilon_0^2(\boldsymbol{\psi}) + \left(\frac{\lambda}{2\lambda_0}\right)^2 2 \|\nabla^{\mathrm{as}} \boldsymbol{a}\|_{L^\infty(K)}^2 \varepsilon_0^2(\boldsymbol{\psi}) \right).$$

Therefore:

$$\left\| \boldsymbol{U} - \tilde{\boldsymbol{U}}_h \right\|_W^2 \leq \sum_K \left(2\eta_s + 3\rho^2 \|\boldsymbol{a}\|_K^2 + \alpha_p \right) \varepsilon_1^2(\boldsymbol{u}) + \sum_K \left(\frac{2}{h^2} + \frac{\alpha_u}{h^2} \right) \varepsilon_0^2(p)$$

$$+ \sum_K \left(\frac{\eta_p}{\lambda_0^2} + \frac{2}{h^2} \frac{\eta_p^2}{\lambda_0^2} \alpha_u + \alpha_\psi \left(\frac{\lambda}{2\lambda_0} \right)^2 \left[\frac{\|\boldsymbol{a}\|_K^2}{h^2} + 2 \|\nabla^{\mathrm{as}} \boldsymbol{a}\|_K^2 \right] \right) \varepsilon_0^2(\boldsymbol{\psi})$$

Now reorganizing the terms and taking into account that $\eta_s = \eta_0 \beta$ and $\eta_p = \eta_0(1 - \beta)$:

$$\left\| \boldsymbol{U} - \tilde{\boldsymbol{U}}_h \right\|_W^2 \leq \eta_0 \sum_K \left(2\beta + \frac{\alpha_p}{\eta_0} \right) \varepsilon_{1,K}^2(\boldsymbol{u}) + \eta_0 \sum_K \rho \frac{\|\boldsymbol{a}\|_K h}{\eta_0} \left(\rho \frac{\|\boldsymbol{a}\|_K}{h} \right) \varepsilon_{1,K}^2(\boldsymbol{u})$$

$$+ \frac{1}{\eta_0} \sum_K \left(\frac{2\eta_0}{h^2} + \frac{\alpha_u \eta_0}{h^2} \right) \varepsilon_{0,K}^2(p)$$

$$+ \frac{\eta_0}{\lambda_0^2} \sum_K (1 - \beta) \left(1 + \frac{2}{h^2} \eta_0 (1 - \beta) \alpha_u + \alpha_\psi \frac{\lambda^2}{4} \frac{1}{\eta_0(1-\beta)} \|\nabla^{\mathrm{as}} \boldsymbol{a}\|_K^2 \right) \varepsilon_{0,K}^2(\boldsymbol{\psi})$$

$$+ \frac{\eta_0}{\lambda_0^2} \sum_K \frac{\lambda \|\boldsymbol{a}\|_K}{h} \left(\frac{\lambda}{4} \frac{1}{\eta_0} \frac{\|\boldsymbol{a}\|_K}{h} \right) \varepsilon_{0,K}^2(\boldsymbol{\psi})$$

$$\leq C \mathcal{E}^2(h)$$

Estimate (6.37) follows form the definitions of the error function and the expression of the stabilization parameters.

Now we will prove (6.36). Taking $\boldsymbol{V}_h = [\boldsymbol{v}_h, q_h, \boldsymbol{\chi}_h]$, we get:

$$B_{\mathrm{stab}} \left(\boldsymbol{U} - \tilde{\boldsymbol{U}}_h, \boldsymbol{V}_h \right) = \frac{\eta_p}{\lambda_0} \left(P_\psi[\boldsymbol{E} \cdot \boldsymbol{e}_\psi], \nabla^{\mathrm{s}} \boldsymbol{v}_h \right) + 2\eta_s \left(\nabla^{\mathrm{s}} \boldsymbol{e}_u, \nabla^{\mathrm{s}} \boldsymbol{v}_h \right)$$

$$+ \langle \rho \boldsymbol{a} \cdot \nabla \boldsymbol{e}_u, \boldsymbol{v}_h \rangle - (\boldsymbol{e}_p, \nabla \cdot \boldsymbol{v}_h)$$

$$+ (\nabla \cdot \boldsymbol{e}_u, q_h) + \frac{1}{2\lambda_0} \left(P_\psi[\boldsymbol{E} \cdot \boldsymbol{e}_\psi], \boldsymbol{\chi}_h \right) - (\nabla^{\mathrm{s}} \boldsymbol{e}_u, \boldsymbol{\chi}_h)$$

$$+ \frac{\lambda}{2\lambda_0} \left(\boldsymbol{a} \cdot \nabla P_\psi[\boldsymbol{E} \cdot \boldsymbol{e}_\psi] + 2\nabla^{\mathrm{s}} \boldsymbol{e}_u, \boldsymbol{\chi}_h \right)$$

$$+ \frac{\lambda}{2\lambda_0} \left(-P_\psi[\boldsymbol{E} \cdot \boldsymbol{e}_\psi] \cdot \nabla \boldsymbol{a} - (\nabla \boldsymbol{a})^T \cdot P_\psi[\boldsymbol{E} \cdot \boldsymbol{e}_\psi], \boldsymbol{\chi}_h \right)$$

$$+ \sum_K \alpha_u \left\langle P_u^\perp \left[-\frac{\eta_p}{\lambda_0} \nabla \cdot P_\psi[\boldsymbol{E} \cdot \boldsymbol{e}_\psi] \right], -\nabla \cdot \boldsymbol{\chi}_h \right\rangle_K$$

$$+ \sum_K \alpha_u \left\langle P_u^\perp [\nabla \boldsymbol{e}_p], \nabla q_h \right\rangle_K$$

$$+ \sum_K \alpha_u \left\langle P_u^\perp [\rho \boldsymbol{a} \cdot \nabla \boldsymbol{e}_u], \rho \boldsymbol{a} \cdot \nabla \boldsymbol{v}_h \right\rangle_K + \sum_K \alpha_p \left\langle P_p^\perp [\nabla \cdot \boldsymbol{e}_u], \nabla \cdot \boldsymbol{v}_h \right\rangle_K$$

$$+ \sum_K \alpha_\psi \left\langle P_\psi^\perp \left[\nabla^{\mathrm{s}} \boldsymbol{e}_u + \frac{\lambda}{2\lambda_0} \left(\boldsymbol{a} \cdot \nabla P_\psi[\boldsymbol{E} \cdot \boldsymbol{e}_\psi] \right) \right. \right.$$

$$\left. \left. - P_\psi[\boldsymbol{E} \cdot \boldsymbol{e}_\psi] \cdot \nabla \boldsymbol{a} - (\nabla \boldsymbol{a})^T \cdot P_\psi[\boldsymbol{E} \cdot \boldsymbol{e}_\psi] \right) \right],$$

$$-\nabla^{\mathrm{s}}\boldsymbol{v}_h + \frac{\lambda}{2\eta_p}\left(\boldsymbol{a}\cdot\nabla\boldsymbol{\chi}_h + \boldsymbol{\chi}_h\cdot(\nabla\boldsymbol{a})^T + \nabla\boldsymbol{a}\cdot\boldsymbol{\chi}_h\right)\Big\rangle_K.$$

Using Schwarz's inequality, integrating by parts the convective term and the continuity equation and using the inverse estimate (6.20) and under the assumption H3:

- $\|\boldsymbol{\chi}_h\| \leq C\,\|P_\psi\,(\boldsymbol{E}\cdot\boldsymbol{\chi}_h)\|$

- $\|\nabla\cdot\boldsymbol{\chi}_h\| \leq C\,\|\nabla\cdot P_\psi\,(\boldsymbol{E}\cdot\boldsymbol{\chi}_h)\|$

- $\left\|\boldsymbol{a}\cdot\nabla\boldsymbol{\chi}_h + \boldsymbol{\chi}_h\cdot(\nabla\boldsymbol{a})^T + \nabla\boldsymbol{a}\cdot\boldsymbol{\chi}_h\right\| \leq$
  $\left\|\left(\boldsymbol{a}\cdot\nabla P_\psi\,[\boldsymbol{E}\cdot\boldsymbol{\chi}_h] + P_\psi\,[\boldsymbol{E}\cdot\boldsymbol{\chi}_h]\cdot(\nabla\boldsymbol{a})^T + \nabla\boldsymbol{a}\cdot P_\psi\,[\boldsymbol{E}\cdot\boldsymbol{\chi}_h]\right)\right\|$

- $\|\rho\boldsymbol{a}\cdot\nabla\boldsymbol{v}_h + \nabla q_h - \nabla\cdot\boldsymbol{\chi}_h\| \leq \|\rho\boldsymbol{a}\cdot\nabla\boldsymbol{v}_h + \nabla q_h - \nabla\cdot P_\psi\,[\boldsymbol{E}\cdot\boldsymbol{\chi}_h]\|$

we get:

$$B_{\mathrm{stab}}(\boldsymbol{U}-\tilde{\boldsymbol{U}}_h,\boldsymbol{V}_h) \leq \frac{\eta_p}{\lambda_0}\varepsilon_0(\boldsymbol{\psi})\,\|\nabla^{\mathrm{s}}\boldsymbol{v}_h\| + 2\eta_s\varepsilon_1(\boldsymbol{u})\,\|\nabla^{\mathrm{s}}\boldsymbol{v}_h\| + \varepsilon_0(p)\,\|\nabla\cdot\boldsymbol{v}_h\|$$

$$+\, h\varepsilon_1(\boldsymbol{u})\,\|\rho\boldsymbol{a}\cdot\nabla\boldsymbol{v}_h + \nabla q_h - \nabla\cdot P_\psi\,[\boldsymbol{E}\cdot\boldsymbol{\chi}_h]\|$$

$$+\left(\frac{1}{2\lambda_0}\varepsilon_0(\boldsymbol{\psi}) + 2\varepsilon_1(\boldsymbol{u})\right)\|P_\psi\,[\boldsymbol{E}\cdot\boldsymbol{\chi}_h]\|$$

$$+\,\frac{\eta_p}{\lambda_0}\varepsilon_0(\boldsymbol{\psi})\left\|\frac{\lambda}{2\eta_p}\left(\boldsymbol{a}\cdot\nabla P_\psi\,[\boldsymbol{E}\cdot\boldsymbol{\chi}_h] + P_\psi\,[\boldsymbol{E}\cdot\boldsymbol{\chi}_h]\cdot(\nabla\boldsymbol{a})^T + \nabla\boldsymbol{a}\cdot P_\psi\,[\boldsymbol{E}\cdot\boldsymbol{\chi}_h]\right)\right\|_K$$

$$+\sum_K \alpha_u\frac{\eta_p}{\lambda_0}\frac{1}{h}\varepsilon_0(\boldsymbol{\psi})\left\|P_u^\perp\,[\nabla\cdot P_\psi\,[\boldsymbol{E}\cdot\boldsymbol{\chi}_h]]\right\|_K + \sum_K \alpha_u\frac{1}{h}\varepsilon_0(p)\left\|P_u^\perp\,[\nabla q_h]\right\|_K$$

$$+\sum_K \alpha_u\rho\,\|\boldsymbol{a}\|_{L^\infty(K)}\varepsilon_1(\boldsymbol{u})\left\|P_u^\perp[\rho\boldsymbol{a}\cdot\nabla\boldsymbol{v}_h]\right\|_K$$

$$+\sum_K \alpha_p\varepsilon_1(\boldsymbol{u})\,\|\nabla\cdot\boldsymbol{v}_h\|_K + \sum_K \alpha_\psi\varepsilon_1(\boldsymbol{u})\,\|\nabla^{\mathrm{s}}\boldsymbol{v}_h\|_K$$

$$+\sum_K \alpha_\psi\varepsilon_1(\boldsymbol{u})\left\|\frac{\lambda}{2\eta_p}\left(\boldsymbol{a}\cdot\nabla P_\psi\,[\boldsymbol{E}\cdot\boldsymbol{\chi}_h] + P_\psi\,[\boldsymbol{E}\cdot\boldsymbol{\chi}_h]\cdot(\nabla\boldsymbol{a})^T + \nabla\boldsymbol{a}\cdot P_\psi\,[\boldsymbol{E}\cdot\boldsymbol{\chi}_h]\right)\right\|_K$$

$$+\sum_K \alpha_\psi\varepsilon_0(\boldsymbol{\psi})\frac{\lambda}{2\lambda_0}\left(\frac{\|\boldsymbol{a}\|_{L^\infty(K)}}{h} + 2\,\|\nabla\boldsymbol{a}\|_{L^\infty(K)}\right)$$

$$\left(\|\nabla^{\mathrm{s}}\boldsymbol{v}_h\|_K + \left\|\frac{\lambda}{2\eta_p}\left(\boldsymbol{a}\cdot\nabla P_\psi\,[\boldsymbol{E}\cdot\boldsymbol{\chi}_h] + P_\psi\,[\boldsymbol{E}\cdot\boldsymbol{\chi}_h]\cdot(\nabla\boldsymbol{a})^T + \nabla\boldsymbol{a}\cdot P_\psi\,[\boldsymbol{E}\cdot\boldsymbol{\chi}_h]\right)\right\|_K\right).$$

Lastly, reorganizing the terms and replacing $\eta_s = \eta_0\beta$: and $\eta_p = \eta_0(1-\beta)$

$$B_{\mathrm{stab}}(\boldsymbol{U}-\tilde{\boldsymbol{U}}_h,\boldsymbol{V}_h)$$

$$\leq \sqrt{\eta_0}\varepsilon_1(\boldsymbol{u})\left(2\beta\sqrt{\eta_0}\,\|\nabla^{\mathrm{s}}\boldsymbol{v}_h\| + \frac{h}{\sqrt{\eta_0}}\,\|\rho\boldsymbol{a}\cdot\nabla\boldsymbol{v}_h + \nabla q_h - \nabla\cdot P_\psi\,[\boldsymbol{E}\cdot\boldsymbol{\chi}_h]\|\right)$$

$$+\sqrt{\eta_0}\varepsilon_1(\boldsymbol{u})\sum_K\left(\frac{\alpha_u}{\sqrt{\eta_0}}\rho\,\|\boldsymbol{a}\|_{L^\infty(K)}\left\|P_u^\perp\,[\rho\boldsymbol{a}\cdot\nabla\boldsymbol{v}_h]\right\|_K\right.$$

$$\left.+\frac{\alpha_p}{\sqrt{\eta_0}}\,\|\nabla\cdot\boldsymbol{v}_h\|_K + \frac{\alpha_\psi}{\sqrt{\eta_0}}\,\|\nabla^{\mathrm{s}}\boldsymbol{v}_h\|_K\right)$$

$$+\sqrt{\eta_0}\varepsilon_1(\boldsymbol{u})\sum_K \frac{\alpha_\psi}{\sqrt{\eta_0}}\left\|\frac{\lambda}{2\eta_0(1-\beta)}\boldsymbol{a}\cdot\nabla P_\psi\,[\boldsymbol{E}\cdot\boldsymbol{\chi}_h]\right.$$

$$+\frac{\lambda}{2\eta_0(1-\beta)}\left(P_\psi\left[\boldsymbol{E}\cdot\boldsymbol{\chi}_h\right]\cdot(\nabla\boldsymbol{a})^T+\nabla\boldsymbol{a}\cdot P_\psi\left[\boldsymbol{E}\cdot\boldsymbol{\chi}_h\right]\right)\Big\|_K$$

$$+\frac{1}{\sqrt{\eta_0}}\varepsilon_0(p)\sqrt{\eta_0}\left(\|\nabla\cdot\boldsymbol{v}_h\|+\sum_K\frac{\alpha_u}{h}\left\|P_u^\perp\left[\nabla q_h\right]\right\|_K\right)$$

$$+\frac{\sqrt{\eta_0}}{\lambda_0}\varepsilon_0(\boldsymbol{\psi})\sqrt{\eta_0}(1-\beta)\left(\|\nabla^s\boldsymbol{v}_h\|+\frac{1}{2\eta_0(1-\beta)}\|P_\psi\left[\boldsymbol{E}\cdot\boldsymbol{\chi}_h\right]\|\right)$$

$$+\frac{\sqrt{\eta_0}}{\lambda_0}\varepsilon_0(\boldsymbol{\psi})\sqrt{\eta_0}(1-\beta)\left\|\frac{\lambda}{\eta_0(1-\beta)}\boldsymbol{a}\cdot\nabla P_\psi\left[\boldsymbol{E}\cdot\boldsymbol{\chi}_h\right]\right.$$

$$\left.+\frac{\lambda}{\eta_0(1-\beta)}\left(P_\psi\left[\boldsymbol{E}\cdot\boldsymbol{\chi}_h\right]\cdot(\nabla\boldsymbol{a})^T+\nabla\boldsymbol{a}\cdot P_\psi\left[\boldsymbol{E}\cdot\boldsymbol{\chi}_h\right]\right)\right\|_K$$

$$+\frac{\sqrt{\eta_0}}{\lambda_0}\varepsilon_0(\boldsymbol{\psi})\sum_K\frac{\alpha_u}{h}\sqrt{\eta_0}(1-\beta)\left\|\nabla\cdot P_\psi\left[\boldsymbol{E}\cdot\boldsymbol{\chi}_h\right]\right\|_K$$

$$+\frac{\sqrt{\eta_0}}{\lambda_0}\varepsilon_0(\boldsymbol{\psi})\sum_K\frac{\alpha_\psi}{\sqrt{\eta_0}}\frac{\lambda}{2}\left(\frac{\|\boldsymbol{a}\|_{L^\infty(K)}}{h}+2\|\nabla\boldsymbol{a}\|_{L^\infty(K)}\right)$$

$$\left(\|\nabla^s\boldsymbol{v}_h\|_K+\left\|\frac{\lambda}{2\eta_0(1-\beta)}\boldsymbol{a}\cdot\nabla P_\psi\left[\boldsymbol{E}\cdot\boldsymbol{\chi}_h\right]\right.\right.$$

$$\left.\left.+\frac{\lambda}{2\eta_0(1-\beta)}\left(P_\psi\left[\boldsymbol{E}\cdot\boldsymbol{\chi}_h\right]\cdot(\nabla\boldsymbol{a})^T+\nabla\boldsymbol{a}\cdot P_\psi\left[\boldsymbol{E}\cdot\boldsymbol{\chi}_h\right]\right)\right\|_K\right)$$

$$\leq C\mathcal{E}(h)\|\boldsymbol{V}_h\|_W.$$

$\square$

Theorem 6.4 (Convergence). *Let $\boldsymbol{U}=[\boldsymbol{u},p,\boldsymbol{\psi}]\in\boldsymbol{\mathcal{X}}$ be the solution of the continuous problem, and suppose that the assumptions of Theorem 1 hold. Then there exist a constant $C>0$ such that*

$$\|\boldsymbol{U}-\boldsymbol{U}_h\|_W\leq C\mathcal{E}(h).$$

Proof. The proof is standard, the only particular point being the weak consistency of the method (see, e.g.,[29]). However, let us include it here. Consider the finite element function $\tilde{\boldsymbol{U}}_h-\boldsymbol{U}_h\in\boldsymbol{\mathcal{X}}_h$, where as Lemma 2, $\tilde{\boldsymbol{U}}_h\in\boldsymbol{\mathcal{X}}_h$ is the best finite element approximation to $\boldsymbol{U}$. Starting from the inf-sup condition, it follows that there exists $\boldsymbol{V}_h\in\boldsymbol{\mathcal{X}}_h$ such that

$$C\left\|\tilde{\boldsymbol{U}}_h-\boldsymbol{U}_h\right\|_W\|\boldsymbol{V}_h\|_W\leq B_{\text{stab}}\left(\tilde{\boldsymbol{U}}_h-\boldsymbol{U}_h,\boldsymbol{V}_h\right)$$

$$=\underbrace{B_{\text{stab}}\left(\tilde{\boldsymbol{U}}_h-\boldsymbol{U},\boldsymbol{V}_h\right)}_{\text{Lemma 6.3 a)}}+\underbrace{B_{\text{stab}}\left(\boldsymbol{U}-\boldsymbol{U}_h,\boldsymbol{V}_h\right)}_{\text{Lemma 6.2}}$$

$$\leq C\mathcal{E}(h)\|\boldsymbol{V}_h\|_W$$

using Lemma 6.2 and Lemma 6.3, in particular inequality (6.36), from where we obtain

$$\left\|\boldsymbol{U}_h-\tilde{\boldsymbol{U}}_h\right\|_W\leq C\mathcal{E}(h).$$

Finally, using the triangle inequality

$$\|\boldsymbol{U}-\boldsymbol{U}_h\|_W\leq\underbrace{\left\|\boldsymbol{U}-\tilde{\boldsymbol{U}}_h\right\|_W}_{\text{Lemma 6.3 b)}}+\left\|\tilde{\boldsymbol{U}}_h-\boldsymbol{U}_h\right\|_W.$$

Theorem follows using Lemma 6.3 inequality (6.37). $\square$

6.5.3   Stability and convergence in natural norms

The next results search prove stability and convergence in a natural norm, in other words, in the norm of the space of the continuous problem, which is not a mesh dependent norm. Since this natural norm does not include any control on the convective terms, stability and convergence in this norm is only meaningful in the case of small cell Reynolds numbers and Weissenberg numbers. In the following, and the contrary to what we have been considering up to his point, generic constants C may depend on these numbers and explode as they increase.

Theorem 6.5 (Stability and convergence in natural norms). *Suppose that the assumptions of Theorem 6.1 hold and the cell Reynolds numbers and cell Weissenberg numbers are small. Then, the solution of the discrete problem $\boldsymbol{U}_h = [\boldsymbol{u}_h, p_h, \boldsymbol{\psi}_h] \in \boldsymbol{\mathcal{X}}_h$ can be bounded as*

$$\sqrt{\eta_0}\, \|\boldsymbol{u}_h\|_{H^1(\Omega)} + \frac{\sqrt{\eta_0}}{\lambda_0}\, \|P_\psi[\boldsymbol{E}\cdot\boldsymbol{\psi}_h]\| + \frac{1}{\sqrt{\eta_0}}\, \|p_h\|$$

$$\leq C\left(\frac{1}{\sqrt{\eta_0}}\, \|\boldsymbol{f}_u\|_{H^{-1}(\Omega)} + \frac{\lambda_0}{\sqrt{\eta_0}}\, \|\boldsymbol{f}_\psi\|\right). \tag{6.38}$$

Moreover, if the solution of the continuous problem $\boldsymbol{U} = [\boldsymbol{u}, p, \boldsymbol{\psi}] \in \boldsymbol{\mathcal{X}}$ is regular enough , the following error estimate holds:

$$\sqrt{\eta_0}\, \|\boldsymbol{u} - \boldsymbol{u}_h\|_{H^1(\Omega)} + \frac{\sqrt{\eta_0}}{\lambda_0}\, \|\boldsymbol{E}\cdot\boldsymbol{\psi} - P_\psi[\boldsymbol{E}\cdot\boldsymbol{\psi}_h]\| + \frac{1}{\sqrt{\eta_0}}\, \|p - p_h\| \leq C\mathcal{E}(h). \tag{6.39}$$

Proof. Firstly we will prove (6.38). We have that

$$B_{\text{stab}}\left(\boldsymbol{U}_h, \boldsymbol{V}_h\right) = \langle \boldsymbol{f}_u, \boldsymbol{v}_h \rangle + \langle \boldsymbol{f}_\psi, \boldsymbol{\chi}_h \rangle$$

$$\leq C\left(\frac{1}{\sqrt{\eta_0}}\, \|\boldsymbol{f}_u\|_{H^{-1}(\Omega)}\, \sqrt{\eta_0}\, \|\boldsymbol{v}_h\|_{H^1(\Omega)} + \sqrt{\eta_0}\, \|\boldsymbol{f}_\psi\|\, \frac{\sqrt{\eta_0}}{\lambda_0}\, \left\| P_\psi\left[\frac{\lambda_0}{\eta_0}\boldsymbol{E}\cdot\boldsymbol{\chi}_h\right]\right\|\right)$$

$$\leq C\left(\frac{1}{\sqrt{\eta_0}}\, \|\boldsymbol{f}_u\|_{H^{-1}(\Omega)} + \sqrt{\eta_0}\, \|\boldsymbol{f}_\psi\|\right) \|\boldsymbol{V}_h\|_W,$$

where $\boldsymbol{V}_h = [\boldsymbol{v}_h, q_h, \boldsymbol{\chi}_h]$ is arbitrary. Therefore, from the inf-sup condition proved in Theorem 6.1 we have

$$C\, \|\boldsymbol{U}_h\|_W\, \|\boldsymbol{V}_h\|_W \leq B_{\text{stab}}\left(\boldsymbol{U}_h, \boldsymbol{V}_h\right) \leq C\left(\frac{1}{\sqrt{\eta_0}}\, \|\boldsymbol{f}_u\|_{H^{-1}(\Omega)} + \sqrt{\eta_0}\, \|\boldsymbol{f}_\psi\|\right) \|\boldsymbol{V}_h\|_W,$$

and this implies that

$$\|\boldsymbol{U}_h\|_W \leq C\left(\frac{1}{\sqrt{\eta_0}}\, \|\boldsymbol{f}_u\|_{H^{-1}(\Omega)} + \sqrt{\eta_0}\, \|\boldsymbol{f}_\psi\|\right).$$

Therefore:

$$\|\boldsymbol{U}_h\|_W^2 = 2\eta_s\, \|\nabla^{\text{s}}\boldsymbol{u}_h\|_K^2 + \frac{\eta_p}{\lambda_0^2}\, \|P_\psi[\boldsymbol{E}\cdot\boldsymbol{\psi}_h]\|_K^2$$

$$+ \sum_K \alpha_u \left\| \rho\boldsymbol{a}\cdot\nabla\boldsymbol{u}_h + \nabla p_h - \frac{\eta_p}{\lambda_0}\nabla\cdot P_\psi[\boldsymbol{E}\cdot\boldsymbol{\psi}_h]\right\|_K^2$$

$$+ \sum_K \alpha_u \left\| P_u^\perp[\rho\boldsymbol{a}\cdot\nabla\boldsymbol{u}_h]\right\|_K^2 + \sum_K \alpha_u \left\| P_u^\perp[\nabla p_h]\right\|_K^2$$

$$+ \sum_K \alpha_u \left\| P_u^\perp \left[\frac{\eta_p}{\lambda_0} \nabla \cdot P_\psi [\boldsymbol{E} \cdot \boldsymbol{\psi}_h] \right] \right\|_K^2$$

$$+ \sum_K \alpha_p \|\nabla \cdot \boldsymbol{u}_h\|_K^2 + \sum_K \alpha_\psi \left\| \frac{\lambda}{2\lambda_0} \left(\boldsymbol{a} \cdot \nabla P_\psi [\boldsymbol{E} \cdot \boldsymbol{\psi}_h] - \dot{\boldsymbol{\psi}}_h^{**} \right) \right\|_K^2$$

$$\leq C \left(\frac{1}{\sqrt{\eta_0}} \|\boldsymbol{f}_u\|_{H^{-1}(\Omega)} + \sqrt{\eta_0} \|\boldsymbol{f}_\psi\| \right)^2 . \tag{6.40}$$

Now, using the inverse inequality, we can write:

$$\sum_K \alpha_u \|\rho \boldsymbol{a} \cdot \nabla \boldsymbol{u}_h + \nabla p_h\|_K^2 \leq \sum_K \alpha_u \left\| \rho \boldsymbol{a} \cdot \nabla \boldsymbol{u}_h + \nabla p_h - \frac{\eta_p}{\lambda_0} \nabla \cdot P_\psi [\boldsymbol{E} \cdot \boldsymbol{\psi}_h] \right\|_K^2$$

$$+ \sum_K \alpha_u \frac{c_{\text{inv}}\eta_0}{\lambda_0} \left(\frac{(1-\beta)}{h} \right)^2 \frac{\eta_0}{\lambda_0} \|P_\psi [\boldsymbol{E} \cdot \boldsymbol{\psi}_h]\|_K^2 .$$

In this expression we only have control on $\rho \boldsymbol{a} \cdot \nabla \boldsymbol{u}_h + \nabla p_h$. There is the possibility of bounding the pressure gradient making use of the control over the viscous term, since

$$\sum_K \alpha_u \|\nabla p_h\|_K^2 \leq \sum_K \alpha_u \|\rho \boldsymbol{a} \cdot \nabla \boldsymbol{u}_h + \nabla p_h\|_K^2 + \sum_K \alpha_u \frac{\eta_0}{h^2} \left(\frac{\rho \|\boldsymbol{a}\|_{L^\infty(K)} h}{\eta_0} \right)^2 \|\nabla \boldsymbol{u}_h\|_K^2 .$$

Note that this expression explodes with the cell Reynolds number Re_K. Then, from inequality (6.40), and using Korn's inequality, the expression of α_u and taking into account that $0 < \beta < 1$, we obtain:

$$\eta_0 \|\boldsymbol{u}_h\|_{H^1(\Omega)}^2 + \frac{\eta_0}{\lambda_0^2} \|P_\psi [\boldsymbol{E} \cdot \boldsymbol{\psi}_h]\|^2 + \frac{h^2}{\eta_0} \sum_K \|\nabla p_h\|_K^2$$

$$\leq C \left(\frac{1}{\sqrt{\eta_0}} \|\boldsymbol{f}_u\|_{H^{-1}(\Omega)} + \sqrt{\eta_0} \|\boldsymbol{f}_\psi\| \right)^2 .$$

For the L^2 stability for the pressure we rely on the inf-sup condition between the velocity and pressure spaces that holds for the continuous problem. See the details in [42].

Now we will prove (6.39). Theorem 6.4 implies that $\|\boldsymbol{U} - \boldsymbol{U}_h\|_W \leq C\mathcal{E}(h)$, and consequently we have that

$$\eta_0 \|\boldsymbol{u} - \boldsymbol{u}_h\|_{H^1(\Omega)}^2 + \frac{\eta_0}{\lambda_0^2} \|\boldsymbol{E} \cdot \boldsymbol{\psi} - P_\psi [\boldsymbol{E} \cdot \boldsymbol{\psi}_h]\|^2$$

$$+ \sum_K \alpha_u \| \rho \boldsymbol{a} \cdot \nabla (\boldsymbol{u} - \boldsymbol{u}_h) + \nabla (p - p_h)$$

$$- \frac{\eta_p}{\lambda_0} \nabla \cdot (\boldsymbol{E} \cdot \boldsymbol{\psi} - P_\psi [\boldsymbol{E} \cdot \boldsymbol{\psi}_h]) \Big\|_K^2$$

$$\leq \mathcal{E}^2(h).$$

Now we will follow the same procedure as the used to prove stability; assuming the cell Reynolds number to be small, we get

$$\sum_K \alpha_u \|\rho \boldsymbol{a} \cdot \nabla (\boldsymbol{u} - \boldsymbol{u}_h) + \nabla (p - p_h)\|_K^2$$

$$\leq \sum_K \alpha_u \|\rho \boldsymbol{a} \cdot \nabla (\boldsymbol{u} - \boldsymbol{u}_h) + \nabla (p - p_h)$$

$$-\frac{\eta_p}{\lambda_0}\nabla\cdot(\boldsymbol{E}\cdot\boldsymbol{\psi}-P_\psi[\boldsymbol{E}\cdot\boldsymbol{\psi}_h])\bigg\|_K^2$$

$$+\sum_K\alpha_u\frac{\eta_0}{\lambda_0^2}\left(\frac{1-\beta}{h}\right)^2\eta_0\varepsilon_{0,K}^2(\boldsymbol{\psi}),$$

and following the same reasoning

$$\sum_K\alpha_u\,\|\nabla\,(p-p_h)\|_K^2$$

$$\leq\sum_K\alpha_u\,\|\rho\boldsymbol{a}\cdot\nabla\,(\boldsymbol{u}-\boldsymbol{u}_h)+\nabla\,(p-p_h)\|_K^2+\sum_K\alpha_u\frac{\eta_0}{h^2}\left(\frac{\rho\,\|\boldsymbol{a}\|_{L^\infty(K)}\,h}{\eta_0}\right)^2\varepsilon_{1,K}^2(\boldsymbol{u}).$$

So, we obtain

$$\eta_0\,\|\boldsymbol{u}-\boldsymbol{u}_h\|_{H^1(\Omega)}^2+\frac{\eta_0}{\lambda_0^2}\,\|\boldsymbol{E}\cdot\boldsymbol{\psi}-P_\psi[\boldsymbol{E}\cdot\boldsymbol{\psi}_h]\|^2$$

$$+\frac{h^2}{\eta_0}\sum_K\|\nabla\,(p-p_h)\|_K^2\leq C\mathcal{E}^2(h).$$

The error estimate to include the L^2 norm of the pressure error can be obtained following the reasoning indicated in [42]. □

Theorem 6.6 (L^2 error estimate for the velocity)**.** *Suppose that the hypothesis of Theorem 6.5 holds and the continuous problem satisfies the elliptic regularity condition*

$$\sqrt{\eta_0}\,\|\boldsymbol{u}\|_{H^2(\Omega)}+\frac{\sqrt{\eta_0}}{\lambda_0}\,\|\boldsymbol{E}\cdot\boldsymbol{\psi}\|_{H^1(\Omega)}+\frac{1}{\sqrt{\eta_0}}\,\|p\|_{H^1(\Omega)}\leq C\frac{1}{\sqrt{\eta_0}}\,\|\boldsymbol{f}_u\|.\qquad(6.41)$$

Then

$$\sqrt{\eta_0}\,\|\boldsymbol{u}-\boldsymbol{u}_h\|\leq Ch\left(\sqrt{\eta_0}\,\|\boldsymbol{u}-\boldsymbol{u}_h\|_{H^1(\Omega)}\right.$$

$$\left.+\frac{\sqrt{\eta_0}}{\lambda_0}\,\|\boldsymbol{E}\cdot\boldsymbol{\psi}-P_\psi[\boldsymbol{E}\cdot\boldsymbol{\psi}_h]\|+\frac{1}{\sqrt{\eta_0}}\,\|p-p_h\|\right)$$

Proof. Let $[\boldsymbol{\omega},\pi,\boldsymbol{S}]\in\boldsymbol{\mathcal{X}}$ be the solution of the following adjoint problem:

$$\nabla\cdot\boldsymbol{S}-2\eta_s\Delta\boldsymbol{\omega}-\rho\boldsymbol{a}\cdot\nabla\boldsymbol{\omega}-\nabla\pi=\frac{\eta_0}{\ell^2}\,(\boldsymbol{u}-\boldsymbol{u}_h)\,,\qquad(6.42)$$

$$-\nabla\cdot\boldsymbol{\omega}=0,\qquad(6.43)$$

$$\frac{1}{2\eta_p}\boldsymbol{S}+\nabla^s\boldsymbol{\omega}-\frac{\lambda}{2\eta_p}\left(\boldsymbol{a}\cdot\nabla\boldsymbol{S}+\boldsymbol{S}\cdot(\nabla\boldsymbol{a})^T+\nabla\boldsymbol{a}\cdot\boldsymbol{S}\right)=\boldsymbol{0},\qquad(6.44)$$

with $\boldsymbol{\omega}=\boldsymbol{0}$ on $\partial\Omega$ and where ℓ is a characteristic length scale of the problem that has only been introduced to keep the dimensionality. Let also $[\tilde{\boldsymbol{\omega}}_h,\tilde{\pi}_h,\tilde{\boldsymbol{S}}_h]$ be the best approximation to $[\boldsymbol{\omega},\pi,\boldsymbol{S}]$ in $\boldsymbol{\mathcal{X}}_h$. Testing (6.42) with $\boldsymbol{u}-\boldsymbol{u}_h$, (6.43) with $p-p_h$ and (6.44) with $\boldsymbol{\psi}-\boldsymbol{\psi}_h$, we can obtain the next expression:

$$\frac{\eta_0}{\ell^2}\,\|\boldsymbol{u}-\boldsymbol{u}_h\|^2=B_\psi\,([\boldsymbol{u}-\boldsymbol{u}_h,p-p_h,\boldsymbol{\psi}-\boldsymbol{\psi}_h],[\boldsymbol{\omega},\pi,\boldsymbol{S}])$$

$$=B_{\text{stab}}\,([\boldsymbol{u}-\boldsymbol{u}_h,p-p_h,\boldsymbol{\psi}-\boldsymbol{\psi}_h],[\boldsymbol{\omega},\pi,\boldsymbol{S}])$$

$$
- \sum_K \alpha_u \left\langle P_u^\perp \left[-\frac{\eta_p}{\lambda_0} \nabla \cdot P_\psi \left[\boldsymbol{E} \cdot \boldsymbol{\psi} - \boldsymbol{E} \cdot \boldsymbol{\psi}_h \right] \right], P_u^\perp [-\nabla \cdot \boldsymbol{S}] \right\rangle_K
$$

$$
- \sum_K \alpha_u \left\langle P_u^\perp \left[\nabla \left(p - p_h \right) \right], P_u^\perp \left[\nabla \pi \right] \right\rangle_K
$$

$$
- \sum_K \left\langle P_u^\perp \left[\rho \boldsymbol{a} \cdot \nabla \left(\boldsymbol{u} - \boldsymbol{u}_h \right) \right], P_u^\perp \left[\rho \boldsymbol{a} \cdot \nabla \boldsymbol{\omega} \right] \right\rangle_K
$$

$$
- \sum_K \alpha_p \left\langle P_p^\perp \left[\nabla \cdot \left(\boldsymbol{u} - \boldsymbol{u}_h \right) \right], P_p^\perp \left[\nabla \cdot \boldsymbol{\omega} \right] \right\rangle_K
$$

$$
- \sum_K \alpha_\psi \left\langle -\nabla^{\mathrm{s}} \left(\boldsymbol{u} - \boldsymbol{u}_h \right) + \frac{\lambda}{2\lambda_0} \left(\boldsymbol{a} \cdot \nabla P_\psi \left[\boldsymbol{E} \cdot \boldsymbol{\psi} - \boldsymbol{E} \cdot \boldsymbol{\psi}_h \right] \right. \right.
$$

$$
- P_\psi \left[\boldsymbol{E} \cdot \boldsymbol{\psi} - \boldsymbol{E} \cdot \boldsymbol{\psi}_h \right] \cdot \nabla \boldsymbol{a}
$$

$$
- \left(\nabla \boldsymbol{a} \right)^T \cdot P_\psi \left[\boldsymbol{E} \cdot \boldsymbol{\psi} - \boldsymbol{E} \cdot \boldsymbol{\psi}_h \right] \right),
$$

$$
\left. -\nabla^{\mathrm{s}} \boldsymbol{\omega} + \frac{\lambda}{2\eta_p} \left(\boldsymbol{a} \cdot \nabla \boldsymbol{S} + \boldsymbol{S} \cdot \left(\nabla \boldsymbol{a} \right)^T + \nabla \boldsymbol{a} \cdot \boldsymbol{S} \right) \right\rangle_K , \tag{6.45}
$$

where we have used the definition of B_{stab} in (6.14). The fifth and sixth terms of (6.45) are zero because of (6.43) and (6.44), respectively. Therefore only four terms need to be bounded. Considering (2.40), these can be written as follows

$$
\frac{\eta_0}{\ell^2} \left\| \boldsymbol{u} - \boldsymbol{u}_h \right\|^2 = B_{\mathrm{stab}} \left([\boldsymbol{u} - \boldsymbol{u}_h, p - p_h, \boldsymbol{\psi} - \boldsymbol{\psi}_h], [\boldsymbol{\omega}, \pi, \boldsymbol{S}] \right)
$$

$$
- \sum_K \alpha_u \left\langle P_u^\perp \left[-\frac{\eta_p}{\lambda_0} \nabla \cdot P_\psi \left[\boldsymbol{E} \cdot \boldsymbol{\psi} - \boldsymbol{E} \cdot \boldsymbol{\psi}_h \right] \right], P_u^\perp [-\nabla \cdot \boldsymbol{S}] \right\rangle_K
$$

$$
- \sum_K \alpha_u \left\langle P_u^\perp \left[\nabla \left(p - p_h \right) \right], P_u^\perp \left[\nabla \pi \right] \right\rangle_K
$$

$$
- \sum_K \left\langle P_u^\perp \left[\rho \boldsymbol{a} \cdot \nabla \left(\boldsymbol{u} - \boldsymbol{u}_h \right) \right], P_u^\perp \left[\rho \boldsymbol{a} \cdot \nabla \boldsymbol{\omega} \right] \right\rangle_K \tag{6.46}
$$

Using the interpolation properties and the shift assumption (6.41) it follows that

$$
\left\| \boldsymbol{\omega} - \tilde{\boldsymbol{\omega}}_h \right\|_{H^1(\Omega)} \leq Ch \left\| \boldsymbol{\omega} \right\|_{H^2(\Omega)} \leq Ch \frac{1}{\ell^2} \left\| \boldsymbol{u} - \boldsymbol{u}_h \right\|,
$$

$$
\left\| \boldsymbol{S} - \tilde{\boldsymbol{S}}_h \right\| \leq Ch \left\| \boldsymbol{S} \right\|_{H^1(\Omega)} \leq Ch \frac{\eta_0}{\ell^2} \left\| \boldsymbol{u} - \boldsymbol{u}_h \right\|,
$$

$$
\left\| \pi - \tilde{\pi}_h \right\| \leq Ch \left\| \pi \right\|_{H^1(\Omega)} \leq Ch \frac{\eta_0}{\ell^2} \left\| \boldsymbol{u} - \boldsymbol{u}_h \right\|.
$$

From these expressions we obtain

$$
B_{\mathrm{stab}} \left([\boldsymbol{u} - \boldsymbol{u}_h, p - p_h, \boldsymbol{\psi} - \boldsymbol{\psi}_h], [\boldsymbol{\omega}, \pi, \boldsymbol{S}] \right)
$$

$$
= B_{\mathrm{stab}} \left([\boldsymbol{u} - \boldsymbol{u}_h, p - p_h, \boldsymbol{\psi} - \boldsymbol{\psi}_h], [\boldsymbol{\omega} - \tilde{\boldsymbol{\omega}}_h, \pi - \tilde{\pi}_h, \boldsymbol{S} - \tilde{\boldsymbol{S}}_h] \right)
$$

$$
\underbrace{- \sum_K \alpha_u \left\langle P_u^\perp \left[-\frac{\eta_p}{\lambda_0} \nabla \cdot P_\psi \left[\boldsymbol{E} \cdot \boldsymbol{\psi} - \boldsymbol{E} \cdot \boldsymbol{\psi}_h \right] \right], P_u^\perp \left[-\nabla \cdot \left(\boldsymbol{S} - \tilde{\boldsymbol{S}}_h \right) \right] \right\rangle_K}_{(2)}
$$

$$
\underbrace{- \sum_K \alpha_u \left\langle P_u^\perp \left[\nabla \left(p - p_h \right) \right], P_u^\perp \left[\nabla \left(\pi - \tilde{\pi}_h \right) \right] \right\rangle_K}_{(3)}
$$

$$-\sum_K \underbrace{\left\langle P_u^\perp \left[\boldsymbol{a} \cdot \nabla \left(\boldsymbol{u} - \boldsymbol{u}_h\right)\right], P_u^\perp \left[\boldsymbol{a} \cdot \nabla \left(\boldsymbol{\omega} - \tilde{\boldsymbol{\omega}}_h\right)\right]\right\rangle_K}_{(4)}. \tag{6.47}$$

Considering these inequalities we can bound terms (2)-(4) easily:

$$(2) \leq \sum_K \alpha_u \frac{\eta_p}{\lambda_0} \frac{1}{h} \left\| P_\psi \left[\boldsymbol{E} \cdot \boldsymbol{\psi} - \boldsymbol{E} \cdot \boldsymbol{\psi}_h\right]\right\|_K \frac{\eta_0}{\ell^2} \left\|\boldsymbol{u} - \boldsymbol{u}_h\right\|_K$$

$$\leq \sum_K \alpha_u \frac{\eta_p}{\lambda_0} \frac{1}{h} \left\|\boldsymbol{E} \cdot \boldsymbol{\psi} - P_\psi[\boldsymbol{E} \cdot \boldsymbol{\psi}_h]\right\|_K \frac{\eta_0}{\ell^2} \left\|\boldsymbol{u} - \boldsymbol{u}_h\right\|_K,$$

$$(3) \leq \sum_K \alpha_u \frac{1}{h} \left\|p - p_h\right\|_K \frac{\eta_0}{\ell^2} \left\|\boldsymbol{u} - \boldsymbol{u}_h\right\|_K,$$

$$(4) \leq \sum_K \alpha_u \left(\rho \left\|\boldsymbol{a}\right\|_{L^\infty(K)}\right)^2 \frac{h}{\ell^2} \left\|\boldsymbol{u} - \boldsymbol{u}_h\right\|_K \left\|\boldsymbol{u} - \boldsymbol{u}_h\right\|_{H^1(\Omega)}.$$

We have to bound the terms of

$$B_{\text{stab}}\left(\left[\boldsymbol{u} - \boldsymbol{u}_h, p - p_h, \boldsymbol{\psi} - \boldsymbol{\psi}_h\right], \left[\boldsymbol{\omega} - \tilde{\boldsymbol{\omega}}_h, \pi - \tilde{\pi}_h, \boldsymbol{S} - \tilde{\boldsymbol{S}}_h\right]\right)$$

for which similar techniques to those used before. Finally we have to combine this bounds in (6.47) and in (6.46) to obtain the next expression:

$$\begin{aligned}
\frac{\eta_0}{l^2} \left\|\boldsymbol{u} - \boldsymbol{u}_h\right\|^2 \leq\ & h \frac{\sqrt{\eta_0}}{\ell^2} \left\|\boldsymbol{u} - \boldsymbol{u}_h\right\| \left(\sqrt{\eta_0} \left\|\boldsymbol{u} - \boldsymbol{u}_h\right\|_{H^1(\Omega)}\right. \\
& + \sum_K \left(\frac{\rho \left\|\boldsymbol{a}\right\|_{L^\infty(K)}}{\eta_0}\right) \sqrt{\eta_0} \left\|\boldsymbol{u} - \boldsymbol{u}_h\right\|_{H^1(K)} \\
& + \frac{\sqrt{\eta_0}}{\lambda_0} \left\|\boldsymbol{E} \cdot \boldsymbol{\psi} - P_\psi[\boldsymbol{E} \cdot \boldsymbol{\psi}_h]\right\|_K \\
& + \frac{\sqrt{\eta_0}}{\lambda_0} \sum_K \left(\frac{\lambda \left\|\boldsymbol{a}\right\|_{L^\infty(K)}}{h}\right) \left\|\boldsymbol{E} \cdot \boldsymbol{\psi} - P_\psi[\boldsymbol{E} \cdot \boldsymbol{\psi}_h]\right\|_K \\
& \left. + \frac{1}{\sqrt{\eta_0}} \left\|p - p_h\right\|_K\right)
\end{aligned}$$

and theorem follows. Note that the bound obtained explodes with the cell Reynolds and the cell Weissenberg numbers. $\square$

6.6 Conclusions

In this chapter we have analyzed the finite element formulation proposed in [120] applied to a linearized form of the logarithmic reformulation of the viscoelastic flow problem. A similar analysis was done in [29] for the standard formulation, and thus the present chapter can be considered a follow-up of the latter. Despite the linearization and the various assumptions that have been needed in our analysis, it serves to draw two main conclusions. The first is that the finite element formulation proposed is effective as stabilization technique, as it allows one to use arbitrary interpolations for all variables in play (we have considered for simplicity the case of continuous interpolations) and yields optimal error estimates, both in the stabilized norm and in the natural norm of the problem, in

the spaces in which the continuous problem is posed. The second conclusion is that the logarithmic reformulation has a significantly better behavior in terms of the Weissenberg number than the standard one, with an error estimate that deteriorates much more slowly when this number increases; this provides some theoretical foundation to justify the use of the logarithmic reformulation to attempt the HWNP, at least using the FE formulation we have introduced.

Chapter 7

Conclusions

In this last chapter the main achievements and conclusions of the work are presented. Moreover, some of the future research lines are enumerated.

7.1 Achievements and concluding remarks

The general aim of this study was the design and implementation of different tools to address the viscoelastic fluid flow problem with a high Weissenberg number, in a stabilized finite element method framework. The main technique implemented, exploited and analyzed in all the chapters, is the called logarithmic conformation reformulation [64]. That formulation is implemented using the in-house finite element code FEMUSS, and stabilized using the Variational Sub-grid Scales method (VMS).

In Chapter 2, the logarithmic formulation is developed for the finite element framework, considering a modification with respect to the original one proposed by Fattal and Kupferman [64], which is non-singular in terms of the relaxation time parameter. Two different stabilized formulations are proposed using that approach: residual-based one and a term-by-term one. Both formulations have optimal convergence order for linear and quadratic elements. The linearization of the problem is particulary detailed in this chapter, emphasizing the treatment of the exponential function. The convergence of the proposed method has a strong dependency on this treatment. Lastly, several numerical results are presented to test the effectiveness of the formulation when elasticity is particularly high and the standard formulation is unable to obtain a converged solution. Therefore, the proposed methods allows to obtain and globally stable solutions, showing accuracy, optimal convergence for smooth solutions, reaching accurate results in comparison with other methods reported in the literature.

The thermal coupling with the viscoelastic fluid flow is investigated in Chapter 3. Also the logarithmic formulation together with the standard one is employed to simulate the cases with high elasticity. The designed algorithm is iterative and non-monolithic, therefore the variables are updated at each iteration. The coupling is established in two directions: viscoelastic parameters are now temperature-dependent, and the energy equation has a term known as *viscous dissipation*. The main effects of that coupling in the viscoelastic fluid flow are studied through two benchmarks, achieving a several conclusions, such as the reduction of stresses when temperature is considered and a higher temperature when the Weissenberg number increases. Also, the flow pattern can be influenced by the parameters that define the problem and for this reason, that influence has been explored varying the Prandtl number and the Brinkman number, apart from the Reynolds and Weissenberg

numbers, as it is proved for the expansion 1:3 benchmark. The conclusion is that the flow is more stable for low Re, high We, low Br and high Pr.

In Chapter 4 the time-dependent sub-grid scales for the viscoelastic fluid-flow problem are developed for both formulations (standard and logarithmic). Again, two different stabilization methods have been designed: one based on the residual of the equations, and the second one based on a split term-by-term stabilization for the momentum equation. The stabilized methods defined allow to solve time-dependent problems in which two different sources of instability can appear simultaneously: the one originated by anisotropic space-time refinement when the time step is small and the well-known stress exponential growth typical of high Weissenberg numbers of viscoelastic problems. The results obtained are particularly remarkable due to the high Weissenberg number reached with the dynamic formulation, which remains stable even if the standard formulation is considered, apart from evident benefits in anisotropic space-time discretizations when the time step is small. Therefore, the combination of dynamic sub-grid scales in the term-by-term stabilization and the logarithmic formulation of the equations is capable of solving problems with higher elasticity than all the other options. Moreover, the numerical analysis in the case of the linearized problem is performed, proving stability for both formulations.

The purely elastic instability is addressed in Chapter 5, where a well documented review is stated. Also, the design of a fractional step scheme for the logarithmic formulation is proposed and validated. The new scheme, in comparison with the monolithic one, allows important savings concerning the computational cost. The fractional step scheme is designed considering a term-by-term stabilization and the time-dependent subgrid scales, allowing the simulation of high Weissenberg problems and anisotropic time-space discretizations. These discretizations are relevant for capturing the purely elastic instability, due to the small time step required in order to capture the physical effect.

In Chapter 6 the finite element formulation proposed in Chapter 2 for the logarithmic formulation is analyzed mathematically, considering the linearized form. Despite the linearization and some hypothesis that have been needed to carry out our analysis, we can arrive to two main conclusions. The first is that the finite element formulation proposed is effective as stabilization technique, as it allows one to use arbitrary interpolations for all variables in play and yields optimal error estimates, both in the stabilized norm and in the natural norm of the problem, in the spaces in which the continuous problem is posed. The second is that the logarithmic reformulation has a significantly better behavior in terms of the Weissenberg number than the standard one, with an error estimate that deteriorates much more slowly when this number increases. Therefore, this provides some theoretical foundation to justify the use of the logarithmic reformulation to attempt the High Weissenberg Number Problem (HWNP).

To sum up, new stabilization techniques have been developed in order to address the well-known High Weissenberg Number Problem, with interesting and robust results.

7.2   Future work

The framework built for the logarithmic formulation along this study is an excellent basis for future developments which involve elastic fluid flows. Apart from the inherent industrial interest, that could be useful to explore deeplier the elastic instabilities.

Fluid-Structure-Interaction with viscoelastic fluid flows
Fluid-structure interaction (FSI) is frequently found in several applications, in particular in biomedical research. For example, the blood flow in arteries and veins, where information

generated by investigation of blood vessel-wall interaction is useful for medical evaluation. In these cases fluids usually have non-Newtonian fluid properties and, in particular, viscoelastic behavior. For such viscoelastic fluid-structure interaction (VFSI) problems the effect of viscoelasticity may play a crucial role when it is comparable to dominant inertial effects and this is the line that could be explored. One of the main difficulties to afford this problem is the stability problem, when elasticity of the fluid is dominant. For example, in [32] the authors investigate this interaction with detail, showing the differences in the FSI if the fluids are viscoelastic instead of purely viscous.

Thermal coupling together with elastic turbulence
One interesting topic is the study of how the heat transfer performance is affected by the elastic turbulence. Heat transfer enhancement is actually a straightforward result from efficient mixing, however, only few works investigated the heat transfer enhancement by elastic turbulence. The evaluations are still confined to the statistical characteristics and they still lack detailed information on how the elastic turbulent flow acts on the heat transfer process. The difficulty to experimentally obtain information such as flow patterns in cross sections or features of stretched polymers and some insights of the heat convection by the disordered fluid motion and the effect of temperature or velocity fields, have seriously limited our understanding. For these reasons, a possible research line is the thermal coupling for elastic turbulence regimes. An interesting benchmark is the one presented in [109], where a three-dimensional curvy channel is simulated for different Weissenberg numbers.

Further Fractional Step Schemes
Fractional schemes for viscoelastic fluid flows can be further investigated. The one studied in Chapter 5 are based on the pressure extrapolation algorithm. There is another family of fractional step schemes that can be designed using the velocity segregation approach. These have a discrete pressure Poisson equation as starting point, and in that case velocities and stresses are extrapolated. That approach permits a second order extrapolation of the velocity and avoids the unstable pressure extrapolations. In the work of Badia and Codina [8] a review of this type of fractional step schemes can be found for Newtonian fluid flows.

Mesh adaptivity
In this dissertation, all the numerical examples are computed using a convenient mesh able to capture suitably the peak of stresses or the large gradients. However for solving problems that exhibit singularities a mesh adaptive refinement method could be employed. In this concern, we found for example the work [166], where an adaptive hp-finite element method is used to solve differential viscoelastic flow problems. In this case, an a posteriori error estimator is employed and the approximation error is reduced to a given level of accuracy with a minimal set of additional degrees of freedom. The derivation of an a posteriori error estimator for the formulation we have proposed would be the first step in this line.

Bibliography

[1] A. Afonso, P. Oliveira, F. Pinho, and M. Alves. Dynamics of high-deborah-number entry flows: a numerical study. *Journal of Fluid Mechanics*, 677:272–304, 2011.

[2] A. Afonso, P. Oliveira, F. T. d. Pinho, and M. Alves. The log-conformation tensor approach in the finite-volume method framework. *Journal of Non-Newtonian Fluid Mechanics*, 157(1-2):55–65, 2009.

[3] A. Afonso, F. Pinho, and M. Alves. The kernel-conformation constitutive laws. *Journal of Non-Newtonian Fluid Mechanics*, 167:30–37, 2012.

[4] M. Alves, F. Pinho, and P. Oliveira. Effect of a high-resolution differencing scheme on finite-volume predictions of viscoelastic flows. *Journal of Non-Newtonian Fluid Mechanics*, 93(2-3):287–314, 2000.

[5] M. Alves, F. Pinho, and P. Oliveira. The flow of viscoelastic fluids past a cylinder: finite-volume high-resolution methods. *Journal of Non-Newtonian Fluid Mechanics*, 97(2-3):207–232, 2001.

[6] P. E. Arratia, G. A. Voth, and J. P. Gollub. Stretching and mixing of non-newtonian fluids in time-periodic flows. *Physics of Fluids*, 17(5):053102, 2005.

[7] H. P. W. Baaijens, G. W. M. Peters, F. P. T. Baaijens, and H. Meijer. Viscoelastic flow past a confined cylinder of a polyisobutylene solution. *Journal of Rheology*, 39(6):1243–1277, 1995.

[8] S. Badia and R. Codina. Algebraic pressure segregation methods for the incompressible navier-stokes equations. *Archives of Computational Methods in Engineering*, 15(3):1–52, 2007.

[9] S. Badia and R. Codina. On a multiscale approach to the transient Stokes problem. *Transient subscales and anisotropic space-time discretization. Preprint*, 2007.

[10] S. Badia, R. Codina, and J. V. Gutiérrez-Santacreu. Long-term stability estimates and existence of a global attractor in a finite element approximation of the Navier–Stokes equations with numerical subgrid scale modeling. *SIAM Journal on Numerical Analysis*, 48(3):1013–1037, 2010.

[11] S. Balay, K. Buschelman, W. D. Gropp, D. Kaushik, M. G. Knepley, L. C. McInnes, B. F. Smith, and H. Zhang. Petsc. *http://www.mcs.anl.gov/petsc*, 2001.

[12] N. Balci, B. Thomases, M. Renardy, and C. R. Doering. Symmetric factorization of the conformation tensor in viscoelastic fluid models. *Journal of Non-Newtonian Fluid Mechanics*, 166(11):546–553, 2011.

[13] J. Baranger and D. Sandri. Finite element approximation of viscoelastic fluid flow: Existence of approximate solutions and error bounds. *Numerische Mathematik*, 63(1):13–27, 1992.

[14] G. Barrenechea, E. Castillo, and R. Codina. Time-dependent semi-discrete analysis of the viscoelastic fluid flow problem using a variational multiscale stabilized formulation. *IMA Journal of Numerical Analysis*, 39:792–819, 2019.

[15] G. R. Barrenechea, E. Castillo, and R. Codina. Time-dependent semidiscrete analysis of the viscoelastic fluid flow problem using a variational multiscale stabilized formulation. *IMA Journal of Numerical Analysis*, 2018.

[16] M. A. Behr, L. Franca, and T. E. Tezduyar. Stabilized finite element methods for the velocity-pressure-stress formulation of incompressible flows. *Computer Methods in Applied Mechanics and Engineering*, 104(1):31–48, 1993.

[17] S. Berti, A. Bistagnino, G. Boffetta, A. Celani, and S. Musacchio. Two-dimensional elastic turbulence. *Physical Review E*, 77(5):055306, 2008.

[18] R. B. Bird, R. C. Armstrong, and O. Hassager. *Dynamics of polymeric liquids. Vol. 1: Fluid mechanics.* 1987.

[19] P. B. Bochev, M. D. Gunzburger, and R. B. Lehoucq. On stabilized finite element methods for the Stokes problem in the small time step limit. *International Journal for Numerical Methods in Fluids*, 53(4):573–597, 2007.

[20] P. B. Bochev, M. D. Gunzburger, and J. N. Shadid. On inf–sup stabilized finite element methods for transient problems. *Computer Methods in Applied Mechanics and Engineering*, 193(15-16):1471–1489, 2004.

[21] G. Boffetta, A. Celani, A. Mazzino, A. Puliafito, and M. Vergassola. The viscoelastic kolmogorov flow: eddy viscosity and linear stability. *Journal of Fluid Mechanics*, 523:161, 2005.

[22] D. V. Boger and K. Walters. *Rheological Phenomena in Focus.* Elsevier, 1993. Amsterdam., 1993.

[23] F. Brezzi and M. Fortin. Mixed and hybrid finite element methods. 1991.

[24] A. Caola, Y. Joo, R. Armstrong, and R. Brown. Highly parallel time integration of viscoelastic flows. *Journal of non-newtonian fluid mechanics*, 100(1-3):191–216, 2001.

[25] E. Castillo and R. Codina. Stabilized stress–velocity–pressure finite element formulations of the Navier–Stokes problem for fluids with non-linear viscosity. *Computer methods in applied mechanics and engineering*, 279:554–578, 2014.

[26] E. Castillo and R. Codina. Variational multi-scale stabilized formulations for the stationary three-field incompressible viscoelastic flow problem. *Computer Methods in Applied Mechanics and Engineering*, 279:579–605, 2014.

[27] E. Castillo and R. Codina. First, second and third order fractional step methods for the three-field viscoelastic flow problem. *Journal of Computational Physics*, 296:113–137, 2015.

[28] E. Castillo and R. Codina. Finite element approximation of the viscoelastic flow problem: A non-residual based stabilized formulation. *Computers & Fluids*, 142:72–78, 2017.

[29] E. Castillo and R. Codina. Numerical analysis of a stabilized finite element approximation for the three-field linearized viscoelastic fluid problem using arbitrary interpolations. *ESAIM: Mathematical Modelling and Numerical Analysis*, 51(4):1407–1427, 2017.

[30] E. Castillo and R. Codina. Dynamic term-by-term stabilized finite element formulation using orthogonal subgrid-scales for the incompressible Navier-Stokes problem. *Computer Methods in Applied Mechanics and Engineering*, 349:701–721, 2019.

[31] E. Castillo, L. Moreno, J. Baiges, and R. Codina. Stabilised variational multi-scale finite element formulations for viscoelastic fluids. *Archives of Computational Methods in Engineering*, 28:1987–2019, 2021.

[32] X. Chen, M. Schäfer, and D. Bothe. Numerical modeling and investigation of viscoelastic fluid–structure interaction applying an implicit partitioned coupling algorithm. *Journal of Fluids and Structures*, 54:390–421, 2015.

[33] C. Chmielewski and K. Jayaraman. The effect of polymer extensibility on crossflow of polymer solutions through cylinder arrays. *Journal of Rheology*, 36(6):1105–1126, 1992.

[34] C. Chmielewski and K. Jayaraman. Elastic instability in crossflow of polymer solutions through periodic arrays of cylinders. *Journal of non-newtonian fluid mechanics*, 48(3):285–301, 1993.

[35] C. Chmielewski, C. A. Petty, and K. Jayaraman. Crossflow of elastic liquids through arrays of cylinders. *Journal of Non-Newtonian Fluid Mechanics*, 35(2-3):309–325, 1990.

[36] A. J. Chorin. A numerical method for solving incompressible viscous flow problems. *Journal of computational physics*, 135(2):118–125, 1997.

[37] P. Christon, P. Gresho, and S. Sutton. Computational predictability of natural convection flow in enclosures. *Computational Fluid and Solid Mechanics*, pages 1465–1468, 2001.

[38] R. Codina. Stabilization of incompressibility and convection through orthogonal sub-scales in finite element methods. *Computer methods in applied mechanics and engineering*, 190(13-14):1579–1599, 2000.

[39] R. Codina. A stabilized finite element method for generalized stationary incompressible flows. *Computer Methods in Applied Mechanics and Engineering*, 190(20-21):2681–2706, 2001.

[40] R. Codina. Stabilized finite element approximation of transient incompressible flows using orthogonal subscales. *Computer Methods in Applied Mechanics and Engineering*, 191(39-40):4295–4321, 2002.

[41] R. Codina. Analysis of a stabilized finite element approximation of the Oseen equations using orthogonal subscales. *Applied Numerical Mathematics*, 58:264 – 283, 2008.

[42] R. Codina. Finite element approximation of the three-field formulation of the stokes problem using arbitrary interpolations. *SIAM Journal on Numerical Analysis*, 47(1):699–718, 2009.

[43] R. Codina and S. Badia. On some pressure segregation methods of fractional-step type for the finite element approximation of incompressible flow problems. *Computer Methods in Applied Mechanics and Engineering*, 195(23-24):2900–2918, 2006.

[44] R. Codina, S. Badia, J. Baiges, and J. Principe. *Variational Multiscale Methods in Computational Fluid Dynamics,* in Encyclopedia of Computational Mechanics (eds E. Stein, R. Borst and T. J. R. Hughes), pages 1–28. John Wiley & Sons Ltd., 2017.

[45] R. Codina and L. Moreno. Analysis of a stabilized finite element approximation for a linearized logarithmic reformulation of the viscoelastic flow problem. *ESAIM. Mathematical Modelling and Numerical Analysis*, 55:279, 2021.

[46] R. Codina, E. Oñate, and M. Cervera. The intrinsic time for the streamline upwind/petrov-galerkin formulation using quadratic elements. *Computer Methods in Applied Mechanics and Engineering*, 94(2):239–262, 1992.

[47] R. Codina, J. Principe, O. Guasch, and S. Badia. Time dependent subscales in the stabilized finite element approximation of incompressible flow problems. *Computer Methods in Applied Mechanics and Engineering*, 196(21-24):2413–2430, 2007.

[48] P. M. Coelho and F. T. Pinho. Fully-developed heat transfer in annuli with viscous dissipation. *International journal of heat and mass transfer*, 49(19-20):3349–3359, 2006.

[49] P. M. Coelho, F. T. Pinho, and P. J. Oliveira. Fully developed forced convection of the Phan-Thien-Tanner fluid in ducts with a constant wall temperature. *International journal of heat and mass transfer*, 45(7):1413–1423, 2002.

[50] O. Colomés, S. Badia, R. Codina, and J. Principe. Assessment of variational multiscale models for the large eddy simulation of turbulent incompressible flows. *Computer Methods in Applied Mechanics and Engineering*, 285:32–63, 2015.

[51] R. Comminal, J. H. Hattel, M. A. Alves, and J. Spangenberg. Vortex behavior of the oldroyd-b fluid in the 4-1 planar contraction simulated with the streamfunction–log-conformation formulation. *Journal of Non-Newtonian Fluid Mechanics*, 237:1–15, 2016.

[52] R. Comminal, J. Spangenberg, and J. H. Hattel. Robust simulations of viscoelastic flows at high weissenberg numbers with the streamfunction/log-conformation formulation. *Journal of Non-Newtonian Fluid Mechanics*, 223:37–61, 2015.

[53] O. M. Coronado, D. Arora, M. Behr, and M. Pasquali. A simple method for simulating general viscoelastic fluid flows with an alternate log-conformation formulation. *Journal of Non-Newtonian Fluid Mechanics*, 147(3):189–199, 2007.

[54] C. L. Cox, H. Lee, and D. C. Szurley. Optimal control of non-isothermal viscous fluid flow. *Mathematical and computer modelling*, 50(7-8):1142–1153, 2009.

[55] M. Crochet and M. Bezy. Numerical solution for the flow of viscoelastic fluids. *Journal of Non-Newtonian fluid mechanics*, 5:201–218, 1979.

[56] H. Damanik, J. Hron, A. Ouazzi, and S. Turek. A monolithic FEM approach for the log-conformation reformulation (LCR) of viscoelastic flow problems. *Journal of Non-Newtonian Fluid Mechanics*, 165(19-20):1105–1113, 2010.

[57] J. Dealy. Weissenberg and deborah numbers-their definition and use. *Rheol. Bull*, 79(2):14–18, 2010.

[58] A. F. Domingues, R. J. Poole, and D. J. Dennis. Inertial instabilities in a microfluidic mixing-separating device. *Physics of Fluids*, 31(7):074101, 2019.

[59] D. Drikakis. Bifurcation phenomena in incompressible sudden expansion flows. *Physics of Fluids*, 9(1):76–87, 1997.

[60] L. Ducloué, L. Casanellas, S. J. Haward, R. J. Poole, M. A. Alves, S. Lerouge, A. Q. Shen, and A. Lindner. Secondary flows of viscoelastic fluids in serpentine microchannels. *Microfluidics and Nanofluidics*, 23(3):33, 2019.

[61] F. Durst, J. C. F. Pereira, and C. Tropea. The plane symmetric sudden-expansion flow at low reynolds numbers. *Journal of Fluid Mechanics*, 248:567–581, 1993.

[62] V. J. Ervin and W. W. Miles. Approximation of time-dependent viscoelastic fluid flow: SUPG approximation. *SIAM Journal on Numerical Analysis*, 41(2):457–486, 2003.

[63] Y. Fan, R. Tanner, and N. Phan-Thien. Galerkin/least-square finite-element methods for steady viscoelastic flows. *Journal of Non-Newtonian Fluid Mechanics*, 84(2-3):233–256, 1999.

[64] R. Fattal and R. Kupferman. Constitutive laws for the matrix-logarithm of the conformation tensor. *Journal of Non-Newtonian Fluid Mechanics*, 123(2-3):281–285, 2004.

[65] R. Fattal and R. Kupferman. Time-dependent simulation of viscoelastic flows at high weissenberg number using the log-conformation representation. *Journal of Non-Newtonian Fluid Mechanics*, 126(1):23–37, 2005.

[66] R. M. Fearn, T. Mullin, and K. A. Cliffe. Nonlinear flow phenomena in a symmetric sudden expansion. *Journal of Fluid Mechanics*, 211:595–608, 1990.

[67] E. Fernández-Cara, F. Guillén, and R. Ortega. Mathematical modeling and analysis of viscoelastic fluids of the Oldroyd kind. 2002.

[68] J. D. Ferry. *Viscoelastic properties of polymers*. John Wiley & Sons, 1980.

[69] M. Fortin and R. Pierre. On the convergence of the mixed method of crochet and marchal for viscoelastic flows. *Computer Methods in Applied Mechanics and Engineering*, 73(3):341–350, 1989.

[70] A. Fouxon and V. Lebedev. Spectra of turbulence in dilute polymer solutions. *Physics of Fluids*, 15(7):2060–2072, 2003.

[71] G. Georgiou, S. Momani, M. J. Crochet, and K. Walters. Newtonian and non-newtonian flow in a channel obstructed by an antisymmetric array of cylinders. *Journal of non-newtonian fluid mechanics*, 40(2):231–260, 1991.

[72] P. Gervasio, F. Saleri, and A. Veneziani. Algebraic fractional-step schemes with spectral methods for the incompressible navier–stokes equations. *Journal of Computational Physics*, 214(1):347–365, 2006.

[73] H. Giesekus. A simple constitutive equation for polymer fluids based on the concept of deformation-dependent tensorial mobility. *Journal of Non-Newtonian Fluid Mechanics*, 11(1-2):69–109, 1982.

[74] R. A. Gingold and J. J. Monaghan. Smoothed particle hydrodynamics: theory and application to non-spherical stars. *Monthly notices of the royal astronomical society*, 181(3):375–389, 1977.

[75] R. Glowinski and O. Pironneau. Finite element methods for navier-stokes equations. *Annual review of fluid mechanics*, 24:167–204, 1992.

[76] M. D. Graham. Drag reduction in turbulent flow of polymer solutions. *Rheology reviews*, 2(2):143–170, 2004.

[77] M. Grilli, A. Vázquez-Quesada, and M. Ellero. Transition to turbulence and mixing in a viscoelastic fluid flowing inside a channel with a periodic array of cylindrical obstacles. *Physical review letters*, 110(17):174501, 2013.

[78] A. Groisman and V. Steinberg. Elastic turbulence in a polymer solution flow. *Nature*, 405(6782):53, 2000.

[79] A. Groisman and V. Steinberg. Efficient mixing at low reynolds numbers using polymer additives. *Nature*, 410(6831):905–908, 2001.

[80] A. Groisman and V. Steinberg. Elastic turbulence in curvilinear flows of polymer solutions. *New Journal of Physics*, 6(1):29, 2004.

[81] J.-L. Guermond, P. Minev, and J. Shen. An overview of projection methods for incompressible flows. *Computer methods in applied mechanics and engineering*, 195(44-47):6011–6045, 2006.

[82] C. Guillopé and J. Saut. Global existence and one-dimensional nonlinear stability of shearing motions of viscoelastic fluids of Oldroyd type. *ESAIM: Mathematical Modelling and Numerical Analysis*, 24(3):369–401, 1990.

[83] A. Gupta and D. Vincenzi. Effect of polymer-stress diffusion in the numerical simulation of elastic turbulence. *Journal of Fluid Mechanics*, 870:405–418, 2019.

[84] F. Habla, A. Woitalka, S. Neuner, and O. Hinrichsen. Development of a methodology for numerical simulation of non-isothermal viscoelastic fluid flows with application to axisymmetric 4: 1 contraction flows. *Chemical engineering journal*, 207:772–784, 2012.

[85] J. Hao and T. Pan. Simulation for high Weissenberg number: viscoelastic flow by a finite element method. *Applied mathematics letters*, 20(9):988–993, 2007.

[86] J. P. Hartnett and M. Kostic. Heat transfer to a viscoelastic fluid in laminar flow through a rectangular channel. *International journal of heat and mass transfer*, 28(6):1147–1155, 1985.

[87] S. Haßler, L. Pauli, and M. Behr. The variational multiscale formulation for the fully-implicit log-morphology equation as a tensor-based blood damage model. *International Journal for Numerical Methods in Biomedical Engineering*, 35:e3262, 2019.

[88] T. Hawa and Z. Rusak. The dynamics of a laminar flow in a symmetric channel with a sudden expansion. *Journal of Fluid Mechanics*, 436:283, 2001.

[89] J. G. Heywood and R. Rannacher. Finite-element approximation of the nonstationary navier–stokes problem. part iv: Error analysis for second-order time discretization. *SIAM Journal on Numerical Analysis*, 27(2):353–384, 1990.

[90] M. Hieber, Y. Naito, and Y. Shibata. Global existence results for Oldroyd-B fluids in exterior domains. *Journal of Differential Equations*, 252(3):2617–2629, 2012.

[91] T. Hughes, G. R. Feijóo, L. Mazzei, and J. Quincy. The variational multiscale method. A paradigm for computational mechanics. *Computer methods in applied mechanics and engineering*, 166(1-2):3–24, 1998.

[92] M. Hulsen, A. Van Heel, and B. Van Den Brule. Simulation of viscoelastic flows using Brownian configuration fields. *Journal of Non-Newtonian Fluid Mechanics*, 70(1-2):79–101, 1997.

[93] M. A. Hulsen, R. Fattal, and R. Kupferman. Flow of viscoelastic fluids past a cylinder at high weissenberg number: stabilized simulations using matrix logarithms. *Journal of Non-Newtonian Fluid Mechanics*, 127(1):27–39, 2005.

[94] A. Jalali, M. A. Hulsen, M. Norouzi, and M. H. Kayhani. Numerical simulation of 3D viscoelastic developing flow and heat transfer in a rectangular duct with a nonlinear constitutive equation. *Korea-Australia Rheology Journal*, 25(2):95–105, 2013.

[95] S. Jin and L. R. Collins. Dynamics of dissolved polymer chains in isotropic turbulence. *New Journal of Physics*, 9(10):360, 2007.

[96] D. M. Jones and K. Walters. The behaviour of polymer solutions in extension-dominated flows, with applications to enhanced oil recovery. *Rheologica Acta*, 28(6):482–498, 1989.

[97] D. D. Joseph. *Fluid dynamics of viscoelastic liquids*, volume 84. Springer Science & Business Media, 2013.

[98] A. Kane, R. Guénette, and A. Fortin. A comparison of four implementations of the log-conformation formulation for viscoelastic fluid flows. *Journal of Non-Newtonian Fluid Mechanics*, 164(1-3):45–50, 2009.

[99] B. Khomami, K. K. Talwar, and H. K. Ganpule. A comparative study of higher- and lower-order finite element techniques for computation of viscoelastic flows. *Journal of Rheology*, 38(2):255–289, 1994.

[100] J. M. Kim, C. Kim, J. H. Kim, C. Chung, K. H. Ahn, and S. J. Lee. High-resolution finite element simulation of 4: 1 planar contraction flow of viscoelastic fluid. *Journal of non-newtonian fluid mechanics*, 129(1):23–37, 2005.

[101] P. Knechtges, M. Behr, and S. Elgeti. Fully-implicit log-conformation formulation of constitutive laws. *Journal of Non-Newtonian Fluid Mechanics*, 214:78–87, 2014.

[102] K. Kunisch and X. Marduel. Optimal control of non-isothermal viscoelastic fluid flow. *Journal of Non-Newtonian Fluid Mechanics*, 88(3):261–301, 2000.

[103] R. Kupferman. A central-difference scheme for a pure stream function formulation of incompressible viscous flow. *SIAM Journal on Scientific Computing*, 23(1):1–18, 2001.

[104] J. Kwack and A. Masud. A three-field formulation for incompressible viscoelastic fluids. *International Journal of Engineering Science*, 48(11):1413–1432, 2010.

[105] J. Kwack, A. Masud, and K. Rajagopal. Stabilized mixed three-field formulation for a generalized incompressible oldroyd-b model. *International Journal for Numerical Methods in Fluids*, 83(9):704–734, 2017.

[106] Y. Kwon. Recent results on the analysis of viscoelastic constitutive equations. *Korea-Australia Rheology Journal*, 14(1):33–45, 2002.

[107] Y. Kwon. Numerical aspects in modeling high deborah number flow and elastic instability. *Journal of Computational Physics*, 265:128–144, 2014.

[108] A. Leonov. Analysis of simple constitutive equations for viscoelastic liquids. *Journal of non-Newtonian fluid mechanics*, 42(3):323–350, 1992.

[109] D.-Y. Li, H. Zhang, J.-P. Cheng, X.-B. Li, F.-C. Li, S. Qian, and S. W. Joo. Numerical simulation of heat transfer enhancement by elastic turbulence in a curvy channel. *Microfluidics and Nanofluidics*, 21(2):25, 2017.

[110] X. Li, X. Han, and X. Wang. Numerical modeling of viscoelastic flows using equal low-order finite elements. *Computer Methods in Applied Mechanics and Engineering*, 199(9-12):570–581, 2010.

[111] A. W. Liu, D. E. Bornside, R. C. Armstrong, and R. A. Brown. Viscoelastic flow of polymer solutions around a periodic, linear array of cylinders: comparisons of predictions for microstructure and flow fields. *Journal of Non-Newtonian Fluid Mechanics*, 77(3):153–190, 1998.

[112] Y. Liu and V. Steinberg. Single polymer dynamics in a random flow. In *Macromolecular Symposia*, volume 337, pages 34–43. Wiley Online Library, 2014.

[113] P. Lomellini. Viscosity-temperature relationships of a polycarbonate melt: Williams-Landel-Ferry versus Arrhenius behaviour. *Die Makromolekulare Chemie*, 193(1):69–79, 1992.

[114] J. López-Herrera, S. Popinet, and A. Castrejón-Pita. An adaptive solver for viscoelastic incompressible two-phase problems applied to the study of the splashing of weakly viscoelastic droplets. *Journal of Non-Newtonian Fluid Mechanics*, 264:144–158, 2019.

[115] M. Lukáčová-Medvidová, B. Mizerová, H.and She, and J. Stebel. Error analysis of finite element and finite volume methods for some viscoelastic fluids. *Journal of Numerical Mathematics*, 24(2):105–123, 2016.

[116] J. Marchal and M. Crochet. A new mixed finite element for calculating viscoelastic flow. *Journal of Non-Newtonian Fluid Mechanics*, 26(1):77–114, 1987.

[117] H. Matallah, P. Townsend, and M. Webster. Recovery and stress-splitting schemes for viscoelastic flows. *Journal of Non-Newtonian Fluid Mechanics*, 75(2-3):139–166, 1998.

[118] S. Mishra and K. Jayaraman. Asymmetric flows in planar symmetric channels with large expansion ratio. *International journal for numerical methods in fluids*, 38(10):945–962, 2002.

[119] L. Moreno, R. Codina, and J. Baiges. Solution of transient viscoelastic flow problems approximated by a term-by-term vms stabilized finite element formulation using time-dependent subgrid-scales. *Computer Methods in Applied Mechanics and Engineering*, 367:113074, 2020.

[120] L. Moreno, R. Codina, J. Baiges, and E. Castillo. Logarithmic conformation reformulation in viscoelastic flow problems approximated by a VMS-type stabilized finite element formulation. *Computer Methods in Applied Mechanics and Engineering*, 354:706–731, 2019.

[121] Y. Mu, G. Zhao, X. Wu, and J. Zhai. Modeling and simulation of three-dimensional planar contraction flow of viscoelastic fluids with PTT, Giesekus and FENE-P constitutive models. *Applied Mathematics and Computation*, 218(17):8429–8443, 2012.

[122] P. Nithiarasu. A fully explicit characteristic based split (cbs) scheme for viscoelastic flow calculations. *International journal for numerical methods in engineering*, 60(5):949–978, 2004.

[123] J. M. Nóbrega, F. T. D. Pinho, P. J. Oliveira, and O. S. Carneiro. Accounting for temperature-dependent properties in viscoelastic duct flows. *International journal of heat and mass transfer*, 47(6-7):1141–1158, 2004.

[124] J. G. Oldroyd. On the formulation of rheological equations of state. *Proceedings of the Royal Society of London. Series A. Mathematical and Physical Sciences*, 200(1063):523–541, 1950.

[125] P. J. Oliveira. Asymmetric flows of viscoelastic fluids in symmetric planar expansion geometries. *Journal of non-newtonian fluid mechanics*, 114(1):33–63, 2003.

[126] F. Olsson and J. Yström. Some properties of the upper convected maxwell model for viscoelastic fluid flow. *Journal of non-newtonian fluid mechanics*, 48(1-2):125–145, 1993.

[127] R. G. Owens, C. Chauvière, and T. N. Philips. A locally-upwinded spectral technique (lust) for viscoelastic flows. *Journal of non-newtonian fluid mechanics*, 108(1-3):49–71, 2002.

[128] R. G. Owens and T. N. Phillips. *Computational rheology*, volume 14. World Scientific, 2002.

[129] P. Pakdel and G. H. McKinley. Elastic instability and curved streamlines. *Physical Review Letters*, 77(12):2459, 1996.

[130] L. Pan, A. Morozov, C. Wagner, and P. Arratia. Nonlinear elastic instability in channel flows at low reynolds numbers. *Physical review letters*, 110(17):174502, 2013.

[131] N. Peres, A. M. Afonso, M. A. Alves, and F. T. Pinho. Heat transfer enhancement in laminar flow of viscoelastic fluids through a rectangular duct. In *Congreso de Métodos Numéricos en Ingeniería*, 2009.

[132] J. B. Perot. An analysis of the fractional step method. *Journal of Computational Physics*, 108(1):51–58, 1993.

[133] G. W. M. Peters and F. P. T. Baaijens. Modelling of non-isothermal viscoelastic flows. *Journal of Non-Newtonian Fluid Mechanics*, 68(2-3):205–224, 1997.

[134] N. Phan-Thien. A nonlinear network viscoelastic model. *Journal of Rheology*, 22(3):259–283, 1978.

[135] N. Phan-Thien and R. I. Tanner. A new constitutive equation derived from network theory. *Journal of Non-Newtonian Fluid Mechanics*, 2(4):353–365, 1977.

[136] T. Phillips and A. Williams. Viscoelastic flow through a planar contraction using a semi-lagrangian finite volume method. *Journal of Non-Newtonian Fluid Mechanics*, 87(2-3):215–246, 1999.

[137] M. Picasso and J. Rappaz. Existence, a priori and a posteriori error estimates for a nonlinear three-field problem arising from Oldroyd-B viscoelastic flows. *ESAIM: Mathematical Modelling and Numerical Analysis*, 35(5):879–897, 2001.

[138] F. Pimenta and M. Alves. Stabilization of an open-source finite-volume solver for viscoelastic fluid flows. *Journal of Non-Newtonian Fluid Mechanics*, 239:85–104, 2017.

[139] F. T. Pinho and P. J. Oliveira. Analysis of forced convection in pipes and channels with the simplified Phan-Thien-Tanner fluid. *International journal of heat and mass transfer*, 43(13):2273–2287, 2000.

[140] E. L. C. V. Plan, A. Gupta, D. Vincenzi, and J. Gibbon. Lyapunov dimension of elastic turbulence. *arXiv preprint arXiv:1701.02366*, 2017.

[141] R. Poole. Three-dimensional viscoelastic instabilities in microchannels. *Journal of Fluid Mechanics*, 870:1–4, 2019.

[142] B. Purnode and M. Crochet. Polymer solution characterization with the fene-p model. *Journal of non-newtonian fluid mechanics*, 77(1-2):1–20, 1998.

[143] T. C. Rebollo. A term by term stabilization algorithm for finite element solution of incompressible flow problems. *Numerische Mathematik*, 79(2):283–319, 1998.

[144] M. Renardy. Mathematical analysis of viscoelastic flows. *Annual review of fluid mechanics*, 21(1):21–34, 1989.

[145] G. N. Rocha, R. J. Poole, and P. J. Oliveira. Bifurcation phenomena in viscoelastic flows through a symmetric 1: 4 expansion. *Journal of non-newtonian fluid mechanics*, 141(1):1–17, 2007.

[146] V. Ruas. Une méthode mixte contrainte-déplacement-pression pour la résolution de problemes de viscoélasticité incompressible en déformations planes. *Comptes rendus de l'Académie des sciences. Série 2, Mécanique, Physique, Chimie, Sciences de l'univers, Sciences de la Terre*, 301(16):1171–1174, 1985.

[147] P. Saramito. A new-scheme algorithm and incompressible fem for viscoelastic fluid flows. *ESAIM: Mathematical Modelling and Numerical Analysis*, 28(1):1–35, 1994.

[148] P. Saramito. On a modified non-singular log-conformation formulation for johnson–segalman viscoelastic fluids. *Journal of Non-Newtonian Fluid Mechanics*, 211:16–30, 2014.

[149] T. Sato and S. M. Richardson. Explicit numerical simulation of time-dependent viscoelastic flow problems by a finite element/finite volume method. *Journal of Non-Newtonian Fluid Mechanics*, 51(3):249–275, 1994.

[150] A. Shahbani-Zahiri, M. M. Shahmardan, H. Hassanzadeh, and M. Norouzi. Effects of fluid inertia and elasticity and expansion angles on recirculation and thermal regions of viscoelastic flow in the symmetric planar gradual expansions. *Journal of the Brazilian Society of Mechanical Sciences and Engineering*, 40(10):480, 2018.

[151] M. A. Sheremet and I. Pop. Natural convection combined with thermal radiation in a square cavity filled with a viscoelastic fluid. *International Journal of Numerical Methods for Heat & Fluid Flow*, 2018.

[152] P. Singh and L. Leal. Finite-element simulation of the start-up problem for a viscoelastic fluid in an eccentric rotating cylinder geometry using a third-order upwind scheme. *Theoretical and Computational Fluid Dynamics*, 5(2):107–137, 1993.

[153] L. Skartsis, B. K., and J. L. K. Polymeric flow through fibrous media. *Journal of Rheology*, 36(4):589–620, 1992.

[154] P. C. Sousa, P. M. Coelho, M. S. N. Oliveira, and M. A. Alves. Effect of the contraction ratio upon viscoelastic fluid flow in three-dimensional square–square contractions. *Chemical Engineering Science*, 66(5):998–1009, 2011.

[155] P. C. Sousa, F. T. Pinho, and M. A. Alves. Purely-elastic flow instabilities and elastic turbulence in microfluidic cross-slot devices. *Soft matter*, 14(8):1344–1354, 2018.

[156] M. M. A. Spanjaards, M. A. Hulsen, and P. D. Anderson. Computational analysis of the extrudate shape of three-dimensional viscoelastic, non-isothermal extrusion flows. *Journal of Non-Newtonian Fluid Mechanics*, 282:104310, 2020.

[157] K. K. Talwar and B. Khomami. Flow of viscoelastic fluids past periodic square arrays of cylinders: inertial and shear thinning viscosity and elasticity effects. *Journal of Non-Newtonian Fluid Mechanics*, 57(2-3):177–202, 1995.

[158] R. Temam. Sur l'approximation de la solution des équations de navier-stokes par la méthode des pas fractionnaires (ii). *Archive for rational mechanics and analysis*, 33(5):377–385, 1969.

[159] B. Traore, C. Castelain, and T. Burghelea. Efficient heat transfer in a regime of elastic turbulence. *Journal of Non-Newtonian Fluid Mechanics*, 223:62–76, 2015.

[160] T. Vaithianathan and L. R. Collins. Numerical approach to simulating turbulent flow of a viscoelastic polymer solution. *Journal of Computational Physics*, 187(1):1–21, 2003.

[161] T. Vaithianathan, A. Robert, J. G. Brasseur, and L. R. Collins. An improved algorithm for simulating three-dimensional, viscoelastic turbulence. *Journal of non-newtonian fluid mechanics*, 140(1-3):3–22, 2006.

[162] R. van Buel, C. Schaaf, and H. Stark. Elastic turbulence in two-dimensional taylor-couette flows. *EPL (Europhysics Letters)*, 124(1):14001, 2018.

[163] A. Vázquez-Quesada and M. Ellero. SPH simulations of a viscoelastic flow around a periodic array of cylinders confined in a channel. *Journal of Non-Newtonian Fluid Mechanics*, 167:1–8, 2012.

[164] S. Vossoughi and F. A. Seyer. Pressure drop for flow of polymer solution in a model porous medium. *Can. J. Chem. Eng.;(Canada)*, 52(5), 1974.

[165] P. Wapperom and M. A. Hulsen. Thermodynamics of viscoelastic fluids: the temperature equation. *Journal of Rheology*, 42(5):999–1019, 1998.

[166] V. Warichet and V. Legat. Adaptive hp-finite element viscoelastic flow calculations. *Computer methods in applied mechanics and engineering*, 136(1-2):93–110, 1996.

[167] C. M. White and M. G. Mungal. Mechanics and prediction of turbulent drag reduction with polymer additives. *Annu. Rev. Fluid Mech.*, 40:235–256, 2008.

[168] M. L. Williams, R. F. Landel, and J. D. Ferry. The temperature dependence of relaxation mechanisms in amorphous polymers and other glass-forming liquids. *Journal of the American Chemical society*, 77(14):3701–3707, 1955.

[169] E. Ziegel. Numerical recipes: The art of scientific computing, 1987.